BIODIESEL AND OXIDES OF NITROGEN: INVESTIGATIONS INTO THEIR RELATIONSHIP

A thesis submitted for the degree of Doctor of Philosophy

By

David Peirce

Department of Mechanical, Aerospace and Civil Engineering

College of Engineering, Design and Physical Sciences

Brunel University

United Kingdom

2016

ABSTRACT

Biodiesel is an alternative fuel that can be produced from a variety of lipid feedstocks. It has a number of perceived advantages over conventional petroleum diesel and as a result world production of biodiesel has increased dramatically since the turn of the century. Amongst its reported disadvantages is a widely observed increase in emissions of oxides of nitrogen, or NO_x. Several explanations have been proposed for this phenomenon; in reality it is likely to be due to a combination of factors.

The interplay of multiple factors affecting NO_x emissions means that the increase in NO_x when fuelling on biodiesel is not consistent or ubiquitous, but is instead dependent upon operating conditions and the specifics of the fuels being compared. The work documented in this thesis explores the nature and causes of the change in NO_x emissions associated with biodiesel. The intention was that, by adjusting operating conditions, and using a wide range of fuels, doped with additives to achieve an even broader range of combustion characteristics, the impact of important variables would be made clearer, making it possible to reduce the problem to its lowest common denominators.

In early experiments it was found that NO_x emissions from biodiesel tended to be lower than those of petrodiesel under conditions where combustion was relatively highly premixed, but higher under more conventional diesel conditions where diffusion combustion constituted a larger proportion of heat release. The main experimental set revealed a definite increase in NO_x emissions when fuelling on biodiesel, for a fixed start of combustion and equivalent degree of premixing. The addition of an oxygenate to petrodiesel elicited comparable NO_x emissions to biodiesel, as a function of fuel-bound oxygen content; the data implies that the like-for-like biodiesel NO_x increase may be a direct result of fuel-bound oxygen. However, the like-for-like biodiesel NO_x increase varies dependent upon operating conditions. In part, this may be related to higher apparent heat release rate (AHRR) through the diffusion burn phase when fuelling on biodiesel. This may result from the extended biodiesel injection duration. Across operating conditions, the extent to which smoke emissions when fuelling on petrodiesel exceeded those when fuelling on biodiesel was generally correlated with the magnitude of the biodiesel NO_x increase; where the difference in smoke emissions was small, the biodiesel NO_x increase was small, and where the difference in smoke emissions was more substantial, so was the difference in NO_x emissions. This suggests a possible connection to changes in mixture stoichiometry.

When differentiating between fuels, increased cetane number reduces NO_x, and increased oxygen content increases NO_x. Biodiesel does not necessarily have higher NO_x emissions than petrodiesel: the biodiesel NO_x increase exists where the difference in cetane number is insufficient to counteract the effects of fuel-bound oxygen content.

ACKNOWLEDGEMENTS

I would like to begin by thanking Dr. Lionel Ganippa, Dr. David Hatherill and Finning for providing me with this opportunity; I hope that I have rewarded their faith by producing something worthwhile. As my supervisor, Lionel has been a constant support and I have learnt a very great deal from him over the past few years. I could not have hoped for a better person to guide me through this process. I have had similar good fortune with my sponsors, and the generosity and enthusiasm of David and Finning have been the motive forces that allowed this research to happen.

A considerable debt is owed to all of the Brunel technical staff who have – in one way or another – made this work possible: to Kenneth Anstiss most of all, as well as to Andrew Selway, Clive Barrett, Costas Xanthos, Peter Wilson, Benjamin McCalla, Christopher Allan, the gentlemen in Civil Engineering who have leant me various bits and pieces, to Leslie Botwright and Minal Shah in stores, and to Lee Charge.

I am grateful to my many colleagues and friends around the engineering department. In the engines lab, to Nehemiah Alozie and Dr. Fanos Christodoulou in particular, and also to the others who have helped me: Dr. Gholamreza Abbaszadeh Mosaiiebi, Dr. Stephen Hemmings, Dr. Pin Lu, Dr. Yan Zhang and Mohammed Abahussain. I spent more of my time at Brunel working with Nehemiah than with anyone else, and the exceptional grace with which he bore my more hurried and abrasive days stands as a solid affirmation of his fine Christian character. Outside the engines lab, I am thankful to Dr. Martin Lawrence for his indispensable expertise during the short but enjoyable time we spent working together on flames. I am grateful to Dr. Radu Beleca for allowing me to work together with him on his very interesting work, for assisting me with less interesting aspects of my own, and for offering up his considerable and multi-faceted wisdom, although I never had very much to offer him in return.

Beyond the department, I would like to thank Dr. Ian Garrard, Dr. Svetalana Ignatova and Prof. Tony Anson for helping to facilitate the gas chromatography that I performed, Dr. Garrard especially, who gave up his time to assist me with my work. I am also grateful

to Dr. Manickam Jayamurthy for allowing Marcos Pereira and I to work in his laboratory.

Beyond the UK, I would like to thank those who I met at the Indian Institute of Science, Prof. Ravikrishna for inviting Nehemiah and I to visit his laboratory, and to Prasad, Saurabh and Kajal, Krishna and Madan for making our time there so pleasant. I'm also grateful to Dr. Hayder Dhahad of the University of Technology, Baghdad, for his help and company during his visit to the UK.

As the number of hours I spent in the laboratory grew, I also came to realise how much I owed to those students that came before me, the products of whose labour I made use of every time I entered the lab, and entirely took for granted. Without their efforts, my work could not have run as smoothly as it did. That is not to say that it always ran smoothly, however: it did not. I am grateful to the engine in TB012c for its endurance, and for giving me many lessons in patience, humility and fastidiousness.

Finally, I would like to thank my parents and grandparents, without whom I would not be here, as well as Oanh and Emily, who have made my work far more difficult, but my life far, far happier.

CONTENTS

LIST OF FIGURES

LIST OF TABLES

NOMENCLATURE

1-MN	1-Methylnaphthalene
2-EHN	2-Ethylhexyl nitrate
a	Crank radius
AFT	Adiabatic flame temperature
AFR	Air:fuel ratio
AHRR	Apparent heat release rate
ANR	Analyser rack
ATDC	After top dead centre
B	Cylinder bore
BDC	Bottom dead centre
BDE	Bond dissociation energy
BHA	Butylated hydroxyanisole
BHT	Butylated hydroxytoluene
BMEP	Brake mean effective pressure
BSFC	Brake specific fuel consumption
BTDC	Before top dead centre
BXX	Biodiesel blend containing XX% biodiesel (e.g. B20)
c	Speed of sound
C_n	Carbon number, where n is the number of carbon atoms in the molecule (e.g. C_{12})
C_p	Constant pressure specific heat
CA	Crank angle degrees
CAXX	Crank angle at which XX% of total apparent heat release is reached (e.g. CA10)
CAPF	Centre for Advanced Powertrain and Fuels Research
CBP	Consolidated bioprocessing
CFPP	Cold filter-plugging point
CLA	Chemiluminescence analyser
CME	Coconut methyl esters
CN	Cetane number
CO	Carbon monoxide
CO_2	Carbon dioxide
COHb	Carboxyhemoglobin
CSFT	Cold soak filtration test
CX:Y	Lipid number, where X is number of carbon atoms in the fatty acid, and Y is the number of double bonds (e.g. C18:1)
d_o	Nozzle hole diameter
D_p	Particle diameter
DG	Diglyceride
DGDE	Diethylene glycol diethyl ether
DN	Double bond number
DPPD	*N-N'*-diphenyl-*p*-phenylenediamine
E_v	Bulk modulus
EB	Electron beam

ECA	Emission Control Area
EGR	Exhaust gas recirculation
EOC	End of combustion
EOPMB	End of premixed burn
ETC	Experimental Techniques Centre
FAEE	Fatty acid ethyl esters
FAME	Fatty acid methyl esters
FEE	Fish ethyl esters
FEG-TEM	Field emission gun transmission electron microscope
FFA	Free fatty acid
FH	Forced heating
FID	Flame ionisation detector
FSN	Filter smoke number
FTL	Fischer-Tropsch liquids
FWHM	Full width at half maximum
GC	Gas chromatography
GHG	Greenhouse Gas
H	Lift-off length
h_{vap}	Latent heat of vaporisation
HACA	Hydrogen abstraction C_2H_2 addition
HC	Hydrocarbons
HEAR	High erucic acid rapeseed
HHV	Higher heating value
HPLC	High-performance liquid chromatography
HSDI	High speed direct injection
ICCD	Intensified charge-coupled device
ID	Ignition delay
IFC	Interface controller
l	Connecting rod length
L	Stroke
LEAR	Low erucic acid rapeseed
LHV	Lower heating value
LII	Laser-induced incandescence
LIF	Laser-induced fluorescence
LNT	Lean NO_x trap
$(m_{fuel}/m_{air})_{st}$	Stoichiometric fuel:air ratio
MCU	Main control unit
MG	Monoglyceride
MPD	Magnetic pressure detection
MW	Microwave
Nd:YAG	Neodymium-doped yttrium aluminium garnet
NO_x	Oxides of nitrogen
NAC	NO_x adsorber catalyst
NDIR	Non-dispersive infrared
NFH	No forced heating
NPAA	4-nonylphenoxy acetic acid
NSC	NO_x storage catalyst
NTC	Negative temperature coefficient
NTPR	Non-thermal plasma reactor
OVN	Heated analysis unit (Oven)
P	In-cylinder pressure
P_{max}	Maximum in-cylinder pressure
PAH	Polycyclic aromatic hydrocarbon

PLN	Pump-line-nozzle
PM	Particulate matter
PPD	*p*-Phenylenediamine
ppm	Parts per million
ppmC	Parts per million carbon
ppr	Pulses per revolution
PSU	Power supply unit
PY	Pyrogallol
Q	Heat energy
RME	Rapeseed methyl esters
RME2	Rapeseed methyl esters (from an alternative source)
ROS	Reactive oxygen species
RSFR	Resonantly stabilised free radical
SCR	Selective catalytic reduction
SINL	Spatially integrated natural luminosity
SME	Sunflower methyl esters
SHS	Sample handling system
SO_x	Oxides of sulphur
SOC	Start of combustion
SOI	Start of injection
SKLE	State Key Laboratory of Engines
SVF	Soot volume fraction
SVO	Straight vegetable oil
SVS	Solenoid valve system
T	Temperature
$T_{b,fuel}$	Fuel boiling point
TBHQ	*tert*-Butylhydroquinone
TDC	Top dead centre
TEM	Transmission electron microscope
TG	Triglyceride
THC	Total hydrocarbons
TME	Tallow methyl esters
TPGME	Tripropylene glycol methyl ether
TWC	Three-way catalyst
UCOME	Used cooking oil methyl esters
ULSD	Ultra-low sulphur diesel
UV	Ultra-violet
V	In-cylinder volume
V_c	Clearance volume
V_d	Displaced volume
VI	Virtual Instrument
VOC	Volatile organic compound
VLM	Visible light microscope
x_{liq}	Liquid length
γ	Ratio of specific heats
ΔP_{diff}	Pressure rise across the diffusion burn phase (between EOPMB and Θ_{Pmax})
ΔP_{inj}	Injector pressure drop
ΔP_{pmb}	Pressure rise across the premixed burn phase (between SOC and EOPMB)
Θ	Crank angle
Θ_{10J}	Angle at which AHRR first exceeds 10 J/deg

Θ_{Pmax}	Angle of maximum in-cylinder pressure
ρ	Density
ϕ	Equivalence ratio
ϕ_{LOL}	Equivalence ratio at the lift-off length
ϕ_{Ω}	Oxygen equivalence ratio
Ω	Oxygen ratio
Ω_{H}	Oxygen ratio at the lift-off length

Chapter 1

INTRODUCTION

1.1 MOTIVATION

It is hard to overstate the current dependence of mankind on fossil fuels. In *Billions & Billions*, Sagan [1] paints the following unpleasant picture:

> *"Our civilization runs by burning the remains of humble creatures who inhabited the Earth hundreds of millions of years before the first humans came on the scene. Like some ghastly cannibal cult, we subsist on the dead bodies of our ancestors and distant relatives."*

Modern life, or more specifically the machines that make the modern lifestyle possible, demand an abundant supply of energy – wars are fought *for* it, and wars are fought *with* it, and failure to secure it fosters political and economic instability. Over the last few centuries, fossil fuels have provided a plentiful, reasonably accessible and affordable fuel source, but today global demand is higher than ever and much of the low-hanging fruit has already been harvested, meaning that prices can be volatile, with many countries entirely or partially dependent upon others to provide for their needs. To some of those situated on top of the world's coal, oil and gas reserves this dependence has delivered great wealth and power; to others it has brought a great deal of trouble.

There is also substantial concern about the detrimental environmental effects which wanton fossil fuel consumption has had, and continues to have, on the planet. On a global scale, man-made climate change appears to be a reality well supported by the scientific evidence [2], although amongst the general public scepticism about this is relatively widespread [3]. On a more local scale, exposure to gaseous pollutants and particulate emissions from vehicles, and other sources, can damage the health of the population, and degrade the living environment.

The diesel engine is an efficient, robust and widely employed prime mover, found in many passenger cars (around half, within the EU) and the majority of commercial vehicles [4], in some trains (diesel traction accounts for around 20% of EU rail traffic [5]), and almost all ships; on a tons per kilometre basis 94% of global trade is diesel-powered [6]. The prevalence of diesel engines within the transport sector (and, to a lesser extent, within small-scale power generation) means that they make a significant cumulative contribution to total anthropogenic greenhouse gas emissions (14% of which is attributed to transportation as a whole [2]), as well as both the quantity and toxicity of air pollution – particulate matter especially [7, 8].

The manufacturers of engines and vehicles, and the suppliers of fuels, have little private interest in protecting public health or the environment for their own sakes, and so it is necessary for governments to enforce legal restrictions. How best to regulate emissions from road vehicles is a matter of current concern, following the implementation of the Euro 6 emissions standards, and the revelation that while vehicles produced by many major carmakers are able to pass the regulatory tests (by hook or by crook), when actually driven under normal conditions as many as 90% of new diesel cars may exceed the limits defined [9, 10]. The Euro 6 (2014) limits can be seen in Figure 1.1, and the scale of the reduction demanded since Euro 1 (1992) is clear. It appears to be emissions of oxides of nitrogen (NO_x) which pose particular recent difficulty, being restricted by Euro 6 to less than 50% of the Euro 5 (2009) values, and to only 16% of the Euro 3 standard (2000).

Biodiesel offers a potential solution to many of the problems associated with conventional petrodiesel. Technically, it provides a means for improving the lubricity of modern ultra-low sulphur petrodiesel, which is itself deficient in this respect [11]. Politically, it helps to provide a domestic fuel source for nations without their own oil fields, creates jobs in rural areas, and offers an alternative revenue stream to farmers. Environmentally, the use of biodiesel is understood to reduce net carbon dioxide emissions (that is, although combustion of biodiesel still releases CO_2 into the atmosphere, this release is largely offset by the consumption of CO_2 during the growth of the crop from which the fuel was derived [12]), and also typically reduces emissions of carbon monoxide (CO), unburned hydrocarbons (HC) and particulate matter (PM) [13]. Perhaps most importantly, the fact that biodiesel is derived from renewable resources means that it may plausibly contribute to a sustainable energy economy of the future.

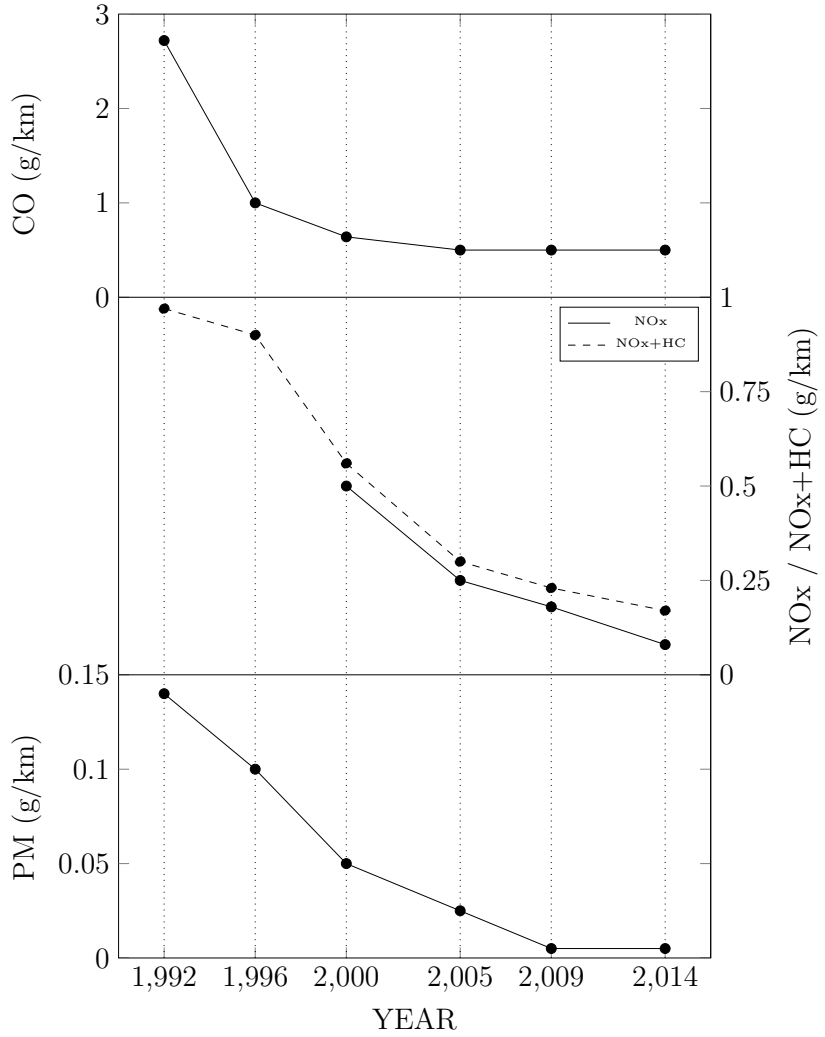

Figure 1.1: European emission standards for light-duty diesel passenger vehicles (note that particulate matter emissions are also restricted in number by Euro 6, to 6×10^{11} particles per km).

However, biodiesel is by no means a total solution, and is not without difficulties of its own. The issue with which this thesis is particularly concerned is the widely reported increase in emissions of oxides of nitrogen that occurs when substituting biodiesel for petrodiesel, either in toto or as part of a blend. Given the concerns associated with NO_x emissions from diesel engines, the fact that fuelling on biodiesel is normally understood to increase NO_x is something of a stain on the potential of a promising alternative fuel.

A lot has been written about possible reasons for the purported biodiesel NO_x increase, but a number of question marks remain, not least because the effect varies from engine to engine, from fuel to fuel, and in some cases biodiesel NO_x emissions are actually lower than those from petrodiesel.

1.2 OBJECTIVE

The primary objective of the work documented in this thesis was to gain an improved understanding of the underlying physical and chemical reasons for the commonly observed increase in NO_x emissions when fuelling on biodiesel. Particular emphasis was placed on the possible influence of factors related to fuel composition, ignition delay and fuel-bound oxygen content, and it was towards these three aspects of the problem that experimental enquiry was directed.

1.3 THESIS OUTLINE

The thesis begins in Chapter 1 by offering a short explanation of the reasons for undertaking the project, and of the experimental and research focus. An overview of the thesis is given, and the relevance of the author's research to the field – how the work makes a contribution to knowledge – is highlighted.

This is followed in Chapter 2 by a literature review covering the nature of biodiesel, its production, factors influencing its physical and chemical properties, and how these properties differ from those of petrodiesel. Armed with this understanding, an attempt is made to describe the processes to which a fuel is exposed and the types of reactions that it may undergo. Primarily, emphasis is on combustion and emissions formation mechanisms, and how the differing chemical composition of fuels can effect them. These processes are placed in context with a description of how they may occur inside a typical diesel engine, and the effects that the different properties of a fuel may have. This section concludes with a discussion of the various means by which NO_x emissions are thought to be affected by replacing petrodiesel with biodiesel.

In Chapter 3, aspects of the experimental equipment employed for the work are described, with insight given into the principles of operation where appropriate. Changes and refinements made to the system are discussed and justified. Generalities of operational procedure are described, but the specifics of each experiment are reserved to their respective chapters. Similarly, an overview of the methodology of data analysis is provided, but more detailed explanations appear alongside the relevant experimental work. Variations observed in the experimental data are analysed and remedial precautions highlighted.

Chapters 4–6 document experiments employing a Ford Duratorq "Puma" 2 litre, 4 cylinder high speed direct injection (HSDI) diesel engine, which were focussed on the

collection and analysis of emissions data, in-cylinder pressure data, and calculated apparent heat release rates. The first set of experiments, forming the basis of Chapter 4, was motivated by the observation that, in the Brunel laboratory diesel engine, as well as in various reports available in the literature, the increase in NO_x emissions when fuelling on biodiesel depends upon load, injection timing, and other operational variables. By sweeping injection timing across a relatively wide range, and comparing the heat release and NO_x emissions data generated by combustion of petro- and biodiesel at two different loads, it was possible to gain some insight into why the variations in relative NO_x emissions might occur. It appeared that the increase in NO_x emissions when fuelling on biodiesel was connected to the magnitude of the so-called premixed burn phase. Under conditions where the premixed burn phase was large, biodiesel had relatively low NO_x emissions, but under conditions where the premixed phase was smaller, NO_x emissions from biodiesel increased relative to those of petrodiesel.

The main set of experiments, documented in Chapter 5, aimed to test the conclusions of Chapter 4, and expand upon them by experimenting with a wider range of fuels under conditions selected and controlled to provide a less obscured view of the important variables identified in the previous chapter. An ignition enhancer was used to extend the range of premixing conditions; an oxygenate was added to the petrodiesel to enable the isolation of the effects of fuel-bound oxygen content; biodiesels from different feedstocks were tested to investigate the influence of fuel composition; injection pressure and engine load were varied to assess the generalisability of the trends observed; a complete set of gaseous emissions and filter smoke numbers were collected to provide insight into existing interrelationships; and steps were taken to synchronise combustion to minimise the considerable differences which changes in phasing can introduce into a comparison between fuels. The results suggest that the conclusions of Chapter 4 are correct in part, but are oversimplified. The discussion and conclusions in Chapter 5 offer a deeper understanding of the factors underlying the biodiesel NO_x increase, complementary to the background literature.

Chapters 6–8 document studies which are, to varying extents, detached from the central theme of the thesis, although still addressing questions related to fuel properties and pollutants. Chapter 6 looks at the effect that the addition of antioxidants to biodiesel has on diesel engine exhaust emissions. Some of the available literature suggests that certain antioxidants may be associated with significant reductions in NO_x emissions, via chemical

mechanisms (namely, the prompt NO pathways) with possible relevance to the biodiesel NO_x increase. However, little evidence of any effect of antioxidants on NO_x emissions was found.

Chapter 7 documents several connected experiments involving wick-generated biodiesel flames. Laser-induced incandescence, as well as more rudimentary sooting height and temperature measurement techniques, were employed to characterise diffusion flames from different biodiesels, petrodiesel, and oxygenated petrodiesel blends. Soot samples were collected using a pneumatic thermophoretic sampler, and studied using a transmission electron microscope. Petrodiesel flames were sootier than those of the biodiesels, and those of the oxygenated blends. In general, the biodiesels derived from more highly unsaturated feedstocks produced slightly sootier flames than the more highly saturated fuels.

Chapter 8 discusses the development of a non-thermal plasma exhaust aftertreatment system for marine applications. Preliminary results suggested a high removal rate of oxides of nitrogen and sulphur.

In Chapter 9 the conclusions of the thesis are summarised and recommendations for future work are made.

1.4 CONTRIBUTION TO KNOWLEDGE

Much of the ground covered in the core of this thesis (primarily Chapters 4 and 5) is already well-trodden, although it has seldom been systematised into a cohesive whole. Consequently, the majority of what will be discussed is unique primarily with respect to the manner in which pre-existing information has been arranged and synthesised. The original contributions to knowledge claimed herein are as follows:

1. The demonstration of a definite separation between petrodiesel and biodiesel NO_x emissions as a function of premixed burn fraction, which varies dependent upon operating conditions.

2. Evidence that this separation between fuels is related to fuel-bound oxygen content.

3. A thorough comparison of petrodiesel and biodiesel apparent heat release rates, illustrating the relative variations of the two over the course of the combustion process.

4. Confirmation of the higher biodiesel diffusion AHRR (previously identified in [14])

and evidence of its relation to increased NO_x emissions via increased maximum in-cylinder pressures. Also, the suggestion of a connection to the duration of the biodiesel injection event.

Chapter 2

LITERATURE REVIEW

2.1 AN INTRODUCTION TO BIODIESEL

Biodiesel is a renewable alternative fuel suitable for use in compression ignition engines and produced by the transesterification, or alcholysis, of natural lipids [15]. Certain legislation (e.g. [16, 17]) currently extends only as far as considering fatty acid methyl esters (FAME), but a complete definition of biodiesel properly includes all mono-alkyl esters of fatty acids. That is to say, the transesterification process, although most commonly utilising methanol for reaction with the triglyceride feedstock (for reasons of low cost and high reactivity) [18, 19], can actually be undertaken with a range of different alcohols, yielding biodiesels with slightly varying physicochemical properties [20, 21].

Straight vegetable oils (SVOs) can be used in diesel engines directly, although systematic adaptations are recommended (fuel pre-heating, for instance) [22, 23], and the practice is generally discouraged in automotive engines [24] due to problems like injector coking, the formation of engine deposits, filter and fuel-line clogging and contamination of the lubricating oil [25]. The primary cause of most of these issues is the relatively high viscosity of SVOs. Transesterification is a means of reducing the fuel's viscosity to levels more closely compatible with existing engine technology. At 40 °C the kinematic viscosity of rapeseed oil is around 35 mm^2/s, compared to about 4.4 mm^2/s for rapeseed methyl esters (RME) [26]; the viscosity of petrodiesel at the same temperature is legally required to be between 2–4.5 mm^2/s [16].

2.1.1 TRANSESTERIFICATION

Generically, transesterification is the name given to a process whereby one alkoxy group is substituted for another [27, 28]. In the case of biodiesel specifically, the alkoxy groups from three molecules of an alcohol are substituted for those of a triol: glycerol. Thus,

a single large triglyceride molecule is broken into three smaller, more mobile, alkyl ester molecules, which have accordingly lower viscosities.

Homogeneous (so called because the catalyst is in phase with the reactants) base catalysed transesterification is the approach most frequently employed in the production of biodiesel [29] because it is faster and currently more economical than other methods [30]; common alkali catalysts include sodium or potassium hydroxides and methoxides, with alternatives including metal complexes, amines and guanidines [31, 32]. Figure 2.1A (slightly modified from [33] on the basis of [34]) illustrates the process by which a single substitution reaction occurs under homogenous base catalysed conditions. In the first step, the base reacts with the alcohol to form an alkoxide ion (RO^-) which goes on to attack a triglyceride carbonyl group (C=O) in step two, forming a tetrahedral intermediate which breaks down in step three. In step four, the hydrogen atom removed from the active species in step one is returned to complete a diglyceride molecule. This process is repeated to produce second and third alkyl ester molecules, reducing the diglyceride to a monoglyceride, then to glycerol.

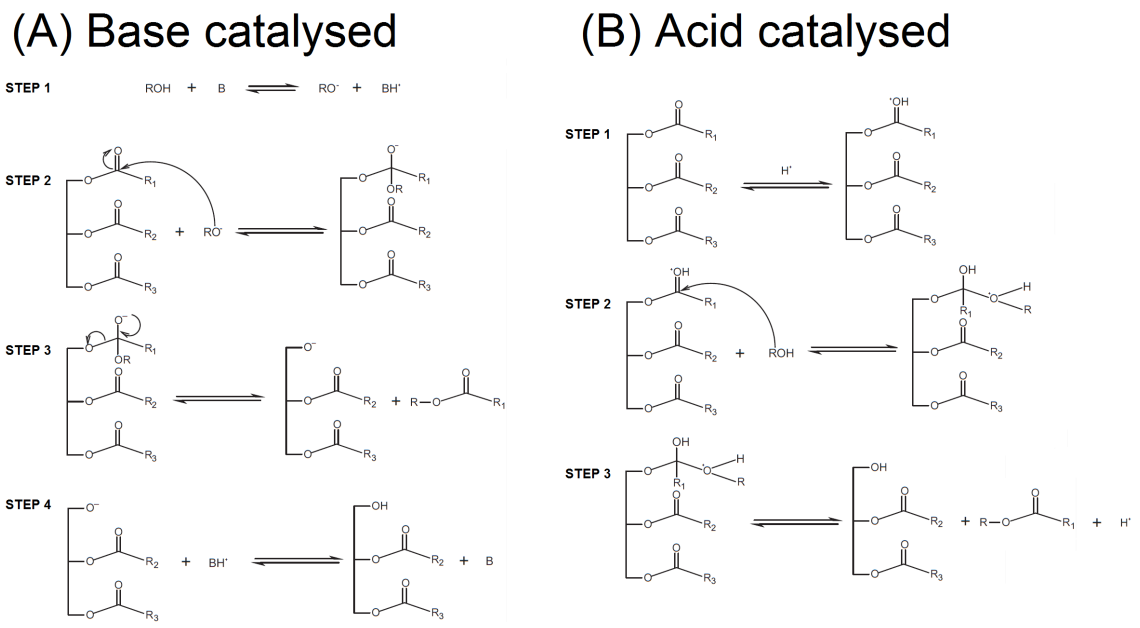

Figure 2.1: Homogeneous base and acid catalysed mechanisms for the transesterification of triglycerides [33, 34].

Homogeneous catalysis can also be acidic [34] or enzymatic [35, 36]. Acid and enzyme catalysed transesterification have the benefit of being able to cope with larger concentrations of free fatty acids (FFAs) and water in the oil-alcohol solution than their alkaline alternative, which enables them to operate with low quality feedstocks, like used cooking oil [30]. These factors may cause a problem when an alkaline catalyst is used because the

presence of FFAs in quantities exceeding approximately 0.5% leads to saponification (such issues may be alleviated by making use of more expensive alkoxides, instead of hydroxides, although alkoxides have other associated difficulties [37]). The presence of water can lead to the formation of FFAs by hydrolysis, along with mono- and diglycerides, which hinder separation of the ester-rich and glycerol-rich phases later in the production process [33], since they act as surfactants [38]. For this reason a pre-treatment stage is usual in commercial biodiesel production, in order to reduce quantities of FFAs to manageable levels. Ways of achieving this reduction include deliberate saponification [39], steam distillation, extraction with alcohol, reaction with glycerol to form triglycerides, or esterification of FFAs using iodine as a catalyst [40]. Also, because acid catalysed transesterification is able to both esterify and transesterify simultaneously (i.e. it accommodates the conversion of FFAs to alkyl esters, alongside the conversion of triglycerides), it is common to precede the base catalysed process with an acid catalysed stage.

Homogenous acid catalysed transesterification is illustrated in Figure 2.1B. Step one sees the protonation of the carbonyl group by the acid, encouraging the attack at this site by the alcohol in step two. As in base catalysed transesterification, a tetrahedral intermediate forms, which breaks down, yielding an alkyl ester [34]. Acidic catalysts that have been employed for the production of biodiesel include sulphuric, sulphonic, phosphoric and hydrochloric acids, and boron trifluoride [41]. The primary disadvantage of acid catalysed transesterification is speed [42]. Despite this fact it has still been suggested that the process may have good overall economic viability, due to the cheaper feedstocks that it would enable producers to operate with directly [43, 44].

Enzyme catalysed transesterification, like acid catalysed transesterification, has the advantage of being able to esterify FFAs, but it is an even slower process than acidic catalysis and is currently prohibitively expensive [40]. The enzymes used for biodiesel production – lipases, a class of hydrolases, including *Candida antarctica* and *Rhizomucor miehei* as examples [40] (a more exhaustive list is provided by Ghaly et al [45]) – nominally catalyse hydrolysis, cleaving ester bonds, and producing FFAs from triglycerides [46]. However, since the reverse reaction, whereby ester bonds are formed, is also catalysed under the correct conditions (viz. microaqueous, as opposed to macroaqueous), by correctly controlling the concentrations of water and the different reactants and products, it is possible to promote a range of chemical processes, including transesterification [46, 47]. Enzymatic transesterification is somewhat more environmentally friendly than

other homogenous processes, because it requires very little heating and doesn't involve the generation of such large quantities of toxic wastewater later in the production process [36, 45]. However, total yields can be lower (with final conversion being reduced by approximately 10%), accumulated glycerol may cover the lipase and inhibit its action, and some alcohols – methanol in particular – can reduce the activity of the enzyme when added in high concentrations, requiring carefully structured alcohol addition [48, 49]. Use of different alcohols [35], and replacement of the alcohol with an acetate [50–52] have been explored as viable alternatives.

Enzymatic transesterification also allows for the catalyst to be recovered from the product for reuse – a process made easier by immobilisation of the lipase [30]. Methods involving heterogeneous catalysts share this benefit, reducing waste and expense compared to their homogeneous counterparts, with resulting economic and environmental benefits. Heterogeneous catalysts may provide additional economic advantages by facilitating continuous fixed bed processing [32]. Alkali heterogeneous catalysts include alkaline earth metal oxides (e.g. calcium oxide and magnesium oxide), aluminium-magnesium hydrotalcites, basic zeolites and heterogenised guanidines [30, 32]. Heterogeneous acid catalysts include oxides of zirconium, titanium and tin, sulphonic acid silicas, sulphated metal oxides and heteropoly acids [30, 32, 53]. The problems associated with heterogeneous catalysts are mainly related to increased capital costs, higher risks of end product contamination due to leaching and in some cases more energy intensive reaction condition requirements and reduced yields [30, 54].

Non-catalytic transesterification is also a possibility, under supercritical conditions [54–56]. This process involves high temperatures and pressures (43 MPa and 350 °C, for example [57]) in order to get the alcohol into the supercritical state, where its polarity effectively drops to a level comparable to that of vegetable oil, enabling the two liquids to form a homogeneous mixture. Under these conditions, as well as being a reactant, methanol acts like an acid catalyst [57]. Due to the single phase solution that forms, reaction takes place very quickly (a matter of minutes rather than hours [55]), with very high conversion rates (reportedly, even higher with ethanol than methanol [58]), no problems with FFA (the process allows esterification and transesterification to occur simultaneously) or water contamination of the feedstock [57] and minimal requirement for product purification. The high pressure and temperature requirements make energy costs high, but because of the shorter processing time and reduced need for aftertreatment the process is

still economical [55] and can, as with the techniques employing heterogeneous catalysts, be incorporated into a continuous production process [59]. Further, the development of supercritical reactive extraction processes may eventually allow complete integration of both the extraction and transesterification processes [60]. The high temperature conditions can cause problems with thermal decomposition, particularly when utilising more highly unsaturated feedstocks [54]. The use of a co-solvent can improve miscibility and reduce the necessary operating temperatures and pressures, and therefore minimise issues related to thermal degradation, and also reduce energy consumption [61] (co-solvents can also increase reaction speed and conversion efficiency in catalytic transesterification processes [62]).

Improved mixing between the alcohol and oil phases, in order to obtain faster and more efficient conversion, can be achieved by employing oscillatory flow [63], ultrasonic and other types of cavitational reactors [64, 65]. Reaction rates may also be increased by the application of microwave irradiation [66].

2.1.2 FEEDSTOCK

With reference to biofuels in general, it is common to refer to first- and second-generation fuels, and, less commonly, to third- and fourth-generation fuels [67]; although these terms do not seem to be rigidly or consistently defined in the literature, they are employed here to provide structure. The categories are dependent upon feedstock, but also relate to different processing methods and fuel technologies, and as such provide a helpful description of the projected evolution of biofuels as a whole.

First-generation biofuels remain the most widely produced and used, and are derived largely from edible sources, including cereals and sugar crops – for the production of bioethanol – and oil crops (or, less commonly, animal fats) for the production of biodiesel. The feedstocks employed for the production of biodiesel vary by region. National contributions to total global biodiesel production can be seen in Figure 2.2A, with the EU contingent subdivided into its component states in Figure 2.2B.

In the EU most biodiesel is derived from rapeseed, in the USA, Brazil and Argentina soybeans are the predominant oil source, and in South East Asia palm oil is most commonly utilised [68–70]. Biodiesel feedstock trends in the EU and US are illustrated in Figure 2.3. It is interesting to note that despite there being no native production of palm oil in the EU, this feedstock constitutes an increasing proportion of overall EU biodiesel production,

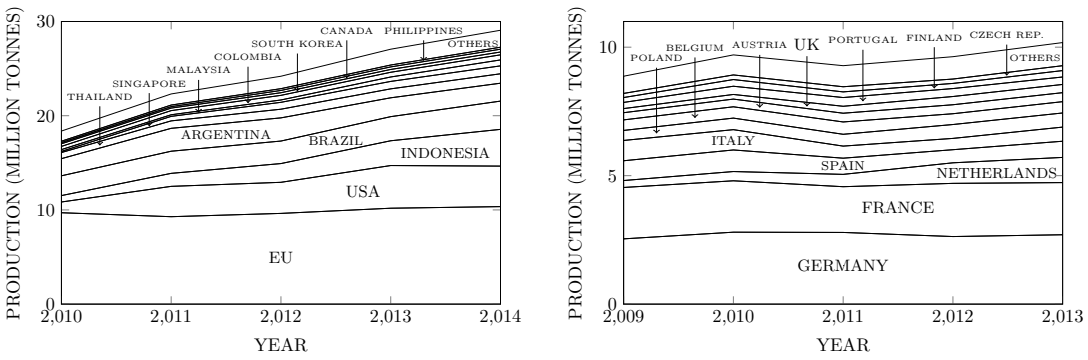

Figure 2.2: (A) Biodiesel production amongst the largest global producers, 2010–2014. (B) Biodiesel production amongst the largest EU producers, 2009–2013. (Data from [68].)

while the production of biodiesel from rapeseed appears to have plateaued. It is reported that palm oil can be produced and processed to biodiesel more economically than rapeseed, despite the added logistical costs involved in transporting it to Europe [71]. Coupled to the sizeable increase in biodiesel output from palm oil producing nations themselves – Indonesia in particular, which saw a 470% increase in biodiesel production between 2010–2014 – the increasing importance of palm oil as a feedstock becomes clear.

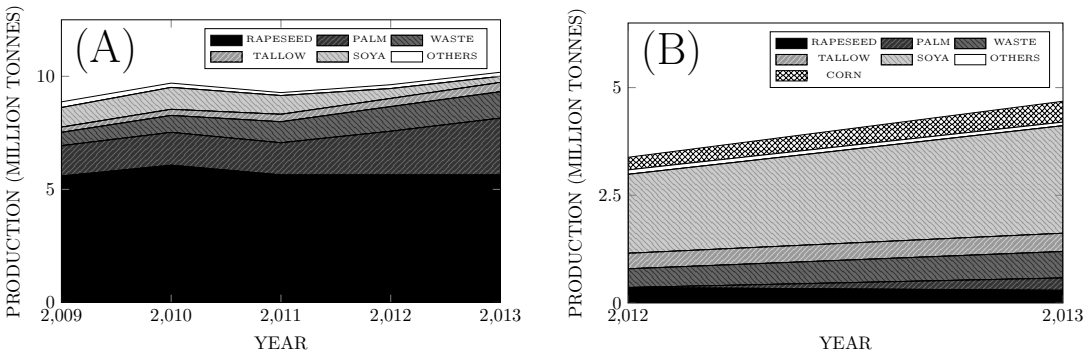

Figure 2.3: (A) Feedstocks used for biodiesel production in the EU, 2009–2013. (B) Feedstocks used for biodiesel production in the USA, 2012–2013. (Data from [68].)

One conspicuous disadvantage of first-generation biofuels is that they interfere with the food supply, either by directly consuming otherwise edible commodities, or by taking up agricultural land which could instead be used to grow food-crops [72].

Second-generation biofuels are produced from sources that circumvent the *food versus fuel* dilemma (to some extent, at least) – largely waste products and crops which can be grown on marginal land. Lignocellulosic materials, which can be retrieved in abundance from a wide variety of agricultural, industrial and domestic wastes [73], from woody biomass, or from grasses such as miscanthus [74], can be fermented to produce bioethanol (following pretreatment [73, 75]). However, although bioethanol has been the predominant first-generation fermentative biofuel, biobutanol (see [76, 77]) may achieve increasing

importance amongst the second-generation fuels. Beyond the biochemically produced alcohols, thermochemically produced synthetic liquid fuels (including Fischer-Tropsch liquids (FTL), dimethyl ether, biomethanol and other heavier bio-alcohols), formed via the gasification of biomass [78, 79] have the potential to become significant energy carriers – FTL, in particular [80]. Generation of gaseous fuels, like synthetic natural gas and biohydrogen, can be achieved by a similar process of gasification and synthesis; additionally, biogas, which can be upgraded to biomethane, may be produced by anaerobic microbial digestion of a variety of waste feedstocks [81]. Other thermochemically produced fuels include bio-char and bio-oil, which may be obtained as by-products of gasification, or by deliberate lower temperature pyrolysis of biomass (temperatures in the range of 250–350 °C are applied to produce bio-char, 550–750 °C to produce bio-oil, whereas gasification takes place at 750–1200 °C and in the presence of restricted oxygen levels) [82].

Second-generation biodiesel feedstocks include non-edible oils from crops which can be grown with relative ease on low quality land – such as jatropha and pongamia [83] – and wastes from food preparation, like used cooking oil and waste animal and fish fats [56]. Jatropha has been given a high priority in India, where 400,000 square kilometers of marginal land have been identified for cultivation, in the hope of replacing a significant proportion (around 20%) of the national diesel fuel demand [83]. The quantity of biodiesel being produced from recycled oils has increased in the West (see Figure 2.3); in 2013 waste oil was the second most common feedstock in the USA, and the third most common in the EU (its use doubled in the EU between 2009–2013), accounting for around 13% and 11.5% of production, respectively [68]. In China, the potential for production of biodiesel from waste oil is very high; in particular 'gutter oil' (a term which refers to waste oils and fats from restaurants and slaughterhouses, as well as oils dredged from sewers and retrieved from rotten meat – to be processed and resold, illegally [84]), which reportedly finds it's way into a disturbing proportion of Chinese cooking oil, might provide a potential waste feedstock almost 3 times the size of that available to the EU, US and Canada, combined [85].

In what may be a slight conflation of terminology – albeit one that one that does little harm to the overall trajectory of the discussion – the alternative oil and fat derivative variously called renewable diesel [86], green diesel [87], hydrotreated vegetable oil (HVO) [88] and NExBTL [89] is also referred to as a second-generation biofuel, although the feedstock from which it is made is not necessarily any different to that of a first-generation

biodiesel. It is produced by hydrogenation of triglycerides (or free fatty acids), followed by deoxygenation, decarbonylation or decarboxylation, yielding alkanes of which some portion may then be converted to *iso*-alkanes in order to improve the low-temperature properties of the fuel and modify other properties (e.g. cetane number) as desired [90].

The *third-generation* designation is widely applied to biofuels derived from algae [82]. Although some authors apply the term to fuels still derived from land-based biomass, they refer to fuels produced by processes focussed more explicitly on specialised micro-organisms, either as a means of consolidated bioprocessing (CBP) [91], or microbial oil production [92], and thus in some sense there is a similar shift in emphasis: away from the plant matter itself, and towards other – smaller, and possibly more manipulable – lifeforms.

Biofuels can be derived from macroalgae (i.e. seaweed), microalgae and varieties of cyanobacteria (often called blue-green algae). As regards macroalgae, its possible roles in fuel production seem to have some similarity to those of plant biomass; it may be processed to yield fermentable sugars [93, 94] or treated directly with metabolically engineered micro-organisms for the production of bioethanol [95], or used to generate methane via anaerobic digestion [96]. However, gasification and pyrolysis may be more problematic than with terrestrial crops [97]. There have also been reports which discuss the production of biodiesel from macroalgae, which suggest that this may be viable although lipid content is typically quite low [98, 99].

For biodiesel production, microalgae and cyanobacteria have far more promising compositions, with oil content commonly between 20–50% of dry mass, and in some cases exceeding 80% [100]. Not only is the oil content of microalgae high, but potential yields vastly exceed those of the oil crops currently grown for biodiesel; Christi [100] estimates possible per hectare oil yields 50–115 times greater than those of rapeseed (canola), and 10–23 times greater than those of oil palm (ranges based on estimates for microalgae species which are 30–70% oil by weight). Scott et al [101] provide more conservative, but still impressive, estimated increases in oil yield of around 5–22 times compared to rapeseed; the estimates given by Demirbas [102] fall between these, specifying yields 7–31 times greater than those of oil palm. The fatty acid composition of algal lipids can vary widely, depending upon both species and growing conditions, but they often contain significant proportions of highly unsaturated species [103, 104], which could be problematic for derived biodiesels in terms of oxidative stability and cetane number regulations [105].

However, examples of very highly saturated algal lipids can also be found in the literature [106].

Currently, the economics and energy balance of the algal biodiesel production process are problematic [101, 107]; the cost of the necessary infrastructure is high, and, in particular, the need to dry to the algal slurry before oil extraction can involve a significant energy input [108], although wet processing methods which reduce the energy demand have been reported [109]. Following lipid extraction, fermentation of algal residuals to produce bioethanol, and subsequent anaerobic digestion of the remains to produce biogas could significantly improve the overall economic and energetic balance of biofuel production from algae [110]. The ability of microalgae to feed on the nutrients in wastewater, and hence combine the growth of an oil crop with an effective wastewater treatment system (phycoremediation) may also make the process more economically and ecologically appealing [111]. However, even if the economic barriers could be overcome, the supply of nutrients, particular phosphorous, may still impose a limitation on the ultimate scalability of algal biodiesel production [112, 113].

Fourth generation biofuels can also include those derived from algae, but the apparent distinction (made in [114]) is that while third-generation fuels are produced by the processing of algal biomass, fourth-generation biofuels are – or rather, will be – derived from metabolically engineered algae. It is hoped that the genetic modification of microalgae might offer improved photosynthetic efficiencies, higher growth rates and lipid concentrations [115, 116], and even direct secretion of fuels, or fuel feedstocks, out of the cells and into the growth medium, in order to reduce the high costs associated with processing algal biomass [114, 117]. Under the fourth-generation header, Gressel [67] discusses biological systems, including combinations of algae, yeasts, and bacteria, which may be able to produce biohydrogen and bioelectricity directly.

2.1.2.1 FATTY ACID COMPOSITION

Triglycerides, composed of fatty acids esterified to glycerol, make up the bulk of most oils and fats [118] (algal lipids are somewhat different in this sense, as they may be comprised of significant proportions of phospho- and glycolipids [119, 120]). The three fatty acid moieties within an individual triglyceride may be the same (mono-acid) but natural fats and oils tend to contain predominantly mixed-acid triglycerides [121]. When transesterified to produce mono alkyl esters, the fatty acids become separate (as discussed in Section 2.1.1),

and this is the form in which they exist in biodiesel.

Most natural fatty acids are straight chain aliphatic carboxylic acids, usually with main chains between 4 and 22 carbon atoms in length (i.e. C_4–C_{22}), having varying degrees of unsaturation [118]. In general, C_{18} fats are most common, and as a result of this the majority of current biodiesels can be represented as mixtures of five dominant species [122], which are depicted in Figure 2.4. The varying proportions in which these species are present in a range of biodiesels can be seen in Figure 2.5.

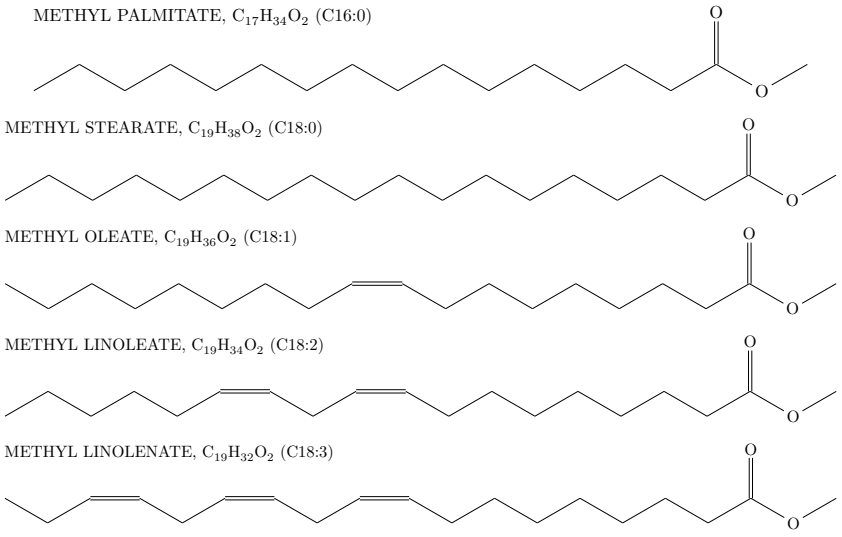

Figure 2.4: Chemical structures of the five methyl esters which comprise the majority of current biodiesels.

As Figure 2.5 shows, in the more commonly used biodiesels (refer to Figure 2.3), it tends to be only a small fraction of the composition which is comprised of species other than C16:0, C18:0, C18:1, C18:2 and C18:3 (note that these are lipid numbers of the form CX:Y, where X is the number of carbon atoms in the fatty acid main chain, and Y is the number of double bonds). In the case of rapeseed, the fatty acid composition can vary significantly depending upon cultivar, but although some regions still grow what is known as high erucic acid rapeseed (HEAR, where erucic acid is a C22:1 fatty acid that has been identified as a health concern), in the West low erucic acid (LEAR), canola-like varieties – high in oleic acid, C18:1 (approximately 60%) – are predominant. HEAR may have C22:1 content of around 45%, but the most significant marginal compound in Western rapeseed feedstocks is likely to be gondoic acid (C20:1), present at around 1–2% [123].

The composition of biodiesel derived from soya oil is ordinarily more highly unsaturated than that from rapeseed, being mostly the C18:2 ester, methyl linoleate (around 55%); although different soybean strains may yield varying proportions of the compounds in Figure 2.4, the five main species generally represent soybean derivatives well [124]. Palm

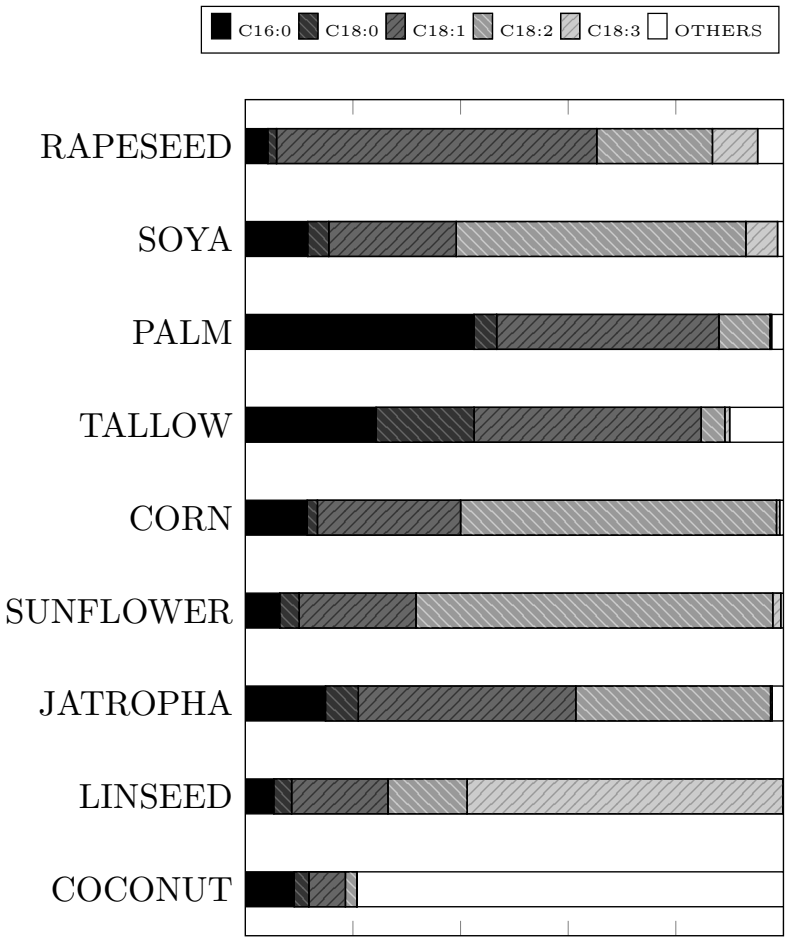

Figure 2.5: Fatty acid compositions of several biodiesel feedstocks in terms of the five most common species (data from [103]).

oil and derived biodiesels are more highly saturated, with methyl palmitate, C16:0, constituting the largest fraction, followed by C18:1 (both present at a little over 40%). Tallow biodiesels are also relatively highly saturated; although C18:1 compounds are present in the largest proportion (around 40%), the quantities of C16:0 and C18:0 saturates are substantial (20–25% and 15–20%, respectively). The fraction of tallow components falling outside the five species depicted in Figure 2.4 is large compared to most of the fuels based on vegetable fats, and includes C14:0, C16:1 and C_{17} fatty acids, amongst others [125]. Corn oil has a composition comparable to that of soybean (around 60% C18:2 and 25% C18:1 in US varieties, although this balance may be shifted somewhat towards C18:1 in non-US corn [126]), as does sunflower oil (around 65% C18:2 and 20% C18:1). Jatropha oil has more equal quantities of C18:1 and C18:2, present at around 40% and 35%, respectively. Linseed is one example (camelina, perilla and chia are others) of an oil crop containing a larger proportion (around 60% for linseed) of the more highly unsaturated C18:3 compound, linolenic acid [127].

There are instances in which the five species in Figure 2.4 are insufficient to provide

an adequate characterisation of an oil feedstock – as the coconut oil plot in Figure 2.5 illustrates. Coconut oil derived biodiesel is largely comprised of methyl laurate (C12:0, 45–50%) and methyl myristate (C14:0, 15–20%), making it a particularly highly saturated biodiesel. Palm kernel, babassu, cuphea and cohune oils are amongst the few vegetable sources with similarly highly saturated lipid compositions [128]. These oils can also contain significant amounts of caprylic acid (C8:0); even shorter chain fatty acids, such as C4:0, butyric acid, may be present in small quantities in biodiesels derived from butter fats, for example [129]. As with tallow, other fats derived from animals and animal products tend to contain more highly saturated overall compositions than most vegetable oils (although less so than coconut, etc.), posses shorter average chain lengths, and be based in larger proportion on compounds beyond those shown in Figure 2.4 [130]. They may also contain some quantity of *trans* fats.

Lipids from fish and algae, while still containing some proportion of the C_{18} fats common in vegetable oils, are typically constituted in large part of saturated and unsaturated C_{14}–C_{16} compounds, in addition to often substantial quantities of polyunsaturated C_{20}–C_{22} species [103, 131, 132]. In particular, eicosapentanoic acid (EPA, C20:5) and docosahexaenoic acid (DHA, C22:6), can be present in high concentrations in many varieties of both fish and algae.

More unusual fatty acids may contain hydroxyl groups (as in ricinoleic acid, C18:1-OH, which makes up around 90% of castor oil), epoxides (as in vernolic acid, C18:1>0, present at approximately 75% in ironweed oil) [133] and other features [134]; biodiesels derived from castor [135] and ironweed oils [136] may contain the former types of compounds, but they are not found in common biodiesel fuels.

2.1.2.2 MINOR CONSTITUENTS

In the BS EN 14214 [17] standard, relatively little is explicitly specified about the bulk of the fatty acid composition; linoleic acid methyl ester (C18:2) must not exceed 12% of the fuel, and less than 1% of the fuel should be comprised of methyl esters with 4 or more double bonds (the specified maximum iodine value also directly limits the overall degree of unsaturation of a biodiesel). Upper limits are also defined for a range of minor species which are of some technical significance.

Methanol, which can remain in biodiesel in small quantities after the washing stage of production, must not be present at a weighting beyond 0.2%. Increased methanol levels

are associated with a reduction in flash point (0.5% methanol is associated with a 50 °C reduction in flash point [137]), which is a safety concern. A limit of 0.2% aims to keep the biodiesel flash point above at least 100 °C. Methanol can also be corrosive to some metals, including aluminium and zinc [138].

Like methanol, residual catalyst alkalis (such as sodium hydroxide and potassium hydroxide) may promote the corrosion of aluminium [139]. In addition to this, if the remnants of the catalyst reach the combustion chamber they form ash when they burn [140]. Alkali catalysts can also react with free fatty acids (either formed by hydrolysis or left over from the production process) to form soaps, which can damage injectors [138]. Group I metals, sodium and potassium, are limited to 5 mg/kg by BS EN 14214 [17], as are Group II metals, calcium and magnesium. These metals will also count towards the sulphated ash limit of 0.02% by mass (high sulphated ash measurements can be associated with problems involving injector coking and filter clogging [137]). Certain metals also catalyse autoxidation reactions, and hence significantly reduce the oxidative stability of a biodiesel; transition metals like copper and iron (which aren't explicitly regulated by the standard) are most effective in this respect [141], but are more likely to come into contact with the fuel during transportation and storage [142], than to be native constituents. No limitations are explicitly defined for FFAs, although high levels would be expected to cause a biodiesel to exceed the specified maximum acid value.

Mono-, di- and triglycerides (MGs, DGs and TGs) of fatty acids must constitute less than 0.7%, 0.2% and 0.2% of a biodiesel, respectively [17]; all three are evidence of incomplete transesterification of the oil feedstock. Free glycerol content (resulting from inadequate separation of the glycerol phase following transesterification, and/or insufficient subsequent washing of the biodiesel) is limited to 0.02% of the fuel by BS EN 14214, and total glycerol, which includes both free glycerol and glycerol bound into MGs, DGs and TGs, is required to be below 0.25%. The presence of MGs, DGs and TGs (particularly those of saturated fatty acids, due to their higher melting points), can significantly degrade the cold flow properties of a biodiesel, causing crystallisation problems at low temperatures; in practice, the deposits found on plugged fuel filters have been reported to contain large quantities of saturated MGs and DGs [140, 143]. Steryl glucosides (SGs) are another high melting point trace species which can cause similar problems with low temperature operability and filtration. SGs are present in both free and acylated forms in vegetable oils, but acylated SGs are converted to the free form during the transester-

ification process [144]. The free form has increased polarity, and therefore precipitates out of biodiesel more readily, and even more readily out of biodiesel-petrodiesel blends [143, 145]. It has been reported that concentrations of SGs as low as 10–90 mg/kg can cause haziness in biodiesel at room temperatures [143], and 10 mg/kg contamination can cause an increase in filtration time comparable to 3000–4000 mg/kg of MGs [146].

Like SGs, free glycerol can also separate out during storage, due to its relatively low solubility in biodiesel. Glycerol in the fuel may add to deposit formation within the engine [140], and might also increase exhaust emissions of acrolein [13] and other aldehydes [147]. The high affinity of glycerol for MGs and water means that they may attract one another and accumulate. Water, which is limited to 500 mg/kg by BS EN 14214, can promote corrosion (rusting, etc.) and can also facilitate hydrolytic degradation of biodiesel (forming FFAs) and microbial growth; such microbes may produce sludges that contribute to filter plugging, or acids – such as sulphuric acid, derived from fuel-bound sulphur – which cause corrosion [140, 148].

The maximum allowable sulphur content of a biodiesel is 10 mg/kg, the same as for an ultra-low sulphur diesel. Typically, biodiesel has far less than this; of the 33 biodiesels (from different feedstocks) tested by Sanford et al [26], 29 were beneath this limit and most had less than 5 mg/kg. However, some oils yield biodiesels that are particularly high in sulphur. In [26], biodiesel derived from neem oil was the highest in sulphur, with 473.8 mg/kg, and elsewhere [149] biodiesel derived from the oil of *Salvadora oleoides* has been found to contain 1200 mg/kg. The latter was also found to be corrosive to engine components, and this was attributed to the higher levels of sulphurous compounds [149]. In general, the reasons for limiting fuel-bound sulphur are to reduce emissions of oxides of sulphur (SO_x), to reduce the sulphate contribution to particulate matter emissions, and because sulphur is a catalyst poison. Phosphorous is also a catalyst poison, restricted to a maximum of 4 mg/kg by BS EN 14214, and although levels are typical low in biodiesels [26], more phosphorous may be present in fuels derived from algal oils, which often contain high proportions of phospholipids; prior to purification, a crude biodiesel derived from *Scenedesmus* sp. was reported to have a phosphorous content of 295.6 mg/kg [150].

2.1.3 ALCOHOL

Methanol is currently the alcohol most commonly employed for large scale biodiesel production [33]. Most methanol is produced from syngas, which is a combination of hydrogen,

carbon monoxide and carbon dioxide, itself produced primarily from natural gas, although it can also be generated by the partial oxidation of heavy oils or by the gasification of solid feedstocks like coal or biomass [151, 152]. Ultimately, the majority of methanol is derived from non-renewable sources (although there are exceptions [153]), which is somewhat out of keeping with the biofuel ethos.

A shift towards biodiesels transesterified using bioethanol, to produce fatty acid ethyl esters (FAEE), would be desirable in terms of sustainability, but higher costs and possible production complications mean that FAEE is less widely utilised, although this may change in the future [33].

Various esters with longer and/or branched alcohol moieties have been investigated in engines [154], ignition quality testers [155] and flames [156], but such experiments seem mainly to have involved single component fuels rather than practical biodiesels. However, Kinoshita et al [157, 158] produced and engine tested esters of palm and coconut oils using a range of different alcohols, achieving positive results with butyl and *iso*-butyl esters, and finding some distinct advantages in terms of cold flow properties.

2.1.4 DIFFERENCES BETWEEN PETRO- AND BIODIESEL

A discussion of the differences between petrodiesel and biodiesel is complicated by the varying compositions that the two types of fuel may have. Petrodiesel would be expected to contain a greater variety of species than biodiesel. Petrodiesel is based upon raw middle-distillate compounds, boiling between approximately 180–380 °C, and can also include products of hydrocracking, whereby thermal decomposition of higher boiling point compounds yields lower boiling point products [159]. Although the balance of compounds may vary significantly (see [160]), the final blend of distillate fractions is controlled and adjusted in order to meet the specifications required by different fuel quality standards [161]; further hydroprocessing techniques (e.g. desulphurisation and denitrogenation) may also be necessary.

Figure 2.6 gives an indication of the make-up of petrodiesel, in terms of the classes and proportions of compounds which are likely to be present, along with examples of species which may be employed as representative surrogates in computational simulations [162]. Middle-distillates contain mostly saturated hydrocarbons and aromatics, having carbon numbers ranging from approximately C_{10}–C_{24} [159, 160]. The *iso*-alkanes present typically contain only one or two methyl substitutions, often towards the extremities of the chain;

amongst the cyclo-alkanes, cyclohexanes with multiple side-chains are most common; and aromatics consist mainly of alkylbenzenes and substituted naphthalenes [159, 160, 163].

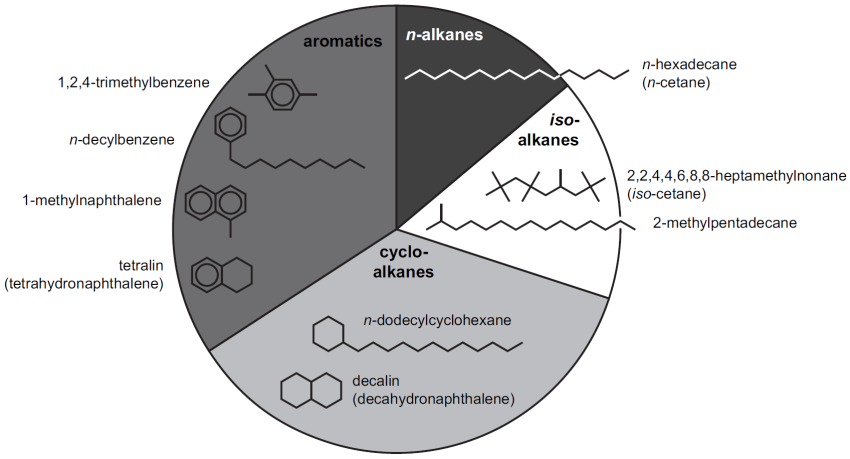

Figure 2.6: Relative amounts of various chemical classes in diesel fuel and possible compounds to represent these chemical classes in a diesel surrogate fuel [162].

As discussed in Section 2.1.2.1, biodiesel contains the alkyl esters of those fatty acids which naturally occur in the oil feedstock from which the fuel is derived and although different feedstocks have different major and minor components, they often draw from the same restricted selection of species, and are almost always structurally similar. Elementally, apart from trace quantities of sulphur, nitrogen and oxygen containing species petrodiesel is purely hydrogen and carbon. Biodiesel, on the other hand, always contains two atoms of oxygen in the ester group of each molecule, equating to around 11% by mass on average.

Figure 2.7 shows gas chromatography results (data collected for work documented in Chapter 5 and Chapter 7, in which the methodology behind them will be explained) for typical petrodiesel and biodiesel (in this case, RME) samples. These plots show the retention times after which portions of the fuels were eluted from the GC; shorter retention times are characteristic of more volatile species and each fuel component is represented by a single peak whose magnitude is dependent upon concentration. Figure 2.7 shows clearly the higher complexity of the petrodiesel sample, and the higher volatility of the compounds of which it was comprised.

2.1.4.1 BOILING POINT

The boiling range of petrodiesel is approximately 180–380 °C [161], and BS EN 590 [16] dictates that no more than 65% of automotive diesel fuel must boil below 250 °C, no less that 85% must boil below 350 °C, and 95% of the fuel must evaporate when heated

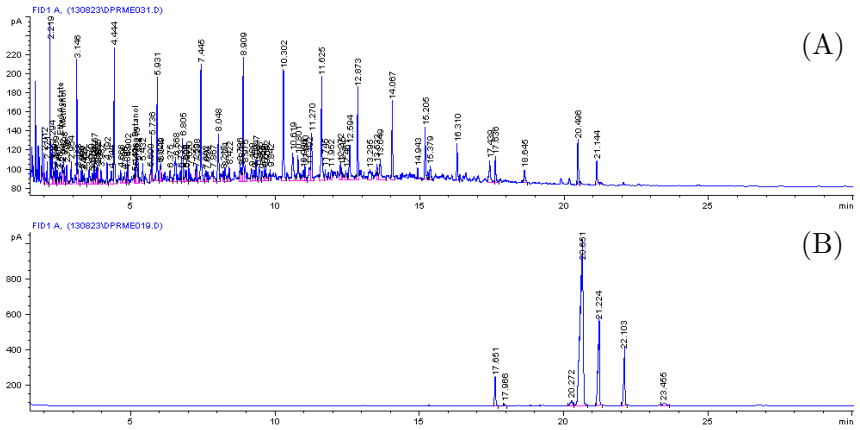

Figure 2.7: Chromatograms of (A) petrodiesel (ultra-low sulphur diesel, ULSD) and (B) biodiesel (rapeseed methyl esters, RME).

to 360 °C. The boiling range of biodiesel depends upon the feedstock from which it is derived, but is higher overall than that of petrodiesel. As is illustrated by Figure 2.8, boiling point is most strongly dependent upon chain length, increasing as chain length increases. The values plotted in Figure 2.8 are estimates calculated by an adapted Stein and Brown group contribution method (EPISuite predictions available from ChemSpider, e.g. [164]), and indicate a tendency towards increasing boiling point with increasing degree of unsaturation; however, experimental measurements of boiling point have suggested that the relationship with unsaturation may be relatively minor [165]. Boiling point predicted by the same method also increases with the length of the alcohol moiety, and is on average around 12 °C higher for the ethyl ester equivalents (e.g. [166]) of the methyl esters plotted in Figure 2.8.

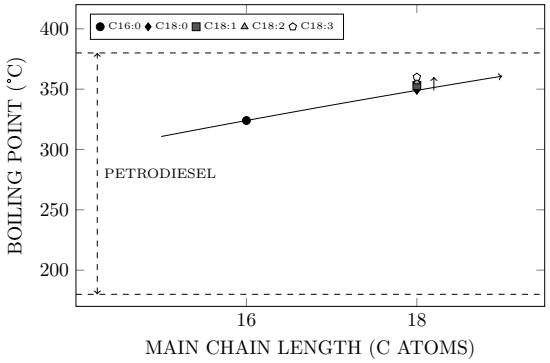

Figure 2.8: Estimated boiling points of methyl esters relative to the approximate petrodiesel boiling range (data from [161, 164]).

The predictions in Figure 2.8 put the majority boiling range of a typical biodiesel between approximately 320–360 °C – which is a little higher than some sources suggest [167], but a little lower than others [165]. In any event, the conclusion to be drawn remains the same; that the boiling points of the common biodiesel components lie within

a relatively narrow window towards the upper end of the petrodiesel boiling range – and beyond the majority of petrodiesel constituents, as seen in Figure 2.7. Correspondingly, the overall vapour pressure of biodiesel will generally be lower than that of petrodiesel.

2.1.4.2 COLD FLOW PROPERTIES

2.1.4.2.1 MELTING POINT

Making a comparison with petrodiesel in terms of the chemical constituents of biodiesel is problematic, because although the cold flow properties of a single compound may be adequately defined in terms of melting point, those of a multicomponent fuel like petro- or biodiesel are more correctly characterised using quantifiers such as cloud point, pour point, cold filter-plugging point (CFPP) or cold soak filtration test (CSFT) [168]. That said, the melting points of the component methyl esters are informative in the sense that it is the higher melting point compounds which are most influential in determining the overall cold flow properties of a biodiesel [169]. As Figure 2.9 shows, melting point increases with chain length, and is drastically reduced by unsaturation of the molecule.

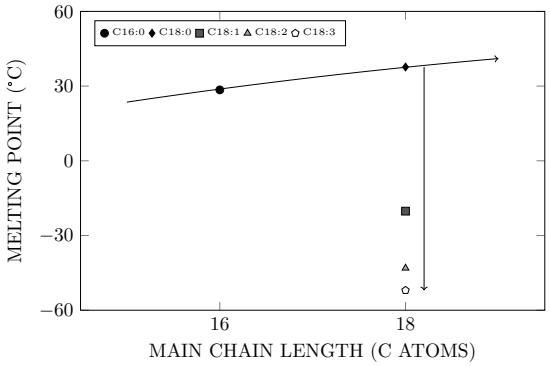

Figure 2.9: Melting points of methyl esters (data from [168, 170]).

It is important to note that although there is a general increase in melting point with chain length, this trend is actually rather more complicated when odd length alkyl esters (e.g. methyl margarate, C17:0) are considered alongside even ones – this is explained by Knothe and Dunn [170]. Increasing the length of the alcohol moiety seems initially to reduce melting point; methyl, ethyl, propyl and butyl stearate have melting points of 37.7 °C, 33 °C, 28.1 °C and 25.6 °C [170]. However, pentyl stearate has a reported melting point of 30 °C, and cetyl stearate of 57 °C [171], which is consistent with the finding that beyond butyl/pentyl esters there is no advantage to further extension in terms of cold flow properties [157]. Several authors have referred to the possible low temperature

advantages of branched alcohol moieties [157, 172, 173], although the available melting point data does not unambiguously coincide with this – for example, the reported melting point for *iso*-butyl stearate is 2 °C higher than that of butyl stearate, whilst, on the other hand, values for *iso*-propyl palmitate are 3 °C lower than those of propyl palmitate [171].

Additionally, *trans* fats have far higher melting points than their *cis* counterparts; the melting point of methyl elaidate (C18:1 Δ9 *trans*) is around 30 °C higher than that of methyl oleate (C18:1 Δ9 *cis*) [170].

2.1.4.2.2 COLD FILTER-PLUGGING POINT

For temperate climates, BS EN 590 specifies the low temperature requirements for fuel in terms of CFPP. The CFPP is defined as the *"highest temperature at which a given volume of fuel fails to pass through a standardized filtration device in a specified time, when cooled under standardized conditions"* [174]. Neat fuel, whether petro- or biodiesel, is required to have a CFPP below the UK Grade C limit of -5 °C between 16 Mar and 15 Oct, and below the Grade E limit of -15 °C between 16 Oct and 15 Mar [16, 17]. Biodiesel for use up to a blending percentage of 7% in an EN 590 compliant petrodiesel must meet slightly less stringent requirements – a CFPP below 5 °C in the summer and -5 °C in the winter.

Based on these criteria (and CFPP data from [103]), it seems that no common biodiesel feedstocks are suitable unblended for year-round automotive usage in the UK. Biodiesels derived from rapeseed, corn and possibly soya (with CFPPs of -12, -8 and -4±2 °C, respectively) are suitable for summer-time use and year-round blending, but feedstocks like palm and tallow (CFPPs of 9 and 13 °C) could only meet legislative limits if they were used in blends in conjunction with biodiesel from another source, or treated with a cold flow improver [175]. This is attributable to their higher percentages of saturated species, C16:0 and C18:0, with significantly higher melting points. The deleterious effect of saturated species on cold flow properties increases with increasing chain length (and hence increasing melting point). Biodiesels from feedstocks containing even small quantities of arachidic (C20:0), behenic (C22:0) or lignoceric (C24:0) acids are likely to have high CFPPs; peanut oil, for instance, which contains around 3% behenic acid and 1.8% lignoceric acid, yields a biodiesel with a CFPP of 17 °C [169].

Other types of compound with even higher melting points, present in biodiesel in only trace quantities, particularly saturated monoglycerides (e.g. monopalmitin and monostearin, with melting points of 77 °C and 82 °C, respectively) and steryl glucosides (e.g.

β-sitosteryl glucoside, with a melting point of 240 °C), are also understood to negatively affect fuel quality under cold conditions [143]. However, removal of these minor components does not improve CFPP [176]. Monoglycerides and steryl glucosides may form solid precipitates when biodiesel is stored at low temperature, and it is these precipitates that constitute a quality concern. Since CFPP does not quantify the propensity of a fuel to form precipitates, it is (in the case of biodiesel, at least) a somewhat inadequate means of assessing cold weather suitability; this is an issue that the cold soak filtration test (CSFT) aims to overcome [143].

2.1.4.3 DENSITY

BS EN 590 specifies that the density of automotive petrodiesel should be between 820–845 kg/m^3 at a temperature of 15 °C; biodiesel has a slightly higher density, and accordingly the allowable density range specified by BS EN 14214 (at the same temperature) is higher, 860–900 kg/m^3 [16, 17] (the density of RME, for example, is approximately 880 kg/m^3 [26]). As Figure 2.10 shows, there is a small decrease in density with increasing chain length, but a significant increase in density with increasing degree of unsaturation [177, 178]. The density of ethyl esters is lower than that of equivalent methyl esters, but the reduction is typically less than 1%.

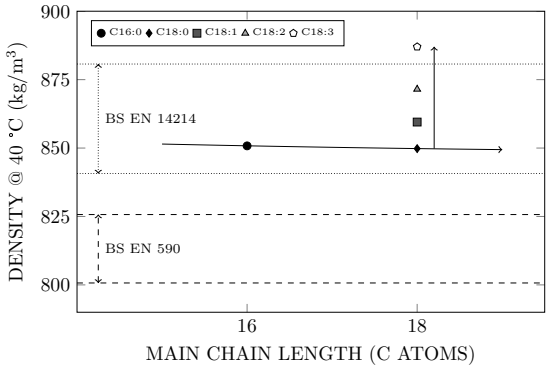

Figure 2.10: Densities of methyl esters at 40 °C, along with petrodiesel and biodiesel standards (data from [177, 178]). (NB. Standards are specified at a temperature of 15 °C, but here these values have been adjusted for the purposes of comparison. Methyl ester data at source shows a decrease in density of 19.3±1.2 kg/m^3 between 15 °C and 40 °C and this is the adjustment that has been applied.)

2.1.4.4 BULK MODULUS AND SPEED OF SOUND

The bulk modulus and speed of sound are two connected properties having to do with the compressibility of a fluid. The bulk modulus (E_v) is defined by Equation 2.1, where ∂P is

the change in pressure required to create a change in volume, ∂V. The speed of sound (c) is the familiar acoustic velocity, which describes the rate of propagation of a disturbance through a fluid, and is related to bulk modulus by Equation 2.2 (where ρ is density) [179].

$$E_v = -\frac{\partial P}{\partial V/V} \tag{2.1}$$

$$c = \sqrt{\frac{E_v}{\rho}} \tag{2.2}$$

As Figures 2.11A and 2.11B show, biodiesel typically has a higher bulk modulus and speed of sound than petrodiesel. Under the conditions studied by Tat and Van Gerpen [180], the biodiesel bulk modulus was 7.5–14% higher than that of petrodiesel, and its speed of sound was 1.5–4.5% higher. However, bulk modulus is also dependent upon the temperature and pressure of the fluid, increasing with pressure and decreasing with temperature [181]. The bulk moduli of petro- and biodiesel change at different rates as functions of pressure and temperature, and as a result the bulk modulus of biodiesel exceeds that of petrodiesel to a lesser extent as pressure increases [180, 182]. There is a similar convergence of speed of sound towards higher pressures [180, 183].

Both properties increase with increasing chain length and with increasing degree of unsaturation, and are fractionally lower with ethyl esters compared to methyl esters (the bulk moduli of ethyl stearate and linoleate are 2.7% and 1.4% lower than those of their methyl ester counterparts at 60 °C; the acoustic velocities of the ethyl esters are reduced by less, 0.7% and 0.5% respectively) [180, 184].

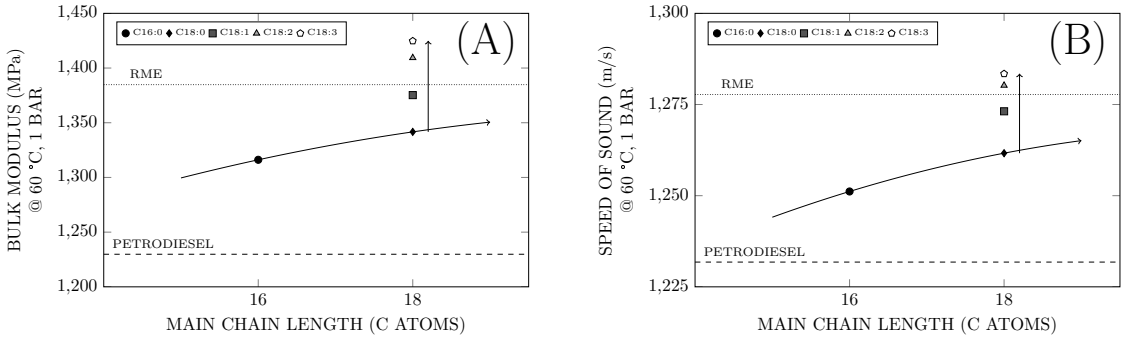

Figure 2.11: (A) Bulk moduli and (B) speeds of sound of methyl esters, rapeseed methyl esters and petrodiesel at 60 °C and 1 bar (data from [180]). (NB. RME plot is based on canola data at source, and petrodiesel on number 2 diesel.)

2.1.4.5 VISCOSITY

BS EN 590 specifies that the viscosity of automotive petrodiesel should be between 2–4.5 mm^2/s at a temperature of 40 °C; biodiesel has a slightly higher viscosity, and accordingly the allowable viscosity range specified by BS EN 14214 (at the same temperature) is higher – 3.5–5 mm^2/s [16, 17] (the value for RME is approximately 4.4 mm^2/s [26]). As Figure 2.12 shows, there is an increase in viscosity with increasing chain length, but a significant reduction with increasing degree of unsaturation [177, 178]. The viscosity of ethyl esters is slightly higher, by between 0.05–0.3 mm^2/s, compared to the methyl esters depicted.

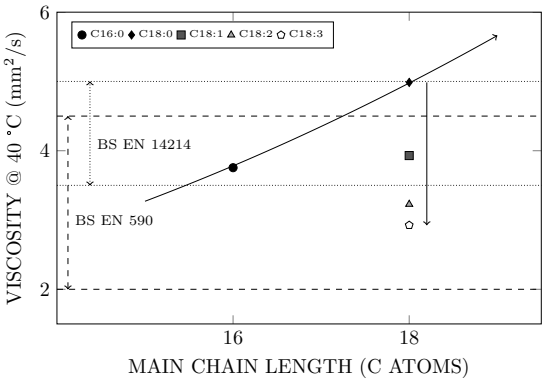

Figure 2.12: Measured viscosities of methyl esters at 40 °C, along with petrodiesel and biodiesel standards (data from [177, 178]).

2.1.4.6 SURFACE TENSION

The surface tension of biodiesel is likely to be higher than that of petrodiesel; representative estimates (from [185]) are illustrated in Figure 2.13. Surface tension increases with main chain length [186], and probably increases with increasing degree of unsaturation [185, 187] (although the latter trend is not always clear [186]). The length of the alcohol moiety has been found to have no significant effect, but the introduction of branching has been associated with a reduction in surface tension; in *iso*-propyl or *iso*-butyl esters of oleic acid, for instance, surface tension is 0.5 m/Nm and 1.5 m/Nm lower than in the equivalent methyl ester [187].

2.1.4.7 LUBRICITY

Lubricity is defined in terms of maximum wear scar diameter in BS EN 590, but is not addressed in BS EN 14214 [16, 17]. A standardised wear scar is produced by an oscillating

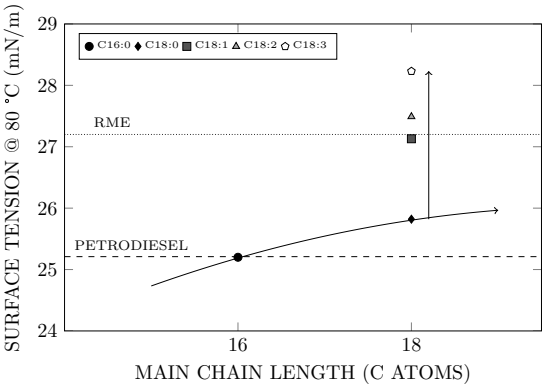

Figure 2.13: Estimated surface tensions of methyl esters, rapeseed methyl esters and petrodiesel at 80 °C (data from [185]). (NB. RME plot is based on canola data at source, and petrodiesel on number 2 diesel.)

ball in contact with a stationary plate immersed in the fuel [188]. The maximum wear scar diameter specified in BS EN 590 is 460 μm at a temperature of 60 °C.

The desulphurisation of petrodiesel is responsible for a substantial reduction in lubricity, not primarily because of the removal of the sulphur containing compounds themselves, but due to the loss of more highly polar nitrogen and oxygen containing compounds, as a consequence of the severe hydrotreatment processes used to produce ultra-low sulphur diesel (ULSD) [189]. As a result, petrodiesel meeting the ultra-low sulphur requirements of BS EN 590 (less than 10 mg/kg) cannot readily meet the lubricity standard without the use of additives (lubricity improving additives are usually acid or ester based [190]), making the lubricity imparting properties of biodiesel a distinct technical advantage.

As can be seen in Figure 2.14A, the average wear scar diameter is far lower for biodiesel than for an untreated ultra-low sulphur petrodiesel. Wear scar diameter is reduced with increasing chain length and generally with increasing degree of unsaturation, although the average methyl oleate value reported at the source [11] is slightly higher than that of methyl stearate. However, one can also see that the wear scar diameter of RME is smaller than that of any of the neat methyl esters. This is because some of the trace constituents, nominally contaminants, present in a typical biodiesel bestow greater lubricity upon the fuel – as evidenced by the reduced lubricity associated with refined biodiesels [191]. Especially, as Figure 2.14B shows, monoglycerides and free fatty acids are found to provide effective lubricity enhancement at low concentrations [11].

The data for butyl oleate presented in Figure 2.14B suggests that extension of the alcohol moiety does not offer any clear benefit in terms of lubricity over methyl oleate, although other sources report a consistent reduction in wear scar diameter with ethyl esters

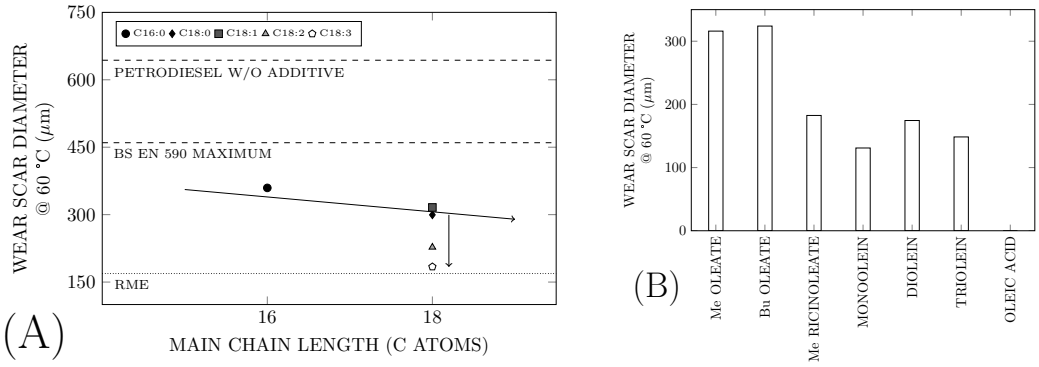

Figure 2.14: (A) Average wear scar diameters for methyl esters, rapeseed methyl esters and petrodiesel at 60 °C. (B) Average wear scar diameter for methyl oleate, compared to those of the equivalent butyl ester, the methyl ester of the equivalent hydroxylated fatty acid, mono-, di- and triglycerides of oleic acid, and the free fatty acid itself. (Data from [11, 192].)

compared to methyl esters [193]. The hydroxylated C18:1 methyl ester, methyl ricinoleate (C18:1-OH), exhibits superior lubricity, and its presence in high concentration in castor oil derived biodiesel facilitates significant lubricity enhancement of petrodiesel at very low blending ratios [194].

2.1.4.8 OXIDATION STABILITY

In the legislative standards oxidation stability is expressed in terms of induction period, which is the time for which a fuel sample can be exposed to air at a temperature of 110 °C before the rapid formation of oxidation products is detected [195, 196].

BS EN 590 specifies that automotive diesel should have an induction period exceeding 20 hours – a limit which accommodates biodiesel admixture into the fuel. It has been reported that after 24 hours at the standard conditions petrodiesel remained unoxidised [197], and based on data for low percentage (B2) biodiesel blends the petrodiesel induction period could be significantly longer than this [198]. BS EN 14214 specifies a minimum induction time of 8 hours for biodiesel, and this is a limit which biodiesels from many feedstocks are unable to meet without antioxidant treatment [26, 148].

Saturated alkyl esters tend to be highly stable (with induction times in excess of 40 hours at the standard conditions) [199]; it has been reported that the induction period of a highly saturated coconut oil derived biodiesel may even exceed that of petrodiesel [200]. Stability is lost with increasing degree of unsaturation, as is seen in Figure 2.15. In this case, the illustrated variation with chain length is based upon the monounsaturated esters of each given chain length (for all other properties – Figures 2.8–2.14 – it was based upon the saturates); an increase in stability is observed with increasing chain length. However,

oxidation onset temperature data shows that this trend does not hold for saturated esters, whose stability decreases slightly with molecular weight [199].

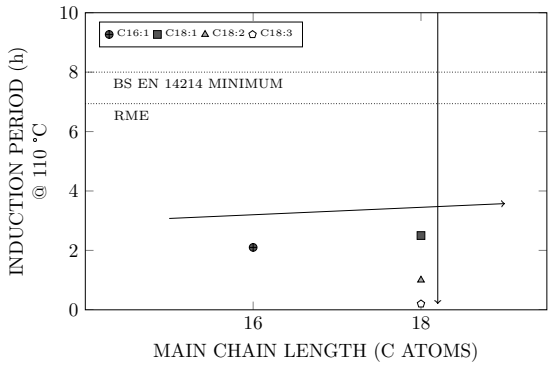

Figure 2.15: Oxidation stability – in terms of induction time – of unsaturated methyl esters and rapeseed methyl esters at 110 °C (data from [199, 201]).

Degree of unsaturation is seen to be the most critical factor affecting oxidation stability, with the introduction of even one double bond causing a very large reduction relative to the >40 hour induction period of saturated esters. *Trans* double bonds do not reduce stability by as much as their *cis* equivalents [199]. There is some indication that stability increases with length of the alcohol moiety (for unsaturated compounds) [141], although this is not entirely clear [199].

Note also that, as with lubricity, the oxidation stability of RME as a whole is better than that which might be anticipated on the basis of its major constituents; largely, this may be associated with the presence of natural antioxidants [201]. In vegetable oils tocopherols are generally the most important antioxidants [202], although in palm oil, for example, tocotrienols and carotenoids may also be present in significant quantities [203], and olive oil can contain large amounts of phenolic compounds [204]; however, tocopherols possess a greater degree of thermal stability and are therefore likely to remain in greater concentrations within a refined oil [202]. Synthetic antioxidants may also be added to biodiesel in order to improve stability [205].

Fats and oils, and the resulting biodiesels, may also contain trace species which promote oxidation and reduce stability. Chlorophyll and other pigments can increase sensitivity to photooxidation, preformed peroxides and hydroperoxides provide a ready source of initiation, and certain metals can catalyse the autoxidation process [202].

2.1.4.9 HEATING VALUE

The heating value of a fuel is the amount of heat released by its complete combustion, returning the products to the same state as the reactants, and is therefore equivalent to the difference in enthalpy between products and reactants [206]. Heating value is specified either as the higher heating value (HHV) or lower heating value (LHV). The distinction is that for the HHV the water returns to a liquid state, whereas for the LHV it remains as a vapour, and therefore the numerical difference between the two is equal to the latent heat of vaporization of the water in the products. The HHVs of both petrodiesel and biodiesel are approximately 7% higher than their respective LHVs, although for fuels with lower C/H ratios this difference is larger (e.g. 13.9% for methanol and 13.5% for liquified natural gas) [207]. In Figure 2.16A HHVs for methyl esters [208] and petrodiesel [207] are given. In Figure 2.16B, the heating values are converted into a volumetric form, indicative of the energy density of the fuel.

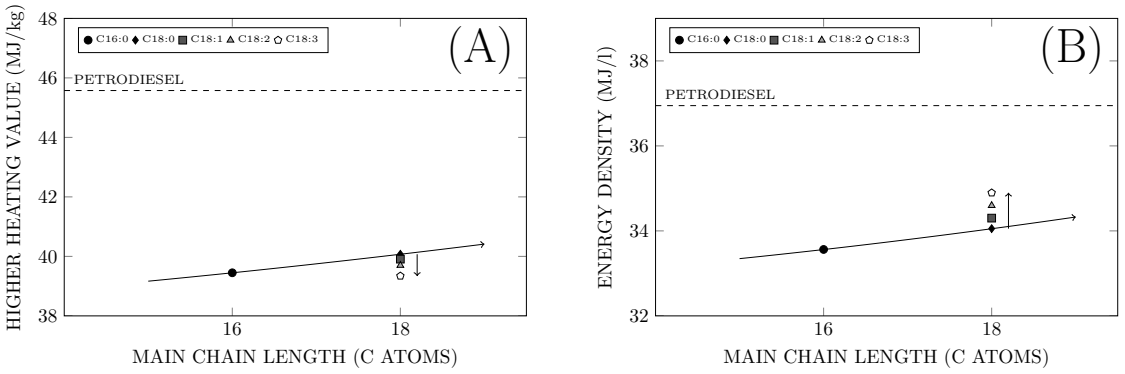

Figure 2.16: (A) Higher heating values and (B) energy densities of methyl esters and petrodiesel (data from [207, 208]). (NB. Petrodiesel plots are based on low-sulphur diesel data at source, and energy density values are calculated from densities at 40 °C as in Figure 2.10.)

By both metrics, the energy content of the biodiesel compounds is seen to be lower than that of petrodiesel. The methyl ester HHVs illustrated are 12–13.7% lower; this reduction is slightly larger than the values provided for a range of biodiesels in the review of Hoekman et al [103] suggest (10.1±4.1%), but in good accordance with the values compiled in *The Biodiesel Handbook* [209] (which show an average reduction of 12.9±1.6% compared to the petrodiesel value in Figure 2.16A). On a volumetric basis, the greater density of biodiesel (see Section 2.1.4.3) offsets its reduced HHV, so that the reduction in energy density relative to petrodiesel is not as large as the reduction in heating value. The energy density of the methyl esters depicted in Figure 2.16B is between 5.6–9.2% lower than that of petrodiesel.

Heating value and energy density both increase with increasing main chain length. Although HHV decreases with increasing degree of unsaturation, energy content in volumetric terms increases, due to the higher density of the unsaturated esters. The difference between methyl and ethyl esters in unclear, but based upon predicted enthalpy values (estimations by the Benson-Groups method given in [210]) the HHVs of saturated ethyl esters are slightly higher than those of saturated methyl esters (by less than 1%), but with increasing degree of unsaturation ethyl ester HHVs appear to be relatively reduced – the predicted HHV of ethyl linolenate is 2% lower than that of methyl linolenate. In volumetric terms, the lower density of ethyl esters means that there is little difference between the energy densities of saturated methyl and ethyl esters, but that unsaturated ethyl esters have a greater deficiency in energy content – the predicted energy density of ethyl linolenate (again, based on the enthalpy estimates in [210]) is 3% less than that of methyl linolenate.

2.1.4.10 CETANE NUMBER

Cetane number (CN) is a quantity representative of the ignition quality of a fuel. Fuels with a higher cetane number have higher ignition quality, autoignite more readily and hence have a shorter ignition delay when employed in a diesel engine. The CN scale was originally defined relative to 1-methylnaphthalene ($C_{11}H_{10}$) with a CN of 0, and *n*-hexadecane ($C_{16}H_{34}$, also called cetane) with a CN of 100. Cetane number and ignition delay are properties which will have particular relevance over the course of this thesis.

BS EN 590 specifies that automotive diesel must have a cetane number in excess of 51, and the same limit is also set for biodiesel in BS EN 14214. The CN of biodiesel often exceeds this value, but – as Figure 2.17 indicates – CN may be significantly affected by differing feedstock characteristics.

The *n*-alkanes in petrodiesel have higher CNs than their methyl ester counterparts; *n*-hexadecane, for example, has a CN around 17 points in excess of that of methyl palmitate (C16:1) [155]. However, the other classes of molecule found in petrodiesel act to suppress the CN of the fuel as a whole.

The branching present in *iso*-alkanes reduces CN; for example, 2-methylheptadecane has a CN 14 points lower than *n*-heptadecane (which has a CN of 105), and when the branch is located closer to the centre of the main chain, as in the case of 9-methylheptadecane, the reported cetane number is lower still, reduced by a further 25 points

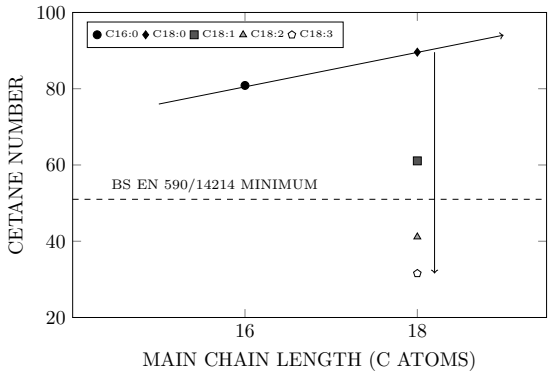

Figure 2.17: Average measured cetane numbers of methyl esters, along with petrodiesel and biodiesel standards (data from [155]).

[155]. Cycloalkanes also have lower cetane numbers than their straight equivalents – around 16 for cyclohexane compared to 46 for hexane, 40 for decalin compared to 72 for decane – but the addition and extension of straight alkyl side chains tends to progressively increase cetane number – methyl-, ethyl- and butylcyclohexane have cetane numbers of approximately 22, 36 and 48, respectively. Aromatics have the lowest cetane numbers of all; benzene has a CN of around 5, naphthalene of around 22. Although the presence of short side chains may actually reduce cetane number (due to effects associated with easily abstractable benzylic hydrogen atoms [211]), the tendency is for alkylbenzenes with longer straight alkyl side chains have higher cetane numbers – octylbenzene, for example has a reported CN of around 38 [155].

In general, increasing straight chain length increases cetane number, and this is reflected in the biodiesel data in Figure 2.17. However, the most significant difference in CN between the biodiesel constituents depicted in Figure 2.17 is the degree of unsaturation, with increasing unsaturation being associated with a sharp decline in CN; methyl linolenate (C18:3), which has three double bonds, has a CN of only 32, which is almost 50 points lower than that of the saturated equivalent, methyl stearate [155]. As with branching, the effect of the presence of a double bond on ignition tends to increase as it moves towards the centre of the main chain [212], although this relationship may not be entirely linear [213]. It is also reported that *trans* double bonds reduce CN more than their *cis* equivalents [213].

It is expected that increasing the length of the alcohol moiety will increase cetane number, however the available CN data is not conclusive in this regard, particularly when dealing with the relatively small differences that exist between methyl and ethyl esters. The average reported change in CN from methyl to ethyl esters of the species depicted in

Figure 2.17 is roughly -1±6, which is not very meaningful. C_3 alcohol (i.e. propyl and *iso*-propyl) esters have CN values roughly 1±5 points higher than methyl esters, while for C_4 alcohol (i.e. butyl, *iso*-butyl, 2-butyl) esters they are 5±5 higher, and with larger alcohol moieties (hexyl, 2-ethylhexyl, octyl and decyl esters) the reported increase over methyl esters becomes large, although still irregular – the CN difference ranging from 6–50 points [155]. Based on this, it appears reasonable to suggest that the length of the alcohol moiety does affect CN positively, although small changes may be masked by inaccuracies and inconsistencies in cetane number determination.

As an additional note, the oxidation of biodiesel as it ages has been reported to increase the cetane number of the fuel by 5–10 points [140].

2.2 OXIDATIVE AND PYROLYTIC PROCESSES AND PRODUCTS

In this section, the topics of fuel oxidation, ignition and pollutant formation will be introduced and then integrated into an explanation of the diesel combustion process. Although many of the processes of interest can be described by overall global reactions, a better understanding of the effects of fuel chemistry is obtained by considering the elementary reactions involved.

2.2.1 AUTOXIDATION

Autoxidation refers to the spontaneous oxidative deterioration that occurs when a compound is exposed to atmospheric oxygen [27]. Unlike the other processes discussed in this chapter, autoxidation is not a factor during combustion itself; rather, it can affect a fuel over the relatively prolonged time-period prior to its utilisation within an engine. It is an issue of critical importance to the practicalities of biodiesel usage, and warrants discussion here logically prior to the high-temperature in-cylinder chemistry that follows. As well as being the cause of the degradation of biodiesel, autoxidation is one of the processes responsible for the rancidification of fatty foods (alongside hydrolysis)[214], leading initially to the formation of hydroperoxides, which can then react and decompose to form a wide possible range of hydrocarbon species, including aldehydes, ketones, epoxides, furans, alcohols, acids and polymeric gums [215–217].

Autoxidation is an auto-catalytic process (meaning that the reaction products catalyse further reactions, such that the rate of reaction will typically increase with time [218])

involving a free radical chain mechanism (whereby radicals are formed by chain initiation, multiplied by chain branching, removed by chain termination, and numerically conserved in chain propagation reactions). The rate of autoxidation is accelerated by additional energy input, and practically this energy will ordinarily come in the form of heat – strictly, the application of heat makes the process one of thermal-oxidation [219], but here autoxidation will be taken as encompassing all unintentional liquid-phase oxidation of hydrocarbons. In relation to biodiesel, autoxidation is a concern under both the relatively cool conditions of storage, and the considerably warmer conditions encountered upon biodiesel contamination of the engine lubricating oil [220–222].

The autoxidation of a hydrocarbon (RH) is generally considered to begin with the formation of an alkyl radical (R) due to the presence or action of a catalyst or initiator (I), as described by Equation 2.3 [202].

$$\mathrm{RH} \xrightarrow{I} \mathrm{IH} + \mathrm{R} \tag{2.3}$$

The process of initiation can be effectively promoted by the generation of radicals catalysed by a variety of means, including (vastly simplified from source [215]):

- The presence of trace quantities of particular metals (such as cobalt, copper, iron, magnesium, manganese and vanadium; reports have indicated that copper appears to be an especially effective catalyst of autoxidation [141, 223]).
  - Processes involving direct electron transfer between the metal and a bond in the hydrocarbon offer the simplest route to metal-catalysed radical formation.
  - Metals may also catalyse the decomposition of existing hydroperoxides (ROOH), to form alkoxyl (RO) and hydroxyl (OH) radicals, or peroxyl (ROO) radicals and hydrogen.
- Exposure to light.
  - Although it is possible for ultra-violet (UV) light to generate hydrocarbon radicals directly, the process is primarily indirect, generating RO and OH radicals from preformed ROOH.
  - As well as being absorbed by peroxide O-O bonds, UV energy can also act upon carbonyl C=O bonds (as found in the biodiesel ester function) and C=C bonds found in unsaturated hydrocarbons.

– Photosensitizing compounds, including pigments (like chlorophyll) and molecules containing a carbonyl group, absorb energy from visible light which can be used to drive chemical reactions and form free radicals.

- The application of heat provides the energy required to break chemical bonds, create radicals and initiate autoxidation; in particular, thermal decomposition of preformed ROOH, breaking the O-O bond, is more likely at milder temperatures.

These points underline the importance of trace compounds in the initiation of the oxidation process, and also the critical role which is played, subsequent to global initiation, by oxidation products – namely, hydroperoxides. With regard to the bulk composition of a fuel, the ease with which radicals are able to abstract hydrogen atoms is critical to the rate at which autoxidation reactions proceed. Hydrogen abstraction is most facile at sites where the bond dissociation energy (BDE) is low; in Figure 2.18 the methyl linoleate (C18:2) molecule is presented, along with approximate BDE values for the different types of hydrogen-carbon (H-C) bonds that are found.

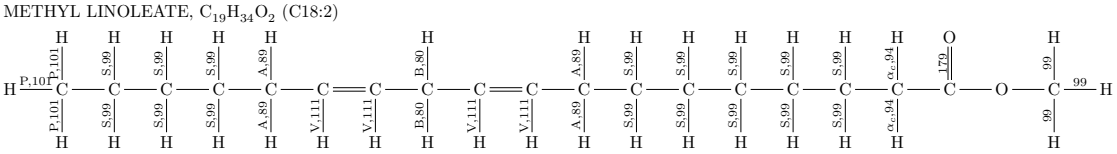

Figure 2.18: Bond dissociation energies in kcal/mol for methyl linoleate (bond dissociation energy data from [224, 225]). P: Primary H-C bonds. S: Secondary H-C bonds. A: Allylic H-C bonds. V: Vinylic H-C bonds. B: Bisallylic H-C bonds. α_c: H-C bonds at the α-carbonyl position.

The weakest H-C bonds in methyl linoleate are located at the bisallylic site, which is situated between the two double bonds. This site exists in all methylene-interrupted polyenes – a category which also includes methyl linolenate (C18:3), which has two such sites between its three double bonds. In methyl oleate (C18:1), which has only one double bond, the weakest H-C bonds are at the allylic sites, which are positioned at one remove from the double bond, as illustrated for methyl linoleate in Figure 2.18. The BDE of an allylic H-C bond (89 kcal/mol) is higher than that of a bisallylic H-C bond (80 kcal/mol), but still significantly lower than the BDE of a standard secondary H-C bond (99 kcal/mol) [224]. In saturated methyl esters, like methyl palmitate (C16:0) and methyl stearate (C18:0), the weakest H-C bonds are located at the α-carbonyl position (i.e. the carbon atom adjacent to the C=O bond) and have BDEs which are lower (94 kcal/mol) than those at other secondary sites, but higher than those of allylic and bisallylic H-C bonds [224]; this provides some explanation for the significant decline in oxidation stability with

increasing degree of unsaturation, described in Section 2.1.4.8.

The bisallylic H-C bond dissociation energy in methyl linoleate is likely to be lower than any equivalent found in petrodiesel. The saturated alkanes in petrodiesel have their weakest H-C bonds at secondary sites in *n*-alkanes, and tertiary sites in *iso*-alkanes and cycloalkanes with alkyl side-chains (with BDEs around 97 kcal/mol). In aromatic hydrocarbons, H-C BDEs are highest at sites within the aromatic ring (113 kcal/mol), but lowest at sites immediately adjacent to the ring – i.e. at benzylic sites (BDE around 90 kcal/mol), as found in alkyl-benzenes [224].

Although in general the BDEs of carbon-carbon (C-C) bonds are lower than those of H-C bonds, C-C bonds are largely broken in unimolecular decomposition reactions (which occur either at higher temperatures or by β-cission following hydrogen abstraction), rather than in the sorts of bimolecular abstraction reactions by which H-C bonds can be broken under relatively cool conditions. However, the BDE of the O-O bond which exists in ROOH is low enough (approximately 34 kcal/mol [226]) that unimolecular decomposition is possible under moderately elevated temperatures, or via exposure to UV light, or in the presence of a catalysing metal; hence, the importance of ROOH as a source of radicals.

The formation of the initial radical, R, is followed by the addition of molecular oxygen to the radical site to form a peroxyl radical, ROO. However, it is not necessarily as straightforward as the radical site being located at the position of the abstracted hydrogen; instead, in the case of the methyl linoleate molecule depicted in Figure 2.18, for example, where H-abstraction would be expected to occur at the bisallylic site, 11 (counting left, starting from the carbonyl group), following this abstraction electrons are delocalized across the double bonds, with greatest density existing at the center, such that oxygen addition occurs mostly at the electron deficient extremities of the double bonds, sites 9 and 13. Oxygen addition at site 9, and the accompanying relocation of double bonds is illustrated in Figure 2.19. For methyl linolenate, whose bisallylic sites are at 11 and 14, oxygen addition is mainly at 9 and 16 (although a significant fraction also occurs at the central 12 and 13 sites); for methyl oleate, with only one double bond, and allylic sites at 8 and 11, oxygen addition is distributed across sites 8–11 [215].

The ROO radical formed by O_2 addition to R can go on to abstract hydrogen from another RH, to form a new R radical, propagating the chain reaction. H-abstraction by ROO from RH is slow and highly selective, with a strong preference for bisallylic hydrogen atoms. H-abstraction by ROO from R'OOH (to form ROOH and R'OO) occurs

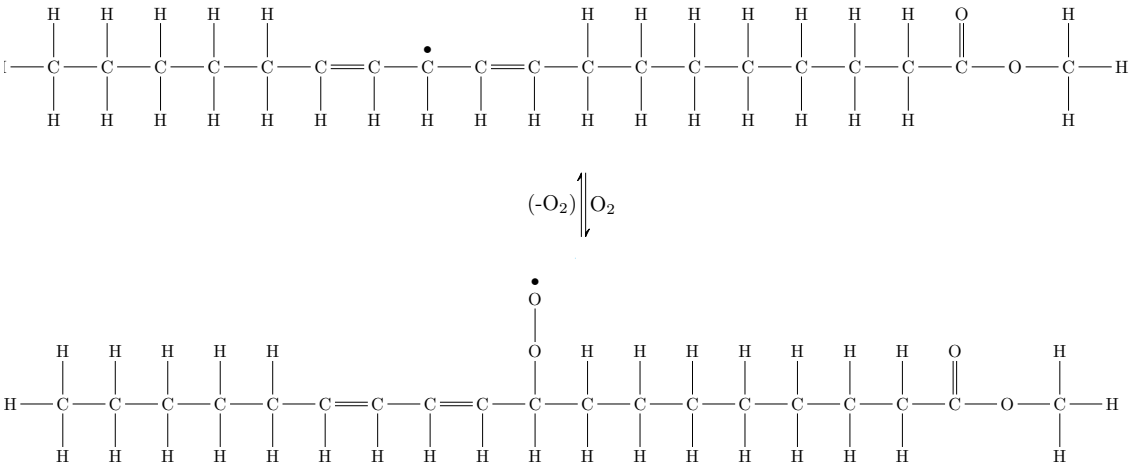

Figure 2.19: Addition of molecular oxygen to the alkyl radical derived by hydrogen abstraction from methyl linoleate [215].

relatively quickly – many times faster than H-abstraction by ROO from bisallylic RH sites, despite the higher BDE of the ROO-H bond (85 kcal/mol) – which affects reaction kinetics and product distributions, but not the overall scheme of oxidation. In the early stages of autoxidation, ROO is the main chain carrier; repeatedly initiating chains by the formation of R from RH, and forming the degenerate branching agent ROOH.

When ROOH decomposes to give RO and OH, both of which are far more reactive radicals than ROO, the system is driven towards rapid oxidation. RO reacts more quickly than ROO, and is able to abstract hydrogen from both allylic and bisallylic sites. OH reacts extremely quickly, and abstracts hydrogen atoms non-specifically; radical sites may then migrate to bisallylic positions where they exist, or alternatively the alkyl radicals formed may abstract hydrogen from unexploited bisallylic sites in other hydrocarbons.

However, because H-abstraction by ROO is slow, ROOH is not necessarily formed immediately, and other reaction pathways involving the ROO radical are also important – these include cyclisation (to form internal peroxides, and potentially polyperoxides, where 3 or more double bonds are present) and β-scission at the peroxide C-O bond (returning ROO to R and O_2 – the reverse of Figure 2.19). Once formed from ROOH, RO radicals can undergo similar types of reactions – cyclisation to form epoxides and epoxyallylic radicals, and β-cission, this time of a C-C bond, to form further alkyl radicals, along with alkanes and aldehydes or other oxo-compounds (which may remain among the final products of autoxidation, or undergo subsequent oxidation).

Alkyl, peroxyl and alkoxyl radicals may also recombine with one another, in what are often termination reactions. Recombination of two RO radicals forms a dimer peroxide

(R_1OOR_2), reaction of RO with R forms an ether (R_1OR_2) and reaction of two R radicals can form an alkane polymer (R_1-R_2). Reaction of two ROO radicals can be a termination step (Equation 2.4) but more usually contributes to a rapid increase in oxidation rates (Equation 2.5).

$$R_1OO + R_2OO \longrightarrow R_1OOR_2 + O_2 \tag{2.4}$$

$$R_1OO + R_2OO \longrightarrow R_1O + R_2O + O_2 \tag{2.5}$$

In summary, autoxidation is initiated by the generation of a radical, due to interaction of either the bulk hydrocarbon (RH) or some contaminant thereof (e.g. ROOH) with redox-active metals, or light, or heat. Directly or indirectly, this process forms an alkyl radical (R), which reacts with molecular oxygen to form a peroxyl radical (ROO). This radical can propagate autoxidation by abstracting further hydrogen atoms to form additional R radicals, and ROOH. Decomposition of ROOH yields more reactive alkoxyl (RO) and hydroxyl (OH) radicals, which abstract hydrogen atoms far more rapidly and accelerate the oxidation process. Cyclisation, cission and recombination of the radicals leads to the formation of a range of stable products.

Antioxidants can interfere with this process in a variety of ways [227]. Primary, or chain-breaking, antioxidants (AH) can donate hydrogen to R, RO or ROO radicals – having highest affinity for the latter – and hence prevent the formation of additional radical species by providing an alternative target for H-abstraction. The A radical formed is relatively stable, and does not itself readily participate in propagation reactions. Instead, it may recombine with other radicals, further reducing the radical pool. Hindered phenols and aromatic amines (like those studied in Chapter 6) are examples of primary antioxidants. Secondary antioxidants can affect autoxidation in different ways, interrupting the process at the point of induction by oxygen scavenging or quenching singlet oxygen, or by chelating metals and reducing their pro-oxidant activity.

2.2.2 IGNITION

2.2.2.1 OVERVIEW OF THE PROCESS

As an introduction to this section, the following quotation from Walker and Morley's chapter in Pilling's *Low-Temperature Combustion and Autoignition* [228] provides a valuable insight:

"In essence, the low-temperature chemistry prepares the mixture for ignition, the intermediate chemistry ignites it and the high-temperature chemistry burns it."

The boundaries between low, intermediate and high-temperature regimes are all dependent upon pressure and the low/intermediate division is strongly affected by the chemical structure of the fuel, as can be seen in Figure 2.20. The different regimes and the position of the boundaries between them result from the varying relative importance of several main kinetic pathways to chain-branching.

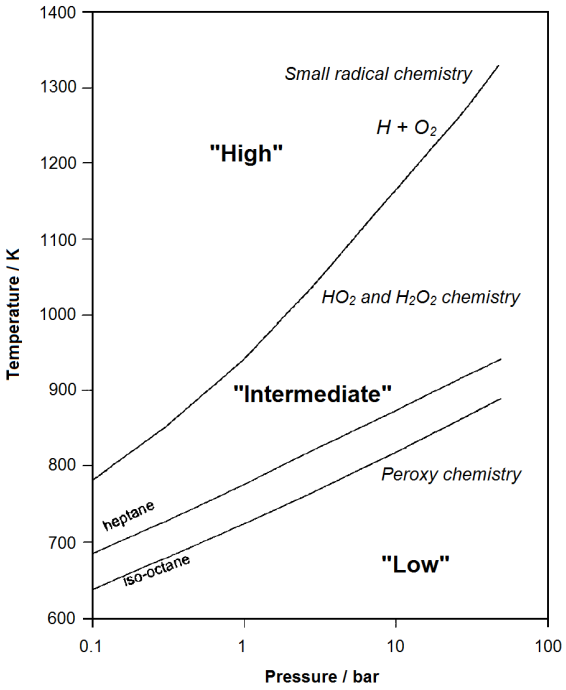

Figure 2.20: Regimes of hydrocarbon oxidation chemistry as delineated by the main kinetic chain-branching processes [229].

At low temperatures (below approximately 850 K under conditions relevant to a diesel engine), repeated oxidation and isomerisation of large alkyl radicals (R) leads to the formation of meta-stable ketohydroperoxide species, which provide chain-branching when they decompose at around 800 K [230]. The low temperature regime is terminated when the equilibrium of Equation 2.6 shifts to the left (which it does as temperature increases), such that dissociation of the peroxyl radical (ROO which is formed following O_2 addition to R) is favoured over stabilisation and subsequent isomerisation; below the *n*-heptane and *iso*-octane boundaries illustrated in Figure 2.20, peroxy chemistry is net-branching, above them, net-terminating [229].

$$R + O_2 \rightleftharpoons ROO \tag{2.6}$$

This gives rise to what is known as negative temperature coefficient (NTC) behaviour, which describes the phenomenon of decreasing reactivity with increasing temperature (in opposition to the usual trend) which is observed around the low/intermediate regime transition [231]; it appears to be within this region that reactivity differences between fuels are maximised (see, e.g., [232, 233]).

The pressure dependence of these boundaries is due to the collisional stabilisation of ROO involving a third body, which occurs more rapidly at high pressures, deterring dissociation [234]. However, for larger molecules stabilisation by these means is less important, because energy is able to be dissipated vibrationally [235]. The fuel dependence of the lower boundary is related to the strength of the bond that forms between R and O_2, and the ease with which isomerisation reactions are able to proceed [233].

At intermediate temperatures (between approximately 850–1200 K) branching via the low temperature pathways is diminished, and the high temperature branching pathways are not yet active. Towards the lower end of this range, reactions forming HOO, and from it H_2O_2 (Equations 2.7–2.9), are of the utmost importance.

$$H + O_2 + M \longrightarrow HOO \tag{2.7}$$

$$RH + HOO \longrightarrow R + H_2O_2 \tag{2.8}$$

$$HOO + HOO \longrightarrow H_2O_2 + O_2 \tag{2.9}$$

The species from which hydrogen is abstracted in Equation 2.8 is denoted here as RH, but this does not necessarily represent a parent hydrocarbon directly from the fuel (except in the very earliest stages of combustion); abstraction will occur where H-C bonds are weak, which may be at allylic or bisallylic sites in unsaturated components of the fuel, or may equally involve intermediate combustion products like aldehydes [229].

H_2O_2 is, like a kethydroperoxide species, essentially meta-stable and accumulates while the temperature is below approximately 1000 K, but once this temperature is attained it decomposes rapidly in the chain branching reaction given in Equation 2.10, rapidly increasing the radical population, leading to ignition and propelling the system towards the high temperature regime [230].

$$H_2O_2 + M \longrightarrow OH + OH + M \tag{2.10}$$

The upper demarcation in Figure 2.20 reflects the competition between Equations 2.7 and 2.11, with the former being increasingly competitive at higher pressures.

$$H + O_2 \longrightarrow OH + O \tag{2.11}$$

Although Equation 2.7 contributes to the ignition process in the intermediate regime, the relative unreactivity of HOO means that at higher temperatures it effectively becomes a termination reaction, while Equation 2.11 leads to a very fast multiplication in the quantities of highly reactive radicals that act to oxidise available hydrocarbons to ultimate products of mostly CO_2 and H_2O, accounting for the larger part of total heat release.

Fundamentally then, ignition occurs when a temperature is reached at which H_2O_2 decomposes to 2 OH, leading to a rapid rise in radical concentration, and pushing the system towards the high temperature regime; therefore, any factor which advances the point at which this critical temperature is attained will tend to lead to an advance in ignition. The highly fuel dependent low temperature peroxy chemistry is vital in this respect, since even a small quantity of additional low temperature heat release will expedite H_2O_2 decomposition, particularly in a diesel engine where the effects of early temperature rises are accentuated by compression. In terms of ignition behaviour in a diesel engine, it is largely the low temperature chemical kinetics that differentiate one fuel from another; in the following section the nature and causes of the differences between fuels will be explored.

2.2.2.2 LOW TEMPERATURE COMBUSTION CHEMISTRY

The oxidation scheme for alkanes illustrated in Figure 2.21 provides a foundational explanation of the process that is, for the most part, directly applicable to saturated alkyl esters and is also, with some added complexity, extendible to alkenes as well as the unsaturated esters of which biodiesel is predominantly composed.

At low temperatures oxidation is generally initiated by hydrogen abstraction from the fuel by O_2, to form an alkyl radical (R) and HOO. This reaction is slow beneath around 600 K, and this lower limit will change depending upon the strength of the relevant H-C bonds (increasing with increasing bond strength). Early in the reaction process, secondary initiation (i.e. H-abstraction by radicals, like OH, O and H) overtakes and dominates as by far the most significant means of initiation, simply because these reactions occur much more readily than those with molecular oxygen [228, 237]. When temperatures exceed

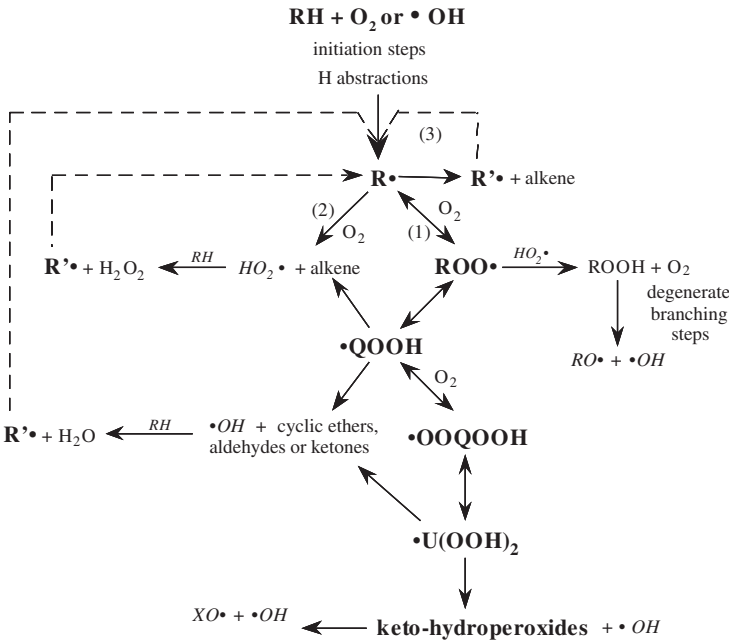

Figure 2.21: Simplified scheme for the primary mechanism of oxidation of alkanes [236].

around 1000–1200 K initiation by unimolecular decomposition (i.e. scission of C-C bonds) becomes dominant.

The alkyl radical can progress in a variety of ways. Decomposition by β-scission (i.e. breaking the bond between atoms 1 and 2 positions away from the radical site) becomes important at somewhat higher temperatures, around 850 K, and is a chain propagating step forming a smaller alkyl radical (R') alongside an alkene. The reaction of O_2 with an alkyl radical can generate a peroxyl radical (ROO) – illustrated for *n*-heptane in Figure 2.22 (and previously for methyl linoleate in Figure 2.19) or it can produce HOO and a conjugate alkene (*conjugate* meaning that it has the same number of carbon atoms as the parent alkyl radical [229]) via a concerted elimination reaction [238]. When low temperatures and small hydrocarbons are involved, conjugate alkenes are the major initial products of oxidation, but it is suggested that with increasing hydrocarbon chain length the conjugate alkene yield may be significantly reduced; this is related to the issue of vibrational stabilisation, mentioned previously [228, 235].

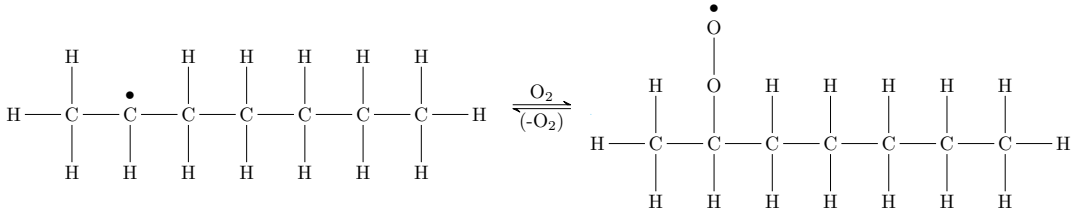

Figure 2.22: Addition of molecular oxygen to an alkyl radical (R) derived by hydrogen abstraction from *n*-heptane.

Note also that O_2 addition to ROO is reversible, as discussed earlier in relation to Equation 2.6; as temperature increases, the equilibrium of Equation 2.6 shifts to the left and dissociation is favoured. Dissociation of ROO occurs more readily when O_2 addition follows H-abstraction from a location where the original H-C bond was weak [233, 239]. As discussed in Section 2.2.1, H-C bond dissociation energies (BDEs) of common petro- and biodiesel constituents generally increase in the order (from weakest to strongest): bis-allylic, allylic, benzylic, tertiary, secondary, primary, vinylic, aromatic [224]. Note also that increasing BDE parallels reduced stability in the resultant radicals [240]. An explanatory illustration of the location and approximate strength of different bond types can be seen in Figure 2.23.

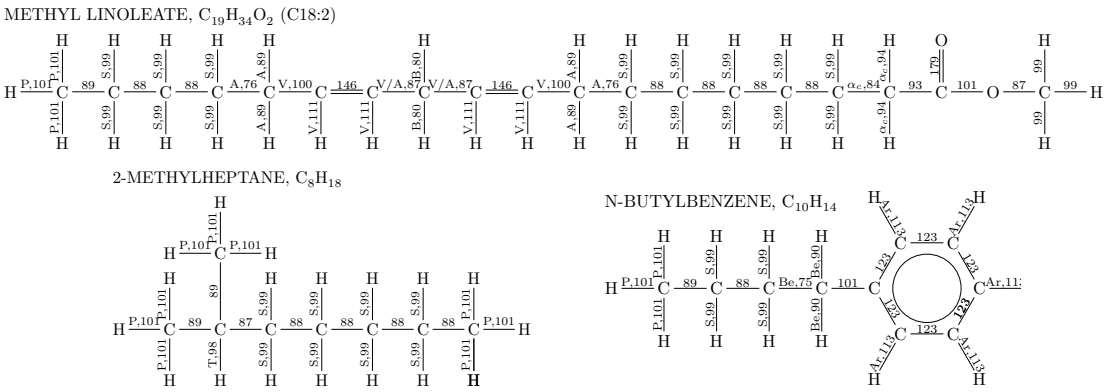

Figure 2.23: Bond dissociation energies in kcal/mol for methyl linoleate, 2-methylheptane and n-butylbenzene (bond dissociation energy data from [224, 225, 241]). P: Primary H-C bonds. S: Secondary H-C bonds. A: Allylic H-C and C-C bonds. V: Vinylic H-C and C-C bonds. B: Bisallylic H-C bonds. α_c: H-C and C-C bonds at the α-carbonyl position. T: Tertiary H-C bonds. Be: Benzylic H-C and C-C bonds. Ar: Aromatic H-C bonds.

Disproportionation reactions of ROO with other radicals (with HOO, for example, leading to chain branching via ROOH as shown in Figure 2.21) are possible, but above 600 K the rate at which isomerisation occurs is high enough that radical-ROO reactions become unimportant [236].

The most important route to low temperature chain branching involves isomerisation of ROO by internal hydrogen atom transfer to form a hydroperoxyalkyl radical, QOOH, where Q denotes a C_nH_{2n} hydrocarbon structure [235]. This is shown for *n*-heptane in Figure 2.24. The rates suggested for the isomerisation of ROO to QOOH depend upon the type of hydrogen atom being abstracted, as well as the ring strain of the isomerisation transition state formed. Suggested values vary between institutions [236]; in general, smaller (i.e. 5-membered) ring-states are less favourable, because they are essentially too tight and highly strained, whereas larger (6–8 membered) rings are less highly strained

and therefore more facile. In some reports, 8-membered rings are considered to be slightly more highly strained [242] (on the basis of a sort of over-extension [243]), but in other studies activation energy continues to decline with ring-size [228, 237, 244].

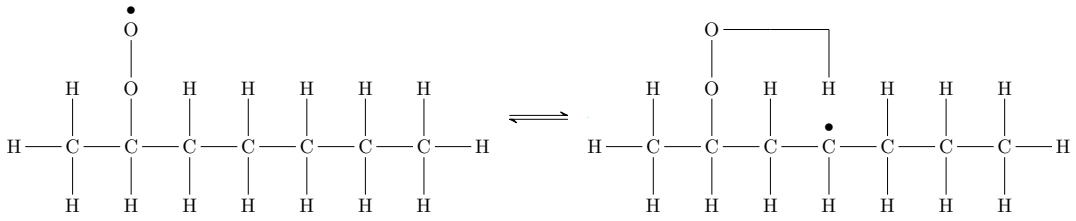

Figure 2.24: Internal hydrogen abstraction, forming a hydroperoxyalkyl radical (QOOH) from a peroxyl radical (ROO) via isomerisation through a 6-centred transition state.

The implication of this is that isomerisation to QOOH occurs most easily where transition states of a favourable size are best able to form; that is, when the saturated chain length is adequate.

The QOOH radical, like ROO before it, may either decompose or form an adduct with O_2 and isomerise. This is influenced by the size of the transition state ring through which QOOH formed [231]. Those formed through smaller (i.e. 5-membered) states primarily decompose to form an HOO radical and an alkene, whilst those formed through larger (i.e. 7- or 8-membered) states are more likely to react to form cyclic ethers and OH radicals – although this is a possibility for all QOOH species [231]. The type of cyclic ether that forms depends upon the proximity of the radical centre to the hydroperoxy group, which again depends upon the size of the transition state by which QOOH was formed. Cyclic ethers having 3-, 4-, 5- and 6-membered rings – called oxiranes, oxetanes, oxalanes (or tetrahydrofurans; these are the most abundant oxygenated products of low temperature *n*-alkane oxidation [245]) and oxanes (or tertahydropyrans), respectively – form following ROO to QOOH isomerisations through 5-, 6-, 7- and 8-membered transition states [239]. QOOH radicals formed through 6-membered [231, 246] or 7-membered [122, 247] isomerisations have the highest probability of subsequent O_2 addition and further isomerisation, progressing along the pathway to chain branching (although the 6-membered isomerisation state appears to have formerly been preferred in the literature [231], the 7-membered state has apparently replaced it, on the basis that the 6-membered ring may lead to decomposition to an alkene, an aldehyde and an OH radical [247]).

Addition of O_2 to QOOH forms a peroxyhydroperoxyalkyl radical, OOQOOH, and this is followed by an internal hydrogen abstraction to form a dihydroperoxyalkyl radical, $U(OOH)_2$. In practice $U(OOH)_2$ radicals can be involved in a range of different reactions

and isomerisations, but, particularly in the case of an alkane, the most common subsequent operation is decomposition to form a ketohydroperoxide (OQOOH) and OH, as shown in Figure 2.25 [248]. This is on the basis that the second isomerisation, OOQOOH to $U(OOH)_2$, would be likely to abstract the remaining hydrogen attached to the other carbon atom bonded to a hydroperoxy group, since the barrier to abstraction is slightly lower at this location [235]. OQOOH acts as a degenerate branching agent, decomposing by scission of the O-O bond upon reaching a temperature of around 800 K, to yield OH and an oxygenated alkyl radical species [236].

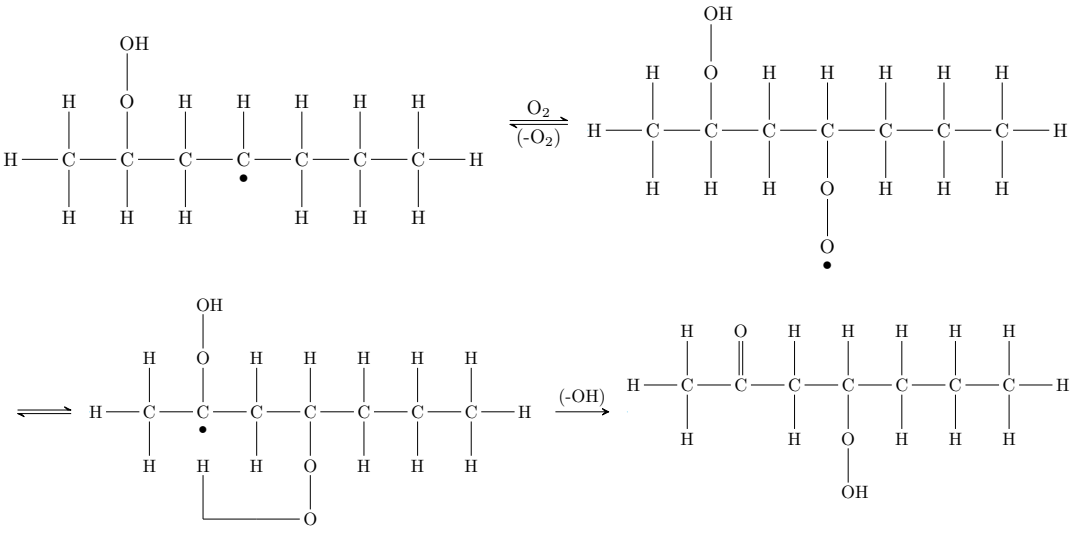

Figure 2.25: Addition of molecular oxygen to an hydroperoxyalkyl radical (QOOH) to form a peroxyhydroperoxyalkyl radical (OOQOOH), followed by isomerisation to form a dihydroperoxyalkyl radical ($U(OOH)_2$), and subsequent decomposition, liberating an alkoxyl radical (OH) and leaving a meta-stable ketohydroperoxide.

The presence of double bonds, in alkenes and unsaturated alkyl esters, affects both low and high temperature reaction chemistry. At higher temperatures, where initiation is largely by cleavage of C-C bonds, the reduced dissociation energies of allylic C-C bonds (76 kcal/mol, compared to 88 kcal/mol for standard secondary C-C bonds, as seen in Figure 2.23 [224]) make them the preferred breaking points. Double bonds themselves are far more resistant to cleavage, as are the adjacent vinylic C-C bonds. By influencing surrounding H-C bond strengths, and hence determining the likely H-abstraction sites, the position of double bonds also affects where β-scission will occur, and the products generated [249].

The low temperature pathway to chain branching is essentially the same for alkenes as for alkanes, as illustrated by Figure 2.26, but with the extra possibility of radical additions to the double bond. However, critical changes to the thermochemistry of oxygen addi-

tion and isomerisation reactions mean that alkenes suffer a reduction in low temperature reactivity in comparison with alkanes.

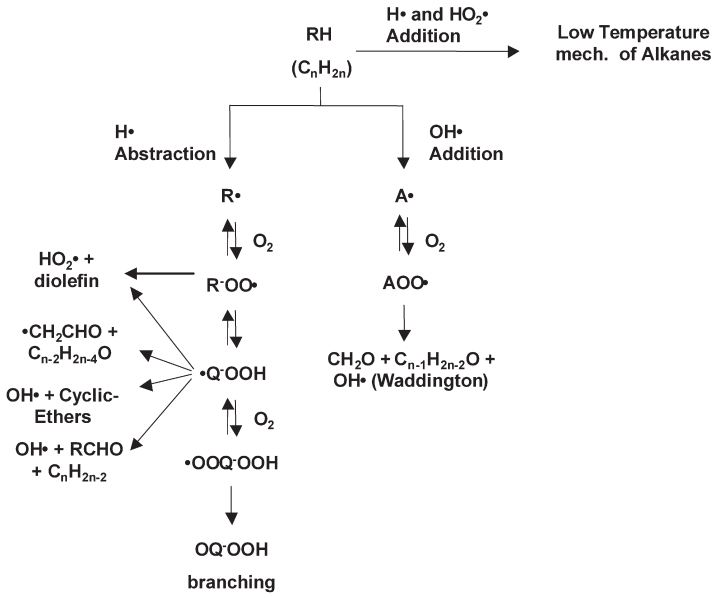

Figure 2.26: Primary oxidation reactions of alkenes [249].

H-abstraction from an alkene is most facile from allylic sites (see Figure 2.23). However, subsequent addition of O_2 to the allylic alkenyl radical formed by such an abstraction, first, occurs less readily than addition to a secondary site, and, second, forms a less stable ROO adduct, which is more prone to decomposition [233, 249]. The lower BDE of allylic H-C bonds may also promote the concerted elimination of HOO (along with the formation of an alkadiene), relative to the equivalent reaction forming HOO and an alkene from an alkyl radical and O_2 [249]. As a result of these factors, ROO levels are lower during alkene oxidation than alkane oxidation [233].

The low stability of ROO adducts formed from allylic alkenyl radicals means that they provide less support for the isomerisation reactions which lead to chain branching [233]. Therefore, although H-abstraction from allylic sites is favoured, H-abstraction from standard secondary sites in alkenes still plays an important role in low temperature chemistry [249].

Isomerisations of alkenyl ROO radicals to form QOOH may be impeded by double bonds, making the transition state ring more highly strained and therefore render its formation less favourable [233, 250]; the available saturated chain length adjacent to the peroxy group is critical to the size of the transition ring which is able to form (which is part of the explanation given for the decline in reactivity often observed as the double bond moves towards the centre of the chain, as mentioned in Section 2.1.4.10). Where

possible, isomerisation reactions abstracting hydrogen from an allylic site are faster than those abstracting from secondary sites [249].

Further addition of O_2 to QOOH and isomerisation to form OOQOOH is encumbered by the same complications as described above; allylic sites encourage H-abstraction, but form relatively weak bonds with O_2 that provide less support for isomerisation, and transition states are inhibited by the presence of double bonds. The products of alkenyl QOOH decomposition – by cission of C-O, O-O or C-C bonds, or cyclisation – differ from those of alkyl QOOH, but are similar in kind.

The possibility of radical addition to the alkene double bond is a point of novelty, but does not lead to a significant departure from the alkane mechanism. Addition of H forms an alkyl radical, R, and the addition of HOO forms a cyclic ether and an OH radical [236]. The most common products of radical addition are hydroxyalkyl radicals (A), formed when OH adds to the double bond. Subsequent O_2 addition forms an unstable hydroxyalkylperoxyl (AOO) radical which decomposes to form an aldehyde and an OH radical; this pathway becomes less significant with increasing saturated chain length [249].

The presence of branching in *iso*-alkanes also reduces low temperature reactivity, and increases ignition delay times. Referring once more to Figure 2.23, it can be seen that, in the case of 2-methylheptane, the weakest H-C bond (though only by a small margin) is located at the tertiary position [224]. As a result this is the preferential site for initial H-abstraction. Subsequent O_2 addition to form ROO, isomerisation to form QOOH, and O_2 addition at the new radical site to form OOQOOH, occur without significant deviation from the alkane mechanism illustrated in Figures 2.24 and 2.25. However, the second internal H-abstraction to form $U(OOH)_2$, which in an alkane is most facile when abstracting from the carbon bonded to the OOH moiety (as in Figure 2.25) due to the slightly reduced BDE at this site, may have to proceed differently for an *iso*-alkane in which, if the initial abstraction was from the tertiary carbon, there is not a weakened secondary hydrogen atom to abstract from this position [232]. This means that the second internal hydrogen abstraction must be of a more strongly bonded hydrogen atom, and therefore occurs less quickly; Figure 2.27 can be compared with the equivalent steps in Figure 2.25 for clarification.

Following this, the resulting $U(OOH)_2$ progresses somewhat differently to that formed in the alkane system, but still forms OH and a degenerate branching agent. It is the second isomerisation step which is most substantially affected by the presence of branching. As the

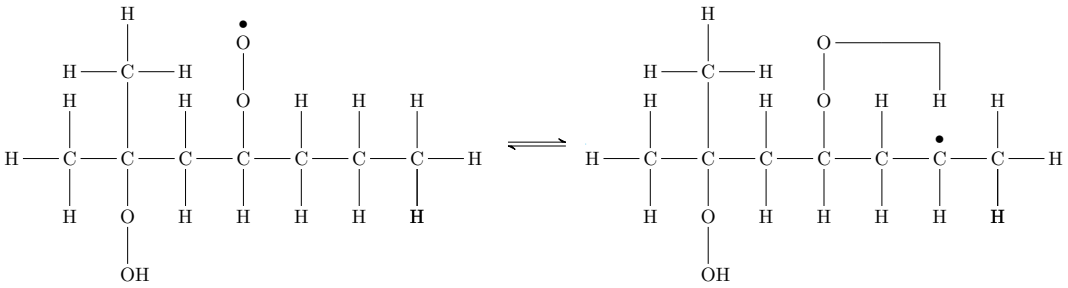

Figure 2.27: Second isomerisation, to form $U(OOH)_2$ from QOOH, in the low temperature oxidation of 2-methylheptane.

length of the straight chain in an *iso*-alkane increases, the overall probability of initiation occurring at the tertiary site is reduced (although it remains the most viable single site), and so the difference in low temperature reactivity between *n*- and *iso*-alkanes is reduced [232]. The presence of additional strong primary H-C bonds is also a factor which tends to depress low temperature reactivity, although, again, as the chain length increases the effect that these have on the branching pathways diminishes [232].

Aromatic species have relatively little low temperature reactivity; their low temperature ignition depends upon the presence of either a single sufficiently long alkyl side chain (e.g. *n*-propylbenzene) or multiple alkyl chains sufficiently close to one another (e.g. *o*-xylene) which may react through paths similar to those described above [251]. The presence of the aromatic ring increases resistance to ignition for several reasons. The high BDE of aromatic H-C bonds (see Figure 2.23) makes abstraction from the ring unlikely at low temperatures, even for highly unselective OH radicals [228]. Besides ipso-addition reactions – in which alkyl side chains are replaced by radicals [252] – and O atom additions (a factor which may also contribute to reduced reactivity [211]), the ring itself remains largely unaffected until higher temperatures are reached [228].

Critically, alkyl side chains introduce low BDE benzylic H-C bonds (shown for *n*-butylbenzene in Figure 2.23), which are favourable sites for H-abstraction, but do not lend themselves as well as secondary sites to subsequent O_2 addition [253]. Although O_2 addition at the benzylic site, followed by the familiar pathway to chain branching, does have a significant probability at low temperatures, the relative unreactivity of the initial R in this case means that reactions with other radicals (such as HOO), to form RO, which subsequently decomposes to form benzaldehyde and an alkyl radical, are also important [254]. As alkyl side chain length increases, the proportion of initial H-abstractions made from the benzylic site decreases, and O_2 addition and isomerisation steps become more

favourable, which is why the ignition delay of an aromatic decreases with increasing length of the alkyl side chain (as discussed in connection to cetane number in Section 2.1.4.10) [252].

Alkylated cyclohexanes generally possess greater low temperature reactivity than alkylbenzenes, but still significantly less than *n*-alkanes of equivalent carbon number [253]; the reactivity of ethylcyclohexane (C_8H_{16}) is reportedly close to that of an alkene with the same chemical formula, 1-octene [255]. Like *iso*-alkanes, cycloalkanes with an alkyl side chain also contain a weakened tertiary H-C bond, and like aromatics they contain a ring structure, although in this case it is saturated. As for *iso*-alkanes, there is a slight preference for abstraction of the tertiary hydrogen, and abstraction from the primary site is less probable, but rates from all sites are comparable [256]. At low temperatures, formation of R is almost always followed by O_2 addition to form ROO, just as with other alkanes. However, isomerisation to form QOOH is not as facile for transition states including the cyclohexane ring, because the CH_2 groups within the ring are unable to rotate [246]. Isomerisation to QOOH appears to be more favourable when the initial H-abstraction is from cyclic carbon sites adjacent to the alkyl chain [256], or from non-cyclic sites [257]; formation of QOOH is considerably reduced when the initial abstraction is from the tertiary site, or from the three cyclic sites across the ring from the alkyl chain [256].

In summary, low temperature oxidation is initiated most frequently by hydrogen abstraction from the sites with the weakest H-C bonds – secondary sites in *n*-alkanes, allylic sites in *n*-alkenes (bisallylic in alkadienes), tertiary sites in *iso*-alkanes and alkylated cyclohexanes and benzylic sites in alkylbenzenes. This is a matter of probability, and so as the length of the saturated chain in any compound increases, the probability of abstraction from secondary sites becomes higher. The R radical formed following H-abstraction can subsequently react with O_2 to form ROO, which may then isomerise to form QOOH. The ability of a molecule to facilitate this transition depends, first, upon the reactivity of the R radical and the stability of the ROO adduct (these factors are related to the initial H-C bond strength, and are less favourable at allylic and benzylic sites, for example); second, the ease with which a suitably sized transition ring is able to form (ideally requires 2 or 3 saturated carbon atoms adjacent to the peroxy site, and may be impeded by the presence of double bonds or ring structures); third, the strength of the H-C bond being broken by the isomerisation. Other pathways can propagate the chain reaction, but the route to chain branching passes through this isomerisation. Following isomerisation, a further

O_2 addition can occur, and subsequently another isomerisation to form $U(OOH)_2$. Unless more weakly bound hydrogen atoms are available, the second internal H-abstraction is typically from the carbon atom at which the initial O_2 addition occurred; in *iso*-alkanes, this path is not available, and so the second isomerisation may be slower. $U(OOH)_2$ decomposes to produce an OH radical and a ketohydroperoxide – the degenerate branching agent whose own decomposition at around 800 K increases the radical population, generates heat release and drives the system towards ignition.

2.2.2.3 BIODIESEL AND ITS EFFECTS

In general, biodiesel is subject to the same mechanisms described above for alkanes and alkenes. The additional feature which requires some further consideration is the ester group. Approximate bond strengths surrounding the group are shown for methyl linoleate in Figure 2.23 (although there is some variety in the literature values [258], the values provided give a reasonable reflection of the pertinent trends). The carbonyl C=O bond itself is very strong, and may remain unbroken throughout the entire combustion process [259]. The C-O bond between the carbonyl C and the alkoxy group is also relatively strong, but the C-O bond to the alkyl group is weaker than a typical secondary C-C bond [225], and the α-carbonyl C-C bond even more so, making these two sites favourable for unimolecular decomposition at higher temperatures.

The α-carbonyl H-C bonds are also significantly weakened, and in saturated fatty acid alkyl esters abstractions of these hydrogen atoms are therefore thought to be the preferred means of low temperature initiation [250, 260, 261]. It may also be the case that slightly reduced H-C BDEs within the alkyl ester group at the site adjacent to the oxygen atom (i.e. the primary C in a methyl ester, where H-C BDEs are 99 kcal/mol in Figure 2.23, compared to typical primary H-C BDEs of 101 kcal/mol, or the secondary carbon in an ethyl ester – BDEs of around 97 kcal/mol compared to typically 99 kcal/mol – again, these values are drawn from [225]) increase the competitiveness of these sites, as seen for methyl decanoate in [258]. In unsaturated biodiesel compounds, H-abstraction from allylic and bisallylic sites is strongly favoured [233].

The differences in probable sites of initiation, for both saturated and unsaturated fatty acid alkyl esters, also affect the location, likelihood and products of subsequent decompositions by β-scission – becoming increasingly important as temperatures increase; for example, β-scission to form methyl acrylate ($C_4H_6O_2$, or C3:1), following H-abstraction

from the α-carbonyl site, is of relatively minor importance at lower temperatures [261] but is highly significant once O_2 addition becomes thermodynamically unfavourable [260, 262].

Following O_2 addition to R, radicals formed via abstraction from sites along the main alkyl chain proceed much the same way as those formed from alkanes or alkenes. O_2 addition to an R radical formed via H-abstraction from a bisallylic site forms an even less stable ROO adduct than O_2 addition to an allylic alkyl radical [233]. For ROO radicals initiated by abstraction from sites within the alcohol moiety, ROO to QOOH isomerisation may progress through a 7- or 8-membered transition state including the ester group; such a ring is slightly more highly strained and hence isomerisation is less facile than would ordinarily be the case [263]. Evidence for the latter reaction has been observed, based on the presence of 5-membered ring cyclic ethers (which form following isomerisation to QOOH through a 7-membered ring state) with the ester group within the ring, found in the oxidation products of methyl palmitate [264] and methyl decanoate [263]. However, experimental results also indicate that the current models overpredict the quantity of cyclic ethers based on hydrogen abstractions from all sites around the ester function [263].

Overall, the oxidation models seem to predict similar low temperature reactivity for methyl esters and *n*-alkanes of closely equivalent size. Herbinet et al [265] report slightly higher conversion of *n*-hexadecane compared to a range of saturated methyl esters (from methyl decanoate to methyl stearate) at the lowest temperatures, but slightly lower conversion of *n*-hexadecane through the negative temperature coefficient zone, as seen in Figure 2.28.

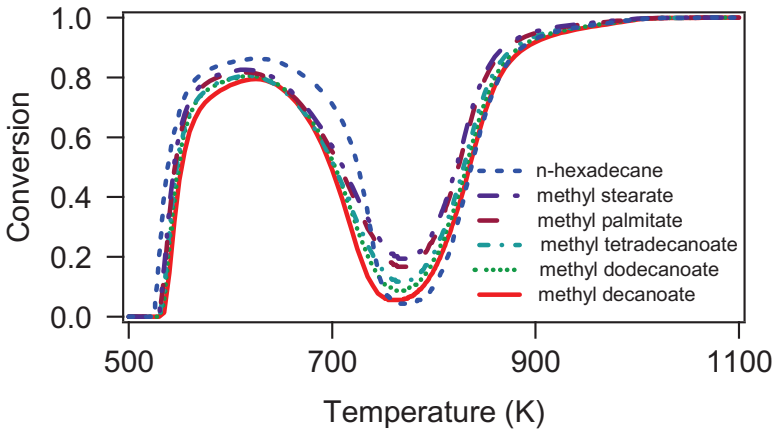

Figure 2.28: Comparison of the conversion of methyl esters from C_{11} to C_{19} and *n*-hexadecane in a jet-stirred reactor [265].

Some possible differences in the pathway to branching are illustrated by Figure 2.29 [263]. Most significant is an apparent increase in the rate of formation of cyclic ethers

from the QOOH radical ($HOOC_{11}H_{20}O_2$), and consequently reduced formation of the ketohydroperoxides which provide chain branching. This could plausibly provide some explanation for the lower reported cetane numbers of methyl esters compared to *n*-alkanes, discussed in Section 2.1.4.10. However, since larger amounts of cyclic ethers have been observed in the oxidation of *n*-hexadecane compared to methyl palmitate [264], this may not be a hypothesis entirely in accordance with the experimental results.

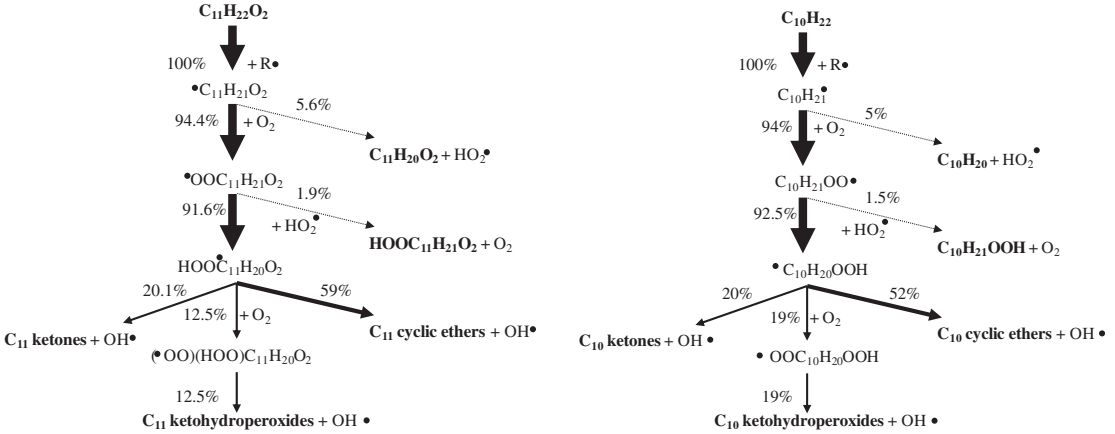

Figure 2.29: Flow rate analyses for the oxidation of methyl decanoate ($C_{11}H_{22}O_2$) and *n*-decane ($C_{10}H_{22}$) in a jet-stirred reactor; 650 K, 1.06 bar, $\phi = 1$, inlet fuel mole fraction of 0.0021 and residence time of 1.5 seconds [263].

Although the modelling literature does not currently appear to offer any definitive explanation for the lower cetane number of alkyl esters relative to their equivalent *n*-alkanes (except for the smallest examples [266], where the explanations are not necessarily scalable to actual biodiesel constituents), the discussion in Section 2.2.2.2 hopefully makes plain why the cetane number of biodiesel is typically higher than that of petrodiesel – i.e. the relative lack of branching, ring structures and aromaticity in biodiesel – and what factors determine whether or not this will be the case in practice; for example, a more highly unsaturated biodiesel, whose molecules contain more double bonds will be likely to have a lower CN, whilst a low aromatic content petrodiesel, on the other hand, will be likely to have a higher CN.

2.2.3 PARTICULATE

2.2.3.1 DEFINITION

Eastwood [267] defines particulate as all emissions from a combustor which deposit on a filter, and further divides the category into five more specific classes, three of them volatile – the sulphate fraction, nitrate fraction and organic fraction – and two of them non-volatile

– the carbonaceous and ash fractions. The first division, of volatility, differentiates the portion of deposits that will evaporate when heated, from those that won't; the latter are generally formed within the combustor itself, the former adhere to existing particles or condense subsequent to the end of combustion (i.e. in the exhaust system). Particulate is also commonly divided according to solubility (in dichloromethane), rather than volatility, but although the volatile and soluble fractions include largely the same components, some of the volatile species are insoluble, and so the volatile fraction is generally slightly larger [268].

The volatile sulphate fraction is comprised mostly of sulphuric acid (H_2SO_4) and associated water, the nitrate fraction primarily of nitric acid (HNO_3), and the organic fraction refers to any of a wide range of condensed species that may either be original constituents of the fuel or lubricating oil (alkanes, aromatics, esters, etc.) or intermediate remnants of incomplete combustion (aldehydes, ketones, ethers, etc.). The non-volatile ash fraction is a collection of inorganic compounds, mostly metals, and the carbonaceous fraction is the solid black matter that gives smoke its colour, being made mostly of carbon and roughly approximated at eight parts carbon to one part hydrogen (on a molecular basis, i.e. C_8H) [267, 269].

There are a variety of size categorisations applied to particulate; it is common to talk about nucleation (D_p (particle diameter) < 50 nm), accumulation (50 nm $< D_p < 1000$ nm) and coarse ($D_p < 1000$ nm) mode particles, because these groupings represent the trimodal lognormal distribution that mass weighted particle concentrations tend to follow [270]. Other classifications include PM10 ($D_p < 10$ μm), PM2.5 (also called fine particles, $D_p < 2.5$ μm), ultrafine particles ($D_p < 100$ nm) and nanoparticles ($D_p < 50$ nm). All of these are shown, along with an example of mass and number weighted size distributions from a diesel engine, in Figure 2.30 [270].

2.2.3.2 MOTIVATION OF INTEREST

Particulate emissions have detrimental environmental and health effects, making them a serious cause for concern [271]. Unlike pollutants such as CO_2 and NO_x, which are ecologically undesirable but are not necessarily an engineering problem, per se, particulate formation is evidence of inefficient combustion and can exacerbate maintenance issues (for instance, by contamination of the lubricating oil, leading to abrasion [272–274], and reduced pumpability as a result of increased oil viscosity [275]). The fact that particulate

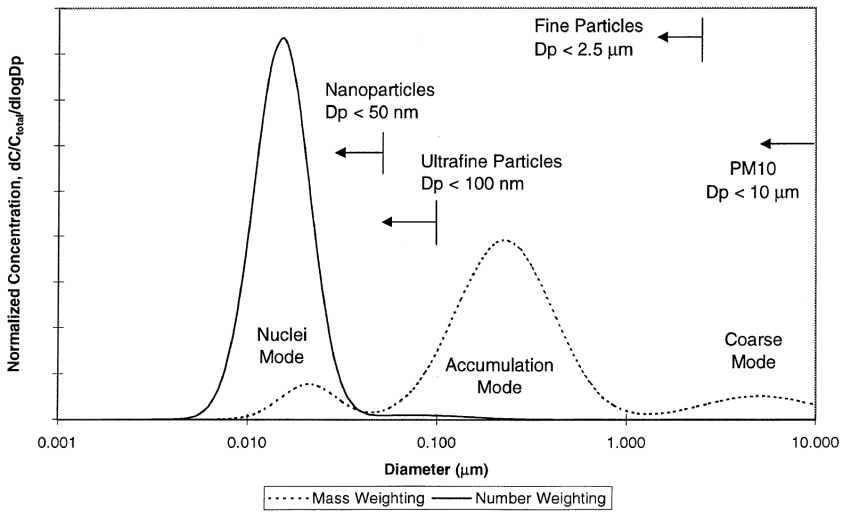

Figure 2.30: Example of a diesel engine exhaust particle size distribution with both mass and number weightings shown [270].

is associated with both political and technical disadvantages makes knowledge relating to its formation and abatement an attractive strategic research focus [276].

The presence of soot particles in the atmosphere, or deposited on the Earth's surface (in snow or sea ice, for instance [277]), alters the planetary albedo; that is, the global mean planetary reflectance, or the proportion of solar radiation incident upon the Earth which is reflected or scattered back into space without absorption (this value is estimated at approximately 30–34%) [278]. The extent to which an aerosol or contaminant affects the albedo depends upon the extent to which it scatters or absorbs radiation, and therefore soot, being darkly coloured, decreases mean reflectance and contributes to global warming [279–281]. Additionally, because soot radiates heat to its surrounding air, it reduces relative humidity and therefore cloudiness [282]; and, of course, soot inclusion in snow and ice, has both an immediate darkening effect, and the resulting longer-term consequence that the snow and ice warms and melts more readily in sunlight, and may eventually disappear entirely, further reducing the reflectance ratio of the planet. It is suggested that black carbon emissions make the second largest contribution to global warming, after CO_2 [283]. By absorbing light on its way to the surface, soot may also make the world dimmer, in some regions by as much as 10% [283].

Increased daily concentrations of fine particulate have been consistently linked to increased rates of mortality and higher hospital admissions [284, 285]. In the short term, existing respiratory and cardiovascular problems can be made worse by inhalation of airborne soot, and long term exposure may cause cancer, diseases of the heart and lungs, and can stunt lung development in children [286].

Some studies have found that carbon black alone doesn't cause an inflammatory response when inhaled, suggesting that it is the organic compounds that soot transports into the body (and possible interactions between these compounds and metallic elements also contained in particulate) that cause inflammation [286]. However, it has been indicated elsewhere that certain inflammatory responses see greater expression under exposure to diesel soot stripped of its organic fraction, than they do when exposed to either the organic fraction itself, or to carbon black, implying that it is not only the organic compounds, but the surface properties and shape of soot that affect its toxicity [287]. Polycyclic aromatic hydrocarbons (PAH) and other adsorbed organic species can transfer directly from a particle to a cell membrane, without the particle itself being uptaken [288, 289]; although there is some variation in opinion, it has been found that even very small ultrafine particles do not themselves pass into systemic circulation [290]. Ultrafine particles are, however, able to penetrate more deeply into the lungs, and have more damaging health effects as a consequence of their ability to enter into the interstitium [291].

In addition to the chemicals of which a soot particle is natively comprised, species that can be generated by (or formed by the body in response to) particulate are also important [286]. In particular, the production of reactive oxygen species (ROS), like peroxides and hydroxyl radicals, is induced by the presence of soot both in vivo and in vitro [292, 293], and these species put oxidative stress on living cells [294]. A large proportion of the pathways leading to the formation of ROS are dependent upon the trace quantities of transition metals found in soot from diesel engines, and where these metals are absent (or significantly less abundant, in soot from flames, for example) ROS generation is reduced – although not entirely nullified [295]. ROS may result from the metabolism of PAH [293], but the presence of large quantities of quinoid radicals in soot has been put forward as the most significant factor [286]. These quinoid radicals can, by a process of redox cycling, repeatedly generate ROS whilst being regenerated by other reducing agents [296]; hence, simultaneously promoting oxidative attack and depleting the antioxidants required to assuage oxidation.

2.2.3.3 MECHANISMS OF FORMATION

In the following sections, it is primarily the formation of soot, or the carbonaceous fraction of particulate, that is discussed. The treatment of the subject is general; the specificities of soot formation within a diesel engine are included in the broader description of diesel

combustion provided in Section 2.2.6. However, some reference to the exhaust process is made in the final section (Section 2.2.3.3.5), in order to incorporate details relevant to the volatile fraction of particulate, and the effects of cooling and dilution on the development of particulate as a whole.

Soot forms, develops and is consumed by the following set of processes [297]:

1. Fuel decomposition and precursor formation.
2. Nucleation or inception of particles from PAHs.
3. Particle growth by surface addition of gas phase species, particle coalescence and agglomeration.
4. Carbonisation.
5. Oxidation.

Although it is conceptually useful to consider these steps in sequence (as a description of the evolution of an individual soot particle), in any practical combustion system they will be to some extent coincident, with the degree of spatial and temporal separation depending upon the type of combustor; a laminar diffusion flame occupies the most sequential extreme, a well-stirred reactor the least [298].

2.2.3.3.1 PRECURSOR FORMATION

In the presence of sufficient oxygen, fuel hydrocarbons will undergo division into progressively smaller intermediate compounds, before complete conversion to CO_2 and H_2O. The early stages of fuel oxidation have been described in Section 2.2.2. Where temperatures are high enough to facilitate reaction but the requisite oxygen is unavailable, the small hydrocarbons formed by scission of larger species can instead react with one another, to form mono- and bicyclic aromatic molecules, which subsequently grow to form polycyclic compounds of increasing molecular weight. The varieties of hydrocarbon formed from the decomposition of a fuel depend upon environmental factors like temperature and oxygen availability, but also upon the chemistry of the fuel itself. The presence of features like double and triple bonds, or cyclic and aromatic structures, alters bond strengths within a molecule (as seen in Figure 2.23) and shifts the preferential sites of hydrogen abstraction (and subsequent β-scission), and unimolecular dissociation [276]. Consequently, the proportions and quantities of the different soot precursors which are generated is altered by the chemistry of the fuel, and hence the rate at which the processes of soot inception and growth proceed is also affected.

It is the formation – or, when using fuels containing aromatic species, the addition [276] – of the first ring structures that is considered to be the rate controlling element in the soot formation process; this is because the growth steps of the large polycyclic molecules which lead to soot nucleation are far more rapid than the production of the first aromatic rings [299]. Additionally, it is the rate of initial ring formation that is most significantly affected by changes to the fuel. That is to say, fuel chemistry affects the pathways of fuel decomposition, these pathways determine the concentrations and varieties of resulting breakdown products, and the types of breakdown products available influences the relative importance of the different routes by which aromatics may ultimately be generated [300].

Figure 2.31 [276] shows a variety of reactions forming one- and two-ringed aromatic species from smaller hydrocarbons. These are instructive because they indicate the types of species that are likely to be critical to the formation of soot, chart progress from the realm of small precursors to aromatics, and show the beginnings of typical aromatic growth processes.

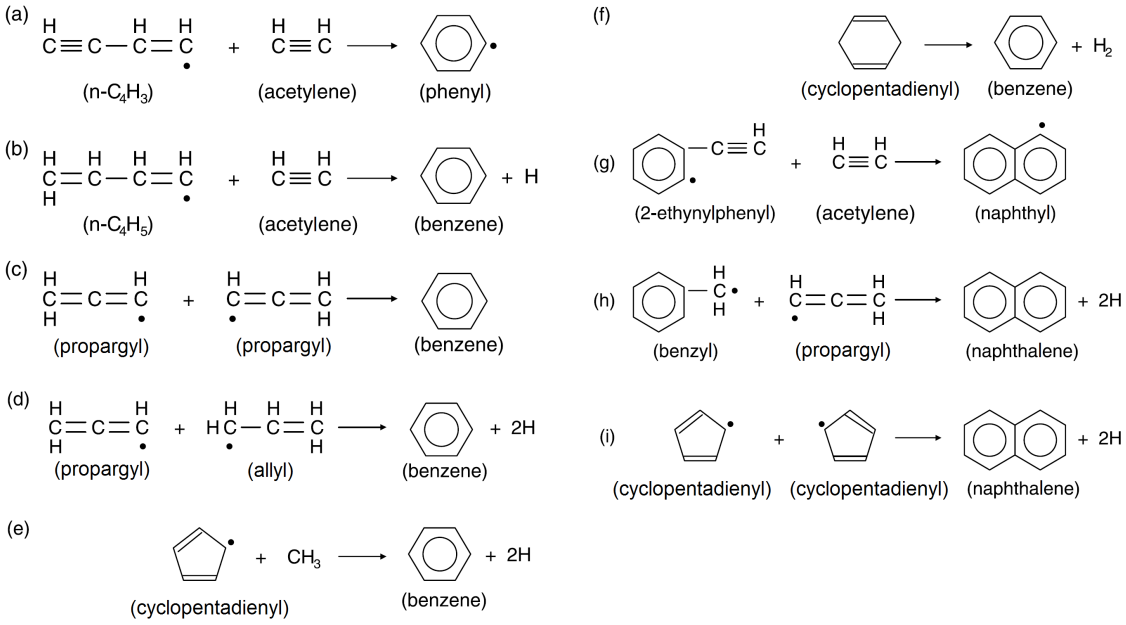

Figure 2.31: Important reactions that form single- and two-ring aromatic hydrocarbons [276].

Historically, reactions involving acetylene (C_2H_2) seem to have been at the heart of the proposed models of soot chemistry [297]. In Figure 2.31 (a) and (b), the first aromatic ring forms following the reaction of C_2H_2 with n-C_4H_3 and n-C_4H_5. n-C_4H_3 and n-C_4H_5 may themselves be formed by reactions involving C_2H_2 [301], but in the case of higher molecular weight fuels they are more likely to be derived from fuel molecules or intermediate species which decompose to form 1,3-butadiene (C_4H_5); this potentially includes any alkene whose double bond is not terminal [302]. These reactions provide an ostensibly favourable means

of aromatic formation, because C_2H_2 is always readily available in hydrocarbon flames [276]; Frenklach refers to acetylene as *"the most abundant building block"* [303]. However, it appears that, although acetylene retains a critical position in the overall soot formation process, emphasis has shifted to other reactions with respect to initial ring formation [304] – specifically, Miller et al [305] identify the reactions depicted in Figure 2.31 (c), (d) and (i) as being probably the most important.

The propargyl radical (C_3H_3) is important because it is readily formed and relatively stable at high temperatures [306]. These properties are a consequence of electron delocalisation; i.e. propargyl is a resonantly stabilised free radical (RSFR), as are allyl (C_3H_5), cyclopentadienyl (C_5H_5) and benzyl (C_7H_7) radicals. Formation rates of RSFRs are higher, because hydrocarbons preferentially decompose to resonantly stabilised configurations, as bond dissociation energy is negatively correlated with the stability of the resulting radical [240], making reactions leading to the formation of RSFRs particularly facile. For related reasons, RSFRs react slowly and form only relatively weak bonds with stable molecules like O_2, leading to low rates of destruction [276, 305]. The combination of high formation rates and low consumption rates inevitably leads to the possible accumulation of relatively high concentrations of C_3H_3 (and other RSFRs).

While *n*-C_4H_3 and *n*-C_4H_5 are not resonantly stabilised, their isomers *i*-C_4H_3 and *i*-C_4H_5 are, which may mean that the concentrations of the *n*- isomers are relatively low, therefore rendering the reactions depicted in Figure 2.31 (a) and (b) somewhat less important [307]. However, other investigators [303] contend that this is dependent upon the difference in stability between the *n*- and *i*- isomers, and, based on lower estimates of the difference, the reactions in Figures 2.31 (a) and (b) may still be significant. Alternatively, it has been proposed that, although the reaction between *i*-C_4H_5 and C_2H_2 is slower than that involving *n*-C_4H_5, greater quantities of the former isomer may make its reaction with acetylene an important contributor to the formation of aromatics [308]. However, even if concentrations of *i*-C_4H_5 are high, it is expected to react quickly with H to form propargyl and a methyl radical, which may limit the quantities of benzene that are formed from it, via addition of C_2H_2 [309].

Propargyl recombination, as seen in Figure 2.31 (c), is the simplest RSFR + RSFR reaction, directly forming a non-cyclic C_6H_6 product, which can undergo rapid sequences of isomerisation to form more stable aromatic C_6H_6 species including benzene and fulvene [310]. This is thought to be the most important reaction in the cyclisation process in the

majority of flames [311]. The reaction of propargyl with allyl, shown in Figure 2.31 (d), is given secondary status, and proceeds through non-cyclic and cyclic intermediates to form fulvene, which can be converted to benzene by H-atom assisted isomerisation [311]. Propargyl can be formed by the reaction of methylene (CH_2) and acetylene (C_2H_2), and by hydrogen abstraction from the C_3H_4 isomers propyne and allene [306], but when using larger hydrocarbon fuels it is primarily produced by the latter process [312]. Since the majority of C_3H_4 species form from the allyl radical (C_3H_5), it follows that most extant C_3H_3 is also formed through C_3H_5, and the importance of allyl in the soot formation process becomes clear. This explanation is aided by Figure 2.32 [313], which shows reaction pathways in an *n*-butane flame. Although the chemistry of *n*-butane itself is not representative of a typical diesel fuel, the allyl radical is formed directly from the unimolecular decomposition of most 1-alkenes [302], and 1-alkenes are the most common decomposition product of alkyl radicals at temperatures above 900–1000 K [236].

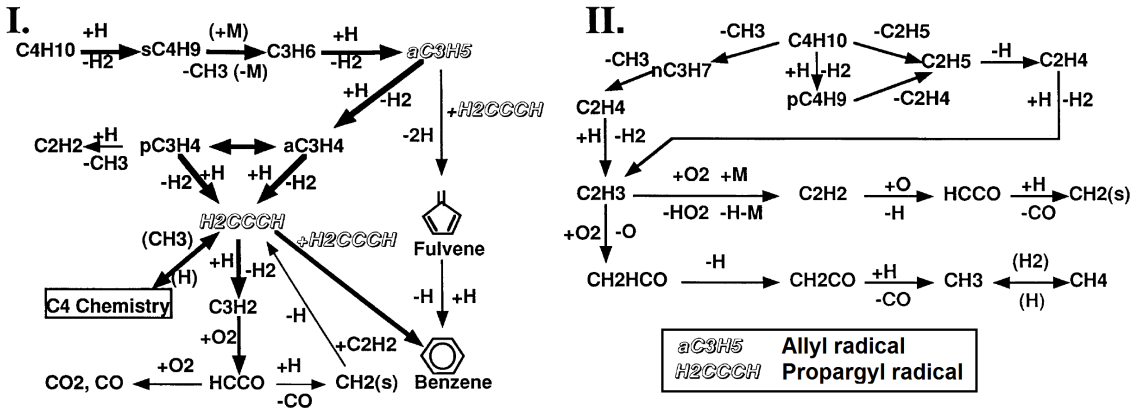

Figure 2.32: Reaction flux/pathway diagrams for the two important reaction sequences leading to reaction intermediates and combustion by-products that occur in an *n*-butane-oxygen-argon flame. I: Pathways initiated by hydrogen abstraction from a secondary carbon. II: Pathways initiated by H-abstraction from a primary carbon (down) or unimolecular decomposition (left and right). Resonantly stabilised free radicals italicised and inset, arrow thickness represents relative importance of pathway [313].

Reactions involving the cyclopentadienyl radical (C_5H_5) have also received attention, although they are likely to be of lesser importance except in those cases where there is the possibility of direct formation from the fuel of either the radical itself [309] or of an alternative C_5 RSFR which could subsequently be cyclised and dehydrogenated to form C_5H_5 [314]. In lieu of formation from the fuel, production of the radical, or larger radicals containing the same cyclopentadienyl moiety, via the oxidation of other aromatic species is also possible [315, 316]. Two pathways involving C_5H_5 are depicted in Figure 2.31 (e) and (i). In Figure 2.31 (e) cyclopentadienyl undergoes ring expansion following reaction with a methyl radical. Although the methyl radical is not resonantly stabilised it is relatively

unreactive and is therefore able to accumulate in significant quantities [276]. It is also possible for the bicyclic aromatic naphthalene ($C_{10}H_8$) to form from the reaction of two cyclopentadienyl radicals, as seen in Figure 2.31 (i), and by similar pathways ring addition to larger species such as indenyl (C_9H_7) may occur [315, 317]. As such, this last process can contribute to both the formation of the first aromatic rings and to further aromatic growth.

Where fuels contain cyclohexane, the formation of benzene is possible by stepwise radical dehydrogenation [318]. Cyclohexadiene can be converted to benzene, as in Figure 2.31 (f), by two further hydrogen abstractions [276]. However, in typical flames, where fuel decomposition is dominated by unimolecular decomposition rather than hydrogen abstraction, dehydrogenation is a less significant source of aromatics [319].

2.2.3.3.2 AROMATIC GROWTH

Figure 2.31 (g) depicts the addition of acetylene to a 2-ethynlphenyl radical (C_8H_5) to form naphthalene, and is an example of one stage of one version of the HACA or hydrogen abstraction C_2H_2 addition mechanism of aromatic growth. A complete illustration [320] of the same theoretical sequence from the phenyl radical (C_6H_5) to the naphthyl radical ($C_{10}H_7$) can be seen in Figure 2.33A; in Figure 2.33B, a similar route to naphthalene (proposed by Bittner and Howard [321]) is presented. In Figure 2.33A, the second acetylene molecule is added to the aromatic ring, and in Figure 2.33B it adds to the end of the first acetylene.

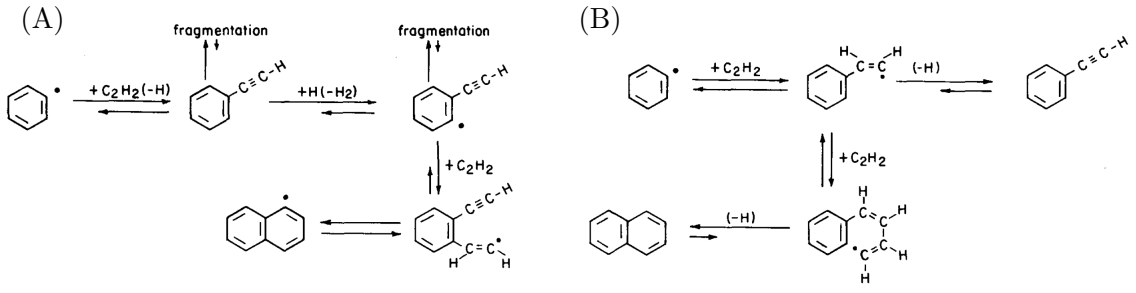

Figure 2.33: Reaction pathways for the formation of two-ring aromatics in (A) the original Frenklach mechanism [320] and (B) the Bittner-Howard mechanism [321].

It has been suggested [322], based on experimental results which provided evidence of reaction pathways similar to those in Figure 2.33, that the Frenklach route (Figure 2.33A) may be more likely to proceed by hydrogen migration around C_8H_7, rather than hydrogen abstraction to form C_8H_5 – the intermediate seen in Figure 2.31 (g) and Figure 2.33A. The process incorporating hydrogen migration is shown on the central path in Figure 2.34

[323].

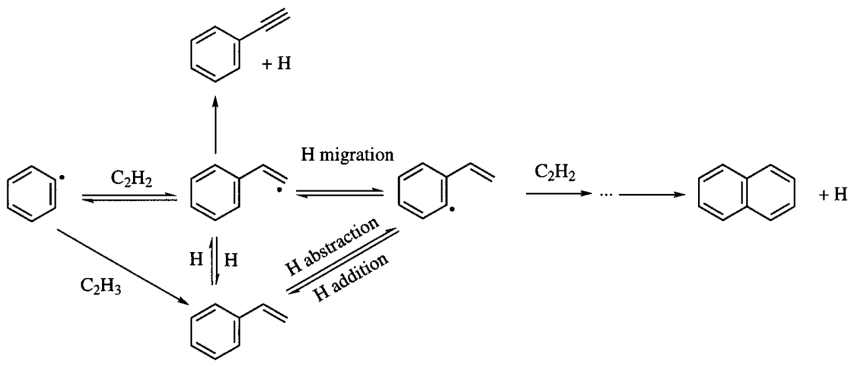

Figure 2.34: Reaction path diagram showing the role of H migration in the overall reaction path from phenyl to naphthalene [323].

Following the addition of the second ring, the HACA mechanism is thought to proceed through the type of reactions depicted in Figure 2.35, to ever larger PAH species. Possibly, considerations relating to hydrogen migration will also have some bearing on the later process; in principle one can see that Figure 2.35 is generally an extension of Figure 2.33A, and that any systematic adjustment affecting the latter might apply equally to the former.

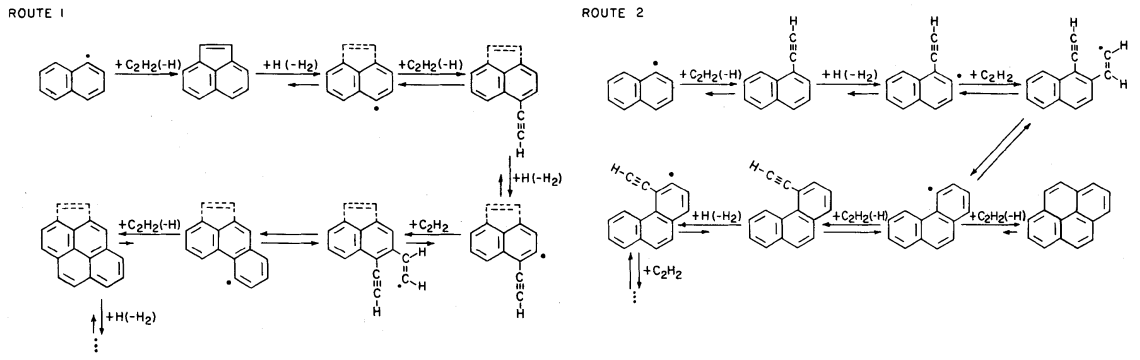

Figure 2.35: Reaction pathways for the formation of fused polycyclic aromatics [320].

Another mechanism of hydrogen abstraction and acetylene addition, proposed as an explanation for the evolution of larger polycyclic aromatic hydrocarbons, involves Diels-Alder reactions in a bay closure mechanism, potentially following dimerisation of smaller PAH species [324]. This also provides an explanation for the types of PAHs observed in flames, particularly with regards to their compactness. An illustration of the system can be seen in Figure 2.36, with Figure 2.36A showing the bay closure mechanism, and Figure 2.36B showing examples of PAH dimerisation, followed by subsequent bay closure. It has been reported, however, that this process is likely to be too slow to compete with the conventional HACA mechanisms [325].

Figure 2.31 (h) shows the reaction between two RSFRs, benzyl (C_7H_7) and propargyl (C_3H_3) radicals, as a potential route to naphthalene. Further aromatic growth by similar

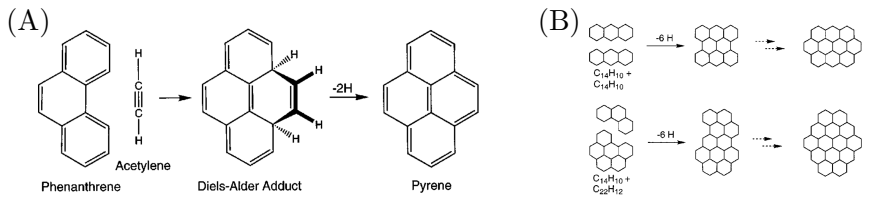

Figure 2.36: (A) The "benzogenic Diels-Alder reaction" with phenathrene (as an example) and acetylene. (B) Examples of condensation reactions of small PAHs, followed by Diels-Alder reactions forming the most compact PAHs [324].

additions of C_3H_3 to naphthyl ($C_{10}H_7$) and phenalenyl ($C_{13}H_9$) radicals have also been proposed [326]. As mentioned in the previous section, reactions like that depicted in Figure 2.31 (i), involving cyclopentadienyl and larger PAHs containing the cyclopentadienyl moiety, are also thought to contribute to aromatic growth [315, 317].

2.2.3.3.3 PARTICLE INCEPTION AND GROWTH

Although it is commonly understood that soot particles develop from PAH species, the means by which the transformation occurs remains to be clarified [327]. Continuation of the processes of aromatic growth, such that a single PAH might keep on expanding and expanding by the steady addition of precursor species, until reaching size enough to condense, has been found to be an insufficient theoretical model to explain the size of observed particles and the time scale of soot inception [303, 328]. The combination of multiple PAHs is therefore a necessary consideration.

How PAH species combine is the subject of debate. Dimerisation of PAHs as small as pyrene ($C_{16}H_{10}$), forming stacks held together by van der Waals forces, has been proposed as a possible first step in the nucleation of soot [328]. Collisions between these dimers and other PAH species could lead to the formation of trimers, tetramers, etc., chemical growth reactions would simultaneously continue the expansion of each PAH sheet within the stack/cluster, and subsequent collisions would continue to increase the size of the body until it evolved into a solid particle [303]. Although subsequent studies have suggested that under flame conditions the dimerisation of pyrene is unlikely to be important [329], larger PAHs, particularly those with attached aliphatic chains through which collisional energy can be dispersed, are believed to facilitate dimerisation and the growth of clusters [330, 331]. Differences in the structure and functionalisation of a PAH may also contribute to localised π-electronic states, which induce radical characteristics and can increase the strength of the binding forces holding dimers together [332]. Another suggestion is that hydrogen abstraction from PAHs to produce aromatic radicals could lead to chemical

coalescence, forming aromatic structures with aliphatic linkages [332, 333].

Nascent soot particles can continue to grow by the same types of processes as large PAHs, colliding and reacting with surrounding gaseous hydrocarbon species [334]. However, reactions between gas phase species and PAHs within a particle are thought to be slower than those involving gas phase PAHs, on the basis that growth species do not have the same degree of access to the reactive sites [335]. Collisions between particles and uncondensed PAH clusters allow the clusters to condense on particle surfaces, adding to total particle mass whilst leaving total particle number unchanged. As the quantity of particles within the reaction zone increases, and the individual particles grow and become less reactive, condensation becomes a significant means of particle mass growth [336]. Generally, surface growth reactions which add mass to existing nuclei are likely to be responsible for a greater proportion of total mass growth than particle inception, although this is dependent upon combustion conditions [267].

As the quantities of soot particles increase, collisions between them, resulting in the formation of agglomerates, become more important; agglomeration decreases the total particle number without affecting total particle mass. Single particles are initially approximately spherical, but depending upon their size and age may possess varying degrees of solidity [267]. For instance, younger, smaller particles may be sufficiently malleable and yielding to permit total coalescence of multiple bodies into a single larger spherule. Older particles, on the other hand, may have a larger solid core, with a relatively thin viscous outer layer that allows them to stick together upon impact, but without merging into one another. It is collisions of this second type that lead to the typical soot aggregate morphology, seen in Figure 2.37 (image from Chapter 7). Further surface growth can round off aggregates somewhat, continuing the increase in total particle mass, and making differentiation between individual spherules more difficult.

It has been observed that the C/H ratio of particles increases as they mature, and that this process of dehydrogenisation/carbonisation is associated with an increasingly orderly, graphitic structural arrangement [297, 337]. In part, this can be attributed to the growth of the PAHs within the particulate [337, 338]; as PAHs grow, their C/H ratio naturally decreases as they tend to follow the path of highest stability (related to the 'stabilomer' class of compact PAHs [339]), wherein the area to perimeter ratio steadily increases and it is only at the perimeter that hydrogen atoms are bound. Beyond this, non-planar, bent PAH structures, ranging from disorderly partial shells to highly ordered closed-shell

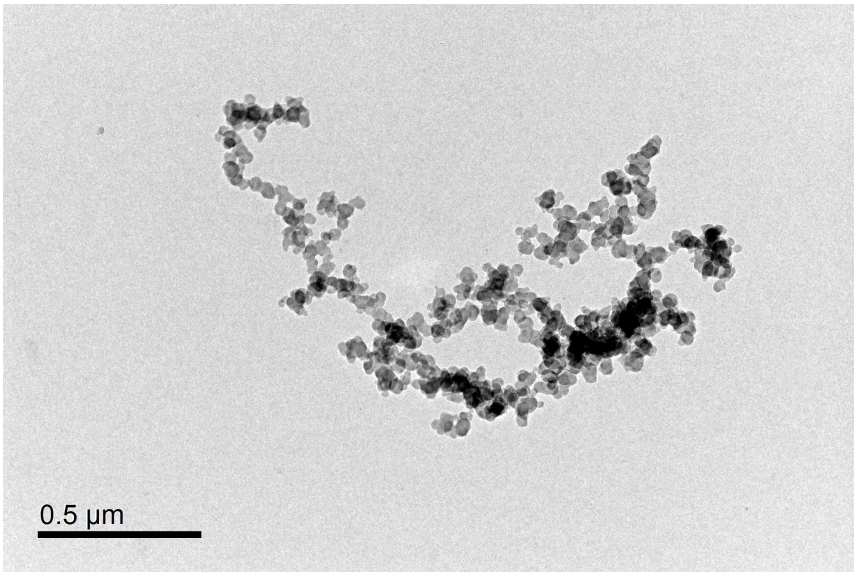

Figure 2.37: Soot aggregate collected from a petrodiesel flame (image taken at a magnification of x10000).

structures including fullerenes and carbon nanotubes can form in flames, and may contain little or no hydrogen [337, 340, 341]. Fullerenes may be formed by reactions between multiple PAHs, gas phase additions to PAHs and internal rearrangement [342]. However, while these structures are known to form in flames, the high pressure environment of a diesel engine may not be so conducive to their growth [343], although defective fullerenic arrangements have reportedly been identified in diesel engine particulate [344].

2.2.3.3.4 OXIDATION

Unless a mixture is entirely depleted of oxygen and oxidising radicals, the process of oxidation will run parallel to the pyrolytic processes which lead to the inception and growth of soot. At lower temperatures, in premixed and partially premixed flames, the oxidation of fuel is primarily initiated by hydrogen abstraction by O_2, and, once the radical pool develops and temperatures increase, oxidising radicals – particularly OH – react rapidly with the fuel. Oxidation reduces the carbon mass available for further growth; once a C-O bond is formed, the attached carbon is less likely to contribute to soot formation. Within a laminar diffusion flame, oxidation occurs at the flame front under approximately stoichiometric conditions, and reactions towards the core are driven by the diffusion of heat and radicals, inwards [345]. At higher temperatures, unimolecular decomposition reactions (C-C fission, β-scission) become dominant, as a means of initiation and consumption of both fuel hydrocarbons and the intermediate species formed during combustion. Progressively smaller alkyl radicals and alkenes are produced, and the types

of stable, unsaturated precursor species depicted in Figure 2.31 can accumulate in high concentrations, if not subjected to oxidative attack. Soot precursors subsequently react with one another to form aromatic and polycyclic aromatic structures.

Most oxidation of aromatics generally occurs early in the growth process, because this tends to be when oxygen availability is highest [303]. The oxidation of soot itself begins at a temperature of around 1300 K. In premixed flames, oxidation and pyrolysis occur simultaneously and hence compete. An increase in temperature increases the rate of both oxidation and pyrolysis, but because the effect of temperature on the rate of oxidation is larger, sooting tendency in a premixed flame declines with increasing temperature. On the other hand, in a diffusion flame, where pyrolysis takes place within the oxygen depleted core, an increase in temperature leads to the formation of greater quantities of soot [299].

O_2 and OH are typically regarded as the main oxidants of soot, but they may vary in relative importance and mode of action. In the near vicinity of a diffusion flame front, for example, OH is likely to be the most abundant and effective oxidising agent, whereas outside the flame where conditions are leaner and cooler O_2 may become a more significant consumer of soot [267, 346]. Because OH is the more highly reactive of the two, it may attack soot mostly at the periphery, while less reactive O_2 could penetrate further into the porous structure of the particle and oxidise the internal regions [267].

Aspects of the internal structure of the primary particles from which soot is comprised may also have a substantial effect on oxidation; higher oxidation rates are associated with soot containing graphene layer planes that are smaller, more highly curved and disordered [347]. This is because carbon atoms located on edge sites are more susceptible to oxidative attack [267]; defect sites are also prone to oxidation [348].

Surface oxygen groups, which form primarily at the edge of the carbon layers, may also increase the rate of oxidation, and alter the nature of the structural transformations which occur as soot is oxidised [349]. However, it has been suggested that the amount of oxygenated surface functional groups may be less important than the quantity of aliphatic C-H groups [350].

In general, oxidation reduces particle mass, but partial oxidation may increase particle number by fragmentation of agglomerates [351]. In the early stages of oxidation, the specific surface area of soot may increase, due to increasing porosity, and the removal of more highly ordered graphitic outer layers, exposing the more amorphous soot core [351, 352]; such an increase in surface area might be expected to increase reactivity. Such

changes in structure may also influence the manner in which particle size varies throughout oxidation – internal burning, for instance, may rapidly reduce mass while leaving apparent particle size unchanged [349].

2.2.3.3.5 EXHAUST

At the beginning of the diesel exhaust process (i.e. when the exhaust valves open), the bulk gas temperature remains high enough for soot growth and oxidation reactions to continue, and so the character of existing particulate matter may continue to evolve. Particulate may be deposited upon surfaces within the exhaust system, and re-entrained into the exhaust flow following a later cycle. Deposits may build-up before becoming dislodged, and such build-up within the exhaust system is thought to be the source of the larger coarse mode of particulate emissions [267].

As the temperature drops, volatile species within the exhaust condense, adhering to existing particulate, or forming new nucleation mode particles [267]. Condensing species may be absorbed by, or adsorbed onto, existing particles (initially comprised of non-volatile carbon and ash), driving particle growth. Where the initial concentration of particles is lower, nucleation of new particles from volatile species is favourable; this means that emissions of nanoparticles may increase as soot emissions decline (i.e. lower particulate *mass* emissions may be associated with higher particulate *number* emissions) [353, 354]. Of the nanoparticles emitted from a diesel engine, upwards of 90% may form from volatile compounds during exhaust dilution [353].

Of the volatile fraction, the quantity of sulphates is primarily determined by fuel-bound sulphur content (sulphur compounds in lubricating oil make a far smaller contribution to particulate emissions [355]), while organics may be derived from both the fuel and lubricating oil, ranging from the heaviest products of pyrolysis (PAHs), to the lightest compounds which do not fall instead under the category of hydrocarbon emissions (see Section 2.2.5.1).

Nucleation is expected to begin where hot exhaust and cold dilution air meet [356], that is, essentially at the tailpipe exit, and within a short period the particle size distribution reaches approximate stability [357, 358]. It has been suggested that nucleation of sulphuric acid and water clusters drives the formation of nucleation mode particles, with even low-volatility organic species only condensing on nucleated cores, or accumulation mode particulate [359]. Some reports suggest that low-volatility oxygenated hydrocar-

bons could contribute to nucleation at lightly loaded conditions [360], and others that nanoparticles may condense around a preformed non-volatile core [358]; a recent modelling study suggests that the participation of semi-volatile organic acids accounts well for observed nucleation and growth rates [361].

2.2.3.4 BIODIESEL AND ITS EFFECTS

The majority of the literature (around 95%) reports a decrease in particulate emissions when a diesel engine is fuelled on biodiesel rather than petrodiesel [13]. The United States Environmental Protection Agency reports that the use of a B100 biodiesel is associated with an average reduction in particulate matter emissions of around 45–50%, compared to petrodiesel [362]. For the most part, this reduction in particulate is attributable to the absence of the highly sooting aromatic species, present at between 15–40% in a typical petrodiesel [160], coupled with the fuel-bound oxygen content of biodiesel, at around 11% by mass.

Fuel-bound oxygen content has been widely associated with a reduction in diesel engine particulate emissions and smoke opacity, in-cylinder soot formation and soot concentrations in jets and flames. Oxygenated hydrocarbons contain C-O bonds which may remain intact throughout ignition and prevent the attached carbon atom from participating in soot formation processes [259]. Superficially, it might therefore be inferred that one atom of fuel-bound oxygen will remove one atom of fuel carbon from the potential sooting pool, and hence reduce the sooting tendency of a molecule, C_n, to that of an equivalent unoxygenated fuel, C_{n-1}. In the case of aldehydes and ketones, for example, this is approximately correct [156]. However, this represents a best case scenario, and the possibility of other possible consumption pathways, elimination reactions in particular, limits the efficacy with which fuel-bound oxygen is able to sequester carbon and reduce sooting.

Since the biodiesel ester group contains 2 oxygen atoms, ideally the sooting tendency of a saturated methyl ester, C_n, would be equal to that of an *n*-alkane, C_{n-2}; McEnally and Pfefferle [156] report that, in practice, a methyl ester produces comparable soot to an *n*-alkane between C_{n-1} and C_{n-2}. The reason for this less than ideal reduction in sooting is the possibility of direct formation of CO_2 from alkyl esters, whereby 2 fuel-bound oxygen atoms only sequester one atom of fuel-carbon between them [259, 363].

The results of carbon labelling experiments suggest that the carbonyl C=O bond is rarely broken during combustion, because the attached carbon atom makes a negligible

contribution to soot [364, 365]. However, Westbrook et al [259] estimate that under conditions representative of fuel-rich diesel ignition (ϕ = 3, P = 10 MPa, initial T = 767 K), during combustion of a biodiesel surrogate (methyl butanoate) around half of the reaction pathways left both O atoms bonded to this single carbon – that is, led to direct formation of CO_2 from the fuel, rather than 2CO.

At higher temperatures the formation of CO_2 from the fuel may occur via unimolecular cleavage of the alkoxy C-O bond and subsequent β-scission, as seen for methyl pentanoate in Figure 2.38 (figures are based on those at [366]).

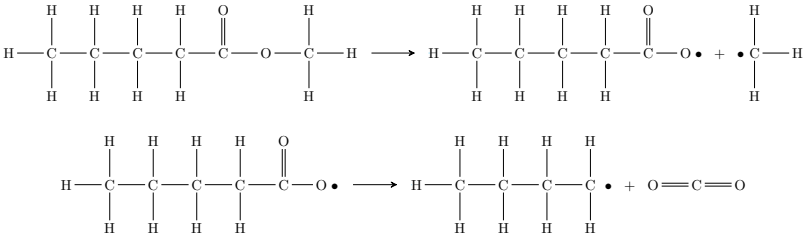

Figure 2.38: High temperature pathway for CO_2 formation from methyl pentanoate (based on diagrams in [366]).

At lower temperatures hydrogen abstractions from sites 2 and 3 carbon atoms from the carbonyl group lead to β-scission reactions forming the $COOCH_3$ and CH_2COOCH_3 radicals depicted in Figures 2.39 and 2.40. The $COOCH_3$ radical can break down into either CO_2 + CH_3 (as in Figure 2.39) or CO + CH_3O, but the former products are more likely [367, 368]. The CH_2OOCH_3 radical can progress in a variety of ways [366], with particular importance ascribed to the pathway involving O_2 addition and subsequent isomerisations, forming the OCHO radical, which decomposes to form CO_2 + H (as in Figure 2.40) [369]. The same route to OCHO and hence CO_2 is possible following initial hydrogen abstraction from the α-carbonyl site, although the pathway may not be preferable in radicals possessing alternative sites for internal hydrogen abstraction (other than the primary carbon in the alcohol moiety, as in CH_2OOCH_3 in Figure 2.40) [370]. Another important source of CO_2 derived from fuel-bound oxygen is HOCHO, formed via the addition of OH to formaldehyde [369].

Given that a typical biodiesel contains, on average, approximately C_{18}–C_{19} methyl esters, whereas a typical petrodiesel contains, on average, C_{14}–C_{15} hydrocarbon species, it is apparent that the sequestration of 1 or 2 carbon atoms by fuel-bound oxygen is not, on its own, sufficient to explain the reduction in particulate which is observed when fuelling on biodiesel. Even optimum removal of 2 carbon atoms would only reduce the sooting

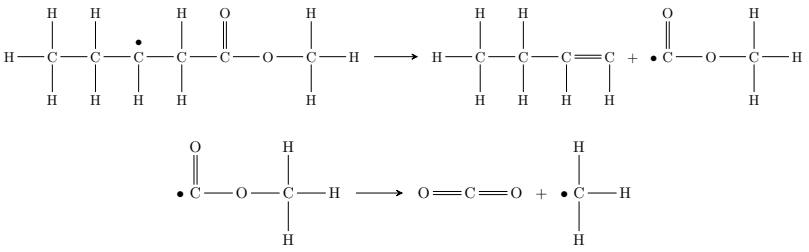

Figure 2.39: Low temperature pathway for CO_2 formation from methyl pentanoate, via the $COOCH_3$ radical (based on diagrams in [366]).

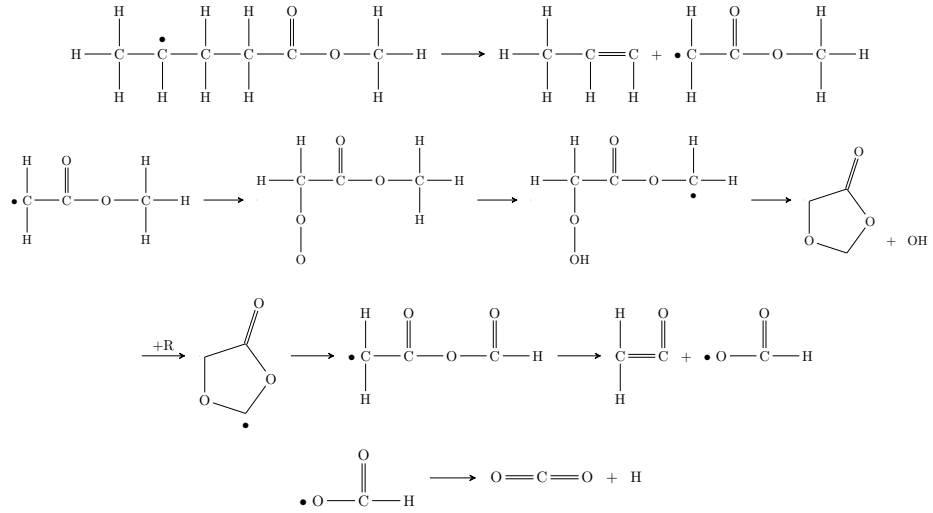

Figure 2.40: Low temperature pathway for CO_2 formation from methyl pentanoate, via the CH_2OOCH_3 and OCHO radicals (based on diagrams in [366] and [369]).

potential of a saturated C_{18}–C_{19} methyl ester to that of an equivalent C_{16}–C_{17} *n*-alkane.

Of course, it is unrealistic to discuss biodiesel as if it were comprised solely of long-chain saturated species, and equally *n*-alkanes are not a suitable representative of petrodiesel. Both petro- and biodiesel contain species more liable to produce soot: in biodiesel, mono- and polyunsaturated alkyl esters have higher sooting tendencies than their saturated equivalents, and in petrodiesel, the *iso*-alkanes, cycloalkanes, and most significantly the aromatic species, substantially increase sooting. This is illustrated in Figure 2.41. The sooting data presented in Figure 2.41 is drawn from investigations pertaining to non-premixed diffusion flames; to some extent, the effect of fuel properties on sooting may be different under the partially-premixed conditions encountered in diesel combustion [259], although the general trends are still likely to be relevant.

With regards to petrodiesel, as Figure 2.41A shows, branching increases the sooting tendency of a molecule such that, for example, a 2-methyl analogue, C_n (which Farrell et al [160] reports to be the most common variety of *iso*-alkane in a typical petrodiesel), yields soot at a level approximately equivalent to that of an *n*-alkane, C_{n+1}. An alkyl-

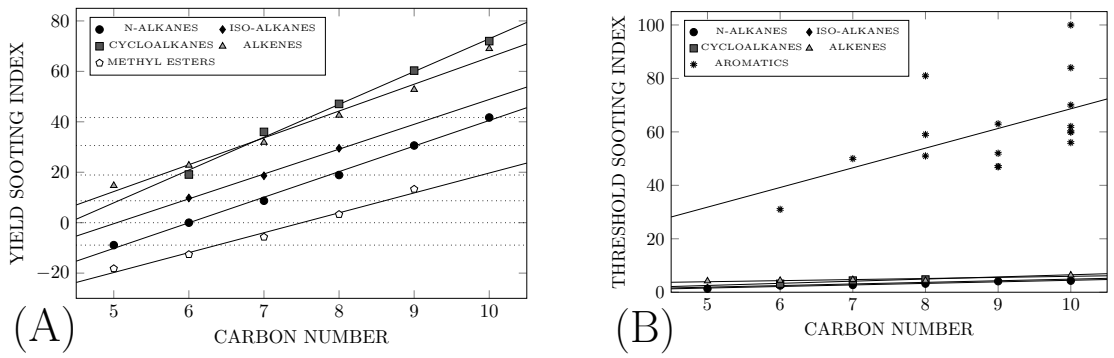

Figure 2.41: (A) Yield sooting indices for *n*-alkanes, *iso*-alkanes, cycloalkanes, alkenes and methyl esters as a function of carbon number (data from [156], available at [371]). (B) Threshold sooting indices for *n*-alkanes, *iso*-alkanes, cycloalkanes, *n*-alkenes and aromatics as a function of carbon number (data from [372]). Note that all *iso*-alkanes values are for 2-methyl analogues, cycloalkane values are for cyclohexane and alkyl-cyclohexanes, alkenes are average values for all available C_n *n*-alkenes at source, and methyl ester values are for saturated species.

cyclohexane, C_n, soots at a level tending to somewhat exceed that of an *n*-alkane, C_{n+2}. However, as Figure 2.41B makes clear, the level of sooting associated with aromatic species is so high that differences between the other species become comparatively minor.

Aromatic species are associated with high sooting in both premixed and diffusion flames [299]. Reflecting upon Section 2.2.3.3.1, it is easy to imagine why this should be the case; when burning non-aromatic fuels, the formation of the first aromatic rings is the rate controlling step in soot formation, but when aromatics are already present in the fuel the importance of this relatively slow first stage is reduced.

With regards to biodiesel, the presence of a single double bond is seen in Figure 2.41A to increase the sooting tendency of a molecule, such that an *n*-alkene, C_n, has a sooting tendency in excess of that of an *n*-alkane, C_{n+2}. The results of Das et al [373], looking specifically at the effect of unsaturation on the sooting tendency of C_4–C_7 alkyl esters, are not entirely consistent with this, but in general confirm that an unsaturated alkyl ester is likely to soot more than a saturated one, and may in some cases soot as much or more than an equivalent *n*-alkane; a lot hinges on the position of the double bond. Feng et al [374] report significantly higher soot volume fractions in flames of unsaturated methyl esters, compared to their saturated equivalents. Sooting tendency also increases with the length of alcohol moiety, due to the facilitation of six-centre elimination reactions by which small unsaturated hydrocarbons can be formed directly [156].

The lack of highly sooting aromatic species and the sequestration of fuel-carbon by fuel-bound oxygen are certainly a significant part of the explanation for reduced soot formation when fuelling on biodiesel and other oxygenated fuels. However, in a practical

combustion device, like a diesel engine, other factors may also contribute. In engine tests, Knothe et al [375] found that methyl palmitate ($C_{17}H_{34}O_2$) produced significantly less soot, not only than hexadecane ($C_{16}H_{34}$), but also than dodecane ($C_{12}H_{26}$). On the basis of Figure 2.41A (and consistent with the proposed carbon sequestration mechanism [259]), the expectation might be that a pure C_{16} *n*-alkane would soot slightly more than a C_{17} methyl ester, but a C_{12} *n*-alkane, like dodecane, should soot considerably less than either.

Many of the factors which effect levels of sooting within a diesel engine are related to mixing processes and the complex phenomena associated with the lifted jet; these aspects are dealt with more thoroughly in Section 2.2.6. The ignition quality of a fuel affects the initial mixing time (viz. the ignition delay), and hence the amount of fuel consumed in the premixed combustion phase. Fuels with reduced ignition quality and prolonged mixing times consequently combust under more highly premixed conditions, and this is associated with a reduction in sooting (as will be seen in Chapter 5). Ignition quality is also generally correlated with the lift-off length of the diesel jet, with lower ignition quality fuels tending to have longer lift-off lengths, and hence entraining more in-cylinder air into the fuel-rich core of the jet [376, 377]. Given that dodecane has a lower cetane number than methyl palmitate (making reference again to [375]), and is therefore likely to have both a longer ignition delay, which increases initial premixing, and a longer lift-off length, which increases air entrainment into the core of the jet, this does not explain the observation that particulate matter emissions when fuelling a diesel engine on dodecane exceed those when fuelling on methyl palmitate – in fact, it tends to suggest that mixing conditions would favour dodecane in terms of soot reduction.

However, due to the fuel-bound oxygen content of biodiesel, it effectively has a head start over petrodiesel and other unoxygenated fuels in terms of mixing, with a greater proportion of the stoichiometric oxygen required for complete combustion available for a given degree of air entrainment. As a result, partially-premixed fuel-rich reactions within the core of the diesel jet consume biodiesel more completely, and restrict soot formation more exclusively to the centre of the jet, where equivalence ratios remain high enough to facilitate soot formation [378].

Following the fuel-rich premixed ignition of *n*-heptane at an equivalence ratio of 4 (which Dec [379] suggests is representative of diesel ignition within the standing premixed reaction zone), Curran et al [380] estimate that 22% of fuel-carbon would be converted to soot precursor species. However, at an equivalence ratio of 2, the calculated formation

of soot precursors was reportedly negligible – consistent with the approximate negation of soot incandescence observed under comparable mixing conditions [381]. Petrodiesel attains an oxygen equivalence ratio (ϕ_Ω, see [382]) of 4 at an air:fuel ratio (AFR) of around 3.5:1. Due to its fuel-bound oxygen and lower stoichiometric air requirement, at the same AFR a typical biodiesel is mixed to an oxygen equivalence ratio closer to 3 (this point is clarified graphically later, in Section 2.3.5).

Cheng et al [383] attribute the reduction in sooting with increasing fuel-bound oxygen addition to increased concentrations of O, OH and HCO radicals within the flame. Inside the premixed reaction zone, these radicals oxidise carbon and prevent it from contributing to the formation of soot precursors, and further downstream, increased radical populations – of OH in particular – inhibit the growth of aromatic and polycyclic aromatic species. Chen et al [384] report a reduction in all precursor species with the addition of oxygenates to a premixed *n*-heptane flame.

In a diesel engine, soot emissions are strongly influenced by the efficacy of the burnout process, with most soot generally being destroyed prior to exhaust [267, 385]. Hence, the possible effects of biodiesel, and fuel oxygenation in general, on soot oxidation and reactivity may also be significant. It has been reported that biodiesel soot is more reactive than that produced when fuelling on petrodiesel, and a variety of hypotheses have been put forward to explain this [386]. Song et al [349] reported capsule-type oxidation of biodiesel soot, depicted in Figure 2.42. Lapuerta et al [386] suggest that this may be because the smaller size of biodiesel primary particles means that carbon layers on the surface of the particles are more stretched, making them more likely to break into smaller parts, facilitating internal burning; smaller primary particle sizes also increase reactivity by increasing the specific surface area available for oxidative attack. Other explanations focus on the increased tortuosity of biodiesel soot, which increases the availability of edge-site carbon atoms for oxidation [387]. A possible explanation for increased tortuosity is greater inclusion of C_5 ring-structures into the soot nanostructure, generating curvature; because formation of C_5 rings is dependent upon partial oxidation, addition of biodiesel to a fuel blend may increase this effect, up to a point [388]. Some authors [349] have suggested that greater surface oxygen functionality of biodiesel soot is an important factor, but others attribute less significance to this aspect [387].

When fuelling on biodiesel, although reductions in smoke and particle mass emissions are commonly observed, this is frequently accompanied by a larger soluble organic fraction

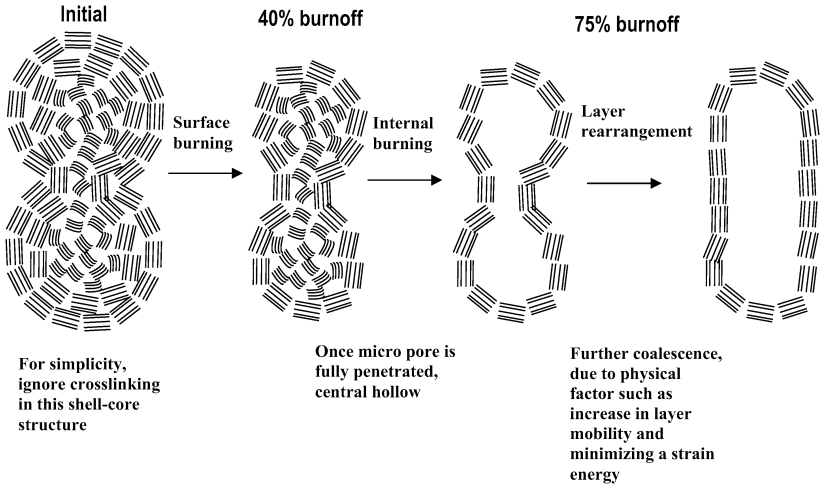

Figure 2.42: Simplified oxidation progression model for biodiesel soot [349].

[375] and an increased number of smaller, nucleation mode particles [389, 390]. Given the reported dependence of nucleation mode particulate on fuel-bound sulphur [359], this increase in low diameter particles when fuelling on biodiesel (which generally contains almost no sulphur), requires some explanation. Tan et al [391] offer 3 possible mechanisms. First, reduction of accumulation mode particulate reduces the concentration of soot available for volatile species to condense on, and hence tends to increase nucleation. Second, the lower volatility of biodiesel may increase the size of the volatile fraction – given that the soluble and volatile fractions are correlated, this is consistent with the literature [375]. Third, the oxygen content of biodiesel may lead to a reduction in the size of emitted carbonaceous particulate, which could consequently be small enough to count towards the nucleation mode. It is also worth noting that some studies have indicated that biodiesel, or certain biodiesel blends, may increase the mutagenic effects of particulate relative to petrodiesel [392, 393]; however, reduced mutagenicity has also been reported in many cases [394].

2.2.4 OXIDES OF NITROGEN

2.2.4.1 DEFINITION

The term oxides of nitrogen, commonly abbreviated to NO_x, generally refers to the combination of nitric oxide (NO) and nitrogen dioxide (NO_2), with emissions from combustion devices under most conditions being predominantly comprised of the former [395]. However, roadside measurements suggest that the percentage of exhaust NO_x comprised of NO_2 has risen significantly in recent years (from around 5–10% in 1999, to around 15–20% in 2009), due to the increasing use of oxidation catalysts and particulate filters [396].

NO is a clear, odourless gas, whereas NO_2 has a pungent acidic odour and brownish colour [397]. It is assumed that after exhaust all NO is eventually oxidised to NO_2 and so, for regulative purposes, when emissions are considered in terms of mass, the mass of NO_x is generally calculated as if it were all NO_2 [395].

Overlapping and related to the NO_x category, several other nitrogen oxides can exist and are generated by combustion processes. Nitrous oxide (N_2O) is only a very minor exhaust constituent in most instances, but has importance as an intermediate species in the NO_x formation process [398], and as a potent greenhouse gas [399] (which may also be generated during the production of biodiesel [400]). Nitrite (NO_2^-) and nitrate (NO_3^-) ions are also present in vehicle exhaust, but in vanishingly small quantities [401]; the majority of nitrate formation occurs in the atmosphere and plays an important role in the atmospheric chemistry of NO_x.

A wider denomination, reactive odd nitrogen, or NO_y, includes NO_x and also encompasses the many products of its oxidation in the atmosphere, largely nitric (HNO_3) and nitrous (HONO) acids, but also dinitrogen pentoxide (N_2O_5) and the various peroxyacyl nitrate species ($RC(O)OONO_2$), or PANs [278].

2.2.4.2 MOTIVATION OF INTEREST

NO_x emissions cause concern amongst legislators primarily because of their contribution to the formation of photochemical smog and acid rain [402]. Some immediate insight can be gained into how NO_x contributes to these processes by considering Figure 2.43 which shows the boundary layer NO_y system through day and night (illustration from [403], original source unavailable). The boundary layer refers to approximately the lowest 1 km of the troposphere, which is the portion of the atmosphere extending from the ground to around 10–15 km altitude [278].

In the daytime, NO can react with O_3 to form NO_2 and molecular oxygen (O_2), the photolysis of NO_2 by ultraviolet light forms NO and an oxygen atom (O), and O can then react with O_2 to form ozone (O_3) through a termolecular reaction; Equations 2.12–2.14.

$$NO + O_3 \longrightarrow NO_2 + O_2 \tag{2.12}$$

$$NO_2 + h\nu(300nm \leqslant \lambda \leqslant 420nm) \longrightarrow NO + O \tag{2.13}$$

$$O + O_2 + M \longrightarrow O_3 \tag{2.14}$$

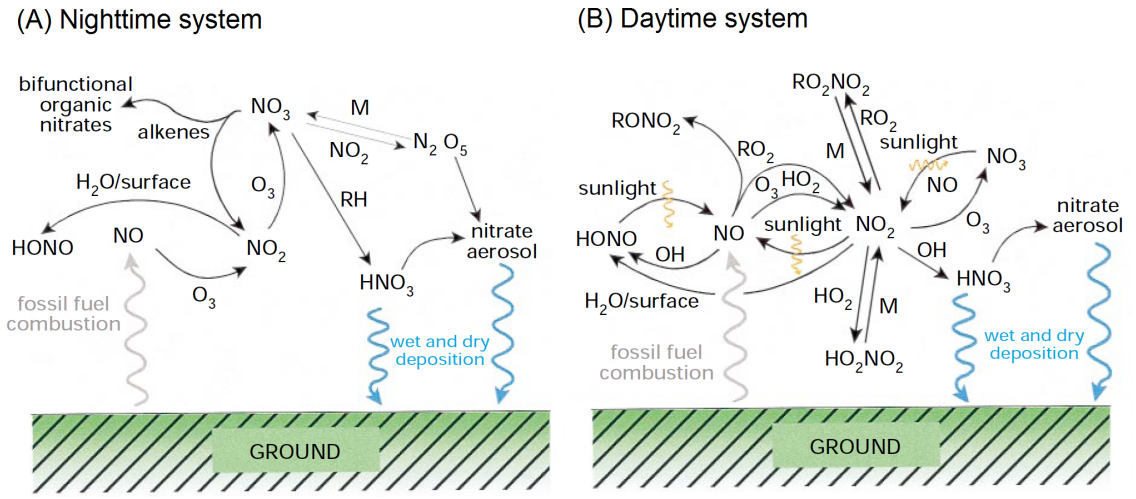

Figure 2.43: Atmospheric chemistry of nitrogen oxides in the boundary layer [403].

However, this is an incomplete description of the actual processes at play, as Figure 2.43B illustrates, particularly in polluted regions where the NO_y system is profoundly affected by interactions with the oxidation products of volatile organic compounds (VOCs), including – but not limited to – the volatile hydrocarbons found in exhaust. Exhaust is by no means the sole origin of such chemicals in the atmosphere; other anthropogenic VOC sources include the evaporation of solvents, use of aerosol sprays and the production of alcoholic beverages; biogenic sources include trees and grasses [404].

Hydrogen abstraction from volatile hydrocarbons, followed by reaction with O_2, yields alkylperoxy radicals (RO_2), but while these alkylperoxy radicals can react with hydroperoxy radicals (HO_2) or each other, they can also react with NO to form alkyl nitrates ($RONO_2$) or with NO_2 to form peroxynitrates (RO_2NO_2). In the case of unsaturated hydrocarbons, radical species can react additively with the double bond, giving products that include nitratoalkyl peroxy radicals ($CH_3CH(O_2)CH_2ONO_2$) and carbonyl containing molecules. Amongst the organic compounds that form as a result of substitution and combination reactions between the oxygen, nitrogen and carbon containing molecules deriving from pollutants and their products, peroxyacyl nitrates (PANs) are of particular interest as a photochemical oxidant contributing to smog [278].

The critical point, in terms of ground-level ozone, is that, in addition to the reaction with ozone given in Equation 2.12, NO can make the transition to NO_2 by reacting with RO_2 or HO_2 radicals [278]. This is important because it means that, instead of O_3 being simply created via Equation 2.12 and then consumed via Equation 2.14, NO_2 formation is supplemented by alternative pathways, effectively bypassing a proportion of the reactions that would otherwise lead to the recycling of ozone. This leads to net ozone production,

and causes increased tropospheric ozone concentrations [403]. Ozone is another of the chemicals that contribute to the broader photochemical smog phenomenon.

In the nighttime system, Figure 2.43A, NO is converted to NO_2 by reaction with O_3, but absent of the photolytic effect there is little reversion and concentrations of NO and O_3 are rapidly depleted [403]. The photolysis of nitrate occurs rapidly during the daytime, and since NO_3^- also reacts very readily with available NO to form $2NO_2$ the path through the nitrate ion is not significant when the sun is up. However, when the sun is down and photolysis no longer occurs, the NO_2/NO ratio increases dramatically as NO_2 ceases to dissociate and NO ceases to be formed. Under these conditions (absent of both photolytic effects and NO to react with) NO_3^- endures for long enough to react with NO_2 to form dinitrogen pentoxide (N_2O_5). N_2O_5 can react with water to form $2HNO_3$ and usually does so heterogeneously on the surface of a water containing aerosol. Nitric acid is also (and primarily) formed during the daytime via NO_2 reaction with the hydroxyl radical (OH) [405]. Reactions between NO_3^- and VOCs can also form NHO_3. Nitric acid is highly soluble in water, and reduces the pH of any that it is dissolved in; hence, the contribution of NO_x to acid rain.

Photochemical smog consists of several main elements, four of which have now been introduced: NO_x, VOCs, O_3 and PANs. Aerosols are considered to be a constituent of smog [269], but their genesis is not linked to NO_x emissions in the same sense as that of ozone or PANs; at any rate, the connection between fine particulate and morbidity has been made [284]. Oxides of sulphur (SO_x), primarily sulphur dioxide (SO_2), are also a smog ingredient, although less critically from vehicles than from combustors burning sulphur-rich fuels like coal; the 1952 London 'Great Smog' was an example of highly sulphurous pollution, and may have been responsible for as many as 12,000 deaths [406], but research suggests that even low levels of atmospheric SO_x may have a serious effect on health [407].

Both NO and NO_2 are considered to be toxic, but at ambient concentrations do not pose a significant threat on their own; largely, it is the products of atmospheric NO_x chemistry that are responsible for the more considerable problems [408]. That said, there is believed to be a link between long-term exposure to NO_2 and decreased lung function, and asthmatics and children may be more acutely affected in the short-term. An association between NO_2 and arrhythmia has also been reported [284]. Additionally, the presence of NO_2 leads to the murky brown colouring of smog and contributes to reduced visibility.

The most serious health issues associated with ozone concern its effects upon the respiratory system [409]; in the short-term, leading to temporary degradation of lung function and athletic performance, decreased lung capacity, inflammation and coughing. There is a link between short-term increases in environmental ozone concentration and mortality [410], although the effect of ozone in this regard is apparently less pronounced than that of PM2.5 [408]. In the long-term, increased exposure to ozone coincides with increased risk of death from respiratory disease [411]. O_3 causes considerable damage to crops, forests and other vegetation [412], is damaging to some paints and plastics, and to rubber [404].

Peroxyacyl nitrates, amongst which peroxyacetyl nitrate is the most common and simplest, were unknown compounds before they were discovered in smog. PANs are highly toxic to plants – 10–50 times more so than ozone – are potent eye irritants and are stable enough to be transported over long distances [413]. An important point is that they can be formed directly from aldehydes, and therefore fuels which increase aldehyde emissions, as oxygenated fuels including biodiesel might (this is discussed further in Section 2.2.5.1), may more readily facilitate the formation of PANs .

2.2.4.3 MECHANISMS OF FORMATION

There are several distinct mechanisms by which NO can be formed in combustion devices, the relative contributions of which depend upon local reaction temperatures, equivalence ratios, and fuel chemistry. Not all are thought to be of significance under diesel engine conditions, but may have more applicability to experiments in flames [414] and will be briefly outlined here, if only for the sake of completeness.

The thermal route to NO, described by the extended Zel'dovich mechanism, involves the oxidation of atmospheric nitrogen, and is generally understood to be the dominant means of NO_x formation within a traditional diesel engine [415–417]. It is most important at close to stoichiometric equivalence ratios ($\phi = 0.8$–1), and strongly influenced by temperature, with rates of NO_x formation by the thermal route increasing dramatically as temperature increases [398, 418]. Since nitrogen naturally occurs as the triple-bonded N_2 molecule, it is highly stable, and will not begin to react at an appreciable rate until the temperature exceeds approximately 1800 K [345]. The Zel'dovich mechanism begins with Equation 2.15:

$$N_2 + O \rightleftharpoons NO + N \tag{2.15}$$

Equation 2.15 is the rate controlling step, and after atomic nitrogen has been formed it reacts rapidly with O_2 in Equation 2.16:

$$N + O_2 \rightleftharpoons NO + O \tag{2.16}$$

Under slightly richer conditions [419] where O_2 is less abundant, nitrogen may also react with OH radicals, in the final equation of the extended mechanism:

$$N + OH \rightleftharpoons NO + H \tag{2.17}$$

In addition to the strength of the N_2 triple-bond, the temperature dependence of the thermal mechanism is a result of the positive temperature sensitivity of the equilibrium O atom concentration [420]. N atom concentrations are very low (a mole fraction of the order of 10^{-8} is typical), and reactions consuming N proceed far more quickly than those forming it, so the steady-state approximation is made, meaning that the variation in N over time is quantitatively insignificant enough that it can be assumed to be equal to zero [418]. Generally, the thermal NO formation process is slow enough, relative to the oxidation of the fuel, that equilibrium radical concentrations can be used when modelling NO production by this pathway. However, because the equilibrium values are often many times lower than the radical concentrations present during the initial reaction process, actual NO formation rates may exceed those predicted, although the discrepancy is reduced as temperatures increase [398]. When measured oxygen radical concentrations are used to predict thermal NO formation, accuracy improves [421].

Bowman defines prompt NO as *"NO that is formed at a rate faster than that calculated from the simple equilibrium thermal NO mechanism"*; super-equilibrium concentrations of O and OH radicals during the initial reaction process are therefore considered to contribute to prompt NO [402]. However, it has been noted in connection with flames that although super-equilibrium concentrations of oxygen radicals are observed, they are not present in regions of the flame hot enough to promote substantial thermal NO production [398], emphasising the point that the location of radical species is also a critical factor.

Prompt NO contributes to total NO_x formation most significantly under conditions somewhat richer and cooler than those at which the thermal mechanism is dominant [398]. Often synonymous with prompt NO (and also considered to be an important means of NO_x formation within diesel engines [415]), is NO formed via fuel derived hydrocarbon radicals through pathways related to those first proposed by Fenimore [422], primarily:

$$CH + N_2 \rightleftharpoons HCN + N \tag{2.18}$$

Currently, it appears that although the suggested reactants in Equation 2.18 are correct, the more likely pathway at typical temperatures is [423]:

$$CH + N_2 \rightleftharpoons NCN + H \tag{2.19}$$

This is because Equation 2.19 conserves electron spin, whereas Equation 2.18 requires a change in spin between reactants (s = 1/2) and products (s = 3/2), and this transition is expected to make the reaction relatively slow [305]. In terms of the NO concentrations predicted, the effect of replacing the former reaction with the latter within larger computational kinetic mechanisms is said to be small; this is because the it is the oxidation rather than initiation steps that determine the concentrations reached [424, 425]. One reaction directly consuming NCN at combustion temperatures, Equation 2.20, leads to the same products as Equation 2.18 [426, 427] (indeed, there are modelling studies in which total conversion of NCN to HCN is assumed [428]). HCN, and a range of other fixed nitrogen species, may ultimately be oxidised to NO by pathways including those depicted in Figure 2.44 [429].

$$NCN + H \rightleftharpoons HCN + N \tag{2.20}$$

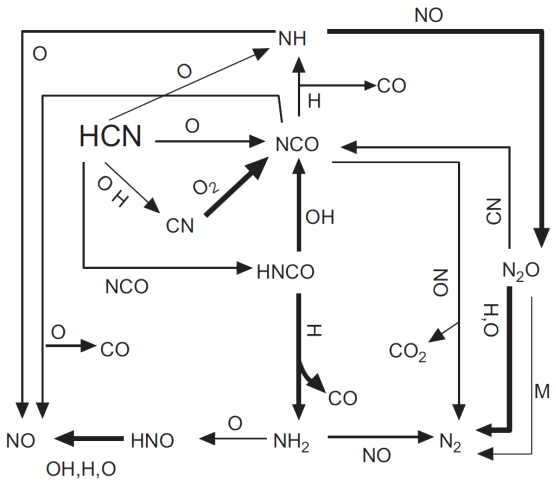

Figure 2.44: Main reaction paths for HCN oxidation (arrow thickness represents relative importance of pathway) [429].

In simulations representative of diesel engine operating conditions ($\phi = 3$, P = 50 atm, T = 1200 K), Garner et al [430, 431] highlight the possible importance of a path from acetylene, given in Equations 2.21–2.25. It has been proposed that this may have a direct

association with the biodiesel NO_x increase – this will be addressed in Section 2.3.

$$C_2H_2 + O \rightleftharpoons CH_2 + CO \tag{2.21}$$

$$CH_2 + H \rightleftharpoons CH + H_2 \tag{2.22}$$

$$CH + N_2 + M \rightleftharpoons HCNN + M \tag{2.23}$$

$$HCNN + O_2 \rightleftharpoons CNN + HO_2 \tag{2.24}$$

$$CNN + HO_2 \rightleftharpoons NO + NCO \tag{2.25}$$

At similarly high pressures, reactions involving HNCN may also be important; Equation 2.26 can both produce and consume NCN, HNCN can react with O to form NO directly, or generate other fixed nitrogen species like NH, NCO, CN and HNO (which may be subsequently oxidised to NO via the pathways shown in Figure 2.44) [426].

$$HNCN + M \rightleftharpoons H + NCN + M \tag{2.26}$$

Additionally, Equation 2.27 is sometimes considered to be an important alternative initiation step, increasing in influence with increasing molecular weight of the hydrocarbon fuel [426] (although other authors suggest that it may be of less consequence [432]).

$$C_2O + N_2 \rightleftharpoons NCN + CO \tag{2.27}$$

Diazomethane (CH_2N_2) produced by reaction of CH_2 radicals with molecular nitrogen has also been proposed as a participant in the prompt NO formation process, being particularly important under lean, low pressure conditions [433, 434]. Additionally, it has been suggested that reactions between small hydrocarbon radicals and N_2O and NNH may be a possible source of HCN in flames [435]

Certainly, N_2O and NNH are often considered to be important intermediates in the NO_x formation process in their own right. N_2O is an important intermediate under lean, relatively low temperature (less than 1800 K) conditions, where super-equilibrium concentrations of oxygen atoms exist [436, 437]. N_2O is formed by Equation 2.28 and converted to NO by Equations 2.29–2.30.

$$N_2 + O + M \rightleftharpoons N_2O + M \tag{2.28}$$

$$N_2O + O \rightleftharpoons NO + NO \tag{2.29}$$

$$N_2O + H \rightleftharpoons NO + NH \tag{2.30}$$

Some authors accord the N_2O mechanism a degree of importance in diesel engine NO_x formation second only to the thermal mechanism [416, 417, 438], although others suggest that its influence is less significant [415]. It is the high pressures encountered in diesel engines that make the termolecular reaction, Equation 2.28, more important than may be the case in flames, particularly in the burnt gases, post-combustion [438].

In regions where the concentrations of both H and O atoms are high, such as flame fronts, the NNH mechanism may also contribute to NO_x formation [436, 439, 440]. NNH is formed by Equation 2.31 and converted to NO by Equation 2.32. However, under diesel engine conditions, reactions forming NNH from NO rather than the other way around may predominate [441], meaning that NNH chemistry could actually provide a means for NO_x reduction, as it does in the thermal de-NO_x process [442].

$$N_2 + H \rightleftharpoons NNH \tag{2.31}$$

$$NNH + O \rightleftharpoons NO + NH \tag{2.32}$$

As has been mentioned, typically the bulk of NO_x emissions exist initially as NO rather than NO_2. However, particularly under cooler, more highly stratified and fuel-lean engine operating conditions, significant proportions of NO_2 can remain. NO formed in the vicinity of the flame can be oxidised by HO_2 radicals via Equation 2.33 [418, 443].

$$NO + HO_2 \rightleftharpoons NO_2 + OH \tag{2.33}$$

Where temperatures are high and O radicals are plentiful, reversion to NO is anticipated, by:

$$NO_2 + O \rightleftharpoons NO + O_2 \tag{2.34}$$

However, if NO_2 is transported or diluted such that local conditions no longer favour Equation 2.34, conversion back to NO does not occur. One can easily imagine that rapid mixing and widespread cool in-cylinder regions would encourage this quenching of NO_2 and increase the NO_2/NO emissions ratio [418].

2.2.5 OTHER EMISSIONS

2.2.5.1 TOTAL HYDROCARBONS

Hydrocarbon emissions from diesel engines range from unburned fuel and oil, up to the high molecular weight products of pyrolysis (like polycyclic aromatic hydrocarbons), and down to the low molecular weight products of fuel decomposition and incomplete oxidation (including carbonyl species) [418]. However, heavier species are likely to condense during the expansion stroke and exhaust process, either independently or on the surface of soot particles, contributing to the volatile (or soluble) fraction of particulate matter. The total hydrocarbons (THC) measurement includes all organic compounds whose boiling point is low enough that they do not condense within the filtered line leading to the measurement device; in the case of a flame ionisation detector (as was employed for THC measurement during the bulk of the work documented in this thesis) the line and heated filter are typically maintained at a temperature of around 191 °C [444]. This is sufficient to allow the measurement of most unburned hydrocarbons and the products of their thermal degradation, but not all; a useful characterisation of diesel engine hydrocarbon emissions and their measurement is provided in Figure 2.45.

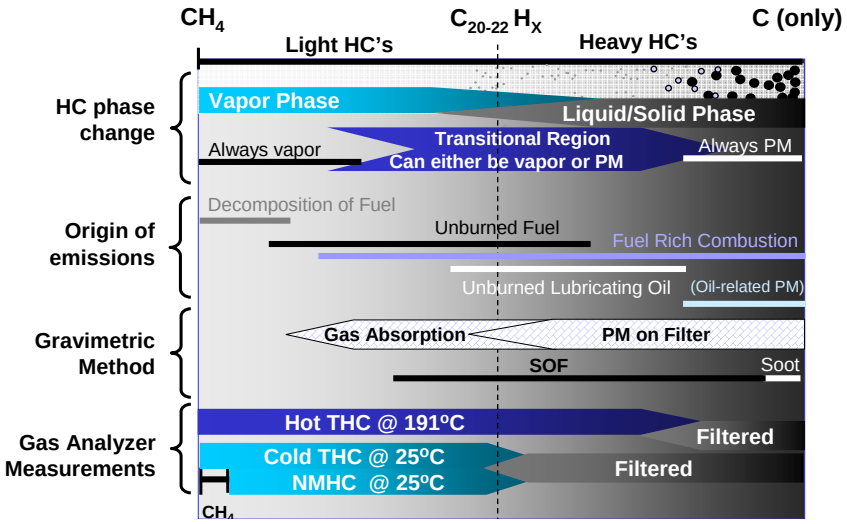

Figure 2.45: Measurement and composition of diesel engine emissions of gaseous hydrocarbons, the soluble organic fraction and soot (from a presentation by Horiba Automotive Test Systems [445]).

The lighter compounds, expected to be gaseous at measurement temperatures include alkanes, alkenes, aromatics, aldehydes and other oxygenated species, many of which are considered to be toxic [446]. Between them, they also contribute to the formation of tropospheric ozone and smog (as discussed in Section 2.2.4.2 and shown in Figure 2.43),

aerosols and peroxyacyl nitrates [278].

Over-leaning is a significant cause of unburned and partially burnt fuel hydrocarbons in diesel exhaust. During the ignition delay the injected fuel mixes with in-cylinder air until a region of the mixture reaches a temperature and equivalence ratio suitable to facilitate autoignition. The initial ignition sites are usually located in fuel-rich regions of the jet [447], but further downstream and away from the jet axis the equivalence ratio is lower and in the most peripheral regions may fall below the lean combustion limit ($\phi \sim 0.3$) [418]. Fuel diluted to this extent is likely to remain unburned or to be only partially oxidised, leading to the formation of combustion intermediates like carbonyls and other oxygenates.

Undermixing of fuel that enters the combustion chamber at low velocity towards the end of the injection event can contribute to incomplete combustion and unburned hydrocarbon emissions, although this contribution is minimised when employing injectors capable of a sharper end of injection cut-off (to prevent 'dribbling') or having a reduced nozzle sac volume [395, 418]. Depending upon the operating conditions, lubricating oil may also contribute significantly to hydrocarbon emissions [448]. Under transient or low temperature operating conditions, wall effects may also be important [449, 450].

The majority of the literature (around 95%) reports a decrease in THC emissions when a diesel engine is fuelled on biodiesel rather than petrodiesel [13]. The United States Environmental Protection Agency reports that the use of a B100 biodiesel is associated with an average reduction in hydrocarbon emissions of around 65–70%, compared to petrodiesel [362]. In part, this is because biodiesel typically has a higher cetane number and therefore a shorter ignition delay than petrodiesel, meaning that there is less pre-ignition mixing time within which to form over-lean regions. More rapid combustion recession following the end of injection when operating on fuels with increased ignition quality [451] may also have some relation to reduced hydrocarbon emissions. Under certain conditions, it has been observed [452] that fuels with higher cetane numbers are able to combust at leaner equivalence ratios (although the difference becomes substantially smaller at compression ratios typical of an operational diesel engine); potentially, this factor may make some small contribution to the correlation between ignition delay and THC emissions. Reduced ignition delay would also tend to advance combustion, and under some conditions this would be expected to reduce THC emissions. In practice, although a general correlation is observed between ignition delay and THC emissions (as will be seen in Chapter 5), the reduction in THC which is observed when fuelling on biodiesel often exceeds that which

would be expected on the basis of reduced ignition delay alone. Reduced hydrocarbon emissions are also reported when comparing oxygenated blends that have lower cetane numbers with petrodiesel [453, 454].

It is plausible that the oxygen content of biodiesel might reduce THC emissions by encouraging more complete combustion [455]; oxygen enrichment of either the fuel or the intake air is normally associated with reduced THC emissions [456]. However, this is not always the case and, as the data presented in Chapter 5 also demonstrates, where an oxygenated fuel or additive possesses a lower cetane number than the petrodiesel to which it is being compared, or a particularly high viscosity, its use may lead to an increase in hydrocarbon emissions [457].

Some portion of the measured reduction in THC emissions when fuelling on biodiesel may be a function of measurement technique – that is to say, greater adsorbtion of hydrocarbons onto particulate (as discussed in Section 2.2.3.4 biodiesel is understood to generate particulate with a larger volatile fraction) or a greater degree of hydrocarbon condensation prior to measurement (on account of the higher boiling range of biodiesel compared to petrodiesel) may mean that more of the unburned biodiesel is filtered out before it can be quantified [458, 459]. Additionally, it may be that the reduced sensitivity of flame ionisation detectors to oxygenated compounds leads to an underestimation of biodiesel THC [13].

Beyond these explanations, it is conceivable that a possibly slightly narrower spray angle [460, 461] when fuelling on biodiesel may restrict the extent to which over-leaning is able to occur during the ignition delay. Hence, the physical properties of biodiesel may also play a role in the reduction of THC emissions. On the other hand, the increased biodiesel liquid length, resulting largely from its higher boiling range, may be responsible for the increased THC emissions sometimes associated with lower load, lower temperature biodiesel operation [462, 463], by causing increased wall-wetting.

One category of hydrocarbon emissions that may be of concern with respect to the use of biodiesel, and oxygenated fuels in general, is carbonyl species. The uptake of ethanol as a replacement for gasoline in Brazil, for example, was initially associated with a substantial increase in ambient aldehydes [464]. Reports on the effects of biodiesel on these species are mixed [13]. Some studies show a general increase in carbonyl emissions when fuelling on biodiesel [465–467], whilst others demonstrate variation dependent upon the biodiesel feedstock [468] (also, compare [469] with [470]), and others report substantial reductions

in carbonyls [471]. Without any obvious trend having been described, the nature and causes of any possible change in emissions of aldehydes or ketones remain to be clarified.

2.2.5.2 CARBON MONOXIDE

Carbon monoxide (CO) is a colourless, odourless and poisonous gas, which is naturally present in the atmosphere in low concentrations (around 100 ppb) [278, 472]. Although CO plays a small role in the chemistry of tropospheric ozone formation [278], its potential to damage human health is a greater cause for concern. The high affinity of haemoglobin for CO (reportedly 240 times its affinity for O_2 [472]) means that significant replacement of oxygen in the bloodstream (as oxyhemoglobin) by carbon monoxide (as carboxyhemoglobin, COHb) is possible at relatively low ambient concentrations; a prediction of COHb levels resulting from CO exposure can be seen in Figure 2.46 [473]. Although the correlation between COHb levels and the symptoms and severity of CO poisoning is not entirely consistent [474], details of general symptoms are included for indicative purposes [475].

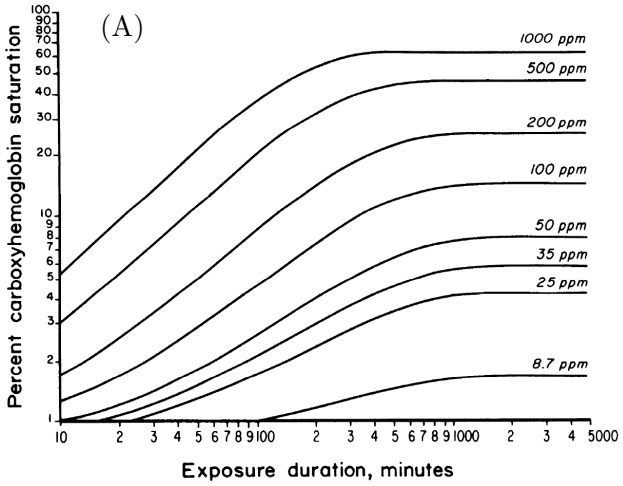

(B)

Blood Level of COHb, percent	Symptoms
0-10	Usually none in healthy individuals; reduced exercise tolerance in patients with pulmonary disease; decreased threshold for angina in patients with coronary heart disease
10-20	Headache; dyspnea on mild exertion; angina in patients with coronary heart disease; dilation of cutaneous vessels
20-30	Throbbing headache; nausea or vomiting (or both); easy fatigability and irritability; difficulty with concentration
30-40	Severe headache; dizziness; fatigue and weakness; syncope on exertion; impaired thought processes
40-50	Tachypnea; tachycardia; syncope; confusion
50-60	Respiratory failure; collapse; intermittent convulsions or seizures; coma
60-70	Respiratory failure; severe hypotension; coma, frequently fatal
>70	Coma, rapidly fatal

Figure 2.46: (A) Carboxyhemoglobin levels for man as a function of exposure duration and of carbon monoxide concentration determined by solving the Coburn-Forster-Kane equation [473]. (B) Symptoms commonly found with different carboxyhemoglobin levels [475].

Ostensibly, the causes of CO emissions are similar to those of unburned hydrocarbons [476]; in-cylinder regions that are either too cool (due to over-leaning or wall-quenching), or without sufficient oxygen to facilitate complete combustion. In practice (as will be shown in Chapter 5), changes in operating conditions that elicit increases in CO emissions do not necessarily cause the same change in THC emissions. This may be because factors related to fuel-rich combustion are more influential in terms of exhaust CO than they are in terms of THC, where the effects of over-leaning predominate. Carbon monoxide

emissions from diesel engines are generally far less of a concern than those from gasoline engines, because the latter operate under far richer global conditions than the former [418].

The majority of the literature (around 90%) reports a decrease in CO emissions when a diesel engine is fuelled on biodiesel rather than petrodiesel [13]. The United States Environmental Protection Agency reports that the use of a B100 biodiesel is associated with an average reduction in carbon monoxide emissions of around 45–50%, compared to petrodiesel [362]. As with THC, this can be attributed in part to the generally reduced ignition delay of biodiesel, which permits less fuel to be diluted to equivalence ratios which preclude the fast, high temperature reactions likely to result in complete oxidation of the fuel. Beyond this, the oxygen content of biodiesel may encourage greater conversion of fuel-carbon to CO_2 in the fuel-rich regions of the flame, and the often faster combustion of biodiesel (see Chapters 4 and 5) may mean that temperatures are higher following the collapse of the diffusion flame, allowing the enduring products of incomplete fuel-rich combustion to be more thoroughly oxidised during the expansion stroke.

2.2.5.3 CARBON DIOXIDE

Carbon dioxide (CO_2) is a transparent and odourless gas, whose presence in the atmosphere has increased from a pre-industrial era global mean level of around 280 ppm [278] to around 400 ppm in 2015 [477]. Although in the very distant past atmospheric CO_2 levels are thought to have dramatically exceeded modern values [478], CO_2 trends over the past few million years exhibit cyclical variations between approximately 200–300 ppm (in parallel with glacial/interglacial cycles), from which the recent rapid increase constitutes a significant and worrying departure [479, 480].

CO_2 is a greenhouse gas (GHG), which absorbs infrared radiation and hence contributes to radiative forcing. Higher levels of CO_2 in the atmosphere increase radiative forcing and are therefore associated with an increase in mean global temperatures – that is, global warming and climate change. Increased anthropogenic CO_2 emissions, primarily via the combustion of fossil fuels and other industrial processes, are considered to be the most important driver of this phenomenon [2]. A host of detrimental effects on the physical environment (e.g. ice and snow melting, flooding and drought, extreme weather events, rising sea levels, etc.), terrestrial and marine ecosystems (e.g. changes in the behaviour, abundance and balance of species, etc.), as well as inevitable impacts on human systems (e.g. reduced crop yields, food insecurity, destruction of homes, etc.), have been widely

attributed to climate change [2]. Other environmental effects of CO_2, such as acidification of the oceans, are also highly damaging. These issues threaten to become more severe as CO_2 levels continue to rise, with potentially more catastrophic consequences looming in the not-too-distant future.

As regards human health, CO_2 is a potential asphyxiate, and excessive exposure can cause acidosis [481]. At atmospheric concentrations it is not problematic, but it may accumulate under certain conditions, due to poor ventilation (particularly close to the ground, due to its relatively high density). Concentrations in excess of 2000 ppm are necessary before physiological effects like shortness of breath are likely to be experienced [481], but it has been reported that less elevated levels may have a detrimental effect on decision making performance [482]. Indirect effects on health, like a reduction in the nutritional value of certain crops, are also amongst the possible negative outcomes of increased atmospheric CO_2 [483].

Unlike the other pollutants that have been discussed, CO_2 is an unavoidable product of complete hydrocarbon oxidation, as illustrated by the idealised reaction:

$$C_xH_y + (x + \frac{y}{4})O_2 \longrightarrow xCO_2 + \frac{y}{2}H_2O \tag{2.35}$$

Hence, the CO_2 emitted from a diesel engine when fuelling on any particular fuel is directly related to brake specific fuel consumption (BSFC), with the vast majority of fuel-carbon injected into the engine leaving the exhaust as CO_2. However, since the relationship between CO_2 emissions and fuel consumption depends upon the weight percentage of the fuel which is comprised of carbon, CO_2 emissions per fuel unit will vary dependent upon fuel composition. The review of Xue et al [484] finds inconsistency in the literature as regards the change in CO_2 emissions when fuelling on biodiesel. Biodiesel contains less carbon by mass (around 77% is typical, compared to approximately 86–88% for petrodiesel), and hence generates less CO_2 per unit of fuel consumed, but because it also has a lower heating value, a greater mass flow rate of biodiesel is required to maintain the same power output. In the studies documented in Chapter 5, CO_2 emissions tended to be marginally higher when fuelling on biodiesel compared to petrodiesel.

Broadly speaking, in the literature more emphasis is placed on the difference in life-cycle carbon dioxide emissions between petro- and biodiesel, rather than exhaust CO_2 concentrations. Combustion of petrodiesel restores carbon to the atmosphere which had formerly been captured and stored within the Earth for many millions of years. Combus-

tion of biodiesel, on the other hand, restores carbon to the atmosphere which was captured and stored by plants far more recently. In this sense, the intended benefit of biodiesel is that it does not contribute to net atmospheric carbon; whereas petrodiesel combustion effectively constitutes an unmitigated addition to modern global CO_2 levels, biodiesel combustion only returns to the atmosphere carbon removed by crop growth earlier in the season. However, this ignores the fossil-derived carbon released throughout the biodiesel life-cycle. Including all energy inputs into the biodiesel production process, it has been estimated that soybean derived biodiesel reduces net CO_2 emissions by 78.45% compared to petrodiesel [12]. Extending consideration to all GHGs, emissions across the life-cycle of soybean biodiesel have been estimated to be reduced by 41% relative to petrodiesel [485]; it is emissions of nitrous oxide (N_2O) resulting from the growth of oil crops that reduces the overall GHG advantage of soybean biodiesel, and for rapeseed derived biodiesel it has been suggested that N_2O emissions may more than totally offset the positive effect of CO_2 reduction [400]. Any positive effects that biodiesel may have on global GHGs are also decimated by the impact of massive land clearance for oil crop growth, particularly in nations like Indonesia, where the destruction of rainforest can incur a 'carbon debt' so large that several centuries of biodiesel usage are theoretically required to undo the initial damage done to the CO_2 balance [486].

It is apparent that a lot depends on what factors are included in the life-cycle analysis, and although most analyses find that the GHG balance is improved by adoption of biodiesel, some authors disagree [487]. In a now very widely cited study, Pimentel and Patzek [488] reported that soybean biodiesel requires 27% more fossil energy to produce than it ultimately yields – but this conclusion and other aspects of the work were subsequently challenged [489].

2.2.6 PROCESSES WITHIN THE DIESEL ENGINE

The following description is an effort to incorporate the fundamental insights provided in the previous sections – alongside other relevant background – into a reasonably functional overall picture of the processes as they occur within a conventional diesel engine. This information is drawn from a range of sources, largely [267, 379, 490–494]; some illustrations from these sources are reproduced over the course of the section, to provide a means of visualising the system in a more understandable way. Largely, the conceptual models described in the literature treat (and are based on) free-jets combusting under quiescent

conditions, and therefore differ from the internal reality of a diesel engine in the sense that neither wall-impingement nor swirl are considered. Despite these simplifications, free-jet descriptions still accurately reflect initial diesel jet development, and the general processes of mixing and combustion [495]. An attempt will be made to integrate descriptions from papers treating impinging or swirling jets, where possible.

Let us begin at the point where the needle valve inside the injector opens, releasing pressurised fuel into the cylinder. In the case of the engine and operating conditions employed for a large part of the experimental work presented in this thesis, fuel was injected at a pressure of 800 bar, through 6 nozzle holes of 0.154 mm diameter, with the 6 holes positioned to create a spray cone angle of 154°. For each individual jet, this corresponds to an initial injection velocity in the region of 165 m/s, and a spray angle of around 15°; due to its higher density, the initial spray angle for biodiesel might be expected to be fractionally narrower than that of petrodiesel [460, 461, 496] (any difference is likely to be small – less than 0.5°, based on the equations given in [167, 497]). Injection velocity is reduced by increased in-cylinder gas density, which causes dispersion, and therefore also increases the spray angle [498]. The increased viscosity of biodiesel may also reduce injection velocity by inhibiting nozzle flow [461, 499, 500], although it has been reported that at pressures typical of common-rail injection systems fuel viscosity has little effect on flow rates [501].

Liquid fuel initially penetrates into the cylinder at an approximately linear rate, until reaching the *liquid length*, which is the point past which all fuel is in the vapour phase, with the spray having entrained enough hot in-cylinder gas to elevate the temperature of the fuel above its boiling point [379, 502]. Although the break-up and atomisation of the liquid jet into smaller droplets is an essential part of the process, in general it can be assumed that vaporisation within a diesel engine is mixing limited, in that it is the entrainment of hot air, heating and diluting liquid fuel and fuel vapour, which controls the rate of evaporation [493]; mixing is dependent upon turbulence [503]. However, at low in-cylinder temperatures and gas densities, where biodiesel has been found to have a particularly long liquid-length, atomisation and interphase transport at droplet surfaces may have increased importance [504, 505].

The liquid length reached depends upon injection parameters, in-cylinder conditions and the thermodynamic properties of the fuel; the correlation given in Equations 2.36–2.38 provides an indication of the critical variables [504]. Where x_{liq} is the liquid length, d_o

is the nozzle hole diameter, k, α and β are all empirically determined constants; ρ_{fuel} and ρ_{air} are the densities of fuel and in-cylinder gas, respectively, and A is therefore the density ratio; $C_{p,fuel}$ and $C_{p,air}$ are the constant pressure specific heats of fuel and air, $T_{b,fuel}$ is the boiling point of the fuel, T_{fuel} and T_{air} are the temperatures of fuel and air at the point of injection, h_{vap} is the fuel's latent heat of vaporisation, and B is called the *specific energy ratio*, being the energy required to vaporise a unit mass of fuel, over the energy available per unit mass of in-cylinder gas.

$$\frac{x_{liq}}{d_o} = kA^{\alpha}B^{\beta} \tag{2.36}$$

$$A = \frac{\rho_{fuel}}{\rho_{air}} \tag{2.37}$$

$$B = \frac{C_{p,fuel}(T_{b,fuel} - T_{fuel}) + h_{vap}}{C_{p,air}(T_{air} - T_{b,fuel})} \tag{2.38}$$

Hence, the liquid length increases with increasing nozzle diameter, fuel density, boiling point and heat capacity, and decreases with increasing in-cylinder gas density and temperature [502–504]. Both calculations [506] and experimental results [507–509] indicate a longer liquid length for biodiesel than petrodiesel and, considering the relative properties of the fuels, one can intuitively understand why this is the case; the density, heat capacity and boiling range are all typically higher for biodiesel than petrodiesel [167]. Within a diesel engine the longer biodiesel liquid length may lead to increased wall-wetting, particularly under cooler, lower pressure ambient conditions (e.g. lower load or advanced injection timing) [506].

Past the liquid length, vapour continues to penetrate into the cylinder and entrain hot gas, with the fuel-air mixture progressing to steadily higher temperatures and lower equivalence ratios. These changes are governed by the rate of entrainment, and the rate of entrainment is proportional to in-cylinder air density, nozzle orifice diameter, injected fuel velocity and the tangent of the spray dispersion half angle [498]. It has been suggested that vapour penetration and total entrainment are largely unaffected by differences in physical properties comparable to those which exist between petro- and biodiesel [510].

The radial fuel mass distribution in a free-jet is highest at the jet centreline, decreasing towards the radial periphery and axial positions further downstream of the injector [511]. However, while radial distributions fall progressively, axial fuel concentration falls steeply at the jet tip; this is because the high turbulence at the sides of the jet facilitates fuel-air mixing, whereas turbulence at the tip of the jet is relatively low, resulting in reduced

mixing [512]. Wall impingement causes a local deterioration in mixing in the region where the jet and wall initially collide (and a stagnation point is formed), but enhances mixing at the tip of the jet due to the formation of a jet-wall vortex which generates turbulence [513]. The overall effect of wall impingement on mixing depends on which of these two factors is dominant.

Depending upon the composition of the fuel, the sort of low-temperature chemistry described in Section 2.2.2.2 typically becomes effective within the heated fuel-air mixture at a temperature of around 700–750 K [230, 490]. Pools of metastable intermediates develop and are consumed; below 800 K ketohydroperoxide species accumulate, before decomposing in degenerate branching reactions, increasing in-cylinder temperatures and the size of the radical pool. The first evidence of heat release can be detected (on the basis of the presence of formaldehyde – which forms immediately following the decomposition of the ketohydroperoxides [493]) in an off-axis, upstream position, where the fully-vaporised mixture is still fuel-rich [447, 514]. From here, the cool-flame, first-stage ignition reactions propagate downstream, and throughout the premixed charge [491]. The equivalence ratio within the leading portion of the premixed jet is reported to be mostly between about 2 and 4, although the full range may be wider and include regions both richer and leaner [515]. Idicheria and Pickett [516] report equivalence ratios in the premixed burn region of up to 5, with a mode of approximately 2. When fuelling on biodiesel, equivalence ratios within the premixed burn are likely to be reduced (in terms of oxygen availability, Ω) due to the fuel-bound oxygen inherent to alkyl esters. When the fuel and operating conditions favour prolonged or enhanced premixing equivalence ratios may be lower [517], although under simulated EGR it has been observed that despite longer ignition delays and greater quantities of premixed fuel mass with increasing EGR rate, the equivalence ratios within the charge remain largely unchanged [516].

To aid this description, an illustration of the conceptual model put forward by Bruneaux [491] is given in Figure 2.47, along with a labelled plot typical of conventional diesel engine heat release in Figure 2.48. The labelled heat release plot shows both the approximate combustion stages depicted in the conceptual model (i.e. 1^{-}, 1^{*}, etc.) and the standard divisions of the diesel combustion process: the ignition delay between the start of injection and the beginning of heat release; the so-called premixed burn fraction in which the fuel-air mixture formed prior to ignition is consumed leading to a rapid spike in heat release; the period of mixing controlled combustion following consumption of the premixed

charge and establishment of the diffusion flame; and the late combustion stage in which remaining pockets of fuel, incomplete combustion products and soot are oxidised after the collapse of the diffusion jet. In addition, simulation results showing the evolution of temperature and important chemical species in a constant pressure homogeneous reactor [493] are provided in Figure 2.49, to assist the illustration of the chemistry of the ignition process.

In Figure 2.47 evidence of low temperature first-stage ignition (i.e. formaldehyde) can be seen spreading throughout the jet in stages 1^{-}, 1^{*} and 1^{+}, becoming restricted to the leaner periphery surrounding the diffusion flame front by stage 2^{-}, and by 2^{*} exists only upstream of the lift-off length, in the standing fuel-rich reaction zone. Although comparison of Figure 2.47 with Figure 2.48 shows that heat release in the earliest stage, 1^{-}, may be attributed to purely low temperature chemistry, from 1^{*} onwards evidence of high temperature reactions is increasingly apparent.

In a conventionally operated diesel engine first- and second-stage ignition do not tend to be sufficiently temporally separate for them to be distinguished on the basis of heat release data, with the first-stage rapidly transitioning into the second [493]. However, under more highly premixed, leaner, highly diluted or cooler conditions the portion of heat release attributable to cool-flame reactions is more clearly discernible. This can be seen in Figure 2.50, which shows that under lightly loaded conditions a low level of heat release is observable prior to the rapid increase in HR which constitutes the familiar diesel premixed burn spike; with further advancement of injection timing, the temporal separation of the low level heat release denoting first-stage ignition and the sharp escalation initiated by second-stage ignition becomes more distinct.

In the homogeneous reactor data shown in Figure 2.49 some separation can be seen between first-stage and second-stage ignition, although the degree of separation is far smaller under the rich conditions of Figure 2.49b than the lean conditions of Figure 2.49a. In both cases after the end of first-stage ignition, when all of the ketohydroperoxide species have been consumed, there is a small increase in temperature – the temperature increase is larger under the fuel-rich conditions, because the size of the KHP pool is larger – and significant quantities of hydrogen peroxide (H_2O_2) and formaldehyde (CH_2O) form. Prior to the start of second-stage ignition, concentrations of CH_2O and unburned hydrocarbons (UHC) decline as these species are oxidised, while concentrations of H_2O_2 increase. Temperature continues to rise slowly until the conditions for H_2O_2 decomposition are

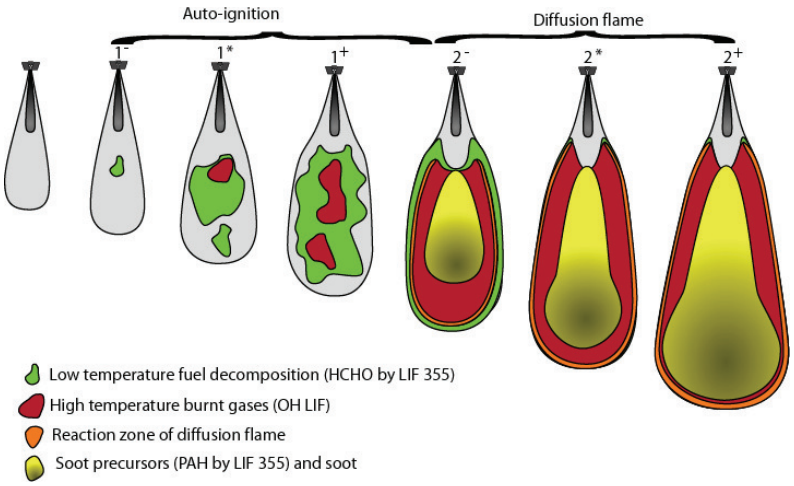

Figure 2.47: Schematic diagram depicting a conceptual model of diesel jet combustion [491].

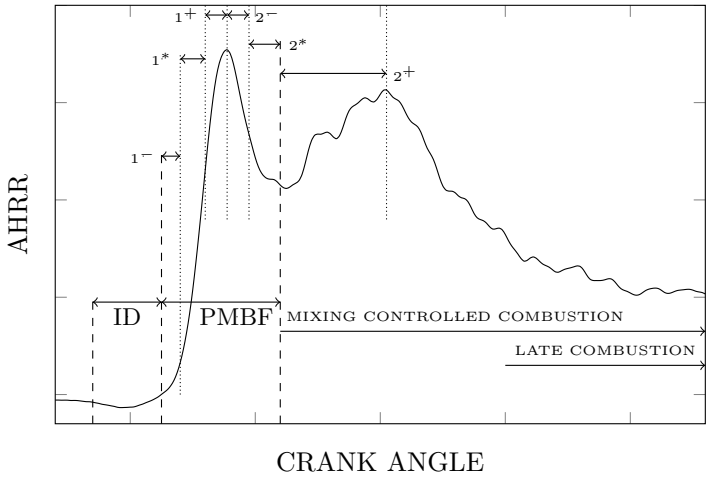

Figure 2.48: Apparent heat release rate plot typical of conventional diesel combustion. Divisions show the key features of the traditional description of diesel combustion: ID, ignition delay; PMBF, premixed burn fraction; followed by mixing controlled and late combustion. Also illustrated are approximate timings of stages 1^-, 1^*, 1^+, 2^-, 2^*, 2^+, to coincide with the conceptual model in Figure 2.47.

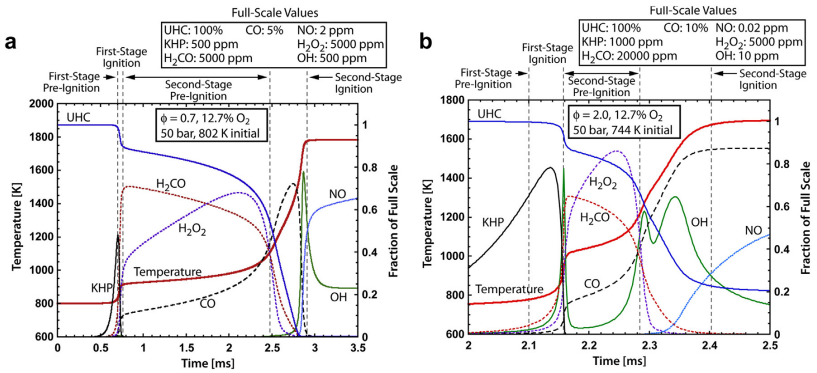

Figure 2.49: Evolution of temperature and important chemical species in homogeneous reactor simulation of ignition of vapour-phase *n*-heptane using the LLNL/Galway-Mayo mechanism [235] for (a) fuel-lean or (b) fuel-rich conditions in 12.7% O_2 and balance N_2 with a constant pressure of 50 bar [493, 518].

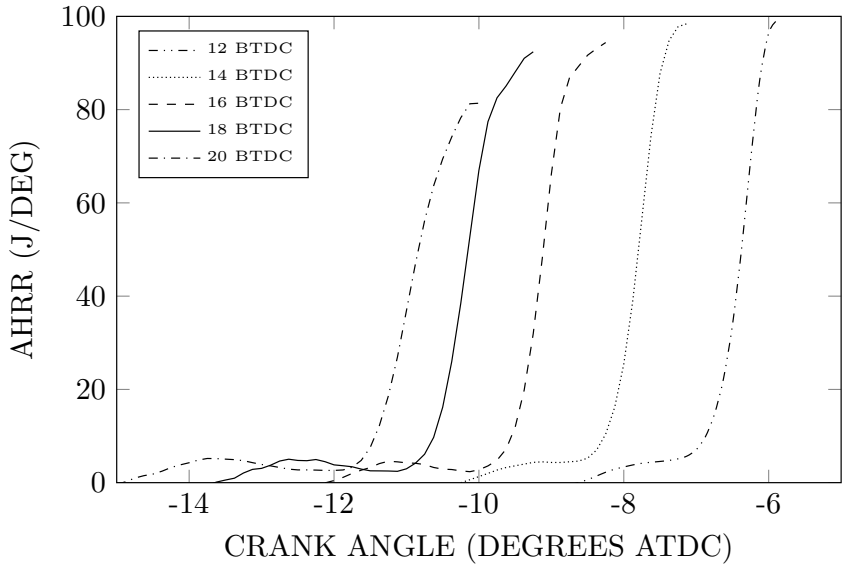

Figure 2.50: Apparent heat release rate between the start of combustion and angle of maximum heat release under very lightly loaded (15 Nm, brake mean effective pressure of 0.94 bar), low speed (1500 rpm) operating conditions. Injection timing swept from 12–20 BTDC. (Data collected in the laboratory engine described in Chapter 3, fuelling on petrodiesel.)

achieved, at which point the H_2O_2 population plummets, producing highly reactive OH radicals which accelerate the rates of hydrocarbon oxidation, rapidly increasing the temperature and quickly reducing the remaining CH_2O pool. In Figure 2.47, evidence of the high temperature reactions that follow second-stage ignition is initially found at the core of the formaldehyde cloud in stage 1^*, expanding throughout the cloud in 1^+, and continuing to expand out into the fuel-lean regions in 2^-.

High temperature reactions begin downstream of the cool-flame reactions, with the degree of separation dependent upon the time taken to transition from first- to second-stage ignition, which is itself dependent upon the type of fuel and the engine operating conditions [376]. Changes in ambient gas temperature may also shift the position of autoignition sites within the jet; Kosaka et al [492] suggest that while ignition occurs in fuel-rich regions towards the core of the jet at temperatures within the negative temperature coefficient (NTC, see Section 2.2.2) range – around 800–1000 K – under hotter or cooler conditions ignition may instead occur closer to the spray periphery, where temperatures are highest. When fuelling on biodiesel autoignition may occur earlier, and further upstream [509], but this is likely to depend upon the cetane number of the biodiesel in question.

The conceptual model depicted in Figure 2.47 shows OH radicals within the jet prior to the establishment of the diffusion flame. However, other prominent conceptual models – particularly that based on the work of Dec [379], and finding its most recent and highly developed expression in Musculus et al [493] – take a slightly different view. In this

embodiment, OH radicals appear at approximately the same time with respect to heat release (approximately within the 1^* to 1^+ demarcations in Figure 2.48), but rather than being located towards the core of the jet, they are at the periphery, in an emerging diffusion flame [379, 493, 519]. First-stage ignition processes sweep through the entirety of the combustible fuel-air mixture within about a degree or so of the start of combustion, approximately equivalent to stage 1^* in Figure 2.48. This is followed in quick succession by second-stage ignition throughout the jet. A diffusion flame is formed at the upstream periphery where the mixture is stoichiometric, with its base in a lifted position (i.e. it does not extend all the way back to the nozzle – the degree of separation, is termed the *lift-off length*), and before peak heat release the reaction front spreads downstream, fully encompassing the jet. In the Bruneaux model, on the other hand, solely premixed combustion is more prolonged, with the diffusion flame being established in stage 2^-, just after the heat release peak. The reason for this difference between the two models is not obvious, but may have some relation to differences in the operating conditions upon which they are based.

In both models, however, it is clear that the diffusion flame establishes itself well within the nominally 'premixed' combustion phase, which makes the traditional division between premixed and mixing-controlled combustion stages, as illustrated in Figure 2.48, somewhat misleading; the premixed burn fraction might therefore be better characterised as premixing *supplemented*. Neither is combustion purely mixing-controlled following the establishment of the diffusion flame; Figure 2.47 stage 2^- sees continued evidence for low temperature premixed reactions in the leaner periphery of the jet, and into 2^* and 2^+, small zones of low temperature reaction products remain visible in the most upstream reacting positions. The Dec model puts greater emphasis on the upstream fuel-rich premixed reaction zone which exists within the fully developed diffusion flame, and can be seen in Figure 2.51 in light blue. In the updated derivative of the Dec model provided by Musculus et al [493] the same reaction zone is identified as the location of fuel-rich second-stage ignition, and is preceded by a large upstream region of low-temperature first-stage ignition reactions (as seen in [514]). The partial oxidation reactions which take place within the fuel-rich premixed flame generate products elevated to a temperature of around 1600–1700 K, which continue into the oxygen depleted core of the jet, in which soot forms and grows.

At its conception the fuel-rich premixed reaction zone was proposed as an explanation for the quantity and location of soot observed within the diffusion jet [379]. In Figure 2.51,

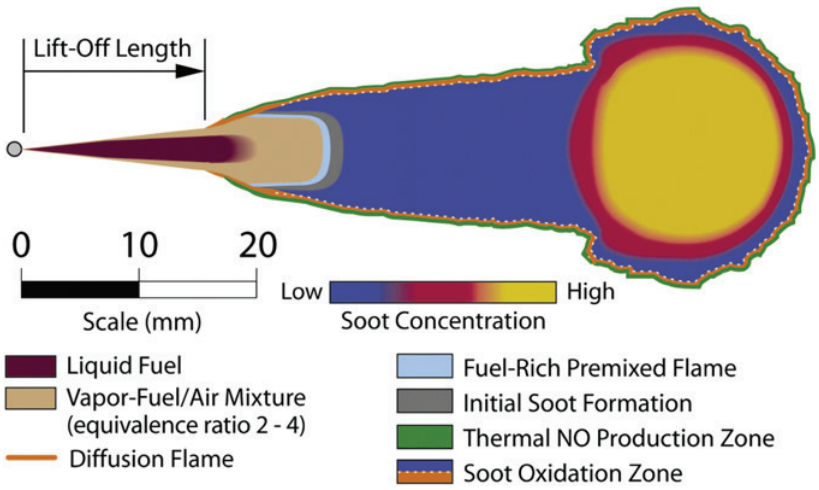

Figure 2.51: Schematic of Dec's conceptual model for conventional diesel combustion during the quasi-steady period (N.B. the 'quasi-steady' period is equivalent to combustion stage 2^+ in Figures 2.47 and 2.48) [379, 493].

past approximately 27 mm, soot exists over the cross-section of the jet: since the air entrained into the jet is not hot enough to induce pyrolysis directly this cannot be the source of soot, and if pyrolysis were due to heat and radicals transported inward from the diffusion flame front, the appearance of soot should be more progressive, from the outside inwards [379]. The presence of a fuel-rich reaction front within the jet, releasing heat and contributing to the formation of soot precursors, helps to explain the way in which soot appears. However, the relationships between first-stage ignition reactions, the premixed reaction zone, and the formation of polycyclic aromatic hydrocarbons (PAH) and soot within the jet are themselves influenced by other factors – in particular, the lift-off length.

The lift-off length is the distance from the nozzle exit to the most upstream extremity of the diffusion flame front, and can be seen illustrated in Figure 2.51. A range of different theories to explain flame lift-off have been proposed [520], and a relationship with autoignition is likely [377]. An empirically derived dependence of the lift-off length on injection and ambient conditions is given in Equation 2.39, where H is lift-off length, ΔP_{inj} is injector pressure drop, T_{air} and ρ_{air} are in-cylinder air temperature and density, respectively, and d_o is the injector orifice diameter [520]. Equation 2.39 suggests that lift-off length should be expected to increase with increasing injection pressure and nozzle hole diameter, whilst falling with increasing in-cylinder air density and temperature.

$$H \propto (\Delta P_{inj})^{0.5} (T_{air})^{-3.74} (\rho_{air})^{-0.85} (d_o)^{0.34} \tag{2.39}$$

In a practical diesel engine lift-off length may be significantly shorter than in the

quiescent jets upon which most models are based [521]. Closer proximity of jets (i.e. more nozzle holes per injector), tends to reduce individual lift-off lengths, and make them less sensitive to the temperature of the in-cylinder air [521]. Any confinement which redirects hot combustion gases back towards either the jet from which they originate, or any neighbouring jet, is likely to cause a reduction in lift-off length [522]. In-cylinder swirl causes asymmetric lift-off, with the lift-off length slightly longer on the upswirl side of the jet [521].

Lift-off length and liquid length both decrease with increasing ambient temperature, but lift-off length decreases more rapidly [523]. At lower temperatures the lift-off length is longer than the liquid length, but at higher temperatures the opposite is true; both lengths are also reduced by increasing in-cylinder pressure, and at higher pressures the crossover (i.e. the temperature above which lift-off length is the shorter of the two) occurs at lower temperatures. Some researchers have associated the difference between liquid length and lift-off length with soot formation, suggesting that a relative reduction in lift-off length may correlate with increased sooting [524].

Although liquid length is unambiguously increased when fuelling on biodiesel, the change in lift-off length is less clear; some reports say that it is shorter with biodiesel [509, 525, 526], while others say that it is longer [527, 528]. It seems likely to be the case that the difference in lift-off lengths between petro- and biodiesel will depend upon the cetane numbers of the particular fuels in question.

The lift-off length itself may or may not change when fuelling on biodiesel, but – critically – the equivalence ratio at the lift-off length, will be reduced, due to the fuel-bound oxygen content, and consequently lower stoichiometric air:fuel ratio of biodiesel (around 13–14% lower than that of petrodiesel). Once the downstream jet is encapsulated by the diffusion flame (as in Figure 2.51, or from 2^- onwards in Figure 2.47), further air cannot be entrained into the jet beyond the lift-off length, and so the equivalence ratio in this region is of high importance, as it determines the environment and reaction conditions which exist within the diffusion flame sheath. The equivalence ratio at the lift-off length can be estimated using Equations 2.40 and 2.41; where ϕ_{LOL} is the equivalence ratio at the lift-off length, H is the lift-off length, x^+ is a characteristic length scale for the fuel jet (calculated using Equation 2.41), $(m_{fuel}/m_{air})_{st}$ is the stoichiometric fuel:air ratio (that is, the reciprocal of the stoichiometric air:fuel ratio), ρ_{fuel} and ρ_{air} are fuel and in-cylinder air densities, d_o is the orifice diameter, Θ is the fuel spray angle and C_a is the area contraction

coefficient of the orifice [529]. Based on Equations 2.40 and 2.41 it can be seen that ϕ_{LOL} decreases as H increases, as $(m_{fuel}/m_{air})_{st}$ increases (and stoichiometric AFR decreases), as the ratio of densities decreases, and as d_o decreases.

$$\phi_{LOL} = \frac{2}{(\sqrt{1+16(H/x^+)^2}-1)(m_{fuel}/m_{air})_{st}} \tag{2.40}$$

$$x^+ = \sqrt{\frac{\rho_{fuel}}{\rho_{air}}}\frac{d_o\sqrt{C_a}}{0.75tan(\Theta/2)} \tag{2.41}$$

There is a decrease in soot formation within the jet with decreasing equivalence ratio at the lift-off length, as can be seen in Figure 2.52 [530]. Once 50–60% of the required oxygen is available at the lift-off length, fuel jets become effectively non-sooting; however, the exact percentage at which it falls to zero, and the level of sooting at higher equivalence ratios is dependent upon the inherent sooting tendency of the fuel, as well as ambient conditions.

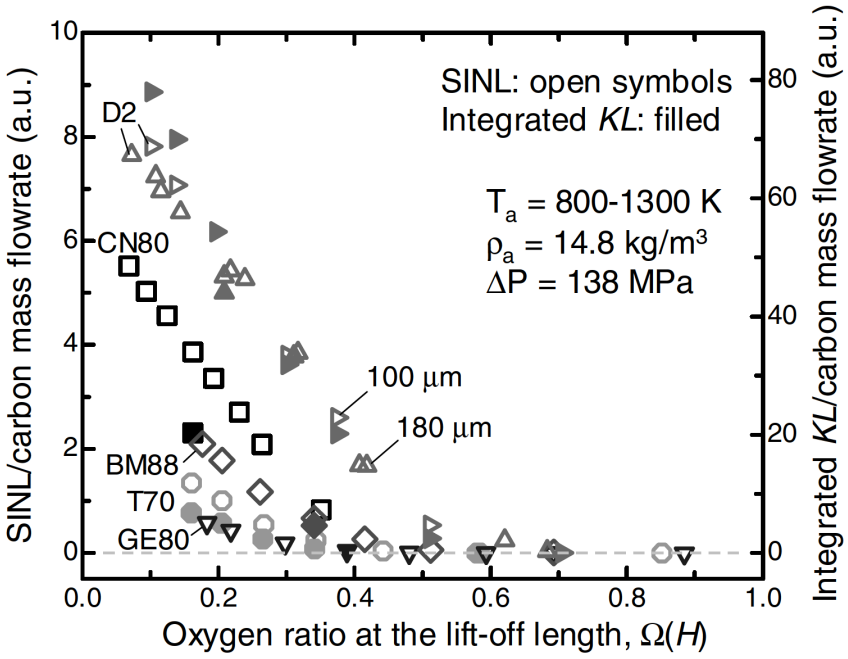

Figure 2.52: Spatially integrated natural luminosity (SINL) and integrated optical thickness (KL) versus oxygen ratio at the lift-off length (Ω_H) for various fuel blends. SINL is plotted in open symbols on the left axis and integrated KL is plotted in filled symbols on the right; both are normalised by carbon mass flow rate for each fuel. The ambient gas density was 14.8 kg/m^3 and the injector pressure drop was 138 MPa. Ω_H changes occurred as a result of changes in lift-off length with changes in ambient gas temperature. D2: number 2 diesel (data provided for two orifice diameters, 100 μm and 180 μm). CN80: 76.5% n-hexadecane, 23.5% heptamethylnonane. BM88: 88% dibutyl maleate, 7% n-hexadecane, 5% 2-ethylhexyl nitrate. T70: 70% tetraethoxypropane, 30% heptamethylnonane. GE80: 80% tripropylene glycol methyl ether, 20% heptamethylnonane [530].

In Figure 2.52 the number 2 diesel (D2) and 76.5% n-hexadecane, 23.5% heptamethylnonane blend (CN80) contain no fuel-bound oxygen, whilst the 88% dibutyl maleate, 7%

n-hexadecane, 5% 2-ethylhexyl nitrate blend (BM88), 70% tetraethoxypropane, the 30% heptamethylnonane blend (T70) and the 80% tripropylene glycol methyl ether, 20% heptamethylnonane blend (GE80) all contain some fuel-bound oxygen, causing an inherent reduction in the oxygen ratio at the lift-off length when fuelling on them. The difference between the sooting of the unoxygenated fuels, D2 and CN80, for a given oxygen ratio at the lift-off length is largely attributable to the presence of aromatics in the former, which are absent from the latter; the difference between the sooting of the oxygenated fuels is attributable in part to differences in the efficacy with which fuel-bound oxygen is utilised for soot reduction [530] (discussed in Section 2.2.3.4). Beyond differences due to molecular structure, and the average cross-sectional oxygen ratio at the lift-off length, it is also important to consider that greater fuel-bound oxygen means that the equivalence ratio at the richer centre of the jet is likely to be reduced more greatly than the cross-sectional average [530].

In Figure 2.52 the range of oxygen ratios for each fuel has been achieved by increasing the ambient temperature, and hence reducing lift-off length and air entrainment prior to lift-off [530]. Figure 2.53 [514] offers a conceptual model based on changes to the sooting propensity of a jet elicited, again, by alteration of ambient temperature (from 850 K in (A), to 900 K in (B) and 1000 K in (C), all at a constant ambient air density of 14.8 kg/m^3), providing insight into the interplay of the first-stage ignition reactions, lift-off length, premixed reaction zone and soot formation processes [514]. Although changes to the lift-off length in Figures 2.52 and 2.53 are the result of changes to ambient temperature, similar changes might also result from variations in fuel reactivity, with more reactive fuels typically having shorter lift-off lengths [376, 377].

The illustrated nature of the premixed combustion zone is slightly different in this embodiment, having a tribrachial appearance, including a small fuel-lean premixed flame on the outside of the diffusion reaction front, in addition to the fuel-rich combustion zone across the core of the jet. Also different from Figure 2.51, initial soot formation does not occur immediately after the fuel-rich premixed flame, but is pushed further downstream. In Figure 2.53A, at the lowest temperature, longest lift-off length conditions, where the oxygen ratio at the centre of the jet is likely to be highest, neither polycyclic aromatics or soot are observed downstream of the premixed combustion zone. The low temperature reactions producing formaldehyde begin upstream of the lift-off length, and the high temperature reactions in which CH_2O is consumed occur across the fuel-rich

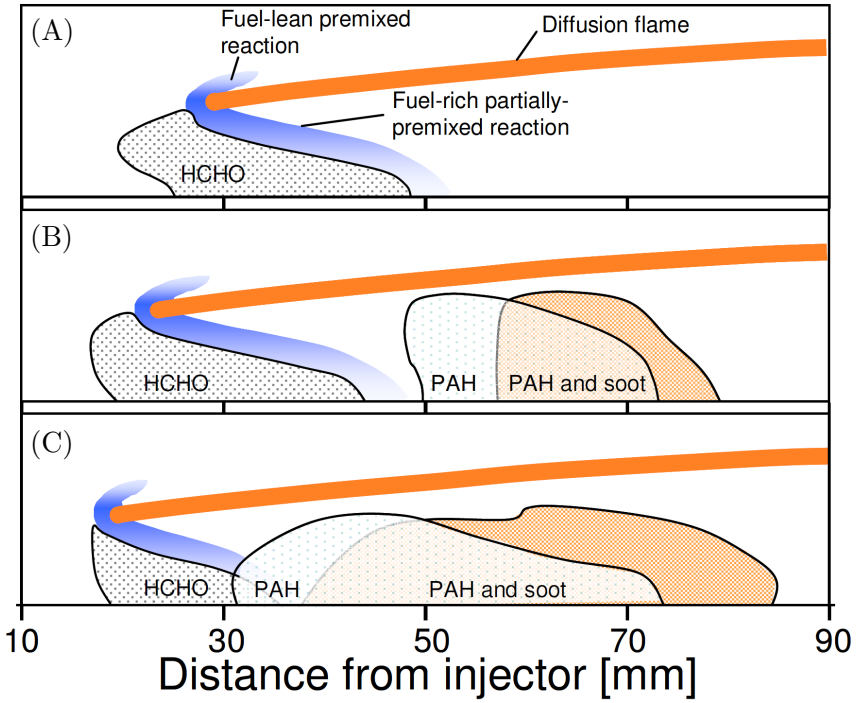

Figure 2.53: Conceptual models of HCHO, PAH and soot formation for (A) no-soot, (B) low-soot and (C) moderate-soot conditions (adapted from [514] and [531]).

reaction zone, progressing from the periphery to the core of the jet. In Figure 2.53B, where the temperature is higher, the lift-off length is shorter, the oxygen ratio at the lift-off length is likely to be lower and consequently the formation of PAH is observed shortly after the fuel-rich combustion zone; moving downstream, the PAH is consumed and a cloud of soot is formed. Although the PAH and soot zones overlap, PAH necessarily arises prior to the formation of soot, because it is from PAH that soot nuclei are formed. In Figure 2.53C, under the hottest illustrated conditions, the lift-off length extends far enough upstream to almost entirely enclose the low temperature reaction zone, likely reducing the oxygen ratio within the jet further still, resulting in the formation of PAH occurring further upstream and in greater quantity. Likewise, the soot cloud begins further upstream and becomes larger under these conditions.

At equivalent operating conditions and lift-off length, the degree of separation between the lift-off length and the location of first soot formation correlates with the sooting tendency of the fuel [378]. That is, progress from the fuel-rich premixed flame, through soot precursors and PAH to soot is more rapid where the structure of the fuel readily lends itself to soot formation – if the fuel naturally contains aromatic species, for example. Absence of such species extends the process of soot formation, increasing both the temporal and spatial gap between high temperature ignition and soot inception. Similarly, the presence of fuel-bound oxygen, by reducing the like-for-like equivalence ratio within the

jet, also delays the inception of soot [378]. Relative to petrodiesel, biodiesel jets have been observed to contain reduced soot concentrations, with soot arising further downstream of the lift-off length [509], delaying subsequent stages of the soot development process [532].

Both the size and concentration of soot particles increases moving further downstream within the jet, reaching maximum values within the head vortex seen in Figure 2.51 [267, 533]. Wall-impinging jets may contain less soot than free-jets, because much of the fuel-rich core is spread across a surface, to which heat is lost, reducing temperatures within the core, and therefore reducing rates of soot formation; additionally, air entrainment into the flame tip is increased by wall-impingement, enhancing soot oxidation [522].

While the diffusion flame is intact, soot exists within it, but not beyond it, because the high temperatures and radical concentrations at the reaction front facilitate the rapid oxidation of soot. For similar reasons, it is approximately coincident with the establishment of the diffusion flame that the formation of NO_x begins [534].

Despite the positive correlation which is commonly observed between the proportion of premixed heat release and NO_x emissions [517], it is reported that in a conventional diesel engine NO_x emissions do not arise from premixed combustion itself, on the basis that it is typically too rich [534]. It is possible that a leaner and consequently hotter premixed burn, as associated with biodiesel, may afford some direct NO_x formation, but the effect on downstream processes is likely to be more significant [525]. It is on the lean periphery of the diffusion flame, where temperatures are high and oxygen and nitrogen are abundant, that the NO_x formation rate is at its maximum [379]. However, because thermal NO formation is a relatively slow process, a large amount of NO_x may also be formed in the hot post-flame gases. Figure 2.54 illustrates the estimated NO production rate throughout the engine cycle [534].

Figure 2.54 shows around 2/3 of NO being formed during heat release and around 1/3 formed after the end of combustion, with NO_x formation continuing for approximately a further 20 CA after heat release concludes. Following the end of injection, but before the end of heat release, regions of NO formation are also observed within the wake of the jet, away from the remaining flame zones. Expansion and dilution of hot post-flame gases determines when they become too cool for NO formation to continue. Hence, the extent to which NO_x formation out-lasts heat release is significantly affected by factors like swirl and combustion duration [534]. Conditions following the collapse of the jet exert a great deal of influence over the quantities of pollutants ultimately emitted from the engine.

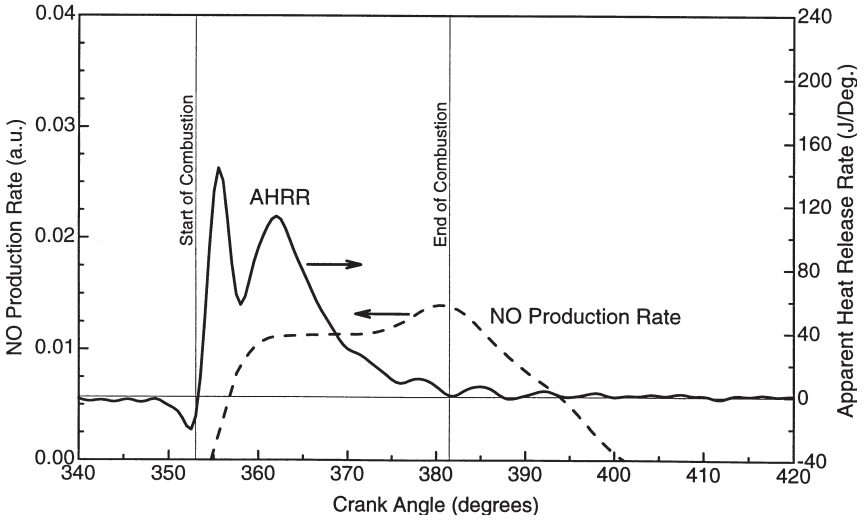

Figure 2.54: Estimated NO production rate throughout the engine cycle, shown alongside apparent heat release rate [534]. (Note that the bump in the NO production-rate curve near the end of combustion is said to be within the noise of the data.)

As injection ends the mass flow rate of fuel into the jet is reduced and, because the downstream flow rate remains constant, greater air entrainment into the spray is required for continuity, generating a more fuel-lean mixture close to the injector [535, 536]. The liquid length and lift-off length both recede back towards the injector, with high-temperature ignition consuming the pools of low-temperature reaction products present upstream of the steady-state lift-off length [451, 537]. At higher temperatures, and with more reactive fuels the recession of lift-off length is more rapid, with implications for unburnt hydrocarbon emissions [451].

The reacting jet becomes entirely encapsulated by the diffusion flame, and is carried downstream as a whole. The plume stem disappears, momentum propels the remains of the burning jet against in-cylinder surfaces, causing it to spread out and collide with the remains of other jets, before being pushed back out into the chamber. As regions of combustion are progressively oxidised and reduced in size, they break-up into smaller pockets [267, 385]. Throughout the expansion stroke soot primary particle diameters fall, and the structure of remaining soot becomes increasingly graphitic and orderly [538].

Insufficient time, excessive cooling or insufficient access to oxidants may prevent total burnout of soot and other products of incomplete combustion. Turbulence assists oxidation in that it improves the availability of oxygen, but by diluting the burnt gases may quench the oxidation process. Ultimately, the vast majority of soot formed in the engine is destroyed before the exhaust valves open [267, 385]. It is possible that by increasing the reactivity of soot, biodiesel may make the burnout process more effective [13]. The

reduced combustion duration often associated with biodiesel fuelling may mean that there is also more time available for burnout, which would also tend to reduce soot emissions.

2.3 HOW BIODIESEL INFLUENCES NO_x EMISSIONS

2.3.1 INTRODUCTION

The majority of the literature reports an increase in NO_x emissions when a diesel engine is fuelled on biodiesel rather than petrodiesel; the review of Lapuerta et al [13] suggests an increase in 85% of cases, while the reviews of Xue et al [484] and Sun et al [539] report unambiguous increases in only 65% and 48.5% of studies, respectively. The United States Environmental Protection Agency reports that the use of a B100 biodiesel is associated with an average increase in NO_x emissions of around 10%, compared to petrodiesel [362].

The commonly reported NO_x increase is not a straightforward, fixed effect of biodiesel; rather, it is the result of the interplay of a variety of factors, related to both the properties of the fuel itself and the characteristics of the engine which it is used to power. A more complete understanding of the causes of the change in NO_x emissions allows associated issues to be considered from a more nuanced perspective.

Many reasons have been posited for the change in NO_x emissions that is observed when fuelling a diesel engine on biodiesel, or biodiesel blends. The differences in chemical and physical properties between petro- and biodiesel (which have been discussed in Section 2.1.4), can affect emissions via, first, changes to the chemistry, thermodynamics and timing of the combustion process itself, second, changes to the fluid dynamics and mechanics of the injection event and mixture preparation, and, third, changes that may take place further upstream in the fuelling system or be induced by the engine management system in response to the properties of the fuel. The latter factors, being dependent upon the specifics of the engine, are the least fundamental and least universal in their applicability. In this overview, the issues of most restricted relevance shall be addressed first, followed by a treatment of those influences for which it is possible to compensate, and, finally, possible substrative and unavoidable differences will be discussed.

2.3.2 INJECTION EVENT

In engines with older pump-line-nozzle (PLN) type injection systems, the start of injection may be artificially advanced when fuelling on biodiesel [180, 540]. The magnitude of this

advance is reported to be around 1–2.5 CA for a pure biodiesel [180, 540–542]. Depending upon the nominal injection timing and operating conditions, advancing injection by 1 CA could be expected to cause an increase in NO_x emissions of 5–10% [543].

Advancing injection timing typically increases NO_x (unless nominal injection timing is already highly advanced [544]) because, if the start of injection (SOI) occurs earlier, then the start of combustion (SOC) also occurs earlier. Heat release earlier in the engine cycle leads to earlier increases in in-cylinder pressure and subsequently to greater compression-heating of reactants, resulting in higher combustion temperatures [517]. Conversely, heat release later in the engine cycle is affected more greatly by expansion-cooling of reactants, associated with a reduction in combustion temperatures. Since much of NO_x formation occurs within the hot post-flame gases, compression and expansion of these is also an important factor [517]. Therefore, advancing the SOC will tend to increase the effects of compression-heating, reduce the effects of expansion-cooling, thus causing a general increase in temperatures, and thereby NO_x formation. Earlier heat release also prolongs high temperature residence times, allowing more time for NO_x formation, and hence contributing to the NO_x increase.

In large part, the biodiesel injection timing advance is due to the higher bulk modulus and higher speed of sound of biodiesel, as discussed in Section 2.1.4.4. The higher speed of sound means that the pressure rise will travel faster from pump to nozzle, and the higher bulk modulus means that a more immediate increase in pressure is elicited by the sudden change in volume caused by the action of the pump [180]. Higher viscosity may also contribute to this effect by reducing fuel leakage past the pump plunger, allowing pressure to develop more rapidly [180].

It would be expected that more highly unsaturated biodiesels will experience a greater artificial timing advance, on account of their higher bulk moduli and speeds of sound; Tat [545] observed a greater advance when fuelling on a soy derived biodiesel (largely C18:2) than when running on a yellow grease biodiesel (mostly C18:1), for example.

In engines equipped with high pressure common rail injection systems the artificial advance in injection timing is not observed [546, 547]. This is because common rail systems decouple pressure generation and injection processes, with a fuel reservoir maintained at high pressure and constantly available for delivery via electronically controlled injectors [548]. Rather than needle lift being a result of instantaneous fuel pressure applied to the base of the needle (as in PLN systems), it depends instead upon pressure relief above

the needle. As such, the transmission of pressure from pump to needle no longer controls injection timing, and so differences in bulk modulus and speed of sound no longer exert as much influence (it should also be noted that the differences in bulk modulus and speed of sound between petro- and biodiesel are smaller at high pressure [182]). Other physical properties may still affect injection timing; the higher viscosity of biodiesel, for example, may cause slight hydraulic delay, particularly at lower injection pressures [549]. However, in practice the difference appears to be negligible [546].

Fuelling on biodiesel also affects the duration of the injection event, although once again the nature of the change depends upon the type of fuel delivery system employed. In PLN systems the injection duration may be reduced when fuelling on biodiesel [540], possibly due to an increase in injection pressure caused, again, by the higher bulk modulus of the fuel [550]. In common rail systems, on the other hand, the injection event is likely to be longer [546, 551] on account of the lower energy density of biodiesel. It has also been suggested that the higher viscosity of biodiesel may reduce the flow rate through the injector, reducing the injection velocity [461, 499] – this factor could also influence the injection duration. However, Dernotte et al [501] report that at higher injection pressures (55–180 MPa in their study), the effect of fuel viscosity on the discharge coefficient is reduced, and mass flow rate is controlled solely by fuel density.

2.3.3 CONTROLLED SYSTEM RESPONSES

Knight et al [551] term the artificial timing advance associated with biodiesel a *passive* system response; this is in opposition to what is referred to as a *controlled* system response, in which a difference in fuel properties causes the engine to actively modify parameter control settings.

Diesel engines are generally designed and calibrated with the intention that they be fuelled on commercial petrodiesel conforming to legislative standards (and hence containing at most only a small percentage – less than 7% [16] – of biodiesel). In many production engines the operation of the engine control system can be affected when fuelling on biodiesel, or biodiesel blends, because the reduced energy density of the fuel necessitates a higher volumetric fuel flow rate (i.e. more fuel per injection event) in order to obtain equivalent power output. Since fuel flow rate is commonly used internally to infer torque, control systems designed to optimise performance and emissions can overestimate engine loading when fuelling on biodiesel and may therefore adjust parameters like exhaust gas

recirculation (EGR) rate, the timing and pressure of injection, the number of injection events, and turbocharger behaviour, compared to when running on petrodiesel [551–553].

The effects of controlled system responses relate to specific engines and operating conditions, and are not generalisable. In some cases the differences in systematic response may increase relative NO_x emissions when fuelling on biodiesel, whilst under alternative conditions they may reduce them; in some cases the effects of the controlled responses are small, in others they can exert more influence on NO_x emissions than the actual combustion differences between petro- and biodiesel. The studies of Eckerle et al [552] and Knight et al [551, 553] offer far greater insight into these issues.

2.3.4 IGNITION DELAY AND PREMIXED BURN FRACTION

Although it depends upon the precise composition of the fuels being compared, as discussed in Section 2.1.4.10, the general expectation is that biodiesel has a shorter ignition delay (i.e. a higher cetane number) than petrodiesel. When this is the case, the SOC is advanced, and as a result the NO_x emissions are higher (ceteris paribus), for the same reasons described in connection with injection timing advance.

However, the reduction in ignition delay also reduces the quantity of premixing that is able to take place prior to ignition. Degree of premixing is positively correlated with NO_x emissions, which means that any reduction in ignition delay encountered when fuelling on biodiesel has two competing effects: a tendency to increase NO_x on account of advanced SOC, and a tendency to reduce NO_x on account of reduced premixed burn fraction (PMBF) [14, 529, 543].

The reasons that PMBF is correlated with increased NO_x emissions are not known with complete certainty, but they involve – or may involve – the following [517]:

- A larger PMBF can result in increased NO_x emissions in a similar manner to advanced SOC; that is, by bringing heat release forward in the cycle, enhancing the effects of compression-heating, reducing the effects of expansion-cooling, increasing temperatures and prolonging high temperature residence times.
- Reduced heat transfer:
  - Under more highly premixed conditions, less soot forms within the jet, and as a result radiant heat transfer and losses (explored in more depth in Section 2.3.8) may be reduced, causing an increase in local temperatures.

  - The rapidity of highly premixed combustion may also mean that there is less suppression of local temperatures by dilution with cooler regions of the in-cylinder gas, or of global temperatures by convective heat transfer [554].

- It is reported that under typical diesel operating conditions the equivalence ratio of the premixed charge is too rich (ϕ = 2–4) for large quantities of NO to be formed by the thermal mechanism; NO production begins when the diffusion flame is established [379, 534]. However, stratification of the premixed charge may mean that in some regions the mixture is lean enough for NO to form directly. Under some conditions (e.g. those affording longer ignition delays) it is also possible that the bulk of the charge may be lean enough for thermal NO formation to occur.

- Even if equivalence ratios are not low enough for thermal NO formation, some reports [555] find that they may well be low enough ($\phi < 1.8$) for prompt NO formation to occur during premixed combustion. However, evidence for this is limited, and the quantities of NO_x formed may be small [556].

Additionally, on the basis that there is a general correlation between degree of premixing and fuel ignition quality, between fuel ignition quality and lift-off length [376, 377] (although this relationship does not always hold [530]), between lift-off length and the equivalence ratio within the autoignition zone [557], and between equivalence ratio within the autoignition zone and NO_x emissions [527], it may be conceived that increased PMBF might also be associated with higher NO_x emissions due to altered mixture stoichiometry within the jet. However, this association would not be *caused by* the degree of premixing, only coincident with it. Another example of a non-causal association between PMBF and NO_x is that fuels containing higher quantities of unsaturated or aromatic compounds, which have relatively low cetane numbers and therefore form relatively large PMBFs, also have relatively high adiabatic flame temperatures, which might also be expected to increase NO_x emissions [517, 558].

There is also the question of how the mixing time afforded by ignition delay relates to the degree of premixing; that is to say, does biodiesel premix to the same degree as petrodiesel given the same time to do so, or does it generate a smaller or larger PMBF for the same ignition delay? On the whole, the results presented in this thesis (see Chapter 4 and Chapter 5) suggest that biodiesel may form a slightly smaller PMBF for the same mixing time. This stands to reason, on the basis that biodiesel is less energy dense than

petrodiesel and so, assuming that both types of fuel are injected at equal volumetric flow rates, it should take longer for the same amount of fuel energy to pass into the cylinder when fuelling on biodiesel. Further discussion of factors influencing differences in mixture preparation extends into the broader topic of mixing and spray characteristics.

2.3.5 MIXING AND SPRAY CHARACTERISTICS

Beyond differences in energy content, other physical and chemical differences between petro- and biodiesel may influence the degree of premixing – both in the sense of the previous section (i.e. mixture preparation prior to the start of combustion), and in the continuous sense of air entrainment into the lifted jet upstream of the lift-off length. There may also be differences in the geometry of the jet that could influence emissions.

The fuel-bound oxygen content of biodiesel is a critical factor in terms of mixture preparation, because it means that a slightly lower AFR is required for complete combustion than is the case for petrodiesel. This is illustrated in Figure 2.55. As a result of this, the proportion of required oxygen which is available – termed the oxygen ratio, or Ω – is higher for a given quantity of fuel-air mixing for biodiesel than for petrodiesel; that is, the biodiesel oxygen equivalence ratio, ϕ_Ω (defined in [382]), is lower, particularly in richer regions of the jet. This is illustrated in Figure 2.56.

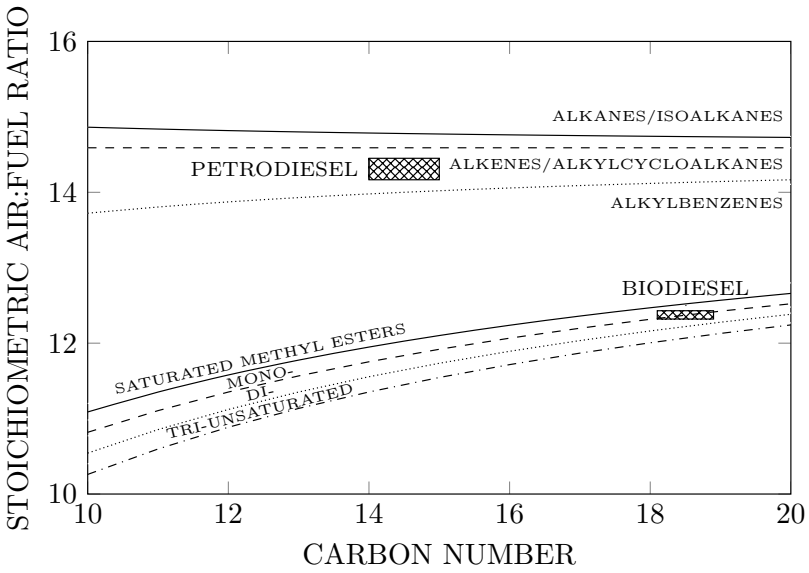

Figure 2.55: Stoichiometric air:fuel ratios for petrodiesel, biodiesel, and their constituents as a function of carbon number. Labelled lines illustrate stoichiometric AFRs of constituents, crosshatched rectangles represent possible overall ranges for the fuels. Petrodiesel rectangle based on average carbon number from 14–15, and H/C ratio of 1.7–1.9. Biodiesel rectangle based on the fatty acid composition of 6 common biodiesels; methyl esters of rapeseed, soya, palm, tallow, jatropha and sunflower oils [103].

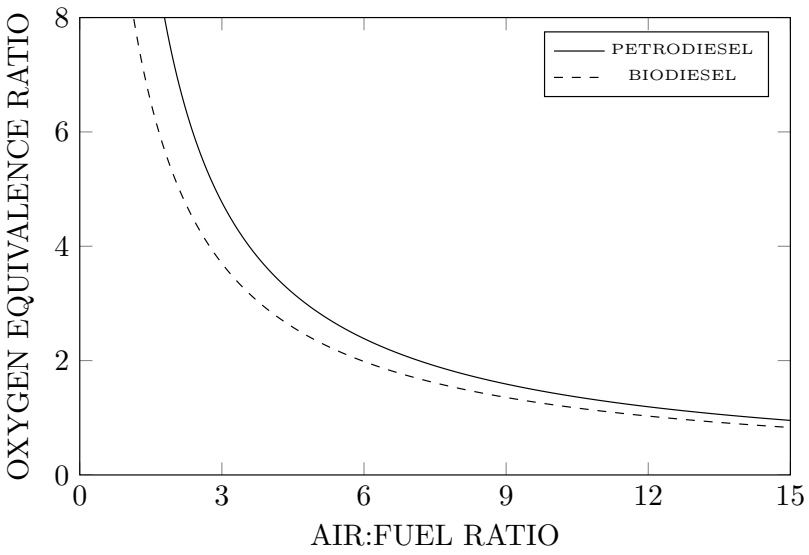

Figure 2.56: Oxygen equivalence ratio (ϕ_Ω, see [382]) as a function of air:fuel ratio for petrodiesel (solid curve) and biodiesel (dashed). Values based upon averages of the same approximations of petro- and biodiesel composition as illustrated in Figure 2.55.

It has been suggested that the fuel-bound oxygen content of biodiesel may encourage the fuel injected during the ignition delay to premix more fully, thus increasing the premixed burn fraction compared to when fuelling on petrodiesel [525]. Although the experimental observations documented here (in Chapters 4 and 5) do not tend to support the argument that the fraction of premixed heat release is larger when fuelling on biodiesel, it is quite possible that the influence of fuel-bound oxygen may counteract the effect of reduced energy density, to some extent, or influence the way in which heat is released during the premixed burn.

Certainly, the oxygen content of biodiesel will affect the stoichiometry of the premixed charge – assuming that the air entrainment rate of a biodiesel jet is equal to that of a petrodiesel jet, local ϕ_Ω values will be reduced. All other things being equal, ϕ_Ω should also be lower at the lift-off length, and hence inside the diffusion flame sheath, when fuelling on an oxygenated fuel. Any reduction in equivalence ratio in the fuel rich regions would be expected to increase NO_x emissions, via possible effects on combustion rates, flame temperatures and heat losses, which will be covered in the following sections. The assumption of equal air entrainment, however, may not be valid.

Due to the typically higher surface tension and viscosity of biodiesel, atomization is likely to be impaired [559], droplet sizes are likely to be larger [560, 561], and given that smaller droplets possess greater total surface area for the same mass, it would be expected that less well atomised fuel would evaporate less quickly [506]. However, although

differences in atomization may be important at lower in-cylinder temperatures and densities [504, 505], the ordinarily mixing limited nature of vaporisation within a diesel engine [503] may mean that the small differences in atomisation which exist between the fuels will make little practical difference with modern injection technology. The higher boiling range (lower volatility), higher density and higher heat of vaporisation of biodiesel, on the other hand, would be expected to delay vaporisation of the fuel under typical diesel conditions; these factors result in the longer biodiesel liquid length [507–509].

Although differences in fuel volatility and density certainly influence liquid penetration, the effects upon vapour penetration are less clear. Experimentally, it appears that biodiesel vapour penetration may be comparable to or slightly higher than that of petrodiesel [509]. Any difference in vapour penetration that does exist may result either from some change in injector flow, which influences the injection velocity and hence the momentum of the jet, or a slightly narrower biodiesel spray angle [509]. In non-evaporating experiments a reduction in spray angle with biodiesel is frequently reported [460], and the same has been suggested by engine modelling results [562]. In experiments conducted at high temperatures (800–1400 K), but still rather low densities (1.2–3 kg/m^3), the initial spray angle was lower for biodiesel, but the spray angles of both petro- and biodiesel ultimately stabilised to similar values [505]; differences were most pronounced under cooler conditions. A common equation used to estimate initial spray angle [167, 497] includes a ρ_{air}/ρ_{fuel} term, suggesting that any reduction in spray angle may be a result of the higher density of biodiesel. In keeping with this, Higgins et al [504] reported reasonably consistent changes in spray angle as a function of ρ_{air}/ρ_{fuel} for all tested fuels, leading to the suggestion that changes in other fuel properties do not have a systematic effect.

It has been reported that reduced spray angle [561], and reduced normal air flow velocity (attributed to poorer spray atomisation) may lead to reduced air entrainment within biodiesel sprays [563]; this could partially or completely offset the equivalence ratio reduction due to the biodiesel oxygen content [561]. However, Kook and Pickett [510] suggest that the differences in vapour penetration and spray angle amongst fuels of varying physical properties are small enough that air entrainment is largely the same.

Ultimately, there does not appear to be any clear evidence that the physical properties of biodiesel will alter the degree of initial premixing which occurs within a modern diesel engine. At the high temperatures and pressures encountered shortly before TDC, when injection typically commences, differences in air entrainment appear likely to be small.

Following the establishment of the diffusion flame air is only entrained upstream of the lift-off length, and so this has a significant effect upon mixture stoichiometry within the fuel rich core of the diesel jet. The lift-off length of biodiesel is typically reported to be shorter than that of petrodiesel and reference fuels [509, 525, 526], although in some cases it has been found to be larger [527, 528]. Some variation may be related to differences in cetane number – a general relationship exists between ignition quality and lift-off length [376, 377] – and the difference between petro- and biodiesel lift-off lengths may also vary throughout the engine cycle [529] and even from jet-to-jet [525].

A reduction in lift-off length is likely to reduce the quantity of air entrained into the core of the diffusion flame, and therefore a shorter biodiesel lift-off length may partially offset the inherently lower oxygen equivalence ratio associated with the fuel. However, although in some cases oxygen availability at the lift-off length is reported to be lower for biodiesel [526], generally the oxygen equivalence ratio at the lift-off length is expected to be somewhat lower, and hence oxygen availability somewhat higher, when fuelling on biodiesel or biodiesel blends [525, 527–529].

2.3.6 COMBUSTION RATES

In general, the phasing of biodiesel combustion is advanced relative to that of petrodiesel by the shift in injection timing (in engines where this effect exerts influence) and reduced ignition delay (for any biodiesel having a higher cetane number than standard petrodiesel), whilst being retarded by the smaller premixed burn fraction. However, significant differences in apparent heat release rate (AHRR) persist between the fuels in the absence of these differences, as will be discussed at length in Chapter 5.

In particular, the AHRR of biodiesel is typically higher through the diffusion combustion phase. Consistent with this, the combustion duration of biodiesel may be shorter than that of petrodiesel under less highly premixed operating conditions (e.g. at higher engine load), despite the combustion retarding effect of the smaller biodiesel PMBF. At more highly premixed conditions (e.g. lower load), on the other hand, the combustion duration of biodiesel may be longer than that of petrodiesel, because the diffusion phase through which biodiesel combustion apparently progresses more quickly becomes less significant. This observation was made by Bittle et al [14], and is in accordance with the results presented in Chapter 4 and the associated publication [543].

Why the biodiesel AHRR is higher through this period remains to be clarified. Bittle

et al [14] attribute it to a faster burn rate. The basis for this is provided by Mueller et al [525]: when fuelling on an oxygenated fuel, the equivalence ratio is closer to stoichiometric (i.e. less rich) past the lift-off length than would be the case with a non-oxygenated fuel, all other things being equal. This results in higher temperatures, higher reaction rates and more complete combustion within the jet core, therefore necessitating less actual mixing-controlled combustion at the flame front, and reducing the total combustion duration.

Other factors may also influence apparent heat release through the post-premixed phase, and these will be discussed in Chapter 5. In particular, the duration of the injection event, which is longer for biodiesel than petrodiesel, due to the difference in energy density between the fuel types, may contribute to the increase in biodiesel diffusion AHRR.

2.3.7 ADIABATIC FLAME TEMPERATURE

Some reports suggest that, in modern diesel engines, adiabatic flame temperature (AFT) differences between fuels are the critical determinant of their relative NO_x emissions [375, 564]. It has been proposed that a higher AFT for biodiesel may be responsible for the associated NO_x increase [415]; this is on the basis that unsaturated compounds have higher AFTs than their saturated equivalents, and biodiesel typically contains a larger proportion of unsaturated species than petrodiesel. This is a hypothesis consistent with the observation that more highly unsaturated biodiesels tend to have higher NO_x emissions [565].

However, AFT calculations for realistic surrogates do not necessarily demonstrate higher values for biodiesel; rather, they suggest that the AFT of a typical biodiesel might actually be lower than that of a conventional petrodiesel [558]. Although degree of unsaturation does indeed correspond to increased AFT, the aromatic species present in petrodiesel (which are also unsaturated) tend to have AFTs higher than most commonly encountered methyl esters. This is illustrated by Figure 2.57 [558]. Note that methyl oleate (an 'Ene FAME'), linoleate (a 'Diene FAME') and linolenate (a 'Triene FAME') have H/C ratios of 1.89, 1.79 and 1.68, respectively; in terms of the aromatics found in petrodiesel, they are primarily alkylbenzenes, and have an average H/C ratio of approximately 1.4–1.5 [566].

The AFTs of saturated methyl esters increase with increasing chain length, as do those of alkanes. However, for unsaturated species and aromatics, increasing alkyl chain length is associated with an increase in H/C ratio and a reduction in AFT. Towards the longest

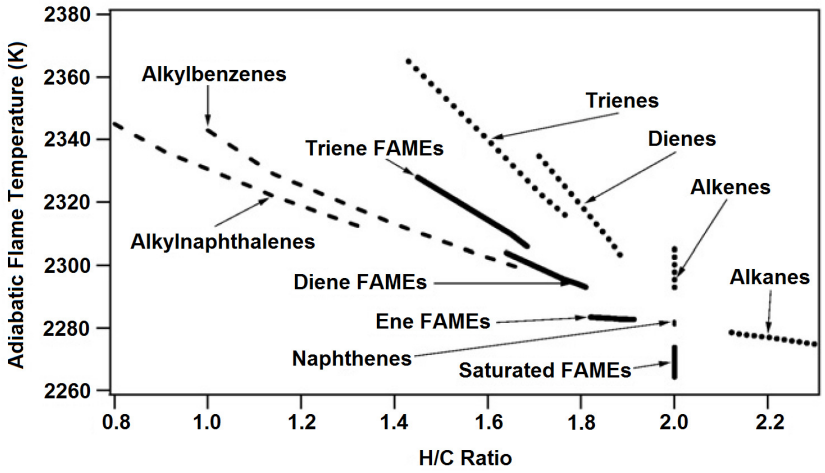

Figure 2.57: Adiabatic flame temperatures of chemical species contained in fuels as a function of H/C ratio [558].

chain lengths, as the H/C ratio converges on 2, calculated AFTs also converge [558].

Examination of Figure 2.57 suggests that any AFT difference between petro- and biodiesel would probably be small (although still potentially significant) – dependent upon the proportion of the petrodiesel comprised of aromatics, and the degree of unsaturation of the biodiesel. Note also that all methyl esters depicted have lower AFTs than their non-oxygenated equivalents (i.e. the AFTs of saturated FAMEs are lower than those of alkanes, 'Ene FAMEs' lower than alkenes, 'Diene FAMEs' lower than alkadienes of the same length, etc.). This is because the ester group itself contributes nothing to the heat of combustion, and in fact the CO_2 molecule commonly formed directly from the fuel consumes sensible heat and reduces flame temperature [558].

In keeping with this, maximum temperatures within modelled *n*-alkane flames are reportedly higher than within flames of equivalent methyl esters; additionally, the maximum flame temperatures of unsaturated methyl esters are found to be higher than those of saturated ones [374]. This corresponds to higher measured NO_x concentrations in *n*-alkane flames and flames of unsaturated methyl esters relative to saturated methyl esters [567].

In probability, the influence of degree of unsaturation over diesel engine NO_x emissions, although sometimes attributed to adiabatic flame temperature, could instead be largely explained with reference to degree of premixing, via the effects of unsaturation on ignition delay (as seen in [568], and discussed further in Chapter 5). However, that is not to entirely discount the importance of adiabatic flame temperature. Schönborn et al [568] performed experiments in which NO_x emissions from a range of fatty acid methyl esters were compared. With start of combustion timing kept constant, NO_x emissions increased

with increasing degree of unsaturation. When the effects of changes in ignition delay (and hence, degree of premixing) were removed – via the addition of a cetane enhancer – NO_x emissions when fuelling on the unsaturated compounds still exceeded those when fuelling on their saturated counterparts, but by a far smaller margin; the remaining differences in NO_x were attributed to differences in AFT. Similarly, without equalisation of ignition delay the NO_x emissions of methyl esters were found to decrease with chain length – due to reduced degree of premixing – but, following the equalisation of ignition delay, the higher molecular weight species generated slightly higher NO_x emissions, attributed to their higher AFTs [568]. However, when parameters like start of combustion and degree of premixing are not controlled, the correlation between the adiabatic flame temperatures of different fuels and their NO_x emissions is not as convincing [525].

All of the above discussion is focussed upon adiabatic flame temperatures under stoichiometric conditions (AFT is at its maximum under approximately stoichiometric conditions, although it actually peaks at an equivalence ratio slightly greater than unity [269]). Since the diffusion flame front is stoichiometric, and it is in proximity to the diffusion flame that temperatures and NO_x formation rates are highest within a diesel engine, stoichiometric flame temperatures are critical. However, although under stoichiometric conditions the difference in AFT between petro- and biodiesel generally appears to be small, it may be the case that more significant differences exist in richer regions [529, 569].

The equivalence ratio in fuel rich regions may be slightly lower when fuelling on biodiesel, due to its fuel-bound oxygen content. The presence of fuel-bound oxygen reduces the stoichiometric air-fuel ratio, and as a result the equivalence ratio of a biodiesel-air mixture is lower than that of a petrodiesel-air mixture for the same quantity of air entrainment. In general, reduction of the equivalence ratio towards 1 increases adiabatic flame temperature, and so adiabatic flame temperatures under rich conditions may be higher when fuelling on biodiesel [569]. However, calculations suggest that as a function of oxygen equivalence ratio, the adiabatic flame temperature of biodiesel may be lower than that of petrodiesel under richer ($\phi_\Omega > 1.5$) conditions. Consequently, although a reduced equivalence ratio with biodiesel under fuel-rich conditions may tend to increase AFT, this influence may be offset by a like-for-like reduction in AFT at any given value of ϕ_Ω [529].

Differences in flame temperatures under rich conditions are unlikely to affect NO_x formation via the thermal NO pathways directly (in that local temperatures will still be

insufficient to facilitate the formation of thermal NO), but may alter prompt NO formation rates [529], or have some effect on subsequent combustion by increasing reaction rates within the jet core [525].

2.3.8 RADIATIVE HEAT TRANSFER

Within an internal combustion engine, heat transfer occurs by a variety of means. Heat is transferred from the in-cylinder gases to the combustion chamber surfaces by convective and radiative process; conductive heat transfer distributes heat throughout the engine structure, and this heat is passed to the coolant by forced convection [570]. Radiative heat transfer refers to heat transfer by electromagnetic waves (in the classical description) or photons (in the quantum mechanical description), which are emitted by hot matter as a result of the oscillation of charged particles (classical description) or energy level transitions (quantum mechanical description) [571]. While conducted and convected heat flux depend linearly on temperature differences, radiative heat flux is proportional to temperature raised to the fourth power, or higher. Therefore, in high temperature applications radiant transfer becomes increasingly important [571].

Radiative transfer occurs from both heated in-cylinder gases and soot. In the low soot environment of a spark-ignition engine gas radiation is the more significant of the two and as a result radiative heat transfer constitutes a small proportion of total heat loss. In a diesel engine, however, soot radiation is generally far more substantial, and may play an influential role in total heat flux [572]; estimates put radiative heat transfer somewhere between 10–40% of the total, although instantaneous proportions vary throughout the engine cycle and under more lightly loaded, low sooting conditions the radiative contribution may be much smaller [573, 574].

As an approximate black body, heated soot emits continuum radiation across visible and infrared ranges [575] which is absorbed by the cylinder walls, as well as other soot particles and in-cylinder gases [576]. While it is radiation to the walls which constitutes effective heat loss, radiation within soot clouds, redistributing heat from hotter to cooler regions and hence reducing maximum values, may also be important [577]. In addition to its strong temperature dependence, the magnitude of radiative heat loss is affected by the optical properties, morphology, distribution and quantities of in-cylinder soot [571], as well as the geometry, optical properties and temperature of the internal surfaces of the combustion chamber [578].

As discussed in Section 2.2.3.4, both soot emissions and in-cylinder soot concentrations tend to be reduced in diesel engines when fuelling on biodiesel. It follows logically that heat losses due to soot radiation are also likely to be reduced, and therefore the cooling effect which radiative transfer has on the flame and hot gases will be depressed when fuelling on biodiesel, encouraging higher local in-cylinder temperatures. Musculus [577] reported that radiative cooling within a diesel engine causes a reduction in flame temperatures of 25–50 K – sufficient to cause a 12–25% reduction in NO_x emissions.

One can imagine that a reduction in soot concentration comparable in magnitude to those that have been reported in diesel engines [579] and combusting sprays [509] might have a significant effect on radiative transfer and NO_x formation. Indeed, Cheng et al [529] found a strong negative correlation between the differences in maximum in-cylinder spatially integrated natural luminosity (SINL – a means of quantifying soot concentration) and NO_x emissions. Mueller et al [525] also reported a correlation between SINL and NO_x emissions when comparing neat biodiesel to a biodiesel doped with 6% phenanthrene ($C_{14}H_{10}$, 3-ring aromatic species). Similarly, the study of Singh et al [580] in partially-premixed flames indicates a reduction in the radiative heat fraction with increasing biodiesel blend percentage and decreasing equivalence ratio; decreasing radiative heat fraction was accompanied by increasing NO_x formation per unit fuel mass.

However, in the Mueller study [525], although the SINL-NO_x relationship holds when comparing biodiesel and the biodiesel-phenanthrene blend, consideration of a non-oxygenated reference fuel with an intermediate SINL but consistently lower NO_x emissions, reveals that differences in SINL do not necessarily correspond to the NO_x differences observed between fuels.

Some further evidence has been presented that a reduction in sooting may occur without any substantial change in NO_x emissions. In a study of the effects of barium addition to fuel on the resulting smoke and NO_x emissions, Song and Jacobs [581, 582] found that although increasing barium concentration was associated with a large reduction in exhaust smoke, the relationship with NO_x was unclear, and any effect on NO_x emissions was relatively slight. Whether or not the reduction in smoke emissions implies reduced *radiative heat transfer* is a question whose answer depends largely upon the mechanism by which the barium additive reduces soot. Although earlier (1970–1980s) accounts suggest some effect of barium on the *formation* of soot [583, 584], emphasis in more recent (1990s) publications appears to be on the *promotion of soot burnout* [585, 586]. If the latter is the case,

reduced smoke emissions in the barium experiments may not be in direct correspondence to the quantity of in-cylinder soot, nor hence be a reliable indicator of the levels of radiative heat transfer; therefore, the conclusion that reduced radiative heat transfer *"likely contributes little"* [581, 582] to the biodiesel NO_x increase is not necessarily supported.

2.3.9 PROMPT NO

It has been suggested that the increase in NO_x with biodiesel is not a result of the thermal NO mechanism, and may instead be related to the *"pre-combustion chemistry of hydrocarbon free radicals"* [587], possibly involving the double bonds present in the various biodiesel constituents [147]. The presence of increased levels of certain hydrocarbon radicals might lead to increased NO_x formation via the Fenimore-type prompt NO pathways [565].

Modelling results indicate that under conditions representative of rich regions of the diesel jet (ϕ = 2–3, 50 atm) larger amounts of NO are formed during the oxidation of an unsaturated methyl ester (methyl *trans*-2-ocetenoate) than a saturated one (methyl ocetanoate), particularly between 1050–1400 K [431]. This is attributed to an experimentally confirmed increase in acetylene (C_2H_2) formation from unsaturated fuels [430], due to the presence of a preferential high temperature decomposition pathway beginning with scission of the allylic C-C bond (which doesn't exist in saturated fuels), and leading to the formation of ethene (C_2H_4) and vinyl radicals (C_2H_3), from which C_2H_2 is derived. C_2H_2 goes on to form CH_2 and then CH, which is the primary hydrocarbon radical which participates in the prompt NO formation mechanism. The presence of the ester group itself may not have much effect on acetylene formation [431].

A numerical study by Som and Longman [461] indicated that concentrations of HCN and CH could indeed be higher when fuelling on biodiesel, and that prompt NO may also be increased, but because prompt NO constitutes a very small fraction of total NO_x formation this seems to be insignificant.

As discussed in Section 2.2.3.3, acetylene is also an important soot precursor. This means that increased soot formation may also have a chemical effect on NO_x formation, due to increased competition for C_2H_2; soot formation consumes C_2H_2 and may therefore reduce prompt NO formation by reducing the availability of hydrocarbon radicals [588, 589]. However, since higher soot formation is likely to be associated with increased C_2H_2 concentrations in the first place, it is not clear that a fuel which reduces sooting will necessarily be associated with higher C_2H_2 availability for prompt NO formation – in fact,

the opposite may be true. In relation to the question of a possible chemical effect of soot on NO_x emissions, Vander Wal et al [532] suggest that the reduction in sooting when fuelling on biodiesel may lead to increased survival of NO_2 (which might otherwise react with any extant soot). Consistent with this hypothesis (but not necessarily in validation of it), data collected by Dhahad [590] does show that NO_2 constitutes a larger proportion of biodiesel NO_x emissions, under a range of operating conditions.

2.3.10 SUMMARY

In the review of Sun et al [539] a useful graphical summary of the factors involved in the change in NO_x emissions when fuelling on biodiesel is provided. In Figure 2.58, an illustration based on similar principles is presented.

Figure 2.58 is complicated, and is more easily appreciated when followed through methodically, than when described. A partial description is furnished below with the intention of providing some introduction to the underlying logic of the diagram, an example to follow, and a clarification of certain points which are not fully explained in Figure 2.58 itself.

Working from the top, downwards, the effect that replacing petrodiesel with biodiesel will have on 5 key properties is depicted qualitatively. The energy density of the fuel will decrease (white arrowhead), as will the aromatic content. The unsaturation of the fuel will typically increase, but this depends upon the feedstock from which the biodiesel is derived (this uncertainty is represented by an open arrowhead). Fuel-bound oxygen content will increase (black arrowhead). *'Physical properties'* is an ambiguous heading, intended as a catch-all for density, viscosity, surface tension, boiling range, bulk modulus, and speed of sound. These are all higher for biodiesel than petrodiesel (hence the black arrowhead), and which ones are relevant to each path will be identified in the following paragraphs.

Taking as a first example the path down the left hand side of the diagram, energy density (which is lower with biodiesel) has 3 main effects with eventual relevance to NO_x emissions. First, it can change the way the engine reacts to the fuel (described in Section 2.3.3), possibly inducing automatic adjustments to EGR rates, injection pressure and injection timing; because these effects are engine dependent the pathline is dotted, and because the effects are uncertain, the arrowhead is open. An increase in EGR would be expected to reduce NO_x emissions (white arrowhead), while an increase in injection pressure would be expected to increase NO_x (black arrowhead). (The mechanisms by which EGR

and injection pressure affect NO_x emissions are beyond the scope of Figure 2.58, which is why they have been reduced to *'etc'*.) Second, increasing energy density increases the degree of premixing (black arrowhead), because it means that a greater quantity of fuel energy can enter the cylinder for a given ignition delay. Third, increasing energy density typically reduces the duration of injection; hence, because biodiesel has reduced energy density, it increases injection duration. An increase in injection duration will alter combustion phasing, although whether it will have a net positive or negative effect is unclear (one would assume that increased injection duration would retard combustion phasing, but the discussion in Chapter 5 suggests the possibility of some positive effect).

Turning, for a second example, to the right hand side of the diagram, to deal with the '*physical properties*' grouping: the effect of an increase in boiling range, density, viscosity and surface tension is an increase in the physical component of ignition delay, hence increasing ignition delay overall (black arrowhead); under cooler conditions (dashed pathline), these properties may reduce air entrainment upstream of the lift-off length and hence increase equivalence ratio at the lift-off length (black arrowhead); also under cooler conditions (dashed pathline) the same properties may affect spray geometry in a way that reduces initial fuel-air premixing (white arrowhead); finally, in older engines with PLN type injection systems (dotted pathline) increased bulk modulus and speed of sound may advance the start of injection (note that a black arrowhead equates to an advance in timing, and that a white arrowhead, such as that connecting ignition delay and advanced start of combustion, would denote a timing retard).

In summary, as Figure 2.58 illustrates, replacing petrodiesel with biodiesel affects NO_x emissions for a variety of reasons, and via a range of mechanisms. At the root of many of the most important changes is the increased fuel-bound oxygen content of biodiesel, and the reduced proportion of low ignition quality, highly sooting aromatic species compared to petrodiesel. Considered independently, not all of the changes caused by biodiesel necessarily increase NO_x emissions; the net outcome is dependent upon the relative magnitude of each contributing factor, and this in turn is likely to be variable, from engine to engine, and from operating condition to operating condition.

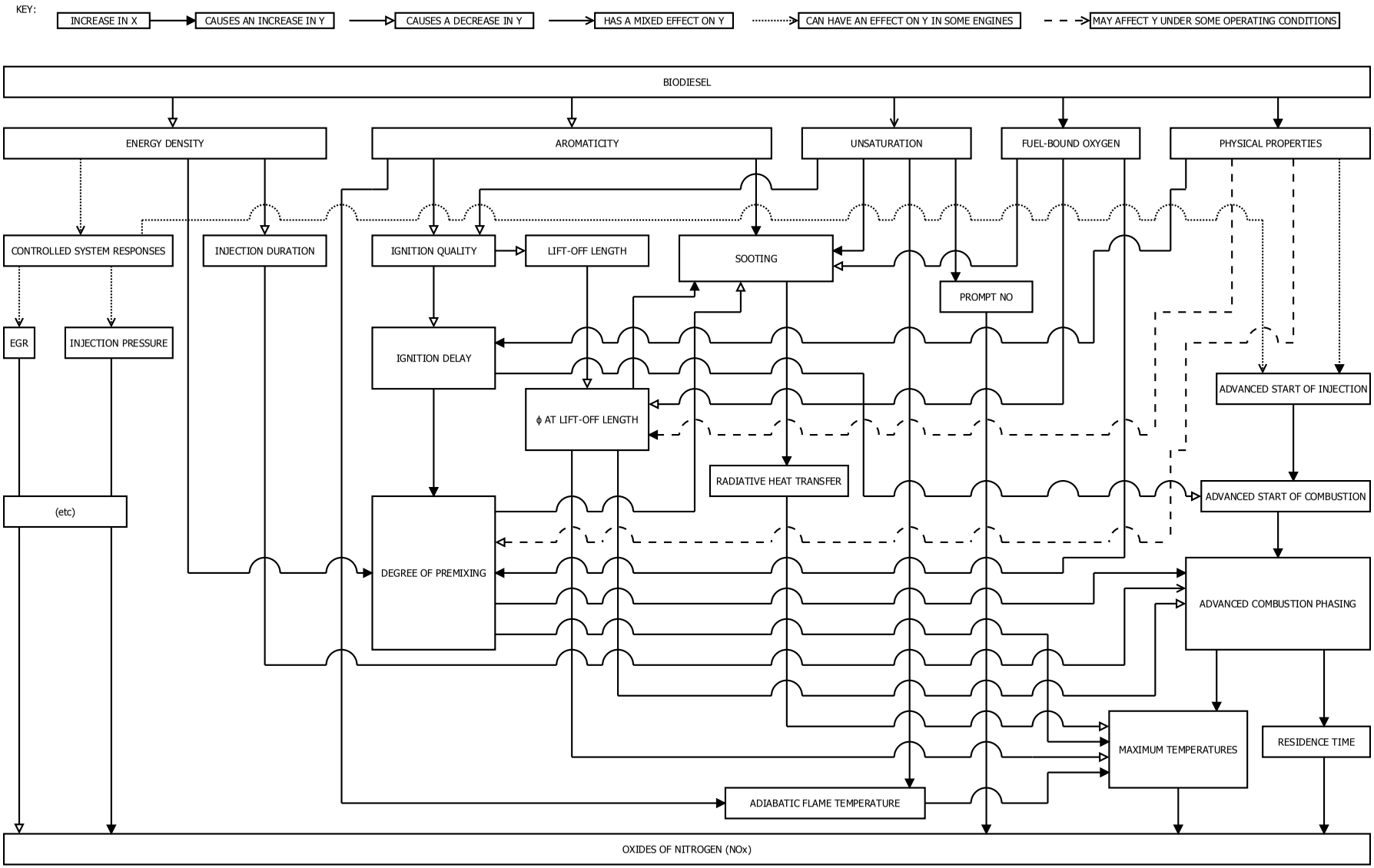

Figure 2.58: Factors contributing to the change in NO_x emissions when fuelling on biodiesel (further explanation of notation provided in the text).

Chapter 3

EXPERIMENTAL EQUIPMENT AND METHODS

3.1 ENGINE SETUP

3.1.1 ENGINE

The engine used to perform the bulk of the experimental work documented in this thesis was a pre-production prototype Ford Duratorq "Puma" 2 litre, 4 cylinder high speed direct injection (HSDI) diesel engine with a common-rail injection system. The closest equivalent production engine is the ZSD 420, a schematic of which can be seen in Figure 3.1. Details of the engine are provided in Table 3.1. A photograph of the laboratory engine can be seen in Figure 3.2. Differences from the commercial ZSD 420 variants include the head, which is from an earlier Ford Zetec engine, the air intake manifold, which has straight cylinder feeds rather than the swirl ports found on production models, and the piston geometry; the pistons inside the laboratory engine have larger bowl volumes, and as a result the engine operates at a lower compression ratio – 18.2:1 rather than 19:1 [591, 592].

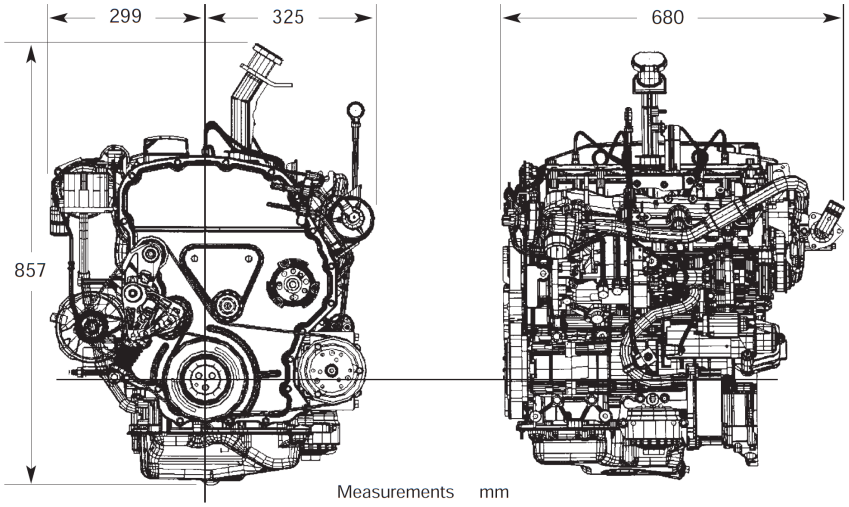

Figure 3.1: Ford Duratorq "Puma" HSDI diesel engine, ZSD 420 engine variant [592].

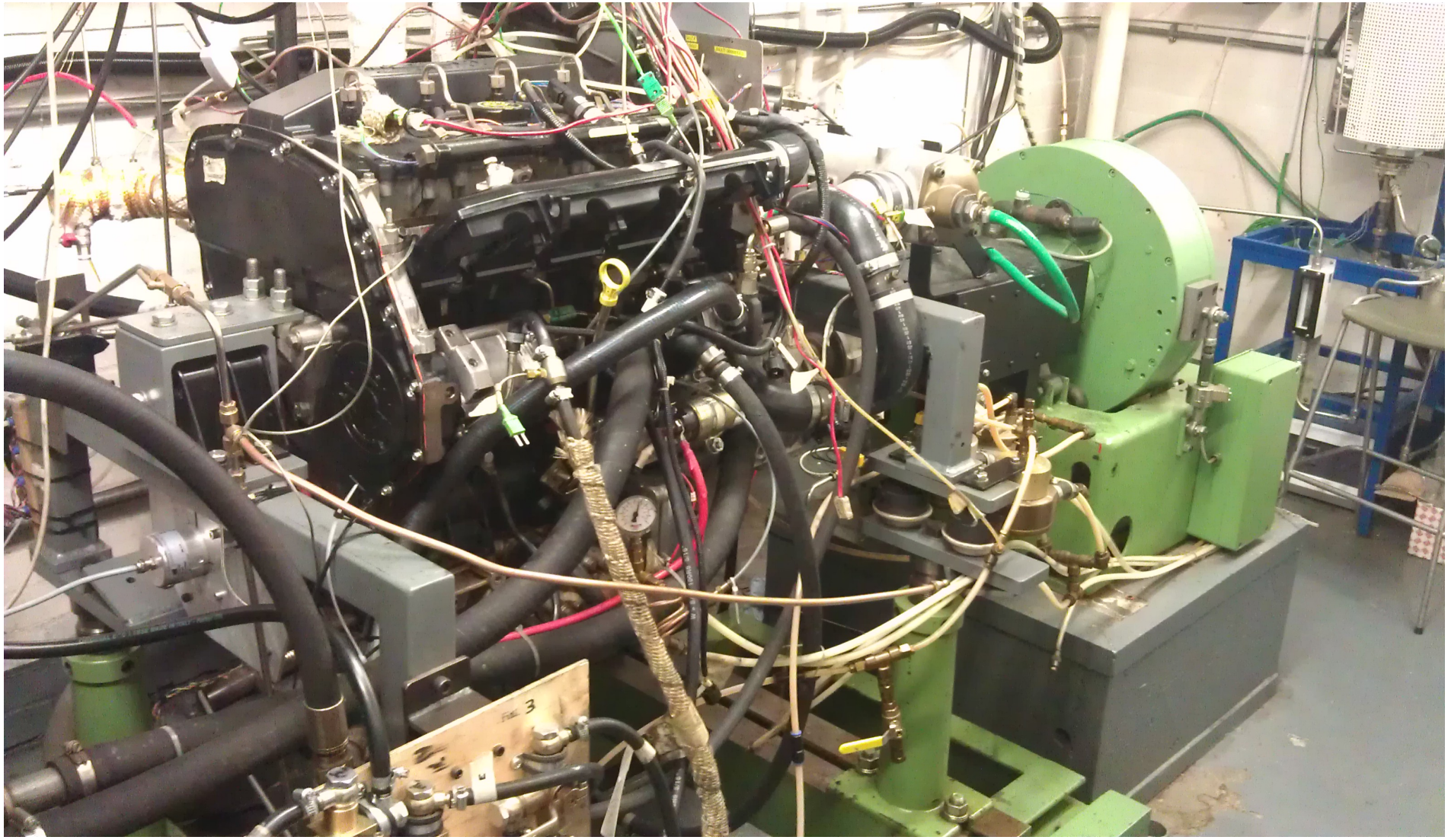

Figure 3.2: Laboratory engine setup.

ENGINE	FORD DURATORQ "PUMA" HSDI DIESEL
SWEPT VOLUME (cc)	1998
NUMBER OF CYLINDERS	4
NUMBER OF VALVES	16
BORE/STROKE (mm)	86/86
COMPRESSION RATIO	18.2:1
CONNECTION ROD LENGTH (mm)	155
PISTON BOWL VOLUME (cc)	21.7
OPERATING COOLANT TEMPERATURE (°C)	77 ± 6 (AUTO-CUTOUT @ 100)

INJECTION SYSTEM	COMMON-RAIL, 1600 BAR MAXIMUM
INJECTORS	DELPHI EJDR00301Z
NUMBER OF HOLES	6
HOLE DIAMETER (mm)	0.154
SPRAY CONE ANGLE	154°

Table 3.1: Engine and injector specifications.

3.1.2 DYNAMOMETER

The engine is coupled to a Schenck W130 eddy current dynamometer, capable of absorbing up to 130 kW of power at a speed of up to 10000 rpm, with a rated torque of 400 Nm. This unit can be seen mounted at the right hand side of the engine in Figure 3.2.

An eddy current dynamometer consists of a conductive rotor which is coupled to the engine drive shaft and rotated between water-cooled heat loss plates, with an electromagentic field applied parallel to the rotational axis [593]. The motion of the rotor causes a change in magnetic flux, inducing eddy currents which, in accordance within Lenz's Law, generate a magnetic field in opposition to the initial change in flux which induced them [594]. This results in a resistive force against the motion of the rotor, and the dissipation of kinetic energy as heat. By varying the strength of the applied electromagnetic field, the strength of the resistive force, and resulting engine load, can be controlled. Although other approaches exist, the laboratory dynamometer system measures torque using a strain gauge transducer. Torque data in conjunction with data from the speed pick-up allow the control system to maintain the desired torque or speed by balancing the eddy current braking forces with the engine output. The user is able to operate in one of two modes, constant speed – wherein an increase in fuelling increases engine load – and constant load – wherein an increase in fuelling increases engine speed.

3.1.3 IN-CYLINDER PRESSURE TRANSDUCER

A Kistler Piezostar 6125A pressure transducer was used to measure in-cylinder pressure. It was fitted within a custom mounting sleeve, inside the glow-plug port of the first cylinder.

Certain types of crystal, including quartz, produce an electric charge when a force is applied to them [595]. However, quartz undergoes a phase transition at 573 °C making it unsuitable where high temperatures may be encountered. In order to perform under the more demanding operating environment which an in-cylinder pressure transducer is subjected to, the Piezostar crystal used in this application is produced from a more expensive and fragile, but highly temperature-stable piezoelectric material, belonging to the family of calcium gallogermanates [596]. This crystal is housed within a stainless steel cylinder, behind a ThermoComp diaphragm for protective purposes [597].

Changes in in-cylinder pressure exert a force on the piezoelectric element, which generates a charge proportional to pressure *change* (in this instance, 16 pC/bar [591]); this necessitates integration by a charge amplifier to convert from charge to a usable voltage proportional to gauge pressure [593] (in this instance, 20 bar/V). Following treatment by the charge amplifier, the signal is discretised using the output from a crank shaft encoder (discussed in the following section) and acquired, via a National Instruments PCI-6070E card, in LabVIEW.

3.1.4 CRANK ANGLE ENCODER

The output from a crank angle encoder was used to discretise the pressure transducer output with reference to engine position. Initially, the engine was fitted with a Lenord+Bauer GEL 244 magnetic pickup and 360 toothed encoder wheel, which provided a means of sampling the pressure signal every 1 CA [591, 598]. However, it is now common for research engines to be fitted with far higher resolution encoders (of the order of 3600 ppr, allowing for sampling at 0.1 CA intervals) [599], in order to assess pressure data and heat release criteria with a greater degree of accuracy. Considering Figure 3.3, for instance, where ignition delay values are plotted to the measured resolution of 1 CA, and a mathematically interpolated accuracy of 0.1 CA, the desirability of finer data can be clearly seen. Although interpolation of low resolution data is a possibility (as seen in Figure 3.3, and Chapter 4), higher resolution 'real' data remains preferable.

For this reason, an Encoder Technology ET758/2 [600] was mounted onto the crank shaft, as a replacement for the GEL 244. The operating principle of the ET758 involves an internal wheel with incremental lines that are optically monitored, rather than the external ferromagnetic toothed wheel required by the GEL 244. The optical system is more compact, and easily affords higher resolution, since lines substantial enough to be optically

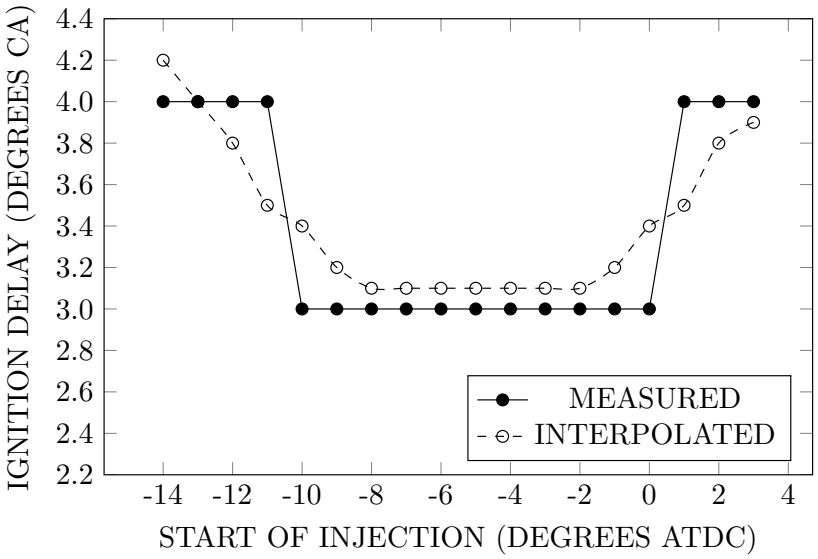

Figure 3.3: Ignition delay as a function of start of injection timing, with data plotted to the 1 CA resolution of the GEL 244 encoder and interpolated to 0.1 CA (plot shows ULSD data from 4, Figure 4.3B).

detectable can be machined far smaller than easily magnetically detectable ferrous teeth. However, the magnetic system has advantages in terms of robustness and longevity. The ET758 fitted to the engine has a 2880 ppr (pulses per revolution) output, providing a sampling interval of 0.125 CA. Images of both systems can be seen in Figure 3.4.

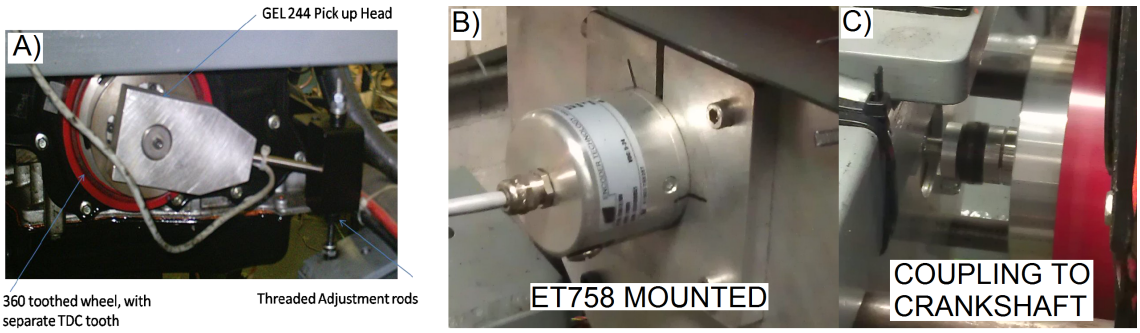

Figure 3.4: Photographs showing the two encoder systems mounted on the engine: A) the GEL 244 [591]; B) and C) the ET758.

When mounting a shaft encoder it is essential that the top dead centre (TDC) reference signal be correctly aligned with physical TDC. Various methods exist for determining physical TDC from thermodynamic analysis of pressure data obtained during non-firing engine operation [601–607]. Motored pressure data alone will display a point of peak pressure that occurs slightly advanced of physical TDC due to heat transfer and mass losses that occur [606]; this slight advance is commonly known as the thermodynamic loss angle. Although attempts were made to calibrate TDC using some of the referenced thermodynamic techniques (particularly that of Staś [602]), the results obtained were not

deemed sufficiently reliable, because the calculated position of TDC varied depending upon the engine speed at which the pressure data sets were recorded. This may be a result of the fact that the laboratory engine was not motored, but rather fired under a highly retarded (4 after TDC) injection timing and idling load to enable prolonged data acquisition whilst minimising the influence of combustion on the near-TDC pressure data. Additionally, filters employed to reduce the effect of noise on first, second and third differentials of pressure data may have contributed to the inconsistency observed.

Ultimately, the TDC reference signal was aligned using the Kistler Type 2926C TDC sensor system [608], with the capacitive displacement sensor inserted into the cylinder through the injector port using a custom built adapter. The displacement data was acquired in LabVIEW and analysed to find the angle of the piston's closest proximity to the probe, which was then used to calculate a TDC offset value that could be input as a correction factor in the LabVIEW VI (virtual instrument) interface.

The immediate benefit of increased angular resolution was, in practice, limited. With a 1 CA sampling interval the pressure data, when averaged over 100 engine cycles, manifested little enough noise that it was possible to calculate apparent heat release rate data directly, without the need for additional filtering or averaging. However, at the higher resolution this becomes impossible, because the differential of pressure is afflicted by excessive spurious fluctuations. This makes the application of some noise reduction technique a necessity; ultimately, a 9-point moving average was used.

Thus, it could be argued that the increased resolution of the encoder did not actually provide higher resolution 'real' data to base analysis upon; instead of mathematical estimates on the basis of interpolation, higher resolution requires mathematical estimates on the basis of averaging. The advantage of averaging over interpolation is that it provides a more clearly defined shape to the pressure curve, and hence the apparent heat release rate data obtained. Fundamentally, a greater quantity of data allows for the exclusion of erroneous measurements, whereas a lesser quantity makes it difficult to ascertain where impropriety may lie. Although the additional resolution obtained was certainly valuable, it was accompanied by an increase in complexity that did not burden earlier lower resolution data acquisition.

3.1.5 ENGINE MANAGEMENT SYSTEM

The fuelling rate is controlled by a potentiometer, which acts analogously to an accelerator pedal, and the speed and torque are controlled by the dynamometer system. All other adjustable variables are controlled using a 486 PC running a piece of software called GrEDI. This offers the user precise real-time control of injection pressure, injection timing (of multiple injection events, if desired) and rates of exhaust gas recirculation (EGR). It can also be used to monitor a wide range of operational parameters – temperatures, pressures, flow rates, etc.

3.1.6 AUXILIARY FUEL SUPPLY

Earlier work with biodiesels by previous researchers in the Brunel Centre for Advanced Powertrain and Fuels Research (CAPF) [462], as well as some of the initial work forming the basis of this thesis (Chapter 4), led to time consuming and expensive injector failures. Such failures are understood to be a potential issue when fuelling on biodiesel [24], but can be avoided, or at least minimised in frequency, by improved control of fuel quality, storage conditions, and proper maintenance of the fuel supply system. Described below are the deficiencies and problems that existed at the outset of experimentation, and the basic steps taken to improve the situation.

3.1.6.1 FUEL QUALITY AND STORAGE

Previous purchases of biodiesel had been delivered in 200 litre barrels. The primary problem with this was that fuel was not consumed quickly enough to warrant such large containers, so between using the top and bottom of the barrel there existed a delay of some several months. At best, this risks changing the condition of the fuel between the beginning and end of the experimental period, by exposure to air, which could lead to varying results. At worst, it allows enough time for serious fuel degradation to take place, leading to increased viscosity and the formation of insolubles, to such a point that filter clogging, fuel pump and fuel injector failure become real possibilities.

It has been seen that prolonged exposure (of the order of several months) to air can cause significant changes to the chemical composition of the fuel [609]. Analysis by gas chromatography (for Chapters 5 and 7) of fuels used over the course of this work reveals the same trend, as is illustrated in Figure 3.5. Note the increase in the proportion of less highly unsaturated compounds (especially C18:1, methyl oleate) at the expense of the more

unsaturated ones (C18:2 and C18:3, methyl linoleate and linolenate, respectively). These changes may have a significant effect upon factors like ignition delay, and consequently engine performance and emissions, and their minimisation is essential.

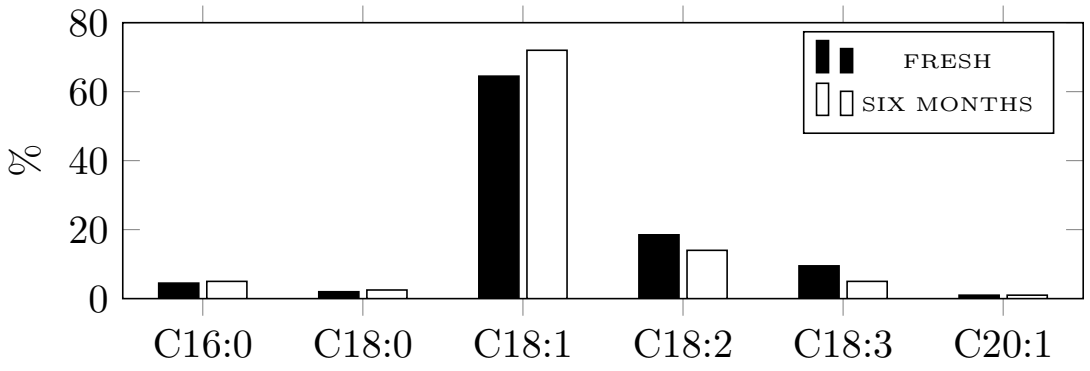

Figure 3.5: Chemical composition of rapeseed methyl esters from a freshly opened can and after being exposed to air for six months.

In Figure 3.6 a sample of jatropha methyl esters taken from an approximately 80% empty barrel opened around a year earlier is seen photographed immediately after being decanted, at subsequent 50 minute intervals, and, in the final (bottom right) image, after being left to settle for a full 20 hours. The initial (top left) image appears fairly innocuous, but as time progresses the fuel separates into three distinct sections: a lighter, transparent layer at the top; a yellow, translucent layer in the middle, similar in appearance to the fuel straight after being poured; and a brown, opaque layer of viscous slime at the bottom.

Later acquisitions of biodiesel were made in containers of a more manageable size (typically around 25 litres) so that they could be more easily stored under appropriate conditions, more easily mixed to ensure a homogeneous test product, and could be consumed within a short period of opening, minimising exposure to air and the possibility of oxidative deterioration. Fuel was decanted into a transparent container and allowed to stand to ensure that it was of an acceptable degree of clarity and without sediment. All opaque containers (namely, jerrycans) were cleaned thoroughly after each use to prevent the accumulation of sediment, paint or fuel remnants.

3.1.6.2 FUEL SUPPLY SYSTEM

Initially, the auxiliary fuel supply system consisted of a one gallon fuel tank connected immediately to a single cleanable but relatively coarse wire mesh diesel filter, then to a hand primer, and then to a switching board which allowed the fuel source to be changed from the laboratory diesel supply to the secondary fuel system. The drawbacks of this

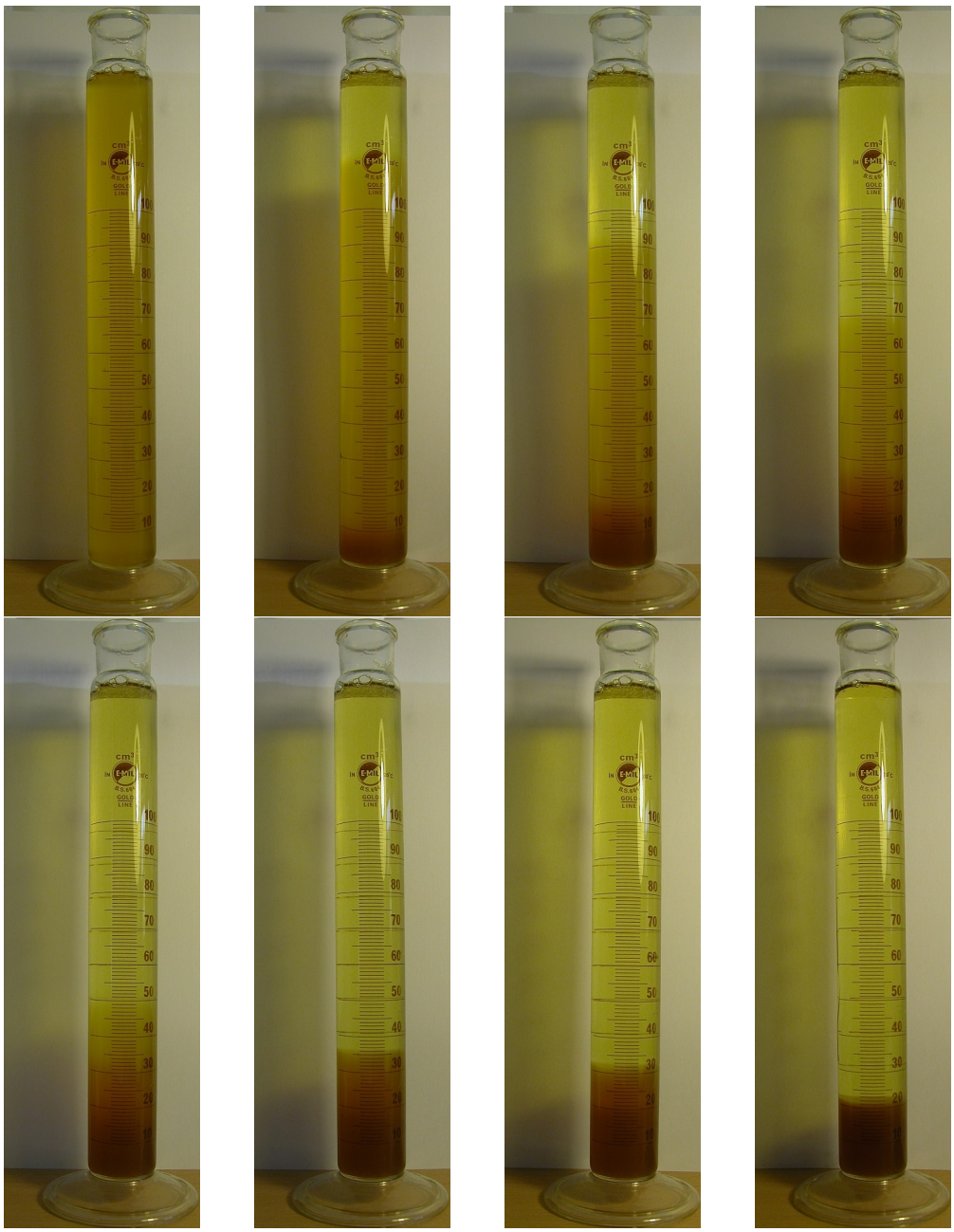

Figure 3.6: Photographs of a sample of jatropha methyl esters at 50 minute intervals (from top left) and finally after 20 hours settling time (bottom right).

system, and the way it was operated, were that the fuel filter was not fine enough, nor was it regularly removed and cleaned, and that the shape of the fuel tank precluded total drainage of the system, which meant that some remnants always remained and sediment was allowed to accumulate. Remedial measures were as follows:

- A two-stage filtration system was put in place, to minimise the risk of introducing contaminants into the fuel-line. After passing through the 100 μm stainless steel strainer filter which was already in place, fuel was subsequently filtered down to 20 μm using nylon and paper inline filters, inside transparent plastic housings to

allow inspection of fuel flow and fouling.

- In addition to the existing precaution of running the engine for a 20–30 minute period on petrodiesel following biodiesel usage in an effort to flush the rail, the entire secondary system was rinsed with diesel at the end of each run, and the strainer filter cartridge was removed from its housing and cleaned.
- The secondary fuel tank was modified to allow total internal access and visibility, and was thereafter emptied and cleaned following every use.

3.2 EMISSIONS MEASUREMENT

3.2.1 HORIBA MEXA 7170 DEGR

The Horiba MEXA 7170 DEGR is an exhaust gas analyser, used to quantify the levels of gaseous emissions, namely carbon monoxide (CO), carbon dioxide (CO_2), oxygen (O_2), total hydrocarbons (THC) and oxides of nitrogen (NO_x). An adapted schematic of the MEXA-7000 series is given in Figure 3.7.

The names and functions of those elements indicated in Figure 3.7 are as follows [610, 611]:

1. Main Control Unit (MCU): the computer used to operate the system.
2. Interface Controller (IFC): the interface between the MCU and the rest of the system.
3. Analyser Rack (ANR): contains the non-heated analysers. In this instance, these are non-dispersive infrared (NDIR) analysers for measurement of CO and CO_2 and a magnetic pressure detection (MPD) analyser for measurement of O_2.
4. Power Supply Unit (PSU).
5. Solenoid Valve System (SVS): switches between calibration and measurement gases.
6. Sample Handling System (SHS): controls and conditions the gas passed to the ANR.
7. Heated Analysis Unit AKA Oven (OVN): heated sampling and analysis system containing a flame ionisation detector (FID) for measurement of THC and a chemiluminescence analyser (CLA) for measurement of NO_x.

The NDIR analysers used by the HORIBA to measure CO and CO_2 function on the basis that these gases absorb infrared radiation in particular wavelength ranges. The

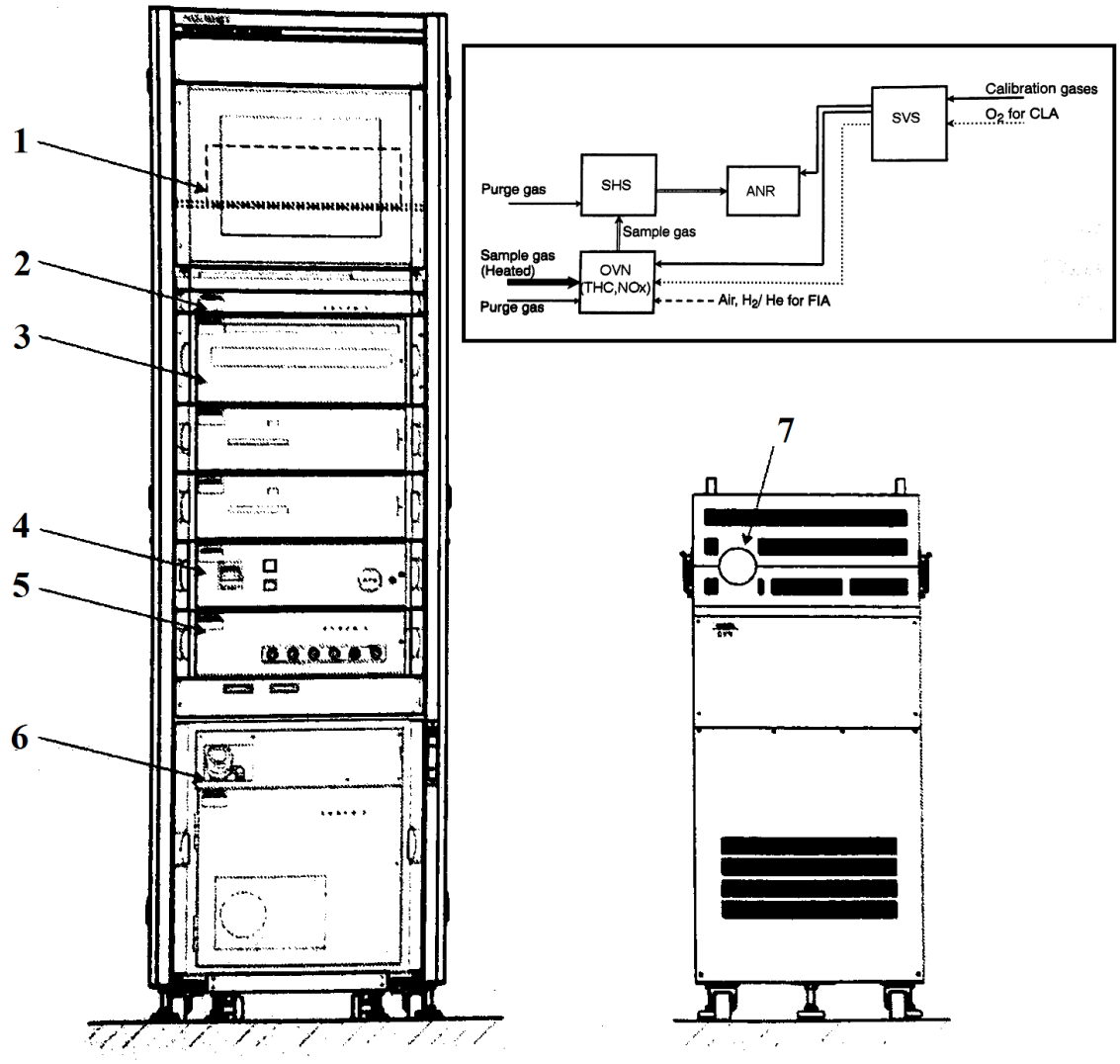

Figure 3.7: External view and layout of the HORIBA MEXA-7000 series (with labels described in the text); inset, illustration of the gas system flow [610].

absorbed wavelength range for any substance corresponds to the natural frequencies of various stretching and bending vibrations that specific molecular bonds and arrangements accommodate [27]. In an NDIR analyser (of the type in question [612], although others exist [613]), an infrared source transmits radiation through two chambers: a reference chamber containing a non-absorbing gas (nitrogen), and a sample chamber containing the gas to be analysed. Optical filters restrict the radiation to a range in which the gas of interest absorbs effectively, and interference from other chemical components is minimised. Detectors measure the intensity of the filtered IR light that has passed through each measurement volume, and by comparing the transmittance of the two chambers, attenuation due to the sample gas and therefore the concentration of the absorbing chemical can be quantified.

The MPD analyser used to measure oxygen functions on the basis that molecular oxy-

gen is paramagnetic (which is unusual for a gas), meaning that it will become magnetised in the direction of an external field, although in the absence of such a field it is not magnetic [171]. This is because O_2 has two unpaired electrons in its π_g^* molecular orbitals [614], and the presence of a magnetic field aligns the spin of these electrons, magnetising the molecule. This characteristic is exploited differently in the various types of paramagnetic oxygen analyser [613, 615], but in this case it is used to induce a change in pressure [612]. Multiple streams of nitrogen pass across a membrane, of which one stream mixes at a later point with the gas sample, in the vicinity of an alternating magnetic field. The oxygen in the sample tends to be drawn into the magnetic field, which causes fluctuations in the incident nitrogen flow, leading to upstream pressure changes and hence deflection of the membrane [615]. The deflection is proportional to the oxygen concentration. This explanation is assisted by Figure 3.8.

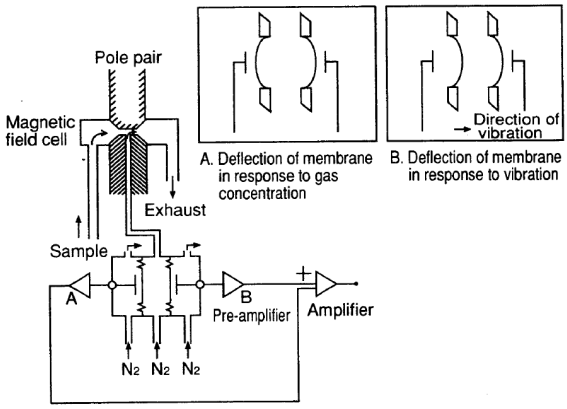

Figure 3.8: Uni-polar single-cell magnetic pressure type oxygen detector [612].

The FID used to measure THC emissions functions on the basis that the addition of organic compounds to a hydrogen flame causes a very substantial increase in the number of ions formed, primarily via Equation 3.1 [615].

$$\mathrm{CH} + \mathrm{O} \longrightarrow \mathrm{CHO}^+ + \mathrm{e}^- \tag{3.1}$$

By applying an electric potential across the flame, ions and electrons can be drawn towards electrodes on either side, generating a small current, which is proportional to the quantity of hydrocarbons present in the exhaust. No differentiation is made between different species of hydrocarbon, and results are indicated in parts per million carbon (ppmC) [613].

The CLA used to measure NO_x emissions functions on the basis that when electronically excited NO_2 transitions to the ground state it emits light in the 590–2600 nm range

[615]. A typical schematic is illustrated in Figure 3.9.

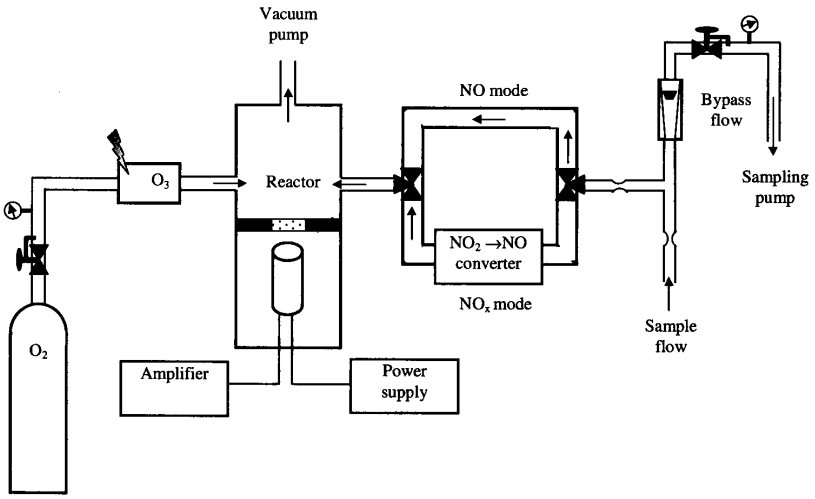

Figure 3.9: Schematic of a chemiluminescence NO_x analyser [613].

Depending on the selected operating mode, the sample may first be passed through an NO_2 to NO converter. Chemiluminescence analysis quantifies NO specifically, and therefore the purpose of the conversion is to include NO_2 in the measurement in order to obtain a total NO_x value. Conversion is achieved by reaction with carbon [612]:

$$NO_2 + C \longrightarrow NO + CO \tag{3.2}$$

Alternatively, exhaust may pass directly to the reactor, excluding any NO_x as NO_2 from the measurement. Ozone (O_3) is also passed to the reactor, having been formed by ultraviolet irradition of oxygen. In the reactor NO reacts with O_3 to produce light by Equations 3.3 and 3.4; the amount of light emitted is proportional to the concentration of NO in the exhaust [613, 615].

$$NO + O_3 \longrightarrow NO_2^* + O_2 \tag{3.3}$$

$$NO_2^* \longrightarrow NO_2 + hv(590nm \leqslant \lambda \leqslant 2600nm) \tag{3.4}$$

3.2.2 AVL 415

The AVL 415 is a filter smoke meter (or spotmeter) used to quantify the levels of soot in the exhaust stream [616]. It functions by drawing a defined amount of exhaust through a piece of filter paper, causing it to blacken. The light reflected by the blackened region is measured by a photoelectric sensor, and compared to the light reflected by an unsoiled portion of the paper [267, 617]. The ratio of the two is directly proportional to the calculated smoke number which, in the case of the AVL 415, ranges from 0–10 (i.e. least

to most blackened by smoke). Filter smoke number is reported to correlate reasonably well with measured soot mass concentrations; over the range typical of the work within this thesis, indicative values are approximately 20 mg/m^3 at a smoke number of 1, and 50 mg/m^3 at a smoke number of 2 [618].

3.2.3 TESTO 350

The Testo 350 is a portable exhaust gas analyser that can be used to quantify all of the same emissions as the Horiba (see Section 3.2.1) in addition to other pollutants including sulphur dioxide (SO_2), and further variables such as temperature and pressure. The Testo employs electrochemical sensors to quantify all emissions except for CO_2, which is measured by a non-dispersive infrared technique, and hydrocarbons which are detected by a Pellistor sensor.

The Testo unit was only employed for the study documented in Chapter 8, where its portability and ease of setup were beneficial because measurements were made outside the laboratory. For the purposes of these experiments, it offers satisfactory performance (with reported relative accuracy of around 5–10% for NO_x measurements, for example [619, 620]), although the performance of the Horiba is superior, subject to correct calibration.

3.3 DATA ANALYSIS

3.3.1 EMISSIONS DATA

Gaseous emissions data are logged in real-time on a computer connected to the Horiba, using software written at the Tianjin University SKLE (State Key Laboratory of Engines) by Dr. Yan Zhang. This samples all emissions 10 times per second over a duration of up to 180 seconds. Typically, the maximum recording duration was used, to avoid biasing the results with short-lived fluctuations in engine behaviour (see Section 3.4). For example, the cooling cycle of the engine is associated with a small periodic variation in emissions as the coolant increases and decreases in temperature.

The data acquisition software exports to Microsoft Excel spreadsheets, which are subsequently processed using a MATLAB module; the core module uses the *uigetfile* function with *multiselect* mode to enable batch processing, and calls a separate function to load the data from the spreadsheets using *xlsread*, average the emissions across the test duration (or make other calculations, estimating variability, for example), and return the results. These can then be imported into Excel as space delimited data, and analysed.

Smoke emissions data are collected manually, reading off the digital display on the AVL 415. The machine itself bases its output on an average of 3 consecutive measurements.

3.3.2 IN-CYLINDER PRESSURE DATA

In-cylinder pressure data are logged and saved using a LabVIEW VI file written by Dr. Lyn McWilliam. The user is required to input the number of samples per revolution at which the encoder operates (set to 360 ppr throughout the earlier work in Chapter 4, but to 2880 ppr in all later work, following replacement of the shaft encoder – see Section 3.1.4), to specify any measured offset to account for misalignment (at the time of writing, 0.7 BTDC), and set the required number of cycles to record (100 cycle data sets have been used throughout the work documented in this thesis, with analysis based on multiple sets). The files generated are extensionless, but can load into Excel as tab delimited data, and into MATLAB using *dlmread*.

The core MATLAB module begins by calling a function to generate arrays containing in-cylinder volume (V) and rate of change of volume ($\partial V/\partial \Theta$) data for angles from 45 BTDC to BDC at 0.125 CA increments. Instantaneous volume is calculated as the sum of clearance volume (29.04 cc) and displaced volume; displaced volume is equal to the instantaneous piston displacement from TDC (calculated using Equation 3.5, the variables in which are illustrated by Figure 3.10) multiplied by the cross-sectional area of the cylinder (58.09 cm^2) [418].

$$s = a cos\Theta + (l^2 - a^2 sin^2\Theta)^{0.5} \tag{3.5}$$

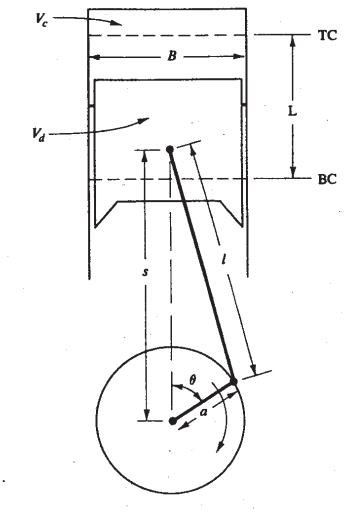

Figure 3.10: Geometry of cylinder, piston, connecting rod and crankshaft, where B = bore (86 mm), L = stroke (86 mm), l = connecting rod length (155 mm), a = crank radius (43 mm), Θ = crank angle [418].

Next, a function is called to process the pressure data, generating arrays containing average in-cylinder pressure (P) and rate of change of pressure ($\partial P/\partial \Theta$) data for the same angular increments, in addition to maximum pressure and angle of maximum pressure values on a cycle-by-cycle basis. As with emissions data, pressure files were loaded using the *uigetfile multiselect* mode for batch processing.

Pressure data were imported using the *dlmread* function and cropped to the relevant angular range. No filtering was needed for the pressure data collected using the 360 ppr encoder, but when using the 2880 ppr encoder a 9-point moving average was applied (i.e. the 0.5 CA data point is an average of data from 0–1 CA) using the *smooth* function. This was necessary to remove noise which made the calculation of apparent heat release rate difficult. Larger averaging windows suppressed features in the resulting AHRR profiles which were short-lived but considered to be 'real', and smaller averaging windows didn't always reduce the noise sufficiently. The 9-point window may not necessarily be optimum, but provides adequate noise reduction for AHRR calculation, whilst allowing the calculated AHRR to retain a similar structure to that generated using pressure data from the 360 ppr encoder – with the benefit of additional detail.

Attempts were also made to filter pressure data using Fourier transform based low pass filters with different bandwidths and roll-off functions. Although noise was successfully reduced while leaving the key features of pressure change intact, this approach influenced the form of the pressure plot, and the resulting AHRR plot, more significantly than the use of a moving average appeared to; for this reason, the moving average was preferred. In hindsight, the noise which is visible on the higher resolution heat release plots (see Chapter 5) does appear to have a degree of periodicity, implying that a well configured Fourier filter may have offered the most effective approach to signal preparation.

Once smoothed, average pressures at each crank angle interval (i.e. every 0.125 CA) are calculated to produce a single pressure profile from each 100 cycle data set. Pressure maxima and their angles of occurrence are calculated immediately after the smoothing filter was applied, but before averaging across the 100 cycles, in order to obtain some insight into cycle-to-cycle variations. The array of data set average pressure data is differentiated to give $\partial P/\partial \Theta$, for the purposes of AHRR calculation.

Arrays of V, $\partial V/\partial \Theta$, P and $\partial P/\partial \Theta$ are passed to another function, which uses them to calculate AHRR and a variety of derived criteria. AHRR, or Q, is calculated over the angular increments using Equation 3.6 [418], where γ is the ratio of specific heats. Q in

this case represents net rather than gross heat release, and as such makes no attempt to account for the proportion of heat which is lost.

$$\frac{\partial Q}{\partial \Theta} = \frac{\gamma}{\gamma - 1} P \frac{\partial V}{\partial \Theta} + \frac{1}{\gamma - 1} V \frac{\partial P}{\partial \Theta} \tag{3.6}$$

Throughout the work documented in this thesis, a constant specific heat ratio of 1.33 has been used. However, this is a simplification, because the ratio of specific heats changes throughout the engine cycle due to the variations in temperature and in-cylinder gas composition [621, 622], falling from approximately 1.35 before combustion, to 1.26–1.3 after it [418]. Heywood suggests that when using a constant value, between 1.3–1.35 is an appropriate range [418]. Initial calculations based on the gradient of ln P versus ln V plots, returned values averaging around 1.33 throughout the engine cycle. This result is broadly consistent with calculations made by Abbaszadehmosayebi [623] on the same laboratory engine, who estimated γ by two methods, at 15 operating conditions, using 3 different fuels, with an overall average of 1.33±0.02. In the Abbaszadehmosayebi study [623] condition-to-condition variation was far larger than that between fuels, and on average very little difference was apparent between petro- and biodiesels; however, calculations from equilibrium species concentrations and thermodynamic data may suggest a very slight reduction in γ when fuelling on biodiesel [624].

An attempt was made to incorporate a ratio of specific heats which varied throughout the combustion process with estimated average in-cylinder temperature (using the equation in [622]). This made only a minor difference to the results and was not finally adopted because it was adjudged to be better for the purposes of the work – specifically, for a comparison between fuels – to apply the same γ value consistently, than to introduce an additional variable and risk unequal treatment of different cases.

From this point onwards, much of the further analysis was done – certainly in the later studies – using Microsoft Excel instead of MATLAB, compiling the arrays of AHRR for all of the data sets for each test case into single spreadsheets, and scrutinising them manually. Exporting to Excel makes analysis considerably more laborious, when most combustion phasing criteria can be calculated quickly and easily using MATLAB scripts. However, the premixed burn fraction in particular is not straightforward to specify algorithmically, primarily because its conclusion possesses different characteristics under different operating conditions.

In the idealised case, the end of premixed burn (EOPMB) is identified as the first

AHRR local minimum following the maximum. However, in practice this point might not be reliable; the first minimum may be located earlier or later than the apparent end of the premixed burn, particularly when calculated from high resolution pressure data.

In the earliest work (see Chapter 4), all heat release parameters were computed automatically, according to the criteria illustrated in Figure 3.11. Except for the EOPMB, all of these values were calculated in the same way in later studies; the only difference being that, whereas the low resolution data was used to interpolate values to 0.1 CA, the higher resolution data was used directly (albeit following filter application) to obtain values to an accuracy of 0.125 CA. Start of injection (SOI) was defined from the commanded SOI specified within the engine management software. Start of combustion (SOC) was defined as the point at which AHRR became positive. The end of combustion (EOC) was defined as the point at which a wide window AHRR moving average (5-point for the 360 ppr data, 45-point for the 2880 ppr data) went below zero. Ignition delay (ID) is the difference between the SOI and the SOC, the premixed burn fraction (PMBF) is the integral of AHRR between SOC and EOPMB, divided by the integral of AHRR between SOC and EOC. Combustion intervals from 10–90% (commonly denoted CA10–CA90) were calculated as the angle, Θ, at which AHRR integrated between SOC and Θ reached the specified percentage of total AHRR.

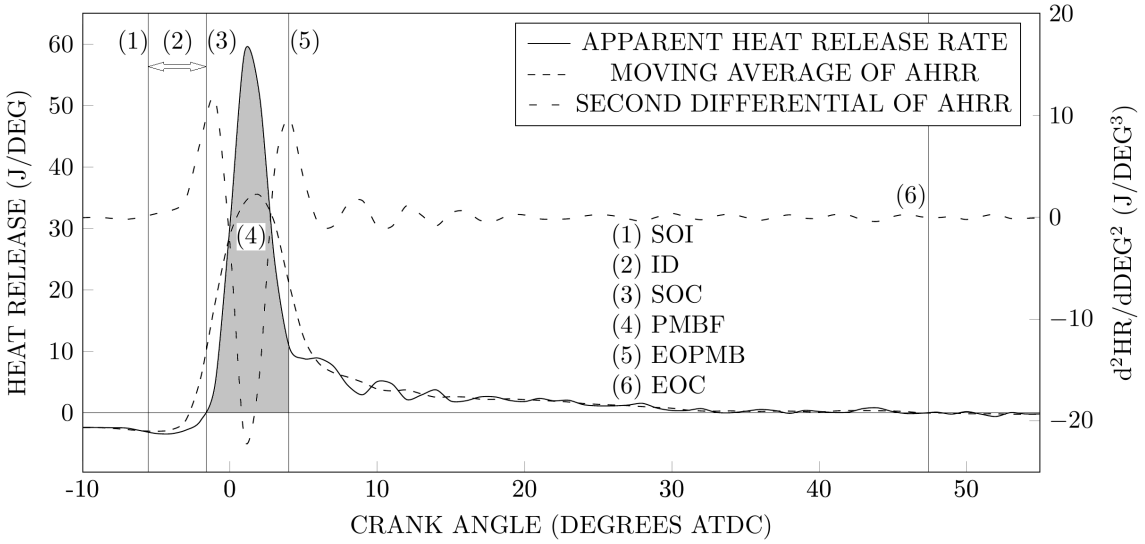

Figure 3.11: Labelled plot of heat release and the derivatives used to calculate combustion criteria. SOI: start of injection. ID: ignition delay. SOC: start of combustion. PMBF: premixed burn fraction. EOPMB: end of premixed burn. EOC: end of combustion.

The EOPMB was calculated as the first local maximum in the second differential of AHRR following peak AHRR. The reason for using this point, instead of the first local AHRR minimum following the maximum, is illustrated by Figure 3.12. Shown are AHRR

plots for petrodiesel (ULSD) and biodiesel (RME) produced from data generated using the 360 ppr encoder (the same data is plotted in Chapter 4, Figure 4.2D with a more complete explanation of the operating condition), along with lines marking the EOPMB determined by the two different definitions. What they show is that, in some cases – for ULSD in Figure 3.12, for instance – there is not a local minimum at what appears to be the end of the premixed burn spike.

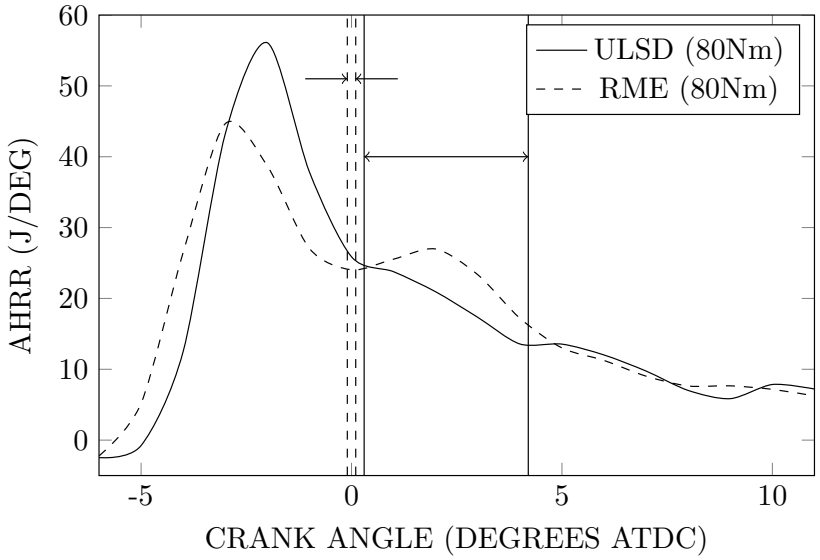

Figure 3.12: Apparent heat release plots (also found in Chapter 4, Figure 4.2D) with vertical lines placed to indicate the end of the premixed burn (EOPMB); solid lines for ULSD, dashed lines for RME. In both cases the leftmost vertical line denotes EOPMB defined as the first local maximum in the second differential of AHRR following peak AHRR, and the rightmost line EOPMB defined as the first AHRR local minimum following the maximum.

The method depicted in Figure 3.11 gave satisfactory EOPMB estimations for the low resolution data, but did not accurately or robustly characterise the high resolution data, due to the greater complexity of the AHRR curve. Ultimately, the premixed burn fraction was identified manually in the high resolution data. This will be addressed in greater depth in Chapter 5.

3.4 OPERATIONAL VARIABILITY

When running the laboratory engine, exhaust emissions might be considered to vary on three different timescales. First, they vary continuously, from instant-to-instant, and from one engine cycle to the next, with every new measurement being slightly different from the last. Second, they vary on an intra-daily basis, hour by hour, as the engine warms up and stabilises, although even at what might be thought of as a fully stabilised condition, measurements taken 10 minutes, or even 10 seconds, apart are unlikely to be identical.

Third, on an inter-daily basis, with changes in atmospheric conditions and the operating state of the engine. Experimentally, the important questions are: what is the extent of the variation associated with each timescale? What can be done to minimise obfuscation of the results?

By analysing all of the data collected at the higher load baseline condition in Chapter 5, a representative picture of the variation in emissions on the shortest (instant-to-instant) and longest (day-to-day) timescales can be obtained. Table 3.2 provides data on the average standard deviation and range of variation for gaseous emissions over 180 seconds. In Figure 3.13, example plots of emissions over this period can be seen.

	NOx (ppm)	**CO** (ppm)	**THC** (ppm)	**CO_2** (%)
AVERAGE	1057	296	115	9.28
STANDARD DEVIATION	7 (0.7%)	4.6 (1.5%)	2.9 (2.5%)	0.04 (0.4%)
MAXIMUM	1075 (+1.7%)	312 (+5.4%)	124 (+8%)	9.36 (+0.9%)
MINIMUM	1039 (-1.7%)	282 (-4.8%)	108 (-6%)	9.19 (-0.9%)

Table 3.2: Data describing the average variability observed across 180 seconds at the higher load baseline from Chapter 5.

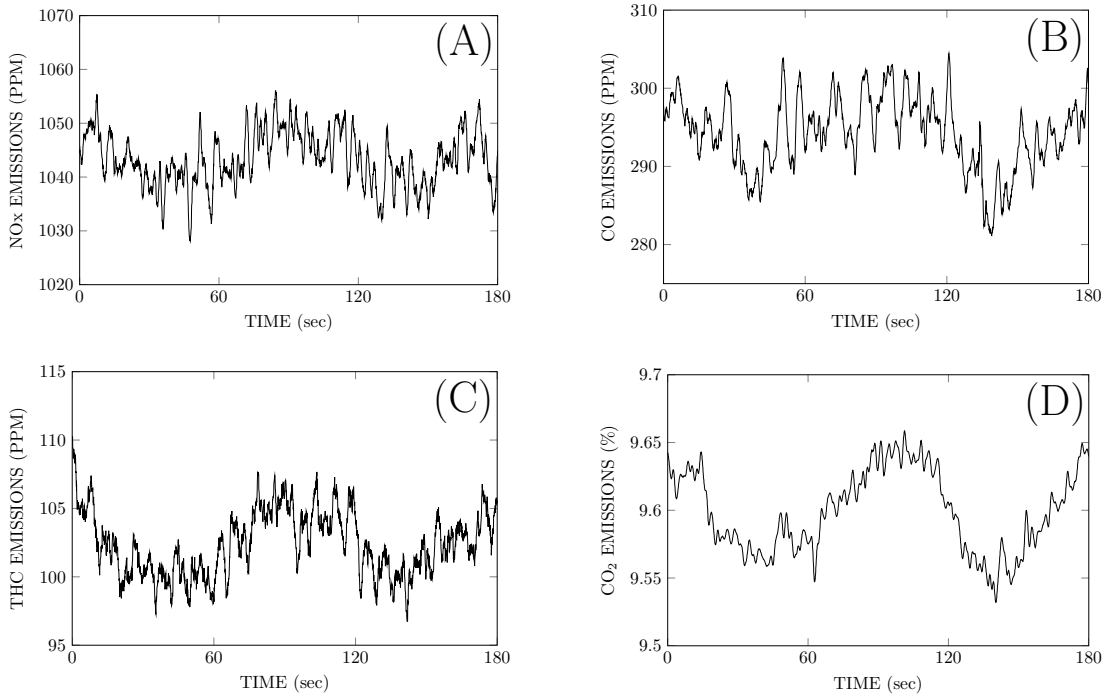

Figure 3.13: Example plots of gaseous emissions over the 180 second measurement period. (A) Emissions of oxides of nitrogen. (B) Carbon monoxide emissions. (C) Total hydrocarbon emissions. (D) Carbon dioxide emissions. (Note that although the variability of these examples is representative of that observed in other cases, the averages, maxima and minima are not necessarily the same as those for the whole data set, as quantified in Table 3.2.)

The data in Table 3.2 makes clear that carbon dioxide is the most stable emission, followed by NO_x, and then carbon monoxide and total hydrocarbons, which are significantly

more variable. However, the plots in Figure 3.13 suggest that much of the variability in levels of the different pollutants may share a common cause. The CO_2 trace (Figure 3.13D), which is evidently the least noisy, exhibits a clear periodic fluctuation, which is also apparent, to a greater or lesser extent, in the plots of NO_x, CO and THC (Figures 3.13A–C). The periodicity seems to coincide with cycling of the engine cooling system, and may therefore be related to changes in heat transfer within the engine. However, the fact that all emissions seem to follow similar trends is strange, given that with an increase in temperature, for example, NO_x emissions would be expected to increase, whilst THC emissions might be anticipated to go down rather than up. It is also noteworthy that CO_2 is fluctuating without any commanded – or registered – change in fuelling rate. Since the torque also fluctuates over the course of the cooling cycle (around 0.5 Nm either side of the designated 80 Nm operating point), it may be that there is some marginal change in the amount of fuel being injected. Alternatively, something may be affecting the exhaust flow to the measurement device, which would be consistent with the fact that all emissions fall and rise together – possibly indicative of changing dilution of the pollutants. However, if the matter were as simple as dilution then one would not expect to see larger proportional changes in one emission than another. Whatever the cause, the fluctuation has a greater proportional influence on THC and CO emissions, than on NO_x and CO_2. Beyond the larger periodic variation, the NO_x, THC and CO plots appear noisier than that of CO_2, and this is probably because the former 3 pollutants are present in far smaller concentrations.

At lower load operating conditions (again, analysing baseline data recorded for the experiments in Chapter 5) the variability in CO and THC emissions is significantly reduced in both absolute and proportional terms; this can be seen by comparing the lower load data in Table 3.3 with the higher load data in Table 3.2. In absolute terms the variations in NO_x and CO_2 emissions over the 180 second measurement period are apparently changed very little. Since the average NO_x emissions are only a little lower in Table 3.3 than in Table 3.2, the standard deviation and range of variation is also similar in percentage terms, whereas the significant reduction in CO_2 emissions at the lower load means that the proportional variability of CO_2 is far greater than at the higher load. The apparent constancy of absolute CO_2 variability possibly implies that the measurement system itself may be the cause.

Although there is still some periodicity to the variation in lower load emissions, it is

	NOx (ppm)	**CO** (ppm)	**THC** (ppm)	**CO_2** (%)
AVERAGE	945	314	206	5.71
STANDARD DEVIATION	6.8 (0.7%)	3.7 (1.2%)	1.9 (0.9%)	0.04 (0.7%)
MAXIMUM	961 (+1.7%)	325 (+3.4%)	211 (+2.5%)	5.8 (+1.4%)
MINIMUM	927 (-1.9%)	302 (-3.9%)	201 (-2.4%)	5.61 (-1.7%)

Table 3.3: Data describing the average variability observed across 180 seconds at the lower load baseline from Chapter 5.

less clear and apparently reduced in frequency compared to higher load; this is consistent with the proposed relation to the cooling system, since at higher load the cooling cycle is shorter due to increased operating temperatures.

Ultimately, it has not been possible to say with certainty what the cause of the short-term variability is, but it is plausible that it is dependent upon both the engine and the measurement system. Ideally, the source of the periodic fluctuation would be identified and removed – possibly by modifying the control parameters of the cooling system, if this does, in fact, play a role. However, simply making recordings over a relatively long time period allows most of the effects of short-term variability to be averaged out, without additional experimental complexity. If the period of the fluctuation could be determined precisely then recording emissions over the duration of a whole number of periods might be a good solution. However, since the period does not appear to be entirely consistent under a given condition, and also varies with fuel and load, this approach is not at all straightforward. The option chosen was to record and average emissions data across the longest time period offered by the acquisition software: 180 seconds. (Note that in the first set of experiments (see Chapter 4), the measurement period was shorter: 60 seconds. At this point the periodic fluctuation had not been discerned in the results.)

On the longest relevant timescale, considering variations in emissions from day-to-day, over the course of the experimental period (several months, in the case of Chapter 5), CO and THC emissions varied substantially more than NO_x and CO_2 emissions, just as they did on the shortest timescale. Filter smoke number (FSN) varied more than any of the gaseous pollutants. This can be seen in Figure 3.14, which shows the standard deviation of the emissions measurements at the daily baseline over the course of the experiments conducted for Chapter 5.

To some extent these variations appear to depend upon atmospheric conditions. As can be seen in Figure 3.15A, baseline NO_x emissions correlate well with atmospheric temperature (that is, the local temperature at the time of the baseline measurement, using

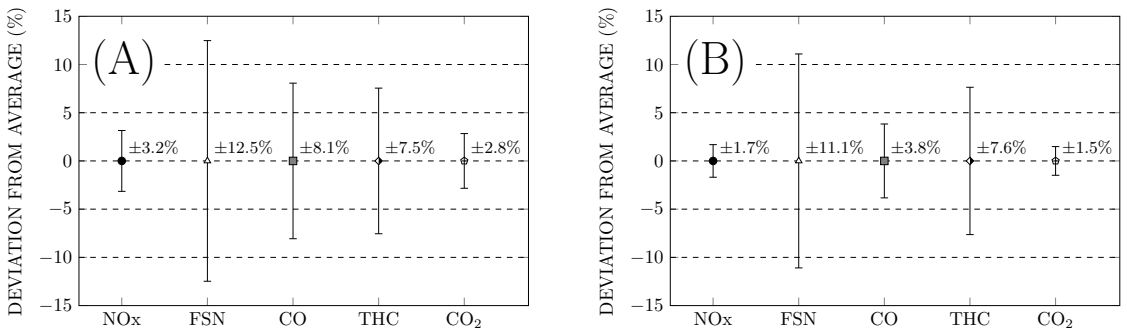

Figure 3.14: Standard deviations of emissions of oxides of nitrogen, carbon monoxide, total hydrocarbons and filter smoke number measured at the Chapter 5 daily baseline under (A) the higher load, (B) the lower load. All deviations given as percentages of the average baseline values.

data available online taken from a nearby weather station [625]), decreasing as temperature increases. This probably has some relationship to the changing density of intake air; start of combustion tended to be advanced and maximum in-cylinder pressures tended to be higher on cooler days. It should be noted that temperature was also monitored within the engine bay, but although the same correlation with NO_x emissions was observed (i.e. a clear reduction in NO_x with increasing temperature), the coefficient of determination was lower.

The relationships between other emissions and atmospheric temperature can be seen in Figures 3.15B–E. Although none correlate as well with temperature as NO_x, and in some cases the degree of correlation is fairly poor, in general the plots offer a reasonable indication that CO, CO_2 and smoke emissions tend to increase with increasing atmospheric temperature, while THC emissions go down a little. In all cases, these trends are consistent with the data collected at the lower load baseline. Baseline CO_2 and CO are well correlated with each other ($r^2 = 0.79$), suggesting both an increase in the necessary fuelling rate and the richness of combustion on hotter days. Baseline CO and FSN are similarly well correlated ($r^2 = 0.8$), further implying some connection to combusting equivalence ratios.

Clearly changes in temperature alone do not provide a full explanation for the degree of variation observed. Other environmental parameters, humidity and atmospheric pressure, for instance, did not appear to have much correspondence to the emissions trends. FSN, seen to have the widest standard deviation in Figure 3.14, is likely to be subject to issues associated with changing and ageing of the engine lubricating oil [626], as well as potentially more drastic problems with the measurement system like partial blockages due to soot accumulation in the sample lines.

In the experiments in this thesis, the approach to coping with day-to-day variations

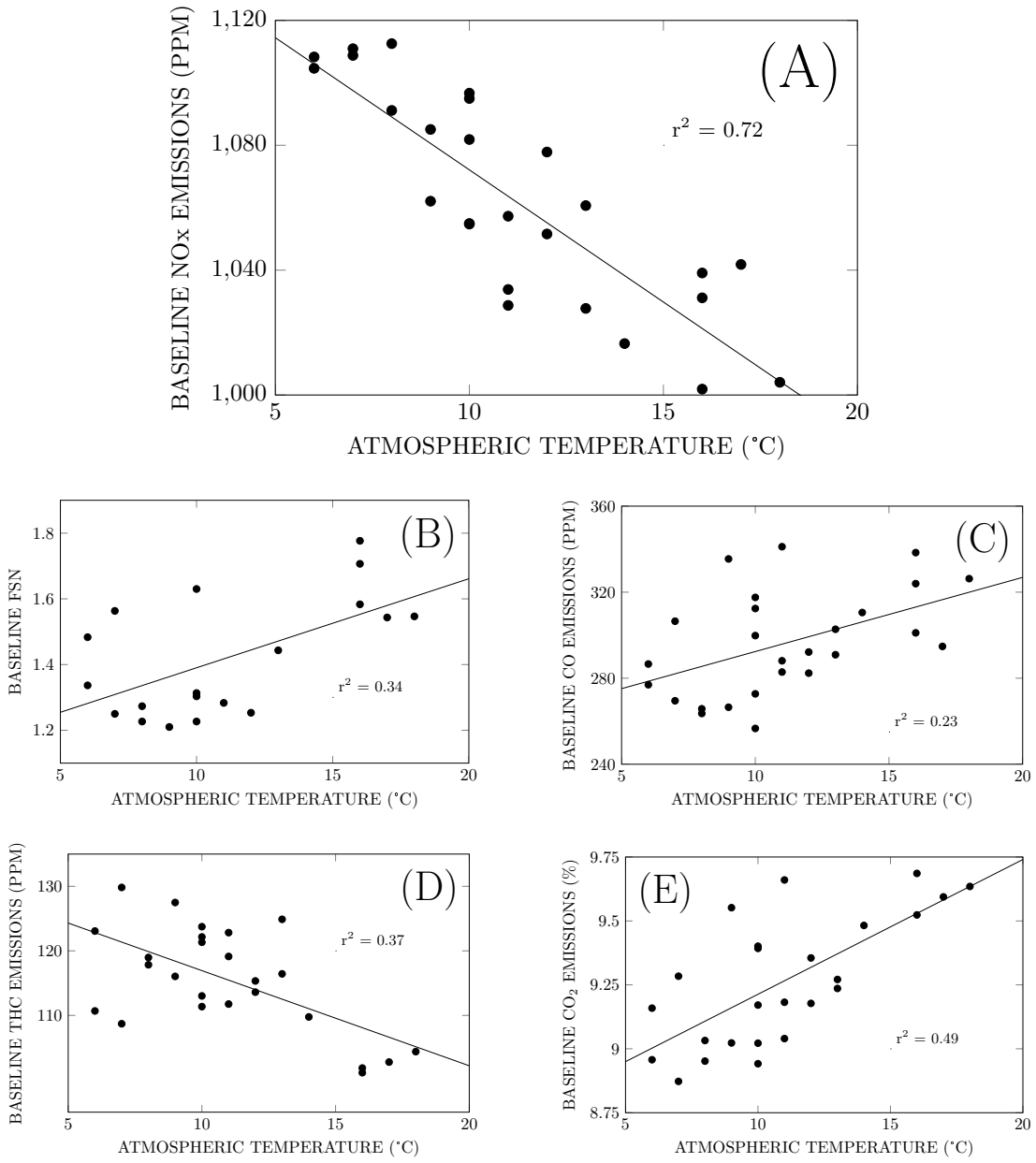

Figure 3.15: Emissions at the daily baseline as a function of atmospheric temperature. (A) Emissions of oxides of nitrogen. (B) Filter smoke number. (C) Carbon monoxide emissions. (D) Total hydrocarbon emissions. (E) Carbon dioxide emissions. (Based on the higher load daily baseline data from Chapter 5.)

was to try to keep the operational environment as consistent as possible, whilst carefully collecting daily baseline data, which could be used either for the purposes of comparison (to identify outliers and discrepancies, and explain unusual results), or for normalisation. Normalisation was avoided where possible, and was only employed where the level of variation was sufficient to affect the *meaning* of the results. Throughout Chapter 4 NO_x emissions are given without any modification or reference to daily values, whereas in Chapters 5 and 6 they are given with an indication of baseline variability, in order to clarify results, but the variations are not significant enough to alter the trends or warrant adjustment; in

Chapter 6, all emissions data is provided with baseline values to improve comprehension and enable meaningful interpretation of the results. Smoke, carbon monoxide and total hydrocarbon emissions are normalised with respect to the daily baseline in the higher load portion of Chapter 5 (Section 5.3.1).

In terms of variations on an intermediate timescale – that is, intra-daily – the data available only provides a partial illustration of the extent of the variations encountered. Although emissions were monitored throughout the experimental period on each day, changes in fuel and operating conditions obscure what could be considered the general trajectory of change. By considering data across the entirety of the 90 minute higher load baseline period in Chapter 5, at which operation on all days was ostensibly identical, it is possible to see how emissions change as the engine warms up and stabilises. In Figure 3.16, average percentage change in all emissions from the end of the warm-up period until the end of the baseline period can be seen (the daily operating schedule and baseline timing are clarified in Chapter 5, Figure 5.1).

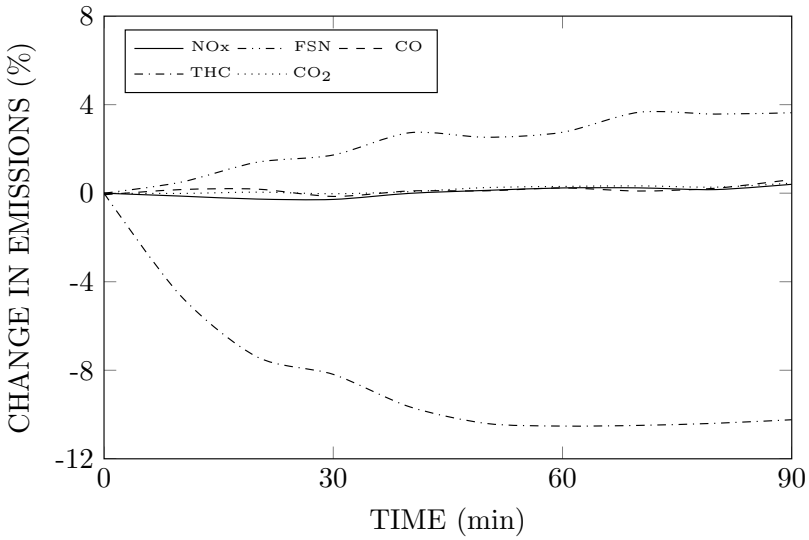

Figure 3.16: Average variation in emissions as a function of time across the 90 minute daily baseline period from Chapter 5.

NO_x, CO and CO_2 emissions were observed to change very little across the 90 minute baseline, on average. After 90 minutes average NO_x emissions were 0.4±1.1% higher than at the start; CO emissions were 0.6±2.5% higher; CO_2 emissions were 0.5±0.6% higher. Hence, it should be understood that the change in emissions of each pollutant is inconsistent, not only in magnitude but also in direction. On 78% of days, NO_x emissions increased over the duration of the baseline, while on the other 22% they fell. CO_2 emissions increased 83% of the time, but CO emissions fell almost as often (44%) as they rose (56%).

THC emissions and smoke number readings changed more dramatically over the baseline period, with THC emissions falling by an average of 10.2±10.3% (declining on 83% of test days) and FSN increasing by an average of 3.6±4.8% (increasing on 75% of test days).

In general, the change in emissions is largest soon after engine start up, and trends gradually settle to a quasi-stable position over a period of several hours. To a certain extent, such quasi-stability appears to be achieved once the engine and test bay have attained an approximate thermal equilibrium. The baseline data presented in Figure 3.16 follows an hour long warm-up period, during which heaters were turned on within the test bay, and the extraction system was not active; this approach raises temperatures more quickly than would otherwise be the case. In experiments conducted earlier than those documented in Chapter 5 (although documented later, in Chapter 6), the same test schedule was used, but the precaution of forced pre-heating of the engine bay had not yet been devised. In this case it can be seen that the change in emissions over the 90 minute baseline was more pronounced, as illustrated in Figure 3.17.

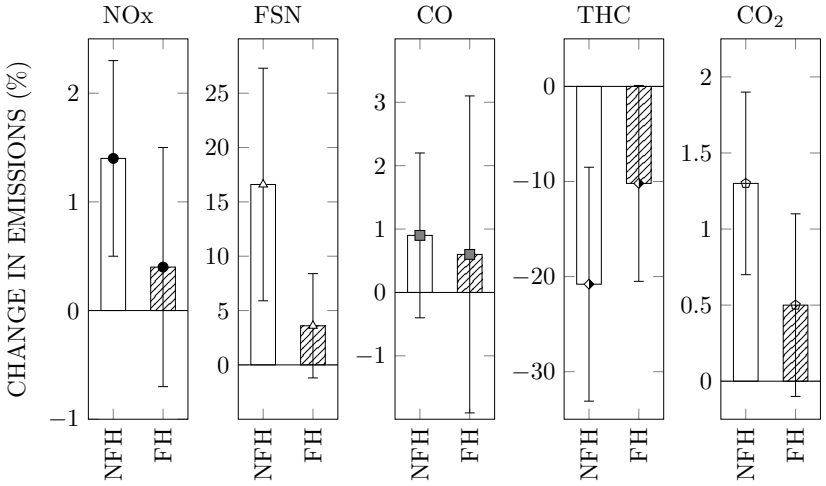

Figure 3.17: Average change in emissions across the 90 minute daily baseline period with and without forced test bay heating during the 60 minute warm-up phase. NFH, no forced heating of the test bay (baseline data from Chapter 6); FH, forced heating of the engine test bay during the warm-up period (baseline data from Chapter 5).

Although other factors may be involved, the reduced change in emissions across the 90 minute baseline when the temperature of the test bay was elevated more rapidly through the warm-up period (that is, in the forced heating cases in Figure 3.17), suggests that the engine and test cell may have reached a condition closer to steady-state by the end of the warm-up period.

For the experiments in Chapter 6, the 90 minute daily baseline was followed by a 90

minute period running on a test fuel, and then a further 90 minutes at the baseline condition. This provides the opportunity to observe the engine operating state immediately after, and then 270 minutes after, the end of the warm-up period, over which time load and engine speed remained basically constant. Because the fuel was changed from petrodiesel, to the test fuel (in all cases, biodiesel with an additive), and back to petrodiesel, it is possible that the interval running on biodiesel may have had lasting effects on the operating state which may have caused deviation from the trends which would be expected based purely on run-time. However, although this data may not be entirely representative, it offers some indication of the trajectory which emissions might be expected follow throughout the day.

NO_x emissions always increased throughout the day, and were, on average 1.2±1% higher 270 minutes after warm-up than at the end of the 90 minute baseline. CO_2 emissions tended to increase slightly between the 90 minute and 270 minute intervals, although in some cases (22%) a reduction was measured; on average, CO_2 emissions were 0.3±0.4% higher at the end of the day than 180 minutes earlier, at the end of the baseline. CO emissions tended to decline, but also rose throughout the day on a significant number of occasions (33%); on average, CO emissions were 1±2% lower 270 minutes after the warm-up, than they were 90 minutes after the warm-up. THC emissions increased across 90–270 minutes on just over half (56%) of test days, with an average increase of 1.7±3.9%. Similarly, smoke number followed no clear trend, increasing throughout the day as often as it fell; on average a reduction of 0.6±5.3% was observed, which illustrates that the general variability of FSN appears to far outweigh the effect of run-time.

The precautions taken to minimise the effects of intra-daily variations (in the main experiments, documented in Chapter 5) were to, as discussed above, encourage rapid heating of the engine and test cell through the warm-up period, to allow sufficient time before data collection for the engine to become relatively settled, and to rigorously test on a daily schedule (see Chapter 5, Figure 5.1) which enforced strict measurement time windows, so that all results would be equally affected by any influence connected to run-time.

In summary, short-term variations were overcome by averaging data over a sufficiently long measurement period, intra-daily variations were minimised by forced initial heating of the test bay and adherence to a fixed experimental schedule, and inter-daily variations were quantified by daily baseline data collection – and, where necessary, normalised with

respect to this data.

Although the experimental protocol was fit for task, and ultimately yielded good quality data and meaningful results, it was a fairly time-inefficient approach. In some cases the daily schedule may have been excessively conservative, and steps taken to avoid the relatively minor effects of intra-daily variations may have incurred a greater penalty in terms of exposure to inter-daily variations. Obtaining an approximate steady-state before data collection is clearly beneficial, but some compression of the schedule may have allowed more data to be collected within the confines of the laboratory opening hours, without invalidating the results. Ideally, test facilities with a high daily time-overhead, in terms of start-up, warm-up, settling, and later, purging, cooling down and cleaning, would be able to operate for periods long enough to reduce this overhead to a small minority of time expenditure; for instance, work undertaken over the course of a fortnight might have been comfortably performed within a single 20 hour access period, without any loss of experimental rigour.

Chapter 4

PREMIXED BURN FRACTION: ITS RELATION TO THE VARIATION IN NO_x EMISSIONS BETWEEN PETRO- AND BIODIESEL

The following chapter is a reproduction of sections from a paper published in Energy & Fuels [543]. Some annotations have been added inside square brackets in italics, and offer expansions upon, and revisions of, the original text. Experimental work was performed with the assistance of N.S.I. Alozie.

4.1 INTRODUCTION

Past and ongoing work undertaken at the Brunel University Centre for Advanced Powertrain and Fuels Research (CAPF) has found both slight increases and decreases in emissions of oxides of nitrogen (NO_x) – dependent upon injection timing and load – when fuelling with biodiesel [462]. Although the literature does account for this kind of variety [13, 484, 539] it is still an inconsistency that requires thorough explanation.

The engine in the Brunel laboratory on which previous tests have been run is typically operated at relatively low loads, and connections have been made in the literature between load and emissions from biodiesel fuelled engines [14, 484, 539, 627–632]. The objective of this study was to monitor operational conditions that were expected to yield both positive and negative changes in NO_x emissions when fuelling with biodiesel, and to identify possible combustion parameters contributing to the variations in relative NO_x emissions between the two fuels.

4.2 METHODOLOGY

4.2.1 EXPERIMENTAL SETUP

The experiment that was performed involved the collection of in-cylinder pressure and emissions data under 40 Nm and 80 Nm loads (BMEPs of 2.5 bar and 5 bar, respectively), running at a constant engine speed of 1800 rpm, fuelling on ultra-low sulphur diesel (ULSD) and rapeseed methyl esters (RME), sweeping start of injection (SOI) timing from 14 BTDC to 3 ATDC in one degree increments. The load was changed by an alteration in fuelling achieved by an elongation of the single injection event.

The experimental setup was as described in Chapter 3, with the original 360 ppr encoder still in place, giving native pressure data resolution of only 1 CA, which was subsequently interpolated to obtain data resolved to 0.1 CA. An in-depth specification of the fuels used was not available.

After start-up, the engine was allowed to warm up until hydrocarbon emissions had settled to an apparent steady state. Following changes to operational conditions, data collection was postponed until all emissions had reached apparent consistency when viewed over a 180 second duration.

In-cylinder pressure data were collected over 100 engine cycles per measurement, and the measurement was repeated 5 times for each point in the experimental matrix. The experimental matrix was completed twice in full, to confirm repeatability. Emissions data were recorded over 60 second intervals, twice for each point in the experimental matrix. Again, this process was repeated for confirmatory purposes.

4.2.2 DATA ANALYSIS

Emissions data files were recorded and analysed as described in Section 3.3.1, in order to provide average values for all gaseous emissions measured by the Horiba. In this study, the discussion is restricted to NO_x emissions in order to narrow the scope to the area of direct relevance. Although data on smoke emissions was also recorded, it has not been included in the analysis, because the smoke meter required recalibration during the period over which experiments were performed, and consequently the collection of a full, repeated data set in parallel to gaseous emissions was not possible. Pressure data were analysed as described in Section 3.3.2, and heat release criteria were calculated as defined in Figure 3.11.

4.3 RESULTS AND DISCUSSION

4.3.1 NO_x EMISSIONS

Figure 4.1 shows the relationship between NO_x emissions and start of injection (SOI) for ULSD and RME under (A) 40 Nm and (B) 80 Nm loads. As can be seen in Figure 4.1A, NO_x emissions were consistently lower for RME than for ULSD under a 40 Nm load, but under an 80 Nm load (Figure 4.1B) the relationship was less consistent. With SOI 14 degrees before TDC, NO_x emissions for both fuels were approximately equal under an 80 Nm load; as injection timing was retarded the RME NO_x emissions became higher than those from ULSD, with the peak difference being recorded at -8 ATDC; from there, the difference declined until both fuels recorded almost equal emissions again at -1 ATDC; and past this point, further retardation led to a relative reduction in RME NO_x emissions, to levels below those of ULSD. (Note that although the differences between the two fuels appear small under some conditions, the trends observed were observed consistently; the average standard deviation of repeated measurements was less than 25 ppm.)

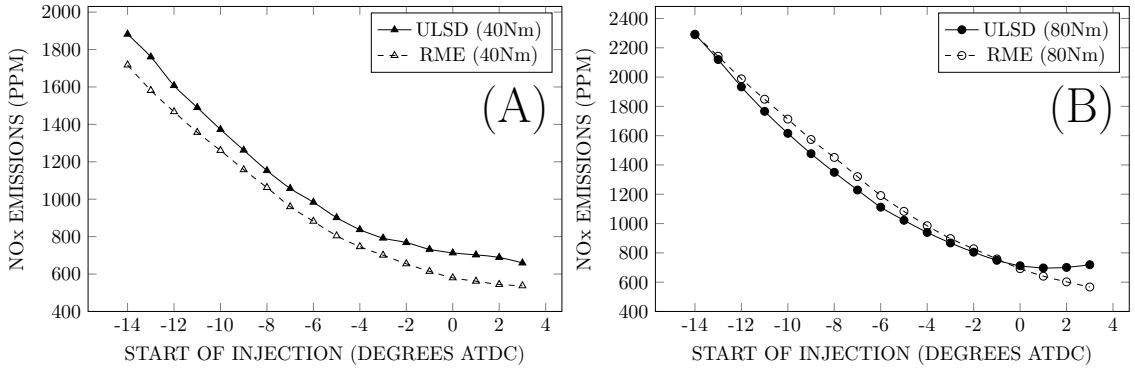

Figure 4.1: NO_x emissions as a function of start of injection timing for ULSD and RME under (A) 40 Nm and (B) 80 Nm loads.

4.3.2 PRESSURE AND HEAT RELEASE

Taking the -8 ATDC SOI position as an initial point of focus (because it was the position at which NO_x emissions from RME were highest relative to ULSD under an 80 Nm load), plots of pressure and apparent heat release rate (AHRR) for both fuels at both loads can be seen in Figure 4.2.

The pressure traces (Figures 4.2A and 4.2B) do not display any vast differences, but there are important points to be drawn from them. The first feature to note is that the RME curves rise earlier in both cases, but are advanced to a slightly greater degree

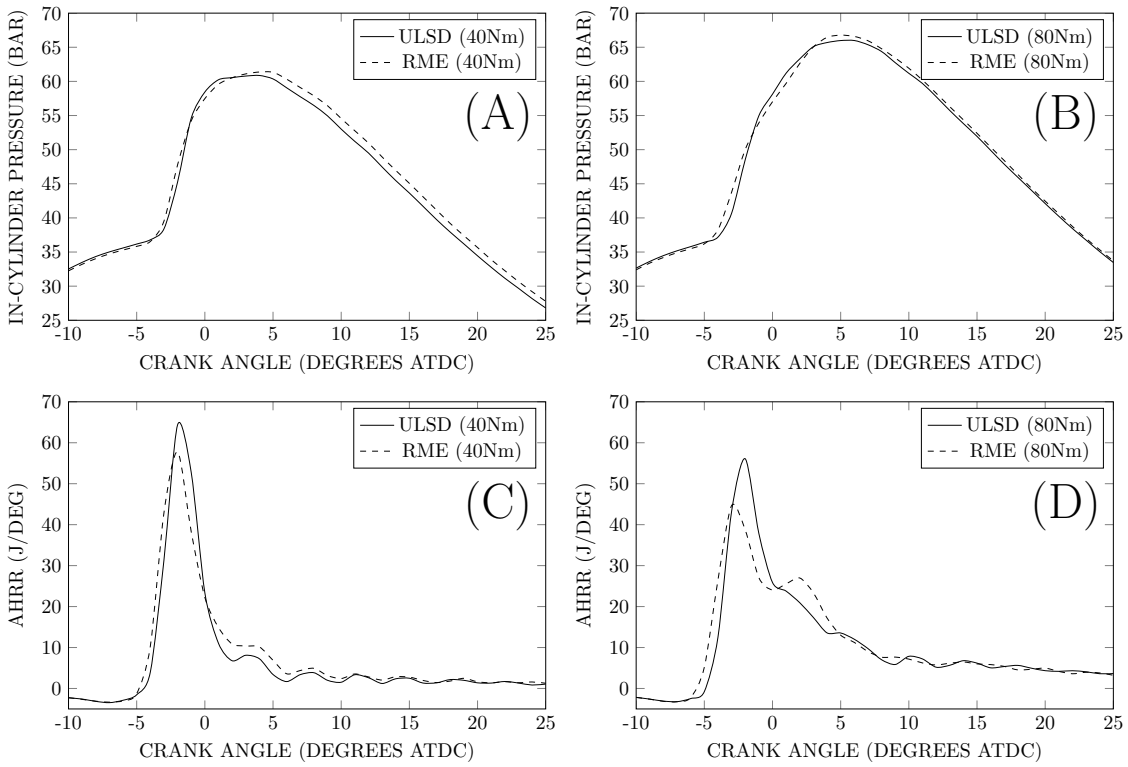

Figure 4.2: In-cylinder pressure (A and B) and apparent heat release rate (C and D) charts for ULSD and RME under 40 Nm and 80 Nm loads at -8 ATDC injection timing.

under the 80 Nm load. This assertion is supported by the heat release plots (Figures 4.2C and 4.2D) which show the same trend, and by the ignition delay (ID) data presented in Figure 4.3, which indicates that the ID of RME was always shorter than that of ULSD, and was reduced to a greater extent by the increase in load. (Note that the average standard deviations of ID values were less than 0.1 CA under the 40 Nm load, and less than 0.2 CA under the 80 Nm load.) When operating temperatures are higher – as they are at higher load (Figure 4.3B) – vaporisation of biodiesel will occur more readily than at lower temperatures, reducing the physical component of ID time [418, 633, 634]. Therefore, it is possible that the larger observed reduction in ID at higher load is related to the impact of temperature change upon the physicochemical properties of biodiesel (its higher viscosity, density, heat capacity and surface tension, reduced vapour pressure, etc., which make the fuel generally more resistant to vaporisation). Although the change in temperature would accelerate the vaporisation of petrodiesel too, it may close the physical delay gap between the two fuels, making the chemical aspect of ID more clearly prominent. *[Some authors suggest that the physical component of ignition delay is significant [635], while others suggest that it isn't [636]. In likelihood, it is the chemical part of ignition delay which is dominant [637].]*

Further to the discussion of ID, Figure 4.4 shows NO_x emissions plotted against start

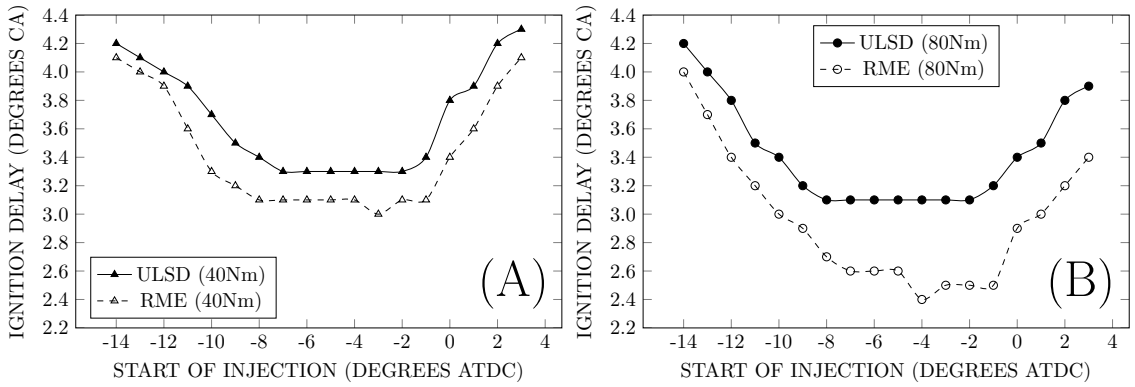

Figure 4.3: Ignition delay as a function of start of injection timing for ULSD and RME under (A) 40 Nm and (B) 80 Nm loads.

of combustion (SOC, as opposed to SOI in Figure 4.1) which serves to demonstrate the immediate impact of RME's shorter ID. Comparing the 80 Nm plots (Figures 4.1B and Figure 4.4B) it can be seen that much of the difference between the two fuels can be directly attributed to the advance in SOC. As a function of SOC, the RME NO_x emissions curve is effectively shifted left, moving it into closer concord with the ULSD curve under the increased load. RME NO_x emissions remain above the ULSD trend for SOI conditions between -10 ATDC and -5 ATDC in Figure 4.4B (as a function of SOC – and equating to SOC timings between approximately -8 ATDC and -2 ATDC), whereas in Figure 4.1B (as a function of SOI) they had exceeded the ULSD trend from -13 ATDC to -2 ATDC. Although it seems that advanced SOC plays a critical, primary role in the increase in NO_x emissions from RME under an 80 Nm load, other secondary differences remain in the absence of this effect. *[The fact that NO_x emissions from the two fuels are almost equal when plotted as a function of SOI does not necessarily mean that differences beyond the change in SOI are of secondary importance, as suggested; it is simply evidence that further differences effectively cancel one another out under this particular operating condition.]*

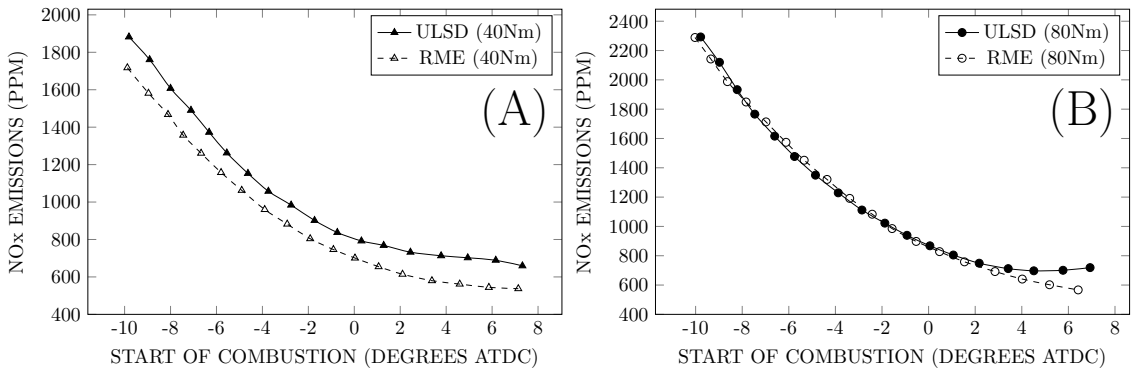

Figure 4.4: NO_x emissions as a function of start of combustion timing for ULSD and RME under (A) 40 Nm and (B) 80 Nm loads.

The second feature to note from the pressure traces (Figures 4.2A and 4.2B) is that the peak in-cylinder pressure reached is higher – albeit modestly – for RME in both instances. This holds true for most injection timings under both load conditions. However, although under an 80 Nm load the difference between peak pressure for ULSD and RME is quite well correlated with the difference in NO_x emissions (with relatively higher peak pressures occurring alongside relatively higher NO_x), at the lower load this is not the case. This can be seen by comparing Figures 4.5A and 4.1A, with Figures 4.5B and 4.1B. This may be because at lower load high temperatures are less widely spread, and so a global pressure value provides a less valuable temperature indicator in terms of the peak temperatures responsible for NO_x formation; for instance, small localities of very high temperature can generate higher NO_x emissions than the same amount of heat-energy evenly distributed, although the two scenarios could yield identical pressure data. It is noteworthy that peak pressure was normally higher when fuelling with RME, even under conditions where NO_x emissions were lower. This is likely to be related to RME's earlier SOC. *[In Chapter 5, with SOC timing equal for all fuels, peak pressure when fuelling on biodiesel still tends to exceed that of petrodiesel.]*

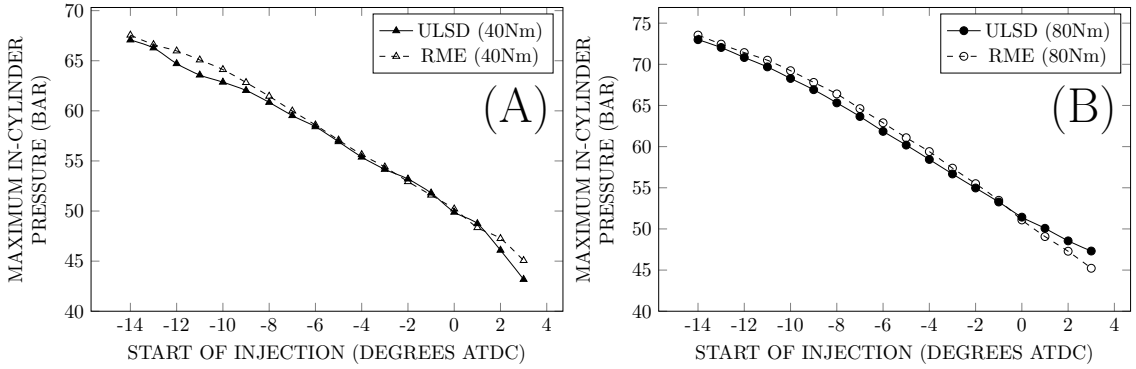

Figure 4.5: Maximum in-cylinder pressure as a function of start of injection timing for ULSD and RME under (A) 40 Nm and (B) 80 Nm loads.

The third feature to note is that, on the 40 Nm pressure trace in Figure 4.2A, the RME curve remains noticeably higher than that of ULSD throughout the decline, indicating that RME combustion continued for longer, lagging behind that of ULSD. This can also be seen in the heat release plot (Figure 4.2C), which shows that ULSD initially released heat more intensely, reaching a higher peak AHRR. On the 80 Nm pressure trace (Figure 4.2B), the RME curve does not lag behind the ULSD curve in the same way. Although, just as at 40 Nm the peak heat release rate is higher for ULSD, the difference is that at 80 Nm a more substantial diffusion burn phase occurs after the premixed burn is completed, as can

be seen from the AHRR plot in Figure 4.2D. This means that, despite the fact that heat is not released as quickly in the premixed phase when fuelling on RME, under increased load an increased rate of post-premixed heat release essentially compensates for the reduction in premixed AHRR. This can be seen more clearly in Figures 4.6–4.8 which show partial combustion durations, relative combustion progress, and average partial heat release rates, respectively.

Figure 4.6A confirms that at the -8 ATDC injection timing combustion proceeded more slowly and took longer to complete (completion here being represented by the 90% burn fraction interval) for RME under the 40 Nm load, and for ULSD under the 80 Nm load. That is to say, generally combustion was more prolonged at each load for the fuel that generated lowest NO_x emissions. It can be seen, under both loads, that the burned fraction curves begin similarly for the two fuels, but for ULSD they become steeper and remain steeper for longer than is the case for RME (indicative of a larger premixed burn fraction). The important difference to note between the 40 Nm and 80 Nm curves is that, following the initial sharper ascent of ULSD, the RME curve remains behind the ULSD curve at 40 Nm but 'overtakes' the ULSD curve at 80 Nm.

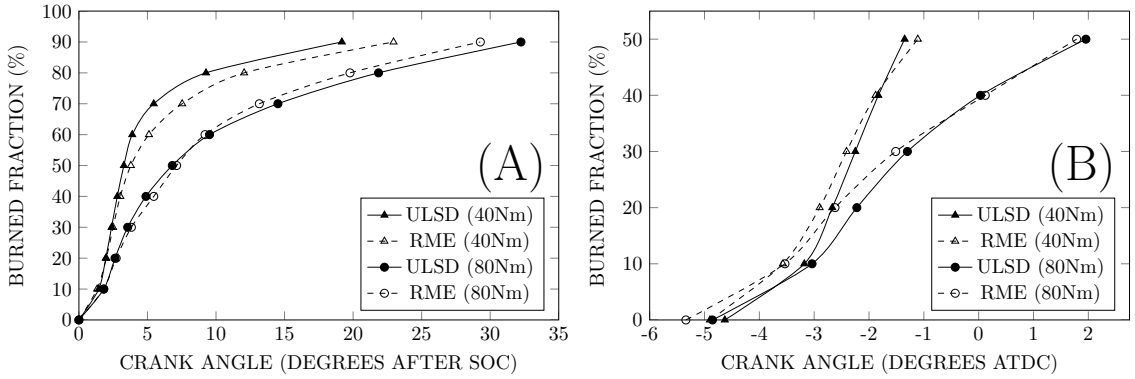

Figure 4.6: Cumulative burned fraction (A) as a function of partial combustion duration (between SOC–CA90) and (B) as a function of crank angle position (between SOC–CA50) for ULSD and RME under 40 Nm and 80 Nm loads at -8 ATDC injection timing.

Figure 4.6B shows absolute combustion intervals through the first half of combustion in terms of crank angle, rather than relative to SOC, and thus includes the direct influence of ID. This affords a clearer examination of differences in the actual combustion progress of the fuels, with RME beginning ahead in both cases and falling behind through the premixed burn phase. (A similar trend – biodiesel combustion being 'overtaken' by petrodiesel through the early burn phase, only to later catch up – has been previously reported by Bittle, Knight and Jacobs [14, 546].) Here, the brevity of the period for which RME falls absolutely behind ULSD under an 80 Nm load at this injection timing can be

seen clearly (with RME trailing only at the 40% combustion interval). This short period of recession seems to be generally characteristic of the SOI timing positions which produced relatively higher NO_x emissions for RME under an 80 Nm load. How combustion progress varies across the full SOI range is qualitatively illustrated in Figure 4.7, which consists of binary plots identifying the fuel that reached each combustion interval earliest under given operational conditions.

Figure 4.7, examined from the left to right, serves to clarify the way in which RME starts out ahead, due to its shorter ID, with SOC and 10–20% burn fraction intervals being reached earlier in all cases. Under the 40 Nm load (Figure 4.7A), ULSD catches up and overtakes RME; under the 80 Nm load (Figure 4.7B), ULSD catches up, overtakes, but then slows down and falls behind again. While at the injection timings between -8 ATDC and -4 ATDC it can be seen that ULSD combustion catches up with RME combustion only briefly under the 80 Nm load, at highly advanced and highly retarded timings the period for which ULSD remains ahead seems to be maximised, to some extent correlating with the reduced relative NO_x emissions from RME that were recorded at these positions, as can be seen in Figures 4.1B and 4.4B.

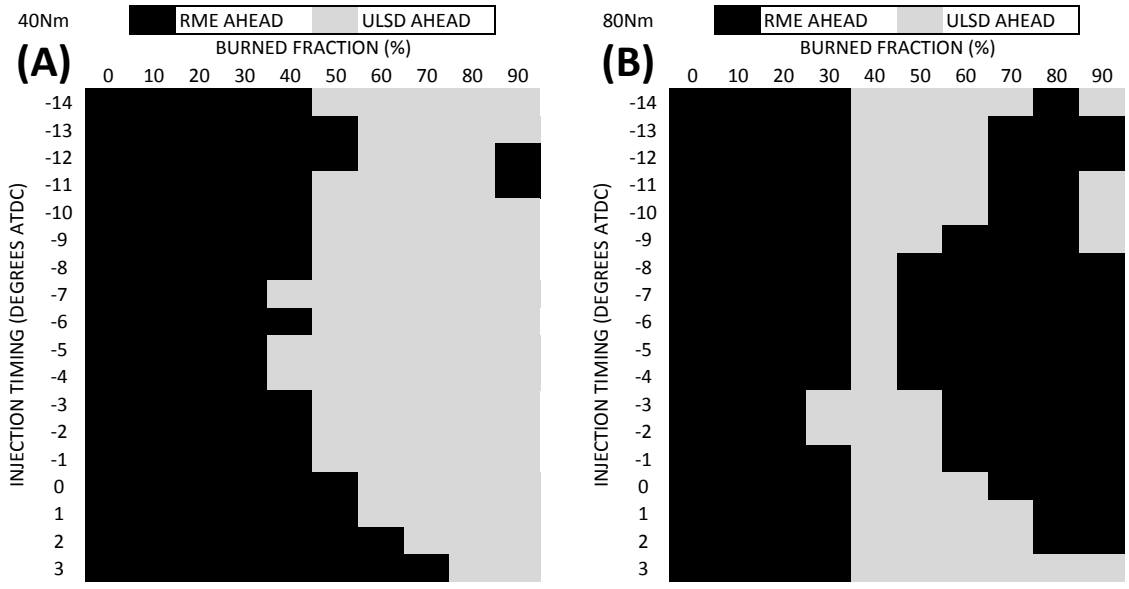

Figure 4.7: Relative combustion progress of ULSD and RME over partial combustion intervals under (A) 40 Nm and (B) 80 Nm loads across injection timings from -14 to 3 ATDC.

At injection conditions from 11–12 BTDC at 40 Nm, and 9–11 BTDC and 14 BTDC at 80 Nm, it appears that behaviour contrary to the wider trends that have been described occurs during the final (80–90%) interval. This is unexpected, but without any good reason to regard the data as erroneous, it can only be suggested that this inconsistency found at some advanced injection timings may come about as a result of late-burn oscillatory

fluctuations in heat release data – like those visible in Figures 4.2C and 4.2D – which can induce variation into the calculation of later burn intervals.

An important difference between the combustion behaviour of the two fuels seems to be related to the gradient profile of the curves in Figure 4.6, which can be thought of as the average fractional burn (or fractional heat release) rate; this data is plotted for the SOI timing of -8 ATDC in Figure 4.8. Since these plots are essentially derived from the AHRR data presented in Figures 4.2C and 4.2D there is a clear similarity in form. As seen in Figure 4.8B, under the 80 Nm load ULSD appears to be faster through the 10–40% burn intervals and slower through 40–70%, which, given the extended duration of the later burn fractions, gives RME adequate time to compensate for its slower early burn rate. From Figure 4.8A the ULSD burn rate under the 40 Nm load can be seen to be significantly higher between the 10% to 70% burn intervals, without the RME having any period of similar advantage during which to 'catch up.'

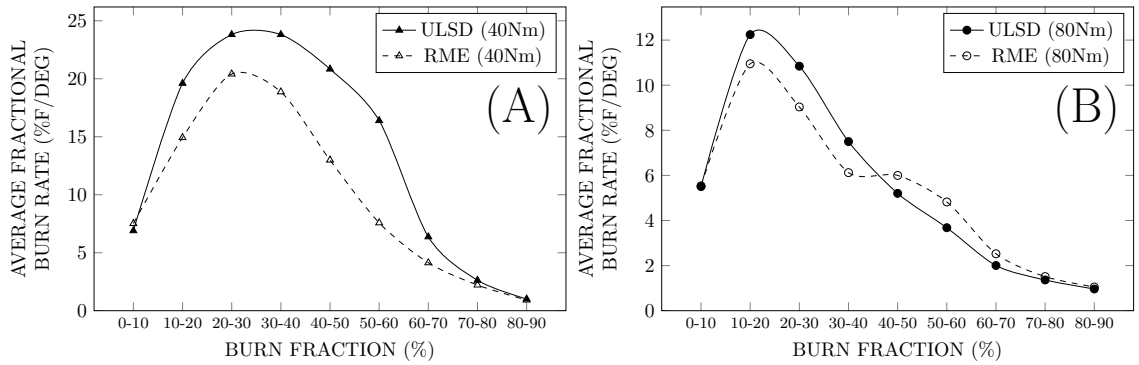

Figure 4.8: Average percentage of total fraction burned per degree over partial combustion intervals for ULSD and RME under (A) 40 Nm and (B) 80 Nm loads at -8 ATDC injection timing.

Largely, it appears that the difference in heat release rates and combustion durations may be correlated with the relative size of the PMBF that each fuel forms under any particular operational condition. At low load, where no fast mixing-controlled burn phase occurs (referring to a period subsequent to the culmination of the premixed burn wherein an obvious increase in AHRR occurs), the fuel with the largest PMBF (i.e. ULSD) invariably combusts more quickly. At higher load, where a more significant diffusion burn phase presents itself, the secondary increase in heat release rate through this diffusion phase tends to cause a relative reduction in the total combustion duration (SOC to CA90) and partial combustion duration (diffusion phase) of the fuel with a smaller PMBF (i.e. RME). Elsewhere [14], it has been suggested that the diffusion burn rate of biodiesel might be higher than that of petrodiesel, which is a tempting and plausible hypothesis. Under the conditions studied here – where the duration of the diffusion burn phase was always

limited – it seemed that both fuels followed broadly similar fractional burn rate patterns when PMBF was approximately the same. That is, the RME diffusion burn rate didn't necessarily appear to be any higher, per se, but because RME always had a smaller PMBF (due largely to its shorter ID) and underwent a relatively pronounced diffusion burn phase – while ULSD transitioned more directly between premixed and slow 'late combustion' phases – post-premixed combustion of RME did occur more quickly. However, the correct controls were not in place to allow a direct comparison between the diffusion burning rates of the two fuels, absent of differences in PMBF and combustion phasing, and hence it is not possible to draw any definitive conclusions about burn rate one way or the other. *[In Chapter 5 the experiments were designed so that a more direct comparison could be made, and the results indicated that AHRR was indeed higher for biodiesel during the diffusion phase of combustion when fuelling on biodiesel, for a given PMBF.]*

As has previously been touched upon with regard to ID, the difference between the efficacy with which the two fuels vaporise and entrain air is likely to be larger at low load, due to the cooler in-cylinder conditions and their effect upon the properties of the fuels. It is therefore possible that differences in fuel atomization, vaporisation and the stoichiometry of the resulting mixture also contribute to the variations observed in heat release rates. Less complete evaporation and poorer distribution of fuel prior to ignition could lead to more locally rich regions throughout the premixed charge, in which total oxidation is not possible. This would be likely to delay heat release, and reduce heat release rates through the premixed phase (as well as reducing flame temperatures, generating soot precursors and otherwise affecting exhaust emissions). Since RME evaporates less readily than ULSD, these locally rich regions may be relatively more prevalent when fuelling with RME under low temperature conditions, detracting from the equivalence ratio reducing effects of the fuel-bound oxygen content, and playing a part in reduced RME heat release rates under the 40 Nm load. Additionally, there may be important differences in the nature and effects of spray-wall impingement and liquid wall film formation.

Figure 4.9 shows how the appearance of the fractional burn rate plots varies with injection timing, allowing for consideration of how this variation may be related to the difference in NO_x emissions from the two fuels under an 80 Nm load. Examining burn rate Figures 4.9A (SOI at -14 ATDC) and 4.9B (-1 ATDC), allows for consideration of two conditions under which the differences in NO_x emissions (as a function of SOI) between ULSD and RME were similar; i.e. close to zero. In Figure 4.9A, the RME curve follows a

shape that closely resembles that of the ULSD curve, only lower, implying that if the two curves were brought into line then RME would be expected to have relatively higher NO_x emissions, all other things remaining the same. In part, this is because combustion begins sooner and therefore much of the heat being released is released slightly earlier.

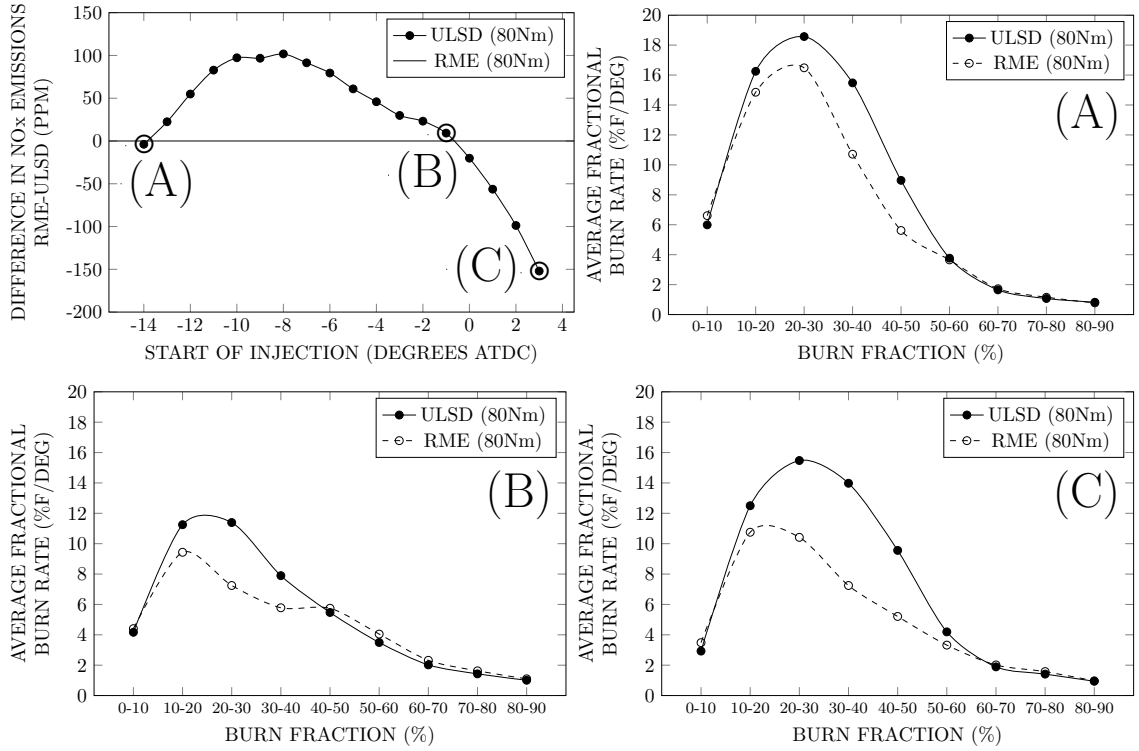

Figure 4.9: Difference in NO_x emissions between ULSD and RME as a function of injection timing under an 80 Nm load. (A–C) Average percentage of total fraction burned per degree over partial combustion intervals for ULSD and RME at injection timings of (A) -14 ATDC, (B) -1 ATDC and (C) 3 ATDC.

In Figure 4.9B, it can be seen that the peak burn rates for both fuels are considerably lower than in Figure 4.9A (on account of reduced PMBF), and that the RME peak is also smaller relative to the ULSD peak. A late increase in burn rate (beyond the 40% interval, as in Figure 4.8B) is visible on the RME plot, and, since the relative NO_x emissions are very similar (between the points illustrated in Figures 4.9A and 4.9B), it appears that this late increase might compensate for some of the reduction in peak burn rate. However, the ID difference between the fuels in Figure 4.9B is considerably larger than in Figure 4.9A, meaning that the effect of advanced SOC on NO_x emissions will be more significant in Figure 4.9B than in Figure 4.9A. That is to say, based on burn rate profile alone, relative RME NO_x emissions would be expected to be lower at B than at A, but that RME's more greatly advanced SOC at this point makes up for the difference. Reflecting back on Figure 4.8B (-8 ATDC), it can be seen that the RME peak burn rate is not relatively lower by such a great extent as in Figure 4.9B, and the late burn rate is more markedly increased.

Consider also that the ID difference at -8 ATDC is smaller than that at point B (see Figure 4.3B), indicating that the larger difference in NO_x emissions between ULSD and RME at -8 ATDC (Figure 4.8B) compared to -1 ATDC (Figure 4.9B) must be dependent upon additional factors associated with combustion behaviour beyond advanced SOC alone.

In Figure 4.9C (3 ATDC), the peak magnitudes for both fuels are higher than in Figure 4.9B, but lower than in Figure 4.9A. Here, it is apparent that the RME peak is relatively very much lower than that of ULSD (indicating a large difference in PMBF between the two fuels), without any late pickup in burn rate, which is a profile consistent with the relatively reduced NO_x emissions from RME at this point.

4.3.3 PREMIXED BURN FRACTION

Figure 4.10A shows PMBF as a function of ID, and Figure 4.10B shows NO_x emissions as a function of PMBF. From Figure 4.10A it can be seen that ID and PMBF correlate positively with a fair degree of linearity (r^2 values: ULSD (40 Nm), 0.88; RME (40 Nm), 0.93; ULSD (80 Nm), 0.92; and RME (80 Nm), 0.96) for each fuel, but that RME tends to generate a smaller PMBF for the same ID. It is anticipated that this is the result of the reduced energy density, poorer mixing properties and slower evaporation of biodiesel. (Note also that the -14 ATDC data point under a 40 Nm load – which had an apparent PMBF of 0.95 and can be seen in Figure 4.10B – has been omitted from Figure 4.10A, and from later PMBF plots; at this point combustion duration for ULSD was consistently too short to allow accurate calculation of PMBF.) *[Results presented in Chapter 5, although indicating a similar reduction in PMBF when fuelling on biodiesel for a given ID, also demonstrate that this reduction is dependent upon the way in which the end of the premixed burn is defined. Additionally, the literature discussed in Section 2.3.5 suggests that physical differences between petro- and biodiesel may not make a significant difference to initial premixing in a modern diesel engine.]*

In Figure 4.10B it can be seen that at all tested conditions PMBF was lower for RME than for ULSD. It is also clear that PMBF values are largest towards the highly advanced and highly retarded injection timing positions, and lowest towards the centre of the timing sweep; these trends are related to ID. Additionally, although at low load the trends for both fuels are generally consistent throughout, under the 80 Nm load there is a marked difference in the PMBF trend towards the most retarded injection timings. At these points, PMBF increases more dramatically for ULSD, leading to a large difference in combustion

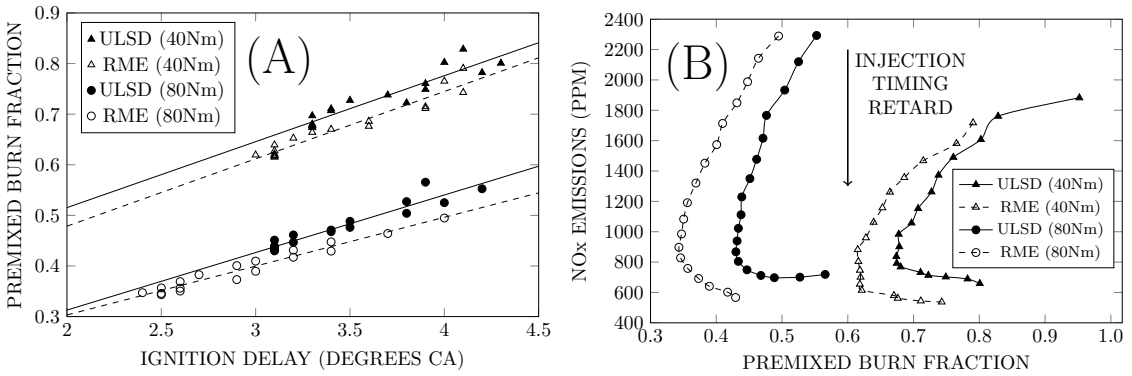

Figure 4.10: (A) Premixed burn fraction as a function of ignition delay and (B) NO_x emissions as a function of premixed burn fraction for ULSD and RME under 40 Nm and 80 Nm loads.

profiles between the fuels (as seen in Figure 4.9C) – a difference large enough to lead to a significant relative reduction in RME NO_x emissions.

The nature of the relationship between PMBF and NO_x emissions is not made clear by Figure 4.10B; the curves take on 'C' shapes due to the influence of SOC timing. Collecting data via injection sweeps has the advantage that it can be used to induce changes in combustion behaviour without making any modification to the properties of the fuels themselves, but it is an approach inevitably encumbered by the inclusion of effects related to changing SOC; predominantly, increased peak in-cylinder pressures and prolonged high-temperature residence times as injection timing is advanced. If, for the sake of simplicity, it is taken that NO_x emissions vary with injection timing due to only three main factors – peak pressure, residence times and combustion profile – then in order to observe the effects of any element alone, it is necessary to take steps to exclude the influence of the others.

This has been achieved here retroactively, by the following process:

1. Two injection timing conditions were identified at which the combustion profiles were similar for each fuel under each load (the same two conditions, -7 ATDC and -2 ATDC, were used for both fuels and under both loads. Quantification of the similarity – ID: maximum variation of ID between -7 ATDC and -2 ATDC of 0.1 CA [where the values were 2.5 CA and 2.6 CA], with a mode difference of 0 CA; PMBF: maximum condition-to-condition variation of 0.02 [between values of 0.35 and 0.37], with a mean difference of 0.015; peak AHRR: maximum condition-to-condition variation of 1.3 J/deg [45 J/deg and 46.3 J/deg], with a mean difference of 0.65 J/deg).

2. The simplistic assumption was then made that – given their similar combustion

profiles – all differences in NO_x emissions between these two points were due to an approximately linear variation in peak pressure and residence time caused by the change in SOC. On this crude basis, a general SOC related NO_x gradient was calculated at each load, by dividing the change in NO_x emissions between the two similar points by the change in SOC.

3. A compensation value was defined using this calculated gradient for every operational condition, as a function of SOC, and this value was subtracted from the measured NO_x emissions to calculate 'SOC compensated relative NO_x emissions.'

SOC compensated relative NO_x emissions derived by this means can be seen in Figure 4.11. There are regions in which these compensated emission values drop below zero which is obviously unrealistic in an absolute sense, but these values are only intended to possess relative validity. The utility of this approach can be seen by comparing Figure 4.10B with Figure 4.12, which shows compensated NO_x emissions as a function of PMBF.

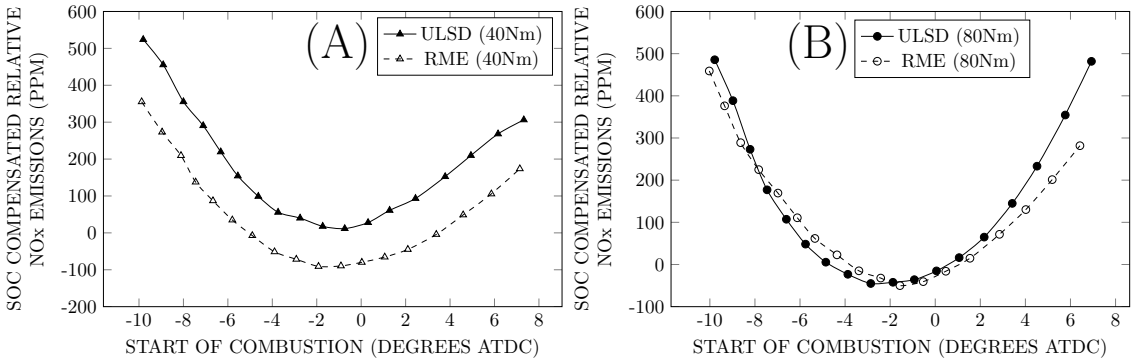

Figure 4.11: Start of combustion compensated relative NO_x emissions as a function of start of combustion timing for ULSD and RME under (A) 40 Nm and (B) 80 Nm loads.

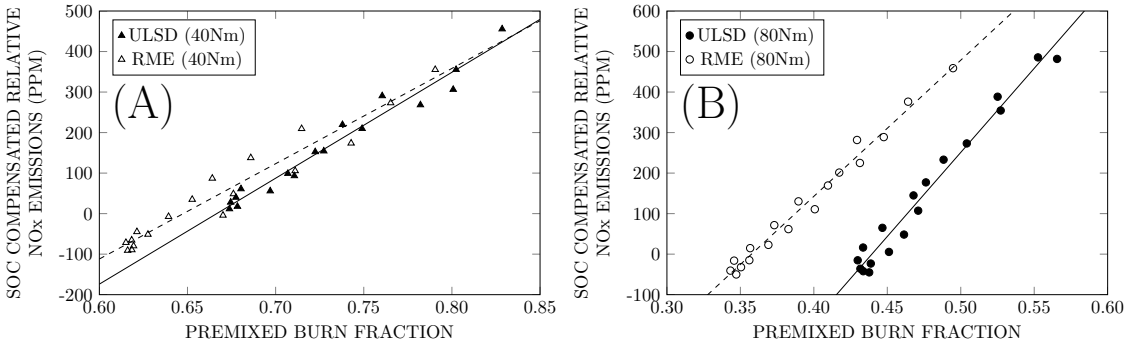

Figure 4.12: Start of combustion compensated relative NO_x emissions as a function of premixed burn fraction for ULSD and RME under (A) 40 Nm and (B) 80 Nm loads.

In Figure 4.12 a fair degree of correlation is apparent between PMBF and the compensated NO_x emissions values, particularly at the higher load (r^2 values: ULSD (40 Nm),

0.97; RME (40 Nm), 0.94; ULSD (80 Nm), 0.98; and RME (80 Nm), 0.97). From these approximately linear relationships it can be seen that SOC compensated relative NO_x emissions increase with increasing PMBF. Under an 80 Nm load (Figure 4.12B) RME clearly generates higher NO_x emissions for the same PMBF, while under a 40 Nm load (Figure 4.12A) the tendency appears to be similar but is less clear-cut. Interestingly it appears that, as PMBF increases, the gap between NO_x emissions from the two fuels narrows. Towards PMBF values of around 0.8, the NO_x gap is nullified completely (based upon extensions of the calculated linear fits). Bearing in mind that RME always had a reduced PMBF, it can be proposed that, beyond the primary effect of advanced SOC when fuelling with biodiesel, the difference in NO_x emissions between the two fuels will be influenced by:

X. The difference between the PMBF of the two fuels.

Y. The size of the NO_x/PMBF correlation gap between the two fuels in the operational PMBF range.

Under all conditions except for those yielding extremely high PMBFs, X and Y will tend to offset each other; a large X and/or a small Y would reduce relative RME NO_x emissions, a small X and/or a large Y would increase relative RME NO_x emissions. X is determined directly from the PMBF of the two fuels. Y is conceptualised as a function of PMBF, being large when PMBF is low and becoming smaller as PMBF increases. Figure 4.13 clarifies this conceptual explanation graphically, with regard to hypothetical NO_x/PMBF relationships for the two fuels extrapolated on the basis of the trends observed in Figure 4.12. *[This hypothesis is examined at length in Chapter 5, and although it has some validity, Figure 4.13 presents an oversimplified explanation.]*

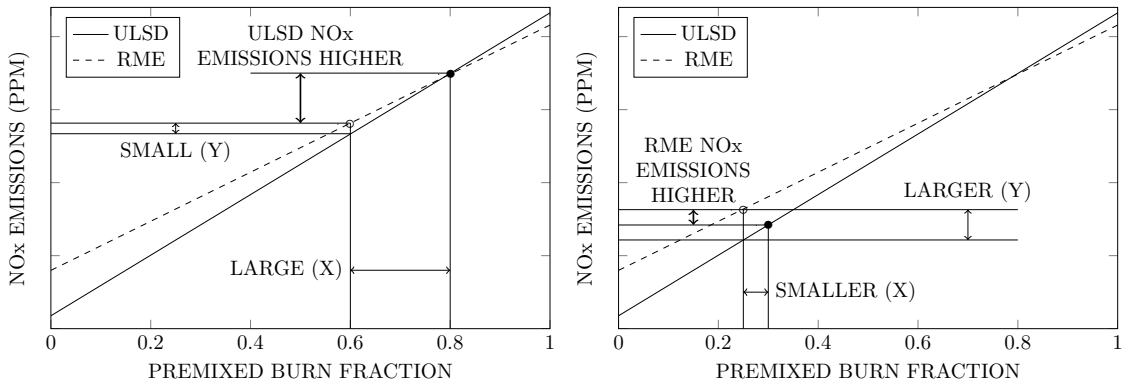

Figure 4.13: Conceptual illustration of the relationship between the premixed burn fraction of the two fuels and the relative NO_x emissions anticipated.

The reason for the correlation gap observed here, and the way that it reduces with increasing PMBF, may be related in part to soot radiative heat losses. It has been reported that as the relative proportion of diffusion burning increases, soot emissions also increase [267, 395, 638]. This being understood, and assuming at least some degree of correlation between soot emissions and in-cylinder soot, it is possible to conceive of the following hypothesis:

- For a large PMBF, in-cylinder soot quantities might be low when fuelling with both ULSD and RME, meaning comparable radiative heat losses, and the tendency to generate lesser differences in NO_x emissions for similar combustion behaviour.
- For a reduced PMBF, in-cylinder soot quantities would be expected to be higher for ULSD than RME, leading to increased heat losses and lower NO_x emissions when fuelling with ULSD.

Although the data collected in this study does not bolster the hypothesis that the diffusion burn rate itself is higher when fuelling with biodiesel, if such were the case – as has been suggested [14, 546] – then that would provide an alternative (or complimentary) explanation for the correlation gap that has been described. That is, as the PMBF becomes smaller, the diffusion burn phase becomes larger, the biodiesel combustion duration would be further reduced relative to that of petrodiesel and therefore heat released earlier due to the increasing prominence of this accelerated diffusion phase; hence, relative biodiesel NO_x emissions would be expected to increase with declining PMBF. Additional factors bearing possible responsibility for the correlation gap may include changes in operational temperatures that alter rates of fuel evaporation and local mixture stoichiometry, changes in combustion chemistry, radical concentrations, flame temperatures and heat transfer. PMBF appears to exert influence over, or be correlated with, the extent to which other inherent differences between petro- and biodiesel are able to affect relative NO_x emissions levels, although the nature of any correlation lines that might be calculated will certainly vary from engine to engine, and depend upon the specific fuels that are utilised.

4.4 CONCLUSIONS

1. The NO_x emissions from RME were lower than those from ULSD under a 40 Nm load, but at an increased load of 80 Nm they were higher at the majority of injection timing conditions.

2. Under all measured conditions, ULSD had a longer ID and a larger PMBF than RME. Additionally, for the same ID ULSD generated a larger PMBF than RME, indicative of the reduced energy density, inferior mixing behaviour and slower evaporation associated with RME.

3. The immediate effect of reduced ID is that SOC is advanced; when NO_x emissions were considered as a function of SOC timing rather than SOI timing, the disparity between NO_x emissions tendencies for the two fuels under an 80 Nm load was considerably reduced, suggesting that advanced SOC was responsible for a significant proportion of the increase in NO_x emissions when fuelling with RME.

4. Under most operational conditions the fuel that combusted most quickly, releasing heat earliest, was the fuel that generated the highest NO_x emissions.

   (a) The rate at which combustion progressed appeared to be related to the size of the PMBF.

   (b) At low load, the PMBF for both fuels was so large that no fast mixing-controlled diffusion burn phase occurred. Under these conditions, ULSD combusted most quickly overall because it had a larger PMBF.

   (c) At increased load, the PMBF for RME was often low enough that a significant fast diffusion burn phase did occur, compensating for the larger, faster PMBF of ULSD. Under these conditions, RME combusted most quickly overall.

5. When the effects of changes in SOC were compensated for, NO_x emissions appeared to correlate fairly linearly (positively) with PMBF at each load.

   (a) Correlations were different for each fuel: RME tended to generate higher NO_x emissions than ULSD for the same PMBF.

   (b) Correlations were different at each load: the magnitude of the difference between RME and ULSD NO_x emissions for the same PMBF was larger under an 80 Nm load than under a 40 Nm load.

   (c) As PMBF increased, the calculated difference between RME and ULSD NO_x emissions for a given PMBF became smaller.

   (d) Some of the differences in correlation may plausibly be related to soot radiative heat transfer, local mixture stoichiometry, and to any extant differences in diffusion burn rate.

6. In-cylinder pressure and heat release data provides useful practical feedback on engine behaviour, and a valuable means for inferring information about in-cylinder phenomena. However, a complete understanding of the petrodiesel/biodiesel NO_x difference will ultimately require more fundamental knowledge of the physical and chemical processes that govern the manner in which these fuels vaporise and combust.

Chapter 5

EFFECTS OF BIODIESEL, OXYGENATES AND DEGREE OF PREMIXING ON EMISSIONS FROM AN HSDI DIESEL ENGINE

The following section documents experimental work performed with the assistance of N.S.I. Alozie. Fuel compositions were analysed with the assistance of Dr. M. Lawrence and Dr. O.A. de la Garza de León (of the Universidad Autónoma de Nuevo León, Mexico).

5.1 INTRODUCTION

In Chapter 4 it was observed that emissions of oxides of nitrogen (NO_x), and the size of the petrodiesel-biodiesel NO_x difference, varied with alterations in engine load and injection timing. As is well understood and ordinarily expected, NO_x emissions from both fuels (in *absolute* terms – i.e. considered in terms of concentration in the exhaust gases (ppm) rather than in *output specific* (g/kWh) or *fuel specific* (g/kg_{fuel}) terms) tended to decline with the retardation of injection timing and the reduction of engine load. When changes in start of combustion (SOC) timing were compensated for, biodiesel typically had higher NO_x emissions than petrodiesel for a given premixed burn fraction (PMBF). However, the relative increase in NO_x emissions when fuelling on biodiesel was not consistent, but rather appeared to vary with degree of premixing; under conditions where the PMBF was large (i.e. lower load and highly advanced/retarded injection timings) NO_x emissions from biodiesel were relatively low, whereas under less highly premixed conditions (i.e. higher load, and more conventional injection timing conditions) NO_x emissions from biodiesel were relatively high. It was proposed that the ostensible relationship between the degree of premixing and the resulting difference in NO_x emissions from petro- and biodiesel may be related to differences in radiative heat transfer, diffusion burn speeds and local

equivalence ratios encountered when operating on the two fuels.

The purposes of the experimental work documented in this chapter were as follows:

- To test the conclusions of the previous study under a wider range of operating conditions, and with controls in place to allow direct investigation of the variables of interest. Specifically, to assess the following criteria:
  - The causality of the relationship between premixing and NO_x emissions; whether these factors are directly connected, or instead linked by their co-relation to another variable.
  - The linearity of the relationship between premixing and NO_x emissions.
  - The generalisability of these relationships.
  - The possible convergence of the NO_x emissions from petro- and biodiesel with increasing degree of premixing.
- To compare biodiesels derived from different feedstocks, in a manner that (as far as is possible) excludes differences in timing in order to more clearly observe differences in emissions related to the properties of the fuels themselves, without the inclusion of effects attributable to, and manageable via, engine controls. This requires:
  - Removal of the effect of variations in start of combustion (SOC) timing, to be achieved by synchronising this point across all test fuels.
  - A means of accounting for differences in the degree of premixing, to be achieved by extending the experimental range of mixing conditions using an ignition promoter, in order to quantify the relationship between NO_x emissions and PMBF and provide a general gradient with which results can be compared.
- To observe the effect of petrodiesel oxygenation, comparing emissions and combustion characteristics with those of the baseline petrodiesel and various biodiesels; further, isolating those effects directly due to fuel-bound oxygen content.

5.2 EXPERIMENTAL METHODOLOGY

5.2.1 EQUIPMENT

The equipment employed for the experiments documented in this chapter is described in more detail in Chapter 3. The engine used was the laboratory Ford Duratorq 2 litre, 4

cylinder HSDI diesel engine with common-rail injection system (see Section 3.1.1). In-cylinder pressure data were collected via a Kistler Piezostar 6125A transducer (described in Section 3.1.3), emissions data were collected using a Horiba MEXA 7170 DEGR exhaust gas analyser (Section 3.2.1), and smoke numbers were measured with an AVL 415 smoke meter (Section 3.2.2).

The experimental setup varied only slightly from that used in Chapter 4; a higher resolution 2880 ppr crank encoder replaced the 360 ppr encoder used in the previous experiments (see Section 3.1.4), to give pressure data resolution of 0.125 CA, and a more thorough fuel filtration system (described in Section 3.1.6.2) was also installed in the intervening period.

5.2.2 PROCEDURE

This set of experiments consisted of three separate, but connected, studies – details of which are provided in Table 5.1.

EXPERIMENT	ENGINE LOAD AND SPEED	INJECTION PRESSURE(S)	START OF COMBUSTION	NEAT FUELS [DENOTATION]	ADDITIVES [WEIGHTING (%)]
STUDY 1: HIGHER LOAD	80 Nm (5 bar BMEP) 2000 rpm	800 bar	3.25 BTDC	Petrodiesel [PETRODIESEL]	2-EHN [1%, 2%] TPGME [15%, 30%]
				Rapeseed methyl esters [BIODIESEL]	2-EHN [0.5%, 1%, 2%]
				Rapeseed methyl esters [RME2]	
				Used cooking oil methyl esters [UCOME]	
				Sunflower methyl esters [SME]	
				Fish oil ethyl esters [FEE]	
STUDY 2: VARYING INJECTION PRESSURE	80 Nm (5 bar BMEP) 2000 rpm	800 bar 1000 bar 1200 bar	3.25 BTDC	Petrodiesel [PETRODIESEL]	
				Rapeseed methyl esters [BIODIESEL]	
STUDY 3: LOWER LOAD	40 Nm (2.5 bar BMEP) 2000 rpm	800 bar	2.875 BTDC	Petrodiesel [PETRODIESEL]	2-EHN [0.5%, 2%] TPGME [30%]
				Rapeseed methyl esters [BIODIESEL]	2-EHN [0.5%, 2%] 1-MN [5.3%]
				Sunflower methyl esters [SME]	

Table 5.1: Outline of the three component studies, including details of the operating conditions and the fuels and additives used.

Study 1 was undertaken at a higher load, 80 Nm, equating to a brake mean effective pressure (BMEP) of 5 bar, and an engine speed of 2000 rpm. While the load is the same as the higher load case in Chapter 4, the speed was increased slightly (from 1800 rpm). The purpose of the increase in speed, and the purpose of using this operating condition for the larger part of the fuel comparison work in these experiments, was to reduce ignition delay and thus restrict mixing time, and to extend the injection event, in order to achieve combustion that was less highly premixed and therefore provided a more accurate reflection of conventional diesel combustion. If one considers the lower load apparent heat release plots later in this chapter, those in Chapter 4, or those in the work of other researchers who

have used the same engine [462, 591, 639–645], it can be seen that the quantity of mixing-controlled heat release is rather small compared to that which characterises the familiar diesel heat release pattern seen in standard texts (e.g. [379, 418]). Since the results of the previous chapter suggest that the diffusion combustion phase may play an important role in the biodiesel NO_x increase, results collected under highly premixed conditions may not provide insight which can be reliably extended to real-world diesel engine operation, or may at least have reduced direct relevance.

In Study 1 injection pressure was held constant, at 800 bar, and start of combustion (SOC) was also fixed, at 3.25 BTDC. The SOC timing was based on the PETRODIESEL baseline measurement with start of injection (SOI) at 7 BTDC, and all subsequent higher load experiments were matched to this. A baseline SOI of 7 BTDC was selected, like the engine load and speed, to restrict mixing time and reduce premixing. The reader will note that, although Studies 1 and 2 had SOC fixed at 3.25 BTDC, in Study 3 it was held at 2.875 BTDC; this was the SOC of the lower load PETRODIESEL baseline at an SOI of 7 BTDC.

Various studies (e.g. [529, 568, 646–648]) have controlled combustion phasing in order to gain greater insight into the effects of biodiesels and other oxygenated fuels on diesel engine performance and emissions. In Chapter 4 it was seen that the effects of changing SOC timing obscured other differences between the fuels, requiring variations in SOC to be compensated for mathematically. This kind of post hoc adjustment is undesirable, so being able to negate differences in SOC experimentally is advantageous, and necessary to validate the findings of Chapter 4.

Study 1 employed the widest range of fuels: all of the neat biodiesels, PETRODIESEL blended with 15% and 30% tripropylene glycol methyl ether (TPGME), and both PETRODIESEL and BIODIESEL doped with 2-ethylhexyl nitrate (2-EHN) at weightings of 1% and 2%. These relatively high 2-EHN weightings were employed in order to elicit a wide range of premixing under a single operating condition, and to achieve heat release profiles closely resembling those reported in standard texts (aforementioned), with greater emphasis on the diffusion phase of combustion. The BIODIESEL, BIODIESEL+1% 2-EHN and BIODIESEL+2% 2-EHN points did not give sufficient distribution in terms of premixing, and so a third weighting of 0.5% 2-EHN was also necessary. The purpose of the 2-EHN addition was to systematically reduce ignition delay, and hence PMBF, so that the effect of premixing on NO_x emissions could be observed over a range wide enough for the re-

lationship to be reliably described and quantified. The purpose of TPGME addition to PETRODIESEL was to assess the effect of fuel-bound oxygen content on combustion and emissions.

For the sake of clarity, it should be explained that although BIODIESEL and RME2 were both rapeseed methyl esters, the two were produced at different facilities, and acquired separately (and as Section 5.2.3.1 will show, there was also some difference in composition). The reason for referring to one of the biodiesels by the BIODIESEL denominator, and the other 4 biodiesels by their respective acronyms was to distinguish the fuel which was used throughout all of the experiments, and served as the base for all additive preparations – BIODIESEL – from the other fuels which were available in smaller quantities and only ever used in their neat forms – RME2, SME, UCOME and FEE. When the capitalised form (i.e. PETRODIESEL or BIODIESEL) is used, the reference is to a specific fuel, but when the uncapitalised form (petrodiesel or biodiesel) is used, it is the class of fuel which is being referred to.

In Study 2 only PETRODIESEL and BIODIESEL were used, with the intention being to modify degree of premixing via air entrainment rate rather than changes to fuel composition and combustion chemistry. While the addition of 2-EHN in Study 1 allowed for reductions in premixing to be induced, increasing injection pressure is a known means of increasing the degree of premixing. Higher injection pressures are likely to affect aspects of combustion beyond premixing, and so Study 2 offers a broader scope on the question of the generalisability of relationships between NO_x, PMBF, and fuel type.

Study 3, once again, utilised 2-EHN addition to extend the PMBF range of PETRODIESEL and BIODIESEL, and the oxygenated additive TPGME to increase the fuel-bound oxygen content of PETRODIESEL to a level comparable to that of BIODIESEL. Because the conclusions drawn in Chapter 4 suggested that the reduction in NO_x at lower load when fuelling on biodiesel is due to its reduced ignition delay and hence PMBF, the biodiesel with the longest ignition delay, SME, was also tested at lower load. The aromatic additive, 1-methylnaphthalene (1-MN) was employed to extend the ignition delay of BIODIESEL, and to see if increasing the sooting tendency of the fuel would have a noticeable effect on lower load performance.

In order to mitigate problems associated with transience, both inter- and intra-daily (discussed in Section 3.4), a strict schedule was drawn up and adhered to throughout the experimental period. This can be seen in Figure 5.1.

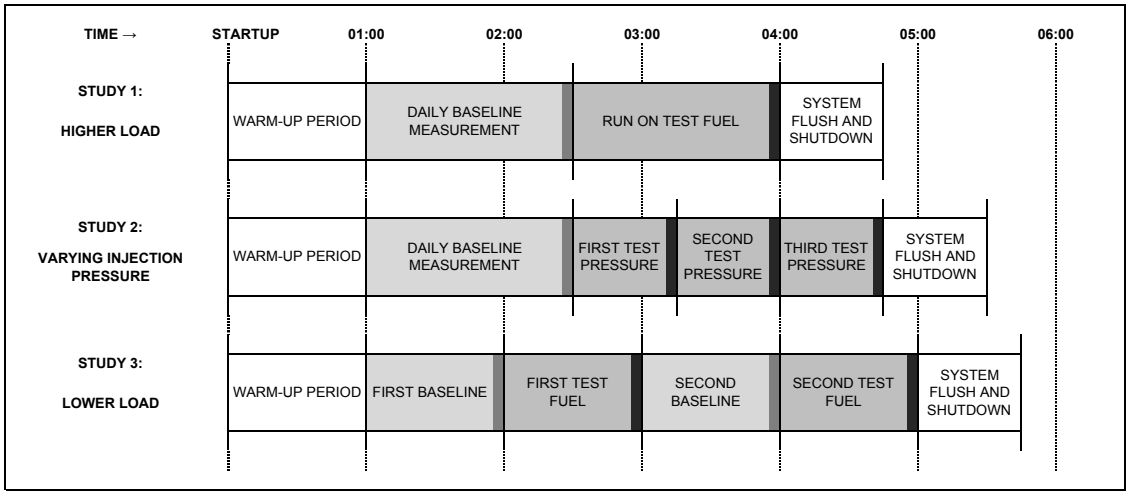

Figure 5.1: Schedule of daily operating procedure.

In all cases, the engine was allowed to warm-up for 60 minutes after being started. This period included a short interval at idling load and low speed, followed by a gradual increase in load to the experimental point, and then a similarly gradual increase in speed. The warm-up period was undertaken with heaters in the engine bay, and the cell extraction system turned off. This measure meant that cell and engine temperatures rose more rapidly through the daily warm-up, which reduced the change in temperature across the remainder of daily operation. After the warm-up, the extraction system was turned on, and an engine fan was used to increase heat transfer from the engine and improve the consistency of operation throughout the day.

In Studies 1 and 2, the baseline condition was maintained and monitored for a 90 minute period each day, while at the lower load, in Study 3, two 60 minute baselines were taken – one before the first test fuel, and the other before the second. In the higher load studies (Studies 1 and 2) the baseline was at 80 Nm, 2000 rpm, with the start of injection at 7 BTDC and injection pressure at 800 bar, running on the laboratory PETRODIESEL supply; in Study 3, all variables were the same except the load, which was at 40 Nm.

The daily baseline measurement was useful for several reasons. First, it gave the engine time to settle to an approximate steady-state; second, collecting data through this period ensured that any unusual behaviour of either the engine or any of the measurement devices wouldn't go unnoticed, and the extent of day-to-day variations could be quantified and considered in the analysis; third, where day-to-day variations were large enough to obscure trends in the data, the baseline provided a reliable datum for normalisation. Although pressure and emissions data were monitored and recorded every 10 minutes for the duration of the baseline window, the reported measurements were always made in

the final 10 minutes of the window, and done so in triplicate; in Figure 5.1 the reported measurement periods are shaded in a darker hue.

In Study 1 the test fuel was run for 90 minutes and, as with the baseline, all parameters were monitored and recorded throughout, but reported data was always collected in the final 10 minutes (again, in triplicate). The 90 minute duration, first, ensured that the engine had adequate time to settle on each test fuel, and also provided sufficient opportunity to adjust injection timing to obtain the necessary start of combustion. In-cylinder pressure data were continuously updated and re-analysed, to ensure that the desired SOC was maintained. All test fuels were repeated to establish consistency, except for FEE, which was not available in sufficient quantities.

In Study 2, all 3 injection pressures were tested on each day, in an effort to reduce the engine running time requirement, and to avoid introducing day-to-day variations. To minimise the problems with changing engine temperature, which the less intensive Study 1 schedule had avoided by testing each fuel on separate days an equal time after engine startup, Study 2 ran both fuels through an ascending injection pressure test day, and a descending injection pressure test day. That is, on the first occasion the fuels were tested at 800 bar, then 1000 bar, then 1200 bar, and on the second they were tested at 1200 bar, then 1000 bar, then 800 bar. It was intended that this approach would help to average out any influence of the differing experimental timing. The test runs were each 45 minutes in duration, because without any requirement to change fuels between test pressures, operational adjustments were more immediate.

In Study 3, the baseline and test runs were 60 minutes in duration, and the first test fuel was separated from the second by an additional baseline. At lower load the engine stabilises more rapidly, and so intra-daily transience does not seem to be such a significant issue (inter-daily variations also tended to be a little lower than at the higher load, as will be seen in Section 5.2.4.4). The second baseline, which was included in order to monitor variation in performance and emissions throughout the day, revealed that after the initial warm-up period subsequent changes were small.

After the tests were completed, the engine was switched to the laboratory petrodiesel supply and in all cases run at the higher load for 20–30 minutes, before being brought down to idling load and low speed before shutdown. Following this, when fuelling on biodiesel the auxiliary fuel system was dissembled and cleaned.

5.2.3 FUELS

5.2.3.1 BIODIESELS

Five different biodiesels were employed for this series of experiments; the feedstocks from which they were derived were detailed in the previous section, in Table 5.1. As already discussed, BIODIESEL and RME2 are both methyl esters of rapeseed oil, but come from different sources. BIODIESEL was produced on a large scale by Shell, whereas RME2 was produced on a smaller scale by Work this Way Oil Works at HMP Standford Hill [649], using a commercial cooking oil (purchased from KTC Edibles). SME and UCOME were also produced by Work this Way, the SME from a commercial sunflower oil (again, from KTC Edibles) and the UCOME from waste cooking oil generated by both HMP Standford Hill itself, and local businesses. The FEE was provided by ReFuel Energy [650], and was derived from a waste fish oil (understood to be largely anchovy) which had been harvested of the majority of its omega-3 content for pharmaceutical use. As such, the FEE is without the sizeable proportions of eicosapentanoic acid (C20:5, or EPA) and docosahexanoic acid (C22:6, DHA) typically found in oily fish like anchovy.

A breakdown of the composition of the fuels is given in Table 5.2. Values are quoted to the nearest 0.5%, and species present in concentrations of less than 1% are not quoted.

METHYL ESTERS

RETENTION TIME (min)		15.342±0.01	17.665±0.027	18.004±0.051	20.283±0.047	20.618±0.067	21.237±0.062	22.105±0.033	23.361±0.044	
FUEL	**FEEDSTOCK**	**C14:0**	**C16:0**	**C16:1**	**C18:0**	**C18:1**	**C18:2**	**C18:3**	**C20:1**	**C22:1**
BIODIESEL	RAPESEED OIL		4.5		2	**64.5**	18.5	9.5	1	
RME2	RAPESEED OIL		4.5		1.5	**60.5**	21	11	1.5	
SME	SUNFLOWER OIL		6.5		3.5	27	**62.5**			
UCOME	USED COOKING OIL		10.5		3.5	**48**	32.5	4.5	1	

ETHYL ESTERS

RETENTION TIME (min)		15.759±0.017	18.142±0.027	18.448±0.025	20.694±0.037	20.972±0.028	21.584±0.02			26.496±0.03
FUEL	**FEEDSTOCK**	**C14:0**	**C16:0**	**C16:1**	**C18:0**	**C18:1**	**C18:2**	**C18:3**	**C20:1**	**C22:1**
FEE	FISH OIL	13.5	**30.5**	14.5	3.5	14	1.5			6

Table 5.2: Results of fuel analysis by gas chromatography (with values as percentages and major species emphasised).

The major chemical components of the biodiesels used in this study were characterised by means of gas chromatography (GC). Chromatography is defined [218] as *"a physical method of separation in which the components to be separated are distributed between two phases, one of which is stationary (stationary phase) while the other (the mobile phase) moves in a definite direction."* In gas chromatography the mobile phase is gaseous, and the sample components are distinguished from one another on the basis of their relative vapour pressures and affinities for the stationary phase [651]. As the column is heated, the

compounds are transferred from the stationary phase to the carrier gas (the mobile phase) and ultimately eluted, in order of descending vapour pressure and ascending solubility in the stationary bed (i.e. lower boiling point, less readily soluble components pass first). Upon leaving the column, the gas passes through a detector to quantify (and in some cases identify – by mass spectrometry, for instance) the eluted species. For a given experimental method, a species will have a characteristic retention time, defined as the time taken to pass through the system, from the injector to the detector, and once characteristic retention times have been ascertained it is possible to analyse the chemical composition of a sample.

Analyses were performed on an Agilent 6890N Gas Chromatograph, with an HP-INNOWax column (19091N-133), having a polyethylene glycol stationary phase [652, 653]. The method used was based upon that recommended by BS EN 14103:2011 [654], with minor alterations. Fuel samples were prepared into a 1:10 fuel:hexanol solution, and 1 μl was injected at a temperature of 300 °C, pressure of 11 psi and split ratio of 50:1. The carrier gas used was hydrogen, at a flow rate of 1.9 ml/min and pressure of 11 psi. As per the cited standard, the oven temperature was initially held at 60 °C for 2 minutes, then raised at a rate of 10 °C/min until reaching 200 °C, then at 5 °C/min up to 240 °C. This was followed by a 6 minute hold, a 20 °C/min rise to 260 °C and a further 4 minute hold, in an effort to ensure complete removal of all injected material from the column. The temperature profile is depicted in Figure 5.2. The system used a flame ionisation detector (FID) to quantify eluted species.

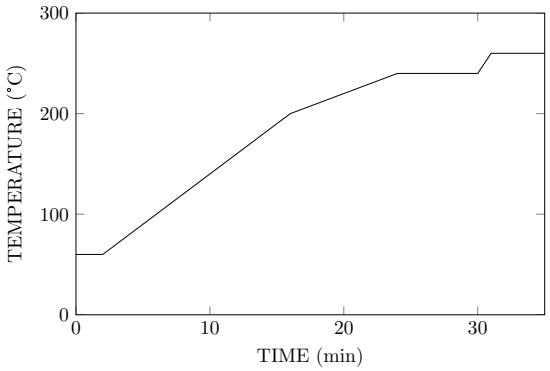

Figure 5.2: Gas chromatograph oven temperature profile.

In lieu of analytical standards, chemical compounds were identified by comparison with the available literature (primarily [103, 131]). This approach is adequate to obtain a fair approximation of fuel composition, but lacks the rigour necessary to be considered an accurately performed analysis. In the case of the vegetable derived biodiesels, with relatively uncomplicated compositions, identification by this method was straightforward,

and provided retention time data for fuel components which reliably informed subsequent analysis. The greater complexity of the fish oil ethyl esters (FEE) meant that certain smaller peaks could not be confidently named; fortunately, the bulk of the fuel did not present a problem.

BIODIESEL, RME2 and UCOME are fully accounted for. SME contained a <1% component likely to be methyl palmitoleate (C16:1), which isn't included in the table. FEE contained 16.5% uncertainly identified species that are not listed above; most unidentified peaks (accounting for around 11% of the total composition) lay between the C16:1 and C18:0 peaks, some probably indicative of more highly unsaturated C16 ethyl esters.

Some estimated properties of the fuels are given in Table 5.3. In all cases these estimates are based upon the fatty acid composition, with double bond number calculated as described in [233], viscosity, cetane number and density as described in [655], and adiabatic flame temperatures calculated (for reactants beginning at the standard state, using the method in [206]) from enthalpy estimations by the Benson-Groups method given in [210]. (Note that the estimated adiabatic flame temperatures are significantly higher than those illustrated in Figure 2.57. This is due to differences in the method of calculation; the trends remain the same.) Energy density values were calculated on the basis of the density and heating value data presented in Section 2.1.4.

Overall values for each biodiesel were calculated by weighted averaging of pure methyl or ethyl ester values. For some properties this approach may be adequate, but in others it is unlikely to give quantitatively reliable results; property estimations are intended only to provide insight into the general differences likely to exist between the tested fuels. For FEE, values are given as ranges, intended to encapsulate the possible properties of the unidentified portions.

FUEL	AVERAGE MAIN CHAIN LENGTH	DOUBLE BOND NUMBER	DENSITY (kg/m^3 @ 20°C)	VISCOSITY (mm^2/s @ 40°C)	CETANE NUMBER	ADIABATIC FLAME TEMPERATURE (°K @ 298.15°K, 10kPa)	ENERGY DENSITY (MJ/kg @ 40°C)
BIODIESEL	17.93	131	878	4.3	55	2430	34.4
RME2	17.94	137	879	4.3	54	2430	34.4
SME	17.86	152.5	881	4.1	50	2435	34.4
UCOME	17.81	127.5	878	4.3	55	2430	34.5
FEE	16.5–16.75	70–100	870–875	2–4.5	57–63	2420–2425	33.9–34
PETRODIESEL	14–15[a]	—	820–845[b]	4.1–4.3	53 (51+)[c]	—	37

Table 5.3: Biodiesel property estimations from their respective fatty acid compositions, provided alongside properties for a typical petrodiesel. Notes: a) These values are indicative of a typical average petrodiesel carbon number, rather than straight chain length. b) This density range is taken from BS EN 590 [16], specified at a temperature of 15 °C; at 20 °C density will be lower by about 4 kg/m^3. c) The minimum cetane number specified in BS EN 590 [16] is 51, but based on the ignition delay data collected in this study a value of 53 was estimated for PETRODIESEL.

Viscosity, cetane number and density calculations used empirical fits determined for

methyl esters [655], so in order to extend the estimation method to ethyl esters (in the case of FEE) it was appropriate to take into account the effect of the alcohol moiety. Viscosity and density were changed on the basis of measurements made in [177, 178], but the estimation of cetane number was left unaltered.

Ethyl esters are slightly more viscous than methyl esters, in general an increase of around 5% appears representative [177, 178]. Ethyl esters are very slightly less dense than methyl esters (for example, ethyl oleate is 0.4% less dense than methyl oleate at 20 °C), and the difference between the two gets smaller with increasing chain length [177, 178]. There is not a clear consensus on how the replacement of a methyl ester with an equivalent ethyl ester affects ignition delay in practical diesel engines [656], although faster ignition of ethyl esters has been observed experimentally [212]. Cetane numbers generally differ relatively little between the two, and not consistently [657]; it may be that the difference between methyl and ethyl esters becomes increasingly insignificant as the length of the main alkyl chain increases [366], and long-chain alkyl esters like those in biodiesel require a more substantial extension of the alcohol moiety (e.g. propyl or butyl esters) before changes in cetane number become readily apparent [658]. Comments on the adiabatic flame temperatures of methyl/ethyl esters suggest that any differences are very small or non-existent [154, 656]; calculations here suggest, for example, that ethyl oleate has an adiabatic flame temperature at standard state conditions which is around 0.1% lower than that of methyl oleate.

From Table 5.3 it can be seen that there is very little difference in average chain length between the vegetable oil derived biodiesels; as Table 5.2 shows, all are derived from feedstocks containing mostly C_{18} fatty acids, and hence have average main chain lengths close to 18, reduced slightly by their varying proportions of C16:0 esters. FEE, of which C16:0 is the largest single constituent, along with a significant quantity of C14:0, has a slightly shorter average chain length, although this is offset to some extent by the remaining longer chain components (in particular, that proportion taken – somewhat speculatively – as being C22:1). Since the unidentified compounds in FEE are largely thought to be derived from C_{16}–C_{18} fatty acids, the possible range of average chain length is small. Of course, because FEE is an ethyl rather than a methyl ester, its carbon number and molecular weight remain similar to those of the other fuels, with the extra length of the alcohol moiety compensating for the relative shortness of the main chain. As Table 5.3 suggests, biodiesels typically contain higher molecular weight compounds than petrodiesel.

The double bond number (DN) is significantly higher for SME than the other fuels, since it has the largest proportion of polyunsaturated methyl linoleate (C18:2). RME2 has a slightly higher DN than BIODIESEL, related to its marginally higher proportions of methyl linoleate and linolenate (C18:3); this may be a result of small differences between the two rapeseed feedstocks, but could also be a reflection of the relative freshness of the fuel (see Section 3.1.6.1). UCOME has a DN slightly lower than these three, but still close to that of BIODIESEL, despite having a relatively large proportion of C18:2. This is due largely to the higher proportion of methyl palmitate (C16:0) in UCOME. FEE has a substantially lower DN than the other fuels, being comprised of almost 50% saturated compounds. However, it is likely to be some of the more highly unsaturated species that have not been identified. The lower limit of the posited range assumes that all unidentified species have 2 double bonds, the upper limit 4. In either case, the DN of FEE is far lower than those of the other biodiesels.

Density is very similar between the four vegetable biodiesels, but slightly lower for FEE. Density decreases with increasing chain length and increases with increasing degree of unsaturation [177, 178]. Primarily, the reason for the lower estimated density of FEE is its lower degree of unsaturation, and once again the range given represents less unsaturated species at the lower limit, and more highly unsaturated at the upper. Additionally, as mentioned already, there is a slight reduction in density due to the fact that it is an ethyl ester. Overall, the small differences in density between the biodiesels are likely to be largely insignificant, aside from possible effects on volumetric fuel consumption. In all cases the density of the biodiesels is significantly higher than that of the petrodiesel.

SME was estimated to have a lower viscosity than the other fuels, on account of its high C18:2 percentage. Viscosity is dependent upon both chain length and degree of saturation, increasing with both. Since chain length is similar between the methyl esters, degree of saturation is the main variable. In the case of FEE, the chain length is shorter, tending to reduce the viscosity, but it is an ethyl ester, tending to increase the viscosity. Although it is highly saturated, the possible presence of highly unsaturated compounds means that, depending on precisely what those compounds are, it could have a viscosity anywhere within the range of the methyl esters – in likelihood, somewhere towards the lower end. All of the biodiesels are likely to have viscosity values towards the upper end of the acceptable range for petrodiesel.

Like viscosity, because the average chain length of the methyl esters is similar, the

main determinant of their respective cetane numbers is degree of saturation; the more highly saturated, the higher the cetane number. As a result, SME has a significantly lower predicted cetane number than the other fuels. FEE, being more highly saturated, had a higher predicted cetane number, despite the slightly shorter length of the main chain (cetane number is positively correlated with chain length [657]); the lower limit of the FEE range represents the most unsaturated possible unknown compounds, the upper limit the least unsaturated. The cetane number of PETRODIESEL is estimated to be below that of all of the biodiesels except for SME.

In terms of adiabatic flame temperature, there is very little difference between the fuels. SME has a slightly higher predicted flame temperature, because it contains a higher percentage of polyunsaturated species. Initially, flame temperature increases with chain length for saturated esters, and falls for unsaturated ones [558], but for esters with chain lengths exceeding about 15 carbons, the main factor influencing flame temperature is degree of unsaturation. Once more, FEE lies at the opposite extreme to SME, being the most saturated, and therefore having the lowest predicted adiabatic flame temperature. As mentioned, the fact that it is an ethyl ester leads to a very minor reduction in adiabatic flame temperature. There is very little to choose between either of the rapeseed derived biodiesels or the UCOME. The difference in adiabatic flame temperature between petro- and biodiesel is unclear, as discussed in greater depth in Section 2.3.7.

It should be apparent that the main factor differentiating the predicted properties of these fuels is the degree of unsaturation. In practice, other aspects, like degree of oxidation, trace constituents, etc., may make a considerable difference, albeit one that has not been quantified in the current study.

5.2.3.2 2-ETHYLHEXYL NITRATE (2-EHN)

2-Ethylhexyl nitrate (2-EHN), also called iso-octyl nitrate, is an ignition improver used to increase the cetane number and therefore reduce the ignition delay of a fuel. Its chemical structure is shown in Figure 5.3A. The 2-EHN used in this work was purchased from Sigma Aldrich (product number 293784).

The additive is reported to fully decompose at temperatures below those at which the low temperature chemistry of typical diesel fuel components become active; in experiments performed at a pressure of 12.5 atm, 2-EHN was entirely consumed beneath 550 K [659]. This decomposition leads to a small amount of heat release and an increase in the size of

the radical pool, advancing the kinetic processes that eventually lead to ignition [230].

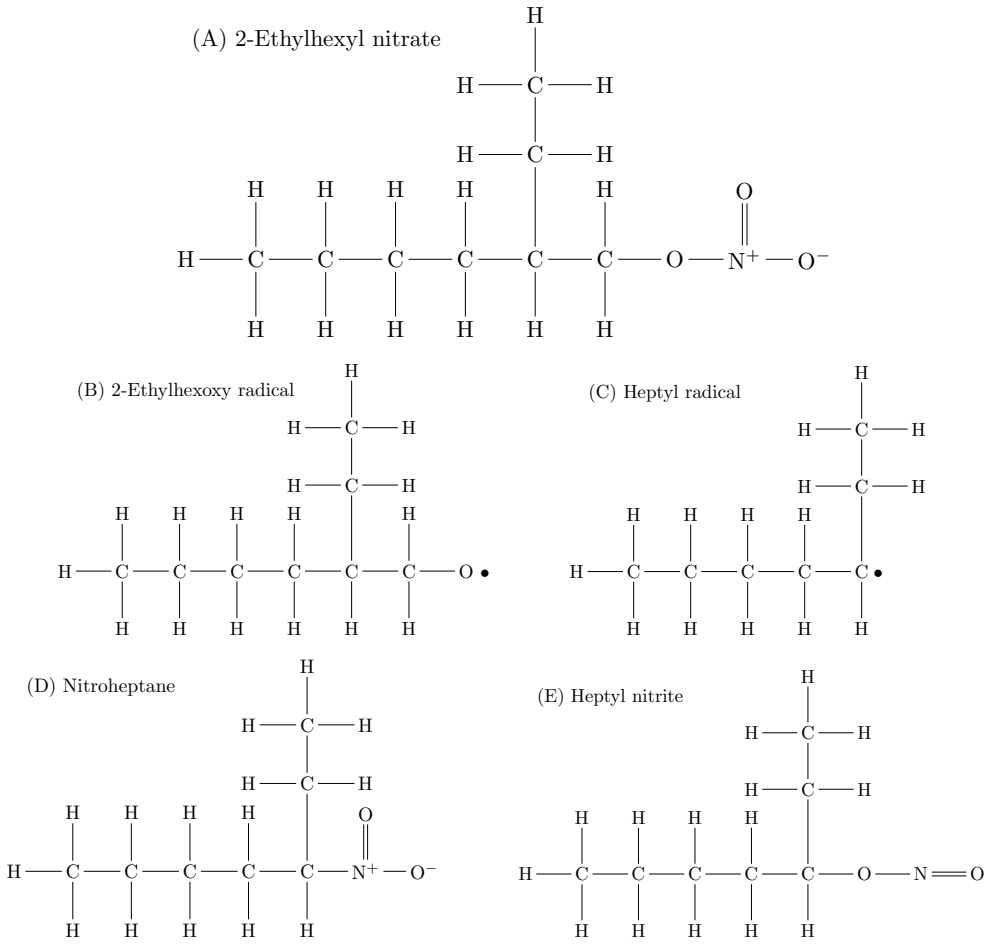

Figure 5.3: Chemical structure of 2-ethylhexyl nitrate and the products of its thermal decomposition.

The first decomposition step is cission of an O-N bond to form a 2-ethylhexoxy radical, like that depicted in Figure 5.3B, and NO_2 [211, 660, 661]. The 2-ethylhexoxy radical undergoes beta-cission, to form formaldehyde (CH_2O) and a heptyl radical, as depicted in Figure 5.3C, with which NO_2 can react to form either nitroheptane, shown in Figure 5.3D, or heptyl nitrite, as shown in Figure 5.3E [659]. In fuel rich regions, CH_2O and nitroheptane are the predominant initial products of 2-EHN decomposition. Nitrites are less stable and decompose to form a heptoxy radical and nitric oxide (NO). At slightly higher temperatures (600–650 K) nitroheptane decomposes, further increasing the concentrations of CH_2O and NO_2 [659, 662].

NO_2 can provide a means for the generation of alkoxy (OH) radicals, by hydrogen abstraction from an available hydrocarbon (abstraction from CH_2O may be important [663], since the aldehydic C-H bond is relatively weak) to form HNO_2, followed by dissociation resulting in NO and OH [211, 664].

The estimated cetane numbers of the fuel blends containing 2-EHN can be seen in Table 5.4. The cetane numbers of the parent fuels were approximated on the basis of fatty acid composition, in the case of BIODIESEL, and by comparison with experimental ignition delay data, in the case of PETRODIESEL. The effect of 2-EHN addition on cetane number is generally understood to be non-linear; this non-linearity was estimated on the basis of the trends reported by Liotta [665]. As a result, PETRODIESEL+2% 2-EHN has an estimated CN 5 points higher than that of PETRODIESEL+1% 2-EHN, whereas PETRODIESEL+1% 2-EHN has a CN around 15 points higher than PETRODIESEL. The blends of 2-EHN with BIODIESEL have slightly higher CN values than those with PETRODIESEL, owing to the higher ignition quality of the parent fuel.

FUEL	CETANE NUMBER
PETRODIESEL+0.5% 2-EHN	62
PETRODIESEL+1% 2-EHN	68
PETRODIESEL+2% 2-EHN	73

FUEL	CETANE NUMBER
BIODIESEL+0.5% 2-EHN	63
BIODIESEL+1% 2-EHN	69
BIODIESEL+2% 2-EHN	75

Table 5.4: Estimated cetane numbers of fuel blends containing 2-ethylhexyl nitrate (2-EHN).

5.2.3.3 TRIPROPYLENE GLYCOL METHYL ETHER (TPGME)

Tripropylene glycol methyl ether, or TPMGE, is a solvent commonly used in inks, as well as in a range of cleaning fluids, coatings and penetrating oils [666]. It is also an effective oxygenated blending component for diesel fuels [667, 668]. The TPGME used in this work was purchased as a mixture of isomers, from Sigma Aldrich (product number 484245). There are 8 isomers of TPGME; each of the three ether linkages may be adjacent to primary or secondary carbon atoms (secondary is favoured) [666, 669]. The alpha isomer is depicted in Figure 5.4.

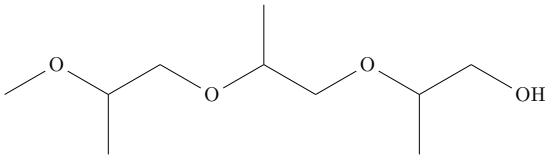

Figure 5.4: Chemical structure of the alpha isomer of tripropylene glycol methyl ether (TPGME).

Having the chemical formula $C_{10}H_{22}O_4$, TPGME contains approximately 31% oxygen by weight. Some estimated properties of the petrodiesel and TPGME blends used in this study are given in Table 5.5.

The lower heating value of TPGME is significantly lower than that of petrodiesel, at 27.15 MJ/kg (based on data at [670]), but TPGME is considerably more dense (968 kg/m^3

FUEL	OXYGEN CONTENT (m/m %)	CETANE NUMBER	ENERGY DENSITY (MJ/kg @ 40°C)
PETRODIESEL+15% TPGME	4.65	56	35.6
PETRODIESEL+30% TPGME	9.3	58	34.3

Table 5.5: Estimated properties of fuel blends containing tripropylene glycol methyl ether (TPGME).

at 20 °C [667]). Consequently, although the heating value of the fuel blend is reduced by increasing addition of TPGME, the reduction is partially offset by the increasing density of the fuel, and as a result PETRODIESEL+30% TPGME has an energy density similar to the biodiesels (compare Table 5.5 with Table 5.3).

The CN values for TPGME provided in the 2014 update of the *Compendium of Experimental Cetane Numbers* [155] vary from 63 to 81.3, and average approximately 70. Despite the lack of consistency, they unanimously suggest that the addition of TPGME will increase the cetane number of a typical petrodiesel. There is also some suggestion in the literature that the addition of TPGME might be expected to reduce adiabatic flame temperature [525, 671].

5.2.3.4 1-METHYLNAPHTHALENE (1-MN)

1-Methylnaphthalene (1-MN) is a polycyclic aromatic, whose chemical structure can be seen in Figure 5.5. Originally used as the cetane number zero reference, it is a low ignition quality fuel, with a relatively high sooting tendency. The 1-MN was amongst remaining stock from past experiments at Brunel, available in only a limited quantity. It was added to BIODIESEL at 5.3% (m/m), because this was the greatest degree of admixture which would permit repeat experimentation at the lower load.

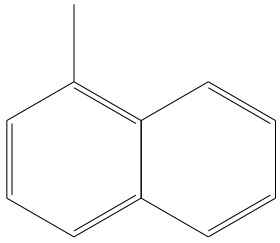

Figure 5.5: Chemical structure of 1-methylnaphthalene (1-MN).

Since it was only blended with BIODIESEL at a relatively low weighting, the effects that 1-MN addition had on the bulk properties of the fuel are expected to be small. Most significantly, the CN of BIODIESEL+5.3% 1-MN is estimated at 52, compared to 55 for BIODIESEL. The density, heating value and adiabatic flame temperature of BIODIESEL

are likely to be slightly increased by the addition of 1-MN, while the viscosity may be a little lower.

5.2.4 DATA ANALYSIS

5.2.4.1 IN-CYLINDER PRESSURE

In-cylinder pressure was collected and analysed as described in Section 3.3.2. Maximum pressure (P_{max}) and angle of maximum pressure (Θ_{Pmax}) values were computed on a cycle-by-cycle basis, so that the averages given are typically representative of around 600 measurements, and are provided with standard deviation estimates which meaningfully describe the distribution of the data. Pressure data was averaged across each 100 cycle data file, and filtered using a 9-point moving average, before being used to calculate apparent heat release rate (AHRR) values across the combustion period.

In Chapter 4, AHRR was analysed as an average over each 100 cycle data set. In the following work, all data for each test fuel were compiled into a single average apparent heat release (AHR) set, and analysed as a unit. Although start of combustion, ignition delay, end of combustion, and all of the percentiles of heat release readily permit automated algorithmic computation, accurate mathematical determination of the end of the premixed burn (EOPMB) was problematic. As a consequence, the EOPMB had to be identified manually, as will be described in the following section. This is the reason that all AHR data for each test fuel were considered as a single lumped set – it is impractical to manually process hundreds of sets of data, and lumping provided a means for reducing the quantity of data to process by over 80%. As such, all heat release parameters are given without error bars, except for the maximum apparent heat release rate, and angle of maximum apparent heat release, which were determined cycle-by-cycle, like P_{max} and Θ_{Pmax}, and are therefore provided with standard deviation estimates.

5.2.4.2 DEFINITION OF THE PREMIXED BURN FRACTION

In the classical description of diesel combustion, the end of the premixed burn phase (EOPMB) is identified as the point at which the apparent heat release rate (AHRR) reaches a local minimum following the maximum of the familiar diesel premixed burn spike; this can be seen in Figure 5.6 [672]. Hence, the premixed burn fraction (PMBF) is the value calculated by dividing the integral of the premixed burn spike by the integral of the AHRR curve from the start of combustion to the end of combustion; that is, by

dividing premixed heat release by total heat release.

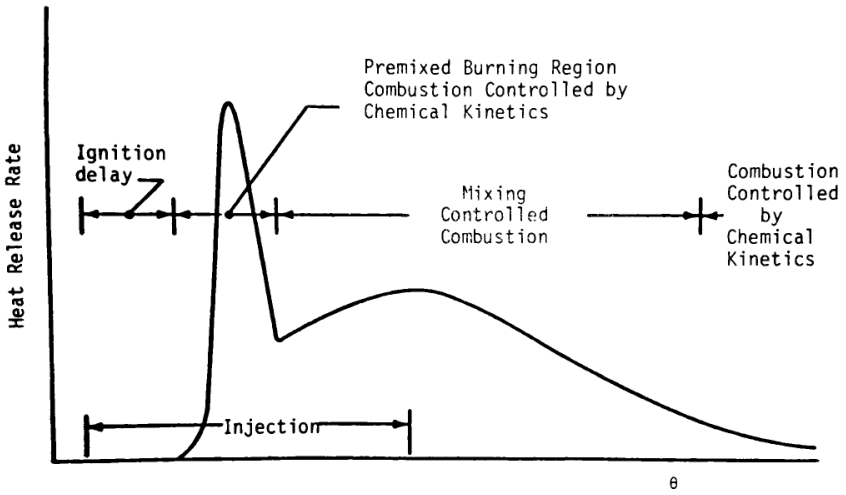

Figure 5.6: Schematic of the heat release rate in a direct-injection diesel engine [672].

However, according to the increasingly comprehensive conceptual models that have been proposed in the literature over the course of the last twenty years [379, 491, 493, 494, 519], purely premixed combustion actually concludes somewhat before even the point of maximum heat release rate, with an encompassing diffusion flame having established itself before maximum AHRR is reached. Therefore, it needs to be acknowledged and understood that the nominal premixed burn fraction does not necessarily correctly quantify the amount of fuel consumed in premixed reactions [494]. Indeed, not only is a substantial proportion of heat release through the premixed combustion phase actually generated by mixing-controlled combustion, but a significant proportion of heat release through the mixing-controlled combustion phase is generated by premixed combustion (that is, in the fuel-rich upstream premixed reaction zone) [490]. These aspects are discussed in greater depth in Section 2.2.6. Spatially, it may be possible to separate one phenomenon from the other, but there is no simple temporal demarcation between premixed and diffusive combustion processes; not, at any rate, one which can be easily discerned from heat release data. Although the relative importance of premixed and mixing-controlled combustion changes drastically throughout the cycle, for much of the combustion duration they occur simultaneously.

Despite this, there is still value in quantification of the so-called premixed burn fraction, since, although the area of the premixed burn spike does not strictly designate actual premixed combustion, its size does tend to correlate with the degree of premixing that takes place, and as a consequence with many other variables related to performance and emissions [517]. In many cases ignition delay would correspond equally well with the same

variables, since it is an explicit measure of pre-combustion mixing time, usually directly correlated with premixed burn fraction, and would therefore function as an adequate alternate means of quantifying the degree of premixing. However, the correlation between ignition delay and degree of premixing depends upon entrainment rates remaining constant and therefore breaks down, for example, when injection pressure changes and degree of premixing increases despite a reduction in ignition delay. For this reason, something akin to the classically defined premixed burn fraction has been used throughout this work as a generally applicable and pragmatic – though objectively inaccurate – estimation of the degree of premixing. It will be referred to frequently as the premixed burn fraction (PMBF) throughout this work, although perhaps *premixing supplemented combustion* or *mostly premixed combustion* [673] would be more strictly correct terms to apply.

In practice, the graphs of AHRR that can be derived from in-cylinder pressure do not replicate the smooth lines and clear transitions of Figure 5.6. Noise can be reduced by filtering, but although some degree of filtering is necessary and beneficial, it was deemed that by the minimum possible processing a less obscured picture of in-cylinder phenomena could be obtained. The location of a feature like the local minimum ordinarily assumed to signify the end of the premixed burn can be drastically altered by noise reduction, or by the frequency at which in-cylinder pressure is sampled. For this reason, in this study EOPMB, and most other heat release criteria, were calculated on the basis of unfiltered AHRR data (although AHRR itself was derived from filtered pressure data).

Figure 5.7 shows AHRR plots for PETRODIESEL (Figure 5.7A) and BIODIESEL (Figure 5.7B) both neat and doped with varying percentages of 2-EHN; in each case the data is presented at the experimental resolution of 8 points per degree, averaged over multiple (6 or more) 100 cycle data sets. The group of vertical lines labelled X represents the EOPMB defined on the basis of either the first local AHRR minimum following the peak, or a suitably located change in gradient. Vertical lines labelled Y are placed at a later point, where a lower minimum is reached; it is this point which has been taken as representing the EOPMB throughout this investigation.

In Figure 5.7A the EOPMBs, as given by Y, were defined as having been reached at 1.625 ATDC for PETRODIESEL, and 1.5 ATDC for PETRODIESEL+1% 2-EHN and PETRODIESEL+2% 2-EHN; these lie around 1.5 CA after their respective X points. The difference between X and Y in Figure 5.7B is similar, with both quantifiers suggesting that the PMBF ends slightly sooner with biodiesel. The reasons for using Y instead of X

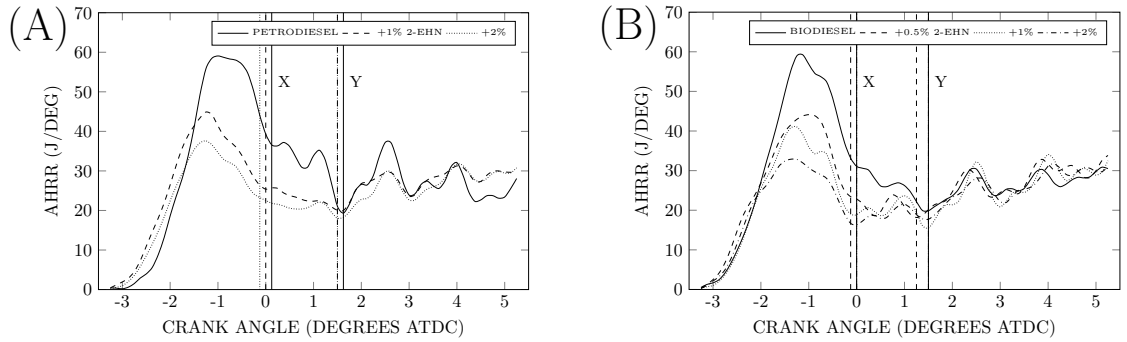

Figure 5.7: Apparent heat release rate at the higher load condition fuelling on (A) PETRODIESEL with 0, 1 and 2 % 2-EHN and (B) BIODIESEL with 0, 0.5, 1 and 2% 2-EHN.

throughout the body of this work are fourfold:

1. More highly premixed operating conditions generally have an AHRR advantage that persists beyond X. That is, in Figure 5.7 both plots show that the AHRR curves are distinctly higher between X and Y for the neat fuels, PETRODIESEL and BIODIESEL, than for those doped with 2-EHN. This suggests that combustion continues to be supplemented by some factor related to premixing; it is anticipated that this may be due to some portion of the premixed charge remaining incompletely combusted. Using Y instead aims to include all effects related to premixing.

2. In most cases the AHRR continues to decline following X. This ought not to be expected if X signalled the end of premixing supplemented combustion; rather, a general increase would be anticipated as the diffusion flame grows, except in highly premixed cases in which the stabilised diffusion phase is absent or small. Using Y instead divides heat release (except in the most highly premixed cases) such that AHRR rises and falls through the premixed phase, rises and falls through the diffusion phase, dying away into late combustion (more closely approximating the divisions of AHRR illustrated in Figure 5.6).

3. X positions are reached at widely varying magnitudes of AHRR. If AHRR at these points were not supplemented by some factor related to premixing then that would suggest some other reason for the difference in AHRR. None is apparent. At Y, all AHRR curves fall to around 20 J/deg, under both higher and lower load conditions (see Figure 5.8) and with all tested fuels. However, when varying injection pressure, it is observed that AHRR at Y increases with increasing injection pressure, as seen in Figure 5.9. This makes sense, because increasing injection pressure could be expected to affect diffusive as well as premixed combustion.

4. Using X leads to a disparity in total premixed apparent heat release as a function of mixing time between load conditions, which widens with increasing ignition delay. Using Y reduces this disparity. This can be seen in Figure 5.10, wherein total AHR up to X (Figure 5.10A) is compared with total AHR up to Y (Figure 5.10B), for all higher and lower load cases. It stands to reason that the quantity of heat released through the PMBF should be close to equal for a given ignition delay, at the two different operating conditions, assuming that the injection event remains the same up to the EOPMB. That is, although the injection event is shorter at lower load, there should not be a large difference in the absolute quantity of premixing able to occur through the ignition delay period. Consider Figure 5.10A, alongside Figures 5.7 and 5.8. Towards longer ignition delays there is a large increase in lower load total premixed heat release; this is a result of X being retarded further towards Y with increasing ignition delay in the lower load case. In general, Y seems to be a more stable point, giving more consistent results between conditions.

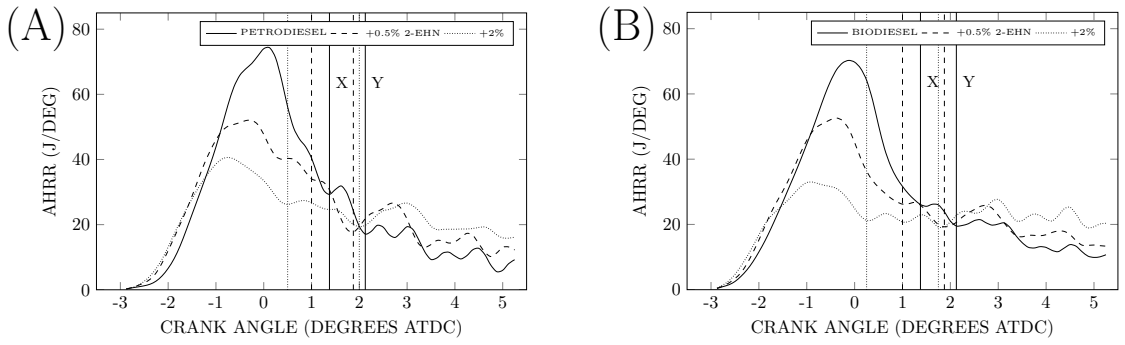

Figure 5.8: Apparent heat release rate at the lower load condition fuelling on (A) PETRODIESEL with 0, 0.5 and 2 % 2-EHN and (B) BIODIESEL with 0, 0.5 and 2% 2-EHN.

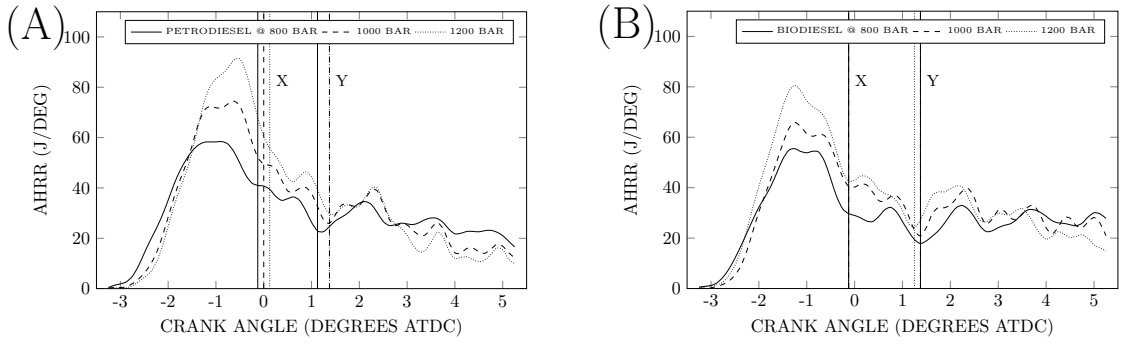

Figure 5.9: Apparent heat release rate at the higher load condition fuelling on (A) PETRODIESEL and (B) BIODIESEL at injection pressures of 800, 1000 and 1200 bar.

The seemingly greater mobility of X under the lower load is possibly a result of the minimisation of the role of stabilised diffusion combustion, and consequently the more

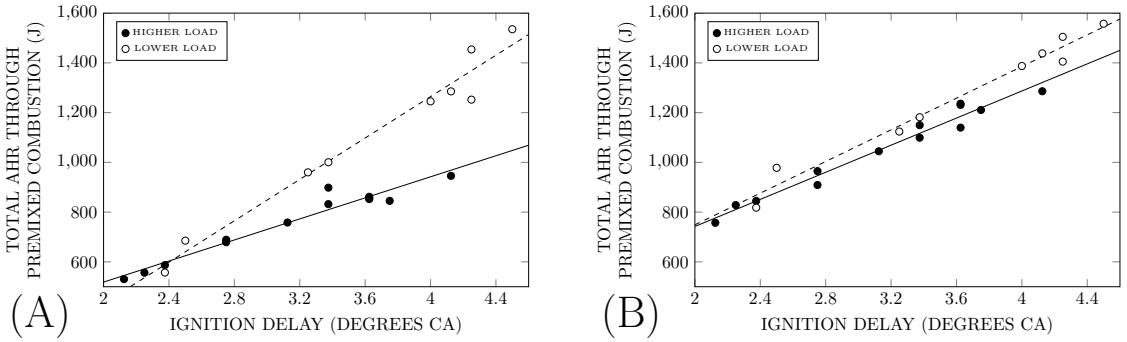

Figure 5.10: Total apparent premixed heat release as a function of ignition delay at higher and lower loads. In (A) the end of premixed combustion is defined at X, in (B) it is defined at Y.

even descent of AHRR following the AHRR maximum. This is particularly pronounced in the most highly premixed, longest ignition delay lower load cases. That is, because the transition between nominally premixed and diffusion combustion, as depicted in Figure 5.6, occurs where the decline in AHRR due to the decline in premixed heat release is exceeded by the increase in AHRR due to increasing diffusion heat release, a change in combustion characteristics which diminishes the role of the diffusion phase will tend to postpone X.

In Figure 5.9 (showing AHRR at varying injection pressures), and particularly in Figure 5.9B (that is, the biodiesel data), the larger PMBF cases have AHRR curves that remain above those of the lower PMBF cases more significantly beyond the designated EOPMB. This is considered to be a result of the higher injection pressures in the more highly premixed cases, which might be expected to cause faster heat release through the diffusion phase as well.

In closing this section, it is necessary to add that the method used herein is not being recommended as a general approach to PMBF calculation; it has been developed iteratively, in response to problems that have been encountered, and is expedient at best. Features of the heat release and pressure data analysed in this study are bound to the engine and sensors that have been employed, and the analysis techniques used are directed toward the identification of particular phenomena. In a different engine, or for a different study, considerations which were important here may be unimportant, and vice versa.

5.2.4.3 EMISSIONS

Emissions data files were recorded and analysed as described in Section 3.3.1, in order to provide average values for all gaseous emissions measured by the Horiba. Emissions data were recorded in triplicate on each test run, and each fuel (with the exception of FEE) was tested at least twice to ensure repeatability. The values presented in the text are averages

of all measurements made for each test fuel, and are provided with standard deviation bars which are intended to provide some indication of experimental consistency, rather than a statistically accurate representation of data distribution. Filter smoke numbers, measured using the AVL 415, were recorded in triplicate for each test run, averaged for each fuel and presented in the same way as the gaseous emissions.

5.2.4.4 VARIATION

As discussed in Section 5.2.2, each higher load (Study 1) data point was collected over the course of a day, to enable the engine to fully stabilise at a given operating point before measurements were taken. Varying injection pressure (Study 2) and lower load (Study 3) experiments saw reportable measurements made more frequently (3 and 2 data points per day, respectively), but still at a reasonably conservative rate, resulting in a prolonged experimental timescale. The Study 1, higher load, testing took place between 21 Oct 2013 and 22 Jan 2014, the Study 2, varying injection pressure, experiments ran from 13-20 Feb 2014, and the Study 3, lower load, data was collected between 4 Dec 2013 and 3 Feb 2014. Because of this, changes in environmental conditions over the period became significant, and the state of the engine cannot be expected to have remained entirely constant. The standard deviation of daily baseline emissions over the course of experiments is illustrated by Figure 5.11, with results from the higher load baseline in Figure 5.11A and the lower load baseline in Figure 5.11B.

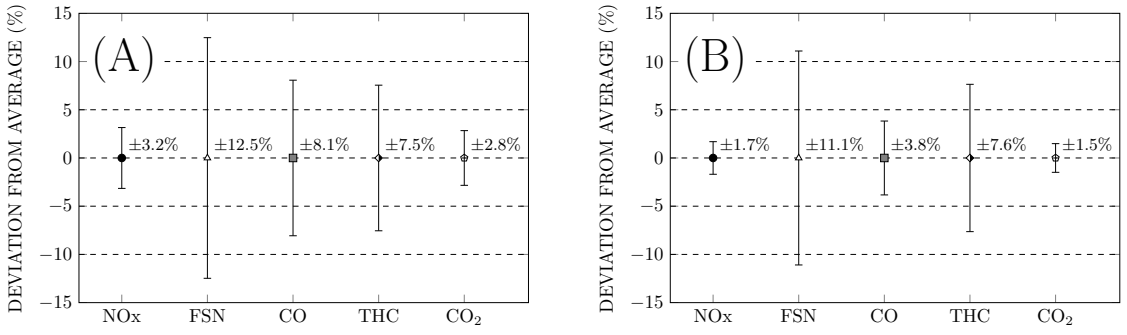

Figure 5.11: Standard deviations of emissions of oxides of nitrogen, carbon monoxide, total hydrocarbons and filter smoke number measured at the daily baseline under (A) the higher load, (B) the lower load. All deviations given as percentages of the average baseline values.

The variation in all emissions is significant, relative to the magnitude of the differences which may be expected to distinguish one fuel from another. NO_x and CO_2 are the most consistent pollutants, at both loads. As such, NO_x and CO_2 emissions data are presented without normalisation in all cases, while FSN, CO and THC all required normalisation

with respect to the daily baseline at the higher load in Study 1. Study 2, which was conducted over a shorter time period, was less problematic. In Study 3, the need for normalisation was also limited; despite the high variability in the lower load FSN baseline illustrated by Figure 5.11B, the repeatability for each test fuel was high.

Overall, the baseline variability adds a degree of uncertainty to the results, but does not appear to be substantial enough to irreparably obscure the trends of interest. With the experiments having been performed to a rigorous daily schedule, the baseline values collected meant that outliers and inconsistencies could be confidently identified and, where necessary, compensated for. The subject of experimental variability is discussed in more depth in Section 3.4.

5.3 RESULTS AND DISCUSSION

5.3.1 STUDY 1: HIGHER LOAD EXPERIMENTS

5.3.1.1 PREMIXING

The first experiment targeted the deliberate alteration of ignition delay and hence premixed burn fraction by the addition of 2-ethylhexyl nitrate (2-EHN) to the parent fuels, under conditions with a combustion regime reasonably representative of typical diesel operation. At first, PETRODIESEL and BIODIESEL were doped at 1 and 2% by mass with 2-EHN, but a further data point, BIODIESEL+0.5% 2-EHN, was deemed necessary due to the limited difference in ignition delay between BIODIESEL+1% 2-EHN and BIODIESEL+2% 2-EHN.

Increasing addition of 2-EHN reduced the ignition delay (ID) of the fuel, as illustrated by Figure 5.12. Note that ignition delays are given to the resolution of the encoder (i.e. to the nearest 0.125 CA); the average measured ID of BIODIESEL was actually 0.11 CA shorter than that of PETRODIESEL, despite the impression given by Figure 5.12 that the two fuels had the same ID. With BIODIESEL, there is strong evidence of diminishing returns, in the sense that the first addition of 2-EHN to the base fuel reduces ignition delay to a greater extent than equivalent subsequent addition. Similar trends have been reported elsewhere (albeit with respect to cetane number rather than ignition delay) [665, 674]. This effect appears to be considerably less pronounced when adding to PETRODIESEL. Particularly at lower concentrations the ignition delay of BIODIESEL was more strongly influenced by 2-EHN addition.

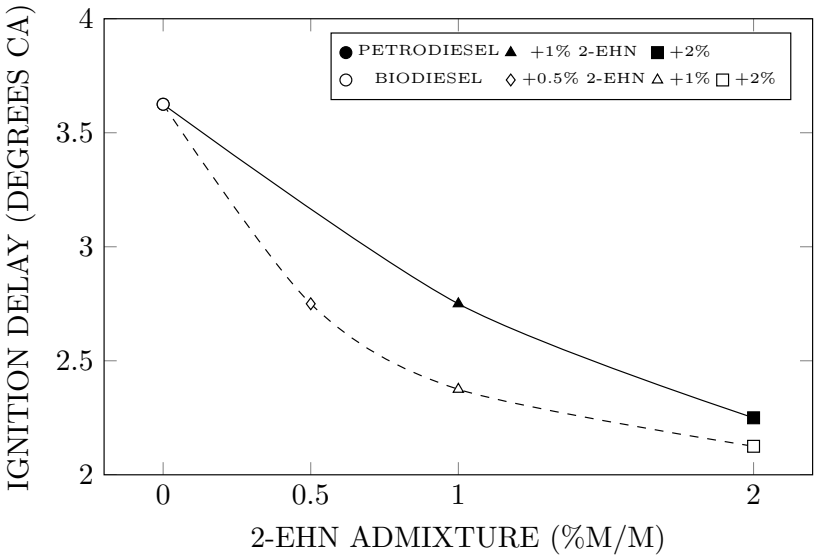

Figure 5.12: Effect of varying levels of 2-ethylhexyl nitrate addition on the ignition delay of PETRODIESEL and BIODIESEL under the higher load condition.

The reason for this difference between the effect of 2-EHN addition on the two fuels is not immediately clear, particularly since the same tendency is not apparent at the lower load (see Section 5.3.3). Liotta [665] added 2-EHN to two fuels, and in his results it also seems that the relationship between 2-EHN admixture and increase in cetane number is more obviously non-linear for the parent fuel with the higher CN.

However, the apparent difference between the fuels here may, instead, be partially due to the method of calculating ignition delay. In this study, ignition delay was calculated as the difference between commanded start of injection and SOC, and SOC was taken as being the point at which AHRR first exceeded zero following injection; this is one commonly employed approach amongst several [636, 675]. Others define SOC at the AHRR minimum that precedes the zero-AHRR point [14], or calculate ignition delay based on a location slightly after the start of combustion – e.g. 5% of peak AHRR [637] – or utilise a third order derivative of the pressure data [675]. Employing any of these other three techniques, non-linearity of approximately the same degree seems to be observed for both fuels (much as is seen at the lower load – see Section 5.3.3). This probably implies that the difference in non-linearity is not significant. Referring back to Figure 5.7A, it can be seen that although AHRR for PETRODIESEL becomes positive at 3.25 BTDC, it doesn't rise significantly until around 3 BTDC (this trend, namely a slow initial increase in AHRR when fuelling on petrodiesel, was also observed at the lower load in Study 3). One can imagine that if this period of inappreciable AHRR were added to the ID, the petrodiesel curve in Figure 5.12

would be significantly more non-linear, and would more closely resemble the biodiesel plot in form.

Across all of the tested fuels, Figure 5.13 shows that there is a fairly good correlation between the estimated cetane numbers and measured ignition delays ($r^2 = 0.91$). The most significant outlier is the PETRODIESEL+30% TPGME point. It appears that ignition delay is slightly increased by further addition of TPGME, although the additive is expected to have a relatively high cetane number (reported values are between 63–81.3 [155]). Because TPGME was provided as mixture of 8 isomers, it may be that the ignition quality varies depending on the balance of isomers. Alternatively, the literature studies may have used the major isomer of TPGME alone, rather than an isomeric mixture.

The 5 neat biodiesels follow approximately the anticipated trend, with the highly unsaturated SME having the lowest CN and longest ID, and the highly saturated FEE having the highest CN and shortest ID. However, the 3 intermediate biodiesels, although appropriately central between SME and FEE, are not entirely as expected; RME2 had a shorter ID than BIODIESEL, despite there being larger proportions of unsaturated species in the former, and its predicted CN therefore being marginally lower. It may be relevant that the GC results were collected in Aug/Sep 2013 (several months before engine tests were performed), after which time the composition of the fuels may have altered somewhat in storage. Because RME2 contained larger proportions of highly unsaturated compounds than BIODIESEL, it may have been more prone to becoming partially oxidised during storage, which can lead to an increase in cetane number and therefore a reduction in ignition delay [676].

The duration of the ignition delay controls the time available for fuel-air premixing. The relationship between ignition delay and premixed burn fraction is shown in Figure 5.14. Again, all values of ID are given to the resolution of the encoder, and none had standard deviations exceeding a single encoder increment, with the exception of UCOME (SD: 0.14 CA). Premixed burn fraction is given without error bars, here and throughout this work, because it has been calculated manually for the average case for each fuel (as explained in Section 5.2.4.2).

The reduction in ignition delay is naturally accompanied by a reduction in the premixed burn fraction, because less mixing time is available. As was seen in Chapter 4, petrodiesel appears to form a slightly larger PMBF than biodiesel for the same ID. However, this trend depends upon the point at which the end of the premixed burn is defined. As will

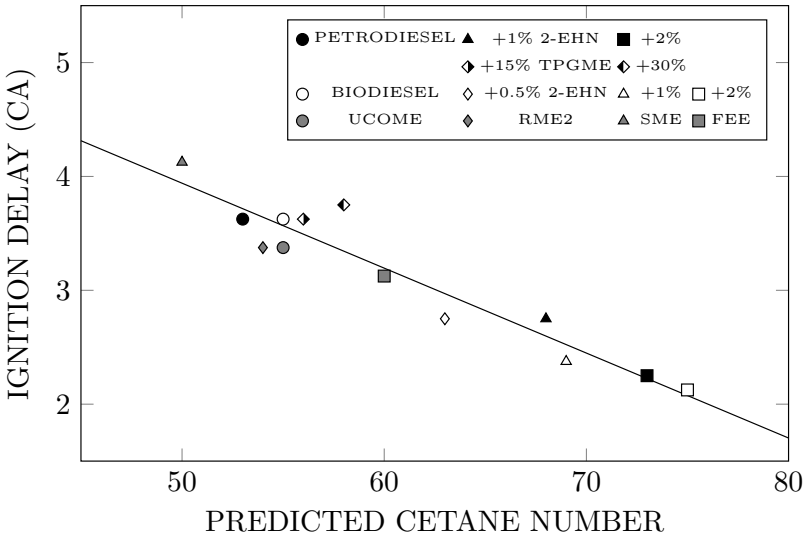

Figure 5.13: Ignition delay as a function of predicted cetane number for all tested fuels under the higher load condition.

be discussed in Section 5.3.1.5, the way the premixed burn appears to proceed varies not only in overall rate between different fuels, but in form. Due to the fact that petrodiesel is faster than biodiesel through the later part of what has been defined as the premixed burn phase, if more of this later section is included in the PMBF, the petrodiesel PMBF appears to be larger than that of biodiesel. Equally, advancing the assigned EOPMB makes the biodiesel PMBF seem larger, because biodiesel AHRR is somewhat higher through the early part of the premixed burn. In Chapter 4 the reduced biodiesel PMBF as a function of ignition delay was attributed to the lower energy density of the fuel, which still seems to be a reasonable explanation for the trend observed, although the trend itself is questionable.

The petrodiesel points in Figure 5.14 are close to being collinear. The linearity of the biodiesel points is fairly high ($r^2 = 0.97$); note that this includes all of the BIODIESEL and 2-EHN blends, in addition to the alternative feedstocks. The only slight outliers are BIODIESEL and RME2; BIODIESEL is slightly below the overall biodiesel trendline, while RME2 is considerably above. BIODIESEL had a longer ignition delay than RME2, and yet had a smaller PMBF. One plausible explanation for this inconsistency is the fact that BIODIESEL data sets were collected earliest, through Oct/Nov 2013, whereas RME2 measurements were performed latest, through Jan 2014; changes in atmospheric conditions and the state of the engine between these periods may have influenced the results.

Other biodiesels had PMBF values appropriate to their ID times. There is a possible reduction in PMBF for a given ID with the addition of the oxygenate TPGME, although

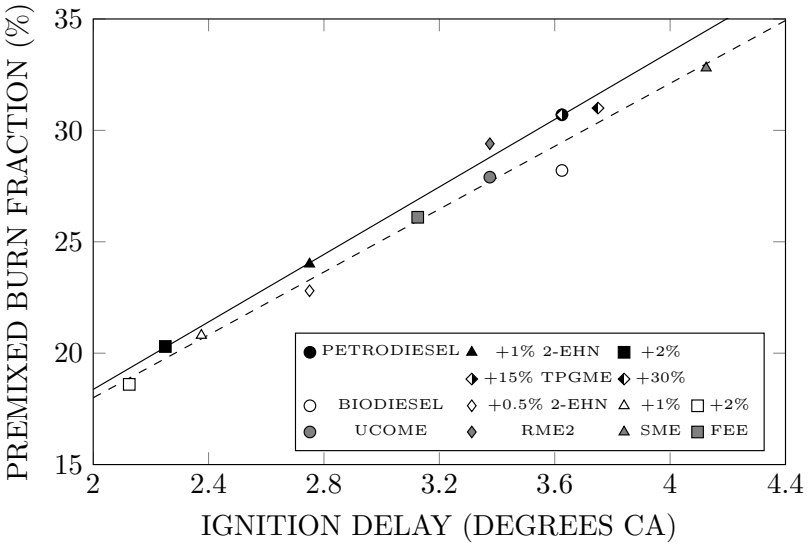

Figure 5.14: Premixed burn fraction as a function of ignition delay for all tested fuels under the higher load condition (solid line represents petrodiesel best fit, dashed line represents best fit through all 8 biodiesel points).

this is not clear. However, such a result may be expected, on account of the lower LHV of the fuel-blend, compared to neat petrodiesel.

5.3.1.2 OXIDES OF NITROGEN (NO_x) EMISSIONS

As proposed on the basis of the mathematical interpretation presented in Chapter 4, it is seen here experimentally that, for a controlled start of combustion (SOC), NO_x emissions decline with a reduction in the premixed burn fraction. This is shown in Figure 5.15. The linearity of the relationship appears to be high; the linear fit through all biodiesel points has an $r^2 = 0.91$. This increases only slightly, to $R^2 = 0.93$, when a second order fit is used, and so any extant non-linearity seems to be slight. The three petrodiesel points are close to collinear.

Possible explanations for the relationship between premixing and NO_x emissions (derived largely from [517]), have been discussed in Section 2.3.4. A general advance in the phasing of combustion, and consequently increased compression heating and/or reduced expansion cooling of both the reactants and the products of combustion is likely to be a significant factor, and the extent to which NO_x emissions correspond to combustion phasing will be considered in detail in later sections. A connection with heat transfer, especially with radiative heat transfer via soot, may also be important, and although in-cylinder soot concentrations and hence levels of soot radiation may not be directly inferable from exhaust smoke opacity, data that will be presented throughout this chapter perhaps offers

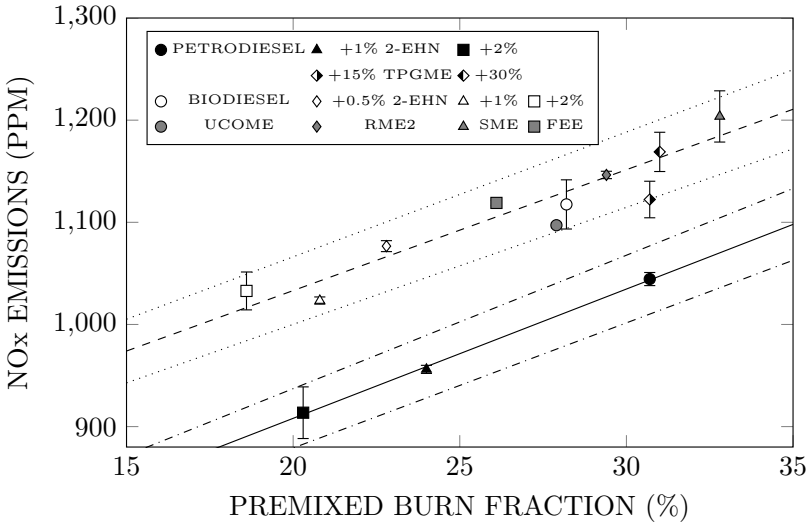

Figure 5.15: Oxides of nitrogen emissions as a function of premixed burn fraction for all tested fuels under the higher load condition (solid line represents petrodiesel best fit, dashed line represents best fit through all 8 biodiesel points, dotdashed and dotted lines lie 3.2% above and below the linear trends and represent possible extent of variations due to external influences).

some support for the plausibility of this mechanism. Factors correlated with, although not causally related to degree of premixing, such as lift-off length and equivalence ratios within the diesel jet, may also contribute significantly to the trends observed.

BIODIESEL NO_x emissions exceed those of PETRODIESEL by 7%. Of the other neat biodiesels, UCOME had NO_x emissions 5% higher than those of PETRODIESEL, when fuelling on FEE NO_x emissions were increased by 7.1%, 9.8% with RME2, and the largest increase of all was 15.2%, when fuelling on SME.

NO_x emissions from BIODIESEL+1% 2-EHN and BIODIESEL+2% 2-EHN are slightly lower than those of PETRODIESEL, implying that in this engine, at this condition (and with SOC held constant), a biodiesel with a cetane number of approximately 70 would run with NO_x emissions lower than, or comparable to, those of PETRODIESEL. This is a very high CN for a biodiesel to have without the addition of cetane enhancers, but is not far above values which have been reported for biodiesel derived from *Moringa oleifera* (with a reported CN of around 67), for example [677].

In some other studies which matched start of combustion, steps were also taken to compare fuels under conditions of equal premixing, by doping each with a calculated level of 2-EHN to achieve matched ignition delay periods (e.g. [568]); this allows a comparison to be made between fuels which overcomes differences in ignition quality. In this work, instead of using 2-EHN addition to remove the effect of variations in the degree of premixing, the different quantities of 2-EHN added to PETRODIESEL and BIODIESEL allow the

influence of changing PMBF to be accounted for. That is, when plotted as a function of PMBF, the magnitude of the change in NO_x emissions which is attributable to degree of premixing becomes visible, allowing for a comparison between fuels which overcomes this variable.

The largest deviation from the biodiesel best-fit line is for UCOME, which is 2.6% lower than the predicted value for the same PMBF. The BIODIESEL+1% 2-EHN point is 1.9% lower, while the SME and BIODIESEL+2% 2-EHN points are 1.6% higher. These are all within the 3.2% error bars indicated in Figure 5.15, which are intended to give a sense of baseline variations over the course of the experimental period; the 3.2% value is the standard deviation of NO_x measurements taken at the daily baseline (discussed in Section 5.2.2). Hence, although there is some variation amongst the different biodiesels, it appears that, when changes in start of combustion are excluded experimentally, and differences in degree of premixing can be accounted for mathematically, the different biodiesel fuels tested all yield NO_x emissions which are within the scale of operational variability inherent to the engine and environment.

However, it is entirely possible that some of the deviations from the overall biodiesel trend are real effects of the fuels themselves. UCOME in particular was associated with rather different trends in other emissions (particularly CO and THC, as discussed in Section 5.3.1.4), which do suggest that this fuel has properties beyond its cetane number which differentiate it from the other biodiesels. Viscosity measurements performed for a later study (by de la Garza and Avulapati) revealed that, while the values predicted in Table 5.3 are the same for both BIODIESEL and UCOME, the actual viscosity of UCOME was around 7% higher than that of BIODIESEL. It has been reported that vegetable oils which have been used for frying may have increased viscosities, due to the range of thermolytic and oxidative reactions which occur when they are heated, forming higher molecular weight dimers and oligomeric compounds [678]. Some portion of the double bonds may also undergo *cis-trans* isomerisation during cooking [679], which would also tend to increase the viscosity. In the review of Hoekman et al [103], biodiesels derived from yellow grease (another term for used cooking oil), are reported to have the highest average viscosity. If the viscosity of the UCOME was relatively high, then this may have altered the spray characteristics in a way which lead to a reduction in NO_x emissions.

It was also proposed in Chapter 4 that NO_x emissions from petro- and biodiesel may converge as PMBF increases; this is the case here, although only to a limited extent, with

the degree of convergence being very slight across the illustrated range. The biodiesel NO_x trend-line is 13.8% higher than that of petrodiesel at a PMBF of 20%, closing to 11.3% at a PMBF of 30%.

The addition of TPGME to PETRODIESEL leads to a considerable increase in NO_x emissions, without a substantial increase in the PMBF. Effectively, it appears that the addition of oxygen 'bridges' the petrodiesel-biodiesel NO_x gap. This is clarified by Figure 5.16.

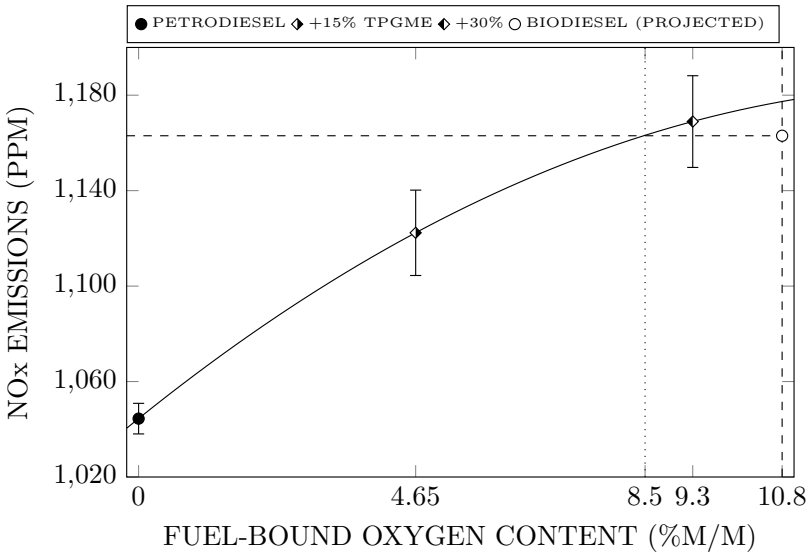

Figure 5.16: Oxides of nitrogen emissions as a function of fuel-bound oxygen content. The biodiesel point represents an approximation of anticipated NO_x emissions at an equivalent degree of premixing, based on the linear correlation illustrated in Figure 5.15.

NO_x emissions increased by 7.5% with the initial addition of 15% TPGME, equating to a fuel-bound oxygen content of 4.65%. Further TPGME addition, to produce a 30% blend, with 9.3% fuel-bound oxygen, caused an additional increase in NO_x of 4.2% – a total increase over PETRODIESEL of 11.9%. Thus, it appears that the effect of oxygenate addition on NO_x emissions is somewhat diminished towards increasing concentrations.

Compared with a biodiesel point projected to the same PMBF, PETRODIESEL+30% TPGME might be expected to produce very slightly higher NO_x emissions (around 0.5%), despite having a lower fuel-bound oxygen content. At the same oxygen content as biodiesel, based on the illustrated curve, an increase in NO_x of 1.2% over biodiesel is expected, and an increase over petrodiesel of 12.7%. Comparable NO_x emissions to biodiesel are predicted for a TPGME blend having an oxygen content of around 8.5%, equating to a TPGME percentage of roughly 27.5%. This may suggest that some structural difference between the way oxygen is bonded into TPGME and biodiesel (i.e. TPGME is an ether, where as

biodiesel is composed of esters) leads to higher NO_x from the TPGME blend, or it may be that there is some other difference between the combustion of these two fuel types, or it may be that the differences observed are simply insignificant, given that the magnitudes of the disparities being considered are well within the variations that may be expected during the day-to-day operation of the engine. It certainly appears that, when SOC is fixed and differences in PMBF are taken into account, a petrodiesel doped with TPGME to a similar oxygen content as biodiesel should be expected to have NO_x emissions very similar to those of an equivalent biodiesel fuel.

It may also be worth considering that the increase in NO_x emissions with increasing TPGME addition to PETRODIESEL occurs despite a likely drop in the adiabatic flame temperature of the blend [525]. On this basis, if the increase in NO_x with TPGME addition has any association with flame temperature, it must be due to variation in mixture stoichiometry or reduced radiative heat transfer, rather than the inherent stoichiometric adiabatic flame temperature of the fuel.

5.3.1.3 FILTER SMOKE NUMBER

In Chapter 4, it was proposed that the converging gap between NO_x emissions from petro- and biodiesels towards higher PMBFs may be related to their relative magnitudes of soot radiative heat losses and varying rates of heat release (in particular, the rate of heat release through the diffusion burn phase).

The basis for the former proposal was that a proportion of heat loss within a diesel engine is typically via radiant transfer from soot to the cylinder walls [572, 573]. Estimated percentages range between about 10–40% [574], although in more modern engines this figure may be lower. It is understood that this heat loss is responsible for a reduction in peak and global temperatures throughout the flame and burnt gases [577]. It has been reported that radiative heat losses are associated with the diffusion phase of combustion, since it is within the diffusion flame sheath that the majority of soot is formed, and during the diffusion burn that in-cylinder soot concentrations are highest [574, 680]. A more pronounced diffusion phase (and a correspondingly reduced premixed phase) may therefore be associated with an increase in radiative heat loss. It is also understood that sooting is considerably reduced when fuelling on biodiesel, with respect to both in-cylinder soot levels, and engine-out emissions. Therefore, the suggestion is that, because petrodiesel soots more, and the presence of soot suppresses temperature, under operating conditions

where a greater fraction of total heat loss is typically due to radiant losses, petrodiesel combustion and post-combustion temperatures may be suppressed more greatly than those of biodiesel.

Figure 5.17 shows the relative levels of soot emissions encountered in this study, quantified by filter smoke number.

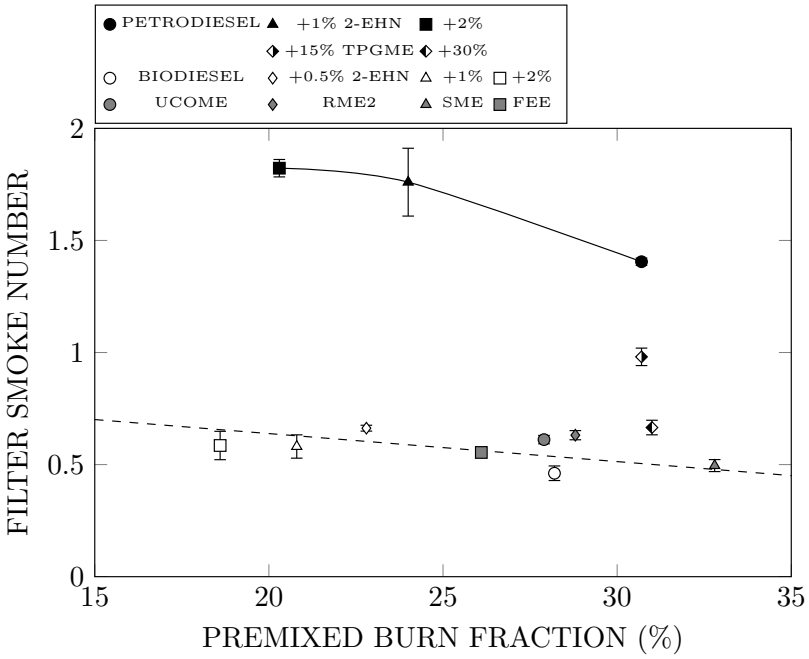

Figure 5.17: Filter smoke number as a function of premixed burn fraction for all tested fuels under the higher load condition (dashed line represents best fit through all 8 biodiesel points).

In general, Figure 5.17 demonstrates an increase in filter smoke number (FSN) with decreasing PMBF, which is as expected. Smoke emissions from petrodiesel were affected more significantly by the change, with FSN rising from 1.41 at a PMBF of 30.7, to 1.82 at a PMBF of 20.3 – an increase of approximately 30%, compared to an estimated increase of 11% for biodiesel across the same range. As a result of the larger increase in FSN from petrodiesel with decreasing PMBF, the difference in smoke emissions between petro- and biodiesel does, as suggested in Chapter 4, become larger towards smaller PMBFs; the estimated biodiesel FSN is 61% lower than that of petrodiesel at a PMBF of 30.7%, becoming 67% lower at a PMBF of 20.3%. However, this relationship is not linear, since the estimated FSN difference is also 67% at the PETRODIESEL+1% 2-EHN point, at a PMBF of 24%.

Despite the general reduction in smoke emissions with increasing PMBF, amongst the neat biodiesels their estimated cetane numbers offer little predictive value in terms of FSN. The highest FSN was observed for RME2 (0.63), and the lowest for BIODIESEL

(0.46) – two fuels with almost identical compositions and cetane numbers (in fact, the estimated CN of RME2 was 1 point lower than that of BIODIESEL, 54 compared to 55). The difference in FSN between these two ostensibly similar fuels, was several times larger than that between the two most dissimilar neat biodiesels, FEE (with an FSN of 0.55) and SME (FSN of 0.5).

It is possible that this unexpected behaviour is due to some undocumented difference between the fuels. UCOME, which had abnormally low NO_x emissions (and abnormally high CO and THC emissions, as will be seen in Section 5.3.1.4), also has a relatively high FSN, suggesting some possible link to the physical properties of the fuels, but the fact that BIODIESEL+0.5% 2-EHN had a higher FSN than all other biodiesels, including BIODIESEL+1% 2-EHN and BIODIESEL+2% 2-EHN, implies that the variability is erroneous rather than some real feature of the fuels.

The FSN values are all normalised on the basis of their respective daily baselines, and as a result the standard deviation for any individual fuel is fairly small, despite repeat measurements typically being conducted some weeks after initial data collection. However, although fuels were not tested consecutively, the experiments with BIODIESEL, BIODIESEL+1% 2-EHN and BIODIESEL+2% 2-EHN, were conducted before those with SME, UCOME, FEE and BIODIESEL+0.5% 2-EHN, with RME2 being tested last. Because FSN is a fairly fickle variable, with regards to changes in engine state and environmental conditions, it may be that a greater quantity of measurements, distributed more evenly in time, would have been necessary to achieve a characterisation of smoke emissions with the accuracy required to clearly perceive the differences between the biodiesels. The overall trend suggested by the biodiesel FSN data in Figure 5.17 is likely to be valid, but apparent differences between the biodiesels ought to be taken with a pinch of salt.

It can be seen that addition of TPGME significantly reduced FSN, but that PETRODIESEL+30% TPGME did not appear have quite as low smoke emissions as a biodiesel under equivalent mixing conditions. This is clarified by Figure 5.18.

Addition of 15% TPGME to PETRODIESEL reduced the FSN by 30%, and the 30% TPGME blend reduced it by a further 32%; giving a total FSN reduction of 53% with the addition of 9.3% fuel-bound oxygen. This is a substantial reduction, but the PETRODIESEL+30% TPGME smoke number remains approximately 7% above the FSN value expected for biodiesel at the same PMBF. Based on an extension of the illustrated curve, showing only a very slight degree of non-linearity, a total fuel-bound oxygen con-

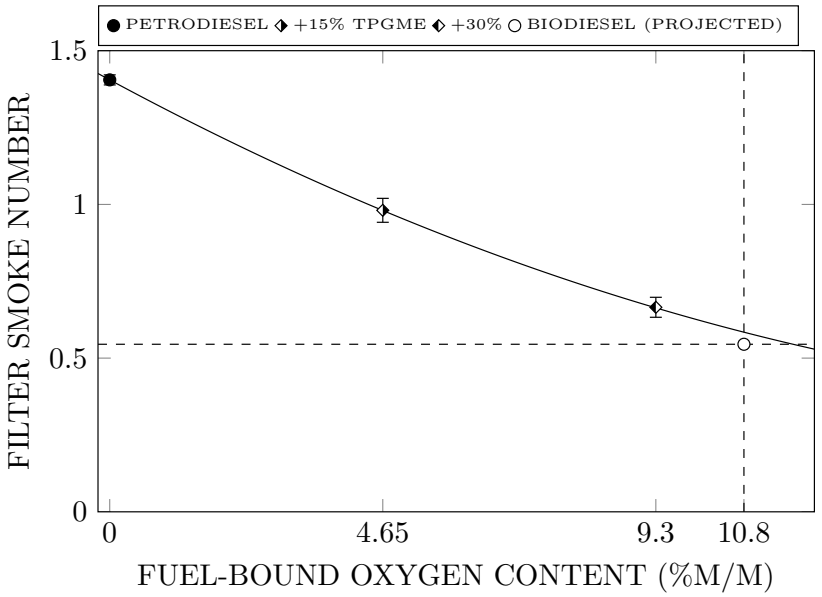

Figure 5.18: Filter smoke number as a function of fuel bound oxygen content. The biodiesel point represents an approximation of anticipated FSN at an equivalent degree of premixing, based on the linear correlation illustrated in Figure 5.17.

tent of somewhere around 11.5% would be necessary to reduce the FSN produced by a PETRODIESEL+TPGME blend (equating to a TPGME percentage of approximately 37.5%) to the same level as that of biodiesel.

However, the reduction in sooting which accompanies the addition of TPGME to PETRODIESEL is not solely a consequence of increased fuel-bound oxygen content. The simple dilution of a petrodiesel by any blending component with a lower propensity to form soot would be expected to reduce FSN; replacing PETRODIESEL (in whole or part) with an *n*-alkane of comparable molecular weight would lead to a significant reduction in smoke emissions, although typically less so than blending with an oxygenated fuel [375, 681]. In particular, it is the sizeable proportion of aromatic species found in petrodiesel which encourage sooting, and the continued presence of these in the PETRODIESEL+TPGME blends – albeit at reduced concentrations – likely contributes to the modestly higher soot emissions relative to an equivalent biodiesel. Greater quantities of oxygen, and lower reacting equivalence ratios, may be required to negate the greater inherent sooting potential of the petrodiesel compounds. Additionally, it has been reported that oxygen bound into an ester group has lower soot reduction potential than that bound into an ether [156, 259, 668, 682], which would suggest that the lower efficacy of the ether in this study on a oxygen percentage basis indicates an even larger effect of the petrodiesel aromatics on sooting.

It is also noteworthy that PETRODIESEL+30% TPGME appeared to have both higher NO_x emissions and a higher FSN than an estimated biodiesel at the same PMBF. This would tend to suggest that it isn't the change in radiative heat loss alone that leads to the increase in NO_x with the addition of the oxygenate.

On the basis of the smoke emissions results presented, there does seem to be some merit to the notion that varying quantities of in-cylinder soot (assuming some correlation between in-cylinder and engine-out soot levels) may be related to the difference between the NO_x emissions when fuelling on petro- and biodiesels, and possibly the way that the calculated trendlines appear to converge (as hypothesised in Chapter 4). There is a clear reduction in soot with the addition of oxygen, and increased degree of premixing, and in both cases this is accompanied by an increase in NO_x emissions. However, the data collected provides no evidence that these relationships are causal.

5.3.1.4 OTHER EMISSIONS

In Figures 5.19 and 5.20 carbon monoxide (CO) and total hydrocarbon (THC) emissions are plotted as functions of premixed burn fraction. In Figure 5.21A carbon dioxide (CO_2) emissions are presented, and Figure 5.21B shows volumetric fuel consumption rates inferred from measured CO_2 emissions and the estimated properties of the individual fuels.

There is a clear increase in both CO and THC emissions with increasing degree of premixing. THC emissions would be expected to increase with increasing PMBF, on the basis that prolonged mixing times encourage overleaning. The reason for the increase in CO emissions is less obvious, since increased premixing is typically associated with leaner combustion conditions which might be expected to reduce CO formation. Potentially, it is the fact that under high PMBF conditions a greater proportion of heat release occurs via fuel-rich premixed reactions, rather than at the stoichiometric diffusion flame front, which causes this increase.

Biodiesel CO emissions are significantly lower than those of the petrodiesels (by around 20%, on average, for a given PMBF), with the exception of UCOME which has comparable CO emissions to a petrodiesel with the same PMBF. Likewise, THC emissions when fuelling on UCOME were higher than on any other fuel; 30% higher than the biodiesel trend. This adds further credence to the suggestion that some effect of the physical properties of UCOME may have negatively affected fuel-air mixing, causing the associated reduction in NO_x, but also the increase in CO and THC emissions.

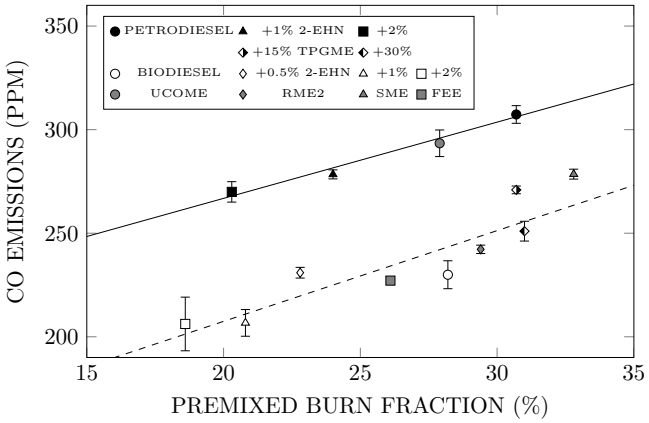

Figure 5.19: Carbon monoxide emissions as a function of premixed burn fraction for all tested fuels under the higher load condition (solid line represents petrodiesel best fit, dashed line represents best fit through biodiesel points, excluding UCOME).

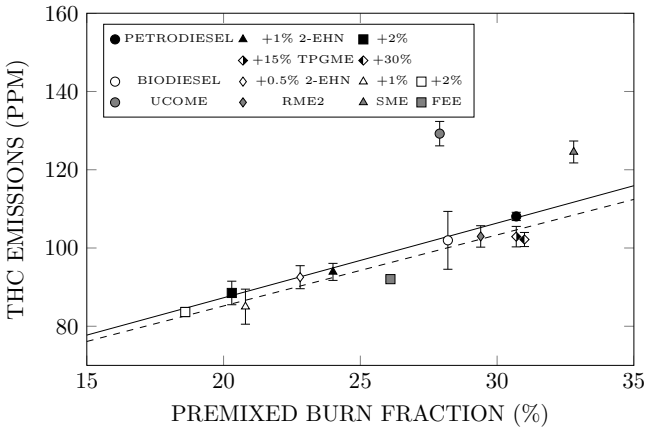

Figure 5.20: Total hydrocarbon emissions as a function of premixed burn fraction for all tested fuels under the higher load condition (solid line represents petrodiesel best fit, dashed line represents best fit through biodiesel points, excluding UCOME and SME).

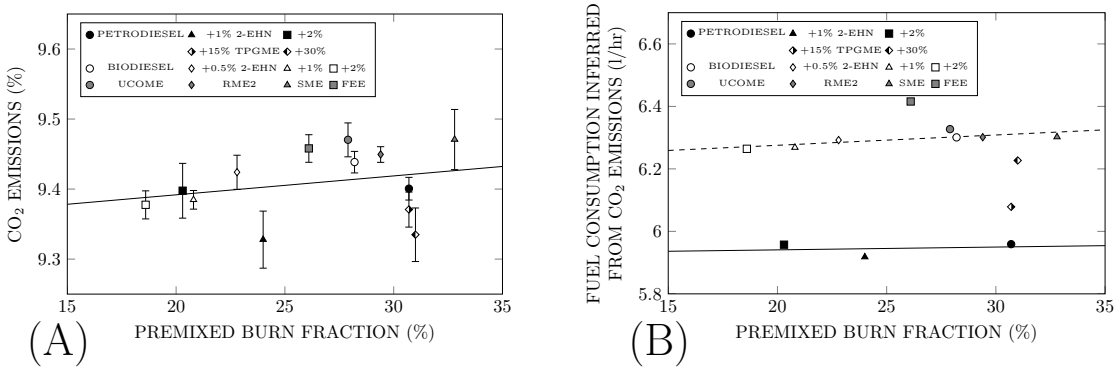

Figure 5.21: (A) Carbon dioxide emissions as a function of premixed burn fraction for all tested fuels under the higher load condition (solid line represents best fit through all points). (B) Volumetric fuel consumption rates inferred from carbon dioxide emissions and fuel properties, as a function of premixed burn fraction for all tested fuels under the higher load condition (solid line represents petrodiesel best fit, dashed line represents best fit through all biodiesel points, excluding FEE).

Biodiesel THC emissions were similar to those of petrodiesel for any given PMBF under the higher load operating condition (reduced by only 2–3%, on average – excluding outliers), apart from those of UCOME and SME. SME exhibited an increase in THC relative to the depicted trends, albeit not one as dramatic as that seen for UCOME (the SME point exceeds the biodiesel trend by around 15%). SME also had CO emissions which exceeded the general biodiesel trend, suggesting that perhaps, like UCOME, the physical properties of the fuel may have negatively affected mixing (although property predictions based on fatty acid composition do not suggest any reason for this, and there is no evidence of a similar reduction in NO_x emissions). It is also possible that the long ignition delay associated with SME may have been sufficient to allow a somewhat higher level of wall impingement to occur.

In general, CO_2 emissions possibly increased slightly with increasing PMBF, and biodiesel appeared to have fractionally higher CO_2 emissions than petrodiesel, but any difference is hard to distinguish. The inferred fuel consumption values suggest increased consumption when fuelling on the biodiesels, which is anticipated on the basis of their lower energy densities. The magnitude of the increase averages around 6%. In the case of FEE, inferred fuel consumption was higher (around 2% higher than the biodiesel trend), due to the shorter average chain length and higher degree of saturation, as a result of which energy density is likely to be lower.

Addition of TPGME to PETRODIESEL reduced CO, THC and CO_2 emissions, although inferred fuel consumption increased. (Practically, the increase in fuel consumption is a result of the lower energy density of the TPGME blends; in terms of the calculation method, the increase in fuel consumption is because the mass percentage of the fuel composed of carbon decreases with addition of TPGME.) With regards to CO and THC, in both cases PETRODIESEL+30% TPGME had comparable emissions to a biodiesel under equivalent mixing conditions. In the case of CO, the same crossing of the gap between petro- and biodiesel trendlines with increasing TPGME addition was apparent, as seen for NO_x (in Figure 5.15) and FSN (in Figure 5.17), clearly implying some relationship with fuel-bound oxygen content and hence mixture stoichiometry within the combusting diesel jet. However, the reduction in CO_2 emissions with increasing TPGME addition is in possible opposition to the biodiesel data.

5.3.1.5 HEAT RELEASE

In Chapter 4 it was reported that, in many cases, the fuel that released heat most quickly overall had the highest NO_x emissions. This is because early heat release tends to promote NO_x emissions, due largely to the effects of greater compression-heating and/or less expansion-cooling, leading to greater maximum temperatures, as well as more prolonged high temperature residence times. In Figure 5.22, plots of relative combustion progress for the various fuels are given, along with relative NO_x emissions. *Relative combustion progress* is intended as a means of comparison between fuels – similar in principle to the binary plot presented in Chapter 4 (Figure 4.7) – and shows the order in which the fuels reached each combustion interval (i.e. CA10 or 10% of total apparent heat release, CA20 or 20% of total heat release, etc.). However, while in Figure 4.7 there were only two fuels to compare, allowing the data to be presented in binary terms, here the larger number of fuels necessitates a slightly different means of presentation. Instead of being distinguished by colour, relative progress is distinguished in Figure 5.22 by Y coordinate, with maximum values attributed to the fuels that reached each interval earliest in the cycle, and the minima to those that reached it latest; other values have been normalised between the maxima and minima, to provide a quantitative indication of temporal separation.

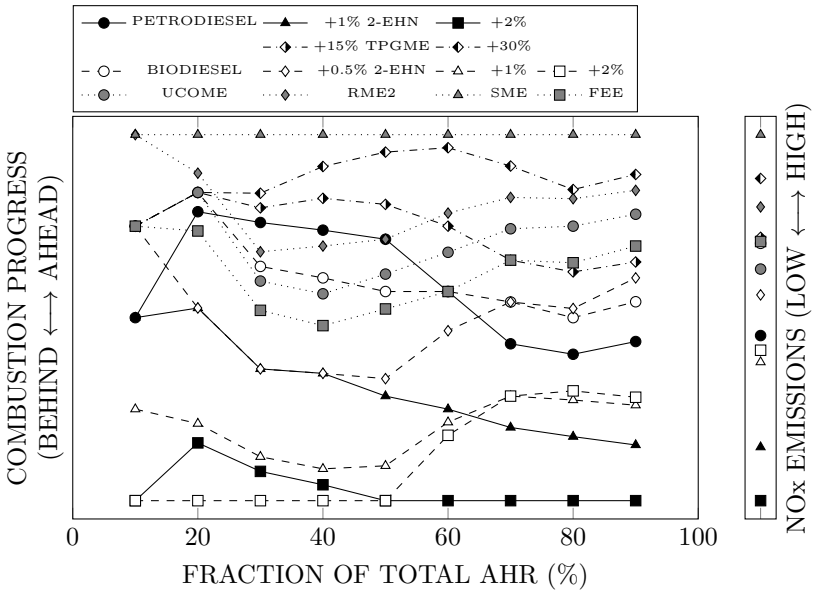

Figure 5.22: Relative combustion progress for all tested fuels under the higher load condition. The vertical position of each fuel indicates how quickly it reached the interval on the x-axis; the fuel that reached the interval earliest is at the top, the fuel that reached it latest is at the bottom, and the other fuels are distributed between based on their timing relative to the slowest and fastest fuels. NO_x emissions distributed similarly are given on the right-hand side.

It can be seen that SME – which is at the top of the plot throughout – combusted most

quickly overall, reaching every interval earlier than the other fuels; SME was the fuel with the largest premixed burn fraction. PETRODIESEL and its blends with TPGME, which had PMBFs larger than all fuels besides SME, began a little more slowly, largely on account of the same sort of sluggish initial pickup in apparent heat release rate, discussed earlier in connection with the PETRODIESEL ignition delay (see Section 5.3.1.1). PETRODIESEL, PETRODIESEL+15% TPGME and PETRODIESEL+30% TPGME then move upwards through the 10–20% fraction, which is where the degree of premixing has the most pronounced effect under these conditions. However, from the 30% interval onwards the three fuels visibly divide, with the PETRODIESEL+30% TPGME curve rising to just below that of SME, the PETRODIESEL curve falling to a position below all of the five pure biodiesels, and the PETRODIESEL+15% TPGME curve remaining approximately equidistant between the other two. This interesting feature replicates the trend which was described in Chapter 4, with biodiesel seemingly releasing heat more rapidly than petrodiesel following the end of the premixed burn. It can be seen that the addition of the oxygenate to petrodiesel makes its pattern of combustion progress increasingly similar to that of the biodiesels.

Examining the biodiesel curves, it can be seen that there is typically a distinct upward gradient from approximately the 40–50% interval, through to 70–80%. The only biodiesel which does not exhibit this trend is the base BIODIESEL, although the gradient of its decline is shallower than those of the petrodiesel fuels. Analysis which will follow later in this section demonstrates that, despite the appearance of Figure 5.22, the BIODIESEL data does share the trait which causes this upward gradient in the other biodiesel plots; namely, an increased rate of heat release through the diffusion burn phase compared to petrodiesel.

The PETRODIESEL+1% 2-EHN and PETRODIESEL+2% 2-EHN curves, as with the PETRODIESEL curve, rise to the 20% interval, but fall consistently throughout the majority of the subsequent combustion process. The initial rise is because the PETRODIESEL and 2-EHN blends had longer ignition delays and larger PMBFs than the BIODIESEL and 2-EHN blends at the same levels of admixture, and the fall is the result of the reduced quantity and rate of mixing-controlled heat release of the petrodiesel fuels.

The correspondence of combustion progress to the relative NO_x emissions data (plotted on the right of Figure 5.22) varies throughout the cycle. By the time that 90% of total AHR has occurred, many of the points are closely aligned (that is, positioned similarly on the

y-axis) to their associated NO_x emissions, while others are a little off; UCOME had lower NO_x emissions than its combustion progress might imply, BIODIESEL had higher, and although the BIODIESEL+1% 2-EHN and BIODIESEL+2% 2-EHN points are ordered correctly with respect to NO_x, they are also a little higher than may be expected on the basis of their combustion progress plots. The separation of the PETRODIESEL, PETRODIESEL+15% TPGME and PETRODIESEL+30% TPGME combustion progress points across the 70–90% intervals corresponds quite accurately to the difference in NO_x emissions observed.

Figure 5.23A gives a quantification of the degree of correlation between NO_x emissions and relative combustion progress, providing r^2 values for linear fits through normalised NO_x emissions (i.e. maximum equal to 1, minimum equal to 0, other values distributed between) as a function of normalised combustion progress. As Figure 5.23A shows, the correlation between combustion progress and NO_x emissions generally increases towards the end of the cycle, peaking at CA70 (at $r^2 = 0.94$), and remaining roughly constant (despite a small decrease, to $r^2 = 0.93$) after that. In Figure 5.23B normalised NO_x emissions are plotted against normalised combustion progress at the CA70 interval. With a few exceptions, the correlation is good.

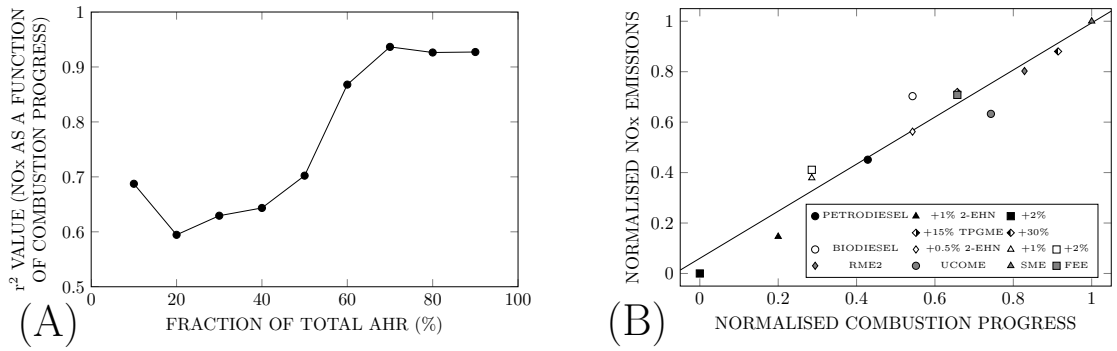

Figure 5.23: (A) r^2 values for linear fits through normalised NO_x emissions as a function of normalised combustion progress, at apparent heat release intervals from 10–90% of total AHR, for all higher load data points. (B) Normalised NO_x emissions as a function of normalised combustion progress at the 70% interval (solid line is linear best fit, the r^2 value of which represents the peak of Figure 5.23A).

Figure 5.23A suggests that even early in the cycle there is some correlation between combustion progress and NO_x emissions, and this is likely to be because more highly premixed combustion is more rapid from the outset, and also generates higher NO_x emissions. Between 50–70% there is a substantial improvement in the correlation, as the biodiesels progress more rapidly through this period, bringing their phasing into accord with their higher NO_x emissions. From 70–90% there is no improvement in the correlation, with heat

release through this period being slow and almost equal for all fuels (although it remains very slightly higher for biodiesel, as will be shown later in this section).

A higher biodiesel diffusion burn rate has been proposed as a possible contributor to the observed increase in NO_x emissions [14]. Chapter 4 and Figure 5.22 provide supporting evidence for the presence of a difference in diffusion heat release rate between petro- and biodiesel. Figure 5.24 confirms that the AHRR through the post-premixed combustion phase is higher when fuelling on biodiesel, after differences in the degree of premixing have been accounted for. Note that the *diffusion phase* is contained within what has been designated instead as *post-premixed combustion*, with the nominal difference indicating that no distinction has been made between the mixing controlled diffusion combustion phase and the late-combustion phase.

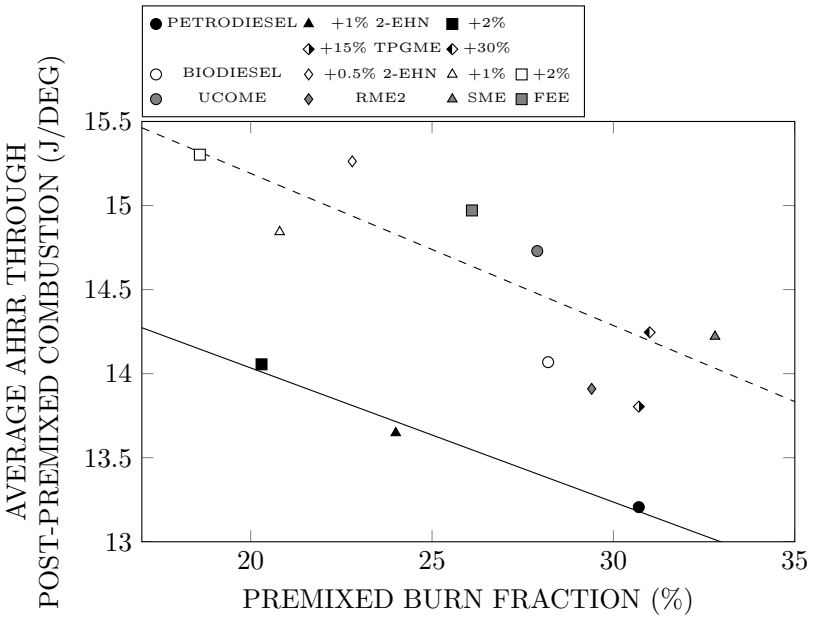

Figure 5.24: Average apparent heat release rate through the post-premixed combustion phase, as a function of premixed burn fraction for all tested fuels under the higher load condition (solid line represents petrodiesel best fit, dashed line represents best fit through all 8 biodiesel points).

The trend-lines for both fuels decline with increasing PMBF, which is likely to be because under more highly premixed conditions, a greater proportion of post-premixed heat release takes place through the slower late-combustion stage, rather than during the more rapid part of the diffusion burn phase. As with the NO_x and FSN results, the petro- and biodiesel post-premixed AHRR trends are clearly separated. The two lines run almost parallel, with the biodiesel points lying at AHRR values approximately 8% higher on average than the petrodiesel ones for the same PMBF; there is a very slight convergence in the trend-lines, with biodiesel being roughly 8.2% higher on average at a

PMBF of 20%, and 7.9% higher at a PMBF of 30%. Although the petrodiesel points all fall close to the trendline given, the biodiesel points are more widely spread ($r^2 = 0.64$); there is no obvious reason for this, besides possible changes in the engine state.

With the addition of TPGME to PETRODIESEL the data points effectively cross the gap from one correlation line to the other, as they did with NO_x and FSN, implying that some factor – common to both the biodiesels and the TPGME blends – is the reason for all of these changes.

The higher average AHRR through this phase could reflect an actually faster rate of biodiesel combustion. A possible explanation for this may be that a reduced equivalence ratio at the lift-off length of the diesel jet could lead to a greater proportion heat release occurring within the upstream fuel-rich premixed reaction zone [525]; as a result of this more completely oxidised fuel fragments and intermediate species would be expected to exist within the core of the jet, potentially allowing combustion at the mixing-controlled flame front to occur more quickly.

However, because the AHRR calculation method used contains no allowance for heat losses, what Figure 5.24 indicates is a difference in *net* apparent heat release rather than *gross*. This means that the higher biodiesel AHRR could instead be a result of reduced heat loss rather than increased heat release. On the basis that biodiesel combustion generates less soot than petrodiesel, the associated reduction in radiative heat transfer may therefore provide a possible explanation for the observed difference in post-premixed AHRR.

By further subdivision of the post-premixed burn phase, it is possible to discern clearly the point at which the oxygenated fuels reach AHRR values most greatly in excess of those calculated for petrodiesel under comparable conditions. In Figure 5.25A the PETRODIESEL+2% 2-EHN post-premixed combustion phase is compared to that of BIODIESEL+1% 2-EHN; these 2 fuels had closely matched PMBFs of 20.3% and 20.8%, respectively. In Figure 5.25B the effect of TPGME addition on the PETRODIESEL post-premixed combustion process is illustrated.

In both cases, it appears that, under the same mixing conditions, the oxygenated fuels have higher AHRR through a large part of the post-premixed combustion phase, between approximately 20–70% of post-premixed combustion. Generally, the discrepancy increases up to the 30–40% interval, and then declines. Under more highly premixed conditions, the point of maximum difference may occur slightly earlier. By the end of combustion, approximately 70–90%, there is very little difference between the AHRR of any of the

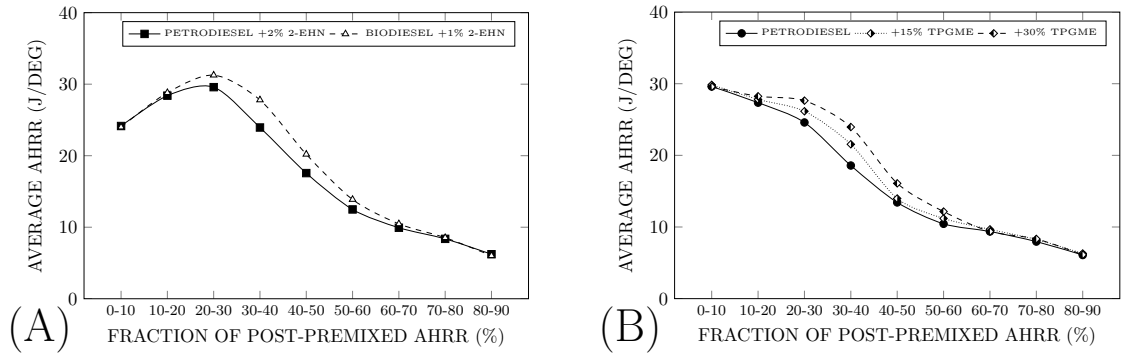

Figure 5.25: Average apparent heat release rate through post-premixed combustion. (A) PETRODIESEL+2% 2-EHN and BIODIESEL+1% 2-EHN (PMBFs of 20.3% and 20.8%, respectively). (B) PETRODIESEL, PETRODIESEL+15% TPGME and PETRODIESEL+30% TPGME (PMBFs of 30.7%, 30.7% and 31%, respectively).

fuels.

Figure 5.26 provides an illustration of the location of the maximum AHRR difference in the engine cycle, and how this corresponds to the overall heat release patterns of the two fuels; again, the comparison is made between PETRODIESEL+2% 2-EHN and BIODIESEL+1% 2-EHN, on the basis that they had similar PMBF values. The region depicted shows both fuels progressing from the end of the premixed burn, to 12 ATDC (which, for PETRODIESEL+2% 2-EHN equates to 65% of the way through the post-premixed portion of combustion, and for BIODIESEL+1% 2-EHN equates to 68%).

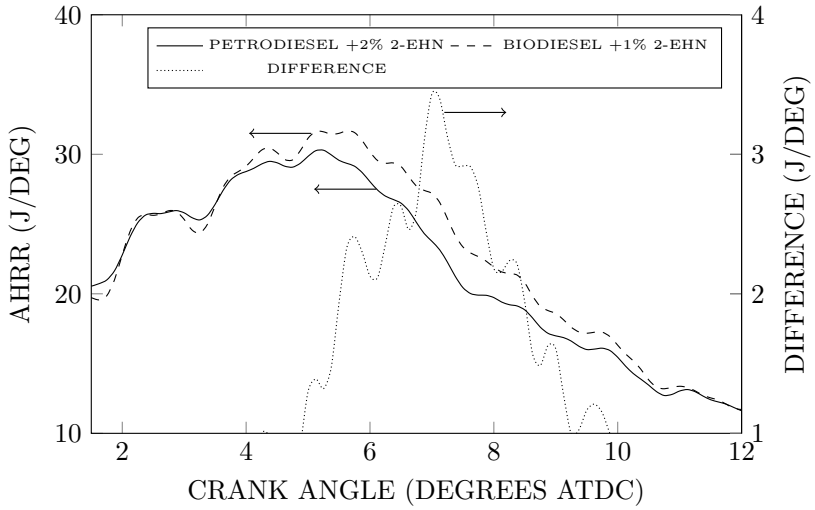

Figure 5.26: Apparent heat release rate from the end of the premixed burn to 12 ATDC, for PETRODIESEL+2% 2-EHN and BIODIESEL+1% 2-EHN (PMBFs of 20.3% and 20.8%, respectively). Based on 9-point moving averages of calculated AHRR data.

It appears that the peak difference is reached slightly after the point of highest post-premixed AHRR, and therefore during the waning of the diffusion flame. However, immediately after the end of the PMBF there is not a significant difference between the AHRR

of the two fuels. This does not conspicuously suggest the conclusion that there is any increase in the biodiesel diffusion heat release rate, per se, as if that were the case one might expect the difference between the two fuels to be discernible earlier and more consistently than is the case. Figure 5.26 indicates an increase in post-premixed AHRR when fuelling on biodiesel which is most significant through a particular period of the diffusion burn, and appears to have some relationship to the magnitude and timing of the post-premixed AHRR maximum.

This is approximately the point at which radiative heat transfer would be expected to peak [574], and hence could possibly correspond to the point at which the difference in radiant losses from the two fuels reached a maximum.

However, a simpler explanation may be as follows. In the test engine employed for these experiments, an individual diffusion flame may never reach a truly steady-state condition. While fuel is supplied to the diesel jet it continues to grow and AHRR increases, until the rate at which fuel is consumed outstrips the rate at which it is being supplied (i.e. injection ramps down and ends), at which point AHRR decreases. (In reality, there is, of course, a delay between fuel passing through the injector and reaching the flame, and so AHRR may continue to rise after the end of injection for a short while.) On account of their lower energy densities the biodiesel fuels would be expected to have prolonged injection events compared to petrodiesel [546]. Interpreted in this light, it may be the case that what Figure 5.26 actually represents is the effect of the somewhat extended biodiesel fuel delivery period, serving to delay and increase the magnitude of peak diffusion heat release.

On this basis, a hypothetical description of Figure 5.26 can be proposed. While the fuels are being supplied at comparable rates (up to approximately 4 ATDC) there is little difference in AHRR, but when the rate of fuel supply decreases, AHRR slows in its ascent and begins to decline. Due, potentially, to its shorter injection event, PETRODIESEL+2% 2-EHN AHRR begins to decline sooner (peaking a little after 5 ATDC), while BIODIESEL+1% 2-EHN AHRR continues to increase for a short additional period (peaking a little before 6 ATDC). This leads to a relative increase in biodiesel AHRR throughout the decline of post-premixed heat release. The increase relative to petrodiesel is maximised in Figure 5.26 at around 7 ATDC, and closes at around 11 ATDC. This may be the result of the later ramping down of the biodiesel injection event, and could be responsible for the higher biodiesel AHRR that persists across approximately 20–70% of

the post-premixed combustion period in Figure 5.25A. Practically, it may be that differences in the magnitude of the fuels' respective AHRR values are related to the size and geometry of the resulting jets.

AHRR data from the TPGME blends, shown in Figure 5.27 is broadly consistent with this explanation, although there is no similar increase in AHRR through the beginning of the diffusion burn, due to the longer ignition delay and more highly premixed conditions. The PETRODIESEL+15% TPGME AHRR curve falls more slowly than that of PETRODIESEL through the diffusion burn, and the PETRODIESEL+30% TPGME curve falls more slowly still. The separation of AHRR curves which occurred at around 4 ATDC in Figure 5.26 occurs a little earlier in Figure 5.27, at around 3 ATDC; the gap is largest at approximately 5 ATDC (compared to 7 ATDC in Figure 5.26), and closes at around 7 ATDC (compared to 11 ATDC). Given that injection began around 1.5 CA earlier when fuelling on the PETRODIESEL and TPGME blends than for the cases shown in Figure 5.26, the injection event would have ended earlier, and so if the difference in AHRR is related to end of injection timing this is consistent with the observed advance of the AHRR gap.

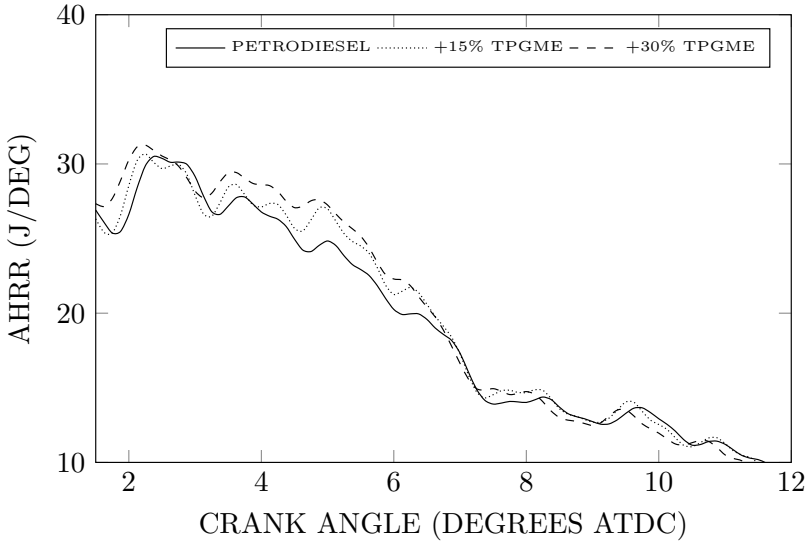

Figure 5.27: Apparent heat release rate from the end of the premixed burn to 12 ATDC, for PETRODIESEL, PETRODIESEL+15% TPGME and PETRODIESEL+30% TPGME (PMBFs of 30.7%, 30.7% and 31%, respectively). Based on 9-point moving averages of calculated AHRR data.

The fact that the addition of TPGME to PETRODIESEL elicited average post-premixed AHRR values and heat release trends similar to those of the biodiesels (given equivalent premixing) may therefore not be a result of the fuel-bound oxygen content common to the biodiesels and TPGME blends (or at least not solely) – instead it may

be, in whole or in part, a consequence of the lower energy density of these fuels which necessitates increased injection duration.

However, given that the total combustion durations of the biodiesels and TPGME blends were also invariably shorter than those of their unoxygenated petrodiesel equivalents (in Figure 5.22 the biodiesels are seen to reach the CA90 earlier than the petrodiesels, and the end of combustion data is consistent with this), it seems unlikely that extended injection duration alone can offer a complete explanation for the increased post-premixed heat release rate of these fuels. Intuitively, a fuel with a longer injection duration might be expected to have a longer combustion duration, if that were the only difference. A contribution from some other factor related to fuel-bound oxygen content, affecting apparent heat release rates through the mixing-controlled and late-combustion phases, is entirely possible.

In summary, under equally premixed conditions, there does appear to be an increase in the post-premixed AHRR when fuelling on biodiesel, or with petrodiesel blended with oxygenates. The cause of the difference is not clear; suggestions relating to the diffusion burn speed [14] and radiant heat losses [543] seem plausible, but based on the position at which the maximum AHRR difference occurs in the engine cycle, it could instead be a result of the slightly prolonged biodiesel injection event. In order to gain clarity on this issue it would be necessary to more closely monitor and/or control the injection event than was the case in this experiment. (An alternative investigation which may provide valuable insight, and would be possible with the current setup – or one similar – is described in Section 9.2.)

Turning attention to the premixed burn phase, Figure 5.28A illustrates that average apparent heat release rate through the premixed phase correlates approximately linearly with the size of the premixed burn fraction, increasing as the PMBF increases. In Figure 5.28A, where average premixed AHRR is plotted as a function of PMBF, some small difference appears to exist between the fuels, with a widening gap between petro- and biodiesel trends, being nil at a PMBF of 20%, but with the biodiesel trend lying about 3.5% above that of petrodiesel at a PMBF of 30%. However, when ignition delay replaces PMBF as the X variable in Figure 5.28B, the gap is largely negated. In part, this suggests that the differences observed in Figure 5.28A may be related to the way PMBF has been calculated, rather than the degree of premixing itself. Ultimately, the change in average premixed AHRR caused by a change in fuel type appears to be relatively minor, beyond

the more significant effect of the degree of premixing that the ignition delay inherent to the fuel allows.

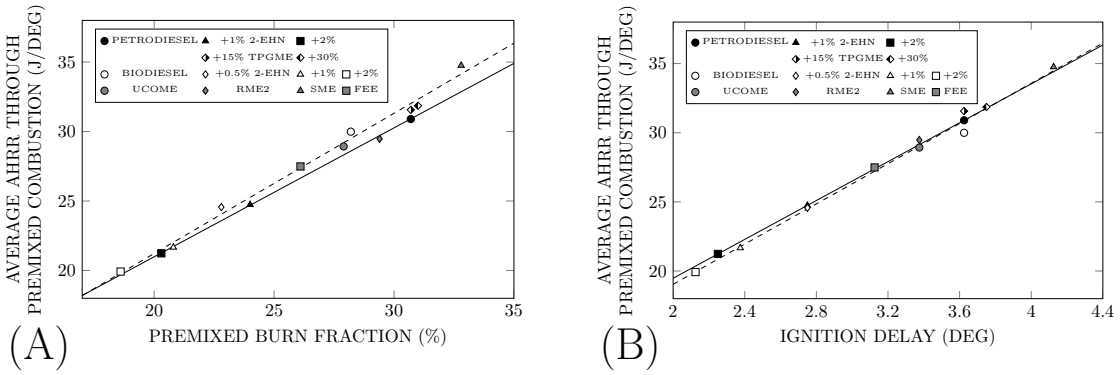

Figure 5.28: Average apparent heat release rate through the premixed combustion phase, as a function of (A) premixed burn fraction and (B) ignition delay, for all tested fuels under the higher load condition (solid lines represent petrodiesel best fits, dashed lines represent best fits through all 8 biodiesel points).

Any further difference which may actually exist between fuels could be linked to the way in which patterns of heat release through the premixed phase vary; a comparison of PETRODIESEL+2% 2-EHN with BIODIESEL+1% 2-EHN is presented in Figure 5.29A, and of PETRODIESEL with PETRODIESEL+15% TPGME and PETRODIESEL+30% TPGME in Figure 5.29B. Biodiesels tended to reach a higher peak AHRR for the same PMBF, as Figure 5.29A reflects, and as supported by Figure 5.30. (Note that maximum apparent heat release rate is calculated cycle-by-cycle and is provided with appropriate error bars, which provide insight into engine variability. Peaks and angles of peaks – both of heat release and pressure – are, in general, approximately normally distributed. Note also that the biodiesel AHRR maximum trend exceeds that of petrodiesel whether the X variable is PMBF or ID, unlike the trends in Figure 5.28.) In contrast, the addition of TPGME to PETRODIESEL appeared to reduce the peak AHRR, as Figure 5.29B and Figure 5.30 illustrate.

In Figure 5.29A, both fuels reach maximum AHRR values in the 20–40% range, and then decline slowly to the 50–60% interval. Here, BIODIESEL+1% 2-EHN AHRR drops sharply, whereas the PETRODIESEL+2% 2-EHN curve continues approximately the same steady rate of decline. After this, the biodiesel has a slightly lower AHRR, on average. In Figure 5.29B, the three fuels reach higher, more enduring peaks through the 20–50% interval, on account of their larger PMBFs (30.7–31%, as opposed to 20.3–20.8% in Figure 5.29A), and then drop away and reach approximate equality by 60–70%. After this point, the PETRODIESEL+30% TPGME curve is noticeably higher than that of

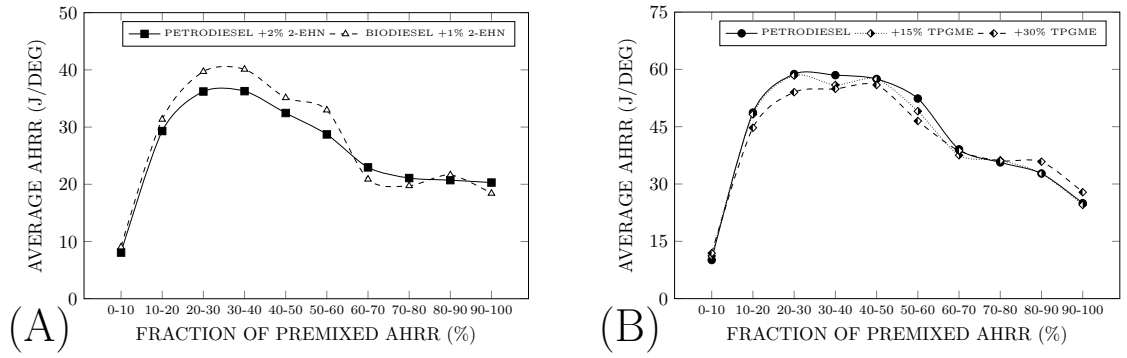

Figure 5.29: Average apparent heat release rate through premixed combustion. (A) PETRODIESEL+2% 2-EHN and BIODIESEL+1% 2-EHN (PMBFs of 20.3% and 20.8%, respectively). (B) PETRODIESEL, PETRODIESEL+15% TPGME and PETRODIESEL+30% TPGME (PMBFs of 30.7%, 30.7% and 31%, respectively).

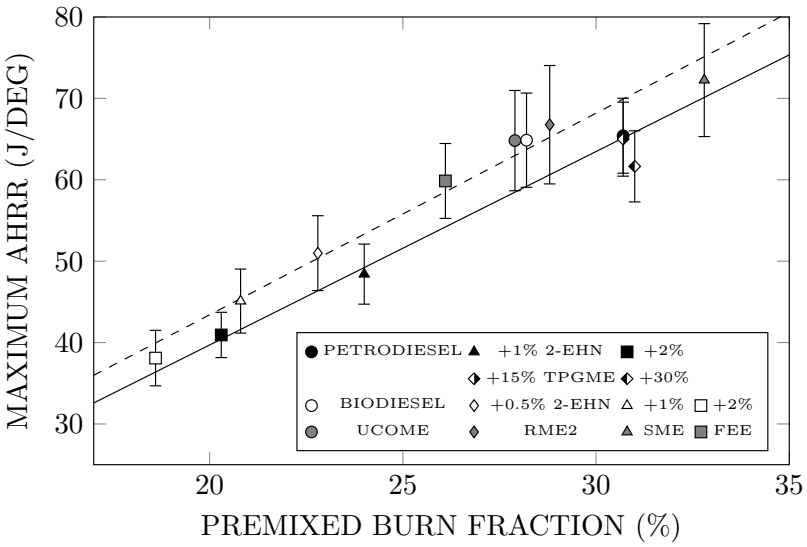

Figure 5.30: Maximum apparent heat release rate as a function of premixed burn fraction for all tested fuels under the higher load condition (solid line represents petrodiesel best fit, dashed line represents best fit through all 8 biodiesel points).

PETRODIESEL.

It is apparent that AHRR is higher for the biodiesel case through approximately the first 60% of the premixed burn fraction, but is then marginally lower than for petrodiesel over the remainder. With the addition of TPGME, this trend is opposite; PETRODIESEL +30% TPGME has a lower AHRR through the first 60%, and is then marginally higher than PETRODIESEL. Hence, it may not be the higher fuel-bound oxygen content of biodiesel which causes its higher maximum AHRR values.

It may instead be possible that it is the narrower range of reactivity which makes the biodiesel AHRR peak higher. That is, biodiesel is comprised of only a handful of different chemical species, with similar structural elements and cetane numbers ranging from around 30–90, whereas petrodiesel contains a far larger variety of species, with cetane

numbers potentially ranging from below 0 to above 100. It may therefore be hypothesised that a less heterogeneous fuel – biodiesel, in this case – may undergo a less protracted premixed burn: more rapid at the outset, and ending more abruptly.

This might go some way towards explaining the increase in the biodiesel peak AHRR, and also the slower decline in AHRR through the back-end of the petrodiesel PMBF. However, it does not offer much insight into the reason for the reduction in maximum AHRR with PETRODIESEL+30% TPGME. It is possible that this is related to the very slight increase in average AHRR through the 0–10% period for PETRODIESEL+30% TPGME (see Figure 5.29B – this small increase is also observed for the biodiesels, as can be seen in Figure 5.29A), which serves to advance rapid heat release by a fraction of a degree; PETRODIESEL reaches 50% of maximum AHRR 1.625 after SOC, whereas PETRODIESEL+30% TPGME exceeds this level of AHRR only 1.375 after SOC. Because this slight advance means that the remainder of the premixed charge is consumed slightly earlier, it may be that it is less well prepared for combustion, and hence releases heat more slowly. Another factor which may have some relevance to the reduction in peak AHRR with the addition of TPGME is the lower adiabatic flame temperature of the oxygenate compared to the parent fuel [525].

All fuels reached maximum AHRR values close to 1 BTDC on average, as can be seen in Figure 5.31, with cycle-to-cycle variation for any given fuel being almost as large as the difference between the fuels (average standard deviation of 0.27 CA, compared to a total range of averages for all fuels of 0.43 CA). The AHRR maximum was slightly retarded with increasing PMBF, occurring around 0.25 CA later at a PMBF of 30% than at a PMBF of 20%. It is also noteworthy that the maximum AHRR of UCOME was retarded by approximately 0.2 CA on average compared to the general trendline, and was later than any other tested fuel; Figure 5.31 shows the linear best fit plus/minus one encoder increment (0.125 CA), and UCOME is the only fuel that deviated beyond this limit.

In summary, the results of this study suggest that fuelling on biodiesel rather than petrodiesel affects heat release approximately as shown in Figure 5.32. Heat release is initially slightly higher for the same degree of premixing with biodiesel, peaks higher through the premixed burn fraction, but is slightly lower through the end of the premixed burn, such that average biodiesel heat release rates through the premixed phase as a whole are similar to those of petrodiesel. Through the diffusion phase biodiesel heat release is significantly higher, and remains very slightly higher through late-combustion. The addition of

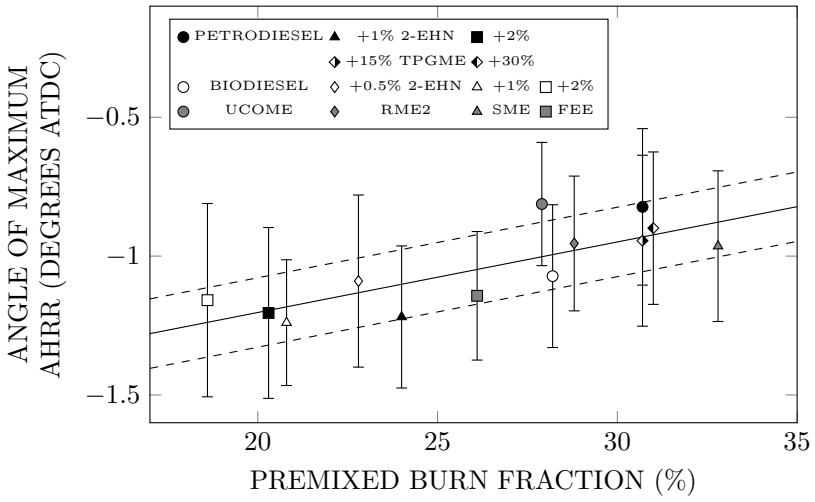

Figure 5.31: Angle of maximum apparent heat release rate as a function of premixed burn fraction for all tested fuels under the higher load condition (solid line represents best fit through all data points, dashed lines are placed at ±0.125 CA to indicate the resolution of the encoder).

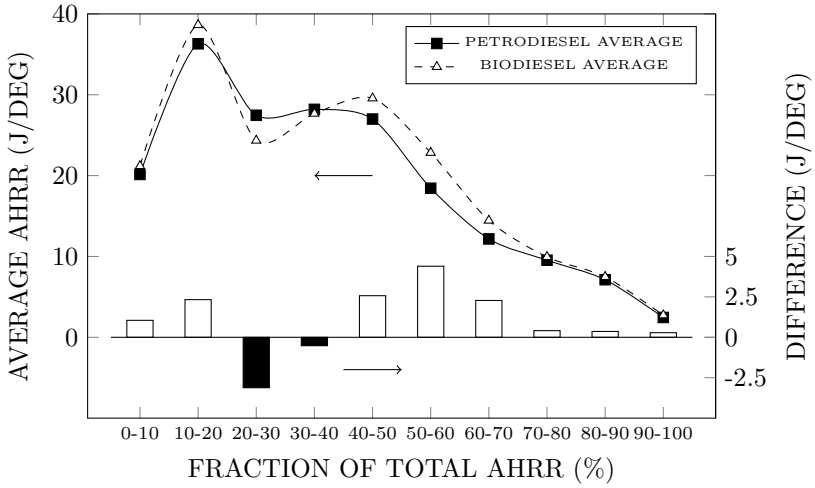

Figure 5.32: Average apparent heat release rate throughout the combustion process for petro- and biodiesel, and the average difference between the two over each period (white bars indicate an increase in AHRR when fuelling on biodiesel, black bars a decrease). Petrodiesel data calculated as the average of PETRODIESEL, PETRODIESEL+1% 2-EHN and PETRODIESEL+2% 2-EHN, with a mean premixed burn fraction of 25%. Biodiesel calculated as the average of all biodiesel data sets except SME, to give an average PMBF of 24.8%.

TPGME to petrodiesel affects post-premixed combustion in essentially the same way as biodiesel does, but was observed to reduce maximum heat release through the premixed phase (i.e. 10–20% in Figure 5.32), and increase it through the end of the premixed phase (i.e. 20–30%). Under the operating conditions of this study, the best correlation between the heat release patterns of the fuels and their respective NO_x emissions is obtained after approximately 70% of combustion is complete (that is, CA70 is the best predictor of NO_x emissions for a fuel), because at this point the contribution of the increased biodiesel apparent heat release rate through the diffusion phase has been incorporated.

5.3.1.6 PRESSURE

The effect of faster heat release through the diffusion phase is evident in the pressure plots. In Figure 5.33, maximum pressure (P_{max}) and angle of maximum pressure (Θ_{Pmax}) are plotted as functions of PMBF. Although in Figure 5.33A many of the biodiesel points exhibit a significant degree of deviation from the trendline (in the case of RME2, for example, it approaches the petrodiesel trend – for the biodiesel trend the overall r^2 = 0.85) it is still evident that P_{max} is consistently higher for the biodiesel fuels than for petrodiesel, given the same degree of premixing. Likewise, the addition of TPGME to PETRODIESEL leads to higher P_{max} values, crossing from one trendline to the other, just as with NO_x, FSN, CO and post-premixed heat release.

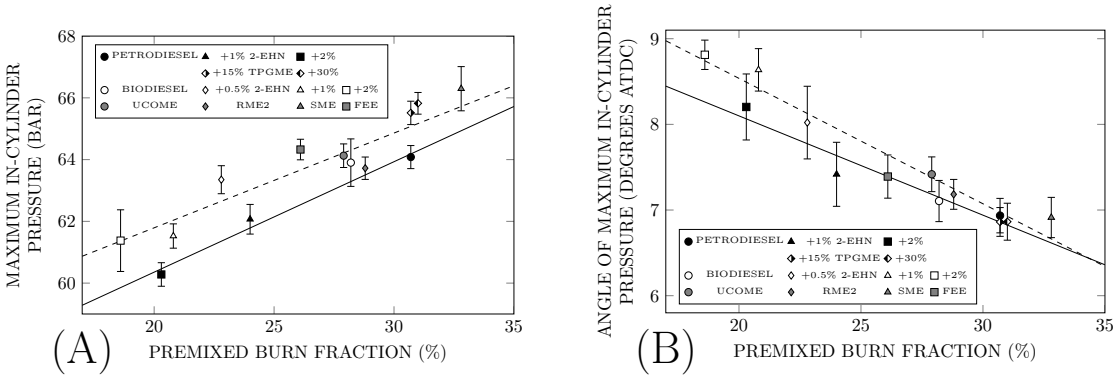

Figure 5.33: (A) Maximum in-cylinder pressure and (B) angle of maximum in-cylinder pressure, as functions of premixed burn fraction for all tested fuels under the higher load condition (solid lines represent petrodiesel best fits, dashed lines represent best fits through all 8 biodiesel points).

Figure 5.33B shows that biodiesel usage was often associated with a retardation of the angle at which P_{max} was reached; in this study, Θ_{Pmax} generally coincided with around 55–60% of total heat release. This difference in Θ_{Pmax} was negated at the more highly premixed conditions, and was not observed when fuelling on the TPGME blends. Referring back to Figures 5.26 and 5.27, and making a comparison between the two:

- In Figure 5.26, which represents less highly premixed combustion, the difference between the AHRR of the two fuels persists further into the cycle than in Figure 5.27, possibly on account of the fact that injection begins and ends later. Consequently, P_{max} is reached while there is still a significant difference in heat release between the fuels (at between 8–9 ATDC). This means that biodiesel heat release is sufficient to maintain rising pressure for a short period after petrodiesel reaches its maximum and begins to fall. This results in BIODIESEL+1% 2-EHN peaking on average 0.4 CA later than PETRODIESEL+2% 2-EHN.

- In Figure 5.27, where combustion is more highly premixed, the AHRR gap between the fuels closes earlier in the cycle than in Figure 5.26, possibly due to the earlier start and end of injection. By the time P_{max} is reached, at around 7 ATDC, no significant difference in AHRR remains, and so pressure rise ends at approximately the same time for PETRODIESEL and its blends with TPGME.

However, even in the absence of any difference in the *timing* of maximum pressure, biodiesel and the oxygenated blends still tend to exceed petrodiesel in terms of the *magnitude* of maximum pressure. In Figure 5.34, total pressure change between the start of combustion and Θ_{Pmax} is divided into that which occurs across the premixed combustion phase (ΔP_{pmb}) and that which occurs across the diffusion combustion phase (ΔP_{diff}). In connection with earlier discussions of heat release rates (regarding Figure 5.24, for example) the term *diffusion* was eschewed in favour of *post-premixed*; here, however, it is appropriate to refer to the diffusion or mixing-controlled combustion phase explicitly, on the grounds that Θ_{Pmax} is likely to occur before *late-combustion* commences.

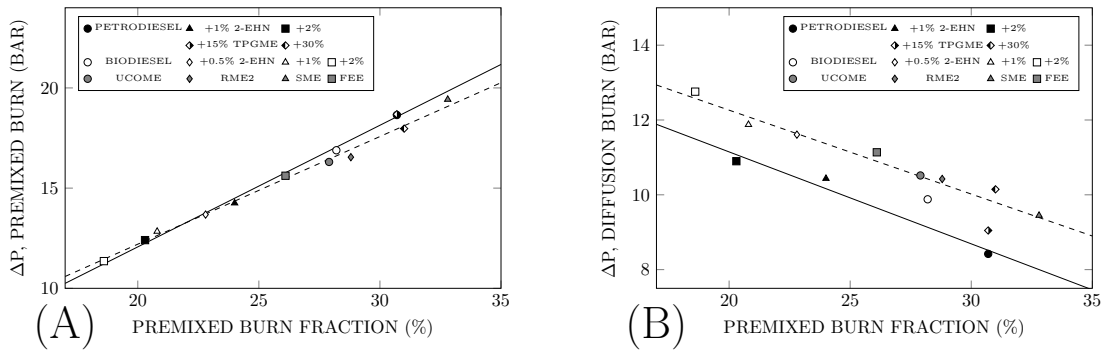

Figure 5.34: Pressure change across the (A) premixed and (B) diffusion burn phases, as a function of premixed burn fraction for all tested fuels under the higher load condition (solid lines represent petrodiesel best fits, dashed lines represent best fits through all 8 biodiesel points).

Figure 5.34A shows that it is not likely to be differences in pressure change across the premixed phase which cause the higher maximum pressures encountered when fuelling on biodiesel; ΔP_{pmb} values are similar for petro- and biodiesel, given the same degree of premixing, which is consistent with the fact that average AHRR values were also similar through the premixed phase (as seen in Figure 5.28). To some extent, ΔP_{pmb} values appear to be slightly lower for biodiesel – particularly in the higher PMBF cases. In fact, it is largely the high values of PETRODIESEL and PETRODIESEL+15% TPGME points which give this impression, and this difference can be attributed to the later end of the premixed burn in these cases (at 1.5–1.625 ATDC), compared to the more highly premixed biodiesels (EOPMB at 1.25–1.375 ATDC).

The slight advance in EOPMB when fuelling on the biodiesels and PETRODIESEL +30% TPGME also contributes to the larger ΔP_{diff}; the increase in ΔP_{diff} for the biodiesels is clear and consistent in Figure 5.34B. At the less premixed conditions it seems that biodiesel has a longer period between EOPMB and Θ_{Pmax} by virtue of a retardation of Θ_{Pmax}, while at the more highly premixed conditions the same phase was instead extended by an advancement of EOPMB. As a result, the biodiesel diffusion phase was consistently longer than that of petrodiesel, as can be seen in Figure 5.35A. However, as Figure 5.35B illustrates, although there is a clear correlation between the duration of the period between EOPMB and Θ_{Pmax}, and ΔP_{diff}, biodiesel also tends to elicit a larger ΔP_{diff} for the same duration of pressure rise.

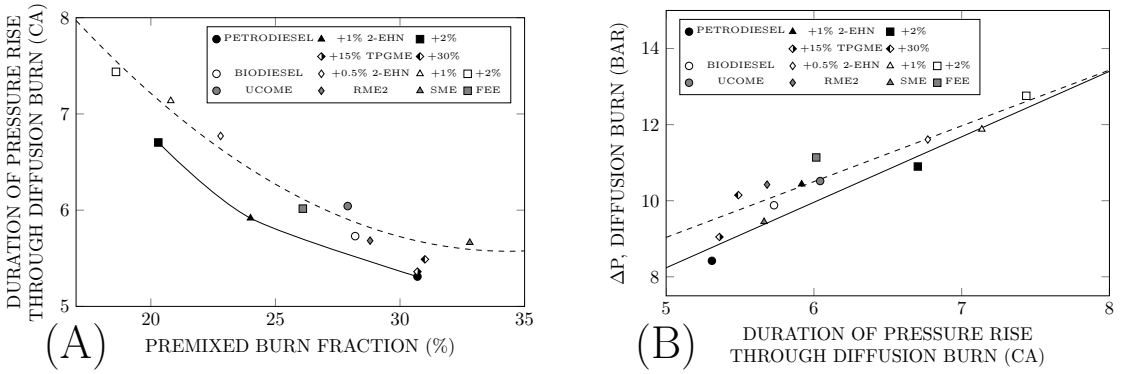

Figure 5.35: (A) Duration of pressure rise through the diffusion phase as a function of premixed burn fraction and (B) pressure rise as a function of duration, for all tested fuels under the higher load condition (solid lines represent petrodiesel best fits, dashed lines represent best fits through all 8 biodiesel points).

For the fuels with shorter ignition delays and lower PMBFs (that is, towards the right side of Figure 5.35B), differences in the duration of pressure rise through the diffusion phase accurately predict the differences in ΔP_{diff}; i.e. petro- and biodiesel have similar ΔP_{diff} values for any given duration. However, the longer ignition delay biodiesels (towards the left side of Figure 5.35B) typically have ΔP_{diff} values larger those of petrodiesel for any given duration of the pressure rise. Similarly, the ΔP_{diff} when fuelling on PETRODIESEL+15% TPGME and PETRODIESEL+30% TPGME exceeds that of PETRODIESEL by far more than would be anticipated on the basis of the extension of the pressure rise duration alone. Thus, it is in the cases in which Θ_{Pmax} is postponed by the use of biodiesel that the *duration* of the pressure rise is the main determinant of ΔP_{diff}. In the cases in which Θ_{Pmax} is not postponed, the *rate* of pressure rise is more significantly increased with biodiesel, and also with the TPGME blends. This is because a greater proportion of the diffusion AHRR gap (refer back to the discussion of Figure 5.33B, and Figures 5.26 and 5.27) has

elapsed by the time Θ_{Pmax} is reached in the cases where Θ_{Pmax} is unaffected by biodiesel usage, meaning that the overall rate of pressure rise is higher, in addition to the increase in duration.

In summary, biodiesel fuels tended to reach higher maximum pressures than petrodiesels for a given degree of premixing. This was primarily a result of the increased apparent heat release rate through the diffusion combustion phase. The increased biodiesel diffusion AHRR caused an increase in the duration and rate of pressure rise through the diffusion phase, resulting in greater pressure rise following the end of the premixed burn, and greater total pressure rise.

5.3.2 STUDY 2: VARYING INJECTION PRESSURES

5.3.2.1 PREMIXING

In the second set of experiments changes to the premixed burn fraction were effected by making alterations to the operating injection pressure. Rather than controlling PMBF via mixing time, as in Study 1, making changes to injection pressure directly influences the rate of in-cylinder air entrainment. As a result, an increase in the degree of premixing is not necessarily accompanied by an increase in the ignition delay.

The effect of injection pressure on ignition delay is illustrated in Figure 5.36. On the basis of the available data, the relationship appears to be reasonably linear, with ignition delay decreasing as injection pressure increases. This is to be anticipated, since the increased rate of air entrainment at higher injection pressure will lead to more rapid vaporisation and heating of the fuel.

In this study, BIODIESEL had a significantly shorter ignition delay than PETRODIESEL. Comparing the 800 bar results in Figure 5.36 with the Study 1, 0% 2-EHN results in Figure 5.12 – which represent ostensibly identical operating conditions and fuels – it is clear that there is a substantial inconsistency between the two studies. The BIODIESEL ignition delay decreased from 3.625 CA to 3.375 CA, and the PETRODIESEL ID increased from 3.625 CA to 3.875 CA. The fact that the ID has increased for BIODIESEL while decreasing for PETRODIESEL suggests that a change common to both fuels (e.g. varying atmospheric conditions or the state of the engine) does not offer a viable explanation. The data for Study 1 was collected in Oct/Nov 2013, and for Study 2 in Feb 2014; between these dates the laboratory PETRODIESEL supply was replenished (although the fuel was nominally the same, in reality the composition is almost certain to have changed to some

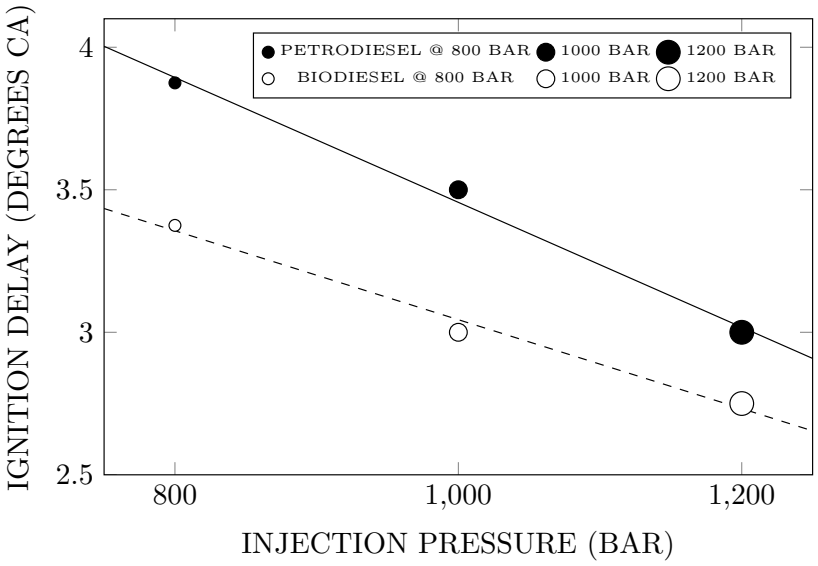

Figure 5.36: Ignition delay as a function of injection pressure for PETRODIESEL and BIODIESEL at injection pressures of 800, 1000 and 1200 bar (solid line represents PETRODIESEL best fit, dashed line represents BIODIESEL best fit.

extent at least, given the potential variability of commercial petrodiesel [160]), and this may account for the increase in the ignition delay when running on PETRODIESEL. (It should also be noted that the slower initial rise in PETRODIESEL AHRR observed in Study 1, and also in Study 3, was not as significant following fuel replenishment in Study 2.) Potentially, the decrease in BIODIESEL ignition delay observed between Study 1 and Study 2 may be attributable to additional ageing and oxidation of the fuel, increasing its cetane number [676].

The trend in Figure 5.36 may suggest a slight reduction in the difference between the IDs of the two fuels with increasing injection pressure, but in fact the relative difference remains approximately constant, with BIODIESEL having an ignition delay about 20% shorter than that of PETRODIESEL at all three injection pressures.

The relationship between ID and PMBF can be seen in Figure 5.37. Whereas in Study 1 (see Figure 5.14) the relationship between ID and PMBF was positive, in Figure 5.37 it is negative, but this is not a causal relationship; PMBF increases with increasing injection pressure *despite* the reduction in ID, not because of it. The important change is to rate of air entrainment, and the dotted lines in Figure 5.37 give some indication as to how this is affected by the change in injection pressure. These lines can be seen to become increasingly steep as injection pressure increases, rising from an increase in PMBF of around 5.6% per degree of the ignition delay period at 800 bar, to an increase of around 29% per degree at 1200 bar. This is a very substantial change, and demonstrates why it is possible for such

a large PMBF to form with such a short mixing interval.

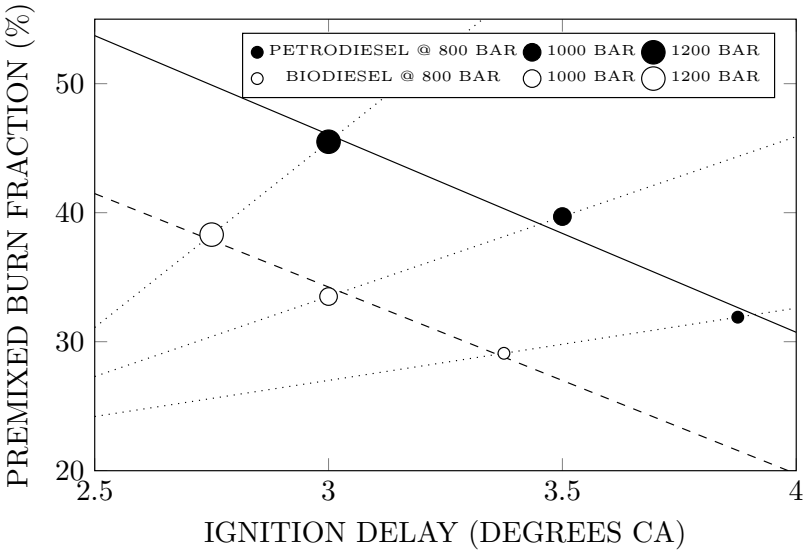

Figure 5.37: Premixed burn fraction as a function of ignition delay for PETRODIESEL and BIODIESEL at injection pressures of 800, 1000 and 1200 bar (solid line represents PETRODIESEL best fit, dashed line represents BIODIESEL best fit, dotted lines give an indication of the rate of air entrainment at each condition).

5.3.2.2 GASEOUS EMISSIONS AND SMOKE

In Study 1 (specifically, Figure 5.15), it was seen that NO_x emissions correlated positively with premixed burn fraction, and that biodiesel had higher NO_x emissions than petrodiesel for a given PMBF. These trends appear to be repeated here, as Figure 5.38 illustrates.

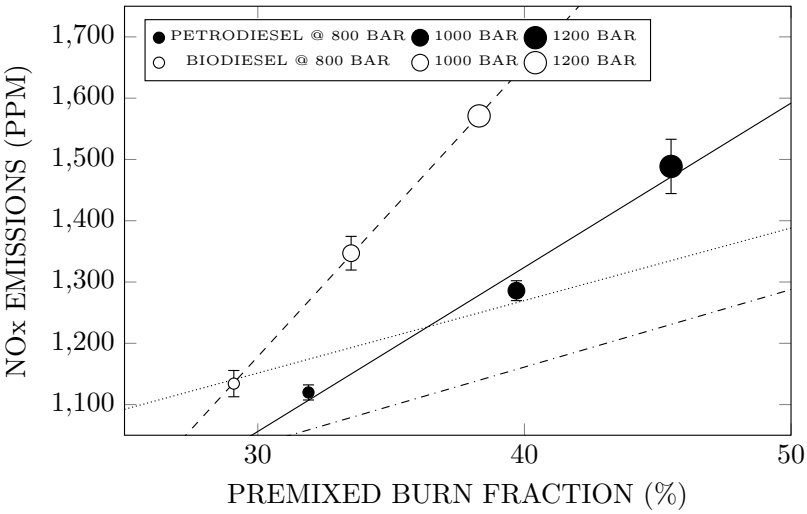

Figure 5.38: Oxides of nitrogen emissions as a function of premixed burn fraction for PETRODIESEL and BIODIESEL at injection pressures of 800, 1000 and 1200 bar (solid line represents PETRODIESEL best fit, dashed line represents BIODIESEL best fit; dashdotted and dotted lines represent continuations of the petro- and biodiesel fits from Study 1, Figure 5.15).

The BIODIESEL points suggest that the relationship is approximately linear, although

the PETRODIESEL data is less clear in this regard; in any case, the data is insufficient to draw a conclusion one way or the other. What is clear (by comparing the trendlines for the varying injection pressure data, with those carried forward from Study 1, Figure 5.15) is that the gradient of the correlation lines is far larger in Figure 5.38 than in Figure 5.15. That is, as a function of PMBF, NO_x emissions are increased more greatly when PMBF is enlarged due to higher injection pressure, than they are when PMBF is enlarged due to prolonged mixing time. In Figure 5.15 the petrodiesel NO_x emissions rise around 12.7 ppm per 1% increase in the PMBF, and the biodiesel NO_x emissions increase 11.8 ppm over the same interval; in Figure 5.38 the petrodiesel NO_x emissions rise 26.8 ppm/%, and biodiesel NO_x emissions rise 47.5 ppm/%.

In Study 1, the slightly higher gradient of the petrodiesel trend relative to the biodiesel trend in Figure 5.15 meant that there was a slight convergence of petro- and biodiesel NO_x emissions with increasing PMBF, as hypothesised in Chapter 4. At varying injection pressures, however, the considerably higher gradient of the BIODIESEL trend relative to the PETRODIESEL one leads the two to diverge with increasing degree of premixing. This means that the hypothesis (from Chapter 4) that biodiesel NO_x emissions might be relatively lower under more highly premixed conditions does not appear to be generalisable to all cases; when modifying injection pressure it was at the more highly premixed conditions that biodiesel had relatively higher NO_x emissions, whereas when modifying engine load and injection timing it appeared to be (based on the analysis in Chapter 4) at the least premixed conditions that biodiesel had the highest surplus. Given that in Study 1 the degree of convergence was minor, and in Study 2 the NO_x trends diverge substantially with increasing PMBF, the conceptual description put forward in Chapter 4, Figure 4.13 seems to be untenable.

In Figure 5.38, and Figure 5.39A, it can be seen that increasing injection pressure from 800 to 1000 bar increased PETRODIESEL NO_x emissions by 14.8%, and from 1000 to 1200 bar by a further 15.7%; a total increase of 32.9% between 800 and 1200 bar. BIODIESEL NO_x emissions increased 18.8% between 800 and 1000 bar, and 16.6% between 1000 and 1200 bar, to make a total increase of 38.5% between 800 and 1200 bar. More clearly visible in Figure 5.39A, BIODIESEL NO_x emissions were 1.3% higher than those from PETRODIESEL at an injection pressure of 800 bar (considerably less than was the case under the same conditions in Study 1 – partially because of the larger difference in ignition delay and hence degree of premixing in Study 2, but also possibly influenced by the change

in composition of the PETRODIESEL between studies), 4.8% higher at 1000 bar and 5.5% higher at 1200 bar. If this trend holds, it may be that operating engines at slightly reduced injection pressures would provide a straightforward means for the mitigation of NO_x emissions when fuelling on BIODIESEL. Such a strategy would, as ever, involve a trade-off, with the primary penalty being in terms of particulate emissions.

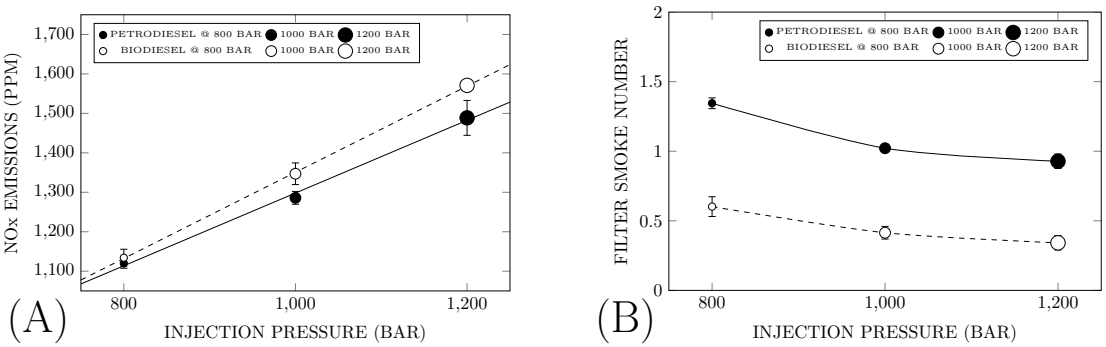

Figure 5.39: (A) Oxides of nitrogen emissions and (B) filter smoke number, as functions of injection pressure for PETRODIESEL and BIODIESEL at injection pressures of 800, 1000 and 1200 bar (solid lines represent PETRODIESEL best fits, dashed lines represent BIODIESEL best fits).

Increased injection pressures have been shown to significantly reduce particulate emissions from diesel engines, under a wide range of operating conditions and using various fuels [683–685]. The same trend in FSN can be seen in Figure 5.39B as a function of injection pressure, and as a function of PMBF in Figure 5.40.

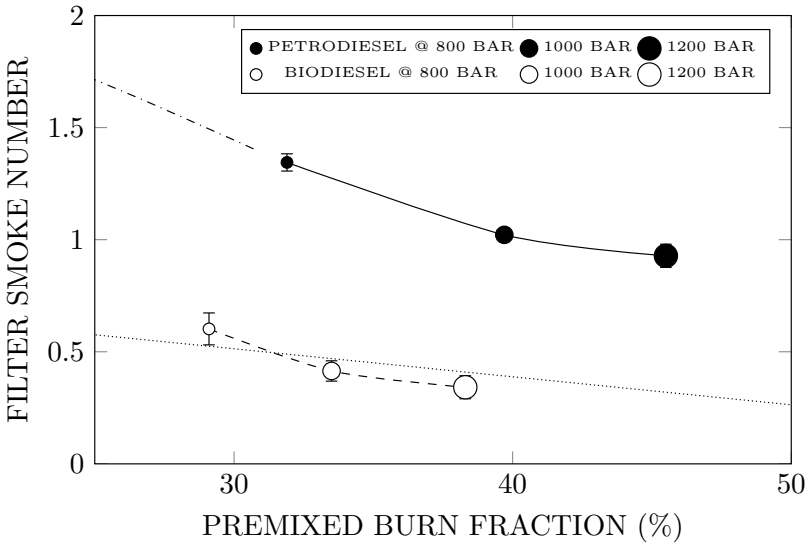

Figure 5.40: Filter smoke number as a function of premixed burn fraction for PETRODIESEL and BIODIESEL at injection pressures of 800, 1000 and 1200 bar (dashdotted and dotted lines represent the petrodiesel data and biodiesel fit from Figure 5.17).

The reduction in soot within the diesel jet is attributed to increased injection velocity,

which increases the lift-off length and therefore affords the opportunity for a greater degree of upstream air entrainment, reducing the equivalence ratio within the diffusion flame sheath. Additionally, increased injection velocity reduces the residence time of fuel and decomposition products within the oxygen depleted core of the jet, and therefore permits less time for soot formation and growth [686]. Within a diesel engine, combustion also concludes earlier at higher injection pressures (as will be seen in Section 5.3.2.3), with temperatures remaining higher for longer. Lower soot levels and higher post-combustion temperatures will tend to lead to lower quantities of soot persisting beyond the bulk gas soot burnout, and subsequently lower soot emissions [385, 686].

Figure 5.39B shows that the FSN measured when fuelling on PETRODIESEL was 1.34 at 800 bar, falling to 1.02 at 1000 bar and 0.93 at 1200 bar – reductions of 24% and 31%, respectively, compared to the 800 bar case. BIODIESEL recorded FSN values of 0.6, 0.41 and 0.34 at injection pressures of 800, 1000 and 1200 bar, respectively. These values mean that an increase in injection pressure from 800 to 1000 bar reduced BIODIESEL FSN by 31% and from 800 to 1200 bar by 43%; hence, increasing the injection pressure reduced BIODIESEL soot emissions more than it did those from PETRODIESEL, in percentage terms. As a result of this, the difference between PETRODIESEL and BIODIESEL soot emissions increases (proportionally) with increasing PMBF, BIODIESEL FSN being 55% lower than that of PETRODIESEL at 800 bar, 59% lower at 1000 bar, and 63% lower at 1200 bar; this is illustrated by Figure 5.40.

This trend is opposite to that observed in Study 1, where the most highly premixed conditions were associated with a smaller, rather than a larger, proportional difference between smoke emissions from petro- and biodiesel. Given that the NO_x trend in Study 2 is also different to that in Study 1 – in the sense that in Study 1 petro- and biodiesel NO_x emissions trends converged very slightly towards higher PMBF values, rather than rapidly diverging, as in Study 2 – it can be seen that in both cases an increase in the difference between FSN values tended to be accompanied by an increase in the difference between NO_x emissions. However, this is only true if the changes to both the FSN and NO_x emissions are considered in *percentage* terms. It can be seen in Figure 5.40 that the *absolute* difference in FSN decreases somewhat as PMBF increases, just as it did in Study 1.

So far as the hypothesis that soot concentrations have a causative effect on NO_x emissions via radiant heat loss, it would seem (intuitively) that the magnitude of the difference

in soot concentrations would be important in an absolute rather than a relative sense. For example, one would imagine that the difference in radiant heat loss would be greater between flames having soot volume fractions of 20 ppm and 8 ppm, than it would be between two having fractions of 8 ppm and 3 ppm; although the percentage difference is larger in the latter case, the absolute difference is larger in the former.

Therefore, although the data shows that a proportional reduction in sooting is associated with a proportional increase in NO_x emissions, it offers no convincing evidence that this relationship is causal. On balance it appears more likely that some factor which contributes to the sooting trends observed also contributes to the NO_x trends. Quite possibly, this factor is mixture stoichiometry.

At varying injection pressures, Figure 5.41 illustrates that CO emissions decline with increasing PMBF, in opposition to the trends observed in Study 1 (see Figure 5.19). The positive relationship between CO and PMBF in Study 1 was speculatively attributed to the increased proportion of combustion taking place under fuel-rich premixed conditions (rather than at the diffusion flame front) as PMBF increased. If this explanation is valid, then the reduction in CO emissions with increasing injection pressure may indicate a reduction in the equivalence ratios encountered within the premixed charge. Once again, CO emissions from BIODIESEL were significantly lower than those from PETRODIESEL (reduced by around 25% on average).

In Study 1 (see Figure 5.20) it was observed that THC emissions increased with increasing degree of premixing, and this trend is repeated at varying injection pressures in Figure 5.42. In Figure 5.41 it is apparent that Study 2 CO emissions for the 800 bar data points lie a little below the trendlines carried forward from Study 1. Similarly, THC emissions are a little lower than they were in Study 1, possibly due to some change in environmental conditions, or the condition of the engine, or the precise properties of the two fuels. However, apart from the slight downward shift, the THC trends are generally consistent between Study 1 and Study 2, although at an injection pressure of 1200 bar THC emissions from both fuels appear to fall a little below the anticipated gradient. This may be related to the more rapid combustion and higher in-cylinder temperatures encountered at higher injection pressures.

In Study 1 biodiesel CO_2 emissions seemed to be slightly higher than those of petrodiesel, and in the Study 2 data presented in Figure 5.43A this difference between the fuels is far clearer. The increase in CO_2 emissions when fuelling on biodiesel also appears to

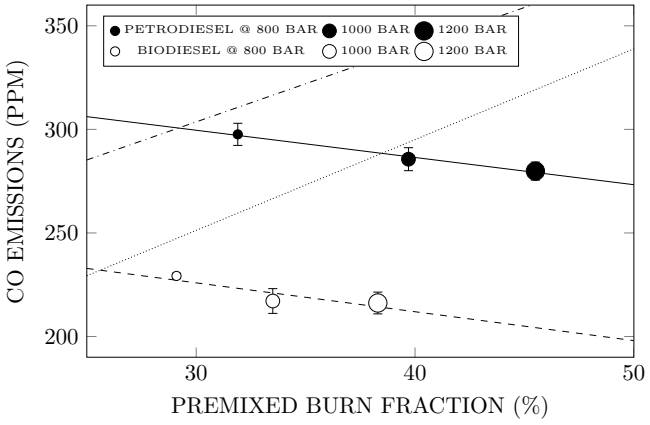

Figure 5.41: Carbon monoxide emissions as a function of premixed burn fraction for PETRODIESEL and BIODIESEL at injection pressures of 800, 1000 and 1200 bar (solid line represents PETRODIESEL best fit, dashed line represents BIODIESEL best fit; dashdotted and dotted lines represent continuations of the petro- and biodiesel fits from Study 1, Figure 5.19).

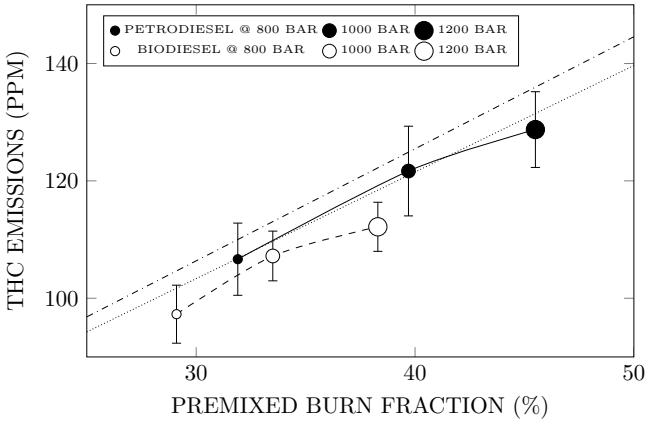

Figure 5.42: Total hydrocarbon emissions as a function of premixed burn fraction for PETRODIESEL and BIODIESEL at injection pressures of 800, 1000 and 1200 bar (dashdotted and dotted lines represent continuations of the petro- and biodiesel fits from Study 1, Figure 5.20).

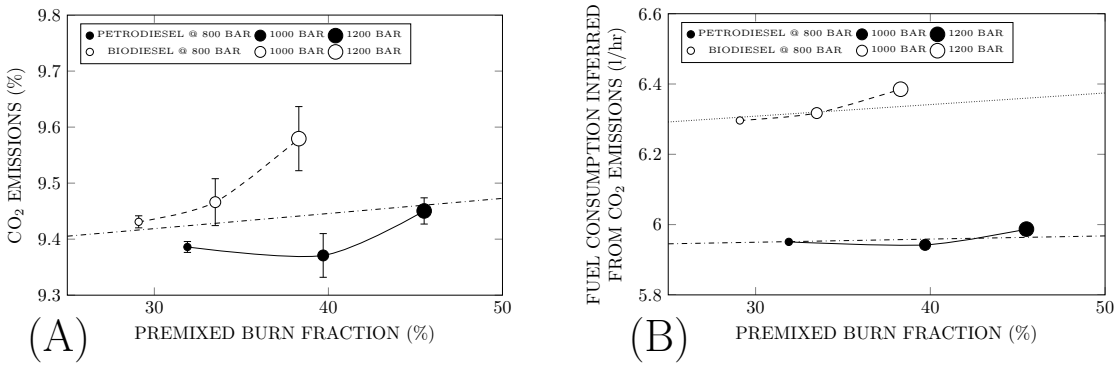

Figure 5.43: (A) Carbon dioxide emissions as a function of premixed burn fraction for PETRODIESEL and BIODIESEL at injection pressures of 800, 1000 and 1200 bar (dashdotted line represents continuation of the overall fit from Study 1, Figure 5.21A). (B) Volumetric fuel consumption rates inferred from carbon dioxide emissions and fuel properties, as a function of premixed burn fraction for PETRODIESEL and BIODIESEL at injection pressures of 800, 1000 and 1200 bar (dashdotted and dotted lines represent continuations of the petro- and biodiesel fits from Study 1, Figure 5.21B).

increase with increasing injection pressure; at 800 bar, BIODIESEL had CO_2 emissions 0.5% higher than those of PETRODIESEL, at 1000 bar they were 1% higher, and at 1200 bar they were 1.4% higher. Consequently, the trends appear to diverge with increasing PMBF. The inferred fuel consumption trends in Figure 5.43B therefore also diverge, fuel consumption being approximately 5.8% higher for BIODIESEL at 800 bar, and 6.6% higher at 1200 bar.

The BIODIESEL data implies that there may be a slight increase in fuel consumption with increasing injection pressure (an increase between BIODIESEL @ 800 BAR and BIODIESEL @ 1200 BAR of 1.5%). Brake specific fuel consumption (BSFC) can be reduced by increasing injection pressure [687], although this depends how other variables are controlled; variations in combustion phasing, for instance, may lead to increases in BSFC with increasing injection pressure [688]. In the laboratory engine, it is likely that reductions in fuel consumption with increasing injection pressure could be achieved if timing were optimised, giving consideration to factors like piston geometry. However, under the studied conditions, with constant SOC, simply increasing the injection pressure appears to impart no advantage in terms of BSFC.

5.3.2.3 HEAT RELEASE AND PRESSURE

Considering the patterns of apparent heat release and how they relate to NO_x emissions for the different fuels, Figure 5.44 illustrates that, as was the case in Study 1 (see Figure 5.22), it appears to be combustion progress in the later stages of heat release that corresponds best to the levels of NO_x emitted. The general trend which was observed in Study 1, with the biodiesel curves falling behind through the premixed burn on account of their lower PMBFs, but in the ascendancy through the later stages of combustion (due to increased diffusion heat release rates), is also demonstrated in Figure 5.44.

By the time that 90% of total AHR has occurred, the order of combustion progress is exactly matched to the order of NO_x emissions; that is to say, the fuel and condition that reached the 90% interval soonest had the highest NO_x emissions, that which reached the interval last had the lowest, and the others between them were also correctly ranked. However, unlike in Figure 5.22 where the ordering was imperfect but the correlation between combustion progress in the later stages and NO_x emissions was reasonably good, in Figure 5.44 the correlation is relatively poor. At 800 bar, where BIODIESEL NO_x emissions were only very slightly higher than those of PETRODIESEL, the difference in combustion

progress between the two fuels is large across the 70–90% intervals, whereas at 1200 bar, where BIODIESEL NO_x emissions were higher than those of PETRODIESEL by a greater margin, BIODIESEL combustion progress does not exceed that of PETRODIESEL at all until relatively late in the process, and even then only by a very small amount.

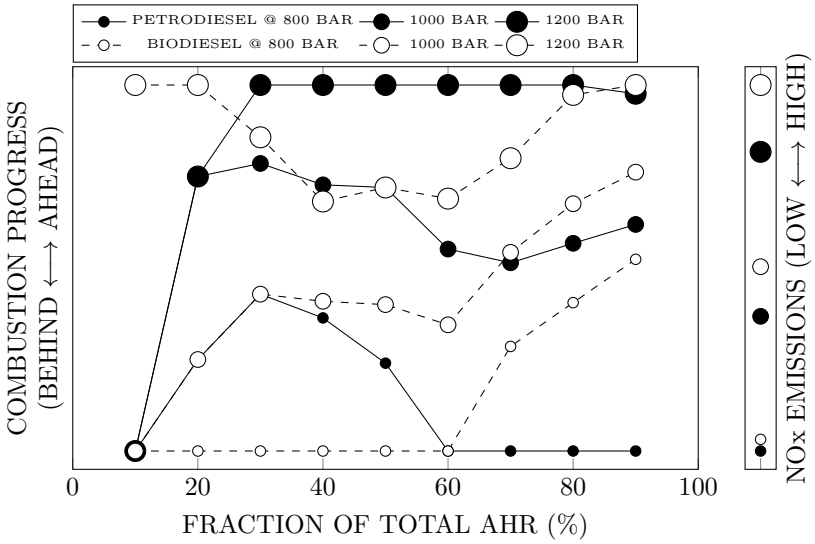

Figure 5.44: Relative combustion progress for PETRODIESEL and BIODIESEL at injection pressures of 800, 1000 and 1200 bar. The vertical position of each fuel indicates how quickly it reached the interval on the x-axis; the fuel that reached the interval earliest is at the top, the fuel that reached it latest is at the bottom, and the other fuels are distributed between based on their timing relative to the slowest and fastest fuels. NO_x emissions distributed similarly are given on the right-hand side.

The highest correlation between combustion progress and NO_x emissions occurs at the 80% interval, where $r^2 = 0.87$ (in Study 1, see Figure 5.23, the maximum $r^2 = 0.94$ and was reached at the 70% interval); this is illustrated in Figure 5.45A. However, as Figure 5.45B shows, even in the best correlated case, there is very little predictive merit to the combustion progress data, beyond the fact that higher injection pressures correspond to an increase in both values. On this basis, it may be reasonable to propose that the difference between the fuels that causes a relative increase in NO_x emissions from biodiesel with increasing injection pressure is not directly related to the rate at which combustion progresses, in and of itself.

It is, however, worth considering that the lack of correlation between combustion progress and NO_x emissions in this case may be because no single interval is a suitable representative for all fuels and conditions. That is, in Figure 5.44, the difference in combustion progress between PETRODIESEL and BIODIESEL corresponds exactly to the difference in NO_x emissions at the 800 bar injection pressure (that is, the vertical separation of the 800 bar combustion progress curves is equal to the vertical separation of

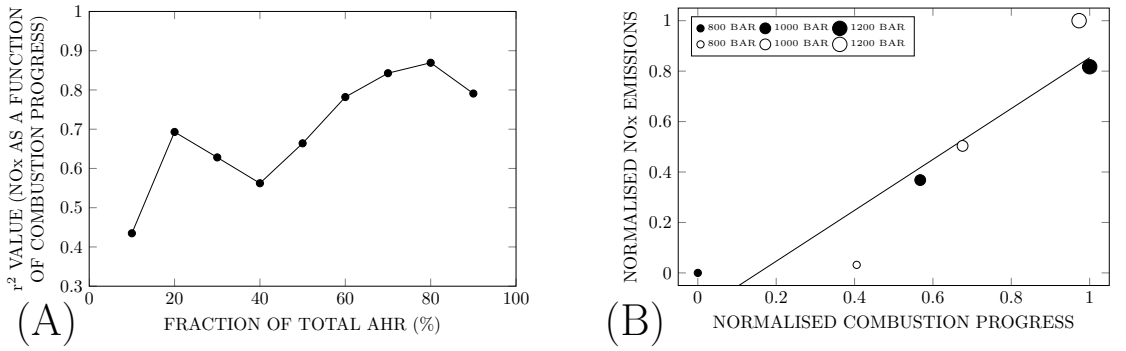

Figure 5.45: (A) r^2 values for linear fits through normalised NO_x emissions as a function of normalised combustion progress, at AHR intervals from 10–90% of total AHR, for PETRODIESEL and BIODIESEL at injection pressures of 800, 1000 and 1200 bar. (B) Normalised NO_x emissions as a function of normalised combustion progress at the 80% interval (solid line is linear best fit).

the associated NO_x points) at a point early in the 60–70% period, while exact correspondence at 1000 bar is reached during the 80–90% period, and (although depicting the 100% interval has been avoided due to the inconsistency associated with its calculation) a closer relationship between the timing of heat release and NO_x emissions at 1200 bar seems to arise in the data as the 100% AHR point (i.e. the end of combustion) is approached. In Study 1, where patterns of heat release and combustion progress were less varied across the data set, a single interval could be identified (the CA70) which gave fair representation to all fuels, but in Study 2, no single point achieves the same, possibly due to the increased range of combustion behaviour.

Overall, for a given PMBF, the differences between the patterns of heat release for the two fuels are much the same at the highly premixed, higher injection pressure conditions as they were in Study 1. This can be seen in Figure 5.46, which shows the BIODIESEL @ 1200 BAR data alongside a plot of the average of PETRODIESEL @ 800 BAR and PETRODIESEL @ 1200 BAR data, in order to make a comparison between the two fuels at a similar degree of premixing (PMBFs of 38.7% and 38.3% for the PETRODIESEL and BIODIESEL plots, respectively).

Just as in Study 1 (see Figure 5.32), in Figure 5.46 the biodiesel AHRR is higher through the first part (0–20%) and slower through the later stages of the premixed burn (20–40%), resulting in an average AHRR through the premixed burn which is approximately the same for both fuels for the same PMBF; consequently, ΔP_{pmb} also shows little dependence on fuel type, as Figure 5.47A shows. The ΔP_{pmb} trends are also largely consistent with the data from Study 1, to the extent that correlation lines can be plotted through petro- and biodiesel data sets from both studies, and, indeed, through the combined set of all Study 1 and 2 data, with $r^2 = 0.99$. However, the difference between

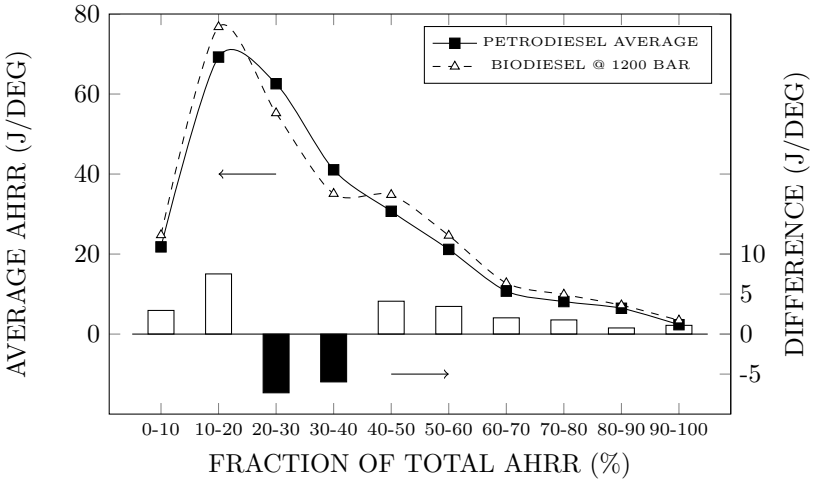

Figure 5.46: Average apparent heat release rate throughout the combustion process for PETRODIESEL and BIODIESEL, and the average difference between the two over each period (white bars indicate an increase in AHRR when fuelling on BIODIESEL, black bars a decrease). PETRODIESEL data calculated as the average of PETRODIESEL @ 800 BAR and PETRODIESEL @ 1200 BAR, with a mean premixed burn fraction of 38.7%. BIODIESEL data represented by the BIODIESEL @ 1200 BAR data set, with a PMBF of 38.3%.

the BIODIESEL @ 1200 BAR and PETRODIESEL @ 1200 BAR points suggests the possibility that ΔP_{pmb} may be slightly higher for the biodiesel points for the same degree of mixing under the higher injection pressure conditions, although the influence which differences in PMBF have on ΔP_{pmb} are far more significant than any other effects of fuel type.

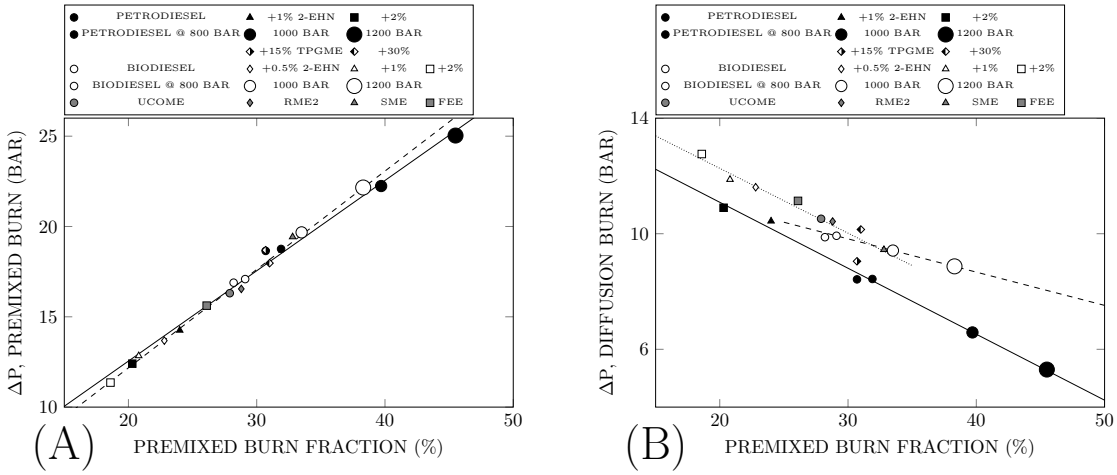

Figure 5.47: Pressure change across (A) the premixed burn phase and (B) the diffusion burn phase, as functions of premixed burn fraction for PETRODIESEL and BIODIESEL at injection pressures of 800, 1000 and 1200 bar, plotted in combination with the complete Study 1 data set (solid lines represent overall petrodiesel best fits; in (A) dashed line represents overall biodiesel best fit, in (B) dashed line represents varying injection pressure BIODIESEL best fit, and dotted line represents Study 1 biodiesel best fit).

In Figure 5.46, like its Study 1 equivalent, Figure 5.32, BIODIESEL AHRR through post-premixed combustion is higher than that of PETRODIESEL. This is also illustrated

in Figure 5.48A, which presents similar trends in average post-premixed AHRR to those seen in Study 1 (see Figure 5.24), both in terms of the gradient of decline with increasing PMBF, and the fact that the BIODIESEL points are consistently above the PETRODIESEL ones. However, both PETRODIESEL and BIODIESEL post-premixed AHRR values are lower, for a given PMBF, than they were in Study 1, more substantially so for PETRODIESEL; this seems to be a result of reduced AHRR through the slower second half of post-premixed combustion – that is, late-combustion. It is possible that the general reduction has some connection to changes in the condition of the engine, and the larger drop between studies with PETRODIESEL could have something to do with slight changes to the composition of the fuel.

Although Figure 5.48A illustrates an increase in post-premixed AHRR, it does not explain the divergence from the Study 1 ΔP_{diff} trend which is seen in Figure 5.47B. In Study 1 ΔP_{diff} was increased when fuelling on biodiesel by an approximately consistent amount at all PMBFs; in Figure 5.47B it can be seen that the Study 1 data, and the associated best fit line (dotted), run approximately parallel to the petrodiesel data and fit (solid). The Study 2 BIODIESEL data, associated with the dashed best fit line in Figure 5.47B, descends at a shallower gradient, and as a result the difference between PETRODIESEL and BIODIESEL ΔP_{diff} in Study 2 appears to become larger towards more highly premixed conditions. Since, for the most part, this isn't due to a variation in the rate of heat release (because the difference in average AHRR between PETRODIESEL and BIODIESEL is essentially constant, as seen in Figure 5.48A), and therefore isn't primarily due to a difference in the *rate* of pressure change, it follows that variation in the *duration* of the pressure change must drive the divergence of the Study 2 ΔP_{diff} trends. In Figure 5.48B, it can be seen that this is the case, with the duration of the diffusion pressure rise falling far less dramatically for BIODIESEL at the highest injection pressures.

The effect of the higher BIODIESEL ΔP_{diff} values is to offset the reduction in ΔP_{pmb} which occurs as a result of the reduced biodiesel ignition delay and PMBF. In Figure 5.49A the maximum in-cylinder pressure data for both fuels at varying injection pressures can be seen. It is clear that the P_{max} trend diverges as a function of PMBF, in keeping with the increased difference in ΔP_{diff}, as degree of premixing increases. Figure 5.49B shows the retardation of the angle of maximum in-cylinder pressure when fuelling on BIODIESEL, and the slight divergence of this trend towards higher PMBFs, consistent with the longer pressure rise duration seen in Figure 5.48B. In Study 1, petro- and biodiesel Θ_{Pmax} trends

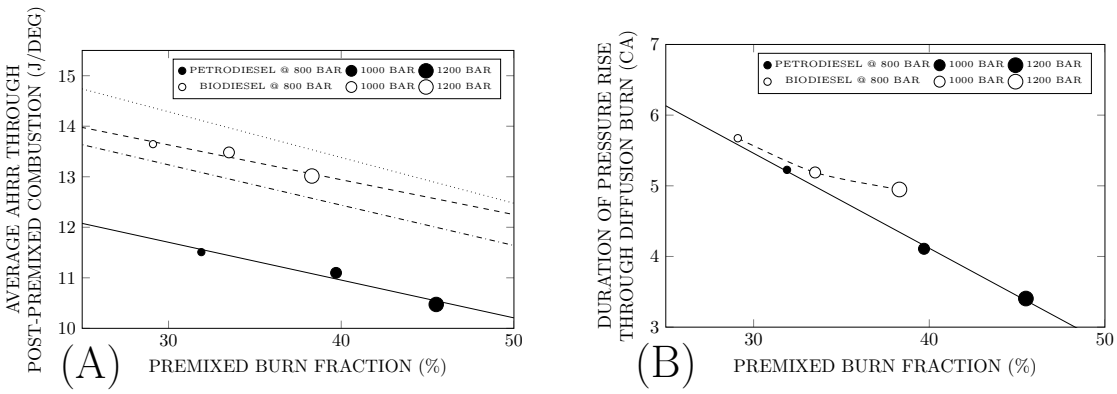

Figure 5.48: (A) Average apparent heat release rate through the post-premixed combustion phase, as a function of premixed burn fraction for PETRODIESEL and BIODIESEL at injection pressures of 800, 1000 and 1200 bar (solid line represents PETRODIESEL best fit, dashed line represents BIODIESEL best fit; dashdotted and dotted lines represent continuations of the petro- and biodiesel fits from Study 1, Figure 5.24). (B) Duration of pressure rise through the diffusion phase, as a function of premixed burn fraction for PETRODIESEL and BIODIESEL at injection pressures of 800, 1000 and 1200 bar (solid line represents PETRODIESEL best fit).

converged with increasing PMBF (see Figure 5.33B), because P_{max} occurred late enough in the cycle under these conditions that the period through the diffusion burn over which biodiesel had higher AHRR was already completed (that is, the period depicted in Figures 5.26 and 5.27). At the higher injection pressures, the more rapid initial heat release, associated with highly premixed combustion, advanced Θ_{Pmax}, such that it occurred while the BIODIESEL AHRR was still significantly above that of PETRODIESEL, leading to relative retardation of the BIODIESEL Θ_{Pmax}. It is possible that a slight increase in fuel consumption at higher injection pressures when fuelling on BIODIESEL, as seen in Figure 5.43B, may also have contributed to this, by necessitating some small further extension of the injection event.

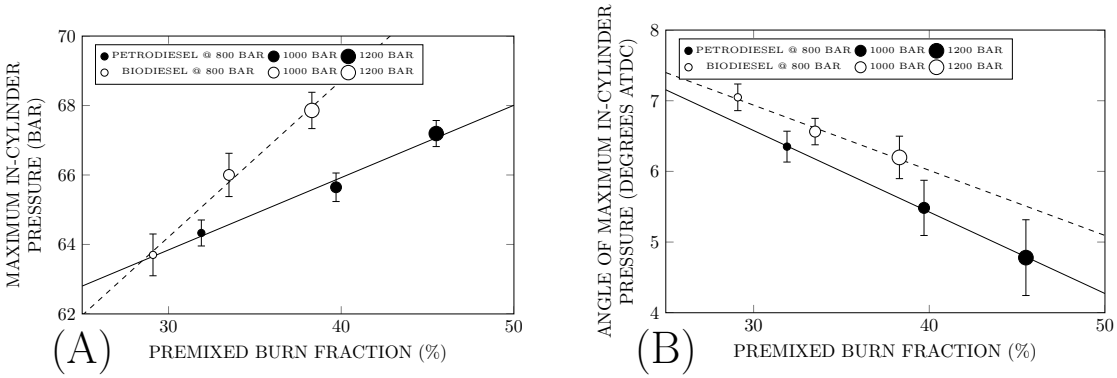

Figure 5.49: (A) Maximum in-cylinder pressure and (B) angle of maximum in-cylinder pressure, as functions of premixed burn fraction for PETRODIESEL and BIODIESEL at injection pressures of 800, 1000 and 1200 bar (solid lines represent petrodiesel best fits, dashed lines represent biodiesel best fits).

Unlike in Study 1 where some of the variation in diffusion pressure rise duration be-

tween petro- and biodiesel was due to changes in the timing of the end of the premixed burn, in Study 2 almost all of the variation in duration appears to be due to changes in the angle of maximum pressure.

In Study 1 (see Figure 5.35) it was seen that ΔP_{diff} was dependent upon the duration of the pressure rise, and that for a given duration of pressure rise the various biodiesels, as well as the PETRODIESEL and TPGME blends, tended to have larger ΔP_{diff} values. Figure 5.50 shows that the varying injection pressure data was consistent with the previously observed trends in this respect. Hence, in Study 2, the slightly higher rate of pressure rise makes a small contribution to the increasing difference between PETRODIESEL and BIODIESEL ΔP_{diff} values, but the most significant driver of this effect is the relative extension of the BIODIESEL pressure rise duration.

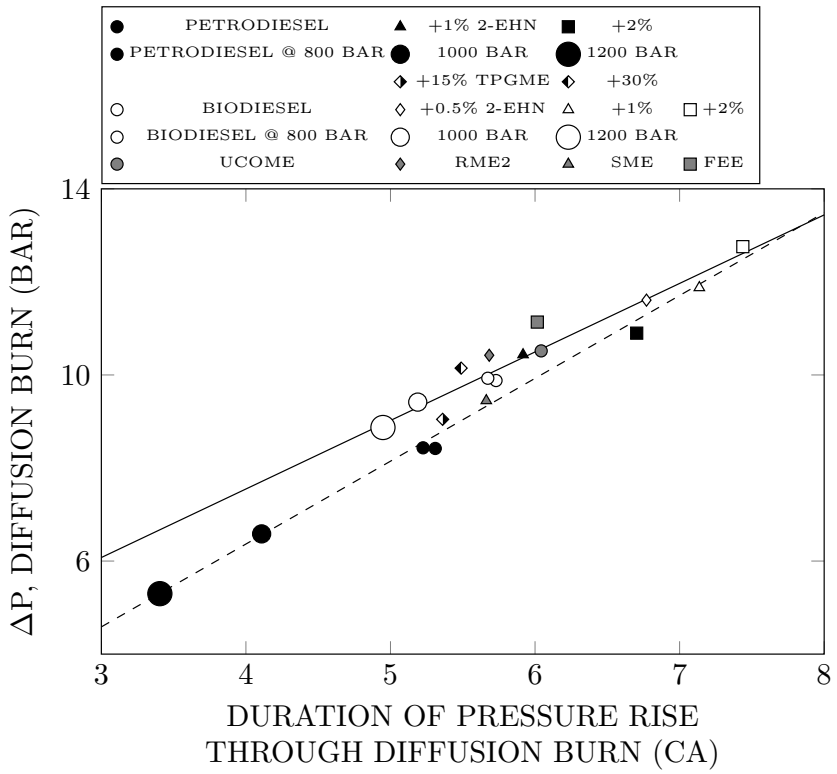

Figure 5.50: Magnitude of pressure rise through the diffusion phase of combustion, as a function of the duration of the diffusion pressure rise period for PETRODIESEL and BIODIESEL at injection pressures of 800, 1000 and 1200 bar, plotted in combination with the complete Study 1 data set (solid line represents overall petrodiesel best fit, dashed line represents overall biodiesel best fit).

The BIODIESEL pressure rise is extended by the retardation of Θ_{Pmax}. This retardation is due to the same period of increased AHRR through the diffusion burn phase when fuelling on BIODIESEL which was important in Study 1. Increasing injection pressure advances Θ_{Pmax}, which brings the pressure maximum forward into the period of higher BIODIESEL AHRR, and this leads to the relative retardation of BIODIESEL Θ_{Pmax}.

That is, when PETRODIESEL AHRR falls below the level sufficient to maintain pressure rise, BIODIESEL AHRR is higher than that of PETRODIESEL by a margin wide enough to prolong pressure rise for a relatively significant period. Although retardation of Θ_{Pmax} is not necessarily associated with higher P_{max} values, in this study the fact that Θ_{Pmax} occurred later when fuelling on BIODIESEL meant that pressure rose further following the EOPMB, leading to increased P_{max}.

Comparing Figures 5.38 and 5.49A, there appears to be a certain similarity in appearance between the P_{max} plot and the NO_x emissions plot. Just as NO_x emissions from the two fuels increase with PMBF, and diverge with increasing PMBF, so do the measured P_{max} values. Maximum in-cylinder pressures at 1000 and 1200 bar injection pressures were significantly higher when fuelling on BIODIESEL than when fuelling on PETRODIESEL, despite the smaller degree of premixing and generally slower heat release observed for BIODIESEL at these conditions. NO_x emissions as a function of P_{max} are shown in Figure 5.51.

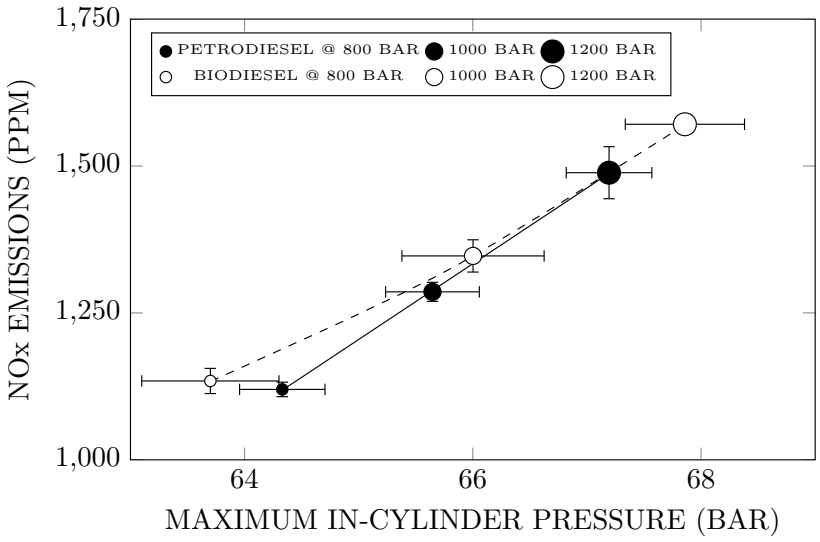

Figure 5.51: Oxides of nitrogen emissions as a function of maximum in-cylinder pressure for PETRODIESEL and BIODIESEL at injection pressures of 800, 1000 and 1200 bar (solid line represents PETRODIESEL best fit, dashed line represents BIODIESEL best fit).

When viewed in this way, NO_x emissions for the two fuels converge with increasing P_{max}, and hence with increasing injection pressure, rather than diverging, as in Figures 5.38 and 5.39A.

In summary, when running at varying injection pressures NO_x emissions do not correspond as well with rates of combustion progress as was the case in Study 1, but the best correlation is still achieved during the later stages of combustion, at around the 80% in-

terval. Differences between the rates of heat release for PETRODIESEL and BIODIESEL follow similar patterns as in Study 1, and this can be seen by comparing Figure 5.46 with Figure 5.32. The most significant difference between the fuels, and the factor which causes the BIODIESEL ΔP_{diff} and P_{max} trends to diverge from the PETRODIESEL trends with increasing injection pressure and PMBF, is the retardation of Θ_{Pmax} when fuelling on BIODIESEL. The retardation of Θ_{Pmax} is due to the higher BIODIESEL diffusion AHRR, and is made more significant at higher injection pressures by the general advance of Θ_{Pmax} to a point at which the instantaneous BIODIESEL AHRR exceeds PETRODIESEL AHRR by a larger margin.

5.3.3 STUDY 3: LOWER LOAD EXPERIMENTS

5.3.3.1 PREMIXING

The third set of experiments involved running the engine at a relatively low load. At such operating conditions, the premixed burn fraction generally comprises a large proportion of total heat release, firstly, because the injection event is shorter and total heat release is reduced, and, secondly, because there is a tendency for ignition delay to be slightly extended, on account of the cooler in-cylinder temperatures, prolonging mixing times. Running at similar conditions, it has been found in the past (see Chapter 4) that NO_x emissions from biodiesel may be lower than those from petrodiesel. This was attributed to the reduced PMBF when fuelling on biodiesel, which was suggested to be of greater importance under more highly premixed conditions for reasons possibly related to radiative heat losses, variations in the diffusion burn rate and changes to the oxygen equivalence ratio [14, 543].

Under the lower load the objective was to establish, by addition of 2-EHN, what the effects of changing degree of premixing would be, and how these effects might compare to those observed at the higher load. If the small relative reduction in ignition delay, and consequently reduced PMBF, when fuelling on biodiesel was the reason that biodiesel NO_x emissions were less than those when fuelling on petrodiesel under the lower load in Chapter 4, then would a biodiesel with a longer ignition delay have NO_x emissions which exceeded those of petrodiesel? Also, by reducing the PMBF to a level comparable to that observed under higher load operating conditions, the hypothesis that the load dependence of the magnitude of the biodiesel NO_x increase is related to premixing might be examined more clearly. That is, if sufficient 2-EHN were added to the fuels that operating PMBF

under lower load were approximately equal to that under the higher load, would the magnitude of the biodiesel NO_x increase also be the same under both conditions?

Unlike in Study 1 at the higher load (see Figure 5.12), Figure 5.52 shows that the addition of 2-EHN reduced the ignition delay of both fuels to approximately the same extent, in both cases with slightly diminishing returns with further addition. Addition of 2-EHN tended to reduce ignition delay more greatly at the lower load than at the higher load. At the higher load PETRODIESEL+2% 2-EHN had an ignition delay 1.375 CA shorter than that of PETRODIESEL, whereas at the lower load it was 1.625 CA shorter; at the higher load the ignition delay of BIODIESEL+2% 2-EHN was shorter than that of BIODIESEL by 1.5 CA, whereas at the lower load it was 1.625 CA shorter. This is consistent with the assertion that 2-EHN is more effective under lower temperature conditions [664]. However, at the higher load the BIODIESEL+0.5% 2-EHN ignition delay was 0.875 CA shorter than that of BIODIESEL, but at the lower load it was 0.75 CA shorter, in seeming contradiction of the trend.

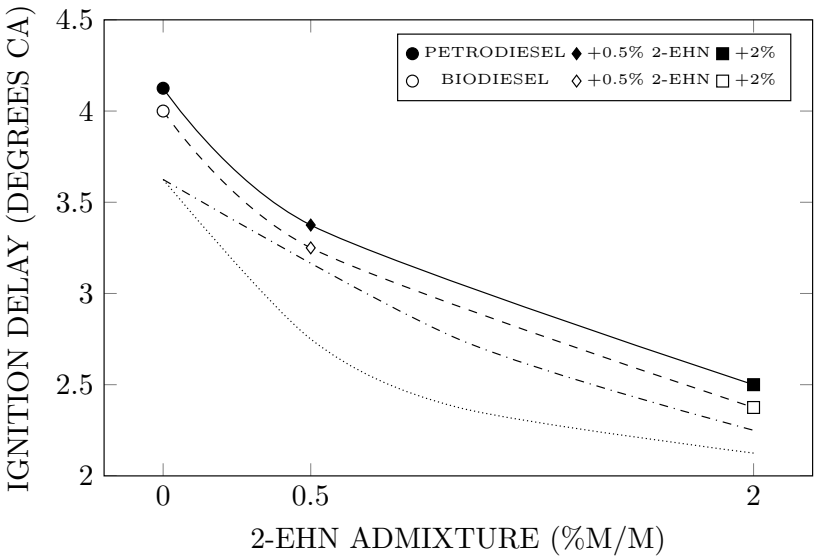

Figure 5.52: Effect of varying levels of 2-ethylhexyl nitrate addition on the ignition delay of PETRODIESEL and BIODIESEL under the lower load condition (the solid line is the PETRODIESEL curve, the dashed line is the BIODIESEL curve; dashdotted and dotted curves are carried forward from Study 1, Figure 5.12.

The BIODIESEL ignition delay was shorter than that of PETRODIESEL at all levels of 2-EHN admixture, consistently reduced by one division of the encoder (0.125 CA). As expected, ignition delay was longer at the lower load in all cases, due to the lower in-cylinder temperatures. Further confirmation of this is seen in Figure 5.53, which shows ignition delay as a function of predicted cetane number for all fuels at the lower load,

alongside the linear fit from Study 1 (Figure 5.13) for the purposes of comparison.

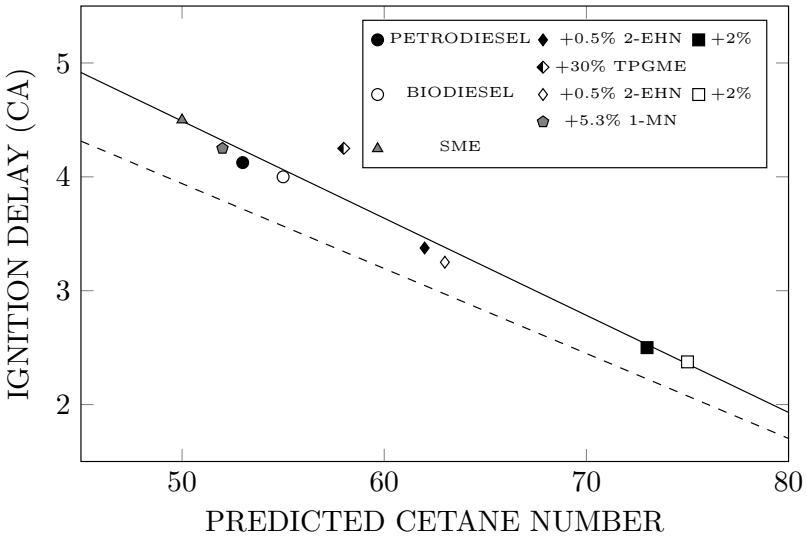

Figure 5.53: Ignition delay as a function of predicted cetane number for all tested fuels under the lower load condition (solid line represents best fit through lower load data, dashed line represents best fit carried forward from higher load data in Study 1, Figure 5.13).

Just as at the higher load in Study 1, the relationship between the estimated cetane numbers and measured ignition delays is reasonably linear ($r^2 = 0.95$), with PETRODIESEL+30% TPGME respresenting the only significant deviation from the trend, providing further evidence that the TPGME used throughout this work was not well represented by the high cetane numbers reported in the literature (for reasons possibly related to the isomeric composition of the TPMGE used). 1-Methylnaphthalene (1-MN), with a CN of 0, reduced the estimated ignition quality of the BIODIESEL to which it was added, and this reduction coincided closely to the increase in ignition delay observed in practice.

In Study 1 (see Figure 5.14) the biodiesels appeared to form a slightly smaller premixed burn fraction than petrodiesel for the same ID; to a limited extent the lower load data is consistent with this, as Figure 5.54 illustrates. However, the gap between the fuel types appears to be nullified at more highly premixed conditions. In connection with the Study 1 results, differences between petro- and biodiesel apparent heat release rates through the later part of premixing supplemented combustion were discussed as a possible contributor to the perceived increase in petrodiesel PMBF as a function of ignition delay. In Figure 5.54, the fact that there is little difference between the more highly premixed fuels may be because heat release through the end of the premixed burn shows less dependence on fuel type at the lower load. This may be related to the point at which the injection event concludes.

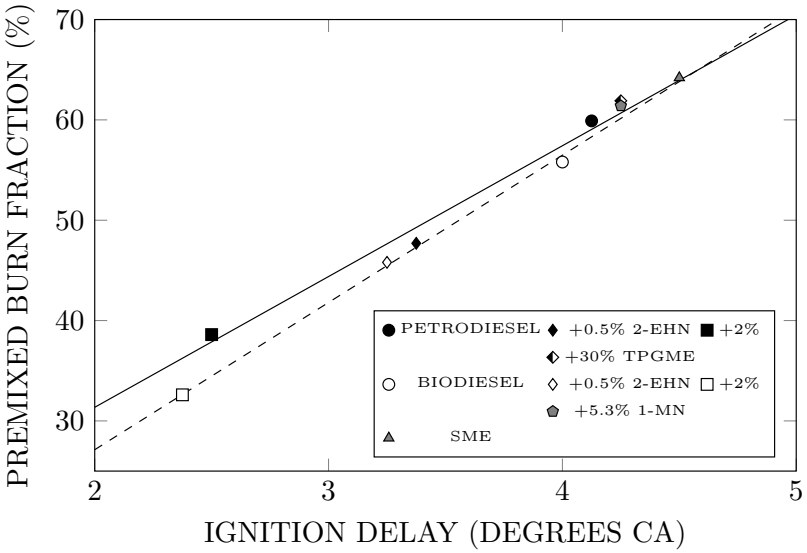

Figure 5.54: Premixed burn fraction as a function of ignition delay for all tested fuels under the lower load condition (solid line represents petrodiesel best fit, dashed line represents best fit through the 4 biodiesel points, including SME but excluding BIODIESEL+5.3% 1-MN).

The addition of TPGME to PETRODIESEL, as at the higher load, increased PMBF slightly, in keeping with the small increase in ID. Likewise, the addition of 1-MN to BIODIESEL increased the degree of premixing. As in Study 1, SME had the longest ignition delay, on account of its highly unsaturated composition, and consequently formed the largest PMBF of all the tested fuels. As at the higher load, the correlation between ignition delay and PMBF appears to be approximately linear, based on the data collected.

5.3.3.2 NO_x EMISSIONS

Under the lower load, NO_x emissions from BIODIESEL were lower than those from PETRODIESEL by around 2.8%. Examination of Figure 5.55 certainly suggests that the relative reduction in BIODIESEL NO_x emissions at this condition (in contrast to the 7% increase measured at the higher load) is associated with the smaller biodiesel PMBF, and the fact that the gap between the petro- and biodiesel trendlines is substantially reduced compared to Study 1 (see Figure 5.15). Fuelling on SME, where the ignition delay is extended and the PMBF is larger than that of PETRODIESEL, NO_x emissions are considerably higher; SME had NO_x emissions 8.3% higher than those of PETRODIESEL, and 11.3% higher than those of BIODIESEL.

This demonstrates that NO_x emissions from any particular biodiesel are not necessarily lower than those of petrodiesel when operating at lower loads, just as they are not necessarily higher than those of petrodiesel at higher loads. Everything hinges on the

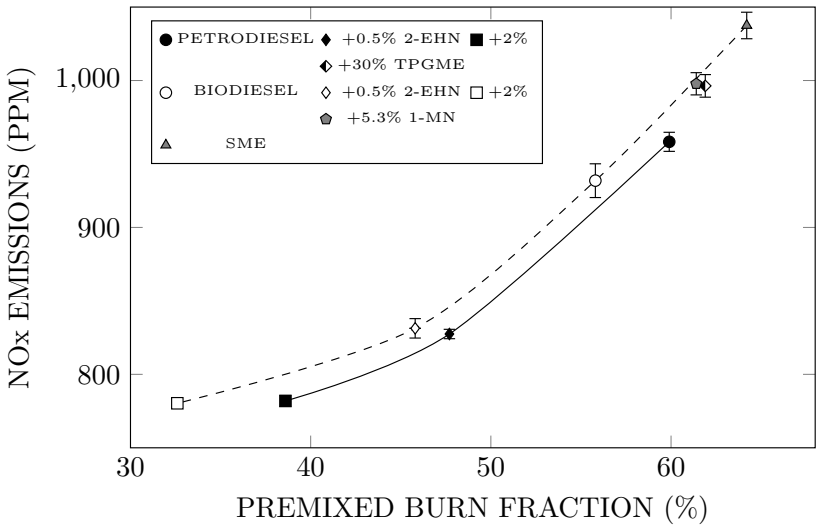

Figure 5.55: Oxides of nitrogen emissions as a function of premixed burn fraction for all tested fuels under the lower load condition (solid line represents petrodiesel best fit, dashed line represents best fit through the 4 biodiesel points, including SME but excluding BIODIESEL+5.3% 1-MN).

properties of the specific fuels being compared, especially their ignition characteristics. In all instances, it appears that fuelling on biodiesel leads to higher NO_x emissions than fuelling on a petrodiesel with the same premixed burn fraction; at lower load, however, the like-for-like difference is smaller.

Unlike at the higher load (in Studies 1 and 2), Figure 5.55 suggests that the relationship between NO_x emissions and PMBF at the lower load is non-linear, appearing to become steeper as PMBF increases. Because the relationship between NO_x and PMBF becomes increasingly steep with increasing PMBF, the effects of small differences in ignition delay and premixing become accentuated and cause significant variations in NO_x emissions. Consequently, despite the biodiesel NO_x trend still exceeding that of petrodiesel for any given PMBF, the small leftward-shift caused by a reduction in ignition delay and PMBF is enough to negate the gap between the correlation lines at lower load, particularly when the PMBF is large. In Chapter 4 it was hypothesised that NO_x emissions from petro- and biodiesel may converge towards more highly premixed conditions, and that this may be why NO_x emissions from biodiesel are reduced relative to those of petrodiesel when the operating PMBF is large. Figure 5.55 shows that this is incorrect. There is less separation between the petro- and biodiesel trends at lower load, regardless of the degree of premixing; that is, PMBF itself is not the determining factor, although the change in the relationship between NO_x emissions and PMBF is critical.

Although in Studies 1 and 2 (Figures 5.15 and 5.38) no significant non-linearity is evident in the relationship between NO_x emissions and PMBF, these data sets cover

smaller PMBF ranges (15–35% and 25–50%, respectively). However, considered over a similar PMBF range (for instance, 30–50%), Figure 5.55 does not suggest significant non-linearity either – it is not until the trend is extended further that this tendency becomes apparent. It may be plausible that, under any operating conditions, if combustion could be varied over a sufficiently wide range of PMBFs, the relationship between NO_x and PMBF would become non-linear, but more experiments would be required to confirm this.

What can be concluded definitively at this stage is that the gap between the petro- and biodiesel PMBF-NO_x correlation lines is not dependent solely on PMBF, and that the conclusions of Chapter 4 (see Figure 4.13) therefore oversimplify the problem. In Study 1, at a PMBF of around 35%, the data trends suggest that biodiesel NO_x emissions would be around 10% higher than those of petrodiesel. At the lower load, at the same PMBF of 35%, extrapolation of the data suggests an increase in biodiesel NO_x emissions of around 3%. Hence, there is clearly some other load dependent variable, or variables, which affect the relationship between premixing and NO_x.

The addition of 1-MN to BIODIESEL caused a significant increase in NO_x emissions; 7.1% over the neat BIODIESEL. This seems to be largely attributable to the increase in PMBF. It may also be possible that the addition of 1-MN could increase NO_x emissions, other things being equal, on account of an increase in adiabatic flame temperature; alkylnaphthalenes have flame temperatures exceeding those of most common biodiesel components [558]. Although in this instance it does not seem to be necessary to invoke this explanation, other studies have reported that the addition of 1-MN to a diesel fuel surrogate (*n*-heptane) increased NO_x emissions beyond what might be expected on the basis of increased mixing time alone [689].

It is noteworthy that BIODIESEL+5.3% 1-MN yielded NO_x emissions almost identical to those from PETRODIESEL+30% TPGME. The intention of these additions was to remove what were viewed to be two of the most significant differences between petro- and biodiesel – that is, aromatic and oxygen content. With these differences reduced, it can be seen that NO_x emissions from the two fuels approached parity. However, this is likely to be – at least in part – the result of a fortunate coincidence, which happened in this case to produce two fuels with similar ignition characteristics.

The addition of TPGME to PETRODIESEL is seen, as in Study 1 (see Figure 5.15) to increase NO_x emissions, by approximately 4% in this case, slightly below the NO_x emissions projected for biodiesel at the same PMBF, and slightly above those projected

for petrodiesel. This is much less than the 12% increase in NO_x emissions observed in the Study 1 higher load experiments when fuelling on PETRODIESEL+30% TPGME, suggesting that fuel oxygenation has a lesser effect on NO_x emissions at lower load (despite the larger impact of the increase in PMBF that accompanies the addition of TPGME). On the whole, this is consistent with the biodiesel NO_x emissions trend, which appears to exceed the petrodiesel trend by around 2–2.5% at PMBFs of 40% and 50% in Figure 5.55, whereas at the higher load in Study 1, NO_x emissions were, on average, around 12.5% higher for biodiesel for a given PMBF.

In summary, at the lower load the relationship between NO_x emissions and degree of premixing appeared to be non-linear. The like-for-like increase in biodiesel NO_x emissions compared to those of petrodiesel was, at any given PMBF, considerably smaller than at higher load. However, the smaller like-for-like NO_x increase at the lower load is not, as suggested in Chapter 4, simply a result of the more highly premixed operating conditions; even where the degree of premixing was apparently the same as at the higher load, the increase in NO_x emissions remained smaller. Due to the reduced biodiesel NO_x increase for a given PMBF, BIODIESEL, which had a slightly shorter ignition delay and smaller PMBF than PETRODIESEL yielded lower NO_x emissions, although SME, which had a longer ignition delay, still had NO_x emissions well in excess of those of PETRODIESEL.

5.3.3.3 FILTER SMOKE NUMBER

At the lower load, filter smoke number is substantially reduced in comparison to the higher load experiments in Study 1 (see Figure 5.17), as Figure 5.56 shows. For PETRODIESEL and BIODIESEL, FSN values are reduced by 85% and 73%, respectively, compared to Study 1, while for PETRODIESEL+2% 2-EHN and BIODIESEL+2% 2-EHN, FSNs are 73% and 61% lower at the lower load. The reduction in FSN is related to the reduction in the quantity of diffusion combustion at the lower load; the total quantity of heat release is lower, and the PMBF constitutes a larger proportion of it. The slightly prolonged ignition delay at lower load further increases the size of the PMBF, and may reduce equivalence ratios throughout the premixed charge. Lower in-cylinder temperatures should also lead to an extension of the lift-off length, reducing the equivalence ratio within the diffusion flame sheath, deterring soot formation.

FSN and PMBF appear to correlate with reasonable linearity, moving towards convergence at more highly premixed conditions. At a PMBF of 38.6%, the biodiesel trend

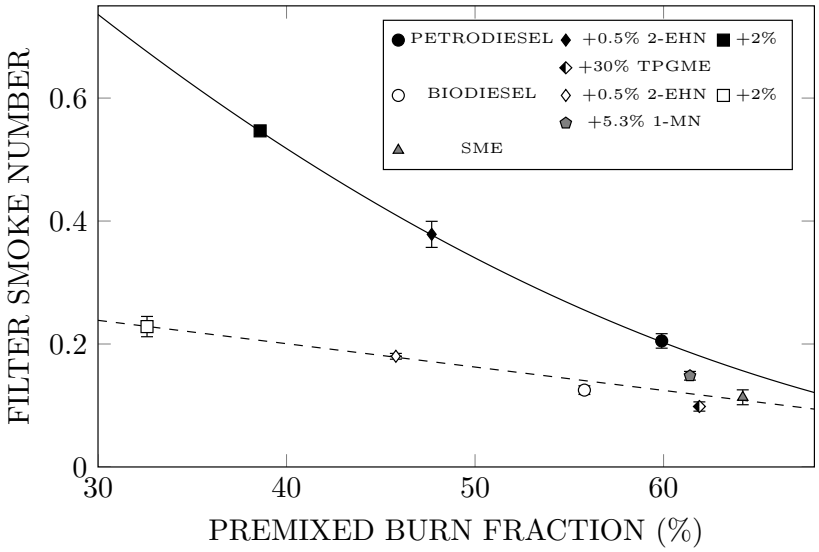

Figure 5.56: Filter smoke number as a function of premixed burn fraction for all tested fuels under the lower load condition (solid line represents petrodiesel best fit, dashed line represents best fit through the 4 biodiesel points, including SME but excluding BIODIESEL+5.3% 1-MN).

lies 62% below the PETRODIESEL+2% 2-EHN data point (comparable to the reduction encountered at the higher load conditions in Study 1), but at a PMBF of 59.9% biodiesel has an estimated FSN 39% lower than the PETRODIESEL.

The addition of 1-MN to BIODIESEL caused an increase in the smoke number, despite the slightly larger PMBF associated with it. The magnitude of the increase is difficult to assess accurately, given that the smoke meter only reads to 2 decimal places, but the BIODIESEL+5.3% 1-MN values were consistently around 25% higher than those of BIODIESEL. An increase in particulate emissions is anticipated when the aromatic content of a fuel is increased, because aromatic hydrocarbons – particularly polycyclic aromatic hydrocarbons, like 1-MN – constitute an immediate source of soot precursors. Under lower load conditions, it can be seen that aromatic addition increases both NO_x emissions (see Figure 5.55) and smoke number compared to the parent BIODIESEL, although only the increase in FSN exceeds that which is attributable to altered ignition quality. Potentially, under a higher load, increased soot formation and radiative heat transfer may act to mitigate NO_x emissions, but here there is no obvious evidence of this.

PETRODIESEL+30% TPGME reduced FSN 52% relative to the parent PETRODIESEL, almost identical to the 53% reduction achieved at the higher load. Hence, whereas the effect of biodiesel on FSN was smaller under high PMBF, lower load conditions, the effect of TPGME was essentially unchanged. This meant that FSN when fuelling on PETRODIESEL+30% TPGME was lower (roughly 20% lower) than the FSN

when fuelling on BIODIESEL. Some portion of this difference is attributable to the larger PMBF of PETRODIESEL+30% TPGME, but even when compared to biodiesel projected to the same PMBF (59.9%), FSN from the TPGME blend remains around 15% lower than that of the biodiesel trend. The PETRODIESEL+30% TPGME smoke number is also lower than that of SME, which had an even higher degree of premixing.

This is interesting, because – although the difference is only slight – it indicates that while PETRODIESEL+30% TPGME appeared to be a less effective soot suppressant than biodiesel at the higher load, it was more effective than biodiesel at the lower load. If this result can be relied upon, it may indicate some effect of the cooler lower load operating conditions on biodiesel air entrainment. In Study 1, where in-cylinder temperatures would have been higher, any differences between biodiesel and PETRODIESEL+30% TPGME jet characteristics and entrainment rates (attributable to the higher biodiesel boiling range, viscosity, etc.) would be smaller than at lower temperatures. While at the higher load the slightly higher biodiesel oxygen content relative to PETRODIESEL+30% TPGME, as well as the total absence of aromatic species, meant that biodiesel smoke emissions were lower, it is possible that, at the lower load, poorer air entrainment into the biodiesel jet may have been sufficient to counteract these factors.

It is also worth noting that, with reference to both Figure 5.55 and Figure 5.56, the PETRODIESEL+30% TPGME data point appears to be below the biodiesel trend in terms of both NO_x emissions and FSN at the lower load, whereas it was above the biodiesel trend in both instances at the higher load (see Figures 5.15 and 5.17).

5.3.3.4 OTHER EMISSIONS

As in Study 1, CO emissions are seen in Figure 5.57 to increase with increasing PMBF. Although the biodiesel trend still exceeds that of petrodiesel, the separation is smaller than in the earlier studies, averaging around 12.5% over the illustrated range. This may give further weight to the argument that any differences in mixture stoichiometry which exist between petrodiesel and biodiesel combustion may be reduced at the lower load; that is, the fuel-bound oxygen content of biodiesel does not make such a significant difference. However, PETRODIESEL+30% TPGME was associated with CO emissions only slightly lower than the petrodiesel trend, and significantly above the biodiesel trend, meaning that there is no direct correspondence between FSN and CO.

Figure 5.58 shows that THC emissions generally increase with PMBF, consistent with

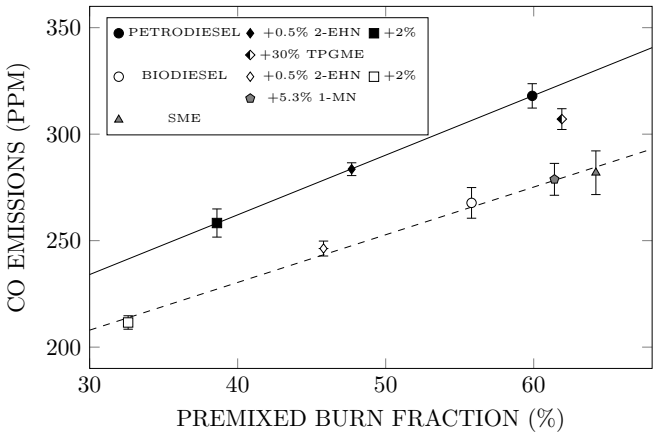

Figure 5.57: Carbon monoxide emissions as a function of premixed burn fraction for all tested fuels under the lower load condition (solid line represents petrodiesel best fit, dashed line represents best fit through the 4 biodiesel points, including SME but excluding BIODIESEL+5.3% 1-MN).

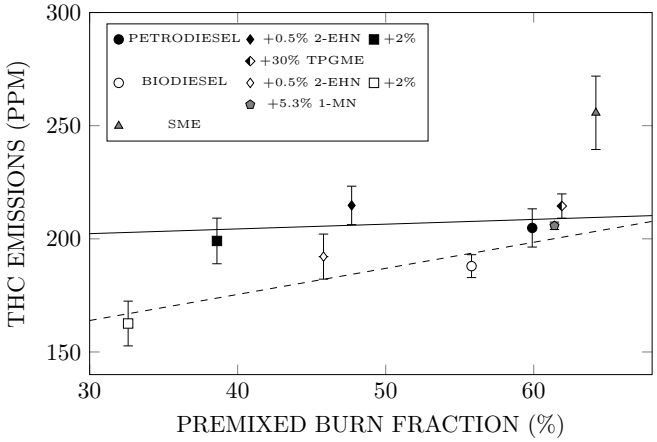

Figure 5.58: Total hydrocarbon emissions as a function of premixed burn fraction for all tested fuels under the lower load condition (solid line represents petrodiesel best fit, dashed line represents best fit through the biodiesel points, excluding both SME and BIODIESEL+5.3% 1-MN).

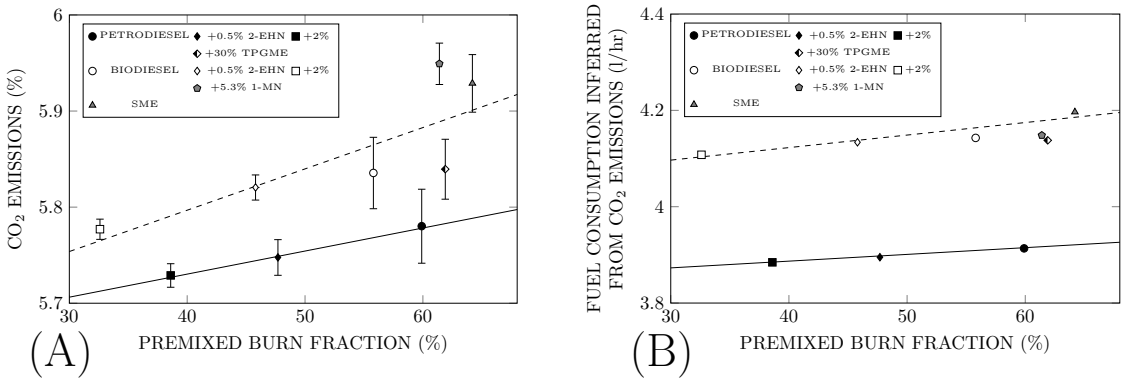

Figure 5.59: (A) Carbon dioxide emissions as a function of premixed burn fraction for all tested fuels under the lower load condition (solid line represents petrodiesel best fit, dashed line represents best fit through the biodiesel points, excluding both SME and BIODIESEL+5.3% 1-MN). (B) Volumetric fuel consumption rates inferred from carbon dioxide emissions and fuel properties as a function of premixed burn fraction for all tested fuels under the lower load condition (solid line represents petrodiesel best fit, dashed line represents best fit through the biodiesel points, excluding both SME and BIODIESEL+5.3% 1-MN).

Studies 1 and 2, although in the lower load petrodiesel data alone there is little evidence of this, and the biodiesel upward trend results largely from the position of the BIODIESEL+2% 2-EHN point. Taken at face value, it seems as if biodiesel THC emissions may be lower than those of petrodiesel at less highly premixed conditions, and similar – if not higher – at more highly premixed conditions. As in Study 1, SME is observed to have particularly high THC emissions (around 26% higher than the biodiesel trend). This would seem to make it more likely that some physical property of the fuel is the cause (as suggested for UCOME in Study 1), rather than increased wall impingement. If wall impingement were the culprit, it might be expected that, under lower temperature, longer ignition delay conditions other fuels would demonstrate the same abnormal increase in THC. In Study 1 SME had an ignition delay of 4.125 CA; in Study 3 PETRODIESEL, PETRODIESEL+30% TPGME and BIODIESEL+5.3% 1-MN all had ignition delays equal to or longer than this, without any similar increase in THC emissions. PETRODIESEL+30% TPGME had THC emissions slightly higher than those of PETRODIESEL, suggesting that the increase in fuel-bound oxygen was either not an effective deterrent of THC, or was offset by some other effect of TPGME addition.

As in Study 2, Figure 5.59A shows that CO_2 emissions were consistently higher for all of the biodiesels at the lower load, particularly for the more highly premixed fuels, BIODIESEL+5.3% 1-MN and SME. On average, biodiesel CO_2 emissions were around 1.5% higher than those of petrodiesel for a given PMBF. Unlike in Study 1, where PETRODIESEL+30% TPGME had lower CO_2 emissions than PETRODIESEL, Figure 5.59A shows an increase in CO_2 following the addition of TPGME. The inferred fuel consumption values indicate an increase of around 6–6.5% when fuelling on biodiesel, although the increase is slightly higher when fuelling on SME (around 7%), in keeping with the increased CO_2 emissions. Although CO_2 emissions were even higher when fuelling on BIODIESEL+5.3% 1-MN, the slightly higher density and mass percentage carbon of the blend lead to its inferred fuel consumption being similar to that of BIODIESEL and PETRODIESEL+30% TPGME.

5.3.3.5 HEAT RELEASE AND PRESSURE

At the lower load, overall rates of combustion progress depend more strongly upon the degree of premixing than at the higher load. Comparing the Study 1 higher load data in Figure 5.22 with the lower load data in Figure 5.60, it can be seen that, by the 60–70%

intervals, at which the biodiesel curves were invariably significantly above their petrodiesel equivalents in Figure 5.22, the progress of the fuels in Figure 5.60 by the same period in the combustion process is basically ordered according to degree of premixing alone. To a large extent, this is because the PMBF for any given fuel is larger at the lower load, primarily on account of the smaller total quantity of heat release (of which the same quantity of premixed heat release naturally constitutes a larger proportion), but also due to a slight extension of ignition delay. In Studies 1 and 2 (as well as Chapter 4) it was observed that biodiesel combustion progressed faster than that of petrodiesel following the end of the premixed burn, and because the premixed burn ends later in Figure 5.60, any possible period of ascent for biodiesel is delayed.

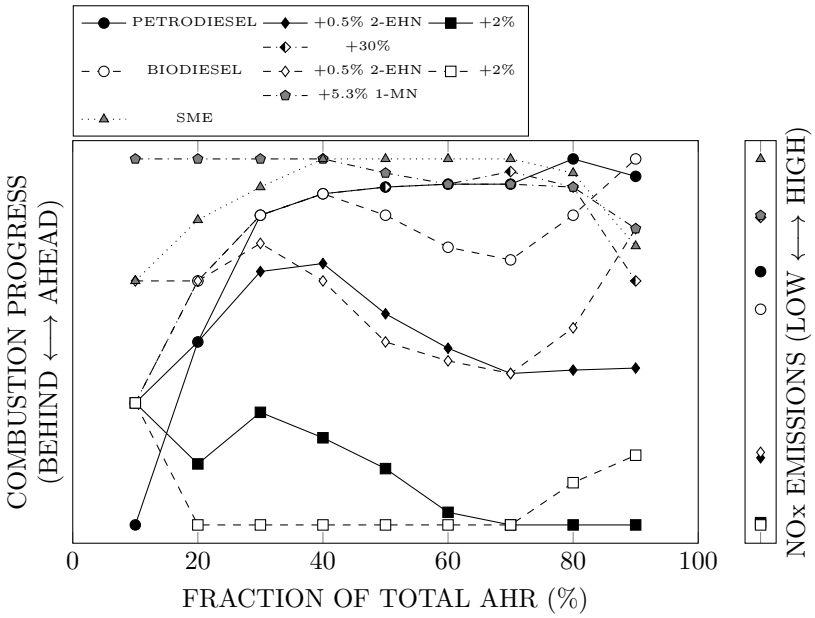

Figure 5.60: Relative combustion progress for all tested fuels under the lower load. The vertical position of each fuel indicates how quickly it reached the interval on the x-axis; the fuel that reached the interval earliest is at the top, the fuel that reached it latest is at the bottom, and the other fuels are distributed between based on their timing relative to the slowest and fastest fuels. NO_x emissions distributed similarly are given on the right-hand side.

The gradient of the BIODIESEL, BIODIESEL+1% 2-EHN and BIODIESEL+2% 2-EHN curves becomes positive after the 70% interval, suggesting an increase in biodiesel heat release through the later part of combustion, similar to that which was observed in Studies 1 and 2. However, over the same period the BIODIESEL+5.3% 1-MN, SME, and PETRODIESEL +30% TPGME curves decline, which is in opposition to the trends which were previously observed for the biodiesels and the oxygenated blends.

It is at the 70% interval that the greatest linear correlation between normalised NO_x emissions and combustion progress exists, where $r^2 = 0.94$, as can be seen in Figure 5.61A.

However, Figure 5.61B seems to suggest that the relationship between the two variables – like that between NO_x and PMBF – is not best described by a linear trend at lower load. A second-order fit offers an improved characterisation of the data in Figure 5.61B (R^2 = 0.98) and, as can be seen in Figure 5.61A, R^2 remains at 0.98 between 40–70% intervals. This adds further evidence for the primacy of the effect of the degree of premixing on lower load NO_x emissions. In fact, simply plotting normalised NO_x emissions as a function of normalised PMBF would offer an even higher degree of non-linear correlation, with an R^2 value of 0.99.

The slower late combustion of BIODIESEL+5.3% 1-MN, SME, and PETRODIESEL +30% TPGME does not seem to have any correspondence to their measured NO_x emissions; as Figure 5.61A shows, after the 70% interval the correlation between combustion progress and NO_x emissions declines substantially. Likewise, the faster heat release of BIODIESEL+0.5% 2-EHN and BIODIESEL+2% 2-EHN through the later intervals moves combustion progress out of accordance with relative NO_x emissions. At the lower load the angle of maximum pressure was typically reached after 65–70% of total AHR.

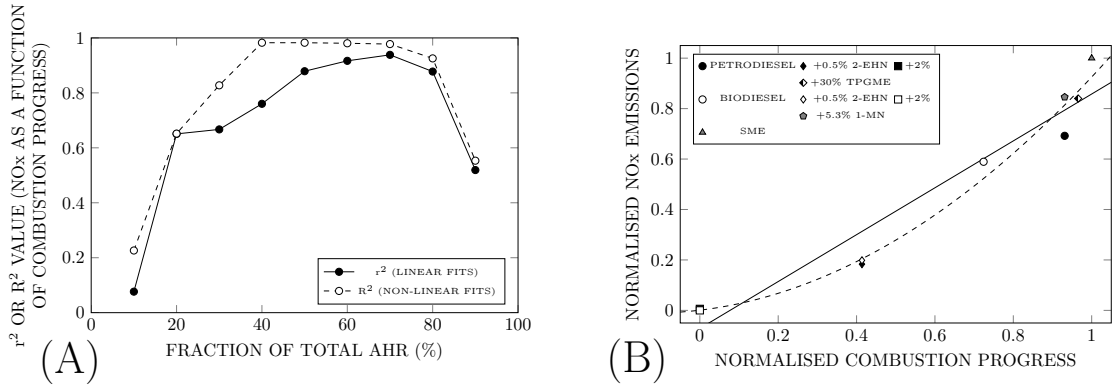

Figure 5.61: (A) r^2 and R^2 values for linear and non-linear fits through normalised NO_x emissions as a function of normalised combustion progress, at AHR intervals from 10–90% of total AHR, for all tested fuels under the lower load. (B) Normalised NO_x emissions as a function of normalised combustion progress at the 70% interval (solid line is linear best fit, dashed curve is second order best fit).

The average AHRR values through the premixed burn are similar for all fuels studied under the lower load, for any given PMBF. At first glance, ΔP_{pmb} values also seem to vary little beyond that which is attributable to the degree of premixing. This can be seen Figure 5.62A. However, it is apparent that the gradient of the biodiesel trendline in Figure 5.62A is slightly steeper than that of petrodiesel, leading to a slight reduction in biodiesel premixed ΔP_{pmb} relative to petrodiesel in the lower PMBF cases, and a slight increase in the high PMBF cases. This is directly related to small changes in the estimated

duration of the premixed burn.

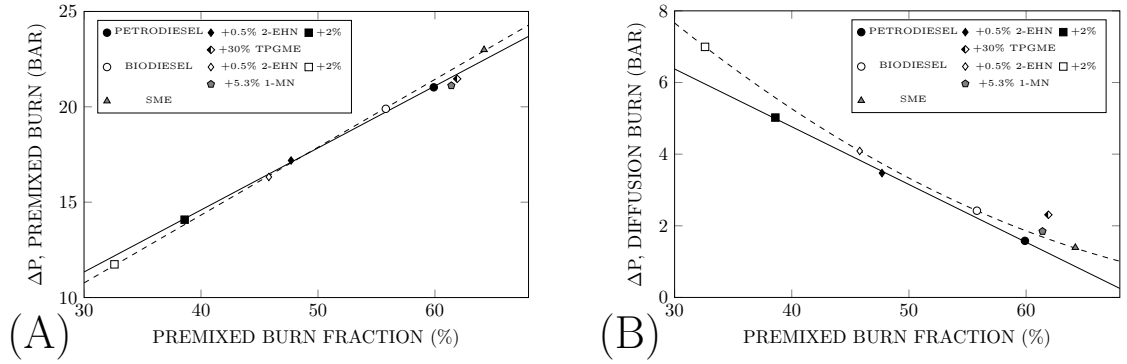

Figure 5.62: Pressure change across (A) the premixed burn phase and (B) the diffusion burn phase, as a function of premixed burn fraction for all tested fuels under the lower load condition (solid lines represent petrodiesel best fits, dashed lines represent best fits through the 4 biodiesel points, including SME but excluding BIODIESEL+5.3% 1-MN).

Figure 5.62B presents ΔP_{diff} values, calculated across the period between the EOPMB and Θ_{Pmax}, which is termed the diffusion phase here as it was in previous sections, although at the lower load this may not include any appreciable period of what could be considered quasi-steady diffusion combustion, as would be expected under typical diesel engine conditions. Biodiesel ΔP_{diff} values are consistently slightly higher than those of petrodiesel, although in general the gap is small compared to that observed in Studies 1 and 2. The increase with biodiesel for any given PMBF appears to be larger towards the extremities of the plot – particularly at the less premixed end of the scale. The higher biodiesel ΔP_{diff} values under lower PMBF conditions (primarily, for BIODIESEL+2% 2-EHN) are attributable to the same factors as at the higher load conditions in Studies 1 and 2: higher average post-premixed AHRR, as shown in Figure 5.63A, and a longer diffusion pressure rise duration, as shown in Figure 5.63B. Both of these factors are themselves attributable to the same period of increased diffusion AHRR when fuelling on biodiesel as was identified at the higher load.

The trends in duration of pressure rise as a function of PMBF are seen in Figure 5.63B to hold reasonably well for all of the fuels, with the difference between petro- and biodiesel being significant under less premixed conditions, but closing as degree of premixing increases. The average post-premixed AHRR data in Figure 5.63A, on the other hand, is less consistent, with BIODIESEL, BIODIESEL+0.5% 2-EHN and BIODIESEL+2% 2-EHN data points lying above the petrodiesel trend (as in Studies 1 and 2) but BIODIESEL+5.3% 1-MN and SME demonstrating no similar increase. If the increase in post-premixed AHRR when fuelling on the biodiesel and TPGME blends

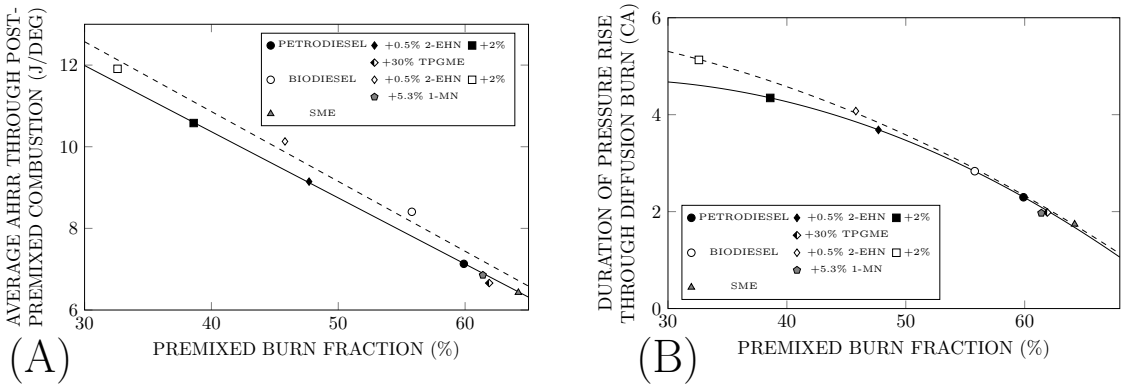

Figure 5.63: (A) Average apparent heat release rate through post-premixed combustion and (B) duration of pressure rise through the diffusion phase, as functions of premixed burn fraction for all tested fuels under the lower load condition (solid lines represent petrodiesel best fits, dashed lines represent biodiesel best fits).

is due to an extension of the injection duration (as speculated in Section 5.3.1.5), then the fact that BIODIESEL+5.3% 1-MN, SME and PETRODIESEL+30% TPGME do not exhibit this trait may be because their injection events conclude early enough to avoid having any effect on post-premixed combustion.

However, BIODIESEL+5.3% 1-MN, SME, and PETRODIESEL+30% TPGME, do appear – in Figure 5.62B – to have relatively high ΔP_{diff} values, compared to the petrodiesel trend, despite no increase in post-premixed AHRR, or the duration of the pressure rise, being evident for these fuels. PETRODIESEL+30% TPGME in particular exceeds both petro- and biodiesel ΔP_{diff} trendlines significantly.

For these more highly premixed fuels, the apparent increase in ΔP_{diff} is a result of fluctuations in the pressure data which appear to be noise rather than anything more significant. Because the pressure rise has been calculated as the difference in pressure between two points, when the magnitude of the difference is small the signal-to-noise ratio effectively drops, and ΔP_{diff} may less accurately characterise the overall pressure rise across the period. This is illustrated by Figure 5.64.

Although the linear gradients depicted in Figure 5.64 do not reflect the actual patterns of pressure rise, they do portray the data in a manner less effected by noise. For the less highly premixed fuels it can be seen that the pressure curves begin and end below the overall gradient lines to a roughly equal extent (that is, the dashed lines in Figure 5.64, which illustrate the average overall gradients of the pressure curves, run approximately parallel to the dotted lines, which represent ΔP_{diff}), such that ΔP_{diff} gives a reasonable account of pressure rise across the period. However, for BIODIESEL+5.3% 1-MN, SME, and most obviously for PETRODIESEL+30% TPGME, the ΔP_{diff} values do not corre-

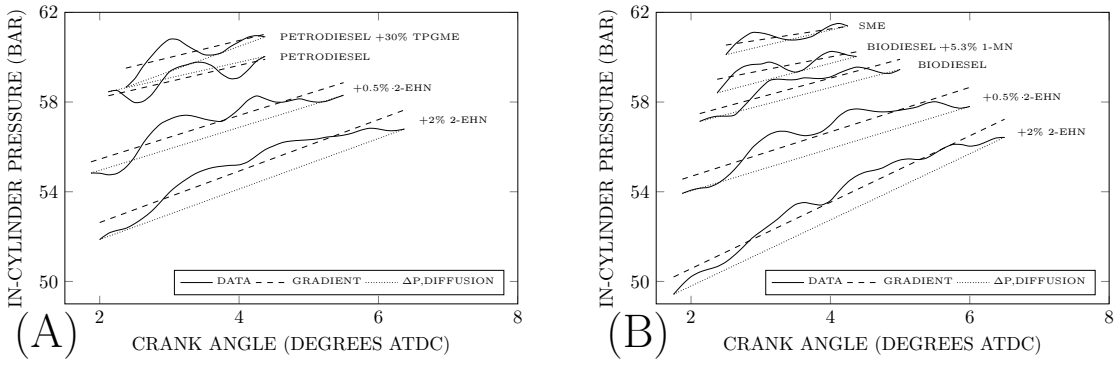

Figure 5.64: Plots showing pressure rise through the diffusion phase (i.e. end of premixed burn to angle of maximum pressure) for (A) petrodiesel and petrodiesel based fuels and (B) biodiesel and biodiesel based fuels, as functions of crank angle under the lower load condition. Solid lines show average pressure plots for each fuel, dashed lines show average gradients of pressure rise, and dotted lines illustrate ΔP across the diffusion phase. (NB. Pressure curves end at the average angles of maximum pressure computed on a cycle-by-cycle basis for each data set, but this is not necessarily the angle at which the average data set pressure curves peak. Consequently, the curves shown do not always end at their peaks, and ΔP_{diff} is not exactly the same as that which has been calculated from the data; however, it is close enough for the figure to provide a faithful representation of the pertinent trends.)

spond as closely to the overall gradient (i.e. the dashed and dotted lines for these fuels in Figure 5.64 are not parallel), because fluctuations in pressure, although not necessarily larger in *magnitude* than for the other fuels are larger in *proportion*, and happen to be timed in a way that gives rise to significant errors. If the trends presented in Figure 5.62 are adjusted in keeping with the overall gradients illustrated in Figure 5.64, in order to eliminate the effects of fluctuations in the pressure data, the most significant changes are that the PETRODIESEL+30% TPGME and BIODIESEL+5.3% 1-MN points in Figure 5.62A are shifted upwards, closer to the biodiesel trend, and in Figure 5.62B the same points are shifted downwards onto the biodiesel trend. Additionally, the biodiesel and petrodiesel trends are more closely aligned than in Figure 5.62B because the SME point is shifted downwards, closer to the petrodiesel trend. Adjusted plots can be seen in Figure 5.65.

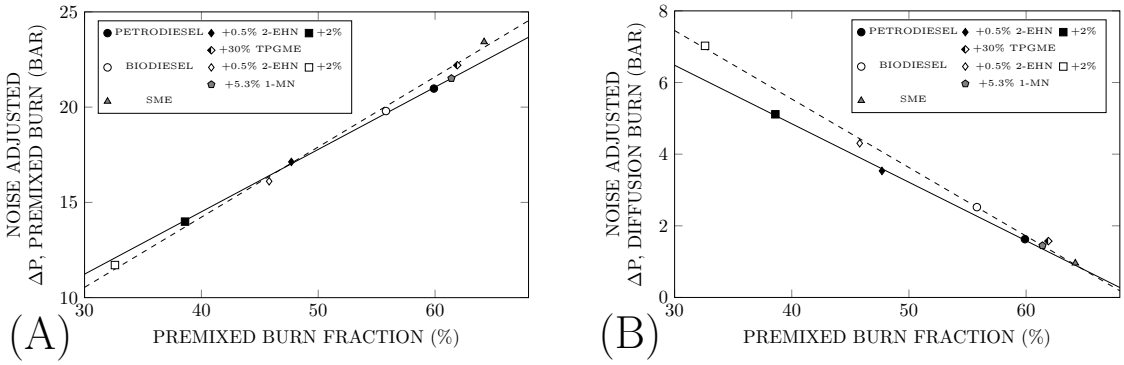

Figure 5.65: Pressure change across (A) the premixed burn phase and (B) the diffusion burn phase, having been adjusted to account for the calculation errors described in connection with Figure 5.64 (the same data is presented without adjustment in Figure 5.62).

Overall, the trend appears to be that the biodiesel fuels have greater ΔP_{diff} values and lower ΔP_{pmb} values when the PMBF is small, but greater ΔP_{pmb} values through the premixed phase and roughly equal ΔP_{diff} values when the PMBF is large. Although the variations in ΔP_{diff} in Figure 5.65B are basically consistent with the explanations that have been put forward, related to higher biodiesel diffusion AHRR, and the possibility of a connection to the injection event, the variations in ΔP_{pmb} are not so easily explained in terms of combustion phenomena. However, the manner in which the ΔP_{pmb} trendlines cross in Figure 5.65A is common to the trend across all higher load data, presented in Study 2 (see Figure 5.47). The reason for this pattern is unclear, but while at the higher load its effect is small (because the variations in maximum pressure due to changes in ΔP_{diff} are far larger), at the lower load it cannot be dismissed as insignificant. At low PMBFs the reduction in biodiesel ΔP_{pmb} seen in Figure 5.65A is sufficient to offset the increase in ΔP_{diff} seen in Figure 5.65B, such that biodiesel P_{max} is only slightly higher than that of petrodiesel. This can be seen in Figure 5.66A. Additionally, the apparent increase in biodiesel ΔP_{pmb} at higher PMBFs is associated with a significant increase in P_{max}.

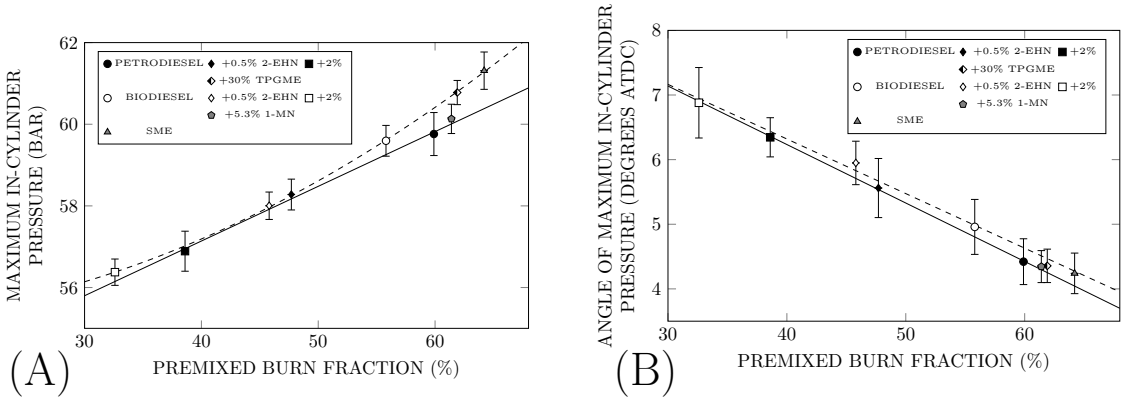

Figure 5.66: (A) Maximum in-cylinder pressure and (B) angle of maximum in-cylinder pressure, as functions of premixed burn fraction for all tested fuels under the lower load condition (solid line represents petrodiesel best fit, dashed line represents biodiesel best fit).

The reason for the increase in ΔP_{pmb}, and consequently in P_{max}, when fuelling on high PMBF biodiesels is not immediately clear, as no consistent pattern providing any explanation is identifiable in the rates of heat release. Figure 5.67A shows that, as was the case at higher load, maximum AHRR tended to be slightly higher for the biodiesels than for the petrodiesels given the same degree of premixing. However, this trend breaks down at higher PMBF conditions, with BIODIESEL, PETRODIESEL, BIODIESEL+5.3% 1-MN and SME all reaching peak values of around 77–80 J/deg, despite their varying degrees of

premixing. Again, as at higher load, the addition of TPGME to PETRODIESEL reduced maximum AHRR.

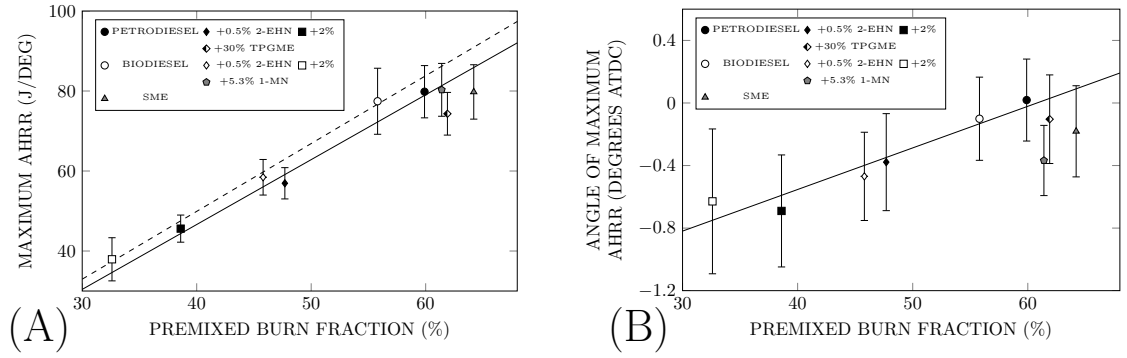

Figure 5.67: (A) Maximum apparent heat release rate as a function of premixed burn fraction for all tested fuels under the lower load (solid line represents petrodiesel best fit, dashed line represents biodiesel best fit, excluding SME and BIODIESEL+5.3% 1-MN). (B) Angle of maximum apparent heat release rate as a function of premixed burn fraction for all tested fuels under the lower load (solid line represents best fit through all fuels, excluding PETRODIESEL+30% TPGME, SME and BIODIESEL+5.3% 1-MN).

Figure 5.67B shows that there is also some change in the timing of maximum AHRR at the most highly premixed conditions. The angle at which maximum AHRR occurs is typically retarded with increasing PMBF, and varies in approximately the same manner for both petro- and biodiesel. However, the PETRODIESEL+30% TPGME point, and even more so the SME and BIODIESEL+5.3% 1-MN points, are advanced relative to the general trend. The reason for this is more clearly seen when the plots of AHRR, presented in Figure 5.68, are considered. (Note that the curves in Figure 5.68 represent smoothed data set averages, whereas Figure 5.67 contains averages collected on a cycle-by-cycle basis. For this reason, the magnitude and timing of maxima are not entirely consistent between the figures, although the general trends remain the same.)

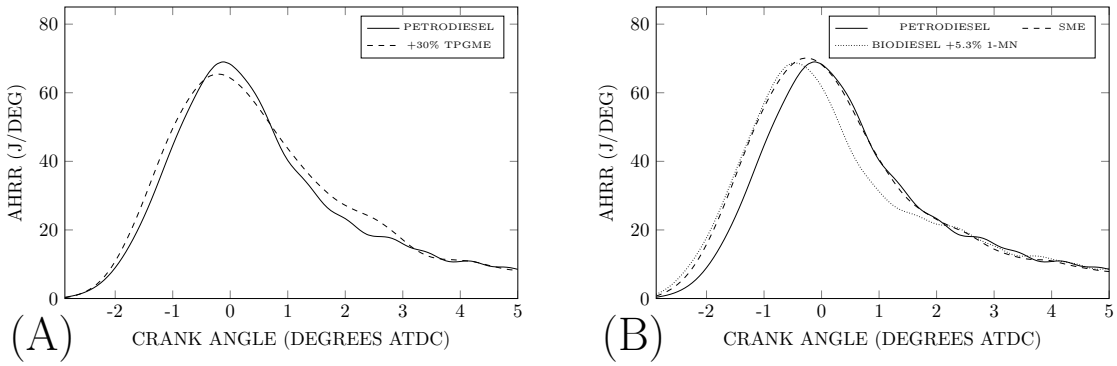

Figure 5.68: Apparent heat release plots at the lower load condition when operating on the fuels that resulted in the most highly premixed combustion.

In Figure 5.68A, the addition of TPGME to PETRODIESEL is seen to have similar effects to those observed at the higher load. Both PETRODIESEL and PETRODIESEL

+30% TPGME begin slowly at first, but PETRODIESEL+30% TPGME picks up more quickly, and is therefore faster through the very first part of AHR, such that subsequent heat release is slightly advanced. PETRODIESEL reaches a higher peak AHRR, but declines more rapidly than PETRODIESEL+30% TPGME through the later part of the heat release attributed to the premixed (or premixing supplemented) phase; the same tendency can be seen in the Study 1 data, in Figure 5.29B. Following the culmination of the PMBF, with EOPMB being reached shortly before 3 ATDC, AHRR from both fuels closely coincides.

In Figure 5.68B PETRODIESEL is compared with the two most highly premixed biodiesel fuels, SME and BIODIESEL+5.3% 1-MN. There is very little difference in either peak magnitude or the form of the plots. SME has a broader premixed burn spike, but through the decline has no AHRR advantage at all over the PETRODIESEL curve, and the BIODIESEL+5.3% 1-MN plot looks very much the same as the PETRODIESEL plot throughout, albeit shifted around 0.3 CA to the left. This brings the discussion to what appears to be a critical factor: a more rapid increase in AHRR is observed for the biodiesels after the nominal start of combustion, resulting in a small advance of peak AHRR, as illustrated in Figure 5.67B. To some extent, this introduces a difference in combustion phasing that may render the comparison between the fuels somewhat unequal. Calculating SOC by a different method and equalising combustion with respect to this point instead, might obviate (or at least reduce) the observed variation in maximum AHRR timing, and in other factors of interest. For the purposes of this study, the important question is to what extent the faster initial ascent of biodiesel AHRR influences NO_x emissions, or – at this point in the discussion – pressure.

Across the operational ranges examined, an advance in SOC of 1 CA corresponds to an increase in NO_x emissions of around 10% and an increase in P_{max} of approximately 1.4 bar (these values are consistent with the data reported in Chapter 4). If, rather than defining SOC as the point at which AHRR exceeds zero, it is defined instead as the point at which AHRR exceeds 10 J/deg (hereafter referred to as Θ_{10J}), the possible impact of variations in the initial rate of AHRR increase may be estimated. That is, by calculating the differences in Θ_{10J}, these factors can be used to make adjustments to NO_x emissions and P_{max} which approximate the results which may be expected if experiments had been performed under conditions holding Θ_{10J} constant, rather than SOC based on the definition employed in the current study.

For example, BIODIESEL reached Θ_{10J} on average 0.17 CA earlier than PETRODIESEL (by interpolation of the 0.125 CA resolution data). Advancing combustion by 0.17 CA is associated with an increase in NO_x of around 1.7%, and an increase in P_{max} of roughly 0.26 bar. Hence, if combustion had been synchronised with respect to Θ_{10J}, BIODIESEL NO_x emissions and P_{max} would be expected to be reduced relative to those of PETRODIESEL by 1.7% and 0.26 bar, respectively. When adjustments are made in this way across the entire data set, compensating for differences in Θ_{10J}, lower load NO_x emissions from the biodiesels exceed those of the petrodiesel based fuels, for a given PMBF, by an even smaller margin than was evident in Figure 5.55. The difference in P_{max} for the more highly premixed biodiesels, seen in Figure 5.66A, is also significantly reduced. Plots of NO_x emissions and P_{max} adjusted in this way can be seen in Figure 5.69.

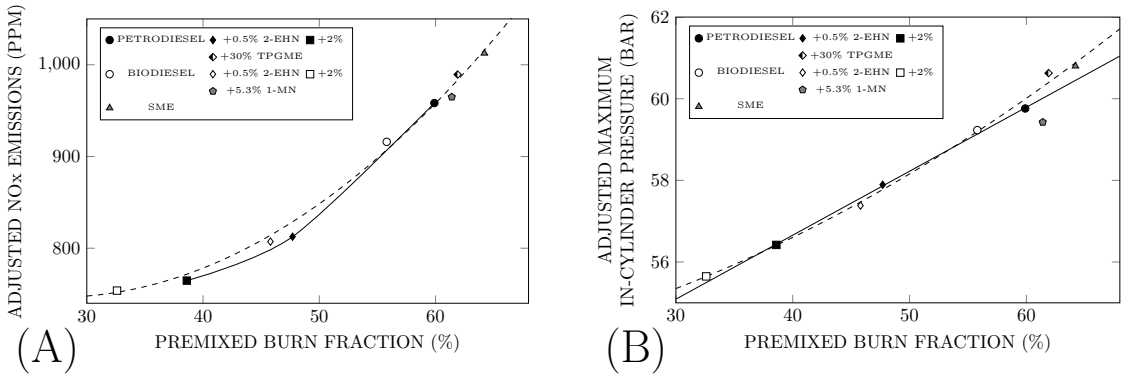

Figure 5.69: (A) Emissions of oxides of nitrogen and (B) maximum in-cylinder pressure as a function of premixed burn fraction for all tested fuels under the lower load condition. Values have been adjusted (from original plots, Figure 5.55 and Figure 5.66A) on the basis of variations in the timing at which apparent heat release rate first exceeded 10 J/deg, with the purpose of approximating the effect of combustion phasing differences induced by differences in rates of heat release immediately after the start of combustion. (Solid lines represent petrodiesel best fits, dashed lines represent best fits through the 4 biodiesel points, including SME but excluding BIODIESEL+5.3% 1-MN).

In general, Figure 5.69 suggests that the small differences in NO_x emissions and P_{max} at the lower load – when both are considered as functions of PMBF, as in Figures 5.55 and 5.66A – may be due in some part to the slight advance of combustion phasing which occurs when the initial rise of AHRR is more rapid. In terms of NO_x, Figure 5.69A illustrates that compensation for the slight difference in phasing reduces the differences between petro- and biodiesel trends basically to the point of negligibility. In all but the most highly premixed cases, differences in P_{max}, seen in Figure 5.69B, also appear to be fairly minor. This explanation is somewhat frustrated, however, by the fact that the most highly advanced fuel of all at the lower load, BIODIESEL+5.3% 1-MN, falls slightly below the NO_x trend when the advancement is adjusted for, as in Figure 5.69A, and more substantially below

the P_{max} trend in Figure 5.69B; this is because its advance was originally associated with no significant increase in either value – in fact, BIODIESEL+5.3% 1-MN P_{max} was already below the biodiesel trend in Figure 5.66A.

Biodiesel exhibited the same faster initial ascent and resulting slight advance of heat release throughout Studies 1 and 3, which may mean that at higher load the increase in NO_x emissions and P_{max} when fuelling on biodiesel is also partially a result of the faster initiation of the premixed burn. However, making similar adjustments as in Figure 5.69 to the Study 1 data has less of a significant impact on emissions and pressure.

In summary, at the lower load the influence of the diffusion combustion phase appears to be insufficient for the biodiesel AHRR increase through this period to significantly effect maximum pressure. Instead, small differences in combustion phasing, induced by a slightly more rapid increase in biodiesel AHRR following the start of combustion, offer a possible explanation for the small variations in P_{max} and NO_x emissions between petro- and biodiesel observed at the lower load.

5.3.4 CONSOLIDATION

Over the course of the preceding discussion, references have been made between the studies, in order to emphasise the points of difference and commonality between them. In the following section, the salient threads are drawn together and an effort is made to bind them where appropriate by way of a generalised explanation.

5.3.4.1 GENERAL

IGNITION DELAY: The addition of 2-ethylhexyl nitrate (2-EHN) reduced the ignition delay of the fuel to which it was added. For the most part, further addition of 2-EHN gave diminishing returns; i.e. doubling the 2-EHN admixture elicited less than double the effect on ignition delay. Increasing injection pressure also reduced ignition delay.

Biodiesels with more highly unsaturated compositions tended to have longer ignition delays. Addition of the oxygenate, tripropylene glycol methyl ether (TPGME), to PETRODIESEL increased the ignition delay of the fuel, as did the addition of the aromatic, 1-methylnaphthalene (1-MN) to BIODIESEL. For the most part, measured ignition delays correlated well with the predicted cetane number (CN) for each fuel; the TPGME blends, which were expected to have shorter ignition delays than PETRODIESEL (on the basis of CN values given in the literature), were the exception. All fuels had shorter

ignition delays at higher load than lower load, due to the higher in-cylinder temperatures.

PREMIXING: Premixed burn fraction (PMBF) correlated approximately linearly with ignition delay (ID) at both higher and lower loads, but the biodiesel fuels tended to form slightly smaller PMBFs for the same ID period. However, this tendency hinges upon the manner in which the end of the premixed burn (EOPMB) is defined. When injection pressure increased, PMBF increased despite the reduction in ignition delay, due to the increased rate of air entrainment.

NO_x EMISSIONS: PMBF was positively correlated with emissions of oxides of nitrogen (NO_x) in all studies. At the higher load, the relationship appeared to be fairly linear, but at the lower load a certain degree of non-linearity was evident. For any given PMBF, NO_x emissions from biodiesel fuels were higher than those of the petrodiesel fuels at all tested conditions. At the higher load, in Study 1, like-for-like NO_x emissions from the biodiesels exceeded those of the petrodiesels by approximately 12.5% on average. At the lower load, in Study 3, like-for-like NO_x emissions from the biodiesels exceeded those of the petrodiesels by around 2–2.5% on average. At both higher and lower loads, the effect of the addition of TPGME to petrodiesel was to increase NO_x emissions. When the fuel-bound oxygen content of a petrodiesel blend approached that of a typical biodiesel, NO_x emissions for a given PMBF also approached those of an equivalent biodiesel. With increasing injection pressure (in Study 2) the biodiesel NO_x increase became progressively larger.

Variations in NO_x emissions between the biodiesels depended largely, but not wholly, on the ignition delay, and hence PMBF, of each fuel, with NO_x emissions being highest in all cases for the biodiesel with the longest ignition delay, sunflower methyl esters (SME). Some of the variation between the fuels may be related to day-to-day variations in engine emissions, but used cooking oil methyl esters (UCOME) in particular had significantly lower NO_x emissions (by 2.6%) than would have been expected based on its CN. This may have been related to its physical properties.

FSN: Under all conditions, the filter smoke number (FSN) declined with increasing PMBF. Biodiesel always had a lower FSN than an equivalent petrodiesel (by between 40–70%), as did the TPGME blends. For a comparable fuel-bound oxygen content and PMBF, biodiesel and the blends of PETRODIESEL and TPGME were associated with similar FSNs. In general, the absolute difference between FSN from oxygenated and non-oxygenated fuels increased as diffusion combustion increased in prominence; this can

be seen in Figure 5.70, where diffusion combustion is quantified by ΔP_{diff}, or pressure change between EOPMB and the angle of maximum pressure. However, some of the data (particularly at varying injection pressures) shows behaviour that suggests additional influences. These may be related to changes in the mixture stoichiometry within the diffusion flame, changes in soot burnout, or may simply reflect that fact that ΔP_{diff} is an imperfect means of quantifying the influence of the diffusion combustion phase.

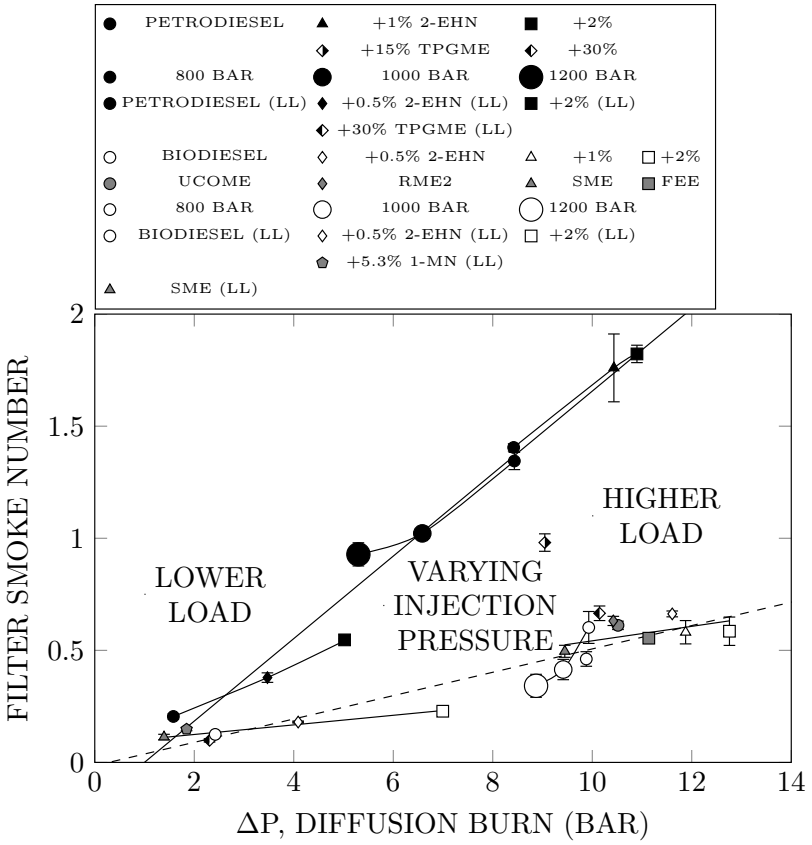

Figure 5.70: Filter smoke number as a function of pressure change across the diffusion combustion phase for all fuels under all tested conditions. Overall linear best fits for petro- and biodiesels are given by solid and dashed lines, respectively. Solid best fits and connecting lines also run through data from the separate studies, to enable differentiation between the various operating conditions, where the same fuels have been used more than once.

OTHER EMISSIONS: Carbon monoxide (CO) emissions increased with increasing PMBF in Study 1 (higher load) and Study 3 (lower load). This was attributed to greater heat release through fuel-rich premixed reactions. In Study 2 (varying injection pressure), CO emissions decreased with increasing PMBF. It was speculated that this may be a result of reduced equivalence ratios throughout the premixed charge at higher injection pressures. Biodiesel CO emissions were lower than those of petrodiesel by around 20–25% at the higher load, and around 12.5% at the lower load. PETRODIESEL+30% TPGME had lower CO emissions than PETRODIESEL. Used cooking oil methyl esters

(UCOME) had significantly higher CO emissions than the other biodiesels (comparable to an equivalent petrodiesel).

Total hydrocarbon emissions (THC) increased with increasing PMBF under all conditions. This may be a result of increased over-leaning. At higher load (in Study 1), the difference between THC emissions from petro- and biodiesel was fairly small (around 2–3%), although in Studies 2 and 3 the difference was a little larger. The addition of TPGME to PETRODIESEL reduced THC emissions slightly at the higher load, and increased them slightly at the lower load. UCOME and SME had THC emissions significantly in excess of the other biodiesels.

Carbon dioxide (CO_2) emissions appeared in most cases to increase a little with increasing PMBF, and were typically slightly higher (by 0–1.5%) when fuelling on biodiesel rather than petrodiesel, with the difference being largest at lower load and at higher injection pressures. Fuel consumption rates inferred from CO_2 emissions also suggest an increase in the volumetric fuel requirement when running on biodiesel, by around 6–6.5%.

APPARENT HEAT RELEASE RATES: Average apparent heat release rate (AHRR) through the premixed burn phase increased with increasing PMBF, and, for a given degree of premixing, average AHRR values through this period were approximately the same for petro- and biodiesel. However, although average values were similar, patterns of AHRR through the premixed phase did vary between fuels. Biodiesel AHRR tended to rise slightly more rapidly following the start of combustion, and reach higher maximum AHRR values than petrodiesel for a given degree of premixing. With the addition of TPGME to PETRODIESEL, maximum AHRR was reduced. The fuels which released heat more slowly through the peak of the premixed burn (i.e. the petrodiesels, and the TPGME blends) had slightly higher AHRR through the later part of the premixed burn; it is because of this that average AHRR values across the PMBF remained roughly the same.

Average AHRR values through post-premixed combustion (i.e. including both diffusion and late-combustion stages) decreased with increasing PMBF, and were in almost all cases higher for biodiesel than for petrodiesel. The only exceptions were in the most highly premixed lower load cases. With the addition of TPGME to PETRODIESEL an increase in average post-premixed AHRR was observed, and the PETRODIESEL+30% TPGME blend had comparable values to those of biodiesel (at the higher load, in Study 1). The increase in post-premixed AHRR when fuelling on biodiesel appears to be at its

most significant around the point at which diffusion heat release rate is maximised. The impression that the data gives is that the decline of diffusion heat release occurs later when fuelling on biodiesel, leading to a period through which biodiesel maintains higher AHRR, before returning to similar (although still marginally higher) levels to petrodiesel through late-combustion.

The effect of variations in diffusion AHRR on overall rates of combustion progress appears to be an important consideration in terms of NO_x emissions; the timing of the 70–80% heat release interval (CA70–CA80) tended to offer the most useful prediction of the NO_x emissions from a given fuel.

PRESSURE: Maximum in-cylinder pressure (P_{max}) increased with increasing PMBF, and tended to be higher for biodiesel than petrodiesel. Addition of TPGME to PETRODIESEL increased P_{max} to levels comparable to those of an equivalent biodiesel. In many cases, the angle at which biodiesel reached maximum pressure (Θ_{Pmax}) was retarded compared to petrodiesel, particularly at higher injection pressures.

Since, for a given PMBF, average AHRR values across the premixed burn fraction were relatively consistent between fuels, pressure change across the premixed burn (ΔP_{pmb}) also tended to vary little between petro- and biodiesel (although at the lower load the variation in ΔP_{pmb} appeared more significant). Due to the increase in post-premixed AHRR when fuelling on biodiesel, particularly through the most rapid period of diffusion heat release, ΔP_{diff} was higher for biodiesel in all but the most highly premixed lower load cases. Generally, it is the increase in ΔP_{diff} which causes the increase in maximum pressure when fuelling on biodiesel. The increase in ΔP_{diff} is due to an increase in both the rate and duration of diffusion pressure rise when fuelling on biodiesel; the increase in the duration of the diffusion pressure rise depends on Θ_{Pmax}, and its proximity to the period of increased biodiesel diffusion AHRR.

5.3.4.2 THE VARYING EFFECT OF BIODIESEL ON NO_x EMISSIONS

Accounting for differences in start of combustion timing and degree of premixing, PETRODIESEL+30% TPGME had similar NO_x emissions to an equivalent biodiesel, as well as typically comparable smoke and CO emissions, maximum pressure and diffusion heat release characteristics. Many of these factors clearly have some connection to the fuel-bound oxygen content of the fuels, and hence the equivalence ratios encountered during their combustion. In simple terms then, the difference in NO_x emissions that remains between

petro- and biodiesel, after differences in start of combustion (SOC) and PMBF have been accounted for, appears to be a function of fuel-bound oxygen content. However, although the difference in fuel-bound oxygen content between petro- and biodiesel is unchanging, the difference in NO_x emissions is not.

Considering all of the higher load data (from both Studies 1 and 2), the NO_x emissions trends most closely correspond to the P_{max} and ΔP_{diff} trends, which are themselves related to the period of the diffusion burn through which biodiesel has significantly higher AHRR than petrodiesel. The next questions are, why does this period exist, and what determines the magnitude and duration of the AHRR difference?

Because diffusion AHRR was increased by the addition of TPGME, it is possible that there is some relationship between the diffusion AHRR increase and fuel-bound oxygen content. Alternatively, it appears possible, due to the timing of the AHRR increase, that it may instead be a result of an increase in the duration of the injection event; this occurs because both the biodiesels and the TPGME blends have lower energy densities than petrodiesel, and hence require an increase in fuelling to maintain the same load.

Although the higher diffusion AHRR of biodiesel causes an increase in P_{max} at the higher load, the difference in NO_x emissions between petro- and biodiesel goes beyond that which is attributable to the P_{max} increase alone. Plotted as a function of P_{max}, in Figure 5.71, NO_x emissions continue to be higher for biodiesel, and the TPGME blends, throughout Study 1 (marked in Figure 5.71 as HIGHER LOAD). In Study 2 (marked as VARYING INJECTION PRESSURE), BIODIESEL NO_x emissions as function of P_{max} were also above those of PETRODIESEL at an injection pressure of 800 bar, but as injection pressure and P_{max} increased, NO_x emissions for the two fuels converged. Although no clear trend is apparent in the Study 3 data (marked as LOWER LOAD in Figure 5.71) considered independently, certainly the differences between petro- and biodiesel in terms of both P_{max} and NO_x emissions were small at this condition.

In summary: the reduced energy density of biodiesel extends the necessary injection duration; it is possible that extended injection duration, and other factors, contribute to increased AHRR through the diffusion burn when fuelling on biodiesel; increased diffusion AHRR increases maximum in-cylinder pressure; for a given value of P_{max}, the increase in NO_x emissions when fuelling on biodiesel generally corresponds to the reduction in FSN, as seen in Figure 5.72; FSN is related to the quantity of diffusion combustion, as well as the fuel-bound oxygen content and inherent sooting tendency of the fuel.

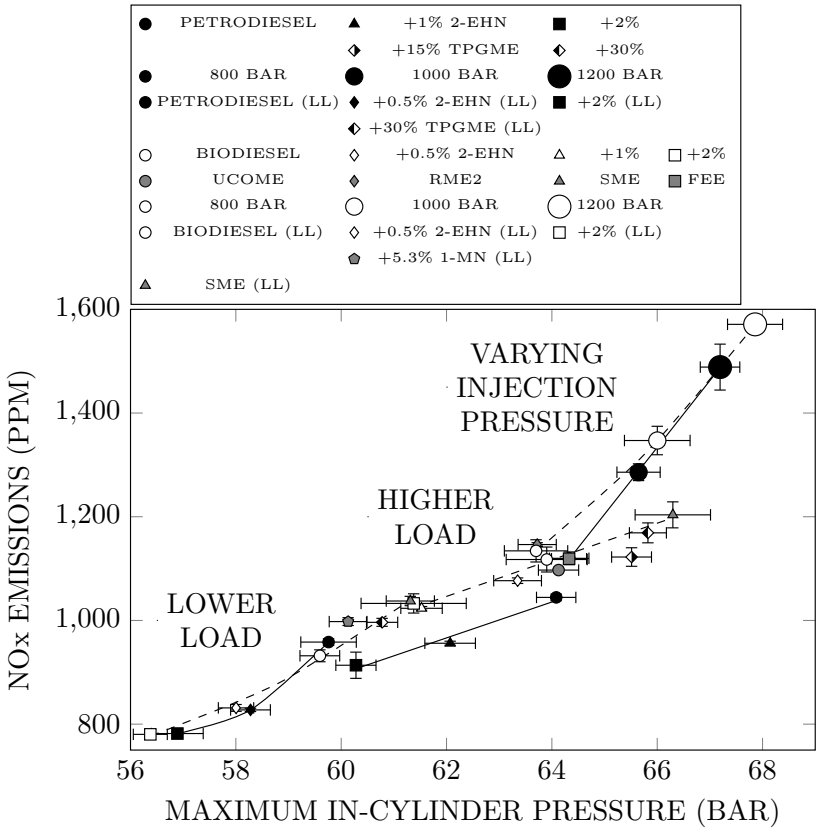

Figure 5.71: Emissions of oxides of nitrogen as a function of maximum in-cylinder pressure for all fuels under all tested conditions. Solid best fits and connecting lines run through petrodiesel data, dashed best fits and connecting lines run through biodiesel data.

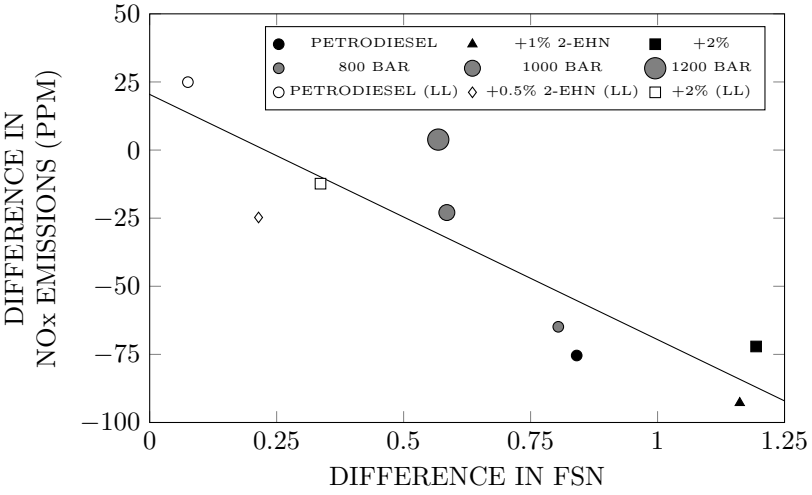

Figure 5.72: Difference in emissions of nitrogen oxides (petrodiesel minus biodiesel) as a function of difference in filter smoke number (petrodiesel minus biodiesel) for all petrodiesel points. Values calculated by comparison with biodiesel data points projected to an equivalent value of maximum in-cylinder pressure, on the basis of best fits through the NO_x and FSN data.

5.4 CONCLUSIONS

Three connected experiments were undertaken, with start of combustion held constant, in order to gain insight into the relationships between biodiesel, degree of premixing, fuel

oxygenation and emissions of oxides of nitrogen. The main conclusions of this work are as follows:

1. Emissions of oxides of nitrogen (NO_x) increased with increasing degree of premixing.

   (a) At higher load, the relationship between NO_x emisisons and premixed burn fraction (PMBF) appeared to be fairly linear.

   (b) At lower load, a degree of non-linearity was apparent.

2. For a given PMBF, the tested biodiesels had higher NO_x emissions than the petrodiesels under all tested conditions.

   (a) The like-for-like increase in biodiesel NO_x emissions was larger at the higher load (around 12.5%) than at the lower load (2–2.5%).

   (b) Addition of the oxygenate, tripropylene glycol methyl ether (TPGME), to petrodiesel increased like-for-like NO_x emissions, such that a petrodiesel blend with comparable fuel-bound oxygen content to biodiesel also had comparable NO_x emissions, for an equivalent PMBF.

   (c) At higher injection pressures the biodiesel NO_x increase relative to petrodiesel became progressively larger.

   (d) It is also possible that physical properties of biodiesel may effect the magnitude of the NO_x increase: a biodiesel derived from used cooking oil, which was possibly more viscous than the other biodiesels, had lower NO_x emissions than the other biodiesels for a given PMBF.

3. Higher cetane number fuels, which have shorter ignition delays and hence reduced PMBFs, have accordingly reduced NO_x emissions. Where a biodiesel CN is higher than that of a petrodiesel, the associated reduction in PMBF can offset the like-for-like biodiesel NO_x increase.

   (a) At higher load, where the like-for-like increase in NO_x is large, a biodiesel would be required to have a very high CN (around 70) in order to elicit NO_x emissions comparable to those of a typical petrodiesel (with start of combustion constant).

   (b) At lower load, where the like-for-like increase in NO_x is smaller, a biodiesel with a CN only modestly higher than that of petrodiesel would be likely to

have lower NO_x emissions as a result of the reduction in PMBF (again, with start of combustion constant).

(c) However, for a low CN biodiesel, like that derived from sunflower oil (which is high in polyunsaturated species), NO_x emissions are significantly higher than those of petrodiesel under either operating condition.

4. Biodiesel typically had a period of higher apparent heat release rate (AHRR) following the end of the premixed burn phase, through the most intense portion of diffusion combustion.

   (a) The timing and nature of the increase suggest a relationship with the duration of the injection event, which is likely to be extended when fuelling on biodiesel due to its reduced energy density.

   (b) The fuel-bound oxygen content of the fuel may also contribute (via mixture stoichiometry, or radiative heat transfer, for example).

   (c) The addition of TPGME to petrodiesel also increased AHRR through this period. Like the biodiesels, the TPGME blends had both extended injection durations and increased oxygen content, compared to the neat petrodiesel.

5. The period of higher diffusion heat release tended to be associated with higher maximum in-cylinder pressure and NO_x emissions.

   (a) In general, trends in maximum pressure as a function of PMBF tended to closely resemble trends in NO_x emissions.

   (b) However, when considered as a function of maximum pressure, biodiesel NO_x emissions continued to exceed those of petrodiesel.

   (c) In general, the difference between petrodiesel and biodiesel NO_x emissions was largest when the difference in filter smoke number was also maximised, possibly implying a relationship with differences in mixture stoichiometry.

6. Filter smoke number (FSN) decreased with increasing degree of premixing.

7. For a given PMBF, the tested biodiesels had lower FSNs than the petrodiesels under all tested conditions.

(a) The difference was at its largest (around 70%) under the least premixed higher load conditions, and at its smallest (around 40%) under the most highly premixed lower load conditions.

(b) Increasing the fuel-bound oxygen content of petrodiesel, via the addition of TPGME, to a level comparable to that of biodiesel, reduced FSN to a level comparable to that of biodiesel.

8. FSN was correlated across all studies with quantities of diffusion combustion.

Addressing explicitly the objectives described in Section 5.1:

- *Is the relationship between premixing and NO_x emissions causal?* No firm conclusion can be drawn on this, because PMBF and other factors associated with increased NO_x emissions could not be separated. However, where the nature of the relationship between PMBF and NO_x varied between the studies, the variation tended to correspond to the changing relationship between PMBF and maximum in-cylinder pressure.

- *Is the relationship between premixing and NO_x emissions linear?* At higher load it appeared to be, but at lower load it did not. It may be necessary to extend the range of PMBFs further in order to accurately assess linearity at the higher load.

- *Is the relationship between premixing and NO_x emissions generalisable?* No, the relationship varies between operating conditions. It is not, as speculated in Chapter 4, necessarily the more highly premixed conditions at which the like-for-like difference in NO_x emissions between petro- and biodiesel is smallest; for instance, with increasing injection pressure PMBF becomes larger and the difference in NO_x emissions between petro- and biodiesel increases.

- *How do biodiesels from different feedstocks vary, when differences in start of combustion timing are removed and differences in degree of premixing are accounted for?* The most significant difference between biodiesels appears to be related to variations in the cetane number of the fuels, resulting largely from variations in the degree of unsaturation of the feedstock. With differences in PMBF, and hence the effects of differences in cetane number, accounted for, the remaining differences between the biodiesels were typically within the scale of variations inherent to the engine. Physi-

cal properties may also exert some influence; a possibly more viscous biodiesel, used cooking oil methyl esters, had significantly reduced NO_x emissions.

- *What is the effect of petrodiesel oxygenation?* In most respects, addition of an oxygenate to petrodiesel made it behave like biodiesel: NO_x increased, FSN decreased, diffusion AHRR and maximum in-cylinder pressure increased. The like-for-like difference in NO_x between petro- and biodiesel is largely negated when fuel-bound oxygen content is comparable. This implies that, beyond differences in combustion phasing and degree of premixing, the biodiesel NO_x emissions increase is related to differences in mixture stoichiometry (although differences in the duration of the injection event may also contribute).

Chapter 6

EFFECTS OF ANTIOXIDANT ADDITION TO BIODIESEL ON EMISSIONS FROM AN HSDI DIESEL ENGINE

The following section documents work performed with the assistance of Dr. H.A. Dhahad (of the University of Technology, Baghdad) and N.S.I. Alozie.

6.1 INTRODUCTION

Reduced oxidative stability is one of the principle drawbacks encountered when using biodiesel (fatty acid alkyl esters, produced by the transesterification of fats and oils) as either a partial constituent of a fuel-blend, or as a total replacement for traditional petrodiesel. The reduced stability of biodiesel compared to petrodiesel is related to the larger quantity of weakly-bound allylic and bis-allylic hydrogen atoms that it contains; as a result, biodiesel stability is dependent upon the feedstock from which the fuel is derived, with more highly unsaturated feedstocks generally yielding less stable biodiesels [148, 690]. Oxidative degradation leads to an increase in the viscosity, peroxide and acid values of the fuel, and can also produce insoluble high molecular weight polymers that are likely to have deleterious effects upon an engine's fuel system, potentially to the point of failure by injector contamination [609].

It has been shown that antioxidants can provide an effective means for preventing oxidative deterioration and can therefore prolong the reasonable shelf-life of biodiesel [691–693], although the efficacy of any particular antioxidant apparently varies dependent on the properties of the fuel to which it is added. In addition to this improvement in stability, there has also been some suggestion in the literature that exhaust emissions – especially those of oxides of nitrogen (NO_x) – might be improved by the addition of antioxidants. It

is with this point that the current article is concerned.

There have been a number of previous studies into the effects of antioxidant addition to biodiesel and biodiesel blends on diesel engine exhaust emissions. Hess et al [694] tested nine antioxidants, added to B20 soybean biodiesel, and their most significant reduction in NO_x emissions was found with the addition of butylated hydroxyanisole (BHA) at a concentration of 1000 ppm, which yielded an average 4.4% reduction in NO_x emissions compared to the baseline B20. Xu et al [695] also report that BHA addition to biodiesel leads to a reduction in NO_x emissions, as well as a reduction in smoke. In the Hess study, butylated hydroxytoluene (BHT) had a slightly lower apparent effect than BHA at the same concentration, corresponding to an average reduction in NO_x emissions of 3%. Varatharajan and Cheralathan (who have published several studies in this area [696–699]) found that BHT addition to a B20 jatropha biodiesel, at the same 1000 ppm concentration, gave a reduction in NO_x emissions of between 4–8%, depending on engine load [697]. Added to jatropha B100, 1000 ppm of BHT was associated with a 10–17% decline in NO_x emissions, but in most cases antioxidant addition was linked to an increase in emissions of CO, HC and smoke [697]. Similarly, Fattah et al [700, 701] added BHA and BHT to B20 blends of palm, coconut and jatropha biodiesels, and found that the antioxidants were generally associated with slightly reduced NO_x emissions but increased CO and HC emissions.

In the study by Ileri and Koçar [702], they reported that BHT was the most effective additive in terms of NO_x reduction, considered alongside BHA and TBHQ (*tert*-butylhydroquinone), when added to B20 canola methyl esters. McCormick et al [587] tested 2000 ppm TBHQ in a B20 soy biodiesel blend and reported a 0.8% reduction in NO_x, although this was accompanied by a 9% increase in particulate matter (PM). Hess et al also tested TBHQ, but found that on average it made little difference to NO_x (a 0.3% reduction), although results varied [694]. Velmurugan and Sathiyagnanam [703] report a reduction in NO_x emissions of around 14% following the addition of 1000 ppm TBHQ to a biodiesel produced from mango seed, and even larger reductions when diethylamine and pyridoxine hydrochloride were added at the same concentration; all of theses additives increased CO, HC and smoke emissions compared to the neat biodiesel.

Varatharajan et al report their most impressive reductions in NO_x emissions with amine antioxidants: *N-N'*-diphenyl-*p*-phenylenediamine (DPPD) was associated with a maximum reduction in excess of 50% at a concentration of 1500 ppm, while *p*-phenylene-

diamine (PPD) was most effective at a concentration of 250 ppm, with NO_x reductions ranging from about 35–45% [697]. Palash et al [704, 705] doped B5, B10, B15 and B20 jatropha blends with 1500 ppm DPPD and also recorded significant reductions in NO_x emissions, ranging from 3.5–16.5%. Again, the reduction in NO_x was accompanied by an increase in CO and HC. Prabu and Anand [706] added combinations of amine antioxidants to jatropha biodiesel at total concentrations between 1500–3000 ppm, achieving NO_x reductions of up to 10% in some cases, but a tendency towards slightly higher CO, HC and smoke emissions compared to the neat biodiesel.

Kalam and Masjuki [707] reported on the effects of 1% 4-nonylphenoxy acetic acid (NPAA) addition to a B20 palm oil biodiesel, documenting a 23% reduction in NO_x emissions compared to the base B20, and even larger reductions in CO and HC emissions. Similarly, Mofijur et al [708] doped a B35 palm biodiesel blend with 1% NPAA, and measured an average reduction in NO_x emissions of 17%, again accompanied by substantial reductions in CO and HC, as well as CO_2 emissions.

On the other hand, Kivevele et al [709] concluded that the addition of 1000 ppm of 1,2,3-trihydrobenzene (pyrogallol, PY) made little difference to emissions when fuelling on methyl esters of croton oil. Jain and Sharma [710] also reported no significant difference in emissions after adding PY to jatropha biodiesel. Likewise, Ryu [711, 712] found that there was no significant trend in emissions differences when five different antioxidants, including BHA, BHT and TBHQ, were added to soybean biodiesel.

In experiments undertaken in a burner rather than an engine, Gan and Ng [713] found that BHA and TBHQ addition reduced NO_x emissions from B10 and B20 palm oil biodiesel blends, while BHT addition was associated with an increase in NO_x emissions; BHA addition was also accompanied by decreased CO emissions, while BHT and TBHQ addition lead to an increase in CO. Antioxidant addition was at concentrations ranging from 250–1000 ppm and, in general, greater additive weighting correlated with a larger change in NO_x emissions. Interestingly, it should also be noted that the studies by Varatharajan et al concluded that the relationship between antioxidant weighting and NO_x reduction is non-linear, and beyond a certain concentration further addition may weaken rather than enhance the capacity for NO_x reduction [697].

It can be seen that a large proportion of the existing literature suggests that antioxidant addition may be an effective way to reduce NO_x emissions and stabilise biodiesel simultaneously (albeit with a possible penalty in terms of CO, HC and PM), and hence

remedy two of the major perceived issues with biodiesel usage in one fell swoop. Unfortunately, there isn't yet anything resembling a consensus on the issue, nor is there a clear explanation of the mechanism by which a large magnitude reduction, or indeed any reduction, might be elicited.

The suggestion seems to be that the purported reduction in NO_x may be related to radical quenching by antioxidants during the combustion process, specifically quenching of the hydrocarbon radicals (CH) involved in the formation of prompt NO (see Section 2.2.4.3). On the face of it (and at the risk of being demonstrably wrong), this appears to be an unlikely proposition. Although it is well understood that small quantities of a compound can have significant effects on combustion [584, 714], the antioxidants under discussion are structurally and chemically similar to common fuel components, and should therefore be expected to behave in keeping with the accepted kinetic models of hydrocarbon oxidation. Practically, the feature that differentiates a primary antioxidant from any other hydrocarbon, and by virtue of which it derives the ability to scavenge radicals and prevent autoxidation, is the possession of particularly weakly bound, easily abstractable, hydrogen atoms [715]. Essentially, these easily abstractable H-atoms provide more favourable targets for radical attack than those of which the fuel itself is comprised, and act as chain-breakers in the early stages of fuel degradation; particularly, primary antioxidants are intended to donate hydrogen to alkylperoxy radicals (RO_2), in order to prevent their creation of further alkyl radicals [227]. Figure 6.1 shows the three antioxidants employed in this study.

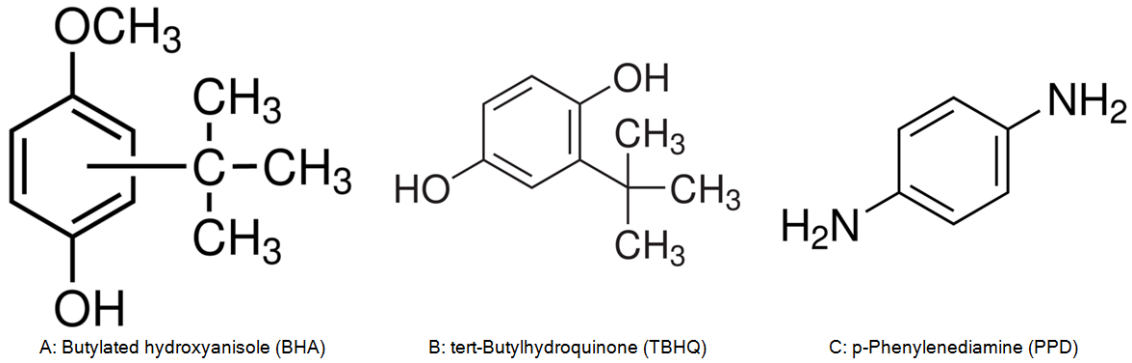

Figure 6.1: Chemical structures of tested antioxidants.

Figures 6.1A and 6.1B are hindered phenols. Phenol (C_6H_6O) itself functions as an antioxidant, but offers only partial quenching of radical activity, because the O-H bond dissociation energy (BDE) is not low enough [716]; it is slightly lower than that of a secondary H-C bond, but higher than an allylic H-C bond. Although phenol will act as

an effective quencher of alkoxy (RO) or hydroxy (OH) radicals, it does not represent a thermochemically attractive target for many alkylperoxy (RO_2) radicals, nor will it draw attack away from the weakest of the H-C bonds present in the fuel. The addition of electron donating groups to the aromatic ring reduces the O-H BDE value by stabilising the radicals formed after hydrogen abstraction through electron delocalisation [716–718]; increased delocalisation is also the reason why the phenol O-H bond is weaker (all other things being equal) than N-H or H-C bonds in the same position, when usually O-H bonds are the stronger of the three [719]. Of the substituents seen in Figure 6.1, the NH_2 group reduces BDE most significantly [717], which is why an amine like PPD is an effective antioxidant despite the slightly higher like for like strength of the aniline N-H bond compared to the phenol O-H bond.

It should be expected that hydrogen will be abstracted very early in the combustion process from viable sites in the antioxidant additives, or lost slightly later homolytically, forming resonantly stabilised aromatic radicals likely to have little low temperature reactivity. A possible exception might exist if the formation of bridged species is possible by reaction with O_2, which could lead to low temperature ring destruction [720]. It seems likely that stabilised aromatic radicals will decompose by pathways similar to those of other aromatic compounds, involving additions at the radical centre, decomposition of side chains, generally retaining the ring until later in the reaction process, and potentially generating significant amounts of soot precursors [720–722]. The implication of this is that any unique radical quenching potential of an antioxidant additive might be lost fairly early in the combustion process, before an opportunity to interfere with NO_x formation might be anticipated to arise.

There is no clear consensus on the proportion of total NO formed in a diesel engine for which the prompt NO pathways bear responsibility. In modelling studies, some researchers report significant formation via the prompt mechanism (around 40% in [589]), others report more modest amounts (around 10% in [415]), and others exclude the pathway entirely on the basis of negligibility [416, 723]. Prompt NO formation occurs at lower temperatures than thermal NO, and in slightly richer mixtures, peaking at an equivalence ratio of about 1.2, whereas thermal NO formation is highest at equivalence ratios between 0.8–1 [398]. However, the equivalence ratios expected within the diffusion flame sheath of a diesel jet are typically considerably higher (2–4) and are therefore not conducive to the formation of NO_x by either route, while, at the lean periphery of the diffusion

flame, temperatures are high enough that the thermal NO mechanism is dominant [379]. However, Dec [379] suggests that nitrogen containing compounds, like HCN, may still form in the fuel-rich core of the jet, and could then react to generate NO at the flame front, and hence Fenimore-type reactions might still contribute to diesel NO_x emissions. Experimentally, it has been observed that NO_x is undetectable in a diesel engine before the establishment of the diffusion flame, indicating that prompt NO is not formed in the rich premixed region itself; further, it is proposed that if large quantities of fixed-nitrogen compounds were being generated in the rich region, then there ought to be a spike in measured NO soon after the diffusion flame appears (because the accumulated nitrogen would be rapidly converted to NO), which isn't the case [534].

Ultimately then, the contribution of the prompt mechanism to NO_x formation in a diesel engine is certainly unclear, quite possibly small, and therefore even if antioxidants did significantly inhibit the prompt pathways, a reduction in NO_x emissions exceeding 10% would seem fairly improbable. Yet, as has been discussed, such reductions have been reported in the literature. On this basis, there may be some other explanation for the reported results.

The objective of the following study was to attempt to emulate the work performed in the aforementioned papers – particularly those of Hess [694] and Varatharajan [697] – to observe the extent and consistency of any possible reduction in NO_x or other emissions, and to identify possible causal influences. The three antioxidants selected were:

- BHA, because Hess et al [694], Gan and Ng [713], and Xu et al [695] each reported NO_x reductions associated with its use.
- TBHQ, because NO_x reductions have been reported by Gan and Ng [713] (and also by Velmurugan and Sathiyagnanam [703], although these had not been reported at the time that this work was undertaken), and Hess et al [694] concluded that further testing was required to determine its efficacy, due to the large variability in data that they recorded.
- PPD, because Varatharajan et al [696, 697] report substantial reductions in NO_x emissions with only very small quantities of the additive.

6.2 EXPERIMENTAL METHODOLOGY

The experimental setup was largely as described in Chapter 3. The study was performed in three parts, which are detailed in Table 6.1. In the first study (Study A) a commercially produced rapeseed biodiesel (rapeseed methyl esters, RME1, provided by Shell) was tested neat, doped with 1000 parts per million (ppm) by mass of butylated hydroxyanisole (BHA, see Figure 6.1A) and with 1000 ppm *tert*-butylhydroquinone (TBHQ, Figure 6.1B). In the second study (Study B) the same RME1 was doped at 250 ppm with *p*-phenylenediamine (PPD, Figure 6.1C).

EXPERIMENT	OPERATING CONDITION	FUEL DENOTATION	PARENT FUEL	ADDITIVE [WEIGHTING]
STUDY A	Engine load: 80 Nm (5 bar BMEP)	BASE	Laboratory petrodiesel supply	—
(Jan–Feb 2013)	Engine speed: 2000 rpm	RME1	Commercial rapeseed methyl esters	—
	Injection pressure: 800 bar	RME1+TBHQ	Commercial rapeseed methyl esters	*tert*-Butylhydroquinone [1000 ppm]
	Start of injection: 9 BTDC	RME1+BHA	Commercial rapeseed methyl esters	Butylated hydroxyanisole [1000 ppm]
STUDY B	Engine load: 80 Nm (5 bar BMEP)	BASE	Laboratory petrodiesel supply	—
(Jun–Jul 2013)	Engine speed: 2000 rpm	RME1	Commercial rapeseed methyl esters	—
	Injection pressure: 800 bar	RME1+PPD	Commercial rapeseed methyl esters	*p*-Phenylenediamine [250 ppm]
	Start of injection: 9 BTDC			
STUDY C	Engine load: 80 Nm (5 bar BMEP)	BASE	Laboratory petrodiesel supply	—
(Jan–Feb 2014)	Engine speed: 2000 rpm	RME2	Small-scale rapeseed methyl esters	—
	Injection pressure: 800 bar	RME2+PPD	Small-scale rapeseed methyl esters	*p*-Phenylenediamine [250 ppm]
	Start of combustion: 3.25 BTDC	RME2+BHA	Small-scale rapeseed methyl esters	Butylated hydroxyanisole [1000 ppm]

Table 6.1: Outline of the three component studies, including details of the operating conditions and the fuels and additives used.

However, because the commercially produced RME1 may have already been treated with an antioxidant preparation (details of which were unavailable) in order to provide oxidative stability meeting the legislative standards, a further biodiesel was procured; again, rapeseed methyl esters, but produced from cooking oil (purchased from KTC Edibles and transesterified by Work this Way Oil Works at HMP Standford Hill). According to the best available information, the only added ingredient in this oil was 5 ppm polydimethylsiloxane (E900, an antifoaming agent [214], commonly added to cooking oil), and there should be no antioxidant content besides that which is naturally present. Naturally occurring tocopherols were not quantified, but a combined tocopherol weighting of between 500–1000 ppm might be a reasonable approximation [123, 226].

In the third study (Study C) the biodiesel produced on a small scale and without prior additive treatment (RME2), was tested with 1000 ppm BHA and 250 ppm PPD. The purpose of this was to examine the possibility that the results of the earlier work had been compromised by antioxidant treatment of the commercial biodiesel during the manufacturing process.

The fuel blends were prepared using a Corning PC-620D stirring hot plate, at a mildly elevated temperature (40–60 °C) and a stirring speed sufficient to generate a vortex without introducing excessive air into the fluid (500–800 rpm). Mixing times varied depending on the additive, with the PPD requiring significantly longer to completely dissolve.

In order to minimise experimental error, all tests were performed on a fixed schedule. Each day, a baseline measurement was made following a 60 minute engine warm-up, and 90 minutes running at the nominal operating condition; by this point temperatures, pressures, fuelling rates and emissions had reached an approximately steady-state. The purpose of this baseline measurement is to provide a reference point which can be used to assess whether or not differences in emissions when operating on the various fuels can be attributed to the fuels themselves, or instead to a more general change in the environment or engine state. After the baseline measurement was made, the engine was switched to the test fuel, given a further 90 minutes to stabilise, and then measurements were taken. The same test schedule was used as in Chapter 5 (see Figure 5.1), but without the precaution of forced preheating of the test bay (discussed in Section 3.4).

Gaseous emissions were recorded over a 120 second duration and averaged. Three sets of emissions data were recorded within the same measurement time window for each test-fuel, and all experiments were repeated in duplicate or triplicate, depending on time and material constraints. Smoke emissions were, likewise, recorded three times within the measurement time window.

6.3 RESULTS

All results in the following section are presented alongside their respective daily petrodiesel baseline measurements. The reason for this is that engine performance and emissions vary day-to-day to a non-negligible extent, as discussed in Section 3.4. Particularly when trying to assess small differences between fuels or additives, changes in emissions which are of research interest can become lost within the noise of the variations inherent to engine operation. The objective is to use the available information to distinguish those changes which are properly attributable to the antioxidant additives themselves, from those changes which are not. Providing daily baseline values informs a more meaningful interpretation of the results, and, unlike normalisation, allows the reader to make their own decisions about the significance of the data collected.

In this section, plots are presented which illustrate emissions data by way of the fol-

lowing graphical elements:

- A dashed horizontal line, denoting the average for the biodiesel data set as a whole, throughout the study. This includes, taking Study A as an example, all of the RME1, RME1+TBHQ and RME1+BHA data. The dashed horizontal line is accompanied by dotted horizontal lines which indicate the standard deviation of the biodiesel data set as a whole, for the individual study.

- White markers and bars, accompanied by error bars, which represent the averages and standard deviations for each individual biodiesel preparation.

- A solid horizontal line, denoting the average baseline petrodiesel measurement across the experimental period. Dashdotted horizontal lines indicate the standard deviation of baseline petrodiesel data throughout the individual study.

- Black markers and cross-hatched bars, accompanied by error bars, which represent the averages and standard deviations for the petrodiesel baselines associated with each of the biodiesel test fuels. In each case, the baseline data is alongside its respective biodiesel data set.

For each pollutant the discussion will consist of the following:

- A comparison of average biodiesel emissions with the average petrodiesel baseline measurement.

- A comparison of the biodiesels containing additives with the neat parent biodiesel. Variations in the average baseline values accompanying each test fuel are discussed when considering the significance of apparent differences.

- A conclusion about the effect of the additives on pollutant emissions.

6.3.1 OXIDES OF NITROGEN

In Figure 6.2A it can be seen that, in Study A, biodiesel NO_x emissions (i.e. emissions from RME1, RME1+TBHQ and RME1+BHA) were, on average, 8.1% greater than those when fuelling on petrodiesel (i.e. at the daily baseline). The standard deviation of the biodiesel points, considered as a single data set, was 1.5%, compared to an overall standard deviation of 0.9% in the daily petrodiesel baseline values.

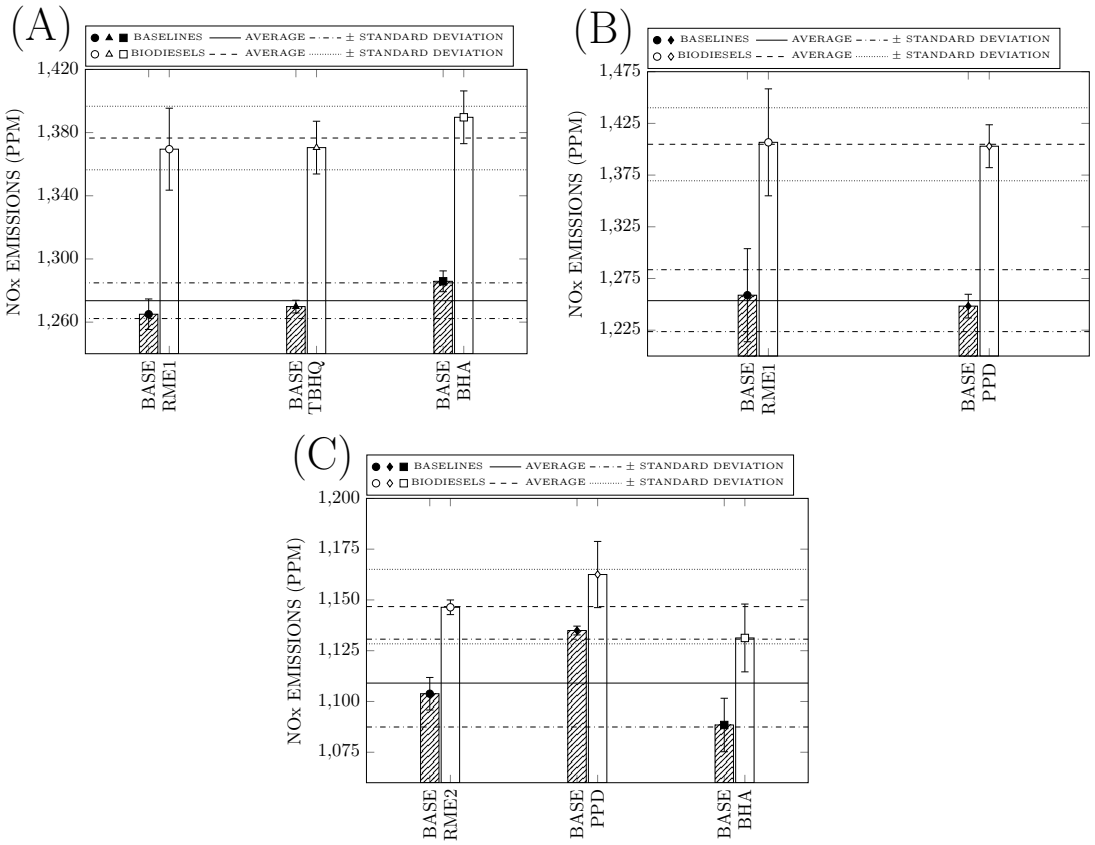

Figure 6.2: Emissions of oxides of nitrogen for biodiesel both neat and doped with antioxidants. In each case, biodiesel results are presented alongside their respective average petrodiesel baseline values. Horizontal lines unify the different sets of biodiesel and petrodiesel baseline results into single groups.

The maximum deviation from the undoped RME1 results was observed for the RME1 +BHA blend, which had NO_x emissions exceeding those of the neat fuel by 1.5%. However, this increase was accompanied by a 1.6% increase in the daily baseline value, effectively negating the change. RME1+TBHQ yielded average NO_x emissions within 0.1% of the neat RME1. Hence, neither additive appeared to cause a meaningful change in NO_x emissions.

In Figure 6.2B it can be seen that, in Study B, biodiesel NO_x emissions were, on average, 12.1% greater than those when fuelling on petrodiesel. Compared to the Study A results, average petrodiesel values were 1.6% lower, whereas average biodiesel values were 2.1% higher, despite the operating condition and fuels being nominally the same as in Study A. Experiments in Study A were undertaken in Jan/Feb 2013, approximately five months prior to the experiments in Study B, which were not performed until Jun/Jul 2013. In the intervening period, all four injectors in the test engine were replaced and it is probable that this, in addition to variations in atmospheric conditions, may bear responsibility for a large part for the differences in measured NO_x emissions. The standard

deviation of the biodiesel points, considered as a single data set, was 2.5%, compared to an overall standard deviation of 2.4% in the daily petrodiesel baseline values.

NO_x emissions from the RME1+PPD blend were, on average, 0.3% lower than those from the undoped RME1. This was accompanied by a 0.8% reduction in the daily petrodiesel baseline, which makes the small observed reduction in NO_x following PPD addition even less significant.

In Figure 6.2C it can be seen that, in Study C, biodiesel NO_x emissions were, on average, 3.3% greater than those when fuelling on petrodiesel. In Study C, NO_x emissions when fuelling on both petro- and biodiesel are substantially reduced in comparison with Studies A and B. The general reduction in magnitude (approximately 12.5% for petrodiesel and 16% for biodiesel) is primarily attributable to the retardation of injection timing in the third experiment, from 9 BTDC in Studies A and B, to 6.9 BTDC and 6.6 BTDC for petro- and biodiesel, repectively, in Study C; the difference in injection timing between petro- and biodiesel was required in order to obtain constant start of combustion timing (required for a parallel experiment, documented in Chapter 5). The disparity between petro- and biodiesel injection timing in Study C, with biodiesel being more greatly retarded, is the reason that biodiesel NO_x emissions were higher than those of petrodiesel by a smaller amount in Study C than in Studies A and B. The standard deviation of the biodiesel points, considered as a single data set, was 1.6%, compared to an overall standard deviation of 1.9% in the daily petrodiesel baseline values.

The RME2+PPD NO_x emissions exceeded those of the undoped RME2 by 1.4%, but this was accompanied by a 2.8% increase in baseline NO_x emissions, which may suggest a small reduction in NO_x emissions when fuelling on the PPD blend in this case. NO_x emissions from RME2+BHA were 1.2% lower than those from neat RME2, but this change is negated by the corresponding 1.2% reduction in the daily baseline.

Overall, the effect of all tested antioxidants on NO_x emissions appeared to be minimal, well within the anticipated day-to-day variation of the test engine. The most significant change in NO_x emissions as a result of antioxidant addition was with the addition of PPD to RME2 in Study C; combined with the daily baseline data, the results suggest a possible reduction in NO_x emissions when fuelling on RME2+PPD of 1–2%, although it remains quite conceivable that this is not meaningful.

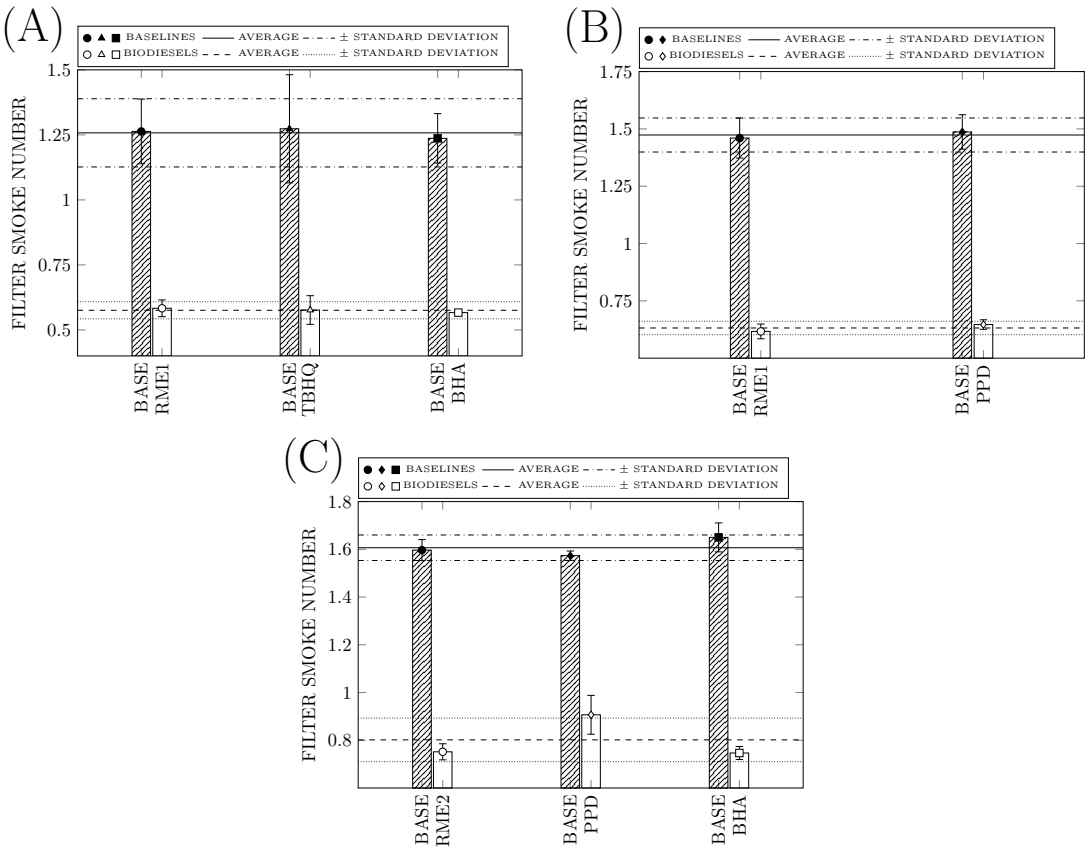

Figure 6.3: Filter smoke numbers for biodiesels both neat and doped with antioxidants. In each case, biodiesel results are presented alongside their respective average petrodiesel baseline values. Horizontal lines unify the different sets of biodiesel and petrodiesel baseline results into single groups.

6.3.2 FILTER SMOKE NUMBER

In Figure 6.3A it can be seen that, in Study A, biodiesel FSN values were, on average, 52.4% lower than when fuelling on petrodiesel. The standard deviation of the biodiesel points, considered as a single data set, was 0.03, compared to an overall standard deviation of 0.13 in the daily petrodiesel baseline values.

The neat RME1 and RME1+TBHQ both had FSNs of 0.58 (averages rounded to the 2 decimal places specified by the smoke meter). When fuelling on RME1+BHA the average FSN was 0.57. This small reduction was associated with a 2% reduction in the average daily baseline, more or less negating the change.

In Figure 6.3B it can be seen that, in Study B, biodiesel FSN values were, on average, 57.1% lower than when fuelling on petrodiesel. The standard deviation of the biodiesel points, considered as a single data set, was 0.03, compared to an overall standard deviation of 0.07 in the daily petrodiesel baseline values.

The FSN was 0.03 higher on average when fuelling on RME1+PPD than when fuelling

on neat RME1. This increase when fuelling on RME1+PPD was accompanied by a 2% increase in the daily baseline, which partially accounts for the change, although not entirely (the 0.03 average increase in FSN approximately equates to a 5% increase over the neat RME1).

In Figure 6.3C it can be seen that, in Study C, biodiesel FSN values were, on average, 49.1% lower than when fuelling on petrodiesel. The standard deviation of the biodiesel points, considered as a single data set, was 0.09, compared to an overall standard deviation of 0.04 in the daily petrodiesel baseline values. This means, that despite a lower variability in the petrodiesel baseline than was the case in Studies B and C, the standard deviation of the biodiesel data set tripled.

Average FSN when fuelling on RME2+PPD was 0.16 higher than when fuelling on either RME2 or RME2+BHA, which both had the same FSN, 0.75. The substantial increase in FSN with PPD addition was not accompanied by any increase in the average petrodiesel baseline value; in fact, the associated baseline was slightly lower for RME2+PPD than for the neat RME2. Hence, it appears that in Study C the addition of PPD may have caused a considerable increase in FSN, to the order of around 20%.

Additionally, in Study C the FSN measured when fuelling on RME+PPD increased as the fuel aged, from an FSN of 0.83 three days after production, to a value of 0.98 a day later. To a lesser extent, the same tendency was extant in Study B, wherein FSNs of 0.64 and 0.63 were measured one and two days after production, but when the next measurement was made a week later the value increased to 0.67.

Overall, PPD was the only antioxidant which was associated with a significant change in FSN, with the results suggesting that PPD addition may have increased smoke emissions significantly.

6.3.3 CARBON MONOXIDE

In Figure 6.4A it can be seen that, in Study A, biodiesel carbon monoxide emissions were, on average, 20.3% lower than when fuelling on petrodiesel. The standard deviation of the biodiesel points, considered as a single data set, was 4.3%, compared to an overall standard deviation of 4.9% in the daily petrodiesel baseline values.

CO emissions when fuelling on RME1 and RME1+TBHQ differed by only 0.1%, but those when fuelling on RME1+BHA were around 4.3% lower. This reduction was accompanied by a 5.9% reduction in the average petrodiesel baseline, effectively negating the

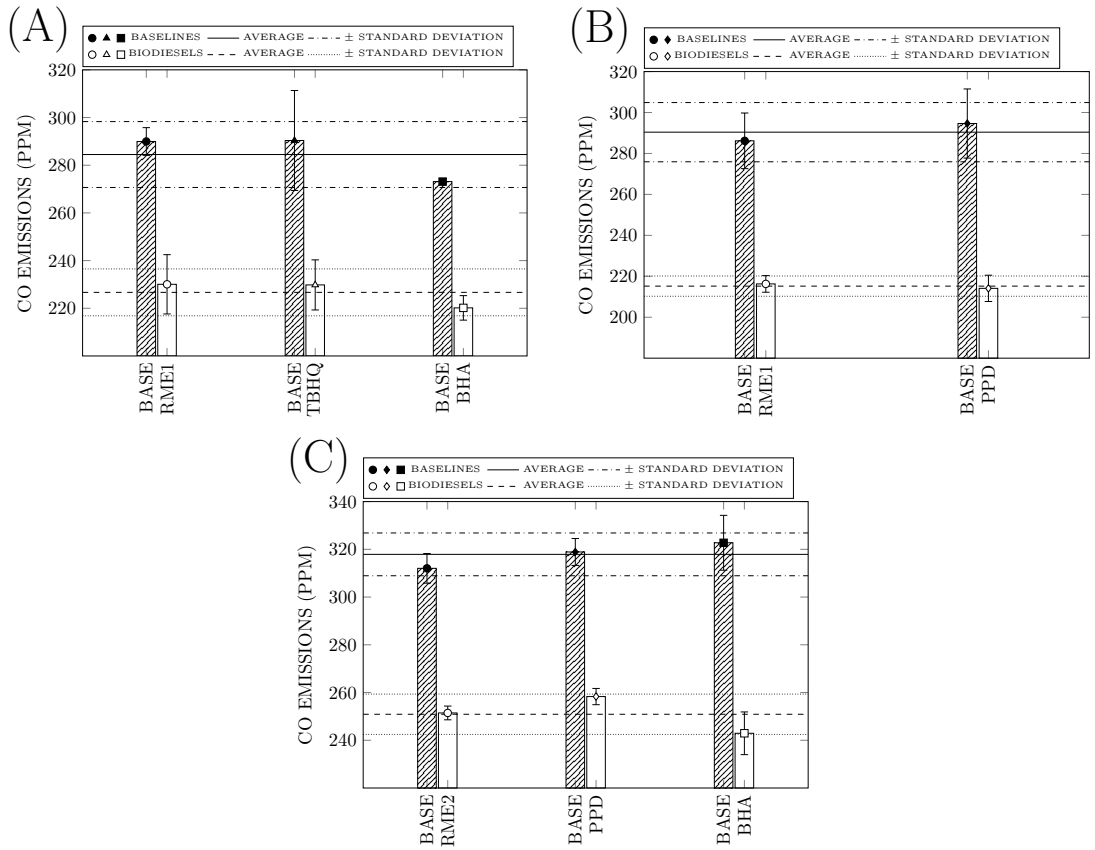

Figure 6.4: Carbon monoxide emissions for biodiesels both neat and doped with antioxidants. In each case, biodiesel results are presented alongside their respective average petrodiesel baseline values. Horizontal lines unify the different sets of biodiesel and petrodiesel baseline results into single groups.

change.

In Figure 6.4B it can be seen that, in Study B, biodiesel carbon monoxide emissions were, on average, 25.9% lower than when fuelling on petrodiesel. The standard deviation of the biodiesel points, considered as a single data set, was 2.3%, compared to an overall standard deviation of 5% in the daily petrodiesel baseline values.

When fuelling on RME1+PPD the CO emissions were 1% lower than when fuelling on the neat RME1. Alone, this is a very small change, but coupled with a 3% increase in the daily baseline, it appears more considerable.

In Figure 6.4C it can be seen that, in Study C, biodiesel carbon monoxide emissions were, on average, 21% lower than when fuelling on petrodiesel. The standard deviation of the biodiesel points, considered as a single data set, was 3.4%, compared to an overall standard deviation of 2.8% in the daily petrodiesel baseline values.

RME2+PPD had CO emissions 2.7% higher than those of RME2, accompanied by a 2.2% increase in the daily baseline, mostly accounting for the change. RME2+BHA recorded a 6% reduction relative to RME2, accompanied by a 3% increase in the daily

baseline. This means that there is an apparently meaningful reduction in CO emissions from biodiesel with the addition of BHA. However, as the wide standard deviation of the RME2+BHA data reflects, there were instances where CO emissions from RME2+BHA were comparable to those of the neat RME2, but these were associated with increased daily baseline emissions.

Overall, the data suggests that BHA addition to biodiesel may be associated with a reduction in CO emissions, although the significance of this is unclear. In Study A the reduction in CO when fuelling on RME1+BHA can be accounted for in terms of the daily baseline values, but in Study C a similar explanation cannot be invoked.

6.3.4 TOTAL HYDROCARBONS

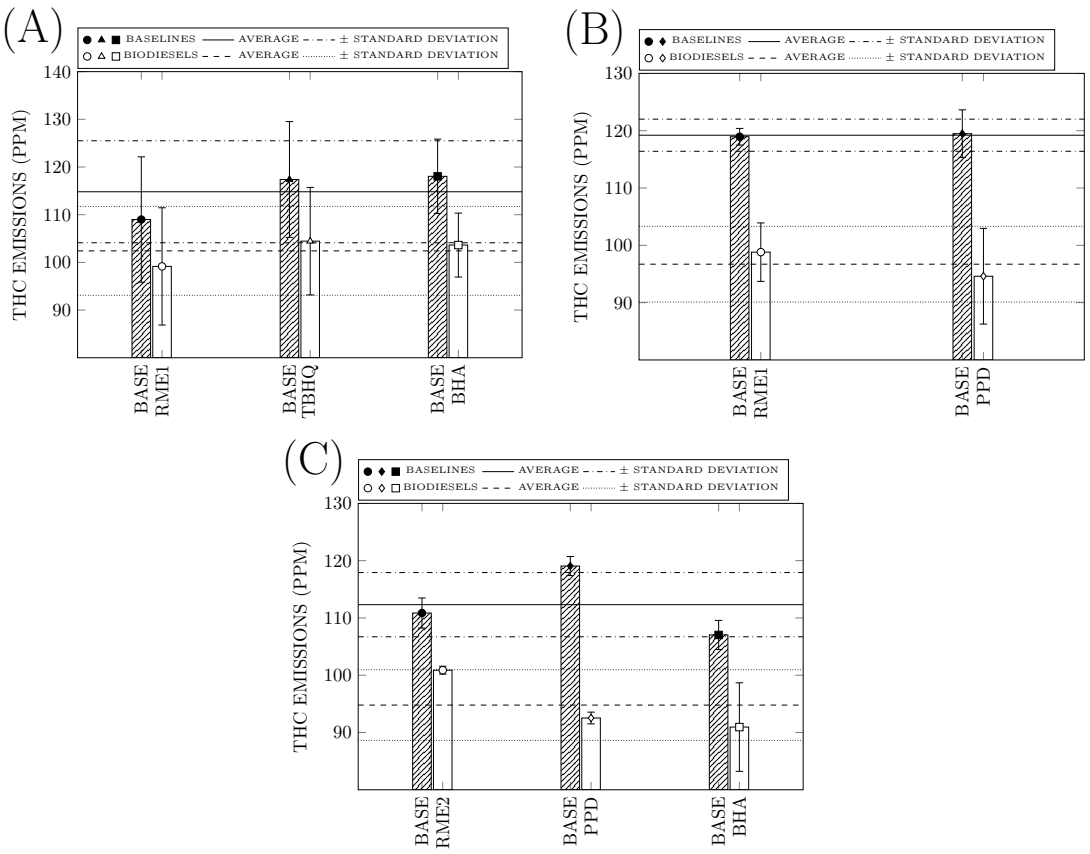

Figure 6.5: Total hydrocarbon emissions for biodiesels both neat and doped with antioxidants. In each case, biodiesel results are presented alongside their respective average petrodiesel baseline values. Horizontal lines unify the different sets of biodiesel and petrodiesel baseline results into single groups.

In Figure 6.5A it can be seen that, in Study A, the biodiesel total hydrocarbon emissions were, on average, 10.8% lower than when fuelling on petrodiesel. The standard deviation of the biodiesel points, considered as a single data set, was 9.1%, compared to an overall standard deviation of 9.3% in the daily petrodiesel baseline values.

Fuelling on RME1+TBHQ saw a 5.3% increase in average THC emissions over neat RME1, and was associated with a 7.7% increase in the daily baseline. Likewise, fuelling on RME1+BHA produced a 4.5% THC increase relative to RME1, accompanied by an 8.3% baseline increase. Even discounting the baseline increases, changes of this magnitude are insignificant due to the large standard deviation of the data for each fuel.

In Figure 6.5B it can be seen that, in Study B, the biodiesel total hydrocarbon emissions were, on average, 18.9% lower than when fuelling on petrodiesel. The standard deviation of the biodiesel points, considered as a single data set, was 6.8%, compared to an overall standard deviation of 2.4% in the daily petrodiesel baseline values.

RME1+PPD generated 4.3% lower THC emissions than RME1, accompanied by a 0.4% increase in the daily baseline. However, this change is likely to be insignificant due to the large variability of the data for each fuel.

In Figure 6.5C it can be seen that, in Study C, the biodiesel total hydrocarbon emissions were, on average, 15.6% lower than when fuelling on petrodiesel. The standard deviation of the biodiesel points, considered as a single data set, was 6.5%, compared to an overall standard deviation of 5.1% in the daily petrodiesel baseline values.

RME2+PPD had THC emissions 8.3% lower than those of the neat RME2, despite a 7.4% increase in the daily baseline. RME2+BHA had 9.8% lower THC emissions compared to the neat RME2, but this was accompanied by a 3.5% reduction in the petrodiesel baseline. Unlike the other THC data collected, there was very little variation amongst the RME2 and RME2+PPD data, and exceptional day-to-day repeatability, as the small standard deviations illustrate. However, this implies a degree of significance that is likely to be undeserved. Although it is possible that the RME2+PPD blend does reduce THC emissions, potentially a more prolonged experimental investigation would have revealed this as an experimental anomaly.

Overall, slight reductions in THC emissions were observed with the addition of PPD in both Studies B and C, but the high variability of THC data in general makes it hard to attribute much significance to the changes observed. If the reduction in CO with PPD addition is a real tendency, it may have some relation to the increase in sooting observed.

6.4 DISCUSSION

There was no substantial change in NO_x emissions elicited by any of the tested additives. This is in minor contradiction of data published by Hess et al [694], major contradiction of

data published by Varatharajan et al [697], but in general agreement with data published by Kivevele [709], Jain and Sharma [710], and Ryu [711, 712]. Why there should be such significant reductions in one study but negligible effects in others is not entirely clear. If the significant reductions seen by Varatharajan were related to combustion chemistry, it should be expected that they would be reproducible in any engine.

A plausible (but perhaps not entirely persuasive) reason for the discrepancy is associated with differences in engine technology. It is likely that the addition of antioxidants affects the physical properties of a fuel, and a change in physical properties would be expected to make a bigger difference in engines employing lower pressure pump-line-nozzle type injection systems, than it would in those utilising a high pressure common-rail. It is also conceivable that the thorough fuel filtration employed in this study may have removed some fraction of the antioxidant from the fuel before it reached the injectors, but given that the antioxidants were rigorously mixed into the biodiesel, and that no deposit accumulation was apparent on any of the fuel filters, this appears to be unlikely.

Additionally, in some cases it may be that the quality of the biodiesel, the manner in which the biodiesel-antioxidant mixture was prepared, and the time for which it was stored prior to use could have affected both the properties of the resulting fuel and the combustion characteristics. The RME1+PPD and RME2+PPD blends that were used darkened slightly as they were prepared and became progressively darker during storage (which wasn't unexpected, because PPD is a dye); the transition from a golden yellow, to a more reddish yellow, and finally to a dark cola-like brown can be seen in Figure 6.6. This process was significantly more rapid and pronounced with RME2+PPD (in Study C) – that is, with the biodiesel which was produced on a smaller scale and was not oxidatively stabilised by the manufacturers. It may also be pertinent that the RME2+PPD mixture was prepared at a slightly higher temperature and mixing speed. It is possible that during preparation and storage the PPD was oxidised and then reacted with some element of the fuel mixture, in order to produce the colour change by mechanisms related to those discussed in [724, 725]. Such a reaction might be expected to produce higher molecular weight compounds, and could therefore have caused an increase in the viscosity and sooting tendency of the fuel.

The production of aromatic oligomers from PPD may explain the slightly increased FSN observed, particularly in Study C, with the addition of PPD to biodiesel. In Study C the increase in FSN when fuelling on RME2+PPD was around 20% on average, compared

Figure 6.6: Colour transition of rapeseed methyl esters mixed with 0.025% m/m p-phenylenediamine. From left to right: before PPD addition, golden yellow; during mixing process, slightly more reddish yellow; several weeks after preparation, dark cola-like brown.

to neat RME2; this was the only case in which an additive caused the quantity of any pollutant to exceed the mean for the overall biodiesel set by more than one standard deviation of the overall set. This increase in smoke emissions when using a fuel doped with aromatic amines was also reported by Varatharajan et al [698].

The literature also generally reports increases in carbon monoxide and total hydrocarbon emissions when antioxidants are added to a biodiesel, as described in Section 6.1. However, here there is no strong evidence to that effect. In fact, CO was reduced in some cases following the addition of antioxidants, most significantly in Study C with RME2+PPD. In Study C THC emissions were also reduced following the addition of PPD to biodiesel, as well as following the addition of BHA. However, the variations in CO observed are insufficient to conclude that the effects are necessarily a result of the addition of antioxidants, and a far larger data set would be required to draw any definitive conclusion. That is to say, the influence of antioxidants is not large enough to be easily distinguishable from experimental error and the inherent variability of the system. In a better controlled environment, smaller changes could be reliably scrutinised.

It should be noted that in-cylinder pressure data was also collected throughout all of the experiments, and heat release parameters were subsequently calculated and analysed. At the outset, it was speculated that differences in factors like ignition delay, or heat release rates, may offer some explanation for the reported reductions in NO_x emissions following antioxidant addition to biodiesel; little information is currently available on this in the literature. However, like the majority of exhaust emissions, heat release characteristics were apparently unaffected by antioxidant addition (a detailed discussion of heat release and its associations with emissions can be found in Chapter 5).

6.5 CONCLUSIONS

Three antioxidant additives – *tert*-butylhydroquinone (TBHQ), butylated hydroxyanisole (BHA) and *p*-phenylenediamine (PPD) – were mixed into two rapeseed derived biodiesels (RME1 and RME2), in order to assess the effects of antioxidant addition on pollutant emissions. RME1 was produced on a large scale by a commercial manufacturer, and was likely to have been oxidatively stabilised with additives during the production process. RME2 was produced on a smaller scale, and was not treated with additives prior to the additions made for the purposes of this study.

In terms of NO_x emissions, none of the antioxidants had any significant effect. There were some changes in CO and THC emissions, but the significance of these is unclear; in all cases the average values for the antioxidant blends were within one standard deviation of the mean for the overall biodiesel set. The most apparently meaningful change observed was an increase in FSN (of around 20%) when fuelling on RME2+PPD. It is hypothesised that this is related to the oxidation of PPD during preparation and storage, followed by reaction with some element of the fuel to form higher molecular weight compounds, and evidenced by the significant observed colour change. This may have occurred more readily with RME2 because, first, it was not oxidatively stabilised during manufacture, and, second, because the blend was prepared at a slightly higher temperature and mixing speed.

An assessment of emissions differences on the scale of those introduced by admixture of antioxidants is problematic, because the inherent variation of the experimental setup is of a comparable magnitude to the changes that are of actual experimental interest. To assess such small changes, either a better controlled and more highly repeatable test system is required, or a far larger data set needs to be collected, in order to allow a comprehensive and statistically valid analysis to be performed.

The results of the work discussed in this chapter suggest the conclusion that changes in pollutant emissions caused by the use of antioxidants at the studied concentrations are small enough that differentiating them from the general variability of experimental engine data is not straightforward. This is with the exception of a possible increase in smoke emissions after the addition of PPD, which may become more pronounced with increasing storage duration.

Chapter 7

RELATIVE SOOTING TENDENCY OF VARIOUS BIODIESELS IN WICK-GENERATED DIFFUSION FLAMES

The following section documents work performed in collaboration with Dr. M. Lawrence, and also incorporates data collected by M.A. Pereira, Jr. (of the Federal University of São Carlos, Brazil) with the author's assistance. A more complete and authoritative description of the optical setup, methodology and analysis is given in [726]. The transmission electron microscope was operated by A. Howkins (of the Brunel University Experimental Techniques Centre).

7.1 INTRODUCTION

In a diesel engine the processes of soot formation are highly convoluted, and sophisticated experimental equipment and diagnostic techniques are necessary in order to obtain a useful characterisation of in-cylinder phenomena. A laboratory flame offers a far more accessible combustion environment, which can be relatively easily controlled, probed physically and optically with a minimum of apparatus, and used to test fuels available in only small quantities and of unknown quality without risk or expense.

The purposes of the following work were: First, to study simple wick-generated diffusion flames fuelled on a range of biodiesels, using an optical technique – namely laser-induced incandescence (LII). These results could then be compared with the respective chemical compositions of the fuels, to gain insight into the practical differences in sooting which the chemical differences between biodiesels might elicit. Second, to conduct similar experiments using petrodiesel, and its blends with biodiesel and other oxygenated fuels, to compare the efficacy of different oxygenated fuels with respect to soot reduction. Third, to collect soot from the flames for examination using a transmission electron microscope

(TEM), with a view to observing possible structural differences resulting from fuel chemistry. Temperature measurements were also made, in part to aid the explanation of the results, but also as a preliminary stage in the investigation of an alternative method of soot measurement; this method was based on [727, 728] but is not discussed here (forming part of a project undertaken by Pereira [729]). In addition, rudimentary sooting height measurements were made, to corroborate and compliment the LII results, and investigate another alternative means of characterising the flames.

7.2 EXPERIMENTAL SETUP

7.2.1 WICK BURNER

In initial experimentation an attempt was made to generate a stable diffusion flame using a vaporiser system, as employed in previous experiments undertaken at Brunel University [372]. However, although it was possible to sustain a satisfactory petrodiesel flame using this equipment, biodiesel posed a greater challenge on account of its higher boiling point, and a greater level of risk on account of its lower autoignition temperature. A biodiesel flame could be produced using the vaporiser, but it was difficult to sustain. However, both petrodiesel and biodiesel, being multi-component fuels, are likely to be unsuitable for use with some vaporiser-type setups, because the different fuel components vaporise at different temperatures and as a result there is a danger of fractionalisation, with the burned mixture not accurately representing the test fuel. This could be avoided if it were possible to ensure complete vaporisation of all constituents, but with the existing equipment the maximum obtainable temperatures were insufficient for this purpose.

The majority of the work documented in this chapter involved the use of a wick generated flame, and the wick burner is illustrated in Figure 7.1. The burner was formed of three parts; a bowl, a cylindrical wick holder which screwed into the base of the bowl, and the wick itself.

The fuel (A) was poured into the bowl, and the geometry of the bowl was designed such that, when full to the brim, the fuel surface remained 5mm below the base of the exposed wick; this prevented pool-burning of the more volatile fuels.

The wick (B) was produced from a calcium-magnesium silicate high temperature insulation wool with a melting point in excess of 1400 °C (Superpak 607 MAX, RS stock number 417-6779 [730]). This wool was not consumed or degraded by the flame itself, although with repeated use wicks would become clogged with soot and fuel residue, neces-

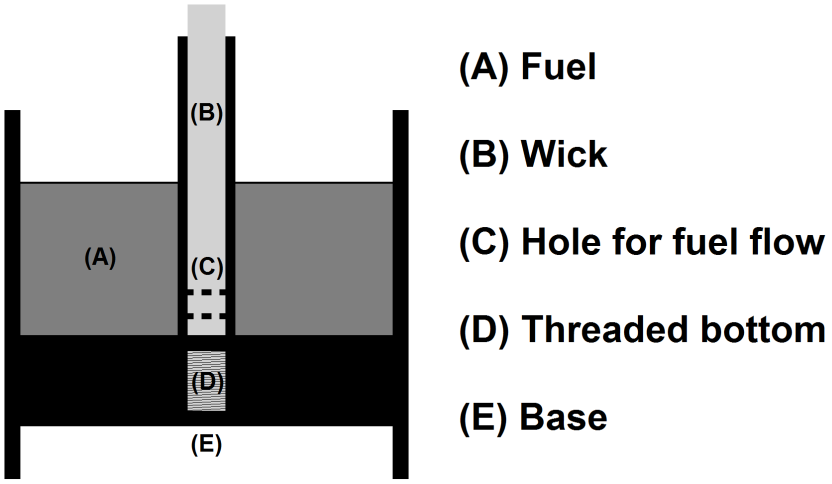

Figure 7.1: Cross-sectional illustration of the wick burner.

sitating periodic replacement. Wicks were hand-rolled to a diameter small enough to allow them to be fed through the 3 mm diameter wick holder. Due to the short fibre length of the ceramic wool, rolling the wicks and threading them through the holder was not straightforward. In an attempt to overcome this difficulty, some of the later experiments – particularly those using the pump (described in Section 7.2.4) – were trialled using a solid ceramic wick from an electronic cigarette (House of Hybrids ceramic wick replacement for the Z-Atty-Pro [731]). This offered advantages in terms of controllability and ease of use, but suffered more rapidly from clogging issues, which made the ceramic wool the preferred option.

Once the wick was inside the cylindrical wick holder, the wick holder was screwed into the base of the bowl. In a burner of this type, flame characteristics are heavily influenced by the shape and geometry of the wick. In order to maintain a degree of consistency, wicks were cut square to the desired length, and (where possible) each fuel was tested multiple times with different wicks to try to overcome any differences induced by changes in wick geometry.

Fuel was soaked into the wick through a hole in the base of the cylindrical wick holder (C), and was transported upwards by capillary motion. Effort was made to roll the wicks in a consistent fashion in order to maintain similar capillary radii; i.e. wicks were rolled to a similar tightness, using similar amounts of the wool. It was essential to thread wicks carefully through the wick holder, rather than packing them into it, because the latter had a negative impact upon wicking, and in some cases prevented flow at a rate sufficient to sustain the flame. In terms of fuel dependent variables, the rate of liquid penetration under capillary motion increases with increasing surface tension and decreases with increasing

viscosity [732]. Certain tested fuels – used cooking oil methyl esters and straight sunflower oil – were found to be excessively viscous to make use of.

The base of the wick burner (E) was shaped in order to enable precise and consistent location of the part with respect to the optical system, using the existing fittings.

7.2.2 OPTICAL DIAGNOSTICS

7.2.2.1 LASER-INDUCED INCANDESCENCE (LII)

Laser-induced incandescence (LII) is an optical diagnostic technique which is widely used to quantify soot volume fraction (SVF) in flames and other combustion systems [733]; it can also be used to predict soot particle sizes [734]. LII involves rapid laser heating of absorbing particles (LII is not restricted to soot, although this is its primary application), followed by photodetection of the resulting black-body radiation. Soot is a broadband absorber, but for the purposes of LII it is usual to irradiate it with an infrared range laser (a 1064 nm Nd:YAG in the case of this study) because this reduces interference in the results (compared to shorter wavelength lasers), from sources such as laser-induced fluorescence (LIF) of polycyclic aromatic hydrocarbons (PAHs) and C_2 fragments [735].

Incandescence of heated particles begins at temperatures above 2500 K, but initially the resulting LII intensity is strongly dependent on the soot temperature and hence the laser fluence, meaning that the effects of soot concentrations on the results are obscured by the effects of the laser settings. By heating the soot to what is known as the vaporisation threshold (approximately 4000 K) a large proportion of any additional energy supplied by the laser is used to vaporise the soot rather than heat it further; hence, past the vaporisation threshold, in the so-called 'plateau region', the influence of laser fluence on the observed LII intensity is reduced [736].

Soot incandescence is spectrally broad, but detection filters are commonly applied in order to restrict quantification to specific wavelengths. The purpose of this is to avoid those frequencies at which interference is likely, while retaining good signal strength, and to enable easier differentiation between LII and the luminosity of the flame [735].

7.2.2.2 OPTICAL SETUP

The optical setup employed for the LII aspect of the experiments can be seen in Figure 7.2.

(A) Camera: Andor InstaSpec V ICCD (intensified charge-coupled device).

(B) Lens: Nikon NIKKOR 50 mm.

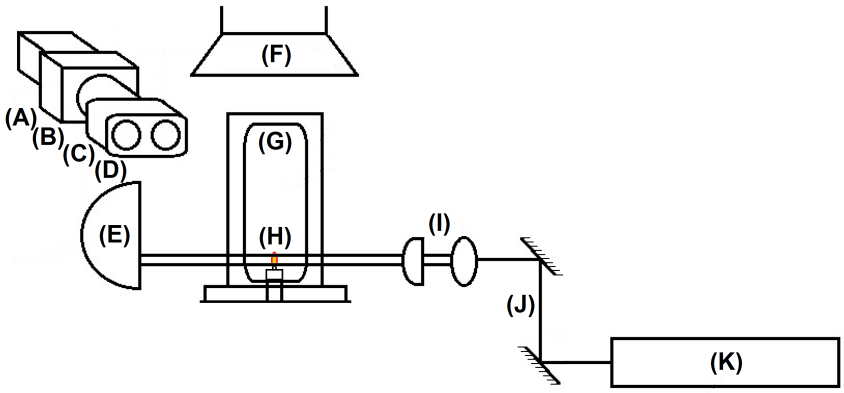

Figure 7.2: Labelled optical setup (label descriptions are given in the text) [726].

(C) LaVision image doubler.

(D) Band pass filters: 415 nm (25 nm FWHM (full width at half maximum)) and 632 nm (11 nm FWHM).

(E) Beam dump.

(F) Extractor.

(G) Flame guard with borosilicate glass windows.

(H) Wick burner (see Section 7.2.1).

(I) Lenses: used to create a laser sheet from the beam. The utilised laser sheet was 10 mm high and 0.5 mm thick.

(J) Mirrors.

(K) Laser: Continuum Surelite Nd:YAG (neodymium-doped yttrium aluminium garnet), with a fundamental wavelength of 1064 nm.

The laser was operated at a 10 Hz pulse frequency, a pulse duration of approximately 8 ns and a pulse energy of 10 mJ, equating to a fluence of 0.25 J/cm^2. The laser was externally triggered, and synchronised with the camera using a Stanford Research DG645 delay generator. The process was controlled via the image acquisition software, Andor MCD.

7.2.3 THERMOPHORETIC SAMPLING

The actuating element of the thermophoretic sampling system was designed and constructed by Stannett for his undergraduate dissertation [737]. It consists of a pneumatic solenoid-driven double acting cylinder, and is illustrated schematically in Figure 7.3.

Stannett also produced circuitry to control the residence time of the probe at its fully extended position, incorporating a reed switch for proximity detection, along with a series of electronic timers. To the end of the sampling probe illustrated in Figure 7.3

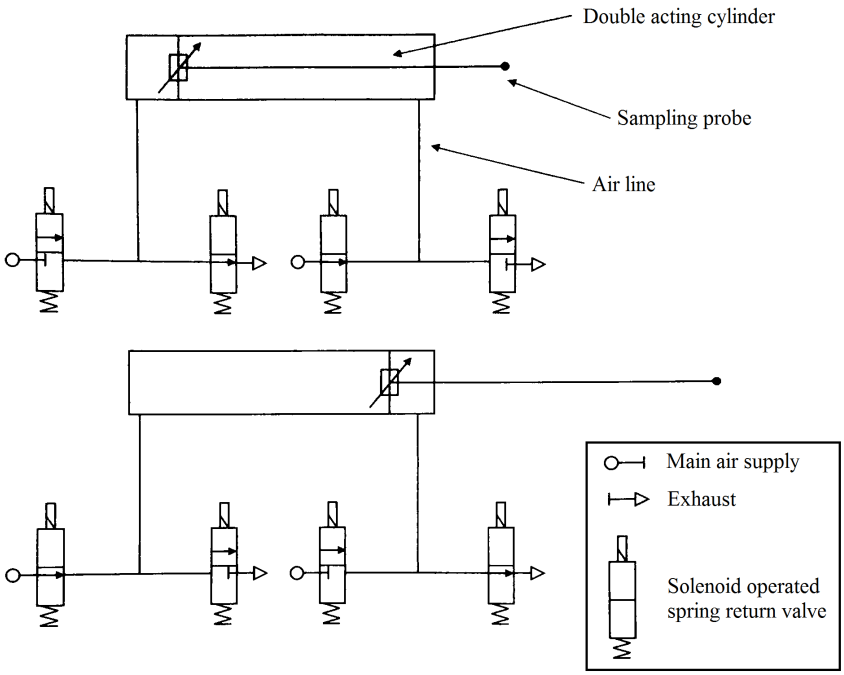

Figure 7.3: Pneumatic double acting cylinder circuit, shown with the sampling probe in the home position (top) and fully extended (bottom) [737].

an additional finger was attached, to enable a TEM grid to be inserted into the flame. A photograph of the sampling finger can be seen in Figure 7.4, with the TEM grid in place (located in the hole to the far right of the image). The grids were clamped between two metal plates, the top one slightly bent to ensure sufficient pressure to keep the grid in place, and the bottom machined with a very small recess to make grid positioning more repeatable and robust.

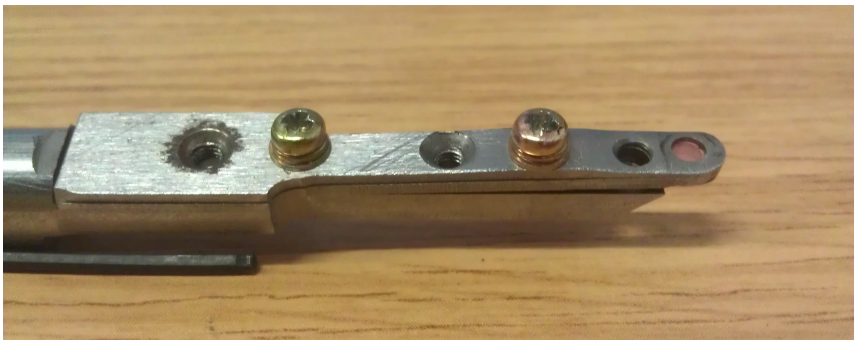

Figure 7.4: Sampling finger with TEM grid in place.

The finger was made reasonably slim, and high-speed video revealed minimal perturbation of the flame during insertion. It also indicated an in-flame residence time of approximately 65 ms. Initially, the sampler was seen to pitch forwards a little upon reaching full extension, leading to a spurious fall in the position of the grid within the flame. This problem was rectified by running the probe along a solid rail.

The TEM grids used were carbon films on 200 mesh copper, with diameters of 3.05 mm (purchased from Agar Scientific and TAAB Laboratories Equipment).

7.2.4 PUMP DRIVEN WICK BURNER

All of the LII, sooting height and TEM experiments were undertaken using the wick burner described in Section 7.2.1. Temperature measurements were performed using a modified setup, incorporating a Shimadzu LC-20AD solvent delivery unit from an high-performance liquid chromatography (HPLC) system. This unit is capable of accurately maintaining a constant rate of flow between 0.0001–10 ml/min, and was included to improve the controllability of the flame by varying the rate at which fuel was supplied to the base of the wick. An illustration of the setup can be seen in Figure 7.5.

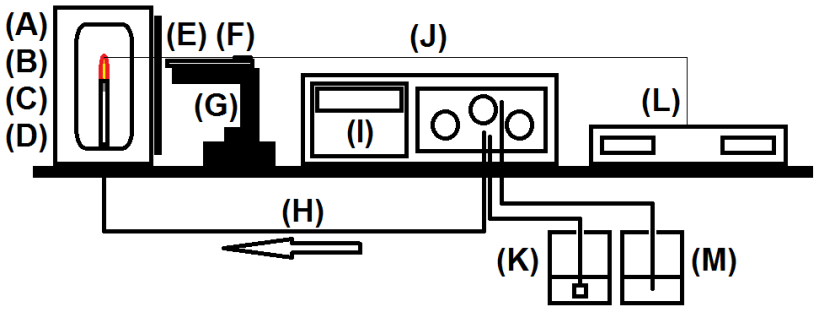

Figure 7.5: Labelled flame setup incorporating solvent delivery unit (label descriptions are given in the text).

(A) Flame guard with borosilicate glass windows.

(B) Wick-generated flame.

(C) Wick: for all reported work the same ceramic wool was used (as described in Section 7.2.1), but attempts were also made using a solid porous ceramic wick from an electronic cigarette [731]. The latter suffered more quickly with fouling.

(D) Glass tube feeding fuel to the wick.

(E) Draft excluder, to prevent perturbations of the flame from the direction of the removed window.

(F) R-type thermocouple (both 0.075 mm and 0.125 mm wire diameters were used).

(G) Positioning stage.

(H) Fuel flow from solvent delivery unit.

(I) Shimadzu LC-20AD solvent delivery unit.

(J) Thermocouple compensation wire.

(K) Fuel supply, induction through a ceramic filter.

(L) Temperature display: running through a Eurotherm 2132 temperature controller [738].

(M) Waste fuel/flushed solvent.

Although the measurements made were intended to have qualitative rather than quantitative validity, temperatures were measured using R-type thermocouples of two different diameters, 0.075 mm and 0.125 mm (purchased from Omega, part numbers P13R-003 and P13R-005, respectively), to provide an approximate indication of the degree of error that may exist as a result of radiant heat loss from the thermocouple [739]. The thermocouple tips were kept a constant shape by reforming them between measurements around a cylinder of 10 mm diameter.

7.2.5 FUELS

The fuels employed for the following experiments were as follows:

- Ultra-low sulphur diesel (ULSD).
- Rapeseed methyl esters (RME).
- Sunflower methyl esters (SME).
- Coconut methyl esters (CME).
- Tallow methyl esters (TME).
- Fish oil ethyl esters (FEE).
- ULSD blended with varying percentages of RME.
- ULSD blended with varying percentages of diethylene glycol diethyl ether (DGDE). The chemical structure of DGDE can be seen in Figure 7.6.

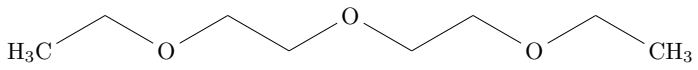

Figure 7.6: Chemical structure of diethylene glycol diethyl ether (DGDE).

The major chemical components of the biodiesels used in this study were characterised by means of gas chromatography. Analyses were performed on an Agilent 6890N Gas Chromatograph, with an HP-INNOWax column (19091N-133), having a polyethylene glycol stationary phase [652, 653]. The method used was based upon that recommended by BS EN 14103:2011 [654], with minor alterations. Fuel samples were prepared into a 1:10 fuel:hexanol solution, and 1 μl was injected at a temperature of 300 °C, pressure of 11 psi and split ratio of 50:1. The carrier gas used was hydrogen, at a flow rate of 1.9 ml/min and pressure of 11 psi. As per the cited standard, the temperature was initially

held at 60 °C for 2 minutes, then raised at a rate of 10 °C/min until reaching 200 °C, then at 5 °C/min up to 240 °C. This was followed by a 6 minute hold, a 20 °C/min rise to 260 °C and a further 4 minute hold, in an effort to ensure complete removal of all injected material from the column. The system used an FID detector to quantify eluted species. Chemical compounds were identified by comparison with the available literature [103, 131]. In the case of the vegetable derived biodiesels, with relatively uncomplicated compositions, identification by this method was straightforward. The greater complexity of the animal derived tallow methyl esters and fish oil ethyl esters meant that certain smaller peaks could not be confidently named; fortunately, the bulk of the fuel did not present a problem.

A breakdown of the composition of the biodiesels is given in Table 7.1. Values are quoted to the nearest 0.5%, and species present in concentrations of less than 1% are not quoted. RME is fully accounted for. SME contained a <1% proportion of methyl palmitoleate (C16:1). CME contained a <1% proportion of methyl caproate (C6:0). TME contained a <1% proportion of methyl laurate, and a further 3.5% of the fuel components could not be certainly identified; most unidentified peaks lay between those attributed to C16:1 and C18:0, and are possibly indicative of methyl esters of more highly unsaturated C_{16} fatty acids. In the case of FEE, 16.5% of the fuel components could not be identified; as with the TME, the majority of unidentified peaks (accounting for around 11% of the total composition) lay between C16:1 and C18:0 peaks – again, some are possibly indicative of ethyl esters of more highly unsaturated C_{16} fatty acids.

METHYL ESTERS

NAME	FEEDSTOCK	C8:0	C10:0	C12:0	C14:0	C16:0	C16:1	C18:0	C18:1	C18:2	C18:3	C20:1	C22:1	AVG. C	DN	AFT (K)
RME	RAPESEED OIL					4.5		2	**64.5**	18.5	9.5	1		17.93	131	2430
SME	SUNFLOWER OIL					6.5		3.5	27	**62.5**				17.86	152.5	2435
CME	COCONUT OIL	7	5.5	**45.5**	18.5	10		2.5	8.5	2				13.13	12.5	2405
TME	TALLOW				2.5	23	2	16.5	**41**	9.5	1.5			17.3	12.5	2420

ETHYL ESTERS

NAME	FEEDSTOCK	C8:0	C10:0	C12:0	C14:0	C16:0	C16:1	C18:0	C18:1	C18:2	C18:3	C20:1	C22:1	AVG. C	DN	AFT (K)
FEE	FISH OIL				13.5	**30.5**	14.5	3.5	14	1.5			6	16.5-16.75	70-100	2420-2425

Table 7.1: Results of fuel analysis by gas chromatography (with major species emphasised). AVG. C is the average main carbon chain length (this value is one less than the carbon number of the fuel for methyl esters, and two less for ethyl esters). DN is the double bond number (calculated as described in [233]) which gives an indication of the degree of unsaturation of a fuel. ATF is the estimated adiabatic flame temperature.

Some estimated properties of the fuels are also given in Table 7.1. In all cases these estimates are based upon the fatty acid composition, with double bond number calculated as described in [233] and adiabatic flame temperatures calculated (for reactants beginning

at the standard state, using the method in [206]) from enthalpy estimations by the Benson-Groups method given in [210]. Overall values for each biodiesel were calculated by weighted averaging of pure methyl/ethyl ester values. In some cases this approach may be adequate, but in others it is unlikely to give quantitatively reliable results; property estimations are intended only to provide qualitative insight. For FEE, values are given as ranges, intended to encapsulate the possible properties of the unidentified portions.

7.3 RESULTS AND DISCUSSION

7.3.1 SOOT VOLUME FRACTION

The addition of either rapeseed methyl esters (RME) or diethylene glycol diethyl ether (DGDE) to neat petrodiesel increases the oxygen content of the fuel, and therefore tends to suppress soot formation. The effects of both oxygenates on planar soot volume fraction (SVF) distributions can be seen in Figures 7.7 and 7.8. In Figure 7.7 petrodiesel is blended with RME at percentages of 10, 20, 25, 30, 45, 50, 60 and 75% (RME %m/m), in addition to neat tests of each fuel; this gives a fuel-bound oxygen content range of approximately 0–11%. In Figure 7.8 petrodiesel is blended with DGDE at percentages of 20, 30, 50 and 75% (DGDE %m/m), equating to a maximum fuel-bound oxygen content of approximately 22% (neat DGDE contains around 29.6% oxygen).

Flame height was kept approximately constant at 15 mm. Dilution of the petrodiesel with either additive tended to reduce flame height, and so it was necessary to increase the length of the exposed wick (and hence fuel mass flow rate) in order to maintain flame height with the additised fuels.

Figure 7.7: Planar soot volume fraction distributions within 15 mm flames of petrodiesel, rapeseed methyl esters and their blends. From top left: petrodiesel, B10 (fuel-bound oxygen content ≈ 1.1%), B20 (≈ 2.2% oxygen), B25 (2.7%), B30 (3.2%), B45 (4.9%), B50 (5.4%), B60 (6.5%), B75 (8.1%) and neat biodiesel (10.8%).

Figure 7.8: Planar soot volume fraction distributions within 15 mm flames of petrodiesel and its blends with diethylene glycol diethyl ether. From top left: petrodiesel, 20% DGDE (fuel-bound oxygen content ≈ 6%), 30% DGDE (≈ 9% O_2), 50% DGDE (15%) and 75% DGDE (22%).

In both cases, there is evidence of a general reduction in soot volume fraction with increasing oxygen content of the fuel. This reduction is quantified in Figure 7.9. However, there is a significant amount of deviation from the general trend; this may result from the small changes that it was necessary to make to the wick in order to maintain flame height, or small alignment errors that could have caused slightly off-centre imaging of the flame.

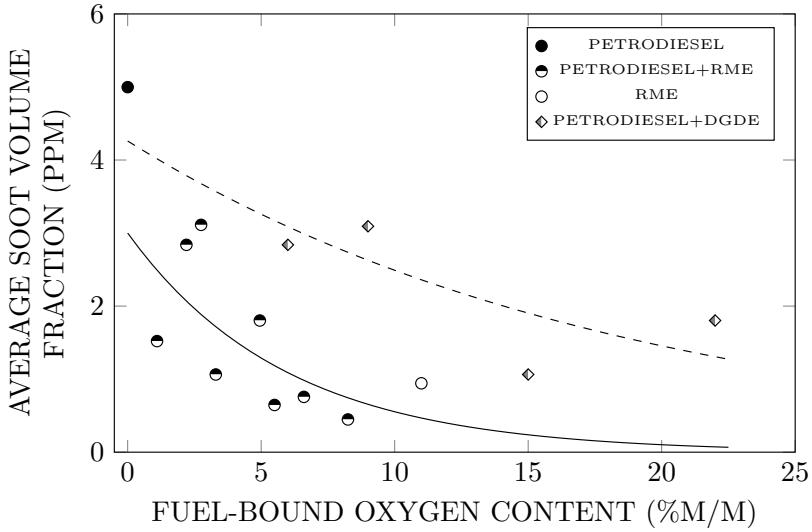

Figure 7.9: Average soot volume fraction within 15 mm flames of petrodiesel, rapeseed methyl esters and blends of petrodiesel with RME and diethylene glycol diethyl ether, given as a function of fuel-bound oxygen content (solid line represents an exponential fit through the petrodiesel+RME data set, including neat petrodiesel and RME; dashed line represents an exponential fit through the petrodiesel+DGDE set, including neat petrodiesel).

It can be seen that although addition of both RME and DGDE reduced average SVF values, RME offered more effective suppression of soot as a function of fuel-bound oxygen content. This is at least partially because a greater admixture of RME was required in order to attain the same level of fuel-bound oxygen content, leading to a greater dilution effect; that is, a larger proportion of the highly sooting parent petrodiesel compounds were replaced with less sooty RME components. Planar SVF results for neat petrodiesel and RME flames of varying heights can be seen in Figures 7.10 and 7.11.

There is no large visible difference to be seen between the petrodiesel and RME plots

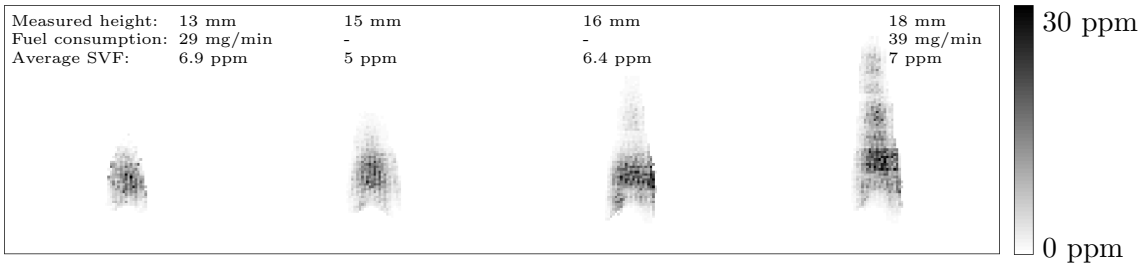

Figure 7.10: Planar soot volume fraction distributions within petrodiesel flames of varying heights (with measured flame heights, fuel mass consumption rates and average soot volume fractions inset).

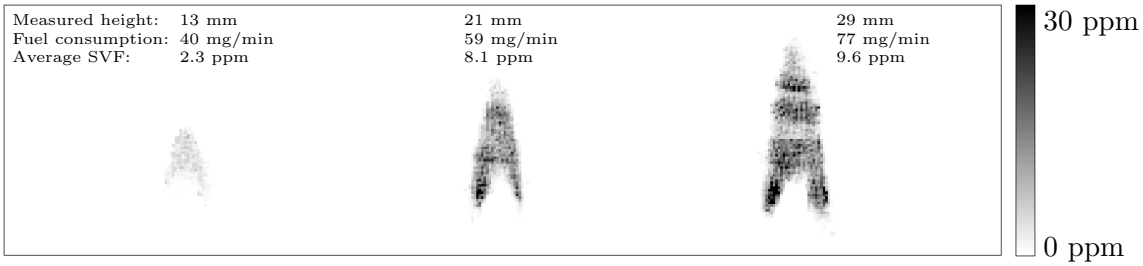

Figure 7.11: Planar soot volume fraction distributions within RME flames of varying heights (with measured flame heights, fuel mass consumption rates and average soot volume fractions inset).

in Figures 7.10 and 7.11, with neither set of flames appearing to be significantly sootier than the other; in fact, contrary to the overall trend observed in Figure 7.7, average SVF values sometimes seem higher within the RME flames in Figure 7.11 than within the petrodiesel flames in Figure 7.10. However, in cases where the planar SVF plots suggest that the petrodiesel and RME flames are of similar sizes, the measured flame heights were actually significantly larger for the RME flames, as were the rates of fuel consumption. What this indicates is that the concentrations of soot throughout the RME flames, and the proportions of fuel-carbon being converted to soot, were reduced relative to petrodiesel, to the extent that a considerably reduced proportion of the full luminous height of the RME flames generated incandescence within the magnitude range that has been illustrated. That is to say, the LII results make the RME flames look smaller due to their reduced soot concentrations. This is true of all of the biodiesels, as Figure 7.12 shows (note that imaged flame height in pixels is determined from the planar SVF plots, counting at the flame centreline).

Within combusting diesel jets, something similar was seen by Nerva et al [509], who observed that soot arose further downstream when fuelling on biodiesel than when fuelling on petrodiesel, and was subsequently removed more quickly; hence, the high SVF region represented a smaller proportion of the actual size of the biodiesel jet. Although the conditions within a partially-premixed jet are different to those within a diffusion flame,

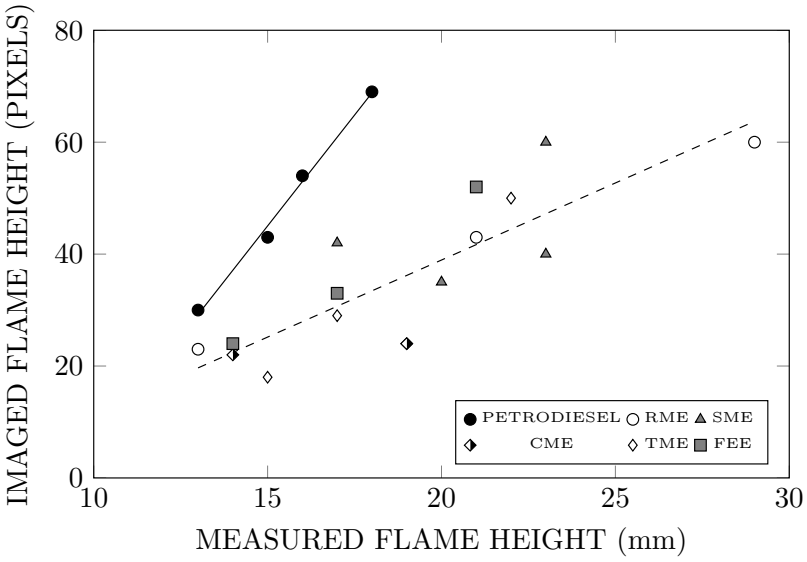

Figure 7.12: Imaged flame height in pixels as a function of measured flame height in millimetres (solid line represents linear petrodiesel best fit, dashed lines represents best fit through all biodiesel points).

in principle the tendency may be the same. If biodiesel retards the processes of soot development such that high concentrations take longer to arise and are more quickly reduced towards the tip, then that could provide some explanation for the trends observed here. However, what may be a little misleading about the SVF plots in Figures 7.10 and 7.11, and in later illustrations, is that the y position of the SVF data is not a constant measure of the height above the burner. Hence, a shorter SVF distribution and imaged flame height may represent reduced soot towards the base of a flame, as well as reduced soot towards the tip.

Figures 7.13–7.15 show planar SVF distributions for methyl esters of sunflower oil (SME), coconut oil (CME) and tallow (TME), and Figure 7.16 for ethyl esters of fish oil (FEE). Figure 7.13 appears to show that the SME flames are somewhat less sooty than the RME ones, although any analysis is encumbered by substantial variations in the imaged flame size. Variability is also apparent in Figure 7.12, which sees two of the SME points falling above the general biodiesel trend, and two of them falling below it. Considering the third and fourth flames from Figure 7.13, both of which were measured at 23 mm but one of which is much larger than the other, it becomes clear that some aspect of the measurement is flawed. Whether the problem lies with the repeatability of the experimental method, or temporary instabilities in the SME flame, it is clear that a greater quantity of data would be required to perform an accurate characterisation of sooting tendency.

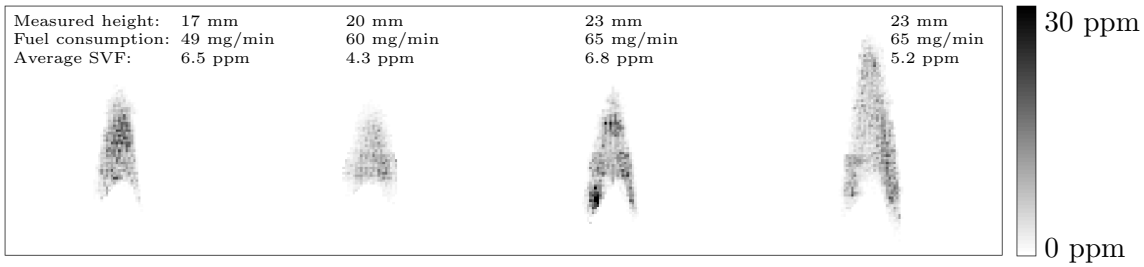

Figure 7.13: Planar soot volume fraction distributions within SME flames of varying heights (with measured flame heights, fuel mass consumption rates and average soot volume fractions inset).

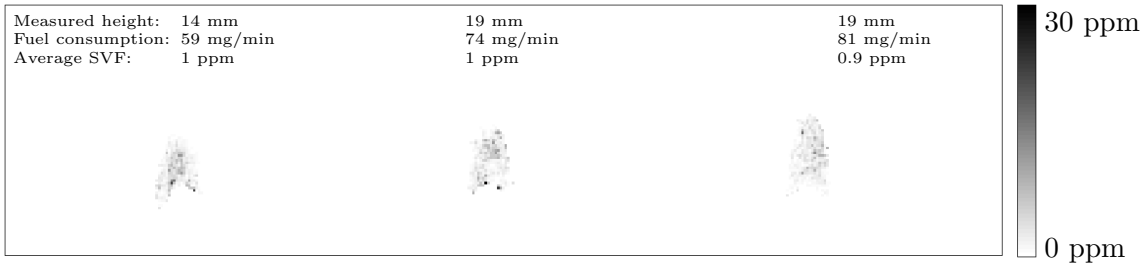

Figure 7.14: Planar soot volume fraction distributions within CME flames of varying heights (with measured flame heights, fuel mass consumption rates and average soot volume fractions inset).

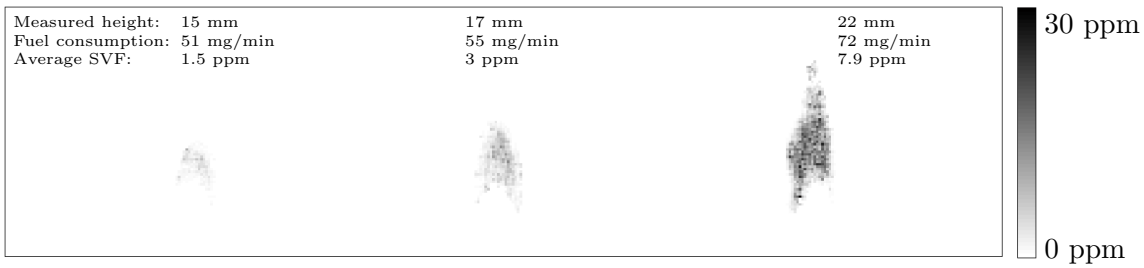

Figure 7.15: Planar soot volume fraction distributions within TME flames of varying heights (with measured flame heights, fuel mass consumption rates and average soot volume fractions inset).

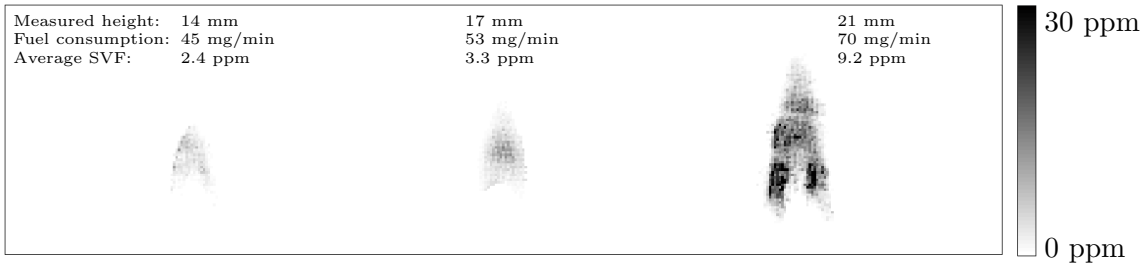

Figure 7.16: Planar soot volume fraction distributions within FEE flames of varying heights (with measured flame heights, fuel mass consumption rates and average soot volume fractions inset).

The CME flames illustrated in Figure 7.14 exhibited occasional flickering, possibly related to the quality of the fuel. However, the CME flames are so starkly different to those of the other tested fuels that any errors induced by flickering are likely to be of minor significance. It is immediately clear from Figure 7.14 that the CME flames had only very low levels of soot. This is likely to be related to the shorter average chain length and highly saturated nature of the CME.

The TME flames shown in Figure 7.15 appear to be slightly lower in soot than the RME and FEE flames (FEE flames are shown in Figure 7.16), and also have significantly higher fuel consumption rates associated with them for the same measured flame height. This is clarified by Figure 7.17.

Note that measured flame height was defined to the tip of the luminous region. For the petrodiesel data in Figure 7.17, a linear fit has been placed though the points for the closed, non-sooting flames, and a second order fit has been placed through all points, including those measurements made for open, sooting petrodiesel flames. Above the sooting height, it can be seen that the height to the peak of the luminous region increases at a lower rate with increasing fuel consumption.

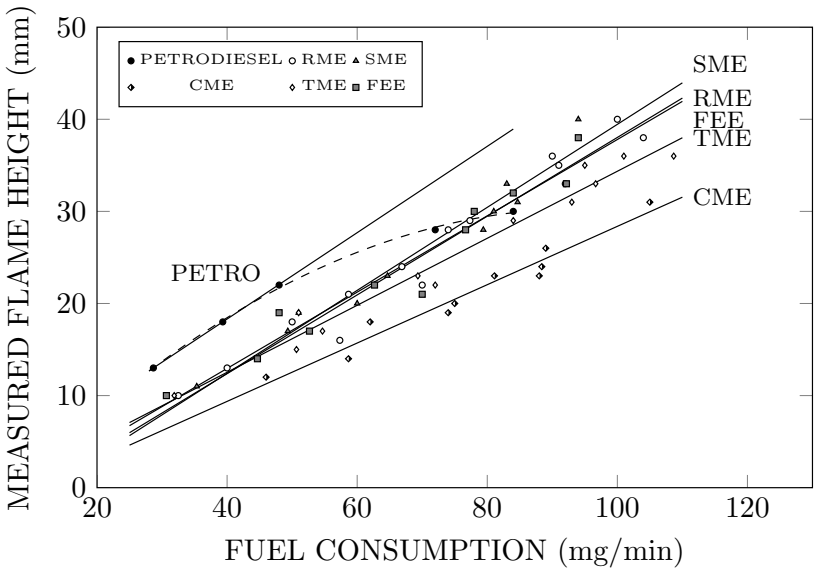

Figure 7.17: Measured flame height as a function of fuel consumption rate. Solid lines represent linear best fits for each tested fuel, labelled accordingly. In the case of petrodiesel, a linear fit runs through those points measured below the sooting height; a dashed second order fit includes those measurements made for open, sooting, petrodiesel flames.

Figure 7.17 shows that the fuel consumption required to generate a flame of any given height was generally higher for the less sooty fuels. Given that soot radiation is responsible for the natural luminosity of a diffusion flame, this is to be expected. CME required a far

higher fuel flow rate than the other fuels (and, accordingly, a significantly larger wick), in order to produce a flame of any particular height, TME flames had the next highest fuel demand, RME and FEE were higher, SME was slightly higher again, and the petrodiesel flames were considerably larger than those of all of the biodiesels for the same rate of fuel consumption.

Recalling the fact that petrodiesel had larger imaged flame heights than the biodiesels for equivalent measured flame heights (see Figure 7.12), it follows that petrodiesel flames which appear similar in terms of planar SVF distribution would be associated with significantly lower rates of fuel consumption; a comparison of the consumption rate values inset on Figure 7.10 to those on Figures 7.11–7.16 confirms that this is the case.

In Figure 7.18 the sooting tendency of each fuel is represented as a product of the apparent imaged flame area and the average SVF – that is, as the summation of calculated SVF throughout the flame. This approach aims to include the effects that fuel chemistry has on both imaged flame size and soot volume fraction, and in this instance appears to offer a clearer perspective than average SVF alone.

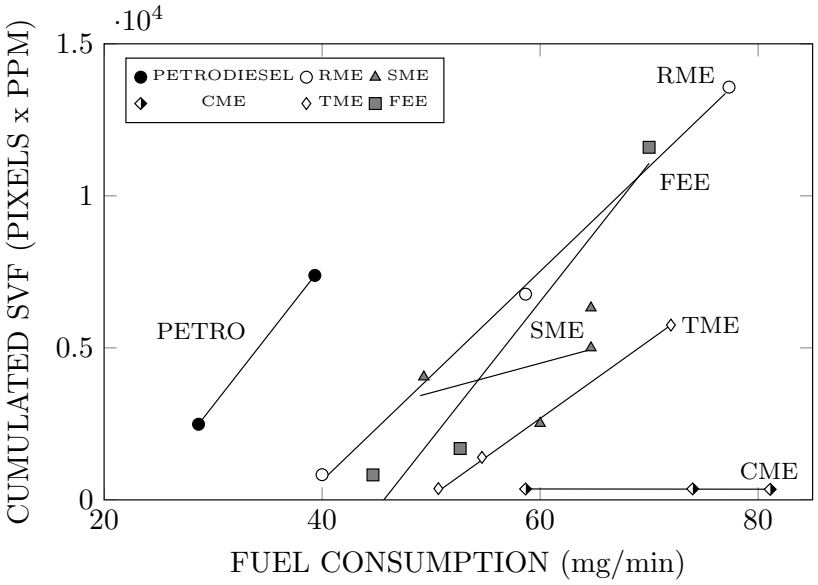

Figure 7.18: Cumulated soot volume fraction as a function of fuel consumption rate. Cumulated SVF is the sum of all SVF values within the imaged flame, and is therefore equal to the product of the total pixel area of the flame and the average SVF value.

Clearly, petrodiesel produces the sootiest flame for a given rate of fuel consumption, with CME occupying the other extreme. TME is the lowest of the other biodiesels, with RME and FEE being the highest, and the SME data points being distributed between the three. To some extent, there is a correspondence between Figure 7.18 and Figure 7.17, with the most significant exception being the SME data. On the basis of its greater proportion

of polyunsaturated species, SME would be expected to produce a sootier flame than the other biodiesels – however, the SVF values do not provide any evidence for this.

7.3.2 SOOTING HEIGHT

To complement the LII results, an attempt was made to quantify the sooting tendency of the fuels by an alternative means; namely, by the measurement of sooting height. The sooting height is generally considered to refer to the flame height at which all of the soot that is formed within the flame is no longer oxidised within the flame envelope. Incomplete soot oxidation within the flame is initially signalled by the appearance of *soot wings*, and this is followed by the opening of the flame tip and an out-pouring of visible black smoke.

Sooting height has been defined as the point at which the soot wings reach the same height as the flame apex [740]. When operating on gaseous fuels, with apparatus that allows immediate and fine modifications to be made to the fuel (and/or air) flow rate, it is a relatively straightforward matter to obtain a steady flame meeting this criterion and perform a measurement. However, using heavy fuels in a wick generated flame, obtaining precisely the correct wick necessary to yield a sooting height flame for each fuel is a more painstaking process.

An alternative approach which has been found to be practicable and effective under the conditions of this experiment involves a dynamic determination of sooting height, by measuring the flame height at the moment of first wing emergence in a transient flame. By using a wick large enough (and hence a fuel flow rate high enough) to produce a stable flame exceeding the sooting height, and monitoring the growth of the flame during the period between ignition and the attainment of steady-state, a reasonably repeatable quantifier can be calculated for each fuel. An illustration of the growth to a sooting flame can be seen in Figure 7.19.

Sooting heights, here called wing emergence heights for the sake of clarity, measured employing the methodology described above are presented in Figure 7.20. For the most part, these values approximately correspond to the trends depicted in Figure 7.18; the petrodiesel flame has the lowest wing emergence height, and is therefore the sootiest of the fuels, CME has the highest wing emergence height and is therefore the least sooty. TME had the second highest flame prior to wing emergence, SME had the second lowest, and RME and FEE were similar, with FEE apparently the sootier of the two. The fact that SME had the lowest wing emergence height is the most significant deviation from the

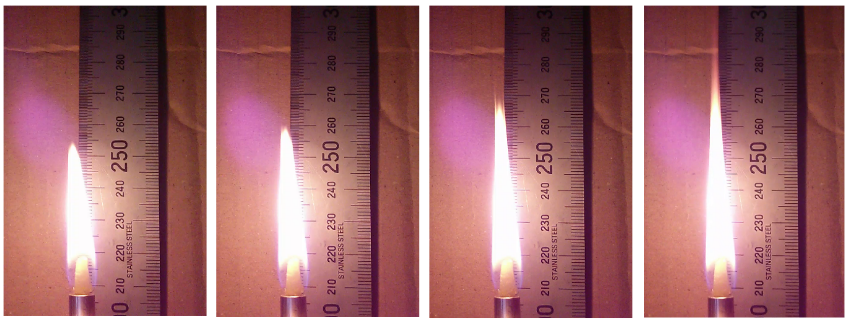

(a) (b) (c) (d)

Figure 7.19: Growth of a transient flame from below to above the sooting height [729]. (a) Closed flame. (b) First appearance of soot wings – sooting height measurement point. (c) Well defined soot wings, exceeding the flame apex. (d) Open sooting flame.

results shown in Figure 7.18, where SME flames appeared to be less sooty than those of RME and FEE. Also, TME was a lot closer to CME in terms of wing emergence height than would be predicted on the basis of the LII results.

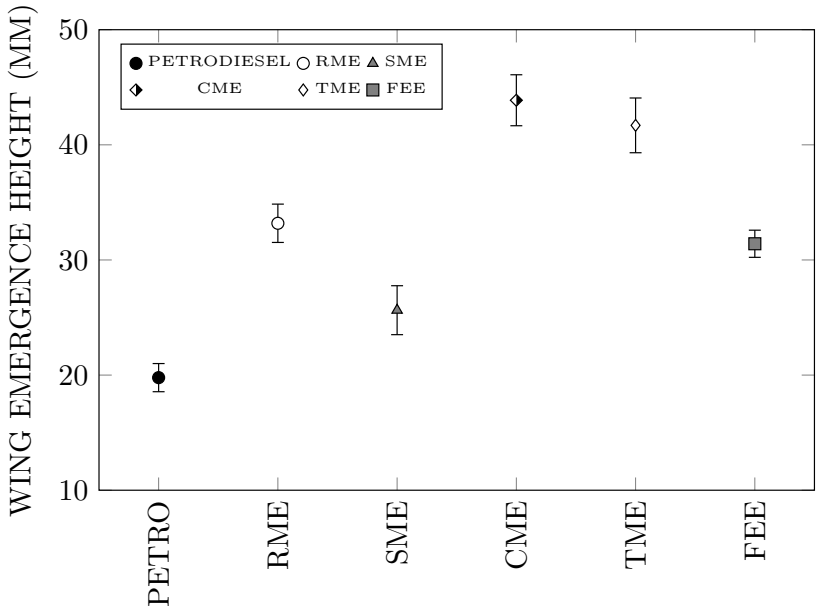

Figure 7.20: Sooting height, given as the height of first soot wing emergence, for petrodiesel and biodiesel flames.

There is seen to be a reasonable correlation between the sooting height data and the chemical composition of the fuels. In Figure 7.21 wing emergence height is plotted as a function of double bond number (DN) (see Table 7.1), and there is a general reduction in wing emergence height with increasing DN, which is in accord with the commonly understood tendency for more highly unsaturated fuels to generate sootier flames. FEE is the exception to this trend, having a lower sooting height than RME, despite a lower estimated double bond number. This may have some relation to the higher sooting tendency

of ethyl esters compared to methyl esters in diffusion flames [156].

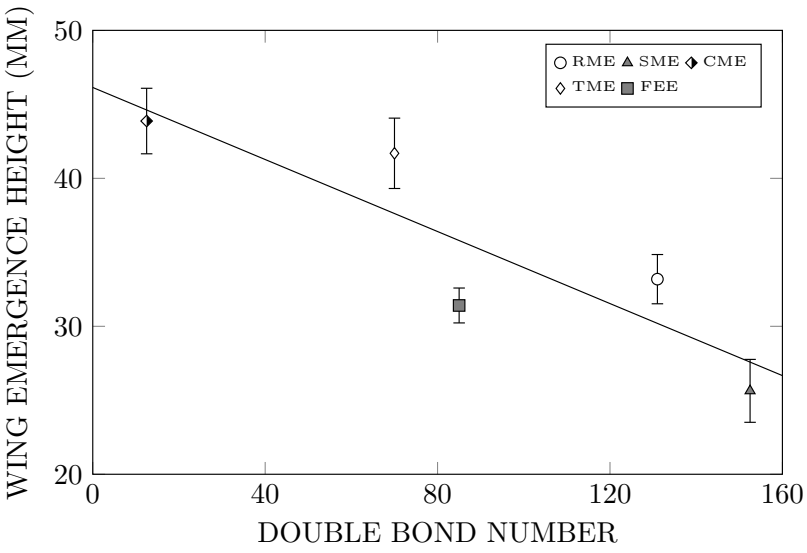

Figure 7.21: Wing emergence height as a function of the double bond number of the tested biodiesels.

7.3.3 TEMPERATURE

The temperatures of the biodiesel flames, measured with both 0.075 mm and 0.125 mm diameter thermocouples, can be seen in Figure 7.22. Measurements were made in flames of a constant height of 18 mm, at a point 2 mm below the tip of the visible flame. This point was used as it avoided problems with soot accumulation on the thermocouple that were encountered when the insertion was made lower down in the core of the flame.

In all cases, it was the maximum temperature that was recorded. This is because small variations in the positioning of the thermocouple cause very significant changes in detected temperature, and the levels of locational precision and flame stability that would be necessary to obtain adequate repeatability were deemed to be beyond the possibilities of this study. Instead, by fixing the height of the flame and thermocouple, and adjusting the radial position of the probe within the flame, reasonably consistent maximum values were measured for each fuel, and repeated experimentation demonstrated relatively small variations in maxima.

RME, CME and FEE all had quite similar maximum temperatures, with the SME maximum being significantly lower on average (by approximately 60 °C), and the TME average being significantly higher (by approximately 75 °C). In terms of the bulk chemical composition of the fuels, there is no obvious reason that the SME should be so significantly lower, or the TME so significantly higher. The estimated adiabatic flame temperatures

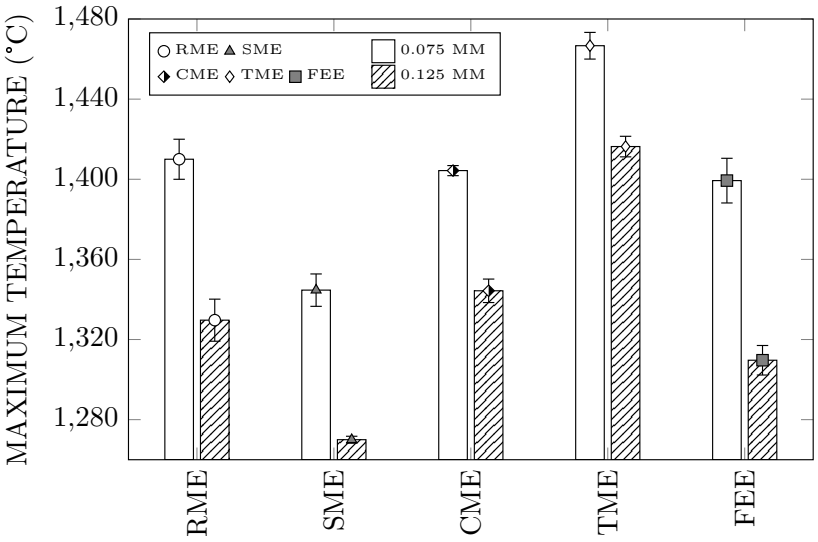

Figure 7.22: Maximum flame temperatures measured 2 mm below the visible apex of 18 mm biodiesel flames. Measurements made with thermocouples 0.075 mm and 0.125 mm in diameter.

presented in Table 7.1 are highest for SME (on account of its more highly unsaturated composition), and the total calculated range for all fuels is 30 °C. On this basis, it appears likely that some factor beyond the bulk composition of the fuels is responsible for the experimental variation observed. Potentially, instabilities in the SME flame may provide some explanation for the relatively low temperature recorded, but the CME flame exhibited more obvious instability and, despite having the lowest estimated adiabatic flame temperature, was amongst the hotter fuels, experimentally.

It is possible that the lower measured temperature of the SME flame is related to the observation that soot concentrations were lower than anticipated in the SME flames; in diffusion flames, incipient soot formation rate increases with temperature [299].

Additionally, it can be seen that measurements made using the 0.075 mm diameter thermocouple were on average around 70 °C higher than those measured using the 0.125 mm thermocouple; evidence of greater radiant heat loss with increasing thermocouple diameter [739]. On this basis, it may be expected that true maximum flame temperatures could be around 100 °C higher than those measured using the 0.075 mm thermocouple.

7.3.4 TRANSMISSION ELECTRON MICROSCOPY

The soot samples were imaged using a JEOL 2100 FEG-TEM (field emission gun transmission electron microscope), a photograph of which can be seen in Figure 7.23. The resolution of a visible-light microscope (VLM) is fundamentally limited by the wavelength

of light (for green light, approximately 550 nm); based on the Rayleigh criterion the smallest resolvable distance using a VLM is around 300 nm [741]. The wavelength of an electron can be related to its energy via the de Broglie equations, and in the operating range of the JEOL 2100 (between 80-200 kV [742]) this equates to an electron wavelength of around 3-4 pm [743]. This reduction in wavelength leads to a significant increase in the maximum possible resolution, allowing samples to be scrutinised at a sub-nanometer level.

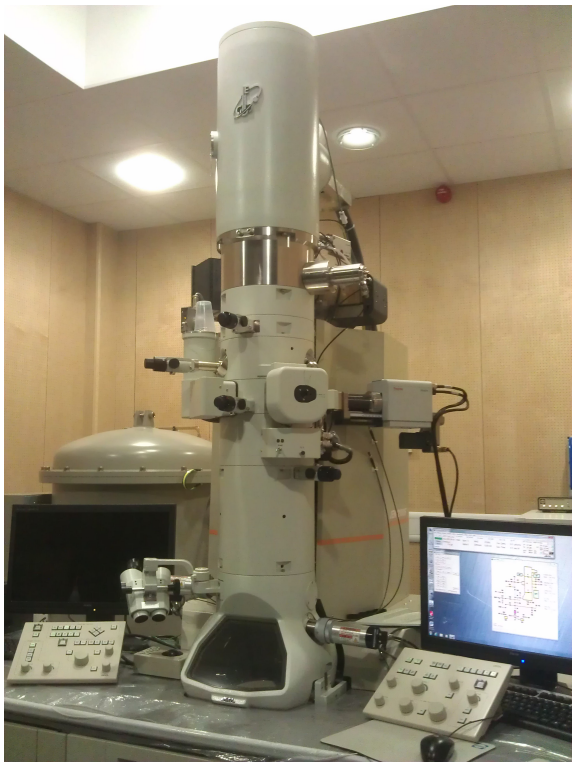

Figure 7.23: The JEOL 2100 FEG-TEM housed in the Brunel University Experimental Techniques Centre (ETC).

It was not possible to get sufficient access to the microscope to perform a statistically valid analysis of the collected soot. Examination of any single TEM grid revealed aggregates varying widely in size and structure, such that only a comprehensive survey of all (or at least a large number) of the aggregates would enable reliable conclusions regarding particle size and morphology to be drawn. In lieu of detailed statistics, in this section some of the more interesting collected images are presented and discussed, along with their possible implications.

In Figure 7.24 two soot particles collected on the same TEM grid can be seen. They were taken from an approximately 20 mm petrodiesel flame, with the grid being inserted 5 mm above the burner. In both cases these are very large soot aggregates, but are significantly different in structure.

The chain-like aggregate in Figure 7.24A is comprised of approximately 400 primary

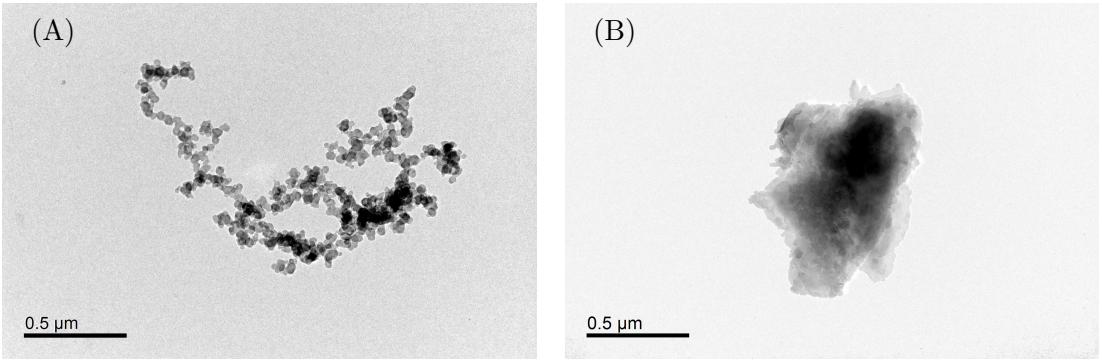

Figure 7.24: TEM images of two soot aggregates collected on a single grid inserted 5 mm from the base of a 20 mm petrodiesel flame (both photographs taken at x10000 magnification).

particles, with an average diameter of approximately 39±9 nm (sizing based on analysis of over 200 particles). As Figure 7.25 illustrates, the primary particle size distribution is approximately normal.

The cluster aggregate in Figure 7.24B does not readily facilitate primary particle size analysis, but based on the total area the cluster appears to be around 50% larger than the chain seen in Figure 7.24A – with a visible area of approximately 0.58 μm^2 compared to 0.39 μm^2 – and is also likely to be thicker, based on the large dark region that can be seen. Additionally, the component spherules are less obvious.

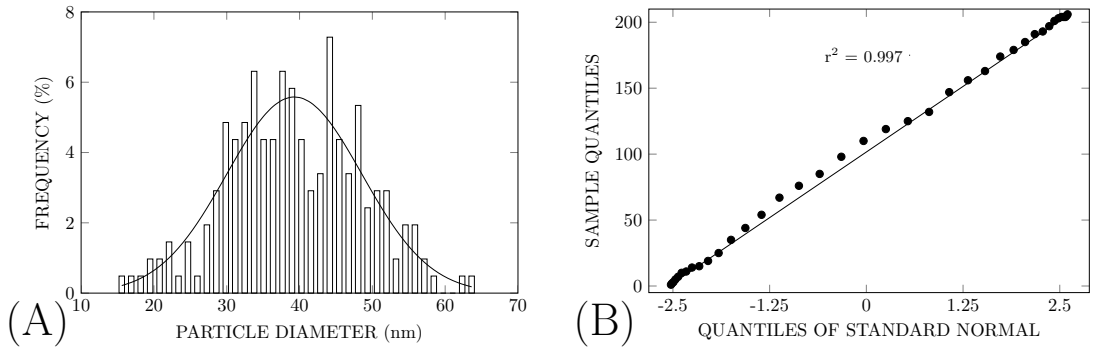

Figure 7.25: (A) Histogram of primary particle sizes within the chain-like soot aggregate seen in Figure 7.24A. (B) Q–Q plot of particle size frequency data against standard normally distributed data.

Figure 7.26 shows images of TEM grids inserted higher in the same flame, Figure 7.26A at 10 mm, and Figure 7.26B at 15 mm. The four aggregates clearly visible in Figure 7.26A range in area from 0.02 μm^2 to 0.11 μm^2 (averaging about 0.06 μm^2), and are therefore substantially smaller than the soot particles observed in Figure 7.24, collected at 5 mm. There are also two smaller particles, with areas of less than 0.01 μm^2. In Figure 7.26B there are more than 10 visible particles, of which only 3 exceed 0.01 μm^2, with the largest having an area of around 0.05 μm^2. It is possible that this suggests a decrease in aggregate particle size for samples collected higher in the flame, but far more detailed analysis would

be required to substantiate this definitively.

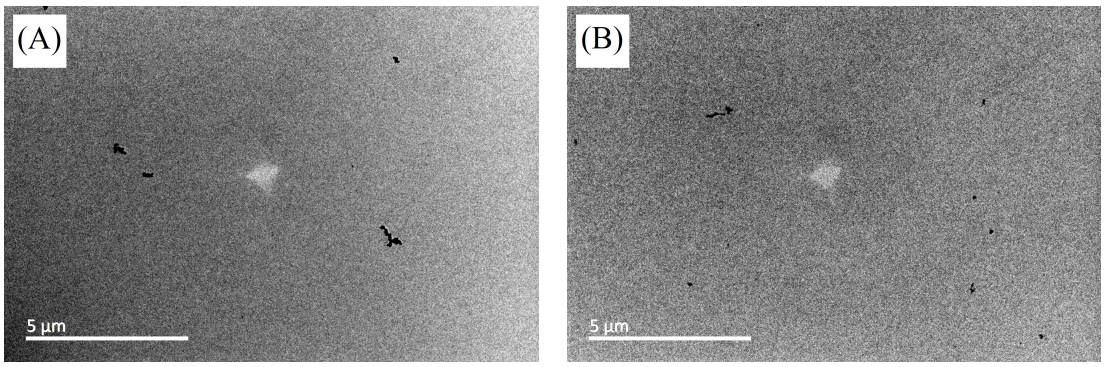

Figure 7.26: TEM images of soot aggregates collected (A) 10 mm and (B) 15 mm from the base of a 20 mm petrodiesel flame (both photographs taken at x1500 magnification).

Figure 7.27 shows two of the soot aggregates collected at 10 mm. The first (Figure 7.27A) consists of around 100 primary particles, with an average diameter of approximately 38±13 nm, the second (Figure 7.27B) of around 25 with an average of diameter of approximately 41±13 nm; hence, there does not appear to be a large difference in the primary particle sizes. Particularly in Figure 7.27A, however, there does seem to be a considerable number of smaller spherules (at the top of the image), possibly showing signs of partial oxidation.

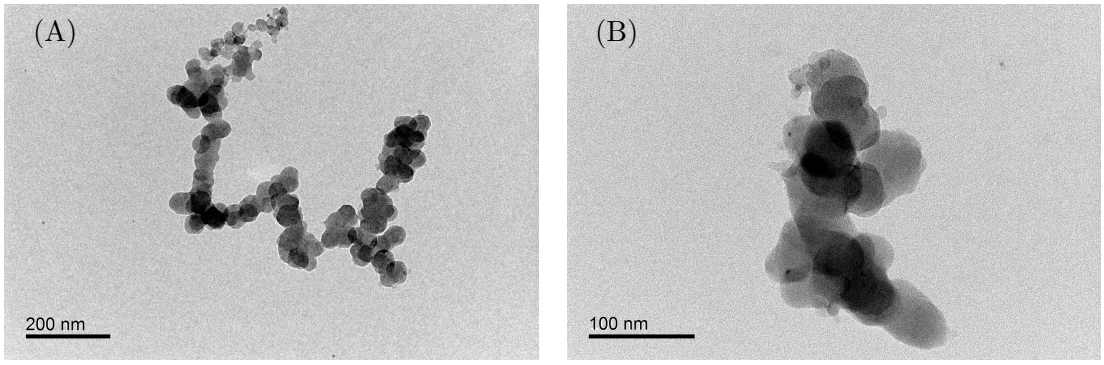

Figure 7.27: TEM images of two soot aggregates collected 10 mm from the base of a 20 mm petrodiesel flame (photograph (A) taken at a magnification of x20000 and (B) at a magnification of x50000.

In the sample collected at 15 mm, the size of the spherules of which the soot particle in Figure 7.28A is composed indicate a larger reduction in average diameter, to approximately 28±5 nm. In Figure 7.28B, the imaged soot appears to be at an even later stage in the oxidation process.

If the tendency is for the size of petrodiesel soot aggregates to decrease as the sampling point moves up the flame, then this trend does not appear to be replicated in the biodiesel images collected. The largest particle seen in the images taken from the RME flame is shown in Figure 7.29A. This is the largest single aggregate observed in this study, with a

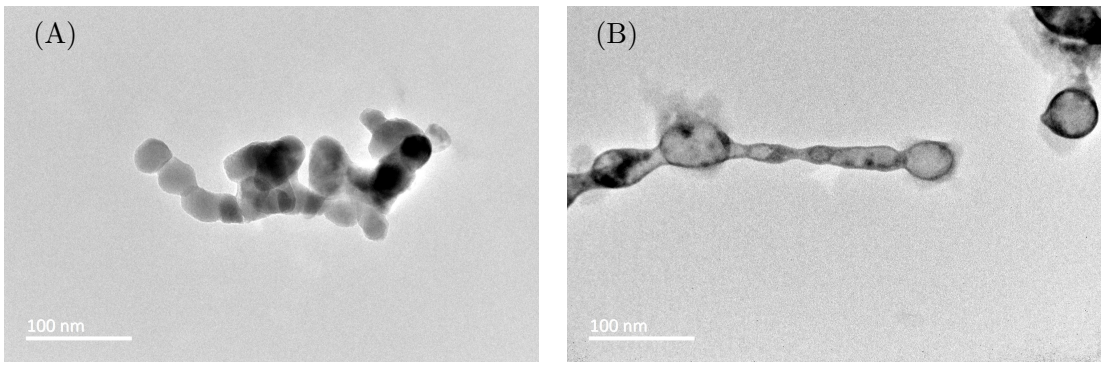

Figure 7.28: TEM images of two soot aggregates collected 15 mm from the base of a 20 mm petrodiesel flame (both photographs taken at x50000 magnification).

visible area of approximately 0.93 μm^2.

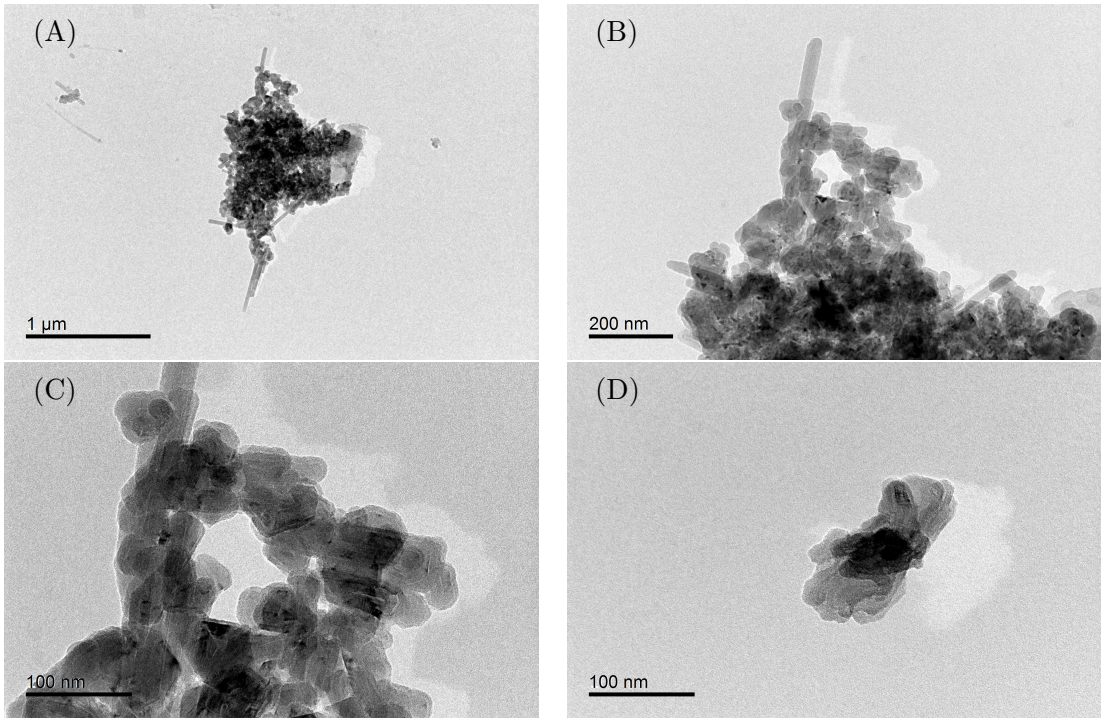

Figure 7.29: TEM images of two particles (the first at varying magnifications in (A)–(C), the second in (D)) found on a grid inserted 15 mm from the base of a 20 mm RME flame (photographs taken at magnifications of (A) x6000, (B) x20000, (C) x50000 and (D) x50000).

Besides the sheer size of this particle, comparison with the previous petrodiesel images suggests that its structural features are also remarkable. In particular, the finger-like features prominent in Figures 7.29A–C were not present in any of the images of petrodiesel soot. Closer examination shows that the primary particles that comprise the aggregate from the grid inserted into the RME flame have a rather planar appearance, compared to the agglomerated spherules found within the petrodiesel flame. The particles on the grid from the RME flame are far from devoid of curvature, but flat faces are abundant and particles of all shapes look distinctly layered. Even in Figure 7.29D, where the particle is relatively small (note that both particles were found on the same TEM grid) there is little

sphericity, and a sense of layering about an amorphous core. Comparing Figure 7.29D with an aggregate from within an equivalent petrodiesel flame – Figure 7.28A, for example – there is a very clear distinction between the two.

Further magnification of the particles seen in Figure 7.28A (petrodiesel at 15 mm) and Figure 7.29D (RME at 15 mm) shows that both contained areas of orderly graphitic layering, and areas in which there was less structural organisation. In the particulate found on the grid inserted into the biodiesel flame, sizable regions of stratification appear to have served as a basis for the apparently flat faces seen in Figure 7.29, whereas in the petrodiesel particulate it seemed that the graphitic areas were buried so deeply beneath less orderly accumulation that their form was not retained and expressed at the body surface. This can be seen in Figure 7.30 and Figure 7.31, for particles from grids inserted into petrodiesel and RME flames, respectively. The spacing of the fringe patterns visible in Figure 7.30B and Figure 7.31B was approximately equal in both cases, at around 0.36 nm peak-to-peak. Similar spacing was also measured in particles found on grids inserted into the other biodiesel flames, and is within the inter-planar spacing range that has been reported in the past [744, 745].

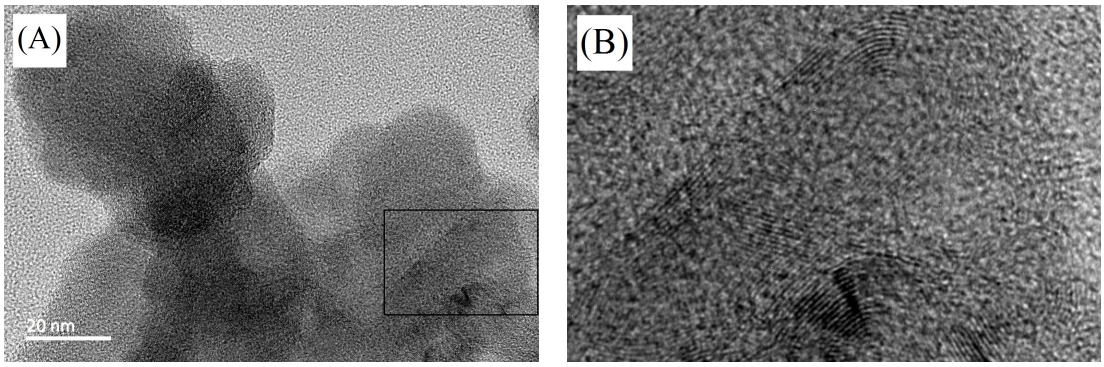

Figure 7.30: (A) TEM image of an aggregate collected 15 mm from the base of a 20 mm petrodiesel flame (photograph taken at a magnification of x200000). (B) Expansion of the selection indicated in (A).

For the other biodiesel flames the primary particles making up the aggregates found on the grids also tended to be less spherical. Even when they were approximately round, the primary particles from the grids inserted into biodiesel flames imaged in this study bore greater resemblance to clods of earth, than to the dough ball shaped primary particles seen in the petrodiesel soot images. In many of the samples found on grids inserted into the other biodiesel flames it was also possible to find the finger-like features seen in Figure 7.29. Images of particles found on grids inserted into FEE, TME, SME and CME flames can be seen in Figure 7.32.

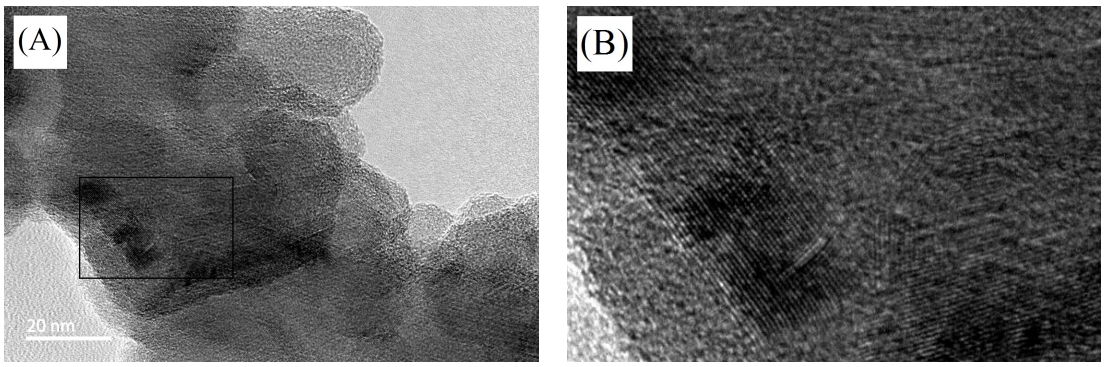

Figure 7.31: (A) TEM image of a particle found on a grid inserted 15 mm from the base of a 20 mm RME flame (photograph taken at a magnification of x200000). (B) Expansion of the selection indicated in (A).

Similarly shaped particles have been documented in previous flame and engine studies and identified as carbon nanotubes [746–750]. However, the same structures have also been observed on unused carbon-film TEM grids [751, 752]. This point is fairly vital: rather than representing some interesting structural difference between soot from petro- and biodiesel flames, the biodiesel TEM images might well reveal instead that actual soot concentrations were sufficiently low that the microscope operator mistook artefacts of the carbon film production process for soot. Although the (possible) contaminants on the carbon-film TEM grid are distinguishable from combustion generated soot, they do possess certain similarities – comparable fringe spacing, for example.

The extent to which the 'biodiesel soot' imaged in this study should be disregarded is not entirely clear. Some may be a genuine indication of carbon nanotube formation within biodiesel diffusion flames, or it may all be spurious. Certainly, future work in this area would be well advised to consider non-carbon support films where viable, or to operate at residence times providing far higher rates of soot deposition, such that contaminants would become a less significant proportion of the total identifiable carbon deposits.

7.4 CONCLUSIONS

Diffusion flames fuelled by a range of biodiesels, and petrodiesel with varying degrees of added oxygenate, were generated using ceramic wool as a wick material. The sooting tendency of the fuels was quantified using both laser induced incandescence (LII) and a more rudimentary sooting height measurement technique.

The addition of either biodiesel or diethylene glycol diethyl ether (DGDE) to petrodiesel reduced the measured soot volume fractions within the resulting flames. With respect to oxygen content, the biodiesel appeared to suppress soot more effectively. Likely,

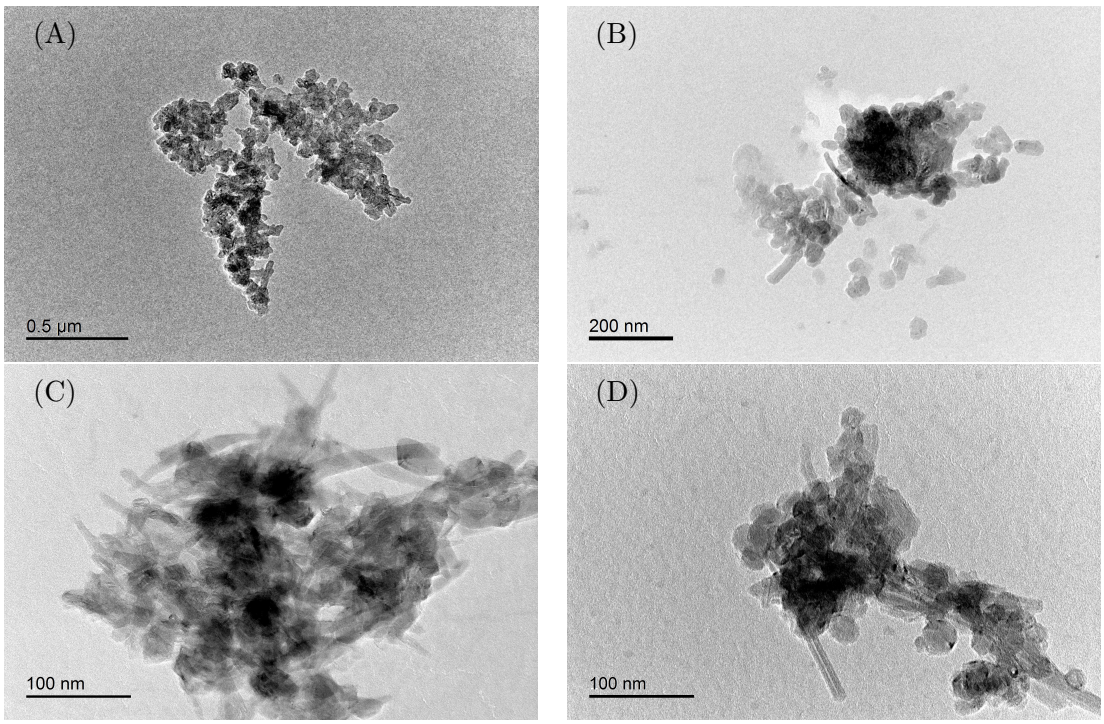

Figure 7.32: TEM images of particles from grids inserted into biodiesel flames. (A) FEE, grid inserted 15 mm from the base of the flame, with the photograph taken at a magnification of x10000. (B) TME, grid inserted at 15 mm, photograph at x20000. (C) SME, grid inserted at 15 mm, photograph at x50000. (D) CME, grid inserted at 5 mm, photograph at x50000.

this is a result of greater dilution of the parent petrodiesel.

Comparison between the sets of optical data collected from flames of petrodiesel and the biodiesels revealed a variety of interconnected relationships, all pertinent to the question of sooting tendency. The imaged heights (i.e. in the LII images) of petrodiesel flames were always larger when compared to biodiesel flames of the same measured height (i.e. measured by eye to the top of the luminous region). The measured heights of petrodiesel flames were also larger than those of any biodiesel flames for a given fuel consumption rate. Presumably, this is because the luminous height is related to the quantities of soot formed within the flame, and petrodiesel flames convert a greater proportion of the fuel to soot than do those of biodiesel. Of the biodiesels, the flames of more highly unsaturated feedstocks, sunflower (SME) and rapeseed methyl esters (RME) were largest for the same fuel flow rate, along with the fish oil ethyl esters (FEE). Since the latter is less unsaturated on average, potentially the ethyl ester moiety contributed to increased sootiness. Tallow methyl esters (TME), which was a more highly saturated biodiesel, generated significantly smaller flames, and coconut methyl esters (CME) – more highly saturated still – produced the smallest flames of all tested fuels for a given rate of fuel flow.

Considering the soot volume fractions within the flames as a function of fuel consump-

tion rate, similar trends were apparent; petrodiesel was the sootiest by a wide margin, followed by RME, then SME and FEE, TME below them and CME significantly lower than all others. Measurements of sooting height ordered the fuels slightly differently; petrodiesel was still the most sooty (with the lowest sooting height), CME and TME were still the least sooty (had the highest sooting heights), but SME had the lowest sooting height of the biodiesels, with RME and FEE being almost equal, and both less sooty than SME. This resulted in a fair, but imperfect, correlation between sooting height and degree of unsaturation.

In terms of temperature, TME flames were found to be the hottest of the tested biodiesels, SME the coolest, with RME, TME and FEE occupying a space somewhere in between. It is not clear why the SME flames were cooler than the others. Temperatures measured using a 0.075 mm thermocouple were on average 70 °C higher than those measured using a 0.125 mm equivalent.

Soot from all of the flames was collected and inspected using a transmission electron microscope (TEM). Based on limited statistical analysis, petrodiesel primary particle diameter appeared to follow an approximately normal distribution, averaging approximately 40 nm in the lower part of the flame, but being reduced to about 30 nm nearer to the top. Particles observed on the grids inserted into the biodiesel flames had different morphology to those from the petrodiesel flame; however, the structures photographed resemble those reported in the literature from unused carbon-film TEM grids, and may therefore be contaminants, remaining from the grid production process, rather than actual soot samples.

Chapter 8

NON-THERMAL PLASMA EXHAUST AFTERTREATMENT SYSTEM FOR THE REDUCTION OF NO_x AND SO_x EMISSIONS FROM MARINE DIESEL ENGINES

The following section documents work on which the author assisted Dr. R. Beleca and other members of the Brunel Centre for Electronics Systems Research; part of a DEECON FP7 European Project entitled "Innovative After-Treatment System for Marine Diesel Engine Emission Control", contract No. 284745. Elements of this work have been presented at the 2014 Transport Research Arena in Paris [753] and the 2012 Electrostatic Joint Conference in Ontario [754].

8.1 INTRODUCTION

A variety of techniques are employed to reduce exhaust emissions from diesel engines. Engine-out (as opposed to exhaust-out) emissions may be improved directly, either by modifications to the design and operation of the combustor itself (e.g. optimisation of injection processes, exhaust gas recirculation (EGR) [755–758], altered geometry, etc.) or by fuel reformulation (desulphurisation [159], dearomatization [759], addition of oxygenates [667], ignition promoters [760, 761], etc.). However, although careful control and tuning can go a long way towards reducing pollution, there is often an inherent trade-off between different pollutants and performance criteria. For instance, higher injection pressures tend to reduce soot formation, but come with a significant penalty in terms of emissions of oxides of nitrogen (NO_x), whilst increasing EGR reduces NO_x, but may increase particulate emissions and fuel consumption – and, further, although it is possible to suppress combustion temperatures sufficiently using EGR and correctly staged injec-

tion to achieve significant concurrent reductions in both NO_x and soot, these combustion modes are associated with degraded fuel economy, and elevated hydrocarbon (HC) and carbon monoxide (CO) emissions [493]. Similarly, fuelling on biodiesel, or biodiesel blends, can significantly improve particulate matter emissions, but typically at the expense of increased NO_x emissions (although the careful adjustment of operating parameters may in some cases make it possible to achieve a trade-off between the two which results in a general improvement compared to standard petrodiesel [762, 763]). The difficulties associated with simultaneously reducing all emissions to below the legally required levels now make exhaust aftertreatment essential.

Aftertreatment of NO_x emissions from diesel engines is a particularly challenging problem, because the excess air present in diesel exhaust discourages the reduction reactions utilised by familiar three-way catalyst (TWC) systems to de-NO_x gasoline exhaust (which is oxygen depleted). The most commonly used alternative for diesel engines is selective catalytic reduction (SCR) [764]. This involves introducing a reducing agent, normally ammonia (NH_3), into the exhaust gas; NH_3 may be introduced directly, but for reasons of safety and toxicity, it is usual to replace it with an aqueous urea ($CO(NH_2)_2$) solution that decomposes and reacts with water in the exhaust to form ultimate products of $2\,NH_3$ and CO_2 [765]. NH_3 reacts preferentially with NO_x, and its high selectivity is the reason that it is possible for NO_x to be reduced despite the excess oxygen available [766]. Reduction occurs over a metal-zeolite or vanadia catalyst, and optimal operation requires that a proportion of NO_x (around 50%) is converted to NO_2 in a prior stage [767]. Drawbacks of SCR include the requirement for an additional consumable (i.e. the reductant solution), diminished efficacy when exhaust temperatures are low, difficulties adjusting for engine transience, and increased emissions of some undesirable species.

Also an important technology for NO_x aftertreatment of diesel exhaust, lean NO_x traps (LNT), also called NO_x storage catalysts (NSC) or NO_x adsorber-catalysts (NAC), circumvent the problem of excess oxygen in a slightly different way. The process is split into two stages: first, a loading stage (30–300 seconds in duration), wherein the NO_x (having been oxidised to NO_2) is trapped as a nitrate, often of barium; second, a regeneration stage (2–10 seconds), in which the NO_x is discharged into a reducing environment, where it reacts with HC and CO [766, 767]. This reducing environment is established either by modifying engine operation so that for a short period engine exhaust is rich – which can cause serious deterioration in performance and other emissions over that time – or

by addition of extra fuel to the exhaust, post-combustion. Problems common to both approaches include the difficulty of supplying precisely the correct levels of reductant, the limited temperature range in which regeneration is effective, and the interference of other pollutants, primarily oxides of sulphur (SO_x), with the storage system [766]. SO_x is an issue because it is more readily absorbed into the storage medium than NO_x, and is also more difficult to regenerate [768]. The 'catalyst poisoning' effect of SO_x is a familiar obstacle in automotive applications [769].

Reduction of SO_x emissions from motor vehicles has largely taken the form of significant fuel desulphurisation – between 1993 and 2013 the maximum automotive diesel sulphur content specified by BS EN 590 fell from 2000 ppm to 10 ppm [16, 770]. Where marine fuels are concerned, however, there has been little legislative restriction over the same time period; the sulphur limits specified in BS ISO 8217 are largely unchanged between 1987 and 2012, remaining at around 10000–20000 ppm for distillate fuels, with up to 35000 ppm sulphur residual fuels still permissible in non-Emission Controlled Areas (ECAs) [771–773]. A map illustrating the location of existing and proposed ECAs can be seen in Figure 8.1. However, by 2015 fuel sulphur content should be below 1000 ppm within any ECA, and by 2020 non-ECA limits will come down to 5000 ppm [773]. The high sulphur content of maritime fuels makes catalytic NO_x reduction problematic, although solutions are certainly available and in use [774]. Currently, shipping accounts for 15% of global NO_x emissions and 3–7% of SO_x, and these numbers are likely to rise unless mitigating steps are taken [775].

Figure 8.1: SO_x Emissions Control Areas (ECAs). Existing ECAs along the North American coast, in the Caribbean, the North Sea and the Baltic Sea are marked in black. Some of the possible future ECAs are also indicated.

Work towards the objective of reduced shipping emissions has been carried out under the DEECON FP7 European Project "Innovative After-Treatment System for Marine Diesel Engine Emission Control", contract No. 284745. The aim of this project is to create a novel, modular, on-board after-treatment unit that combines different sub-units, each of which is optimized to remove specific primary pollutants; namely, SO_x, NO_x, particulate matter (PM), volatile organic compounds (VOCs) and carbon monoxide. This new integrated retrofit system is intended to reduce the environmental footprint of new and existing ships below the limits imposed by current and envisaged future regulations, while giving the EU marine industry a competitive edge. The non-thermal plasma module of this system has been developed by members of the Brunel Centre for Electronics Systems Research, and combines an electron beam (EB) and microwave (MW) for the abatement of submicron PM emissions and the removal of gaseous pollutants, including NO_x and SO_x.

The project proceeded through two development stages:

- A laboratory scale non-thermal plasma system based on AC-Corona and MW.
- A pilot scale non-thermal plasma system based on MW and EB

The solution and results documented in this chapter formed a part of the first development stage, which was presented at the 2014 Transport Research Arena in Paris [753].

8.2 NON-THERMAL PLASMA REACTORS (NTPR)

In SCR and LNT systems, as well as TWC, the aim is to reduce NO_x to nitrogen, with relatively inoffensive co-products, namely carbon dioxide and water. In an NTPR, instead of (or in addition to) reducing NO_x, the objective is to convert both NO_x and SO_x into compounds that can be more easily removed from the exhaust stream.

A plasma is an ionised gas, containing a mixture of positive and negative ions, electrons and radicals, as well as other neutral atoms and molecules [776]. Plasma is the fourth state of matter and results when a gas is heated to the point at which collisions between atoms or molecules are sufficiently energised to remove electrons from their orbits [777]. Since the temperatures required to achieve electron liberation are very high (typically in excess of 0.5 eV, or 5750 K [776]) and therefore difficult to contain, plasmas are commonly generated

by heating the electrons to temperatures far higher than those of the bulk gas. It is this thermal disequilibrium that characterises a non-thermal plasma.

Non-thermal plasmas can be formed by the application of an electrical current or electromagnetic radiation to a gas. Inside an electric field the (initially small number of) existing charge carriers (i.e. ions and electrons) are accelerated, and form additional charge carriers when they collide with neutral atoms/molecules in impact ionisation reactions [776, 778]. Further, ion-molecule reactions, and electron impacts and attachments can lead to molecular dissociation, decomposing the gases within the ionised region into their constituent atoms.

The ionisation and decomposition of pollutant species represents a part of an aftertreatment system, but because the ions and radicals produced by these processes are generally highly reactive, it is necessary to take additional steps to ensure that they subsequently react to form products which can be more easily removed from the exhaust stream. As such, the efficacy with which an NTPR removes pollutants depends on what other reactants are formed from – or introduced into – the exhaust. In diesel exhaust, the predominant constituents include water, oxygen and nitrogen (as well as carbon dioxide), and radicals formed from these chemicals include O, H, OH and N. Reactions with these radicals, when followed by further aftertreatment processes, can offer very high levels of emissions reduction. The removal efficiency of both NO_x and SO_x can be increased by converting them to more highly water-soluble compounds, primarily nitric acid (HNO_3) and sulphuric acid (H_2SO_4) [779]; these acids may then be readily dissolved into sea water [780]. In certain related systems, ammonia may also be added to the exhaust stream in order to facilitate reactions forming ammonium nitrate and sulphate (NH_4NO_3 and $(NH_4)_2SO_4$, respectively), which can be retrieved as solids [781–783].

8.3 EXPERIMENTAL SETUP

The engine employed was the same 2 litre, 4 cylinder Ford Duratorq HSDI diesel engine described in Chapter 3. The constraints placed on engine operation for the purposes of this study were, first, that the temperature of the engine exhaust be ordinarily maintained within a 70–100 °C range at the inlet to the NTPR (although, in some cases it was run somewhat hotter), second, that the exhaust flowrate not exceed the capacity of the design (approximately 2.4 kg/min) and, third, that suitable and consistent levels of NO_x and SO_x be obtained.

The laboratory scale NTPR was based on a modified Samsung CM1919 1850 W microwave oven, and an approximate schematic can be seen in Figure 8.2.

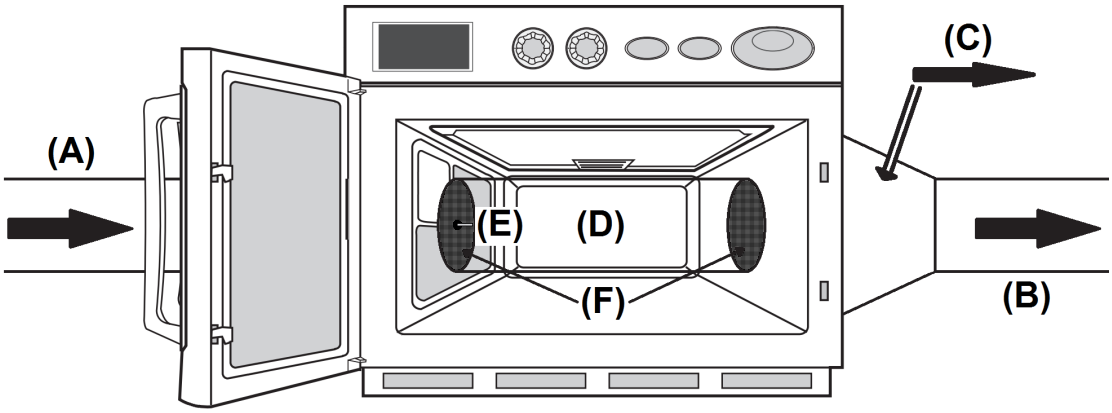

Figure 8.2: Schematic of the microwave based non-thermal plasma reactor. (A) Inlet. (B) Outlet. (C) Testo 350 sample flow. (D) Glass cylinder. (E) AC corona source. (F) Grounded copper meshes.

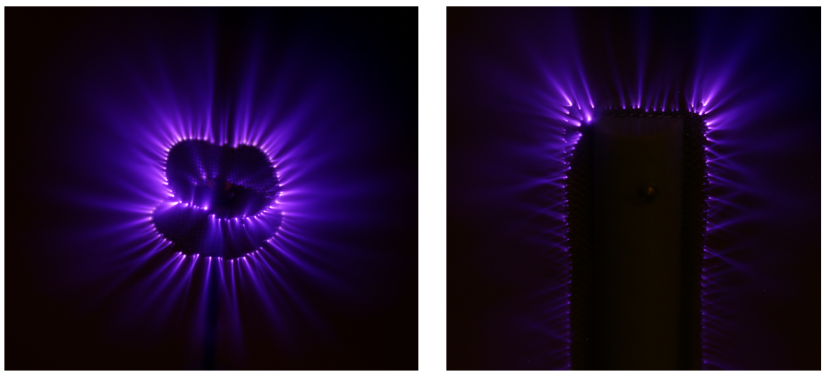

Figure 8.3: AC corona discharges in air using two different electrode designs, operating at 48 kV, 5 MHz [753].

The internal cavity of the microwave itself had dimensions of 370x190x370 mm, and walls made from 1 mm thick stainless steel. (A) and (B) represent the inlets and outlets to the microwave. (C) shows the sample flow to the Testo 350 portable emissions analyser; this device was used to quantify NO, NO_2, O_2, SO_2 and CO emissions. (D) is the glass cylinder which carried the exhaust gas through the microwave. It was made from 5 mm thick glass and had a volume of 2.3 litres. (E) is the electrode of the corona source, an Electro-Technic Products BD-20ACV capable of generating an output between 10–45 kV at a frequency between 4–5 MHz. (F) indicates the two grounded copper meshes positioned at inlet and outlet to prevent plasma leakage.

The nature of the corona discharge is highly dependent upon the electrode geometry, and discharges from two different electrode designs can be seen in Figure 8.3. AC discharge is also divided into positive and negative half cycles. During the positive half-cycle, elec-

trons in the vicinity of the electrode are drawn towards it by electromagnetic attraction, and during the negative half-cycle they are repulsed and move away. Different regimes are encountered depending upon the applied voltage, but in this instance the positive half-cycle generates a non-uniform streamer discharge, and during the negative half-cycle the electrode operates in an homogeneous glow regime.

The purpose of the microwave is to provide additional energy to the free electrons, and has the advantage of being able to achieve a higher degree of ionisation for a given energy consumption than would be possible using the corona source alone. A microwave is also more robust in the sense that it is not prone to contamination in the same way that an electrode is.

The complete laboratory scale NTPR setup can be seen in Figure 8.4. It was located immediately behind the engines laboratory, where it could be connected to a junction in the diesel engine exhaust outlet pipe, which allowed the flow to be diverted round and through the reactor.

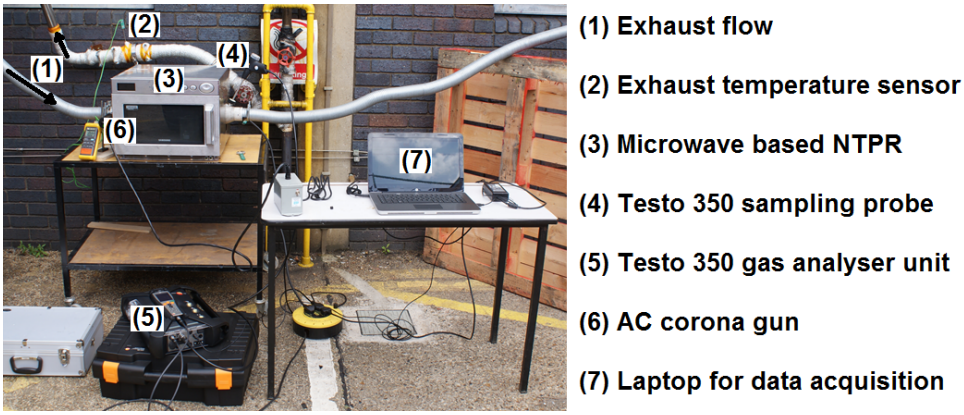

Figure 8.4: Labelled laboratory scale non-thermal plasma reactor setup [753].

8.4 RESULTS

The system was tested across a range of operational settings: varying engine conditions, microwave power and corona voltage and frequency. The results presented in Figure 8.5 were collected with the engine running at 2000 rpm, start of injection 9 degrees before top dead centre, an applied torque of 80 Nm (equating to a brake mean effective pressure of 5 bar), fuelling on ultra-low sulphur diesel. This condition produces relatively high temperature (engine out temperature $\approx$ 550 °C, NTPR inlet $\approx$ 120 °C, exceeding the nominal constraints of the system but sustainable over a short period), sooty exhaust (filter smoke number = 1.3) in comparison to the more lightly loaded states at which the

system was generally trialled. Due to high levels of pollutant emissions at this condition the Testo gas analyser was required to operate at a 5x dilution factor. The emissions reported by the Testo were generally consistent with those from the Horiba connected upstream, but tended to be somewhat lower. The microwave was set to a power of 370 W, constituting 20% of maximum power. The AC corona potential difference used was approximately 40 kV, or roughly 90% of maximum, and a frequency of 5 MHz.

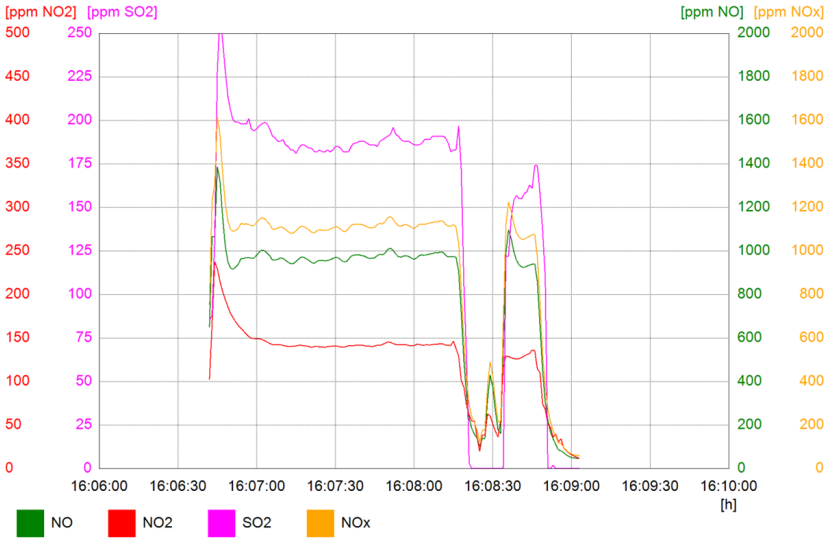

Figure 8.5: NO, NO_2, NO_x and SO_2 plots from the Testo 350, plotted as a function of time when operating the microwave at 370 W and the AC corona at approximately 40 kV, 5 MHz [753].

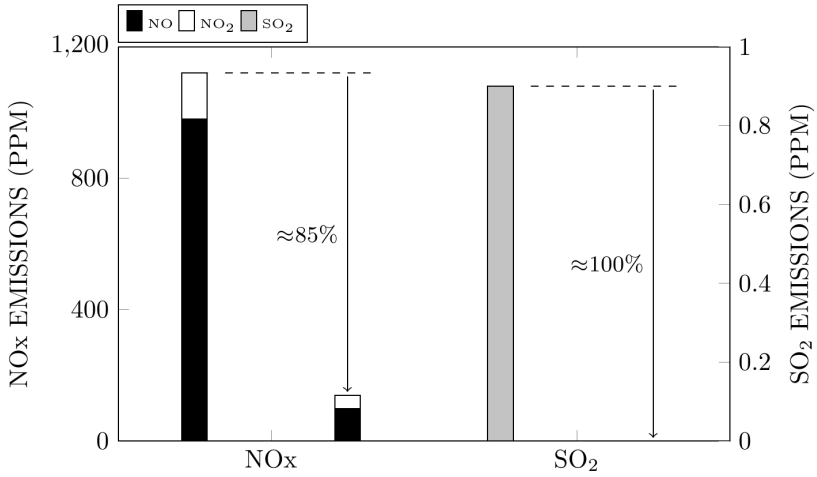

Figure 8.6: NO_x and SO_2 reduction when operating the microwave at 370 W and the AC corona at 40 kV. In each case the left hand bar shows emissions when operating without the NTPR active, and the right shows the corresponding results with the aftertreatment system operational.

As Figure 8.5 shows, there was a brief period (around 10–15 seconds) for which the emissions measured at the NTPR were significantly reduced. The short duration of the reduction is a result of the technical features of the commercial microwave oven employed. Pulse width modulated power is supplied to the magnetron, which is discontinued once the

temperature within the internal cavity is increased beyond a defined limit; the magnetron restarts when the measured temperature has decreased sufficiently.

The extent of the reduction over the active period of the microwave is illustrated in Figure 8.6, and can be seen to reach a removal efficiency around 85% for NO_x and 100% for SO_2. It is also worth noting that although quantities of both oxides of nitrogen were reduced by the treatment, NO was reduced by around 90%, while NO_2 was reduced by only 75%.

8.5 CONCLUSIONS

A laboratory scale non-thermal plasma reactor based on the combination of an AC corona source and a commercial microwave was successfully tested under a range of operating conditions. Exhaust emissions were only reduced over a relatively short period – due to limitations of the microwave – but during that period a very significant reduction in emissions was observed; NO_x emissions decreased by approximately 85% and removal of SO_2 was apparently total.

These experiments provided a useful proving ground for the technology, before it progressed to a larger scale pilot project.

Chapter 9

CONCLUSION

9.1 CONCLUSIONS

The primary focus of this thesis was the increase in emissions of oxides of nitrogen NO_x which is widely reported to occur when fuelling a diesel engine on biodiesel rather than petrodiesel. The objective was to gain some additional insight into why this occurs, with particular emphasis on the effects of fuel composition, cetane number and fuel-bound oxygen content. The most important conclusions to be drawn from this work are as follows:

Chapter 2: Literature Review

1. The techniques used to prepare biodiesel, and the materials from which it is produced continue to advance. If biodiesel endures as an alternative fuel, the lipid feedstock from which it is derived might be expected to shift away from food crops grown on agricultural land, towards waste products, or higher yield oil crops with lower land requirements, particularly microalgae.

2. The fatty acid composition of the lipid feedstock determines the physical and chemical properties of the resulting biodiesel. In general, the most important differentiating factor amongst common biodiesels is degree of unsaturation. Increasing unsaturation extends ignition delay via effects on low temperature chemistry. More highly unsaturated alkyl esters have better cold flow properties and are less viscous than their saturated counterparts, but their oxidative stability can be poor.

3. The biodiesel NO_x increase is a complicated phenomenon, with many contributing factors. The most significant differences between petro- and biodiesel appear to be rooted in the fuel-bound oxygen content of biodiesel, and its lack of aromatic

species. These properties influence combustion via changes in ignition quality, degree of premixing, combustion phasing and mixture stoichiometry.

Chapter 4: Premixed Burn Fraction: Its Relation to the Variation in NO_x Emissions between Petro- and Biodiesel

1. Biodiesel was observed to have higher NO_x emissions than petrodiesel when operating at a higher engine load, but lower NO_x emissions than petrodiesel when operating at a lower load. Towards highly advanced and highly retarded injection timings, biodiesel NO_x emissions were also relatively low.

2. In general, the fuel which combusted most quickly at any given operating condition tended to have the highest NO_x emissions.

3. The ignition delay of the tested biodiesel was consistently shorter than that of the tested petrodiesel. Reduced ignition delay advances start of combustion, for a given injection timing. Advanced start of combustion timing is associated with increased NO_x emissions. However, a shorter ignition delay also reduces the time available for fuel-air premixing, and hence reduces the premixed burn fraction. Reduced PMBF is associated with reduced NO_x emissions. Hence, the shorter ignition delay of biodiesel has conflicting effects on NO_x emissions.

4. When differences in start of combustion timing were adjusted for, biodiesel typically had higher NO_x emissions than petrodiesel for a given premixed burn fraction (PMBF). The extent to which biodiesel NO_x emissions exceeded those of petrodiesel appeared to be correlated with the degree of premixing: under operating conditions where the PMBF was large, the biodiesel NO_x increase was small, but under conditions at which the PMBF was smaller, the biodiesel NO_x increase was larger.

Chapter 5: Effects of Biodiesel, Oxygenates and Degree of Premixing on Emissions from an HSDI Diesel Engine

1. Holding start of combustion constant, the predictions of Chapter 4 (based on mathematical adjustments) were partially validated. Clear relationships between NO_x emissions and premixed burn fraction were observed. At all conditions, biodiesel had higher NO_x emissions than petrodiesel, for a given degree of premixing. However, the biodiesel NO_x increase did not get smaller with increasing premixed burn

fraction, per se (as suggested in Chapter 4), although the like-for-like increase in biodiesel NO_x emissions was far smaller (2–2.5%) at the lower load than it was at the higher load (approximately 12.5%). **With start of combustion constant, there is a definite increase in NO_x emissions for a given PMBF when fuelling on biodiesel; however, the size of the increase depends upon operating conditions.**

2. Although the biodiesels always had higher NO_x emissions for the same premixed burn fraction, variations in PMBF meant that while, for example, a low cetane number (CN) sunflower oil derived biodiesel had higher NO_x emissions than petrodiesel at both higher and lower loads, a rapeseed derived biodiesel with a higher CN, still had higher NO_x emissions than petrodiesel at the higher load, but lower NO_x emissions at the lower load. Therefore, although like-for-like biodiesel NO_x emissions are higher than those of petrodiesel, the increase can be offset by an increase in CN. **Biodiesel NO_x emissions are not necessarily higher than those of petrodiesel; it depends upon the composition of the biodiesel – primarily degree of unsaturation – and operating conditions.**

3. When the fuel-bound oxygen content of petrodiesel was increased, by the addition of an oxygenate (tripropylene glycol methyl ether) to a level comparable to that of biodiesel, the NO_x emissions when fuelling on the blend were also comparable to those of biodiesel, for a given PMBF. This implies that **beyond differences in start of combustion timing and degree of premixing, the difference in NO_x emissions between petro- and biodiesel is largely a consequence of the difference in fuel-bound oxygen content.**

4. There is an increase in apparent heat release rate during diffusion combustion when fuelling on biodiesel. A similar increase is also seen when fuelling on the oxygenated petrodiesel blend. Although this means that the increase in diffusion AHRR may be a consequence of fuel-bound oxygen content, the heat release plots suggest a possible relationship with the duration of the injection event. That is, because both biodiesel and the oxygenated petrodiesel blends have reduced energy density compared to neat petrodiesel, the injection duration is likely to be extended. Whatever the cause, **the increase in diffusion AHRR when fuelling on biodiesel is associated with an increase in maximum in-cylinder pressure; consequently, maximum**

in-cylinder pressure is typically higher when fuelling on biodiesel.

5. For a given maximum in-cylinder pressure biodiesel typically had higher NO_x emissions than petrodiesel. When considered as a function of maximum pressure, the difference in NO_x emissions between petro- and biodiesel tended to be smaller where the difference in smoke emissions was smaller; that is, **biodiesel NO_x emissions generally exceeded those of petrodiesel by a larger amount where petrodiesel smoke emissions exceeded those of biodiesel by a larger amount, possibly implying a relationship with differences in mixture stoichiometry.**

6. Smoke emissions were significantly lower when fuelling on biodiesel, or the oxygenated petrodiesel blends, than when fuelling on neat petrodiesel. The reduction was largest (around 70%) at the low PMBF higher load conditions, and smallest (around 40%) at the most highly premixed lower load conditions. In general, **smoke emissions were correlated across all operating conditions with the magnitude of pressure rise attributable to the diffusion combustion phase.**

Chapter 6: Effects of Antioxidant Addition to Biodiesel on Emissions from an HSDI Diesel Engine

1. Some authors have hypothesised that the biodiesel NO_x increase may be due in part to some effect of fuel chemistry on the prompt NO pathways. Further theories propose that the addition of antioxidants to biodiesel may quench hydrocarbon free-radicals, and hence reduce prompt NO formation and biodiesel NO_x emissions. A review of the relevant literature finds mixed experimental results, and no clear theoretical underpinning.

2. The effect of the tested antioxidants (*tert*-butylhydroquinone, butylated hydroxyanisole and *p*-phenylenediamine) on biodiesel NO_x emissions from the laboratory diesel engine was insignificant. The data therefore provided neither any evidence of an effect of antioxidant addition on NO_x emissions, nor any possible explanation for it. The fact that many prior studies reported antithetical results may be related to differences in engine technology.

3. The effects of antioxidants on all emissions were apparently small enough to be obscured by variations in day-to-day engine performance. The most significant change

in emissions observed was an increase in smoke emissions following the addition of *p*-phenylenediamine. This may be related to oxidation of the additive, and subsequent reactions within the fuel, as evidenced by the change in colour.

Chapter 7: Relative Sooting Tendency of Various Biodiesels in Wick-Generated Diffusion Flames

1. In wick-generated diffusion flames, increasing the fuel-bound oxygen content reduced the soot volume fraction, just as it was observed to reduce smoke emissions from a diesel engine in Chapter 5. Blending petrodiesel with biodiesel reduced soot volume fraction more effectively, as a function of fuel-bound oxygen content, than blending petrodiesel with an oxygenate (in this case, diethylene glycol diethyl ether). This is because greater admixture of biodiesel was required to obtain the same oxygen weighting, and therefore the highly sooting parent petrodiesel was diluted to a greater extent.

2. In general, the more highly unsaturated biodiesels yielded sootier flames. In particular, the highly saturated coconut derived biodiesel produced flames with far lower soot concentrations, and higher sooting heights, than the other biodiesels. However, the correspondence between degree of unsaturation and sooting tendency was imperfect. In the engine tests documented in Chapter 5, the results were also mixed, but smoke emissions tended to go down, rather than up, with increasing degree of unsaturation; this suggests that within a diesel engine differences in fuel-air premixing possibly affect sooting more than small changes in fuel chemistry.

3. Thermophoretic sampling of soot, and subsequent imaging using a transmission electron microscope, identified agglomerates comprised of hundreds of primary particles, with the size of the primary particles being approximately normally distributed, averaging around 30–40 nm. Soot collection and analysis were problematic due to the use of carbon film TEM grids, which contained a range of carbonaceous structures as pre-existing contaminants, remaining from the production process.

Chapter 8: Non-Thermal Plasma Exhaust Aftertreatment System for the Reduction of NO_x and SO_x from Marine Diesel Engines

1. Increasingly stringent emissions legislation has made exhaust aftertreatment a vital part of many diesel engine powered systems. Differences in fuel regulations, amongst

other factors, make the aftertreatment of exhaust from marine diesel engines both particularly challenging, and especially important.

2. Non-thermal plasma aftertreatment may be an effective approach for reducing emissions of both NO_x and SO_x, particularly from larger diesel engines, such as those used in marine applications.

Addressing explicitly the objective and points of focus of the thesis, as defined in Section 1.2:

- *How does fuel composition affect emissions of oxides of nitrogen from a diesel engine?* Based on the evidence of the data collected here, fuel composition should be expected to affect NO_x emissions primarily via its effect on ignition quality, and hence the ignition delay period and degree of premixing.
  - More highly unsaturated compounds in biodiesel and aromatic species in petrodiesel should both be expected to increase ignition delay.
  - If injection timing were constant, the advance in combustion phasing caused by a reduction in ignition delay would tend to increase NO_x emissions, whilst the reduction in degree of premixing caused by a reduction in ignition delay would tend to reduce NO_x emissions. Hence, a change in ignition quality will elicit two opposing effects on NO_x emissions, the net outcome of which depends upon the magnitude of the change and the specific operating conditions.
  - If start of combustion were constant, the effect would become more straightforward – NO_x emissions increase with increasing ignition delay and degree of premixing.
  - Although at lower load the differences in ignition delay and premixing largely account for the differences in NO_x emissions between petro- and biodiesel, at higher load the biodiesel NO_x emissions are larger than can be attributed to differences in degree of premixing alone.
  - Other emissions also demonstrate a dependence on the degree of premixing. For instance, smoke emissions decrease significantly with increasing degree of premixing. As a result, more highly unsaturated biodiesels, which showed some evidence of being sootier in flames, tended to have lower smoke emissions from a diesel engine.

Factors beyond ignition quality may also be significant. In older diesel engines, employing pump-line-nozzle injection systems, physical factors effecting pressure transmission through the system are of well understood importance. The data here suggests that certain fuels – namely, the biodiesel derived from used cooking oil – may have had slightly lower NO_x emissions than the other tested biodiesels on account of some property not conspicuously related to its fatty acid composition, or at least not identified in the analysis performed. On the basis that both later measurements and literature values attribute a higher viscosity to UCOME than to most other biodiesels (on account of structural changes induced by the prolonged heating to which frying oils are subjected), it may be that some effect of the physical properties of the fuel on spray processes is responsible for the slight reduction in NO_x emissions observed.

- *What is the effect of fuel-bound oxygen content?* The data unambiguously suggests that increased fuel-bound oxygen content causes an increase in NO_x emissions, accompanied by a reduction in carbon monoxide emissions and filter smoke number (as well as a reduction in soot volume fraction within flames). Total hydrocarbon emissions were also typically lower from oxygenated fuels. Apparent heat release rate through the diffusion burn phase was generally higher for the oxygenated fuels, and consequently so was maximum in-cylinder pressure, although this may be related – wholly or in part – to extension of the injection event, rather than the fuel-bound oxygen content itself.

  All in all, with start of combustion constant and an equal degree of premixing, the remaining differences between petro- and biodiesel are primarily attributable to differences in fuel-bound oxygen content, possibly implying that mixture stoichiometry is the key causal factor.

- *What insight has been gained into the nature and causes of the biodiesel NO_x increase?*

  1. There is a definite increase in NO_x emissions when fuelling on biodiesel, relative to petrodiesel, which remains once differences in start of combustion timing and degree of premixing have been accounted for.
  2. The remaining increase appears to be largely related to the fuel-bound oxygen content of biodiesel.

3. The magnitude of the increase varies depending upon operating conditions.
4. Biodiesel combustion tends to be associated with higher in-cylinder pressures.
5. The higher in-cylinder pressures are attributable to a period of increased apparent heat release rate through the diffusion phase when fuelling on biodiesel (which may be a result of extended injection duration).
6. For a given maximum in-cylinder pressure, the difference between petro- and biodiesel NO_x emissions is negatively correlated with the difference between petro- and biodiesel filter smoke numbers.

9.2 FURTHER WORK

The major conclusions of this thesis (primarily, those based on the work documented in Chapter 5), raise and leave unanswered several important questions which might be addressed in further experimental work.

First: *what is the reason for the seemingly increased apparent heat release rate through the diffusion burn phase when fuelling on biodiesel, and with the addition of an oxygenate to petrodiesel?* In Chapter 5, two possible causes for this were proposed: either the increase in AHRR is a result of fuel-bound oxygen content, or it is due to the reduction in energy density which causes an extension of injection duration (or, potentially, both factors might play a role). A relatively straightforward means of establishing which, if either, of these suggestions is accurate would involve fuelling an instrumented diesel engine on an unoxygenated fuel with a similar energy density (and hence injection duration) to biodiesel, and comparing the results with those of biodiesel, petrodiesel and an oxygenated petrodiesel blend. If such a fuel is found to exhibit the same increase in AHRR through the diffusion phase, then the increase in diffusion AHRR is likely to be a consequence of the extended injection event; if it displays no similar increase, then it is more likely that the fuel-bound oxygen content bears responsibility. This test may also help to examine the hypothesis that it is increased diffusion AHRR which leads to the increase in maximum in-cylinder pressure when fuelling on biodiesel. It would be necessary to perform this experiment with start of combustion held constant, and degree of premixing equalised between fuels, probably by use of ignition enhancers. The experimental setup would also benefit from instrumentation of the injectors, for accurate determination of the beginning and end of the injection event.

Second: *does the increase in NO_x with increasing fuel-bound oxygen content have any causal connection to in-cylinder soot via radiative heat transfer?* A possible means of testing the role of soot in the NO_x increase would be to test a fuel with a lower sooting tendency to petrodiesel, but no fuel-bound oxygen. This experiment might even employ the same fuel as the energy density test described above; an *n*-alkane in the C_{12}–C_{14} range should have both a similar energy density to biodiesel, and a lower sooting tendency than petrodiesel. If an unoxygenated, low sooting tendency fuel had NO_x emissions similar to those of petrodiesel (at a fixed start of combustion, and for a given premixed burn fraction) then that would suggest that radiative heat transfer is not an important contributor to the like-for-like biodiesel NO_x increase. If, however, an increase in NO_x were observed, then that may imply a significant causal effect of in-cylinder soot on NO_x, rather than just a correspondence based on mixture stoichiometry.

Third: *do more viscous biodiesels have lower NO_x emissions?* In Chapter 5 the biodiesel derived from used cooking oil was observed to have substantially lower NO_x emissions than the biodiesel trend. It was suggested that this may be a result of the higher viscosity of the fuel. A first possible means of testing this would be to find another biodiesel with a higher viscosity (crambe biodiesel, for example [784]), and compare it with other biodiesels in the same way as was done in Chapter 5. Another possible approach, and one which may offer broader interest, would be to subject biodiesel to controlled oxidation, and submit that to engine testing once it reached a range of viscosity milestones. It has been reported in the past that oxidation of the fuel can increase cetane number [140], and would therefore be expected to reduce NO_x emissions in and of itself. However, whether the increasing viscosity would have an effect on emissions beyond that attributable to changes in cetane number may be useful information to have: might controlled oxidation of biodiesel prior to its use offer advantages?

Additional questions of interest which have relevance to experimental work that has been described include:

What is the best way to equalise combustion phasing between fuels? In Chapter 5, it was proposed that, at the lower load where the effect of fuel oxygenation on NO_x emissions is apparently smaller, a large part of the differences in NO_x emissions between the fuels was due to small differences in phasing, despite the start of combustion always being equal. But is start of combustion the best point to use to synchronise combustion? Realistically, this is a very difficult question to get any definite answer to, primarily because it is not

entirely clear what would make one point *better* than another.

How does the addition of p-phenylenediamine influence the physical properties of a biodiesel to which it is added, and does this influence evolve with time? In Chapter 6 it was suggested that the slight increase in sooting following the addition of *p*-phenylenediamine to biodiesel may have resulted from some reaction forming higher molecular weight compounds within the fuel. The fact that the increase in sooting appeared to become more pronounced the longer the fuel was stored before use raises the possibility that the additive takes time to exert its influence. By tracking the development of the fuel, physically and chemically, over a period of days or weeks, greater insight into this might be gained. Accompanied by further engine testing, this might also help to substantiate the conclusions of Chapter 6.

Some progress has been made towards the objective of understanding the biodiesel NO_x increase. However, if the question posed in Section 1.2, nominally forming the basis of the work documented in this thesis, is to be answered more fully by a future student, then they ought to begin with an eye on the fundamentals of the matter, rather than simply causing and observing a range of phenomena, and then attempting to explain them from the top, downwards. The diesel engine is essentially a practical device, rather than a system for scientific experimentation. Although its operation is dependent upon the physical and chemical processes which are of research interest, the level of complexity is too high, and the convolution too great, for fundamental answers to be derived directly from engine tests. Engine tests can be used to identify trends and to validate models, but the core of research into differences between fuels must ultimately be centred around experiments which reduce the subject to its simplest elements, out of which single threads may be drawn and examined. Diesel combustion represents a veritable tapestry of such threads, which one cannot tease apart without extreme difficulty, and certainly not with only in-cylinder pressure and emissions data to base judgements upon.

In the 2007 *Report of the Basic Energy Sciences Workshop for Clean and Efficient Combustion of 21st Century Transport Fuels* [785], a single 'overarching grand challenge' for combustion research is identified:

> *"The development of a validated, predictive, multi-scale, combustion modeling capability to optimize the design and operation of evolving fuels in advanced engines for transportation applications."*

If progress can be made towards this goal, in the future it will not only be possible for researchers to more quickly and thoroughly understand the reasons for the effects of changes in fuel, but the ability of engine manufacturers to achieve optimised configurations will also be significantly enhanced. Ultimately, this is the practical end of experimental work: to improve upon existing technology. With adoption of alternative fuels becoming more widespread, a complete understanding of the differences between them is essential to ensuring that possible benefits are maximised, while associated downsides – like the biodiesel NO_x increase – are avoided or minimised.

PUBLICATIONS AND CONTRIBUTIONS

PUBLISHED

D.M. Peirce, N.S.I. Alozie, D.W. Hatherill, L.C. Ganippa, **Premixed Burn Fraction: Its Relation to the Variation in NOx Emissions between Petro- and Biodiesel**, Energy & Fuels 27 (2013) 3838–3852.

UNDER PREPARATION

D.M. Peirce, N.S.I. Alozie, D.W. Hatherill, L.C. Ganippa, **Effects of Biodiesel, Oxygenates and Degree of Premixing on Emissions from an HSDI Diesel Engine**, *intended for submission to Fuel.*

D.M. Peirce, H.A. Dhahad, N.S.I. Alozie, D.W. Hatherill, L.C. Ganippa, **Effects of Antioxidant Addition to Biodiesel on Emissions from an HSDI Diesel Engine**, *intended for submission to Fuel Processing Technology.*

D.M. Peirce, D.W. Hatherill, L.C. Ganippa, **How Biodiesel Affects Emissions of Oxides of Nitrogen from Diesel Engines**, *intended for submission to Renewable and Sustainable Energy Reviews.*

CONTRIBUTIONS

R. Beleca, N. Manivannan, L. Ganippa, M. Abbod, D.M. Peirce, W. Balachandran, **Microwave Induced Plasmas for Marine Diesel Engine Emission Control**, in: Proceedings of the Electrostatic Joint Conference, Cambridge, ON, Canada, 2012.

N.S.I. Alozie, D.M. Peirce, A. Lindner, W. Winklmayr, L.C. Ganippa, **Influence of Dilution Conditions on Diesel Exhaust Particle Measurement Using a Mixing Tube Diluter**, SAE Paper No. 2014-01-1568, 2014.

N.S.I. Alozie, D.M. Peirce, L.C. Ganippa, **Comparative Influences of Air and Nitrogen as Dilution Gases in Measurement of Diesel Engine Particle Number Concentrations**, SAE Paper No. 2014-01-1576, 2014.

M. Abbod, R. Beleca, D.M. Peirce, L. Ganippa, N. Manivannan, W. Balachandran, **Power Controlled Microwave Reactor for the Removal of NOx and SOx from the Exhaust of Marine Diesel Engine**, in: Transport Research Arena, Paris, France, 2014.

REFERENCES

[1] C. Sagan, Billions & Billions: Thoughts on Life and Death at the Brink of the Millenium, Ballantine Books, New York, USA, 1997.

[2] IPCC Core Writing Team, R.K. Pachauri, L.A. Meyer (Eds.), Climate Change 2014: Synthesis Report, Intergovernmental Panel on Climate Change, Geneva, Switzerland, 2014.

[3] S. Capstick, L. Whitmarsh, W. Poortinga, N. Pidgeon, P. Upham, WIREs Climate Change 6 (2015) 35-61.

[4] P. Mock, European Vehicle Market Statistics: Pocketbook 2014, The International Council on Clean Transportation, Berlin, Germany, 2014.

[5] B. Diczfalusy, J. Wisniewski, Railway Handbook 2012: Energy Consumption and CO_2 Emissions, International Energy Agency/International Union of Railways, Paris, France, 2012.

[6] V. Smil, Prime Movers of Globalization: The History and Impact of Diesel Engines and Gas Turbines, The MIT Press, Cambridge, MA, USA, 2010.

[7] JC. Seagrave, J.D. McDonald, E. Bedrick, E.S. Edgerton, A.P. Gigliotti, J.J. Jansen, L. Ke, L.P. Naeher, S.K. Seilkop, M. Zheng, J.L. Mauderly, Environmental Health Perspectives 114 (2006) 1387-1393.

[8] Y. Zhu, W.C. Hinds, S. Kim, S. Shen, C. Sioutas, Atmospheric Environment 36 (2002) 4323-4335.

[9] D. Carrington, Four More Carmakers Join Diesel Emissions Row, The Guardian, 9 Oct 15 [Online]. Available at: http://www.theguardian.com/environment/2015/oct/09/mercedes-honda-mazda-mitsubishi-diesel-emissions-row [Accessed Oct 2015].

[10] D. Carrington, Nine out of 10 New Diesel Cars Exceed EU Pollution Limits, Report Finds, The Guardian, 14 Sep 15 [Online]. Available at: http://www.theguardian.com/environment/2015/sep/14/nine-out-of-10-new-diesel-cars-in-breach-of-eu-pollution-rules-report-finds [Accessed Oct 2015].

[11] G. Knothe, K.R. Steidley, Energy & Fuels 19 (2005) 1192-1200.

[12] J. Sheehan, V. Camobreco, J. Duffield, M. Graboski, H. Shapouri, An Overview of Biodiesel and Petroleum Diesel Life Cycles, Report No. NREL/TP-580-24772, National Renewable Energy Laboratory, 1998.

[13] M. Lapuerta, O. Armas, J. Rodriguez-Fernandez, Progress in Energy and Combustion Science 34 (2008) 198-223.

[14] J.A. Bittle, B.M. Knight, T.J. Jacobs, Energy & Fuels 24 (2010) 4166-4177.

[15] G. Knothe, J. Van Gerpen, J. Krahl, The Biodiesel Handbook, AOCS Press, Champaign, IL, USA, 2005.

[16] British Standards Institute, Automotive Fuels - Diesel - Requirements and Test Methods, BS EN 590:2013.

[17] British Standards Institute, Liquid Petroleum Products – Fatty Acid Methyl Esters (FAME) for Use in Diesel Engines and Heating Applications – Requirements and Test Methods, BS EN 14214:2012.

[18] N.N.A.N. Yusuf, S.K. Kamarudin, Z. Yaakub, Energy Conversion and Management 52 (2011) 2741-2751.

[19] A. Demirbas, Progress in Energy and Combustion Science 31 (2005) 466-487.

[20] G. Knothe, K.R. Steidley, Fuel 84 (2005) 1059-1065.

[21] G. Knothe, Fuel Processing Technology 86 (2005) 1059-1070.

[22] S.S. Sidibé, J. Blin, G. Vaitilingom, Y. Azoumah, Renewable and Sustainable Energy Reviews 14 (2010) 2748-2759.

[23] M. Basinger, T. Reding, C. Williams, K.S. Lackner, V. Modi, Fuel 89 (2010) 2925-2938.

[24] K.S. Tyson, R.L. McCormick, Biodiesel Handling and Use Guidelines, Report No. NREL/TP-540-43672, National Renewable Energy Laboratory, 2006.

[25] A.K. Agarwal, Progress in Energy and Combustion Science 33 (2007) 233-271.

[26] S.D. Sanford, J.M. White, P.S. Shah, C. Wee, M.A. Valverde, G.R. Meier, Feedstock and Biodiesel Characteristics Report, Renewable Energy Group, Ames, IA, USA, 2009.

[27] L.G. Wade, Organic Chemistry, 6th ed., Pearson Prentice Hall, Upper Saddle River, NJ, USA, 2006.

[28] J. Otera, Chemical Reviews 93 (1993) 1449-1470.

[29] J. Van Gerpen, B. Shanks, R. Pruszko, D. Clements, G. Knothe, Biodiesel Production Technology, Report No. NREL/SR-510-36244, National Renewable Energy Laboratory, 2004.

[30] M.K. Lam, K.T. Lee, A.R. Mohamed, Biotechnology Advances 28 (2010) 500-518.

[31] F. Ma, M.A. Hanna, Bioresource Technology 70 (1999) 1-15.

[32] K. Narasimharao, A. Lee, K. Wilson, Journal of Biobased Materials and Bioenergy 1 (2007) 1-12.

[33] C. Brunschwig, W. Moussavou, J. Blin, Progress in Energy and Combustion Science 38 (2012) 283-301.

[34] E. Lotero, Y. Liu, D.E. Lopez, K. Suwannakarn, D.A. Bruce, J.G. Goodwin, Industrial & Engineering Chemistry Research 44 (2004) 5353-5363.

[35] A. Gog, M. Roman, M. Tosa, C. Paizs, F.D. Irimie, Renewable Energy 39 (2012) 10-16.

[36] L. Fjerbaek, K.V. Christensen, B. Norddahl, Bioetchnology and Bioengineering 102 (2009) 1298-1315.

[37] A.C. Pinto, L.L.N. Guarieiro, M.J.C. Rezende, N.M. Ribeiro, E.A. Torres, W.A. Lopes, P.A.P. Pereira, J.B. de Andrade, Journal of the Brazilian Chemical Society 16 (2005) 1313-1330.

[38] C.E. Stuaffer, Emulsifiers for the Food Industry, in: F. Shahidi (Eds.), Bailey's Industrial Oil and Fat Products, 6th ed., John Wiley & Sons, Hoboken, NJ, USA, 2005.

[39] L.C. Meher, D. Vidya Sagar, S.N. Naik, Renewable and Sustainable Energy Reviews 10 (2006) 248-268.

[40] D.Y.C. Leung, X. Wu, M.K.H. Leung, Applied Energy 87 (2010) 1083-1095.

[41] A.P. Vyas, J.L. Verma, N. Subrahmanyam, Fuel 89 (2010) 1-9.

[42] J. Van Gerpen, Fuel Processing Technology 86 (2005) 1097-1107.

[43] Y. Zhang, M.A. Dubé, D.D. McLean, M. Kates, Bioresource Technology 89 (2003) 1-16.

[44] Y. Zhang, M.A. Dubé, D.D. McLean, M. Kates, Bioresource Technology 90 (2003) 229-240.

[45] A.E. Ghaly, D. Dave, M.S. Brooks, S. Budge, American Journal of Biochemistry and Biotechnology 6 (2010) 54-76.

[46] S. Hari Krishna, N.G. Karanth, Catalysis Reviews 44 (2002) 499-591.

[47] A.L. Paiva, V.M. Balcão, F. Xavier Malcata, Enzyme and Microbial Technology 27 (2000) 187-204.

[48] Y. Shimada, Y. Watanabe, T. Samukawa, A. Sugihara, H. Noda, H. Fukuda, Y. Tominaga, Journal of the American Oil Chemists Society 76 (1999) 789-793.

[49] Y. Watanabe, Y. Shimada, A. Sugihara, Y. Tominaga, Journal of Bioscience and Bioengineering 88 (1999) 622-626.

[50] W. Du, Y. Xu, D. Liu, J. Zeng, Journal of Molecular Catalysis B: Enzymatic 30 (2004) 125-129.

[51] Y. Xu, W. Du, D. Liu, Journal of Molecular Catalysis B: Enzymatic 32 (2005) 241-245.

[52] M.K. Modi, J.R.C. Reddy, B.V.S.K. Rao, R.B.N. Prasad, Bioresource Technology 98 (2007) 1260-1264.

[53] K. Wilson, A.F. Lee, D.J. Macquarrie, J.H. Clark, Applied Catalysis A: General 228 (2002) 127-133.

[54] C. da Silva, J.V. Oliveira, Brazilian Journal of Chemical Engineering 31 (2014) 271-285.

[55] S. Saka, D. Kusdiana, Fuel 80 (2001) 225-231.

[56] L. Coniglio, J.A.P. Coutinho, J.Y. Clavier, F. Jolibert, J. Jose, I. Mokbel, D. Pillot, M.N. Pons, M. Sergent, V. Tschamber, Progress in Energy and Combustion Science (2014) 1-35.

[57] D. Kusdiana, S. Saka, Bioresource Technology 91 (2004) 289-295.

[58] G. Madras, C. Kolluru, R. Kumar, Fuel 83 (2004) 2029-2033.

[59] K. Bunyakiat, S. Makmee, R. Sawangkeaw, S. Ngamprasertsith, Energy & Fuels 20 (2003) 812-817.

[60] K.T. Lee, S. Lim, Y.L. Pang, H.C. Ong, W.T. Chong, Progress in Energy and Combustion Science (2014) 54-78.

[61] W. Cao, H. Han, J. Zhang, Fuel 84 (2005) 347-351.

[62] G. Guan, N. Sakurai, K. Kusakabe, Chemical Engineering Journal 146 (2009) 302-306.

[63] A.P. Harvey, M.R. Mackley, T. Seliger, Journal of Chemical Technology and Biotechnology 78 (2003) 338-341.

[64] J. Ji, J. Wang, Y. Li, Y. Yu, Z. Xu, Ultrasonic 44 (2006) e411-e414.

[65] P.R. Gogate, Chemical Engineering and Processing 47 (2008) 515-527.

[66] T.M. Barnard, N.E. Leadbeater, M.B. Boucher, L.M. Stencel, B.A. Wilhite, Energy & Fuels 21 (2007) 1777-1781.

[67] J. Gressel, Plant Science 174 (2008) 246-263.

[68] T. Mielke, Oil World Annual 2014, Volume 1, ISTA Mielke GmbH, Hamburg, Germany, 2014.

[69] M.F. Milazzo, F. Spina, P. Primerano, J.C.J. Bart, Renewable and Sustainable Energy Reviews 26 (2013) 579-624.

[70] I. Mukherjee, B.K. Sovacool, Renewable and Sustainable Energy Reviews 37 (2014) 1-12.

[71] T. Thamsiriroj, J.D. Murphy, Applied Energy 86 (2009) 595-604.

[72] D. Graham-Rowe, Nature 474 (2011) S6-S8.

[73] Y. Sun, J. Cheng, Bioresource Technology 83 (2002) 1-11.

[74] C. Somerville, H. Youngs, C. Taylor, S.C. Davis, S.P. Long, Science 329 (2010) 790-792.

[75] K. Sanderson, Nature 474 (2011) S12-S14.

[76] P. Dürre, Biotechnology Journal 2 (2007) 1525-1534.

[77] P. Dürre, Current Opinion in Biotechnology 22 (2011) 331-336.

[78] W. Zhang, Fuel Processing Technology 91 (2010) 866-876.

[79] E.D. Larson, Biofuel Production Technologies: Status, Prospects and Implications for Trade and Development, Report No. UNCTAD/DITC/TED/2007/10, United Nations Conference on Trade and Development, New York and Geneva, 2008.

[80] T. Takeshita, K. Yamaji, Energy Policy 36 (2008) 2773-2784.

[81] S. Zinoviev, F. Müller-Langer, P. Das, N. Bertero, P. Fornasiero, M. Kaltschmitt, G. Centi, S. Miertus, ChemSusChem 3 (2010) 1106-1133.

[82] R.A. Lee, J.M. Lavoie, Animal Frontiers 3 (2013) 6-11.

[83] S.K. Lohan, T. Ram, S. Mukesh, M. Ali, S. Arya, Renewable and Sustainable Energy Reviews 25 (2013) 251-259.

[84] F. Lu, X. Wu, Food Control 41 (2014) 134-138.

[85] S. Liang, Z. Liu, M. Xu, T. Zhang, Bioresource Technology 131 (2013) 139-145.

[86] G. Knothe, Progress in Energy and Combustion Science 36 (2010) 364-373.

[87] T. Kalnes, T. Marker, D.R. Shonnard, International Journal of Chemical Reactor Engineering 5 (2007) A48 1-9.

[88] M. Kuronen, S. Mikkonen, P. Aakko, T. Murtonen, SAE Paper No. 2007-01-4031, 2007.

[89] L. Rantanen, R. Linnaila, P. Aakko, T. Harju, SAE Paper No. 2005-01-3771, 2005.

[90] T.G. Smagala, E. Christensen, K.M. Christison, R.E. Mohler, E. Gjersing, R.L. McCormick, Energy & Fuels 27 (2012) 237-246.

[91] C.R. Carlos, R. Sparling, N. Cicek, D.B. Levin, International Journal of Molecular Sciences 9 (2008) 1342-1360.

[92] P.S. Nigam, A. Singh, Progress in Energy and Combustion Science 37 (2011) 52-68.

[93] C.S. Goh, K.T. Lee, Renewable and Sustainable Energy Reviews 14 (2010) 842-848.

[94] S. Kraan, Mitigation and Adaption Strategies for Global Change 18 (2013) 27-46.

[95] A.J. Wargacki, E. Leonard, M.N. Win, D.D. Regitsky, S.N.S. Santos, P.B. Kim, S.R. Cooper, R.M. Raisner, A. Herman, A.B. Sivitz, A. Lakshmanaswamy, Y. Kashiyama, D. Baker, Y. Yoshikuni, Science 335 (2012) 308-313.

[96] D.P. Chynoweth, J.M. Owens, R. Legrand, Renewable Energy 22 (2001) 1-8.

[97] A.B. Ross, J.M. Jones, M.L. Kubacki, T. Bridgeman, Bioresource Technology 99 (2008) 6494-6504.

[98] R. Maceiras, M. Rodríguez, A. Cancela, S. Urréjola, A. Sánchez, Applied Energy 88 (2011) 3318-3323.

[99] S. Bastianoni, F. Coppola, E. Tiezza, A. Colacevich, F. Borghini, S. Focardi, Biomass and Bioenergy 32 (2008) 619-628.

[100] Y. Christi, Biotechnology Advances 25 (2007) 294-306.

[101] S.A. Scott, M.P. Davey, J.S. Dennis, I. Horst, C.J. Howe, D.J. Lea-Smith, A.G. Smith, Current Opinion in Biotechnology 21 (2010) 277-286.

[102] M.F. Demirbas, Applied Energy 88 (2011) 3473-3480.

[103] S.K. Hoekman, A. Broch, C. Robbins, E. Ceniceros, M. Natarajan, Renewable and Sustainable Energy Reviews 16 (2012) 143-169.

[104] O. Levitan, J. Dinamarca, G. Hochman, P.G. Falkowski, Trends in Biotechnology 32 (2014) 117-124.

[105] G. Knothe, Energy & Fuels 26 (2012) 5265-5273.

[106] S. Rasoul-Amini, N. Montazeri-Najafabady, M.A. Mobasher, S. Hoseini-Alhashemi, Y. Ghasemi, Applied Energy 88 (2011) 3354-3356.

[107] C.S. Jones, S.P. Mayfield, Current Opinion in Biotechnology 23 (2012) 346-351.

[108] K. Sander, G.S. Murthy, The International Journal of Life Cycle Assessment 15 (2010) 704-714.

[109] H.K. Reddy, T. Muppaneni, Y. Sun, Y. Li, S. Ponnusamy, P.D. Patil, P. Dailey, T. Schaub, F.O. Holguin, B. Dungan, P. Cooke, P. Lammers, W. Voorhies, X. Lu, S. Deng, Fuel 133 (2014) 73-81.

[110] L. Zhu, Biofuels, Bioproducts & Biorefining 8 (2014) 7-15.

[111] I. Rawat, R.R. Kumar, T. Mutanda, F. Bux, Applied Energy 88 (2011) 3411-3424.

[112] M. Hannon, J. Gimpel, M. Tran, B. Rasala, S. Mayfield, Biofuels 1 (2010) 763-784.

[113] C. Rhodes, Why Algal Biofuels May Never Hold the Key to the Future, 2012 [Online]. Available at: http://oilprice.com/Alternative-Energy/Biofuels/Why-Algal-Biofuels-May-Never-Hold-the-Key-to-the-Future.html[Accessed Nov 2015].

[114] J. Lü, C. Sheahan, P. Fu, Energy & Environmental Science 4 (2011) 2451-2466.

[115] D.R. Georgianna, S.P. Mayfield, Nature 488 (2012) 329-335.

[116] H. Schuhmann, D.K.Y. Lim, P.M. Schenk, Biofuels 3 (2012) 71-86.

[117] R. Radakovits, R.E. Jinkerson, A. Darzins, M.C. Posewitz, Eukaryotic Cell 9 (2010) 486-501.

[118] C. Scrimgeour, Chemistry of Fatty Acids, in: F. Shahidi (Eds.), Bailey's Industrial Oil and Fat Products, 6th ed., John Wiley & Sons, Hoboken, NJ, USA, 2005.

[119] P.J.B. Williams, L.M.L. Laurens, Energy & Environmental Science 3 (2010) 554-590.

[120] J.K. Volkman, S.W. Jeffrey, P.D. Nichols, G.I. Rogers, C.D. Garland, Journal of Experimental Marine Biology and Ecology 128 (1989) 219-240.

[121] K. Sato, S. Ueno, Polymorphism in Fats and Oils, in: F. Shahidi (Eds.), Bailey's Industrial Oil and Fat Products, 6th ed., John Wiley & Sons, Hoboken, NJ, USA, 2005.

[122] C.K. Westbrook, C.V. Naik, O. Herbinet, W.J. Pitz, M. Mehl, S.M. Sarathy, H.J. Curran, Combustion and Flame 158 (2011) 742-755.

[123] R. Przybylski, T. Mag, N.A.M. Eskin, B.E. McDonald, Canola Oil, in: F. Shahidi (Eds.), Bailey's Industrial Oil and Fat Products, 6th ed., John Wiley & Sons, Hoboken, NJ, USA, 2005.

[124] E.G. Hammond, L.A. Johnson, C. Su, T. Wang, P.J. White, Soybean Oil, in: F. Shahidi (Eds.), Bailey's Industrial Oil and Fat Products, 6th ed., John Wiley & Sons, Hoboken, NJ, USA, 2005.

[125] A.P. Bimbo, Rendering, in: F. Shahidi (Eds.), Bailey's Industrial Oil and Fat Products, 6th ed., John Wiley & Sons, Hoboken, NJ, USA, 2005.

[126] R.A. Moreau, Corn Oil, in: F. Shahidi (Eds.), Bailey's Industrial Oil and Fat Products, 6th ed., John Wiley & Sons, Hoboken, NJ, USA, 2005.

[127] R. Przybylski, Flax Oil and High Linolenic Oils, in: F. Shahidi (Eds.), Bailey's Industrial Oil and Fat Products, 6th ed., John Wiley & Sons, Hoboken, NJ, USA, 2005.

[128] E.C. Canapi, Y.T.V. Agustin, E.A. Moro, E. Pedrosa, M.L.J. Bendaño, Coconut Oil, in: F. Shahidi (Eds.), Bailey's Industrial Oil and Fat Products, 6th ed., John Wiley & Sons, Hoboken, NJ, USA, 2005.

[129] H.P. Visser, Biodiesel Production from a Butter Factory Effluent, Masters Dissertation, North-West University, South Africa, 2012.

[130] M.J. Haas, Animal Fats, in: F. Shahidi (Eds.), Bailey's Industrial Oil and Fat Products, 6th ed., John Wiley & Sons, Hoboken, NJ, USA, 2005.

[131] R.G. Ackman, Fish Oils, in: F. Shahidi (Eds.), Bailey's Industrial Oil and Fat Products, 6th ed., John Wiley & Sons, Hoboken, NJ, USA, 2005.

[132] J.P. Wynn, C. Ratledge, Oils from Microorganisms, in: F. Shahidi (Eds.), Bailey's Industrial Oil and Fat Products, 6th ed., John Wiley & Sons, Hoboken, NJ, USA, 2005.

[133] J.C.J. Bart, N. Palmeri, S. Cavallaro, Biodiesel Science and Technology, Woodhead Publishing Limited, Cambridge, UK, 2010.

[134] W.W. Christie, The AOCS Lipid Library, Fatty Acids: Hydroxy and Other Oxygenated Structures, Occurence and Biochemistry [Online]. Available at: http://lipidlibrary.aocs.org/Lipids/fa_oxy/index.htm [Accessed Jan 2015].

[135] N.L. Panwar, H.Y. Shrirame, N.S. Rathore, S. Jindal, A.K. Kurchania, Applied Thermal Engineering 30 (2010) 245-249.

[136] E.A. Alamineh, Biodiesel Production from Vernonia Galamensis Oil Using Ethanol with Alkali Catalyst, Masters Dissertation, Addis Ababa University, Ethiopia, 2012.

[137] P. Felizardo, M.J.N. Correia, I. Raposo, J.F. Mendes, R. Berkemeier, J.M. Bordado, Waste Management 26 (2006) 487-494.

[138] M. Berrios, R.L. Skelton, Chemical Engineering Journal 144 (2008) 459-465.

[139] L. Díaz-Ballote, J.F. López-Sansores, L. Maldonado-López, L.F. Garfias-Mesias, Electrochemistry Communications 11 (2009) 41-44.

[140] J.H. Van Gerpen, E.G. Hammond, L. Yu, A. Monyem, SAE Paper No. 971685, 1997.

[141] G. Knothe, R.O. Dunn, Journal of the American Oil Chemists Society 80 (2003) 1021-1026.

[142] R.L. McCormick, M. Ratcliff, L. Moens, R. Lawrence, Fuel Processing Technology 88 (2007) 651-657.

[143] R.O. Dunn, Progress in Energy and Combustion Science 35 (2009) 481-489.

[144] V. Van Hoed, N. Zyaykina, W. De Greyt, J. Maes, R. Verhé, K. Demeestere, Journal of the American Oil Chemists Society 85 (2008) 701-709.

[145] F. Lacoste, F. Dejean, H. Griffon, C. Rouquette, European Journal of Lipid Science and Technology 111 (2009) 822-828.

[146] L. Pfalzgraf, I. Lee, J. Foster, G. Poppe, The Effect of Minor Components on Cloud Point and Filterability, Biodiesel Magazine, 2007 [Online]. Available at: http://biodieselmagazine.com/articles/1916/the-effect-of-minor-components-on-cloud-point-and-filterability/ [Accessed Nov 2015].

[147] M.S. Graboski, R.L. McCormick, T.L. Alleman, A.M. Herring, The Effect of Biodiesel Composition on Engine Emissions from a DDC Series 60 Diesel Engine, Report No. NREL/SR-510-31461, National Renewable Energy Laboratory, 2003.

[148] G. Knothe, Fuel Processing Technology 88 (2007) 669-677.

[149] S. Kaul, R.C. Saxena, A. Kumar, M.S. Negi, A.K. Bhatnagar, H.B. Goyal, A.K. Gupta, Fuel Processing Technology 88 (2007) 303-307.

[150] L. Chen, T. Liu, W. Zhang, X. Chen, J. Wang, Bioresource Technology 111 (2012) 208-214.

[151] W.H. Cheng, H.H. Kung, Overview, in: W.H. Cheng, H.H. Kung (Eds.), Methanol Production and Use, Marcel Dekker Inc., New York, USA, 1994.

[152] J.R. LeBlanc, R.V. Schneider, R.B. Strait, Production of Methanol, in: W.H. Cheng, H.H. Kung (Eds.), Methanol Production and Use, Marcel Dekker Inc., New York, USA, 1994.

[153] Y. Isayama, S. Saka, Bioresource Technology 99 (2008) 4775-4779.

[154] P. Hellier, N. Ladommatos, R. Allan, J. Rogerson, Energy & Fuels 26 (2012) 1912-1927.

[155] J. Yanowitz, M.A. Ratcliff, R.L. McCormick, J.D. Taylor, M.J. Murphy, Compendium of Experimental Cetane Numbers, Report No. NREL/TP-5400-61693, National Renewable Energy Laboratory, 2014.

[156] C.S. McEnally, L.D. Pfefferle, Environmental Science & Technology 45 (2011) 2498-2503.

[157] E. Kinoshita, Y. Ueda, S. Takata, SAE Paper No. 2011-01-1937, 2011.

[158] E. Kinoshita, A. Itakura, T. Otaka, K. Koide, Y. Yoshimoto, T. Myo, SAE Paper No. 2014-32-0084, 2014.

[159] J.G. Speight, The Chemistry and Technology of Petroleum, 4th ed., CRC Press, Taylor & Francis Group, Boca Raton, FL, USA, 2007.

[160] J.T. Farrell, N.P. Cernansky, F.L. Dryer, D.G. Friend, C.A. Hergart, C.K. Law, R.M. McDavid, C.J. Mueller, A.K. Patel, H. Pitsch, SAE Paper No. 2007-01-0201, 2007.

[161] J.G. Speight, Handbook of Industrial Hydrocarbon Processes, Gulf Professional Publishing, Oxford, UK, 2011.

[162] W.J. Pitz, C.J. Mueller, Progress in Energy and Combustion Science 37 (2011) 330-350.

[163] Y. Briker, Z. Ring, A. Iacchelli, N. McLean, P.M. Rahimi, C. Fairbridge, R. Malhotra, M.A. Coggiola, S.E. Young, Energy & Fuels 15 (2001) 23-27.

[164] Royal Society of Chemistry, ChemSpider Methyl Oleate [Online]. Available at: http://www.chemspider.com/Chemical-Structure.4516661.html [Accessed Jan 2015].

[165] M.S. Graboski, R.L. McCormick, Progress in Energy and Combustion Science 24 (1998) 125-164.

[166] Royal Society of Chemistry, ChemSpider Ethyl Oleate [Online]. Available at: http://www.chemspider.com/Chemical-Structure.4515636.html [Accessed Jan 2015].

[167] C. Rakopoulos, K. Antonopoulos, D. Rakopoulos, Energy Conversion and Management 47 (2006) 1550-1573.

[168] B.R. Moser, Biodiesel Properties and Alternative Feedstocks, in: S.T. Yang, H.A. El-Enshasy, N. Thongchul (Eds.), Bioprocessing Technologies in Biorefinery for Sustainable Production of Fuels, Chemicals and Polymers, John Wiley & Sons, Hoboken, NJ, USA, 2013.

[169] M.J. Ramos, C.M. Fernández, A. Casas, L. Rodríguez, A. Pérez, Bioresource Technology 100 (2009) 261-268.

[170] G. Knothe, R.O. Dunn, Journal of the American Oil Chemists Society 86 (2009) 843-856.

[171] D.R. Lide, W.M. Haynes (Eds.), CRC Handbook of Chemistry and Physics, 90th ed., CRC Press, Boca Raton, FL, USA, 2010.

[172] I. Lee, L.A. Johnson, E.G. Hammond, Journal of the American Oil Chemists Society 72 (1995) 1155-1160.

[173] G. Knothe, Energy & Environmental Science 2 (2009) 759-766.

[174] British Standards Institute, Diesel and Domestic Heating Fuels - Determination of Cold Filter Plugging Point - Linear Cooling Bath Method, BS EN 16329:2013.

[175] C. Boshui, S. Yuqui, F. Jianhua, W. Jiu, W. Jiang, Biomass and Bioenergy 34 (2010) 1309-1313.

[176] C. Echim, J. Maes, W. De Greyt, Fuel 93 (2012) 642-648.

[177] M.J. Pratas, S. Freitas, M.B. Oliveira, S.C. Moneiro, A.S. Lima, J.A.P. Coutinho, Journal of Chemical & Engineering Data 55 (2010) 3983-3990.

[178] M.J. Pratas, S. Freitas, M.B. Oliveira, S.C. Moneiro, A.S. Lima, J.A.P. Coutinho, Journal of Chemical & Engineering Data 56 (2011) 2175-2180.

[179] M.R. Munson, D.F. Young, T.H. Okiishi, Fundamentals of Fluid Mechanics, 5th ed., John Wiley & Sons, Hoboken, NJ, USA, 2006.

[180] M.E. Tat, J.H. Van Gerpen, Measurement of Biodiesel Speed of Sound and Its Impact on Injection Timing, Report No. NREL/SR-510-31462, National Renewable Energy Laboratory, 2003.

[181] L.M. Rodriguez-Anton, J. Casanova-Kindelan, G. Tardajos, SAE Paper No. 2000-01-2046, 2000.

[182] K. Yamane, A. Ueta, Y. Shimamoto, International Journal of Engine Research 2 (2001) 249-261.

[183] M.E. Tat, J.H. Van Gerpen, S. Soylu, M. Canakci, A. Monyem, S. Wormley, Journal of the American Oil Chemists Society 77 (2000) 285-289.

[184] A.F.G. Lopes, M.C. Talavera-Prieto, A.G.M. Ferreira, J.B. Santos, M.J. Santos, A.T.G. Portugal, Fuel 116 (2014) 242-254.

[185] C.E. Ejim, B.A. Fleck, A. Amirfazli, Fuel 86 (2007) 1534-1544.

[186] C.A.W. Allen, K.C. Watts, R.G. Ackman, Journal of the American Oil Chemists Society 76 (1999) 317-323.

[187] K.M. Doll, B.R. Moser, S.Z. Erhan, Energy & Fuels 21 (2007) 3044-3048.

[188] British Standards Institute, Diesel Fuel - Assessment of Lubricity using the High-Frequency Reciprocating Rig (HFRR) - Part 1: Test Method, BS EN ISO 12156-1:2006.

[189] R.H. Barbour, D.J. Rickeard, N.G. Elliott, SAE Paper No. 2000-01-1918, 2000.

[190] S. Cook, J. Barker, J. Reid, P. Richards, SAE Paper No. 2012-01-0867, 2012.

[191] J. Hu, Z. Du, C. Li, E. Min, Fuel 84 (2005) 1601-1606.

[192] B.R. Moser, Energy & Fuels 22 (2008) 4301-4306.

[193] L. Prasad, L.M. Das, S.N. Naik, Energy & Fuels 26 (2012) 5307-5315.

[194] J.W. Goodrum, D.P. Geller, Bioresource Technology 96 (2005) 851-855.

[195] British Standards Institute, Fat and Oil Derivatives - Fatty Acid Methyl Esters (FAME) - Determination of Oxidation Stability (Accelerated Oxidation Test), BS EN 14112:2003.

[196] British Standards Institute, Automotive Fuels - Fatty Acid Methyl Ester (FAME) Fuel and Blends with Diesel Fuel - Determination of Oxidation Stability by Accelerated Oxidation Test, BS EN 15751:2014.

[197] I. Miyata, Y. Takei, K. Tsurutani, M. Okada, SAE Paper No. 2004-01-3031, 2004.

[198] G. Karavalakis, D. Karonis, S. Stournas, SAE Paper No. 2009-01-1828, 2009.

[199] B.R. Moser, Journal of the American Oil Chemists Society 86 (2009) 699-706.

[200] M. Shahabuddin, M.A. Kalam, H.H. Masjuki, M.M.K. Bhuiya, M. Mofijur, Energy 44 (2012) 616-622.

[201] J. Polavka, J. Paligová, J. Cvengroš, P. Šimon, Journal of the American Oil Chemists Society 82 (2005) 519-524.

[202] E.N. Frankel, Lipid Oxidation, 2nd ed., Woodhead Publishing Limited, Cambridge, UK, 2012.

[203] Y. Basiron, Palm Oil, in: F. Shahidi (Eds.), Bailey's Industrial Oil and Fat Products, 6th ed., John Wiley & Sons, Hoboken, NJ, USA, 2005.

[204] R.W. Owen, A. Giacosa, W.E. Hull, R. Haubner, G. Würtele, B. Spiegelhalder, H. Bartsch, The Lancet Oncology 1 (2000) 107-112.

[205] S. Schober, M. Mittelbach, European Journal of Lipid Science and Technology 106 (2004) 382-389.

[206] Y.A. Çengel, M.A. Boles, Thermodynamics: An Engineering Approach, 5th ed., McGraw-Hill, New York, USA, 2005.

[207] US Department of Energy, Biomass Energy Data Book [Online]. Available at: http://cta.ornl.gov/bedb/index.shtml [Accessed Mar 2015].

[208] B. Freedman, M.O. Bagby, Journal of the American Oil Chemists Society 66 (1989) 1601-1605.

[209] G. Knothe, Appendix A – Technical Tables, in: G. Knothe, J. Krahl, J. Van Gerpen, The Biodiesel Handbook, 2nd ed., AOCS Press, Urbana, IL, USA, 2010.

[210] M. Lapuerta, J. Rodríguez-Fernández, F. Oliva, Chemistry and Physics of Lipids 163 (2010) 172-181.

[211] P.Q.E. Clothier, B.D. Aguda, A. Moise, H.O. Pritchard, Chemical Society Reviews 22 (1993) 101-108.

[212] Y. Zhang, Y. Yang, A.L. Boehman, Combustion and Flame 156 (2009) 1202-1213.

[213] P. Hellier, N. Ladommatos, R. Allan, S. Filip, J. Rogerson, Fuel 105 (2013) 477-489.

[214] F. Shahidi, Quality Assurance of Fats and Oils, in: F. Shahidi (Eds.), Bailey's Industrial Oil and Fat Products, 6th ed., John Wiley & Sons, Hoboken, NJ, USA, 2005.

[215] K.M. Schaich, Lipid Oxidation: Theoretical Aspects, in: F. Shahidi (Eds.), Bailey's Industrial Oil and Fat Products, 6th ed., John Wiley & Sons, Hoboken, NJ, USA, 2005.

[216] C.T. Ho, F. Shahidi, Flavor Components of Fats and Oils, in: F. Shahidi (Eds.), Bailey's Industrial Oil and Fat Products, 6th ed., John Wiley & Sons, Hoboken, NJ, USA, 2005.

[217] J. Dong, C.A. Migdal, Antioxidants, in: L.R. Rudnick (Eds.), Lubricant Additives: Chemistry and Applications, CRC Press, Taylor & Francis Group, Boca Raton, FL, USA, 2009.

[218] IUPAC, Compendium of Chemical Terminology: Gold Book (Version 2.3.2), International Union of Pure and Applied Chemistry, Zürich, Switzerland, 2012.

[219] F. Shahidi, Y. Zhong, Lipid Oxidation: Measurement Methods, in: F. Shahidi (Eds.), Bailey's Industrial Oil and Fat Products, 6th ed., John Wiley & Sons, Hoboken, NJ, USA, 2005.

[220] H.L. Fang, S.D. Whitacre, E.S. Yamaguchi, M. Boons, SAE Paper No. 2007-01-4141, 2007.

[221] M. Andreae, H. Fang, K. Bhandary, SAE Paper No. 2007-01-4036, 2007.

[222] K.M. Richard, S. McTavish, SAE Paper No. 2009-01-2660, 2009.

[223] A. Sarin, R. Arora, N.P. Singh, M. Sharma, R.K. Malhotra, Energy 34 (2009) 1271-1275.

[224] S.J. Blanksby, G.B. Ellison, Accounts of Chemical Research 36 (2003) 255-263.

[225] A.M. El-Nahas, M.V. Navarro, J.M. Simmie, J.W. Bozzelli, H.J. Curran, S. Dooley, W. Metcalfe, Journal of Physical Chemistry A 111 (2007) 3727-3739.

[226] R.T. Sanderson, Chemical Bonds and Bond Energy, Academic Press, Inc., New York, USA, 1976.

[227] P.K.J.P.D. Wanasundara, F. Shahidi, Antioxidants: Science, Technology and Applications, in: F. Shahidi (Eds.), Bailey's Industrial Oil and Fat Products, 6th ed., John Wiley & Sons, Hoboken, NJ, USA, 2005.

[228] R.W. Walker, C. Morley, Basic Chemistry of Combustion, in: M.J. Pilling (Eds.), Comprehensive Chemical Kinetics, Volume 35: Low-Temperature Combustion and Autoignition, Elsevier Science, Amsterdam, The Netherlands, 1997.

[229] C. Morley, M.J. Pilling, Introduction, in: M.J. Pilling (Eds.), Comprehensive Chemical Kinetics, Volume 35: Low-Temperature Combustion and Autoignition, Elsevier Science, Amsterdam, The Netherlands, 1997.

[230] C.K. Westbrook, Proceedings of the Combustion Institute 28 (2000) 1563-1577.

[231] C.K. Westbrook, W.J. Pitz, H.J. Curran, Auto-Ignition and Chemical Kinetic Mechanisms of HCCI Combustion, in: H. Zhao (Eds.), HCCI and CAI Engines for the Automotive Industry, Woodhead Publishing Limited, Cambridge, UK, 2007.

[232] S.M. Sarathy, C.K. Westbrook, M. Mehl, W.J. Pitz, C. Togbe, P. Dagaut, H. Wang, M.A. Oehlschlaeger, U. Niemann, K. Seshadri, P.S. Veloo, C. Ji, F.N. Egolfopoulos, T. Lu, Combustion and Flame 158 (2011) 2338-2357.

[233] C.K. Westbrook, W.J. Pitz, S.M. Sarathy, M. Mehl, Proceedings of the Combustion Institute 34 (2013) 3049-3056.

[234] J.K. Merle, C.M. Hadad, Reactive Intermediates in Combustion, in: M.S. Platz, R.A. Moss, M. Jones (Eds.), Reviews of Reactive Intermediate Chemistry, John Wiley & Sons, Hoboken, NJ, USA, 2007.

[235] H.J. Curran, P. Gaffuri, W.J. Pitz, C.K. Westbrook, Combustion and Flame 114 (1997) 149-177.

[236] F. Battin-Leclerc, Progress in Energy and Combustion Science 34 (2008) 440-498.

[237] S.H. Robertson, P.W. Seakins, M.J. Pilling, Elementary Reactions, in: M.J. Pilling (Eds.), Comprehensive Chemical Kinetics, Volume 35: Low-Temperature Combustion and Autoignition, Elsevier Science, Amsterdam, The Netherlands, 1997.

[238] J.C. Rienstra-Kiracofe, W.D. Allen, H.F. Schaefer, Journal of Physical Chemistry A 104 (2000) 9823-9840.

[239] J. Zádor, C.A. Taatjes, R.X. Fernades, Progress in Energy and Combustion Science 37 (2011) 371-421.

[240] T.H. Lowry, K. Schueller Richardson, Mechanism and Theory in Organic Chemistry, Harper & Row, New York, USA, 1976.

[241] Y.R. Luo, Handbook of Bond Dissociation Energies in Organic Compounds, CRC Press LLC, Boca Raton, FL, USA, 2003.

[242] H.J. Curran, P. Gaffuri, W.J. Pitz, C.K. Westbrook, Combustion and Flame 129 (2002) 253-280.

[243] C.K. Westbrook, Combustion Chemistry: Chemical Kinetics and Kinetic Modeling, in: Princeton-CEFRC Combustion Summer School Lectures, Princeton, NJ, USA, 2010. (http://www.princeton.edu/engineering/video/combustion-2012/2010/ - Part 2, 40:20, Accessed Jan 2013).

[244] F. Buda, R. Bounaceur, V. Warth, P.A. Glaude, R. Fournet, F. Battin-Leclerc, Combustion and Flame 142 (2005) 170-186.

[245] O. Herbinet, S. Bax, P.A. Glaude, V. Carré, F. Battin-Leclerc, Fuel 90 (2011) 528-535.

[246] W.J. Pitz, C.V. Naik, T. Ní Mhaoldúin, C.K. Westbrook, H.J. Curran, J.P. Orme, J.M. Simmie, Proceedings of the Combustion Institute 31 (2007) 267-275.

[247] C.K. Westbrook, W.J. Pitz, Fundamental Chemical Kinetics, in: D. Crolla, D.E. Foster, T. Kobayashi, N. Vaughan (Eds.), Encyclopedia of Automotive Engineering (Online), John Wiley & Sons, Hoboken, NJ, USA, 2014.

[248] P.A. Glaude, F. Battin-Leclerc, R. Fournet, V. Warth, G.M. Côme, G. Scacchi, Combustion and Flame 122 (2000) 451-462.

[249] M. Mehl, G. Vanhove, W.J. Pitz, E. Ranzi, Combustion and Flame 155 (2008) 756-772.

[250] O. Herbinet, W.J. Pitz, C.K. Westbrook, Combustion and Flame 157 (2010) 893-908.

[251] A. Roubaud, R. Minetti, L.R. Sochet, Combustion and Flame 121 (2000) 535-541.

[252] F. Battin-Leclerc, V. Warth, R. Bounaceur, B. Husson, O. Herbinet, P.A. Glaude, Proceedings of the Combustion Institute 35 (2015) 349-356.

[253] O. Herbinet, B. Husson, H. Le Gall, F. Battin-Leclerc, Chemical Engineering Science (2015).

[254] H. Nakamura, D. Darcy, M. Mehl, C.J. Tobin, W.K. Metcalfe, W.J. Pitz, C.K. Westbrook, H.J. Curran, Combustion and Flame 161 (2014) 49-64.

[255] B. Husson, O. Herbinet, P.A. Glaude, S.S. Ahmed, F. Battin-Leclerc, Journal of Physical Chemistry A 116 (2012) 5100-5111.

[256] B.W. Weber, W.J. Pitz, M. Mehl, E.J. Silke, A.C. Davis, C.J. Sung, Combustion and Flame 161 (2014) 1972-1983.

[257] R.H. Natelson, M.S. Kurman, N.P. Cernansky, D.L. Miller, Combustion and Flame 158 (2011) 2325-2337.

[258] P. Diévart, S.H. Won, S. Dooley, F.L. Dryer, Y. Ju, Combustion and Flame 159 (2012) 1793-1805.

[259] C.K. Westbrook, W.J. Pitz, H.J. Curran, Journal of Physical Chemistry A 110 (2006) 6912-6922.

[260] G. Dayma, S. Gaïl, P. Dagaut, Energy & Fuels 22 (2008) 1469-1479.

[261] C.V. Naik, C.K. Westbrook, O. Herbinet, W.J. Pitz, M. Mehl, Proceedings of the Combustion Institute 33 (2011) 383-389.

[262] G. Dayma, C. Togbé, P. Dagaut, Energy & Fuels 23 (2009) 4254-4268.

[263] P.A. Glaude, O. Herbinet, S. Bax, J. Biet, V. Warth, F. Battin-Leclerc, Combustion and Flame 157 (2010) 2035-2050.

[264] M.H. Hakka, P.A. Glaude, O. Herbinet, F. Battin-Leclerc, Combustion and Flame 156 (2009) 2129-2144.

[265] O. Herbinet, J. Biet, M.H. Hakka, V. Warth, P.A. Glaude, A. Nicolle, F. Battin-Leclerc, Proceedings of the Combustion Institute 33 (2011) 391-398.

[266] K.C. Lin, J.Y.W. Lai, A. Violi, Fuel 92 (2012) 16-26.

[267] P. Eastwood, Particulate Emissions from Vehicles, John Wiley and Sons Ltd, Chichester, UK, 2008.

[268] M. Lapuerta, R. Ballesteros, J. Rodríguez-Fernández, Measurement Science and Technology 18 (2007) 650-658.

[269] I. Glassman, R.A. Yetter, Combustion, 4th ed., Elsevier Academic Press, Burlington, MA, USA, 2008.

[270] D.B. Kittelson, Journal of Aerosol Science 29 (1998) 575-588.

[271] The World Bank, Reducing Black Carbon Emissions from Diesel Vehicles: Impacts, Control Strategies, and Cost-Benefit Analysis, Report No. 86485, The World Bank Group, Washington, DC, USA, 2014.

[272] S. George, S. Balla, M. Gautam, Wear 262 (2007) 1113-1122.

[273] D.A. Green, R. Lewis, Proceedings of the Institution of Mechanical Engineers, Part D: Journal of Automobile Engineering 222 (2008) 1669-1689.

[274] E. Hu, X. Hu, T. Liu, L. Fang, K.D. Dearn, H. Xu, Wear 304 (2013) 152-161.

[275] S. George, S. Balla, V. Gautam, M. Gautam, Tribology International 40 (2007) 809-818.

[276] C.S. McEnally, L.D. Pfefferle, B. Atakan, K. Kohse-Höinghaus, Progress in Energy and Combustion Science 32 (2006) 247-294.

[277] J. Hansen, L. Nazarenko, Proceedings of the National Academy of Sciences of the United States of America 101 (2004) 423-428.

[278] J.H. Seinfeld, S.N. Pandis, Atmospheric Chemistry and Physics, 2nd ed., John Wiley & Sons, Hoboken, NJ, USA, 2006.

[279] M.O. Andreae, Nature 409 (2001) 671-672.

[280] M.Z. Jacobson, Nature 409 (2001) 695-697.

[281] M.Z. Jacobson, Journal of Geophysical Research 107 (2002) 4410.

[282] M.Z. Jacobson, Journal of Geophysical Research 115 (2010) D1429.

[283] V. Ramanathan, G. Carmichael, Nature Geoscience 1 (2008) 221-227.

[284] B. Brunekreef, S.T. Holgate, The Lancet 360 (2002) 1233-1242.

[285] J.S. Lighty, J.M. Veranth, A.F. Sarofim, Journal of the Air & Waste Management Association 50 (2000) 1565-1618.

[286] B. Kumfer, I. Kennedy, The Role of Soot in the Health Effects of Inhaled Airborne Particles, in: H. Bockhorn, A. D'Anna, A.F. Sarofim, H. Wang (Eds.), Combustion Generated Fine Carbonaceous Particles, KIT Scientific Publishing, Karlsruhe, Germany, 2009.

[287] C.F.A. Vogel, E. Sciullo, P. Wong, P. Kuzmicky, N. Kado, F. Matsumura, Environmental Health Perspectives 113 (2005) 1536-1541.

[288] A. Penn, G. Murphy, S. Barker, W. Henk, L. Penn, Environmental Health Perspectives 113 (2005) 956-963.

[289] G. Murphy, R.L. Rouse, W.W. Polk, W.G. Henk, S.A. Barker, M.J. Boudreaux, Z.E. Floyd, A.L. Penn, American Journal of Respiratory Cell and Molecular Biology 38 (2008) 532-540.

[290] N.L. Mills, N. Amin, S.D. Robinson, A. Anand, J. Davies, D. Patel, J.M. de la Fuente, F.R. Cassee, N.A. Boon, W. MacNee, A.M. Millar, K. Donaldson, D.E. Newby, American Journal of Respiratory and Critical Care Medicine 173 (2006) 426-431.

[291] G. Oberdörster, J. Ferin, R. Gelein, S.C. Soderholm, J. Finkelstein, Environmental Health Perspectives 97 (1992) 193-199.

[292] F. Tao, B. Gonzalez-Flecha, L. Kobzik, Free Radical Biology & Medicine 35 (2003) 327-340.

[293] A. Baulig, M. Garlatti, V. Bonvallot, A. Marchand, R. Barouki, F. Marano, A. Baeza-Squiban, American Journal of Physiology: Lung Cellular and Molecular Physiology 285 (2003) L671-L679.

[294] T. Finkel, N.J. Holbrook, Nature 408 (2000) 239-247.

[295] H. Jung, B. Guo, C. Anastasio, I.M. Kennedy, Atmospheric Environment 40 (2006) 1043-1052.

[296] G.L. Squadrito, R. Cueto, B. Dellinger, W.A. Pryor, Free Radical Biology & Medicine 31 (2001) 1132-1138.

[297] H. Richter, J.B. Howard, Progress in Energy and Combustion Science 26 (2000) 565-608.

[298] D.R. Tree, K.I. Svensson, Progress in Energy and Combustion Science 33 (2007) 272-309.

[299] I. Glassman, Proceedings of the Combustion Institute 22 (1988) 295-311.

[300] H.R. Zhang, E.G. Eddings, A.F. Sarofim, C.K. Westbrook, Proceedings of the Combustion Institute 32 (2009) 377-385.

[301] H. Wang, M. Frenklach, Combustion and Flame 110 (1997) 173-221.

[302] C.S. McEnally, L.D. Pfefferle, Combustion and Flame 143 (2005) 246-263.

[303] M. Frenklach, Physical Chemistry Chemical Physics 4 (2002) 2028-2037.

[304] P.R. Westmoreland, The Prehistory of Soot: Small Rings from Small Molecules, in: H. Bockhorn, A. D'Anna, A.F. Sarofim, H. Wang (Eds.), Combustion Generated Fine Carbonaceous Particles, KIT Scientific Publishing, Karlsruhe, Germany, 2009.

[305] J.A. Miller, M.J. Pilling, J. Troe, Progress in Energy and Combustion Science 30 (2005) 43-88.

[306] S.E. Stein, J.A. Walker, M.M. Suryan, A. Fahr, Proceedings of the Combustion Institute 23 (1990) 85-90.

[307] J.A. Miller, C.F. Melius, Combustion and Flame 91 (1992) 21-39.

[308] J.P. Senosiain, J.A. Miller, Journal of Physical Chemistry A 111 (2007) 3740-3747.

[309] N. Hansen, T. Kasper, B. Yang, T.A. Cool, W. Li, P.R. Westmoreland, P. Oßwald, K. Kohse-Höinghaus, Proceedings of the Combustion Institute 33 (2011) 585-592.

[310] J.A. Miller, S.J. Klippenstein, Journal of Physical Chemistry A 107 (2003) 7783-7799.

[311] J.A. Miller, S.J. Klippenstein, Y. Georgievskii, L.B. Harding, W.D. Allen, A.C. Simmonett, Journal of Physical Chemistry A 114 (2010) 4881-4890.

[312] G. Blanquart, P. Pepiot-Desjardins, H. Pitsch, Combustion and Flame 156 (2009) 588-607.

[313] N.M. Marinov, W.J. Pitz, C.K. Westbrook, A.M. Vincitore, M.J. Castaldi, S.M. Senkan, C.F. Melius, Combustion and Flame 114 (1998) 192-213.

[314] C.S. McEnally, L.D. Pfefferle, Combustion and Flame 152 (2008) 469-481.

[315] C.F. Melius, M.E. Colvin, N.M. Marinov, W.J. Pitz, S.M. Senkan, Proceedings of the Combustion Institute 26 (1996) 685-692.

[316] C.S. McEnally, L.D. Pfefferle, Combustion and Flame 129 (2002) 305-323.

[317] J.A. Mulholland, M. Lu, D.H. Kim, Proceedings of the Combustion Institute 28 (2000) 2593-2599.

[318] M.E. Law, P.R. Westmoreland, T.A. Cool, J. Wang, N. Hansen, C.A. Taatjes, T. Kasper, Proceedings of the Combustion Institute 31 (2007) 565-573.

[319] C.S. McEnally, L.D. Pfefferle, Combustion and Flame 136 (2004) 155-167.

[320] M. Frenklach, D.W. Clary, W.C. Gardiner, S.E. Stein, Proceedings of the Combustion Institute 20 (1984) 887-901.

[321] J.D. Bittner, J.B. Howard, Proceedings of the Combustion Institute 18 (1981) 1105-1116.

[322] D.S.N. Parker, R.I. Kaiser, T.P. Troy, M. Ahmed, Angewandte Chemie International Edition 53 (2014) 7740-7744.

[323] N.W. Moriarty, N.J. Brown, M. Frenklach, Journal of Physical Chemistry A 103 (1999) 7127-7135.

[324] K. Siegmann, K. Sattler, Journal of Chemical Physics 112 (2000) 698-709.

[325] V.V. Kislov, N.I. Islamova, A.M. Kolker, S.H. Lin, A.M. Mebel, Journal of Chemical Theory and Computation 1 (2005) 908-924.

[326] A. Raj, M.J. Al Rashidi, S.H. Chung, S.M. Sarathy, Journal of Physical Chemistry A 118 (2014) 2865-2885.

[327] D. Wong, R. Whitesides, C.A. Schuetz, M. Frenklach, Molecular Dynamics Simulations of PAH Dimerization, in: H. Bockhorn, A. D'Anna, A.F. Sarofim, H. Wang (Eds.), Combustion Generated Fine Carbonaceous Particles, KIT Scientific Publishing, Karlsruhe, Germany, 2009.

[328] C.A. Schuetz, M. Frenklach, Proceedings of the Combustion Institute 29 (2002) 2307-2314.

[329] H. Sabbah, L. Biennier, S.J. Klippenstein, I.R. Sims, B.R. Rowe, Journal of Physical Chemistry Letters 1 (2010) 2962-2967.

[330] S.H. Chung, A. Violi, Proceedings of the Combustion Institute 33 (2011) 693-700.

[331] P. Elvati, A. Violi, Proceedings of the Combustion Institute 34 (2013) 1837-1843.

[332] H. Wang, Proceedings of the Combustion Institute 33 (2011) 41-67.

[333] A. D'Anna, Particle Inception and Growth: Experimental Evidences and a Modelling Attempt, in: H. Bockhorn, A. D'Anna, A.F. Sarofim, H. Wang (Eds.), Combustion Generated Fine Carbonaceous Particles, KIT Scientific Publishing, Karlsruhe, Germany, 2009.

[334] M. Frenklach, Proceedings of the Combustion Institute 26 (1996) 2285-2293.

[335] M. Sander, R.I.A. Patterson, A. Braumann, A. Raj, M. Kraft, Proceedings of the Combustion Institute 33 (2011) 675-683.

[336] F. Bisetti, G. Blanquart, M.E. Mueller, H. Pitsch, Combustion and Flame 159 (2012) 317-335.

[337] K.H. Homann, Angewandte Chemie International Edition 37 (1998) 2434-2451.

[338] J.H. Miller, J.D. Herdman, Computational and Experimental Evidence for Polynuclear Aromatic Hydrocarbon Aggregation in Flames, in: H. Bockhorn, A. D'Anna, A.F. Sarofim, H. Wang (Eds.), Combustion Generated Fine Carbonaceous Particles, KIT Scientific Publishing, Karlsruhe, Germany, 2009.

[339] S.E. Stein, A. Fahr, Journal of Physical Chemistry 89 (1985) 3714-3725.

[340] J.B. Howard, J.T. McKinnon, Y. Makarovsky, A.L. Lafleur, M.E. Johnson, Nature 352 (1991) 139-141.

[341] Z.A. Mansurov, Combustion, Explosion, and Shock Waves 41 (2005) 727-744.

[342] H. Richter, W.J. Grieco, J.B. Howard, Combustion and Flame 119 (1999) 1-22.

[343] J.T. McKinnon, W.L. Bell, R.M. Barkley, Combustion and Flame 88 (1992) 102-112.

[344] D.S. Su, J.O. Müller, R.E. Jentoft, D. Rothe, E. Jacob, R. Schlögl, Topics in Catalysis 30/31 (2004) 241-245.

[345] S.R. Turns, An Introduction to Combustion, 2nd ed., Tata McGraw-Hill, New Delhi, India, 2012.

[346] B.S. Haynes, H.G. Wagner, Progress in Energy and Combustion Science 7 (1981) 229-273.

[347] R.L. Vander Wal, SAE Paper No. 2005-01-0964, 2005.

[348] H.P. Boehm, Carbon 32 (1994) 759-769.

[349] J. Song, M. Alam, A.L. Boehman, U. Kim, Combustion and Flame 146 (2006) 589-604.

[350] L. Wang, C. Song, J. Song, G. Lv, H. Pang, W. Zhang, Proceedings of the Combustion Institute 34 (2013) 3099-3106.

[351] J.S. Lighty, V. Romano, A.F. Sarofim, Soot Oxidation, in: H. Bockhorn, A. D'Anna, A.F. Sarofim, H. Wang (Eds.), Combustion Generated Fine Carbonaceous Particles, KIT Scientific Publishing, Karlsruhe, Germany, 2009.

[352] A.W. Kandas, I.G. Senel, Y. Levendis, Carbon 43 (2005) 241-251.

[353] I.A. Khalek, D.B. Kittelson, SAE Paper No. 2000-01-0515, 2000.

[354] D.B. Kittelson, J. Johnson, W. Watts, Q. Wei, M. Drayton, D. Paulsen, N. Bukowiecki, SAE Paper No. 2000-01-2212, 2000.

[355] D.B. Kittelson, W.F. Watts, J.P. Johnson, C. THorne, C. Higham, M. Payne, S. Goodier, C. Warrens, H. Preston, U. Zink, D. Pickles, C. Goersmann, M.V. Twigg, A.P. Walker, Environmental Science & Technology 42 (2008) 9276-9282.

[356] M. Olin, T. Rönkkö, M. Dal Maso, Atmospheric Chemistry and Physics 15 (2015) 5305-5323.

[357] T. Rönkkö, A. Virtanen, K. Vaaraslahti, J. Keskinen, L. Pirjola, M. Lappi, Atmospheric Environment 40 (2006) 2893-2901.

[358] T. Rönkkö, A. Virtanan, J. Kannosto, J. Kekinen, M. Lappi, L. Pirjola, Environmental Science & Technology 41 (2007) 6384-6389.

[359] J. Schneider, N. Hock, S. Weimer, S. Borrmann, U. Kirchner, Environmental Science & Technology 39 (2005) 6153-6161.

[360] M. Inoue, A. Murase, M. Yamamoto, S. Kubo, Applied Surface Science 252 (2006) 7014-7017.

[361] L. Pirjola, M. Karl, T. Rönkkö, F. Arnold, Atmospheric Chemistry and Physics 15 (2015) 10435-10452.

[362] Office of Air Quality Planning and Standards, A Comprehesive Analysis of Biodiesel Impacts on Exhaust Emissions, Report No. EPA-420-P-02-001, United States Environmental Protection Agency, 2002.

[363] J.P. Szybist, A.L. Boehman, D.C. Haworth, H. Koga, Combustion and Flame 149 (2007) 112-128.

[364] B.A. Buchholz, C.J. Mueller, A. Upatnieks, G.C. Martin, W.J. Pitz, C.K. Westbrook, SAE Paper No. 2004-01-1849, 2004.

[365] A. Eveleigh, N. Ladommatos, R. Balachandran, A. Marca, Combustion and Flame 161 (2014) 2966-2974.

[366] L. Coniglio, H. Bennadji, P.A. Glaude, O. Herbinet, F. Billaud, Progress in Energy and Combustion Science 39 (2013) 340-382.

[367] L.K. Huynh, A. Violi, Journal of Organic Chemistry 73 (2008) 94-101.

[368] P.A. Glaude, W.J. Pitz, M.J. Thomson, Proceedings of the Combustion Institute 30 (2005) 1111-1118.

[369] O. Herbinet, W.J. Pitz, C.K. Westbrook, Combustion and Flame 154 (2008) 507-528.

[370] C.J. Hayes, D.R. Burgess, Proceedings of the Combustion Institute 32 (2009) 263-270.

[371] Haller and Pfefferle Lab Group, Yale University, YSI Database [Online]. Available at: http://pfefferlehallerlabs.yale.edu/ysi-database [Accessed Nov 2015].

[372] N. Ladommatos, P. Rubenstein, P. Bennett, Fuel 75 (1996) 114-124.

[373] D.D. Das, C.S. McEnally, L.D. Pfefferle, Combustion and Flame 162 (2015) 1489-1497.

[374] Q. Feng, A. Jalali, A.M. Fincham, Y.L. Wang, T.T. Tsotsis, F.N. Egolfopoulos, Combustion and Flame 159 (2012) 1876-1893.

[375] G. Knothe, C.A. Sharp, T.W. Ryan, Energy & Fuels 20 (2006) 403-408.

[376] L.M. Pickett, D.L. Siebers, C.A. Idicheria, SAE Paper No. 2005-01-3843, 2005.

[377] C. Pauls, G. Grünefeld, S. Vogel, N. Peters, SAE Paper No. 2007-01-0020, 2007.

[378] L.M. Pickett, D.L. Siebers, International Journal of Engine Research 7 (2006) 103-130.

[379] J.E. Dec, SAE Paper No. 970873, 1997.

[380] H.J. Curran, E.M. Fisher, P.A. Glaude, N.M. Marinov, W.J. Pitz, C.K. Westbrook, D.W. Layton, SAE Paper No. 2001-01-0653, 2001.

[381] D. Siebers, B. Higgins, L. Pickett, SAE Paper No. 2002-01-0890, 2002.

[382] C.J. Mueller, SAE Paper No. 2005-01-3705, 2005.

[383] A.S. Cheng, R.W. Dibble, B.A. Buchholz, SAE Paper No. SAE 2002-01-1705, 2002.

[384] G. Chen, W. Yu, J. Fu, J. Mo, Z. Huang, J. Yang, Z. Wang, H. Jin, F. Qi, Combustion and Flame 159 (2012) 2324-2335.

[385] J.E. Dec, P.L. Kelly-Zion, SAE Paper No. 2000-01-0238, 2000.

[386] M. Lapuerta, F. Oliva, J.R. Agudelo, A.L. Boehman, Combustion and Flame 159 (2012) 844-853.

[387] K. Yehliu, R.L. Vander Wal, O. Armas, A.L. Boehman, Combustion and Flame 159 (2012) 3597-3606.

[388] R.L. Vander Wal, A. Strzelec, T.J. Toops, C.S. Daw, C.L. Genzale, Fuel 113 (2013) 522-526.

[389] A. Tsolakis, Energy & Fuels 20 (2006) 1418-1424.

[390] P.Q. Tan, Z.Y. Hu, D.M. Lou, B. Li, SAE Paper No. 2009-01-2726, 2009.

[391] P.Q. Tan, D.M. Lou, Z.Y. Hu, SAE Paper No. 2010-01-0787, 2010.

[392] O. Schröder, J. Bünger, A. Munack, G. Knothe, J. Krahl, Fuel 103 (2013) 414-420.

[393] E.R. Kisin, X.C. Shi, M.J. Keane, A.B. Bugarski, A.A. Shvedova, Journal of Environmental Engineering & Ecological Science 2 (2013).

[394] J. Bünger, J. Krahl, O. Schröder, L. Schmidt, G.A. Westphal, Critical Reviews in Toxicology 42 (2012) 732-750.

[395] R. Stone, Introduction to Internal Combustion Engines, 3rd ed., Macmillan Press Ltd, London, UK, 1999.

[396] D. Carslaw, S. Beevers, E. Westmoreland, M. Williams, J. Tate, T. Murrells, J. Stedman, Y. Li, S. Grice, A. Kent, I. Tsagatakis, Trends in NO_x and NO_2 Emissions and Ambient Measurements in the UK, Department for Environment, Food and Rural Affairs, 2011.

[397] S. Vilčeková, Indoor Nitrogen Oxides, in: F. Nejadkoorki (Eds.), Advanced Air Pollution, InTech, Rijeka, Croatia, 2011.

[398] J.A. Miller, C.T. Bowman, Progress in Energy and Combustion Science 15 (1989) 287-338.

[399] A.R. Ravishankara, J.S. Daniel, R.W. Portmann, Science 326 (2009) 123-125.

[400] P.J. Crutzen, A.R. Mosier, K.A. Smith, W. Winiwarter, Atmospheric Chemistry and Physics 8 (2008) 389-395.

[401] I.A. Khalek, T.L. Bougher, P.M. Merritt, Phase 1 of the Advanced Collaborative Emissions Study, CRC Report No. ACES Phase 1, Coordinating Research Council, 2009.

[402] C.T. Bowman, Proceedings of the Combustion Institute 24 (1992) 859-878.

[403] D. Fowler, C. Flechard, U. Skiba, M. Coyle, J.N. Cape, New Phytologist 139 (1998) 11-23.

[404] A. Tiwary, J. Colls, Air Pollution: Measurement, Modeling and Mitigation, 3rd ed., Routledge, Abingdon, UK, 2010.

[405] J.S. Gaffney, G.E. Streit, W.D. Spall, J.H. Hall, Environmental Science & Technology 21 (1987) 519-524.

[406] M.L. Bell, D.L. Davis, T. Fletcher, Environmental Health Perspectives 112 (2004) 6-8.

[407] K. Katsouyanni, G. Touloumi, C. Spix, J. Schwartz, F. Balducci, S. Medina, G. Rossi, B. Wojtyniak, J. Sunyer, L. Bacharova, J.P. Schouten, A. Ponka, H.R. Anderson, BMJ 314 (1997) 1658-1663.

[408] WHO Working Group, Health Aspects of Air Pollution with Particulate Matter, Ozone and Nitrogen Dioxide, Report No. EUR/03/5042688, World Health Organisation, Geneva, Switzerland, 2003.

[409] M. Lippmann, Journal of the Air Pollution Control Association 39 (1989) 672-695.

[410] M.L. Bell, A. McDermott, S.L. Zeger, J.M. Samet, F. Dominici, Journal of the American Medical Association 19 (2004) 2372-2378.

[411] M. Jerrett, R.T. Burnett, C.A. Pope, K. Ito, G. Thurston, D. Krewski, Y. Shi, E. Calle, M. Thun, The New England Journal of Medicine 360 (2009) 1085-1095.

[412] S.V. Krupa, W.J. Manning, Environmental Pollution 50 (1988) 101-137.

[413] J.S. Gaffney, N.A. Marley, Peroxyacetyl Nitrate (PAN): Histroical Perspective, ANL/ER/CP-102348, in: 81st American Metereological Society Annual Meeting, Albuquerque, NM, USA, 2001.

[414] A.A. Konnov, M.T. Javed, H. Kassman, N. Irfan, NOx Formation, Control and Reduction Techniques, in: M. Lackner, F. Winter, A.K. Agarwal (Eds.), Handbook of Combustion, Wiley-VCH, Weinheim, Germany, 2010.

[415] G.A. Ban-Weiss, J.Y. Chen, B.A. Buchholz, R.W. Dibble, Fuel Processing Technology 88 (2007) 659-667.

[416] A.M. Mellor, J.P. Mello, K.P. Duffy, W.L. Easley, J.C. Faulkner, SAE Paper No. 981450, 1998.

[417] W.L. Easley, A.M. Mellor, S.L. Plee, SAE Paper No. 2000-01-0582, 2000.

[418] J.B. Heywood, Internal Combustion Engine Fundamentals, McGraw-Hill, New York, USA, 1988.

[419] C.T. Bowman, Progress in Energy and Combustion Science 1 (1975) 33-45.

[420] R.F. Sawyer, Proceedings of the Combustion Institute 18 (1981) 1-22.

[421] S. Hill, L. Douglas Smoot, Progress in Energy and Combustion Science 26 (2000) 417-458.

[422] C.P. Fenimore, Proceedings of the Combustion Institute 13 (1971) 373-380.

[423] L.V. Moskaleva, M.C. Lin, Proceedings of the Combustion Institute 28 (2000) 2393-2401.

[424] A. El bakali, L. Pillier, P. Desgroux, B. Lefort, L. Gasnot, J.F. Pauwels, I. da Costa, Fuel 85 (2006) 896-909.

[425] S.V. Naik, N.M. Laurendeau, Energy & Fuels 22 (2008) 250-261.

[426] A.A. Konnov, Combustion and Flame 156 (2009) 2093-2105.

[427] N. Faßheber, J. Dammeier, G. Friedrichs, Physical Chemistry Chemical Physics 16 (2014) 11647-11657.

[428] T. Yoshikawa, R.D. Reitz, SAE Paper No. 2008-01-2413, 2008.

[429] P. Dagaut, P. Glarborg, M.U. Alzueta, Progress in Energy and Combustion Science 34 (2008) 1-46.

[430] S. Garner, R. Sivaramakrishnan, K. Brezinsky, Proceedings of the Combustion Institute 32 (2009) 461-467.

[431] S. Garner, K. Brezinsky, Combustion and Flame 158 (2011) 2289-2301.

[432] R.S. Zhu, S.C. Xu, M.C. Lin, Chemical Physics Letters 488 (2010) 121-125.

[433] B.A. Williams, J.W. Fleming, Proceedings of the Combustion Institute 31 (2007) 1109-1117.

[434] B.A. Williams, J. A. Sutton, J.W. Fleming, Proceedings of the Combustion Institute 32 (2009) 343-350.

[435] J. Tomeczek, B. Gradoń, Combustion and Flame 133 (2003) 311-322.

[436] A.M. Dean, J.W. Bozzelli, Combustion Chemistry of Nitrogen, in: W.C. Gardiner (Eds.), Gas-Phase Combustion Chemistry, Springer-Verlag, New York, USA, 2000.

[437] P.C. Malte, D.T. Pratt, Combustion Science and Technology 9 (1974) 221-231.

[438] J.J. Hernández, J. Pérez-Collado, J. Sanz-Argent, Energy & Fuels 22 (2008) 262-272.

[439] J.W. Bozzelli, A.M. Dean, International Journal of Chemical Kinetics 27 (1995) 1097-1109.

[440] S.J. Klippenstein, L.B. Harding, P. Glarborg, J.A. Miller, Combustion and Flame 158 (2011) 774-789.

[441] R. Miller, G. Davis, G. Lavoie, C. Newman, T. Gardner, SAE Paper No. 980781, 1998.

[442] J.A. Miller, P. Glarborg, International Journal of Chemical Kinetics 31 (1999) 757-765.

[443] M. Lapuerta, J. José-Hernández, O. Armas, SAE Paper No. 2000-01-2939, 2000.

[444] Cornell University Law School Legal Information Institute, 40 CFR 1065.260 – Flame Ionization Detector [Online]. Available at: http://www.law.cornell.edu/cfr/text/40/1065.260 [Accessed Nov 2014].

[445] L. Hill, Horiba UK (personal communication, Nov 2014).

[446] T.L. Ullman, L.R. Smith, J.W. Anthony, W.J. Slodowske, B. Trestrail, A.L. Cook, W.B. Bunn, C.A. Lapin, K.J. Wright, C.R. Clark, SAE Paper No. 2003-01-1381, 2003.

[447] G. Bruneaux, SAE Paper No. 2007-01-0650, 2007.

[448] S. Brandenberger, M. Kohr, K. Grob, N.P. Neukom, Atmospheric Environment 39 (2005) 6985-6994.

[449] K.A. Raihan, F. Takimoto, H. Ogawa, N. Miyamoto, SAE Paper No. 2001-01-1259, 2001.

[450] S. Mendez, J.T. Kashdan, G. Bruneaux, B. Thirouard, F. Vangraefschepe, SAE Paper No. 2009-01-2729, 2001.

[451] B.W. Knox, C.L. Genzale, L.M. Pickett, J.M. Garcia-Oliver, W. Vera-Tudela, SAE Paper No. 2015-01-0797, 2015.

[452] G.K. Lilik, A.L. Boehman, Energy & Fuels 27 (2013) 1586-1600.

[453] F.J. Liotta, D.M. Montalvo, SAE Paper No. 932734, 1993.

[454] Y. Ren, Z. Huang, H. Miao, Y. Di, D. Jiang, K. Zeng, B. Liu, X. Wang, Fuel 87 (2008) 2691-2697.

[455] J. Song, K. Cheenkachorn, J. Wang, J. Perez, A.L. Boehman, P.J. Young, F.J. Waller, Energy & Fuels 16 (2002) 294-301.

[456] C.D. Rakopoulos, D.T. Hountalas, T.C. Zannis, Y.A. Levendis, SAE Paper No. 2004-01-2924, 2004.

[457] K.D. Vertin, J.M. Ohi, D.W. Naegeli, K.H. Childress, G.P. Hagen, C.I. McCarthy, A.S. Cheng, R.W. Dibble, SAE Paper No. 1999-01-1508, 1999.

[458] K.F. Hansen, M.G. Jensen, SAE Paper No. 971689, 1997.

[459] D.Y. Chang, J.H. Van Gerpen, SAE Paper No. 982527, 1998.

[460] P. Boggavarapu, R.V. Ravikrishna, International Journal of Spray and Combustion Dynamics 5 (2013) 85-121.

[461] S. Som, D.E. Longman, Energy & Fuels 25 (2011) 1373-1386.

[462] L. Labecki, Combustion and Emission Characteristics of Biofuels in Diesel Engines, PhD Thesis, Brunel University, UK, 2010.

[463] G. Fontaras, M. Kousoulidou, G. Karavalakis, T. Tzamkiozis, P. Pistikopoulos, L. Ntziachristos, E. Bakeas, S. Stournas, Z. Samaras, Environmental Pollution 158 (2010) 1451-1460.

[464] S.M. Corrêa, E.M. Martins, G. Arbilla, Atmospheric Environment 37 (2003) 23-29.

[465] S.M. Corrêa, G. Arbilla, Atmospheric Environment 42 (2008) 769-775.

[466] F. Staat, P. Gateau, SAE Paper No. 950053, 1995.

[467] C. He, Y. Ge, J. Tan, K. You, X. Han, J. Wang, Q. You, A.N. Shah, Atmospheric Environment 43 (2009) 3657-3661.

[468] G. Fontaras, G. Karavalakis, M. Kousoulidou, L. Ntziachristos, E. Bakeas, S. Stournas, Z. Samaras, Environmental Pollution 158 (2010) 2496-2503.

[469] G. Karavalakis, S. Stournas, E. Bakeas, Science of the Total Environment 407 (2009) 3338-3346.

[470] G. Karavalakis, S. Stournas, E. Bakeas, Atmospheric Environment 43 (2009) 1745-1752.

[471] C.A. Sharp, S.A. Howell, J. Jobe, SAE Paper No. 2000-01-1968, 2000.

[472] J. Raub, Environmental Health Criteria for Carbon Monoxide, World Health Organisation, Geneva, Switzerland, 2003.

[473] J.E. Peterson, R.D. Stewart, Journal of Applied Physiology 39 (1975) 633-638.

[474] N.B. Hampson, N.M. Hauff, American Journal of Emergency Medicine 26 (2008) 665-669.

[475] A.L. Ilano, T.A. Raffin, Chest 97 (1990) 165-169.

[476] A. Velji, M. Lüft, S. Merkel, Mixture Formation, Combustion and Pollutant Emissions in High-Speed Direct Injection Diesel Engines, in: H. Zhao (Eds.), Advanced Direct Injection Combustion Engine Technologies and Development, Volume 2: Diesel Engines, Woodhead Publishing Limited, Cambridge, UK, 2010.

[477] Earth System Research Laboratory, ESRL Global Monitoring Division – Global Greenhouse Gas Reference Network [Online]. Available at: http://www.esrl.noaa.gov/gmd/ccgg/trends/global.html [Accessed Nov 2015].

[478] P.N. Pearson, M.R. Palmer, Nature 406 (2000) 695-699.

[479] R.M. Rotty, C.D. Masters, History of Carbon Dioxide in the Atmosphere, in: J.R. Trabalka (Eds.), Atmospheric Carbon Dioxide and the Global Carbon Cycle, Report No. DOE/ER-0239, United States Department of Energy, Washington, DC, USA, 1985.

[480] D.M. Sigman, E.A. Boyle, Nature 407 (2000) 859-869.

[481] US Department of the Interior: Bureau of Land Management, Appendix C Health Risk Evaluation for Carbon Dioxide (CO2) [Online]. Available at: http://tinyurl.com/pt3arte [Accessed Nov 2015].

[482] W.J. Fisk, U. Satish, M.J. Mendell, T. Hotchi, D. Sullivan, Is CO_2 an Indoor Pollutant? Higher Levels of CO_2 May Diminish Decision Making Performance, Report No. LBNL-6148E, Ernest Orlando Lawrence Berkeley National Laboratory, Berkeley, CA, USA, 2013.

[483] S.S. Myers, A. Zanobetti, I. Kloog, P. Huybers, A.D.B. Leakey, A.J. Bloom, E. Carlisle, L.H. Dietterich, G. Fitzgerald, T. Hasegawa, N.M. Holbrook, R.L. Nelson, M.J. Ottman, V. Raboy, H. Sakai, K.A. Sartor, J. Schwartz, S. Seneweera, M. Tausz, Y. Usui, Nature 510 (2014) 139-142.

[484] J. Xue, T.E. Grift, A.C. Hansen, Renewable and Sustainable Energy Reviews 15 (2011) 1098-1116.

[485] J. Hill, E. Nelson, D. Tilman, S. Polasky, D. Tiffany, Proceedings of the National Academy of Sciences of the United States of America 103 (2006) 11206-11210.

[486] J. Fargione, Science 319 (2008) 1235-1238.

[487] F. Cherubini, A.H. Strømman, Bioresource Technology 102 (2011) 437-451.

[488] D. Pimentel, T.W. Patzek, Natural Resources Research 14 (2005) 65-76.

[489] National Biodiesel Board, Response to David Pimentel Biodiesel Life Cycle Analysis, 2005 [Online]. Available at: http://tinyurl.com/ndnjgha [Accessed Nov 2015].

[490] P.F. Flynn, R.P. Durrett, G.L. Hunter, A.O. zur Loye, O.C. Akinyemi, J.E. Dec, C.K. Westbrook, SAE Paper No. 1999-01-0509, 1999.

[491] G. Bruneaux, International Journal of Engine Research 9 (2008) 249-265.

[492] H. Kosaka, T. Aizawa, T. Kamimoto, International Journal of Engine Research 6 (2005) 21-42.

[493] M.P.B. Musculus, P.C. Miles, L.M. Pickett, Progress in Energy and Combustion Science 39 (2013) 246-283.

[494] R. Demory, Optical Measurements of Nitric Oxide and Hydroxyl Radicals Distributions in Combusting Diesel Sprays, PhD Thesis, University of Brighton, UK, 2007.

[495] M.P.B. Musculus, L.M. Pickett, In-Cylinder Spray, Mixing, Combustion and Pollutant-Formation Processes in Conventional and Low-Temperature-Combustion Diesel Engines, in: H. Zhao (Eds.), Advanced Direct Injection Combustion Engine Technologies and Development, Volume 2: Diesel Engines, Woodhead Publishing Limited, Cambridge, UK, 2010.

[496] L. Li, X. Zhang, Z. Wu, J. Deng, C. Huang, SAE Paper No. 2006-01-3250, 2006.

[497] H. Hiroyasu, M. Arai, SAE Paper No. 900475, 1990.

[498] J.D. Naber, D.L. Siebers, SAE Paper No. 960034, 1996.

[499] S. Som, D.E. Longman, A.I. Ramrez, S.K. Aggarwal, Fuel 89 (2010) 4014-4024.

[500] H.K. Suh, S.H. Park, C.S. Lee, International Journal of Automotive Technology 9 (2008) 217-224.

[501] J. Dernotte, C. Hespel, F. Foucher, S. Houillé, C. Mounaïm-Rousselle, Fuel 96 (2012) 153-160.

[502] R.E. Canaan, J.E. Dec, R.M. Green, D.T. Daly, SAE Paper No. 980510, 1998.

[503] D.L. Siebers, SAE Paper No. 1999-01-0528, 1999.

[504] B.S. Higgins, C.J. Mueller, D.L. Siebers, SAE Paper No. 1999-01-0519, 1999.

[505] C.L. Genzale, L.M. Pickett, S. Kook, SAE Paper No. 2010-01-0610, 2010.

[506] R. Reitz, L. Pickett, M. Trujillo, Fuel Introduction, in: D. Crolla, D.E. Foster, T. Kobayashi, N. Vaughan (Eds.), Encyclopedia of Automotive Engineering (Online), John Wiley & Sons, Hoboken, NJ, USA, 2014.

[507] J.V. Pastor, R. Payri, J. Gimeno, J.G. Nerva, Energy & Fuels 23 (2009) 5899-5915.

[508] B.T. Fisher, G. Knothe, C.J. Mueller, Energy & Fuels 24 (2010) 5163-5180.

[509] J.G. Nerva, C.L. Genzale, S. Kook, J.M. García-Oliver, L.M. Pickett, International Journal of Engine Research 14 (2013) 373-390.

[510] S. Kook, L.M. Pickett, Fuel 93 (2012) 539-548.

[511] J. Abraham, L.M. Pickett, Atomization and Sprays 20 (2010) 241-250.

[512] G. Bruneaux, SAE Paper No. 2005-01-2100, 2005.

[513] G. Bruneaux, SAE Paper No. 2005-01-2097, 2005.

[514] C.A. Idicheria, L.M. Pickett, SAE Paper No. 2006-01-3434, 2006.

[515] C. Espey, J.E. Dec, T.A. Litzinger, D.A. Santavicca, Combustion and Flame 109 (1997) 65-86.

[516] C.A. Idicheria, L.M. Pickett, Proceedings of the Combustion Institute 31 (2007) 2931-2938.

[517] M.P.B. Musculus, SAE Paper No. 2004-01-1401, 2004.

[518] M.P.B. Musculus, P.C. Miles, L.M. Pickett, Progress in Energy and Combustion Science 31 (2014) 94.

[519] J.E. Dec, E.B. Coy, SAE Paper No. 960831, 1996.

[520] R. Venugopal, J. Abraham, SAE Paper No. 2007-01-0134, 2007.

[521] M.P.B. Musculus, SAE Paper No. 2003-01-0074, 2003.

[522] L.M. Pickett, J.J. López, SAE Paper No. 2005-01-0921, 2005.

[523] D. Siebers, B. Higgins, SAE Paper No. 2001-01-0530, 2001.

[524] M.M. Aye, J. Beeckmann, A. Vanegas, N. Peters, H. Pitsch, SAE Paper No. 2007-01-0134, 2007.

[525] C.J. Mueller, A.L. Boehman, G.C. Martin, SAE Paper No. 2009-01-1792, 2009.

[526] O.A. Kuti, J. Zhu, K. Nishida, X. Wang, Z. Huang, Fuel 104 (2013) 838-846.

[527] P. Ye, A.L. Boehman, Energy & Fuels 24 (2010) 4215-4225.

[528] Y. Wu, R. Huang, Y. Liu, M. Leick, C.F.F. Lee, SAE Paper No. 2010-01-0606, 2010.

[529] A.S. Cheng, A. Upatnieks, C.J. Mueller, International Journal of Engine Research 7 (2006) 297-318.

[530] L.M. Pickett, D.L. Siebers, SAE Paper No. 2003-01-3080, 2003.

[531] L.M. Pickett, Understanding Diesel Spray Combustion, in: 8th International Symposium Towards Clean Diesel Engines, Chester, UK, 2011.

[532] R.L. Vander Wal, A. Strzelec, T.J. Toops, C.S. Daw, Forensics of Soot: Nanostructure as a Diagnostic of In-Cylinder Chemistry, in: Spring Technical Meeting of the Central States Section of the Combustion Institute, Dayton, OH, USA, 2012.

[533] J.E. Dec, SAE Paper No. 920115, 1992.

[534] J.E. Dec, R.E. Canaan, SAE Paper No. 980147, 1998.

[535] M.P.B. Musculus, K. Kattke, SAE Paper No. 2009-01-1355, 2009.

[536] S. Kook, L.M. Pickett, M.P.B. Musculus, SAE Paper No. 2009-01-1356, 2009.

[537] S.A. Skeen, J. Manin, L.M. Pickett, Proceedings of the Combustion Institute 35 (2015) 3167-3174.

[538] J. Song, C. Song, Y. Tao, G. Lv, S. Dong, Combustion and Flame 158 (2011) 446-451.

[539] J. Sun, J.A. Caton, T.J. Jacobs, Progress in Energy and Combustion Science 36 (2010) 677-695.

[540] J.P. Szybist, A.L. Boehman, SAE Paper No. 2003-01-1039, 2003.

[541] A. Monyem, J.H. Van Gerpen, M. Canakci, Transactions of the American Society of Agricultural Engineers 44 (2001) 35-42.

[542] T. Jeyaseelan, A. Krishnasamy, P.S. Mehta, Proceedings of the Institution of Mechanical Engineers, Part D: Journal of Automobile Engineering 228 (2014) 1274-1284.

[543] D.M. Peirce, N.S.I. Alozie, D.W. Hatherill, L.C. Ganippa, Energy & Fuels 27 (2013) 3838-3852.

[544] H. Yun, M. Sellnau, N. Milovanovic, S. Zuelch, SAE Paper No. 2008-01-0639, 2008.

[545] M.E. Tat, Investigation of Oxides of Nitrogen Emissions from Biodiesel-Fueled Engines, PhD Thesis, Iowa State University, USA, 2003.

[546] J.A. Bittle, B.M. Knight, T.J. Jacobs, SAE Paper No. 2009-01-2782, 2009.

[547] T. Fang, Y.C. Lin, T.M. Foong, C.F. Lee, Fuel 88 (2009) 2154-2162.

[548] H. Nanjundaswamy, H.J. Laumen, Diesel Fuel Injection Systems, in: D. Crolla, D.E. Foster, T. Kobayashi, N. Vaughan (Eds.), Encyclopedia of Automotive Engineering (Online), John Wiley & Sons, Hoboken, NJ, USA, 2014.

[549] F.J. Salvador, J. Gimeno, J. De la Morena, M. Carreres, Energy Conversion and Management 54 (2012) 122-132.

[550] A. Senatore, M. Cardone, V. Rocco, M.V. Prati, SAE Paper No. 2000-01-0691, 2000.

[551] B.M. Knight, J.A. Bittle, T.J. Jacobs, International Journal of Engine Research 12 (2011) 336-352.

[552] W.A. Eckerle, E.J. Lyford-Pike, D.W. Stanton, L.A. LaPointe, S.D. Whitacre, J.C. Wall, SAE Paper No. 2008-01-0078, 2008.

[553] B.M. Knight, J.A. Bittle, T.J. Jacobs, SAE Paper No. 2010-01-0565, 2010.

[554] R. Lee, J. Pedley, C. Hobbs, SAE Paper No. 982649, 1998.

[555] K. Verbiezen, A.J. Donkerbroek, R.J.H. Klein-Douwel, A.P. van Vliet, P.J.M. Frijters, X.L.J. Seykens, R.S.G. Baert, W.L. Meerts, N.J. Dam, J.J. ter Meulen, Combustion and Flame 151 (2007) 333-346.

[556] K. Verbiezen, R.J.H. Klein-Douwel, A.P. van Vliet, A.J. Donkerbroek, W.L. Meerts, N.J. Dam, J.J. ter Meulen, Proceedings of the Combustion Institute 31 (2007) 765-773.

[557] C.E. Dumitrescu, C. Polonowski, B.T. Fisher, A.S. Cheng, G.K. Lilik, C.J. Mueller, SAE Paper No. 2014-01-1260, 2014.

[558] P.A. Glaude, R. Fournet, R. Bounaceur, M. Molière, Fuel Processing Technology 91 (2010) 229-235.

[559] S.W. Park, S. Kim, C.S. Lee, Energy & Fuels 20 (2006) 1709-1715.

[560] C.S. Lee, S.W. Park, S.I. Kwon, Energy & Fuels 19 (2005) 2201-2208.

[561] X. Wang, Z. Huang, O.A. Kuti, W. Zhang, K. Nishida, International Journal of Heat and Fluid Flow 31 (2010) 659-666.

[562] W. Yuan, A.C. Hansen, Q. Zhang, International Journal of Vehicle Design 45 (2007) 12-32.

[563] O.A. Kuti, K. Nishida, J. Zhu, Energy 57 (2013) 434-442.

[564] C.A. Sharp, T.W. Ryan, G. Knothe, SAE Paper No. 2005-01-3671, 2005.

[565] R.L. McCormick, M.S. Graboski, T.L. Alleman, A.M. Herring, Environmental Science & Technology 35 (2001) 1742-1747.

[566] S. Sato, Y. Sugimoto, K. Sakanishi, I. Saito, S. Yui, Fuel 83 (2004) 1915-1927.

[567] Q. Feng, Y.L. Wang, T.T. Tsotsis, F.N. Egolfopoulos, Industrial & Engineering Chemistry Research 51 (2012) 9719-9732.

[568] A. Schönborn, N. Ladommatos, J. Williams, R. Allan, J. Rogerson, Combustion and Flame 156 (2009) 1396-1412.

[569] G. Adi, C. Hall, D. Snyder, M. Bunce, C. Satkoski, S. Kumar, P. Garimella, D. Stanton, G. Shaver, Energy & Fuels 23 (2009) 5821-5829.

[570] C.F. Taylor, The Internal-Combustion Engine in Theory and Practice, 2nd ed., The M.I.T. Press, Cambridge, MA, USA, 1985.

[571] M.F. Modest, Radiative Heat Transfer, 3rd ed., Academic Press (Elsevier), Oxford, UK, 2013.

[572] G. Borman, K. Nishiwaki, Progress in Energy and Combustion Science 13 (1987) 1-46.

[573] J. Abraham, V. Magi, SAE Paper No. 970888, 1997.

[574] F.J. Struwe, D.E. Foster, SAE Paper No. 2003-01-0072, 2003.

[575] C.L. Tien, S.C. Lee, Progress in Energy and Combustion Science 8 (1982) 41-59.

[576] P. Furmanski, J. Banaszek, T.S. Wisniewski, SAE Paper No. 980504, 1998.

[577] M.P.B. Musculus, SAE Paper No. 2005-01-0925, 2005.

[578] R. Viskanta, M.P. Mengüç, Progress in Energy and Combustion Science 13 (1987) 97-160.

[579] B. Menkiel, A. Donkerbroek, R. Uitz, R. Cracknell, L. Ganippa, Fuel 118 (2014) 406-415.

[580] V.N. Singh, R.N. Parthasarathy, S.R. Gollahalli, Journal of Petroleum Science Research 2 (2013) 97-103.

[581] H. Song, T.J. Jacobs, The Influence of Soot Radiation on NO Emission in Conventional Diesel and Biodiesel Combustions, in: Spring Technical Meeting of the Central States Section of the Combustion Institute, Dayton, OH, USA, 2012.

[582] H. Song, T.J. Jacobs, Fuel 128 (2014) 281-287.

[583] D.H. Cotton, N.J. Friswell, D.R. Jenkins, Combustion and Flame 17 (1971) 87-98.

[584] J.B. Howard, W.J. Kausch, Progress in Energy and Combustion Science 6 (1980) 263-276.

[585] P.A. Bonczyk, Fuel 70 (1991) 1403-1411.

[586] J.B.A. Mitchell, D.J.M. Miller, M. Sharpe, The Use of Additives in the Control and Elucidation of Soot Formation, in: W.R. Seeker, C.P. Koshland (Eds.), Incineration of Hazardous Waste, Gordon and Breach Science Publishers S.A., Montreux, Switzerland, 1992.

[587] R.L. McCormick, J.R. Alvarez, M.S. Graboski, NO_x Solutions for Biodiesel, Report No. NREL/SR-510-31465, National Renewable Energy Laboratory, 2003.

[588] H. Guo, G.J. Smallwood, Combustion and Flame 149 (2007) 225-233.

[589] Y. Ren, X. Li, SAE Paper No. 2011-01-1385, 2011.

[590] H.A. Dhahad, An Investigation on the Combustion and Emissions Characteristics of HSDI Diesel Engine Fueled with Diesel and Biodiesel, PhD Thesis, University of Technology, Baghdad, Iraq, 2014.

[591] L. McWilliam, Combined Hydrogen Diesel Combustion: An Experimental Investigation into the Effects of Hydrogen Addition on the Exhaust Gas Emissions, Particulate Matter Size Distribution and Chemical Composition, PhD Thesis, Brunel University, UK, 2008.

[592] Ford Power Products, ZSD 420 Range, Ford Land Europe, South Ockendon, UK, 2003.

[593] A.J. Martyr, M.A. Plint, Engine Testing, 3rd ed., Butterworth-Heinemann, Oxford, UK, 2007.

[594] J.S. Killedar, Dynamometer: Theory and Application to Engine Testing, Xlibris Corporation, Bloomington, IN, USA, 2012.

[595] E.H. Higham, J.M. Paros, Measurement of Pressure, in: W. Boyes (Eds.), Instrumentation Reference Book, Butterworth-Heinemann, Burlington, MA, USA, 2010.

[596] C. Cavalloni, R. Sommer, Piezostar Crystals: A New Dimension in Sensor Technology, Kistler Instrumente AG, Winterthur, Switzerland, 2003.

[597] Kistler, Engine Combustion Analysis, Kistler Instrumente AG, Winterthur, Switzerland, 2010.

[598] Lenord+Bauer, GEL 244 Incremental Toothed-Wheel Encoder with Sine or Square Wave Output Signal: Operating Instructions, Lenord, Bauer & Co. GmbH, Oberhausen, Germany, 2003.

[599] U. Asad, R. Kumar, X. Han, M. Zheng, Measurement 44 (2011) 1261-1278.

[600] Encoder Technology, Model ET758 – 58mm Euro-Standard, Encoder Technology, East Preston, UK, 2007.

[601] M. Morishita, T. Kushiyama, SAE Paper No. 980625, 1998.

[602] M.J. Staś, SAE Paper No. 2000-01-0561, 2000.

[603] M. Tazerout, O. Le Corre, P. Stouffs, SAE Paper No. 1999-01-3509, 2000.

[604] Y. Nilsson, L. Eriksson, SAE Paper No. 2004-01-1458, 2004.

[605] E. Pipitone, A. Beccari, S. Beccari, SAE Paper No. 2008-36-0059, 2008.

[606] E. Pipitone, A. Beccari, S. Beccari, SAE Paper No. 2007-24-0052, 2007.

[607] M.J. Staś, SAE Paper No. 960610, 1996.

[608] Kistler, TDC Sensor System Type 2629C, Kistler Instrumente AG, Winterthur, Switzerland, 2010.

[609] C.D. Bannister, C.J. Chuck, M. Bounds, J.G. Hawley, Proceedings of the Institution of Mechanical Engineers, Part D: Journal of Automobile Engineering 225 (2011) 99-114.

[610] Horiba, Horiba MEXA-7000 Instruction Manual, Horiba Ltd., Kyoto, Japan, 2003.

[611] H. Ohashi, J. Saito, Motor Exhaust Gas Analyzer MEXA-7000 Series: 1. Product Concept, Horiba Readout (R011-04-019-E), 1995.

[612] K. Takeda, H. Koike, Motor Exhaust Gas Analyzer MEXA-7000 Series: 2. Downsizing and Modular Configuration of Analyzers, Horiba Readout (R011-05-025-E), 1995.

[613] H. Zhao, N. Ladommatos, Engine Combustion Instrumentation and Diagnostics, Society of Automotive Engineers, Warrendale, PA, USA, 2001.

[614] G.L. Miessler, P.J. Fischer, D.A. Tarr, Inorganic Chemistry, 5th ed., Pearson, Upper Saddle River, NJ, USA, 2013.

[615] C.K. Laird, I. Verhappen, Chemical Analysis: Gas Analysis, in: W. Boyes (Eds.), Instrumentation Reference Book, 4th ed., Elsevier Inc., Burlington, MA, USA, 2010.

[616] AVL, Smoke Value Measurement with the Filter-Paper-Method: Application Notes, AVL List GmbH, Graz, Austria, 2005.

[617] B. Gieschaskiel, M. Maricq, L. Ntziachristos, C. Dardiotis, X. Wang, H. Axmann, A. Bergmann, W. Schindler, Journal of Aerosol Sience 67 (2014) 48-86.

[618] W.F. Northrop, S.V. Bohac, J.Y. Chin, D.N. Assanis, Journal of Engineering for Gas Turbines and Power 133 (2011) 102804-1-102804-6.

[619] Testo, Flue Gas Analyzer for Industry, Testo AG, Lenzkirch, Germany, 2013.

[620] T. Kelly, Y.L. Chou, S.J. Abbgy, P.I. Feder, J.J. Reuther, K. Riggs, Environmental Technology Verification Report: Testo Model 350 Portable Emissions Analyzer, Battelle, Columbus, OH, USA, 1999.

[621] M.F.J. Brunt, H. Rai, A.L. Emtage, SAE Paper No. 981052, 1998.

[622] M.F.J. Brunt, K.C. Platts, SAE Paper No. 1999-01-0187, 1999.

[623] G. Abbaszadehmosayebi, L. Ganippa, Applied Energy 122 (2014) 143-150.

[624] B.T. Tomkins, H. Song, J.A. Bittle, T.J. Jacbos, Applied Energy 98 (2012) 209-218.

[625] Weather Underground, Weather History & Data Archive, The Weather Channel LLC [Online]. Available at: http://www.wunderground.com/history/ [Accessed Mar 2014].

[626] G.E. Andrews, S.M. Abdelhalim, H. Li, SAE Paper No. 1999-01-1135, 1999.

[627] J. Patterson, M.G. Hassan, A. Clarke, G. Shama, K. Hellgardt, R. Chen, SAE Paper No. 2006-01-0234, 2006.

[628] R.L. McCormick, Effects of Biodiesel on NOx Emissions, NREL/PR-540-38296, in: California Air Resources Board Biodiesel Workgroup, Sacramento, CA, USA, 2005.

[629] S.K. Hoekman, A. Broch, C. Robbins, E. Ceniceros, Investigation of Biodiesel Chemistry, Carbon Footprint and Regional Fuel Quality, CRC Report No. AVFL-17a, Coordinating Research Council, 2011.

[630] E.G. Giakoumis, C.D. Rakopoulos, A.M. Dimaratos, D.C. Rakopoulos, Progress in Energy and Combustion Science 38 (2012) 691-715.

[631] M.P. Dorado, E. Ballesteros, J.M. Arnal, J. Gomez, F.J. Lopez, Fuel 82 (2003) 1311-1315.

[632] O. Armas, A. Gomez, M.D. Cardenas, Energy & Fuels 23 (2009) 6168-6180.

[633] E. Rosseel, R. Sierens, SAE Paper No. 961123, 1996.

[634] E.F. Obert, Internal Combustion Engines and Air Pollution, Harper and Row Publishers, New York, USA, 1973.

[635] O. Kuti, K. Nishida, M. Sarathy, J. Zhu, SAE Paper No. 2013-01-2554, 2013.

[636] D.A. Rothamer, L. Murphy, Proceedings of the Combustion Institute 34 (2013) 3021-3029.

[637] L. Hamilton, D. Luning Prak, J. Cowart, Journal of Engineering for Gas Turbines and Power 136 (2014) 071505-1-071505-7.

[638] S.B. Han, P.C. Hinze, Y.J. Kwon, S.S. Mun, SAE Paper No. 971658, 1997.

[639] S. Hemmings, Supporting the Regeneration of a Diesel Particulate Filter with the Addition of Hydrogen and Hydrogen/Carbon Monoxide Mixtures: Diesel Engine Aftertreatment System, PhD Thesis, Brunel University, UK, 2012.

[640] F. Christodoulou, Hydrogen, Nitrogen and Syngas Enriched Diesel Combustion, PhD Thesis, Brunel University, UK, 2014.

[641] F. Christodoulou, A. Megaritis, International Journal of Hydrogen Energy 38 (2013) 10126-10140.

[642] F. Christodoulou, A. Megaritis, International Journal of Hydrogen Energy 39 (2014) 2692-2702.

[643] G. Abbaszadehmosayebi, Diesel Engine Heat Release Analysis by using Newly Defined Dimensionless Parameters, PhD Thesis, Brunel University, UK, 2014.

[644] H.A. Dhahad, M.A. Abdulhadi, E.M. Alfayyah, T. Megaritis, International Journal of Scientific & Engineering Research 5 (2014) 646-653.

[645] H.A. Dhahad, M.A. Abdulhadi, E.M. Alfayyah, T. Megaritis, Engineering & Technology Journal 32 (2014) 2216-2234.

[646] B.E. Hallgreen, J.B. Heywood, SAE Paper No. 2001-01-0648, 2001.

[647] A. Schönborn, N. Ladommatos, R. Allan, J. Williams, J. Rogerson, SAE Paper No. 2008-01-1578, 2008.

[648] P. Hellier, N. Ladommatos, R. Allan, M. Payne, J. Rogerson, SAE Paper No. 2011-01-1922, 2011.

[649] Work This Way, Oil Works [Online]. Available at: http://tinyurl.com/h6a7m7x [Accessed Aug 2015].

[650] UK Renewable Fuels Ltd., ReFuel Energy CHP Biofuel [Online]. Available at: http://www.refuelenergy.co.uk/index.html [Accessed Aug 2015].

[651] H.M. McNair, J.M. Miller, Basic Gas Chromatography, 2nd ed., John Wiley & Sons, Hoboken, NJ, USA, 2009.

[652] Agilent Technologies, Agilent 6890N Netwrok Gas Chromatograph: Data Sheet, Publication No. 5989-3290EN, Agilent Technologies, Inc., Santa Clara, CA, USA, 2007.

[653] Agilent Technologies, A Full Family of Polar PEG Columns from Agilent: Selection Guide, Publication No. 5988-8994EN, Agilent Technologies, Inc., Santa Clara, CA, USA, 2003.

[654] British Standards Institute, Fat and Oil Derivatives – Fatty Acid Methyl Esters (FAME) – Determination of Ester and Linoleic Acid Methyl Ester Contents, BS EN 14103:2011.

[655] L.F. Ramírez-Verduzco, J.E. Rodríguez-Rodríguez, A. del Rayo Jaramillo-Jacob, Fuel 91 (2012) 102-111.

[656] M. Lapuerta, J.M. Herreros, L.L. Lyons, R. García-Contreras, Y. Briceño, Fuel 87 (2008) 3161-3169.

[657] M.J. Murphy, J.D. Taylor, R.L. McCormick, Compendium of Experimental Cetane Number Data, Report No. NREL/SR-540-36805, National Renewable Energy Laboratory, 2004.

[658] W.E. Klopfenstein, Journal of the American Oil Chemists Society 62 (1985) 1029-1031.

[659] Y. Stein, R.A. Yetter, F.L. Dryer, A. Aradi, SAE Paper No. 1999-01-1504, 1999.

[660] H.O. Pritchard, Combustion and Flame 75 (1989) 415-416.

[661] H. Bornemann, F. Scheidt, W. Sander, International Journal of Chemical Kinetics 34 (2002) 34-38.

[662] A.M. Ickes, S.V. Bohac, D.N. Assanis, Energy & Fuels 23 (2009) 4943-4948.

[663] P.Q.E. Clothier, H.O. Pritchard, M.A. Poirier, Combustion and Flame 95 (1995) 427-429.

[664] B. Higgins, D. Siebers, C. Mueller, Effects of 2-Ethylhexyl Nitrate on Diesel-Spray Processes, Report No. SAND98-8243, Sandia National Laboratories, Livermore, CA, USA, 1998.

[665] F.J. Liotta, SAE Paper No. 932767, 1993.

[666] United Nations Environment Programme, Propylene Glycol Ethers, SIDS Initial Assessment Report for SIAM 17, Italy, 2003.

[667] D.W. Naegeli, S. Moulton, E.C. Owens, E.A. Frame, Oxygenates for Advanced Petroleum-Based Diesel Fuels, Report No. TFLRF 357, US Army TARDEC Fuels and Lubricants Research Facility, Southwest Research Institute, San Antonio, TX, USA, 2001.

[668] C.J. Mueller, L.M. Pickett, D.L. Siebers, W.J. Pitz, C.K. Westbrook, G.C. Martin, SAE Paper No. 2003-01-1791, 2003.

[669] R. Stevens, C. English, Rapidly Analyze a Wide Range of Glycol Ethers by GC-MS Using the New Rxi-1301Sil MS Column, Restek Corporation, Bellefonte, PA, USA, 2014.

[670] Sandia National Laboratories, Engine Combustion Network: 2.5 Fuels [Online]. Available at: http://www.sandia.gov/ecn/cvdata/sandiaCV/fuels.php [Accessed Aug 2014].

[671] The Dow Chemical Company, Product Information: DOW P-Series Glycol Ethers, Midland, MI, USA, 2002.

[672] J.I. Ramos, Internal Combustion Engine Modeling, Hemisphere Publishing Corporation, New York, USA, 1989.

[673] P.R. Hellier, The Molecular Structure of Future Fuels, PhD Thesis, University College London, UK, 2013.

[674] C. Ji, J. Dec, J. Dernotte, W. Cannella, SAE Paper No. 2014-01-1282, 2014.

[675] T. Katrašnik, F. Trenc, S.R. Oprešnik, Transactions of the American Society of Mechanical Engineers 128 (2006) 928-933.

[676] J. Van Gerpen, Cetane Number Testing of Biodiesel, in: Proceedings of the Third Liquid Fuel Conference, Nashville, TN, USA, 1996.

[677] U. Rashid, F. Anwar, B.R. Moser, G. Knothe, Bioresource Technology 99 (2008) 8175-8179.

[678] M.G. Kulkarni, A.K. Dalai, Industrial & Engineering Chemistry Research 45 (2006) 2901-2913.

[679] R.O. Dunn, B.R. Moser, Cold Weather Properties and Performance of Biodiesel, in: G. Knothe, J. Krahl, J. Van Gerpen, The Biodiesel Handbook, 2nd ed., AOCS Press, Urbana, IL, USA, 2010.

[680] J.F. Wiedenhoefer, R.D. Reitz, Numerical Heat Transfer Part A 44 (2003) 665-682.

[681] A. Schönborn, N. Ladommatos, J. Williams, R. Allan, J. Rogerson, SAE Paper No. 2007-24-0125, 2007.

[682] P. Pepiot-Desjardins, H. Pitsch, R. Malhotra, S.R. Kirby, A.L. Boehman, Combustion and Flame 154 (2008) 191-205.

[683] D.T. Hountalas, D.A. Kouremenos, K.B. Binder, V. Schwarz, G.C. Mavropoulos, SAE Paper No. 2003-01-0340, 2003.

[684] S.S. Bhusnoor, M.K. Gajendra Babu, J.P. Subrahmanyam, SAE Paper No. 2007-01-0613, 2007.

[685] S. Han, C. Bae, SAE Paper No. 2012-01-1721, 2012.

[686] L.M. Pickett, D.L. Siebers, Combustion and Flame 138 (2004) 114-135.

[687] S. Song, Emission Control Systems—Oxides of Nitrogen, in: D. Crolla, D.E. Foster, T. Kobayashi, N. Vaughan (Eds.), Encyclopedia of Automotive Engineering (Online), John Wiley & Sons, Hoboken, NJ, USA, 2014.

[688] D.A. Pierpoint, R.D. Reitz, SAE Paper No. 950604, 1995.

[689] Z. Xiao, N. Ladommatos, H. Zhao, Proceedings of the Institution of Mechanical Engineers, Part D: Journal of Automobile Engineering 214 (2000) 307-332.

[690] R.O. Dunn, Biofuels, Bioproducts & Biorefining 2 (2008) 304-318.

[691] R.O. Dunn, Fuel Processing Technology 86 (2005) 1071-1085.

[692] M. Mittelbach, S. Schober, Journal of the American Oil Chemists Society 80 (2003) 817-823.

[693] H. Tang, A. Wang, S.O. Salley, K.Y.S. Ng, Journal of the American Oil Chemists Society 85 (2008) 373-382.

[694] M.A. Hess, M.J. Haas, T.A. Foglia, W.N. Marmer, Energy & Fuels 19 (2005) 1749-1754.

[695] G.J. Xu, Z. Wang, G.P. Mao, X.Z. Wang, Transactions of the Chinese Society for Agricultural Machinery 42 (2011) 8-11.

[696] K. Varatharajan, M. Cheralathan, R. Velraj, Fuel 90 (2012) 2721-2725.

[697] K. Varatharajan, Effect of Antioxidant Addition on NOx Emissions from a Jatropha Biodiesel Fuelled DI Diesel Engine, PhD Thesis, SRM University, India, 2012.

[698] K. Varatharajan, M. Cheralathan, Fuel Processing Technology 106 (2013) 526-532.

[699] G. Balaji, M. Cheralathan, International Journal of Ambient Energy 35 (2014) 13-19.

[700] I.M. Rizwanul Fattah, H.H. Masjuki, M.A. Kalam, M.A. Wakil, H.K. Rashedul, M.J. Abedin, Industrial Crops and Products 57 (2014) 132-140.

[701] I.M. Rizwanul Fattah, H.H. Masjuki, M.A. Kalam, M. Mofijur, M.J. Abedin, Energy Conversion and Management 79 (2014) 265-272.

[702] E. Ileri, G. Koçar, Energy Conversion and Management 76 (2013) 145-154.

[703] K. Velmurugan, A.P. Sathiyagnanam, Alexandria Engineering Journal (2015) http://dx.doi.org/10.1016/j.aej.2015.10.004.

[704] S.M. Palash, M.A. Kalam, H.H. Masjuki, B.M. Masum, Advanced Materials Research 774-776 (2013) 784-790.

[705] S.M. Palash, M.A. Kalam, H.H. Masjuki, M.I. Arbab, B.M. Masum, A. Sanjid, Energy Conversion and Management 77 (2014) 577-585.

[706] A. Prabu, R.B. Anand, Frontiers in Energy 9 (2015) 238-245.

[707] M.A. Kalam, H.H. Masjuki, Biomass and Bioenergy 32 (2008) 1116-1122.

[708] M. Mofijur, H.H. Masjuki, M.A. Kalam, M. Shahabuddin, Energy Education Science and Technology Part A: Energy Science and Research 30 (2012) 1-12.

[709] T.T. Kivevele, L. Kristóf, A. Bereczky, M.M. Mbarawa, Fuel 90 (2011) 2782-2789.

[710] S. Jain, M.P. Sharma, Fuel 106 (2013) 152-156.

[711] K. Ryu, Journal of Mechanical Science and Technology 23 (2009) 3105-3113.

[712] K. Ryu, Bioresource Technology 101 (2010) S78-S82.

[713] S. Gan, H.K. Ng, Energy Conversion and Management 51 (2010) 1536-1546.

[714] P. Glarborg, Proceedings of the Combustion Institute 31 (2007) 77-98.

[715] G.F. Pedulli, M. Lucarini, P. Pedrielli, Bond Dissociation Energies of Phenolic and Amine Antioxidants, in: F. Minisci (Eds.), Free Radicals in Biology and Environment, Springer Science+Business Media, Dordrecht, The Netherlands, 1997.

[716] Q. Zhu, X.M. Zhang, A.J. Fry, Polymer Degradation and Stability 57 (1997) 43-50.

[717] F.G. Bordwell, X.M. Zhang, Journal of Physical Organic Chemistry 8 (1995) 529-535.

[718] F.G. Bordwell, J.P. Cheng, Journal of the American Chemical Society 113 (1991) 1736-1743.

[719] K.U. Ingold, J.S. Wright, Journal of Chemical Education 77 (2000) 1062-1064.

[720] K. Brezinsky, Progress in Energy and Combustion Science 12 (1986) 1-24.

[721] K. Brezinsky, G.T. Linteris, T.A. Litzinger, I. Glassman, Proceedings of the Combustion Institute 21 (1986) 833-840.

[722] M. Nowakowska, O. Herbinet, A. Dufour, P.A. Glaude, Combustion and Flame 161 (2014) 1474-1488.

[723] S.C. Kong, Y. Sun, R.D. Reitz, Journal of Engineering for Gas Turbines and Power 129 (2007) 245-251.

[724] J.F. Corbett, Journal of the Society of Cosmetic Chemists 35 (1984) 297-310.

[725] J.F. Corbett, Dyes and Pigments 41 (1999) 127-136.

[726] M. Lawrence, Development of the Gas Phase Induced Phosphorescence Technique and Soot Measurements in Flames Using Laser Induced Incandescence, PhD Thesis, Brunel University, UK, 2014.

[727] A.D. Eisner, D.E. Rosner, Combustion and Flame 61 (1985) 153-166.

[728] C.S. McEnally, Ü.O. Köylü, L.D. Pfefferle, D.E. Rosner, Combustion and Flame 109 (1997) 701-720.

[729] M.A. Pereira, Soot Emissions in Biodiesels, Undergraduate Summer Project (Unpublished), Brunel University, UK, 2014.

[730] Morgan Thermal Ceramics, Superpak 607 MAX Material Safety Data Sheet, Thermal Ceramics Limited, Bromborough, UK, 2001.

[731] UK ECIG STORE, House of Hybrids Ceramic Wick Replacement for the Z-Atty-Pro [Online]. Available at: http://www.ukecigstore.com/ceramic-wick-replacement-for-the-z-atty-pro-by-house-of-hybrids.html [Accessed Sep 2014].

[732] E.W. Washburn, The Physical Review 17 (1921) 273-283.

[733] H. Zhao, N. Ladommatos, Progress in Energy and Combustion Science 24 (1998) 221-225.

[734] R.L. Vander Wal, T.M. Ticich, A.B. Stephens, Combustion and Flame 116 (1999) 291-296.

[735] C. Schulz, B.F. Kock, M. Hoffman, H. Michelsen, S. Will, B. Bougie, R. Suntz, G. Smallwood, Applied Physics B 83 (2006) 333-354.

[736] R.J. Santoro, C.R. Shaddix, Laser-Induced Incandescence, in: K. Kohse-Höinghaus, J.B. Jeffries (Eds.), Applied Combustion Diagnostics, Taylor & Francis, New York, USA, 2002.

[737] P. Stannett, Design and Fabrication of a Rapid Insertion Soot Sampler, Undergraduate Dissertation (Unpublished), Brunel University, UK, 2008.

[738] Eurotherm Controls, 2132 and 2116 PID Temperature Controllers Datasheet No. HA026270, Eurotherm Controls, Durrington, UK, 1998.

[739] J.D. Walker, B.J. Stocks, Fire Technology 4 (1968) 59-62.

[740] I. Glassman, P. Yaccarino, Combustion Science and Technology 24 (1980) 107-114.

[741] D.B. Williams, C.B. Carter, Transmission Electron Microscopy, 2nd ed., Spring Science+Business Media, New York, USA, 2009.

[742] JEOL GmbH, TEMs with 200 kV Acceleration Voltage [Online]. Available at: http://tinyurl.com/mc3xj6s [Accessed Oct 2014].

[743] Australian Microscopy & Microanalysis Research Facility, The Electron Wavelength [Online]. Available at: http://tinyurl.com/megjkcj [Accessed Oct 2014].

[744] A.B. Palotás, L.C. Rainey, C.J. Feldermann, A.F. Sarofim, J.B. Vander Sande, Microscopy Research and Technique 33 (1996) 266-278.

[745] C.R. Shaddix, T.C. Williams, Soot Structure and Dimensionless Extinction Coefficient in Diffusion Flames: Implications and Index of Refraction, in: H. Bockhorn, A. D'Anna, A.F. Sarofim, H. Wang (Eds.), Combustion Generated Fine Carbonaceous Particles, KIT Scientific Publishing, Karlsruhe, Germany, 2009.

[746] A.B. Fialkov, A.N. Hayhurst, S.G. Taylor, S.B. Newcomb, Combustion Science and Technology 185 (2013) 1762-1776.

[747] H.S. Jung, A. Miller, K. Park, D.B. Kittelson, Journal of the Air & Waste Management Association 63 (2013) 1199-1204.

[748] W. Merchan-Merchan, A. Saveliev, L.A. Kennedy, A. Fridman, Chemical Physics Letters 354 (2002) 20-24.

[749] L.E. Murr, J.J. Bang, E.V. Esquivel, P.A. Guerrero, D.A. Lopez, Journal of Nanoparticle Research 6 (2004) 241-251.

[750] L.E. Murr, K.F. Soto, Materials Characterization 55 (2005) 50-65.

[751] P.J.F. Harris, Carbon 39 (2001) 909-913.

[752] R.F. Klie, D. Ciuparu, L. Pfefferle, Y. Zhu, Carbon 42 (2004) 1953-1957.

[753] M. Abbod, R. Beleca, D.M. Peirce, L. Ganippa, N. Manivannan, W. Balachandran, Power Controlled Microwave Reactor for the Removal of NOx and SOx from the Exhaust of Marine Diesel Engine, in: Transport Research Arena, Paris, France, 2014.

[754] R. Beleca, N. Manivannan, L. Ganippa, M. Abbod, D.M. Peirce, W. Balachandran, Microwave Induced Plasmas for Marine Diesel Engine Emission Control, in: Proceedings of the Electrostatic Joint Conference, Cambridge, ON, Canada, 2012.

[755] N. Ladommatos, S.M. Abdelhalim, H. Zhao, Z. Hu, SAE Paper No. 961165, 1996.

[756] N. Ladommatos, S.M. Abdelhalim, H. Zhao, Z. Hu, SAE Paper No. 961167, 1996.

[757] N. Ladommatos, S.M. Abdelhalim, H. Zhao, Z. Hu, SAE Paper No. 971659, 1997.

[758] N. Ladommatos, S.M. Abdelhalim, H. Zhao, Z. Hu, SAE Paper No. 971660, 1997.

[759] C. Song, X. Ma, Applied Catalysis B: Environmental 41 (2003) 207-238.

[760] N.B. Ribeiro, A.C. Pinto, C.M. Quintella, G.O. da Rocha, L.S.G. Teixeira, L.L.N. Guarieiro, M. do Carmo Rangel, M.C.C. Veloso, M.J.C. Rezende, R.S. da Cruz, A.M. de Oliveira, E.A. Torres, J.B. Andrade, Energy & Fuels 21 (2007) 2433-2445.

[761] N. Ladommatos, M. Parsi, A. Knowles, Fuel 75 (1996) 8-14.

[762] D.Y.C. Leung, Y. Luo, T.L. Chan, Energy & Fuels 20 (2006) 1015-1023.

[763] R.L. Muncrief, C.W. Rooks, M. Cruz, M.P. Harold, Energy & Fuels 22 (2008) 1285-1296.

[764] T. Johnson, Overview of Diesel Emissions and Control for Heavy-Duty Diesel Engines, in: H. Zhao (Eds.), Advanced Direct Injection Combustion Engine Technologies and Development, Volume 2: Diesel Engines, Woodhead Publishing Limited, Cambridge, UK, 2010.

[765] M. Koebel, M. Elsener, M. Kleemann, Catalysis Today 59 (2000) 335-345.

[766] P. Eastwood, Exhaust Gas Aftertreatment for Light-Duty Diesel Engines, in: H. Zhao (Eds.), Advanced Direct Injection Combustion Engine Technologies and Development, Volume 2: Diesel Engines, Woodhead Publishing Limited, Cambridge, UK, 2010.

[767] H. Tschoeke, A. Graf, J. Stein, M. Krüger, J. Schaller, N. Breuer, K. Engeljehringer, W. Schindler, Diesel Engine Exhaust Emissions, in: K. Mollenhauer, H. Tschoeke (Eds.), Handbook of Diesel Engines, Springer-Verlag, Berlin, Germany, 2010.

[768] L.J. Gill, P.G. Blakeman, M.V. Twigg, A.P. Walker, Topics in Catalysis 28 (2004) 157-164.

[769] J.A. Rodriguez, J. Hrbek, Accounts of Chemical Research 32 (1999) 719-728.

[770] British Standards Institute, Specification for Automotive Diesel Fuel, BS EN 590:1993.

[771] British Standards Institute, British Standard Marine Series: Specification for Petroleum Fuels for Marine Oil Engines and Boilers, BS ISO 8217:1987.

[772] British Standards Institute, Petroleum Products – Fuels (Class F) – Specifications of Marine Fuels, BS ISO 8217:2012.

[773] Det Norsk Veritas, Marpol 73/78 Annex VI Regulations for the Prevention of Air Pollution from Ships: Technical and Operational Implications, Det Norsk Veritas, Høvik, Norway, 2009.

[774] MAN Diesel & Turbo, SCR: Selective Catalytic Reduction, MAN Diesel & Turbo, Augsburg, Germany, 2011.

[775] D. Neef, The Development of a Global Maritime Emissions Inventory Using Electronic Monitoring and Reporting Techniques, in: Proceedings of the Electrostatic Joint Conference, Cambridge, ON, Canada, 2013.

[776] T.G. Beuthe, J.S. Chang, Gas Discharge Phenomena, in: J.S. Chang, A.J. Kelly, J.M. Crowley (Eds.), Handbook of Electrostatic Processes, Marcel Dekker, New York, USA, 1995.

[777] R.J. Goldston, P.H. Rutherford, Introduction to Plasma Physics, Institute of Physics Publishing, Bristol, UK, 1995.

[778] H. Conrads, M. Schmidt, Plasma Sources Science and Technology 9 (2000) 441-454.

[779] M.B. Chang, H.M. Lee, F. Wu, C.R. Lai, Journal of the Air & Waste Management Association 54 (2004) 941-949.

[780] N. Manivannan, W. Balachandran, R. Beleca, M. Abbod, Journal of Clean Energy Technologies 2 (2014) 233-236.

[781] N.W. Frank, S. Hirano, The History of Electron Beam Processing for Environmental Pollution Control and Work Performed in the United States, in: B.M. Penetrante, S.E. Schultheis (Eds.), Non-Thermal Plasma Techniques for Pollution Control, Part B: Electron Beam and Electrical Discharge Processing, Springer-Verlag, Berlin, Germany, 1993.

[782] H. Namba, O. Tokunaga, T. Tanaka, Y. Ogura, S. Aoki, R. Suzuki, Radiation Physics and Chemistry 42 (1993) 669-672.

[783] A.G. Chmielewski, B. Tymiński, A. Dobrowolski, E. Iller, Z. Zimek, J. Licki, Radiation Physics and Chemistry 57 (2000) 527-530.

[784] K. Anand, A. Ranjan, P.S. Mehta, Energy & Fuels 24 (2010) 664-672.

[785] A. McIlroy, G. McRae, Basic Research Needs for Clean and Efficient Combustion of 21st Century Transportation Fuels, US Department of Energy, Office of Basic Energy Sciences, Washington, DC, USA, 2007.